

Markolf H. Niemz

BIOLOGICAL AND MEDICAL PHYSICS, BIOMEDICAL ENGINEERING

Laser-Tissue Interactions

Fundamentals and Applications

Third, Enlarged Edition

 Springer

**BIOLOGICAL AND MEDICAL PHYSICS,
BIOMEDICAL ENGINEERING**

BIOLOGICAL AND MEDICAL PHYSICS, BIOMEDICAL ENGINEERING

The fields of biological and medical physics and biomedical engineering are broad, multidisciplinary and dynamic. They lie at the crossroads of frontier research in physics, biology, chemistry, and medicine. The Biological and Medical Physics, Biomedical Engineering Series is intended to be comprehensive, covering a broad range of topics important to the study of the physical, chemical and biological sciences. Its goal is to provide scientists and engineers with textbooks, monographs, and reference works to address the growing need for information.

Books in the series emphasize established and emergent areas of science including molecular, membrane, and mathematical biophysics; photosynthetic energy harvesting and conversion; information processing; physical principles of genetics; sensory communications; automata networks, neural networks, and cellular automata. Equally important will be coverage of applied aspects of biological and medical physics and biomedical engineering such as molecular electronic components and devices, biosensors, medicine, imaging, physical principles of renewable energy production, advanced prostheses, and environmental control and engineering.

Editor-in-Chief:

Elias Greenbaum, Oak Ridge National Laboratory,
Oak Ridge, Tennessee, USA

Editorial Board:

Masuo Aizawa, Department of Bioengineering,
Tokyo Institute of Technology, Yokohama, Japan

Olaf S. Andersen, Department of Physiology,
Biophysics & Molecular Medicine,
Cornell University, New York, USA

Robert H. Austin, Department of Physics,
Princeton University, Princeton, New Jersey, USA

James Barber, Department of Biochemistry,
Imperial College of Science, Technology
and Medicine, London, England

Howard C. Berg, Department of Molecular
and Cellular Biology, Harvard University, Cambridge,
Massachusetts, USA

Victor Bloomfield, Department of Biochemistry,
University of Minnesota, St. Paul, Minnesota, USA

Robert Callender, Department of Biochemistry,
Albert Einstein College of Medicine,
Bronx, New York, USA

Britton Chance, Department of Biochemistry/
Biophysics, University of Pennsylvania,
Philadelphia, Pennsylvania, USA

Steven Chu, Department of Physics,
Stanford University, Stanford, California, USA

Louis J. DeFelicis, Department of Pharmacology,
Vanderbilt University, Nashville, Tennessee, USA

Johann Deisenhofer, Howard Hughes Medical Institute,
The University of Texas, Dallas, Texas, USA

George Feher, Department of Physics,
University of California, San Diego, La Jolla,
California, USA

Hans Frauenfelder, CNLS, MS B258,
Los Alamos National Laboratory, Los Alamos,
New Mexico, USA

Ivar Giaever, Rensselaer Polytechnic Institute,
Troy, New York, USA

Sol M. Gruner, Department of Physics,
Princeton University, Princeton, New Jersey, USA

Judith Herzfeld, Department of Chemistry,
Brandeis University, Waltham, Massachusetts, USA

Mark S. Humayun, Doheny Eye Institute,
Los Angeles, California, USA

Pierre Joliot, Institut de Biologie Physico-Chimique,
Fondation Edmond de Rothschild, Paris, France

Lajos Keszthelyi, Institute of Biophysics,
Hungarian Academy of Sciences, Szeged, Hungary

Robert S. Knox, Department of Physics and Astronomy,
University of Rochester, Rochester, New York, USA

Aaron Lewis, Department of Applied Physics,
Hebrew University, Jerusalem, Israel

Stuart M. Lindsay, Department of Physics
and Astronomy, Arizona State University, Tempe,
Arizona, USA

David Mauzerall, Rockefeller University,
New York, New York, USA

Eugenie V. Mielczarek, Department of Physics
and Astronomy, George Mason University, Fairfax,
Virginia, USA

Markolf Niemz, Medical Faculty Mannheim,
University of Heidelberg, Mannheim, Germany

V. Adrian Parsegian, Physical Science Laboratory,
National Institutes of Health, Bethesda, Maryland, USA

Linda S. Powers, NCDMF: Electrical Engineering,
Utah State University, Logan, Utah, USA

Earl W. Prohofsky, Department of Physics,
Purdue University, West Lafayette, Indiana, USA

Andrew Rubin, Department of Biophysics,
Moscow State University, Moscow, Russia

Michael Seibert, National Renewable Energy
Laboratory, Golden, Colorado, USA

David Thomas, Department of Biochemistry,
University of Minnesota Medical School, Minneapolis,
Minnesota, USA

Samuel J. Williamson, Department of Physics,
New York University, New York, New York, USA

Markolf H. Niemz

Laser-Tissue Interactions

Fundamentals and Applications

Third, Enlarged Edition

With 175 Figures, 33 Tables, 40 Problems and Solutions

 Springer

Professor Dr. Markolf H. Niemz
University of Heidelberg
MABEL – Mannheim Biomedical Engineering Laboratories
Germany
E-mail: Markolf.Niemz@urz.uni-heidelberg.de

Library of Congress Control Number: 2007930040

2nd Printing of the 3rd, enlarged edition (ISBN 3-540-40553-4)
ISSN 1618-7210
ISBN 978-3-540-72191-8 3rd Edition Springer Berlin Heidelberg New York
ISBN 3-540-42763-5 2nd Edition Springer Berlin Heidelberg New York

This work is subject to copyright. All rights are reserved, whether the whole or part of the material is concerned, specifically the rights of translation, reprinting, reuse of illustrations, recitation, broadcasting, reproduction on microfilm or in any other way, and storage in data banks. Duplication of this publication or parts thereof is permitted only under the provisions of the German Copyright Law of September 9, 1965, in its current version, and permission for use must always be obtained from Springer. Violations are liable for prosecution under the German Copyright Law.

Springer is a part of Springer Science+Business Media

springer.com

© Springer-Verlag Berlin Heidelberg 2004, 2007

The use of general descriptive names, registered names, trademarks, etc. in this publication does not imply, even in the absence of a specific statement, that such names are exempt from the relevant protective laws and regulations and therefore free for general use.

Typesetting by the authors
Production: LE-TeX Jelonek, Schmidt & Vöckler GbR, Leipzig, Germany
Cover: eStudio Calamar Steinen

Printed on acid-free paper SPIN 11878070 57/3180/YL - 5 4 3 2 1 0

Foreword to the First Edition

Dr. Markolf Niemz has undertaken the formidable task of writing a monograph on virtually all aspects of the current use of lasers in medicine, using laser-tissue interaction mechanisms as a guide throughout this book. The professional background of the author is in physics, in bioengineering, and in biomedical optics. In 1995, he was awarded the Karl-Freudenberg Prize by the Heidelberg Academy of Sciences, Germany, for his basic studies on laser-tissue interactions. Such a background is excellently suited to achieving the goals of this book, which are to offer an interdisciplinary approach to the basics of laser-tissue interactions and to use this knowledge for a review of clinical laser applications including laser safety.

His own research applying ultrashort laser pulses has enabled the author to provide profound discussions on photoablation, plasma-induced ablation, and photodisruption. Several aspects of related effects were first described by himself. Moreover, photodynamic therapy, photothermal applications, and laser-induced interstitial thermotherapy are extensively addressed in this book. The reader thus obtains a comprehensive survey of the present state of the art.

This book is intended mainly for scientists and engineers in this field, but medical staff will also find many important aspects of interest. There is no doubt that this book will fulfil a need for all of us working in the field of lasers in medicine, and I expect that it will be received very well.

Academic Medical Center
Amsterdam, 1996

MARTIN J. C. VAN GEMERT
Director of the Laser Center

Dedicated to my wife Alexandra

Preface to the Second Edition

Since the publication of the first edition of this book six years ago both research and applications in laser medicine have undergone substantial growth. The demand for novel techniques based on minimally invasive surgery has increased tremendously, and there is no end to it yet. Therefore, as the first edition ran out of stock, the publisher has asked me to prepare a second edition taking all these new developments into account.

Well, here it is. Although minor changes and corrections have been made throughout the book, major changes have been limited to Chap. 4. The reason is that the theory presented in Chaps. 2 and 3 is basically complete and does not need any further modifications, except that the discussion on *laser-induced interstitial thermotherapy (LITT)* in Sect. 3.2 has been extended by the technique of a multi-fiber treatment. On the other hand, the contents of Chap. 4 – the chapter on applications – strongly depend on the current state of the art. The second edition of this book covers all applications addressed in the first edition plus novel techniques for refractive corneal surgery and the treatment of caries.

The success in refractive corneal surgery has significantly increased since the introduction of *laser in situ keratomileusis (LASIK)* described in Sect. 4.1. The quality of caries removal can be improved with the application of ultra-short laser pulses with durations in the femtosecond range as discussed in Sect. 4.2. Furthermore, descriptive graphics have been added as in Sects. 3.2 and 4.10, and the reference section has been updated with the newest citations available on each topic.

Enjoy reading your second edition ...

Heidelberg,
January 2002

MARKOLF H. NIEMZ

Preface to the First Edition

This book has emerged from the need for a comprehensive presentation of the recently established field of laser–tissue interactions. So far, only publications dealing with specific issues and conference proceedings with contributions by several authors have been available for this subject. From these multi-author presentations, it is quite difficult for the reader to get to the bottom line of such a novel discipline. A textbook written by a single author is probably better suited for this purpose, although it might not provide the reader with all the details of a specific application.

The basic scope of the book was outlined during several lectures on biomedical optics which I held at the University of Heidelberg in the years 1992–1995. I have tried to include the most significant studies which are related to the field of laser–tissue interactions and which have been published during the past three decades. This comprises the description of experiments and techniques as well as their results and the theoretical background. Some parts of this book, especially the detailed discussion of ultrashort laser pulses, are naturally influenced by my own interests.

Due to the rapidly increasing number of medical laser applications, it is almost impossible to present a complete survey of all publications. Thus, this book will mainly serve as a starting guide for the newcomer and as a quick reference guide for the insider. For discussion of the newest techniques and results, the reader should consult the latest issues of scientific journals rather than a textbook. Regular coverage is provided by the journals *Lasers in Surgery and Medicine*, *Lasers in Medical Science*, *Biomedical Optics*, and the *SPIE Proceedings on Biomedical Optics*. Apart from these, related articles frequently appear in special issues of other journals, e.g. *Applied Physics B* and the *IEEE Journal of Quantum Electronics*, as well.

I wish to thank all authors and publishers who permitted me to reproduce their figures in this book. Some of the figures needed to be redrawn to improve readability and to obtain a uniform presentation. My special thanks are addressed to the participants of the seminar on Biomedical Optics of the *Studienstiftung des Deutschen Volkes* (German National Fellowship Foundation) which was held in Kranjska Gora, Slovenia, in September 1995. Furthermore, I acknowledge Prof. Dr. J. Bille and his students for their valuable advice concerning the manuscript, Dr. T. Pioch for providing several of the

pictures taken with scanning electron microscopy, the editorial and production staff of Springer-Verlag for their care and cooperation in producing this book, and last but definitely not least all friends who spent some of their precious time in reading the manuscript.

In spite of great care and effort on my part, I am fairly sure that some errors still remain in the book. I hope you will bring these to my attention for further improvements.

Heidelberg,
February 1996

MARKOLF H. NIEMZ

Table of Contents

1. Introduction	1
1.1 Historic Review	1
1.2 Goal of the Book	6
1.3 Outlook	7
2. Light and Matter	9
2.1 Reflection and Refraction	10
2.2 Absorption	15
2.3 Scattering	19
2.4 Turbid Media	25
2.5 Photon Transport Theory	27
2.6 Measurement of Optical Tissue Properties	37
2.7 Questions to Chapter 2	43
3. Interaction Mechanisms	45
3.1 Photochemical Interaction	47
3.1.1 Photodynamic Therapy (PDT)	49
3.1.2 Biostimulation	57
3.1.3 Summary of Photochemical Interaction	58
3.2 Thermal Interaction	58
3.2.1 Heat Generation	68
3.2.2 Heat Transport	68
3.2.3 Heat Effects	77
3.2.4 Laser-Induced Interstitial Thermotherapy (LITT)	81
3.2.5 Summary of Thermal Interaction	87
3.3 Photoablation	88
3.3.1 Model of Photoablation	96
3.3.2 Cytotoxicity of UV Radiation	100
3.3.3 Summary of Photoablation	102
3.4 Plasma-Induced Ablation	103
3.4.1 Model of Plasma-Induced Ablation	108
3.4.2 Analysis of Plasma Parameters	121
3.4.3 Summary of Plasma-Induced Ablation	125
3.5 Photodisruption	126
3.5.1 Plasma Formation	131

3.5.2	Shock Wave Generation	135
3.5.3	Cavitation	143
3.5.4	Jet Formation	147
3.5.5	Summary of Photodisruption	149
3.6	Questions to Chapter 3	149
4.	Medical Applications of Lasers	151
4.1	Lasers in Ophthalmology	152
4.2	Lasers in Dentistry	181
4.3	Lasers in Gynecology	201
4.4	Lasers in Urology	207
4.5	Lasers in Neurosurgery	213
4.6	Lasers in Angioplasty and Cardiology	221
4.7	Lasers in Dermatology	227
4.8	Lasers in Orthopedics	232
4.9	Lasers in Gastroenterology	237
4.10	Lasers in Otorhinolaryngology and Pulmology	241
4.11	Questions to Chapter 4	247
5.	Laser Safety	249
5.1	Introduction	249
5.2	Laser Hazards	249
5.3	Eye Hazards	250
5.4	Skin Hazards	251
5.5	Associated Hazards from High Power Lasers	253
5.6	Laser Safety Standards and Hazard Classification	253
5.7	Viewing Laser Radiation	258
5.8	Eye Protection	260
5.9	Laser Beam Calculations	262
5.10	Questions to Chapter 5	263
A.	Appendix	265
A.1	Medical Neodymium Laser System	265
A.2	Physical Constants and Parameters	269
B.	Solutions	273
	References	275
	Index	299
	About the Author	307

1. Introduction

1.1 Historic Review

Since the first report on laser radiation by Maiman (1960), many potential fields for its application have been investigated. Among these, medical laser surgery certainly belongs to the most significant advances of our present century. Actually, various kinds of lasers have already become irreplaceable tools of modern medicine. Although clinical applications were first limited to ophthalmology – the most spectacular and today well-established laser surgery being argon ion laser coagulations in the case of retinal detachment – the fields of medical laser treatment have meanwhile considerably widened. Due to the variety of existing laser systems, the diversity of their physical parameters, and last but not least the enthusiasm of several research groups almost every branch of surgical medicine has been involved. This should not be interpreted as criticism, although much damage has been done in some cases – especially in the field of biostimulation – when researchers have lost orientation due to striving for new publications and success, and industries have praised laser systems that later turned out to be completely useless. In general, though, many really useful laser techniques have been developed and clinically established with the help of all kinds of scientists. These methods of treatment have been reconfirmed by other researchers and properly documented in a variety of well-accepted scientific journals. And, even with early laser applications primarily aimed at therapeutic results, several interesting diagnostic techniques have recently been added. Only some of them will be addressed in this book wherever appropriate, for instance diagnosis of tumors by fluorescence dyes and diagnosis of caries by spectroscopical analysis of laser-induced plasma sparks. However, the discussion of these diagnostic applications is not the main goal of the author, and the interested reader is referred to detailed descriptions found elsewhere.

From the historic point of view, lasers were first applied in ophthalmology. This was obvious, since the eye and its interior belong to the easiest accessible organs because of their high transparency. And it was only a few years earlier that Meyer-Schwickerath (1956) had successfully investigated the coagulative effects of xenon flash lamps on retinal tissue. In 1961, just one year after the invention of the laser, first experimental studies were published by Zaret et al. (1961). Shortly afterwards, patients with retinal de-

tachment were already being treated as reported by Campbell et al. (1963) and Zweng et al. (1964). At the same time, investigations were first carried out in dentistry by Goldman et al. (1964) and Stern and Sognaes (1964). In the beginning, laser treatment was limited to the application of ruby lasers. Later on, other types of lasers followed. And, accordingly, clinical research extended within the disciplines of ophthalmology and dentistry.

Starting in the late 1960s, lasers were introduced to other medical disciplines, as well. And today, a large variety of laser procedures is performed all over the world. Most of them belong to the family of *minimally invasive surgery (MIS)*, a novel term of our decade describing non-contact and bloodless surgical procedures. These two characteristics have mainly promoted the laser to being a universal scalpel and treatment aid. Many patients, and also surgeons as sketched in Fig. 1.1, believed in lasers as if they were some kind of wonder instruments. This attitude evoked misleading statements and unjustified hopes. Careful judgment of new developments is always appropriate, and not every reported laser-induced cure can be taken for granted until it is reconfirmed by independent studies. Laser-induced effects are manifold as will be shown in this book. Most of them can be scientifically explained. However, the same effect which might be good for a certain treatment can be disastrous for another. For instance, heating of cancerous tissue by means of laser radiation might lead to desired tumor necrosis. On the other hand, using the same laser parameters for retinal coagulation can burn the retina, resulting in irreversible blindness. Thermal effects, in particular, tend to be irreversible if temperatures $> 60^{\circ}\text{C}$ are achieved as will be shown in Sect. 3.2.



“Wow, that new wonder laser burns it all away...”

Fig. 1.1. Cartoon

Laser systems can be classified as *continuous wave (CW) lasers* and *pulsed lasers*. Whereas most gas lasers and to some extent also solid-state lasers belong to the first group, the family of pulsed lasers mainly includes solid-state lasers, excimer lasers, and certain dye lasers. In Table 1.1, a list of medical laser types and two of their characteristic parameters are given: *wavelength* and *pulse duration*. The list is arranged with respect to the latter, since the duration of exposure primarily characterizes the type of interaction with biological tissue, as we will evaluate in Chap. 3. The wavelength is a second important laser parameter. It determines how deep laser radiation penetrates into tissue, i.e. how effectively it is absorbed and scattered. Frequently, a third parameter – the applied *energy density* – is also considered as being significant. However, its value only serves as a necessary condition for the occurrence of a certain effect and then determines its extent. Actually, it will be shown in Chap. 3 that all medically relevant effects are achieved at energy densities between 1 J/cm^2 and 1000 J/cm^2 . This is a rather narrow range compared to the 15 orders of magnitude of potential pulse durations. A fourth parameter – the applied *intensity* – is given as the ratio of energy density and pulse duration. For a detailed discussion of all these dependences, the reader is referred to Chap. 3. Each laser type listed in Table 1.1 is used for particular clinical applications as described in Chap. 4.

Table 1.1. List of some medical laser systems

Laser type	Wavelength	Typical pulse duration
Argon ion	488/514 nm	CW
Krypton ion	531/568/647 nm	CW
He-Ne	633 nm	CW
CO ₂	10.6 μm	CW or pulsed
Dye laser	450–900 nm	CW or pulsed
Diode laser	670–900 nm	CW or pulsed
Ruby	694 nm	1–250 μs
Nd:YLF	1053 nm	100 ns – 250 μs
Nd:YAG	1064 nm	100 ns – 250 μs
Ho:YAG	2120 nm	100 ns – 250 μs
Er:YSGG	2780 nm	100 ns – 250 μs
Er:YAG	2940 nm	100 ns – 250 μs
Alexandrite	720–800 nm	50 ns – 100 μs
XeCl	308 nm	20–300 ns
XeF	351 nm	10–20 ns
KrF	248 nm	10–20 ns
ArF	193 nm	10–20 ns
Nd:YLF	1053 nm	30–100 ps
Nd:YAG	1064 nm	30–100 ps
Free electron laser	800–6000 nm	2–10 ps
Ti:Sapphire	700–1000 nm	10 fs – 100 ps

Two recent laser developments have become more and more important for medical research: diode lasers and free electron lasers. Diode lasers can emit either CW or pulsed radiation and are extremely compact. Free electron lasers provide very short laser pulses but are huge machines which are driven by powerful electron accelerators and are available at a few selected locations only.

The progress in laser surgery can be primarily attributed to the rapid development of pulsed laser systems. As already mentioned above, it is the pulse duration which finally determines the effect on biological tissue. In particular, *thermal* and *nonthermal effects* may be distinguished. A rough approximation is the “1 μ s rule” stating that pulse durations $> 1 \mu$ s are often associated with measurable thermal effects. At pulse durations $< 1 \mu$ s, on the other hand, thermal effects usually become negligible if a moderate repetition rate is chosen (see Sect. 3.2 for further details). Without implementation of additional features, many lasers will either emit CW radiation or pulses with durations $> 1 \mu$ s. Investigations are thus limited to the study of potential thermal effects. Only when generating shorter laser pulses do other types of interactions become accessible. Among these are very efficient ablation mechanisms such as photoablation, plasma-induced ablation, and photodisruption which take place on the nanosecond or picosecond scale. Today, even shorter pulses in the femtosecond range can be realized. But their clinical advantage is being disputed as will be explained when comparing the related mechanisms of plasma-induced ablation and photodisruption. Both of them originate from a physical phenomenon called optical breakdown. And, as will be shown in a theoretical analysis in Sect. 3.4, the threshold parameters of optical breakdown do not decrease any further when proceeding from picosecond to femtosecond pulses. In general, though, it can be summarized that the development of laser systems capable of providing shorter pulses has always evoked new and interesting applications, as well.

In Fig. 1.2, the progress in the development of pulsed laser systems is illustrated. In the case of *solid-state lasers*, two milestones were reached when discovering the technique of mode locking and when developing novel laser media with extremely large bandwidths as will be discussed below. These two events are characterized by two steps of the corresponding curve in Fig. 1.2. The other important group of lasers capable of providing ultrashort pulses consists of *dye lasers*. They were invented after the first solid-state lasers. Their progress was not so stepwise but proceeded smoothly. Several new techniques such as colliding pulse mode locking were developed which also lead to very short pulse durations comparable to those of solid-state lasers. However, medical applications of dye lasers will be rather limited because of their inconvenience and complicated maintenance. In contrast to long-living solid-state crystals, dyes need to be recirculated and exchanged on a regular basis which often disables a push-button operation.

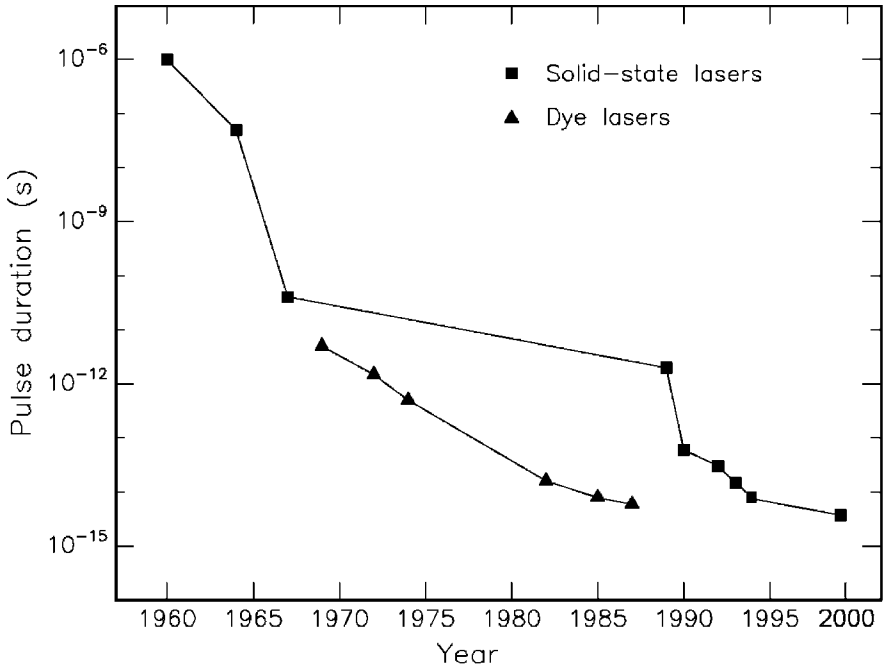


Fig. 1.2. Shortest achieved pulse durations with solid-state lasers and dye lasers

The very first laser was a ruby laser pumped with a xenon flash lamp. The output of such a laser is characterized by several spikes. Their overall duration is determined by the flash itself which is matched to the lifetime of the upper state of the laser transition, in ruby approximately 1 ms. With the invention of *Q-switching*, pulses as short as 50 ns could be obtained. Either mechanical devices (rotating apertures or laser mirrors) or optical devices (electrooptic or acoustooptic Pockels crystals) may serve as a Q-switch. In both cases, losses inside the resonator are kept artificially high until an extremely large inversion of the energy levels is achieved. Then, when removing the artificial losses, all energy stored in the laser medium is suddenly converted by means of stimulated emission. Even shorter pulses were obtained when initiating *mode locking* inside the laser cavity. During mode locking, a modulation of the electromagnetic field is induced by using either fast modulating crystals (active mode locking) or saturable absorbers (passive mode locking). By this means, the phases of all oscillating axial laser modes are forced to coincide, resulting in picosecond pulses. A typical representative is the Nd:YAG laser with an optical bandwidth of the order of 1 nm. This bandwidth limits the shortest achievable pulse duration to a few picoseconds. Thus, the realization of femtosecond lasers mainly depended on the discovery of novel laser media with larger optical bandwidths. These were found in crystals such as Ti:Sapphire or Cr:LiSAF which currently led to the

generation of laser pulses as short as 8.5 fs according to Zhou et al. (1994). This duration is equivalent to a spatial pulse extent of a few wavelengths only. The most significant techniques of pulse generation are described in detail in the excellent book written by Siegman (1986).

1.2 Goal of the Book

The main goal of this book is to offer an interdisciplinary approach to the basics of laser–tissue interactions. It thus addresses all kinds of scientists, engineers, medical doctors, and graduate students involved in this field. Special emphasis is put on

- giving a detailed description of the physical background of potential interaction mechanisms between laser light and biological tissue,
- providing an updated review of clinical laser applications,
- including a chapter on laser safety.

In Chap. 2, mandatory prerequisites are given which are essential for understanding all the interaction mechanisms discussed in Chap. 3. Basic phenomena dealing with light and matter such as *reflection*, *absorption*, and *scattering* are explained by their physical roots. In each case, special attention is paid to their indispensable mathematical handling. The informed reader may well skip these sections and directly proceed with Sect. 2.5. In that section, when discussing *photon transport theory*, important tools will be derived which are of considerable importance in modern theoretical research. In order to solve the governing equation of energy transfer, either the Kubelka–Munk theory, the method of diffusion approximation, or Monte Carlo simulations are most frequently used. All of them will be comprehensively reviewed in Sect. 2.5 and compared to each other along with their advantages and disadvantages. The interested reader, of course, should also consult the original works by Kubelka (1948), Metropolis and Ulam (1949), and the profound theory developed by Ishimaru (1978).

The main chapter of the book is Chap. 3. Whereas Chap. 2 focuses on how matter acts on light, here we will consider the opposite effect, i.e. how light acts on matter. Starting with some general remarks and definitions, a general classification scheme is developed with the exposure duration being the main physical parameter. Five different types of interaction mechanisms are presented: *photochemical interaction*, *thermal interaction*, *photoablation*, *plasma-induced ablation*, and *photodisruption*. Each of them is thoroughly discussed including selected photographs and manifold illustrations. At the end of each section, a comprehensive statement is given summarizing in brief significant features of each interaction mechanism. Special recently developed techniques such as photodynamic therapy (PDT) or laser-induced interstitial thermotherapy (LITT) are explained according to the latest references.

Both of these techniques are concerned with the laser treatment of cancer, either photochemically or thermally, as an alternative to conventional methods which still remain unsatisfactory for a large group of patients. When discussing photoablation, potential risks originating from UV radiation will be surveyed. The differentiation between plasma-induced ablation and photodisruption is emphasized and properly substantiated. Novel theoretical models are introduced describing the basic mechanism of plasma-induced ablation. They help to better understand the physical phenomena associated with optical breakdown and its threshold parameters.

In Chap. 4, the most important clinical applications are reviewed based on the latest results and references. Due to the historic sequence and their present significance, applications in ophthalmology, dentistry, and gynecology are considered first. In ophthalmology, various standard techniques are discussed such as coagulation of the retina, laser treatments of glaucoma, and fragmentation of the lens. The newest methods and results concerning refractive corneal surgery are presented, as well. In dentistry, special emphasis is put on different laser treatments of caries in comparison to conventional drills. In gynecology, various thermal effects of laser radiation have recently been investigated. Major tasks and first clinical results are surveyed. Other disciplines of clinical importance follow as mentioned in the table of contents. In each case, experimental procedures and clinical results are discussed along with any complications arising or technical difficulties. By means of specially selected photographs and artwork, it is intended to pass on clinical relevance and professional insight to the interested reader.

Finally, Chap. 5 comprises the latest standard of laser safety. It outlines a careful selection of essential guidelines published by the Laser Institute of America, Orlando, Florida. Meanwhile, most of them have been adapted by other governments, as well. A laser classification scheme is included which is commonly used all over the world. Moreover, important exposure limits are given to be taken into account when treating patients. In general, this chapter is meant to serve as a quick reference when operating lasers, but it might also be a useful guide for the inexperienced reader.

1.3 Outlook

It is interesting to observe that almost every new technique initially evokes a euphoric reaction among surgeons and patients. This period is often followed by indifference and rejection when long-term effects and limitations become obvious. Eventually, researchers agree on certain indications for applying the new technique which then leads to the final approval. One typical example for the occurrence of this sequence was the introduction of photodisruptive lasers to ophthalmology by Aron-Rosa et al. (1980).

At present, lasers have already contributed to the treatment of a wide variety of maladies. However, today's clinical lasers and their applications

most probably represent only the infancy of laser medicine. In the near future, other lasers will evolve and take their places in hospitals and medical centers. Miniaturization will enhance their usefulness and applicability, and highly specialized delivery optics will expand the surgeon's ability to achieve very precise therapies. Moreover, combinations of different wavelengths – distributed both spatially and temporally – may provide tissue effects superior to those of single wavelengths. Other successful techniques and interesting alternatives will certainly be developed, as well. Even the list of interaction mechanisms known today may not yet be complete.

Ultimately, all these endeavors will advance minimally invasive surgery beyond our present horizon. This progress, however, will rely on our creativity and cooperation. Further scientific research is as essential as the promotion of its results to clinical applications. The future of medical lasers cannot be created by physicists, engineers, or surgeons alone, but must be realized through collective human sources of science, medicine, industry, and government.

2. Light and Matter

In this and the following chapter, we will discuss basic phenomena occurring when matter is exposed to light. While here we will be concerned with various actions of matter on light, the opposite effect will be discussed in Chap. 3. Matter can act on electromagnetic radiation in manifold ways. In Fig. 2.1, a typical situation is shown, where a light beam is incident on a slice of matter. In principle, three effects exist which may interfere with its undisturbed propagation:

- reflection and refraction,
- absorption,
- scattering.

Reflection and refraction are strongly related to each other by *Fresnel's laws*. Therefore, these two effects will be addressed in the same section. In Fig. 2.1, refraction is accounted for by a displacement of the transmitted beam. In medical laser applications, however, refraction plays a significant role only when irradiating transparent media like corneal tissue. In opaque media, usually, the effect of refraction is difficult to measure due to absorption and scattering.

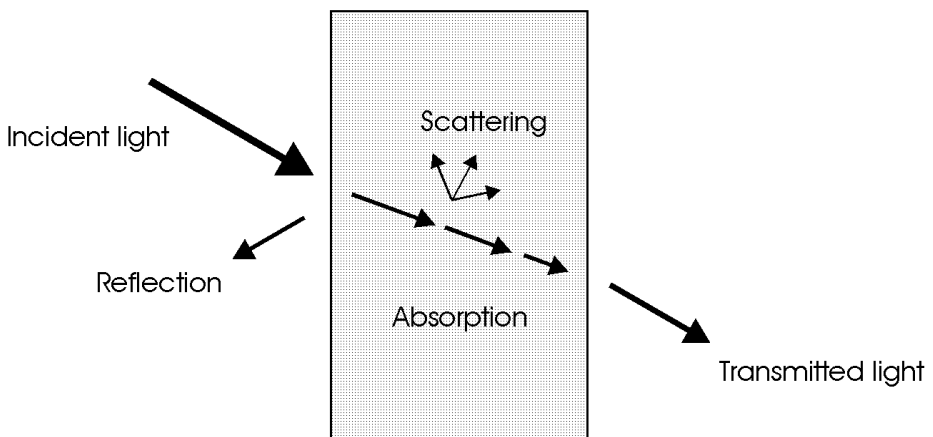


Fig. 2.1. Geometry of reflection, refraction, absorption, and scattering

Only nonreflected and nonabsorbed or forward scattered photons are transmitted by the slice and contribute to the intensity detected behind the slice. The ratio of transmitted and incident intensities is called *transmittance*. Which of the losses – reflection, absorption, or scattering – is dominant primarily depends on the type of material and the incident wavelength. As we will encounter in the following sections, the wavelength is a very important parameter indeed. It determines the index of refraction as well as the absorption and scattering coefficients. The index of refraction governs the overall reflectivity of the target. This index strongly depends on wavelength in regions of high absorption only. The scattering coefficient, on the other hand, can scale inversely with the fourth power of wavelength as will be evaluated in Sect. 2.3 when discussing Rayleigh scattering.

In laser surgery, knowledge of absorbing and scattering properties of a selected tissue is essential for the purpose of predicting successful treatment. The index of refraction might be of considerable interest when applying laser radiation to highly reflecting surfaces such as metallic implants in dentistry or orthopedics. In general, however, no specific kind of target or biological tissue will be assumed unless otherwise stated in certain figures or tables. Instead, emphasis is put on general physical relations which apply for most solids and liquids. In reality, of course, limitations are given by the inhomogeneity of biological tissue which are also responsible for our inability to provide other than mean tissue parameters.

2.1 Reflection and Refraction

Reflection is defined as the returning of electromagnetic radiation by surfaces upon which it is incident. In general, a reflecting surface is the physical boundary between two materials of different indices of refraction such as air and tissue. The simple law of reflection requires the wave normals of the incident and reflected beams and the normal of the reflecting surface to lie within one plane, called the *plane of incidence*. It also states that the reflection angle θ' equals the angle of incidence θ as shown in Fig. 2.2 and expressed by

$$\theta = \theta' . \tag{2.1}$$

The angles θ and θ' are measured between the surface normal and the incident and reflected beams, respectively. The surface itself is assumed to be smooth, with surface irregularities being small compared to the wavelength of radiation. This results in so-called *specular reflection*.

In contrast, i.e. when the roughness of the reflecting surface is comparable or even larger than the wavelength of radiation, *diffuse reflection* occurs. Then, several beams are reflected which do not necessarily lie within the plane of incidence, and (2.1) no longer applies. Diffuse reflection is a common phenomenon of all tissues, since none of them is provided with highly polished

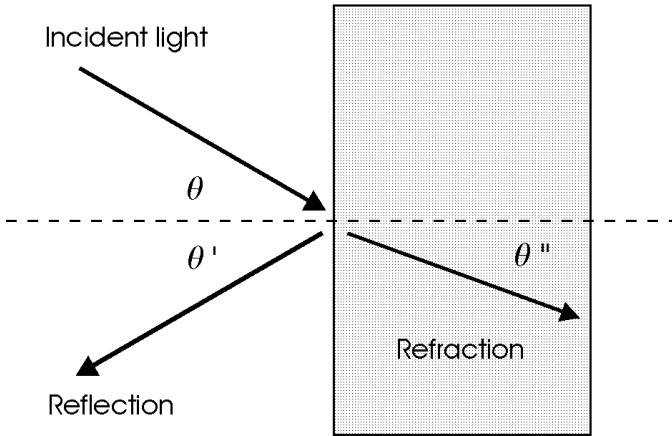


Fig. 2.2. Geometry of specular reflection and refraction

surfaces such as optical mirrors. Only in special cases such as wet tissue surfaces might specular reflection surpass diffuse reflection.

Refraction usually occurs when the reflecting surface separates two media of different indices of refraction. It originates from a change in speed of the light wave. The simple mathematical relation governing refraction is known as *Snell's law*. It is given by

$$\frac{\sin \theta}{\sin \theta''} = \frac{v}{v'} , \quad (2.2)$$

where θ'' is the angle of refraction, and v and v' are the speeds of light in the media before and after the reflecting surface, respectively. Since the corresponding indices of refraction are defined by

$$n = \frac{c}{v} , \quad (2.3)$$

$$n' = \frac{c}{v'} ,$$

where c denotes the speed of light in vacuum, (2.2) turns into

$$n \sin \theta = n' \sin \theta'' . \quad (2.4)$$

Only for $\sin \theta > n'/n$ can (2.4) not be fulfilled, meaning that refraction will not occur. This event is also referred to as *total reflection*.

The *reflectivity* of a surface is a measure of the amount of reflected radiation. It is defined as the ratio of reflected and incident electric field amplitudes. The *reflectance* is the ratio of the corresponding intensities and is thus equal to the square of the reflectivity. Reflectivity and reflectance depend on the angle of incidence, the polarization of radiation, and the indices of

refraction of the materials forming the boundary surface. Relations for reflectivity and refraction are commonly known as *Fresnel's laws*. In this book, we will merely state them and consider their principal physical impact. Exact derivations are found elsewhere, e.g. in books dealing with electrodynamics. Fresnel's laws are given by

$$\frac{E_s'}{E_s} = -\frac{\sin(\theta - \theta'')}{\sin(\theta + \theta'')} , \quad (2.5)$$

$$\frac{E_p'}{E_p} = \frac{\tan(\theta - \theta'')}{\tan(\theta + \theta'')} , \quad (2.6)$$

$$\frac{E_s''}{E_s} = \frac{2 \sin \theta'' \cos \theta}{\sin(\theta + \theta'')} , \quad (2.7)$$

$$\frac{E_p''}{E_p} = \frac{2 \sin \theta'' \cos \theta}{\sin(\theta + \theta'') \cos(\theta - \theta'')} , \quad (2.8)$$

where E , E' , and E'' are amplitudes of the electric field vectors of the incident, reflected, and refracted light, respectively. The subscripts “s” and “p” denote the two planes of oscillation with “s” being perpendicular to the plane of incidence – from the German *senkrecht* – and “p” being parallel to the plane of incidence.

Further interaction of incident light with the slice of matter is limited to the refracted beam. One might expect that the intensity of the refracted beam would be complementary to the reflected one so that the addition of both would give the incident intensity. However, this is not correct, because intensity is defined as the power per unit area, and the cross-section of the refracted beam is different from that of the incident and reflected beams except at normal incidence. It is only the total energy in these beams that is conserved. The reflectances in either plane are given by

$$R_s = \left(\frac{E_s'}{E_s} \right)^2 , \quad (2.9)$$

$$R_p = \left(\frac{E_p'}{E_p} \right)^2 . \quad (2.10)$$

In Fig. 2.3, the reflectances R_s and R_p are plotted as a function of the angle of incidence. It is assumed that $n = 1$ and $n' = 1.33$ which are the indices of refraction of air and water, respectively. Thus, Fig. 2.3 especially describes the specular reflectance on wet surfaces.

The angle at which $R_p = 0$ is called the *Brewster angle*. In the case of water, it is equal to 53° . At normal incidence, i.e. $\theta = 0$, the reflectances in either plane are approximately 2%. This value is not directly evident from (2.5) and (2.6), since insertion of $\theta = \theta'' = 0$ gives an indeterminate result. It can be evaluated, however, as follows. Since both θ and θ'' become

very small when approaching normal incidence, we may set the tangents in (2.6) equal to the sines and obtain

$$R_p \simeq R_s = \frac{\sin^2(\theta - \theta'')}{\sin^2(\theta + \theta'')} = \left(\frac{\sin \theta \cos \theta'' - \cos \theta \sin \theta''}{\sin \theta \cos \theta'' + \cos \theta \sin \theta''} \right)^2. \quad (2.11)$$

When dividing numerator and denominator of (2.11) by $\sin \theta''$ and replacing $\sin \theta / \sin \theta''$ by n' , i.e. assuming $n = 1$, it reduces to

$$R_p \simeq R_s = \left(\frac{n' \cos \theta'' - \cos \theta}{n' \cos \theta'' + \cos \theta} \right)^2 \simeq \left(\frac{n' - 1}{n' + 1} \right)^2. \quad (2.12)$$

The approximate equality becomes exact within the limit of normal incidence. Thus, inserting $n' = 1.33$ yields

$$R_p \simeq R_s \simeq 2\%.$$

In several cases, this fraction of incident radiation is not negligible. Thus, regarding laser safety, it is one of the main reasons why proper eye protection is always required (see Chap. 5).

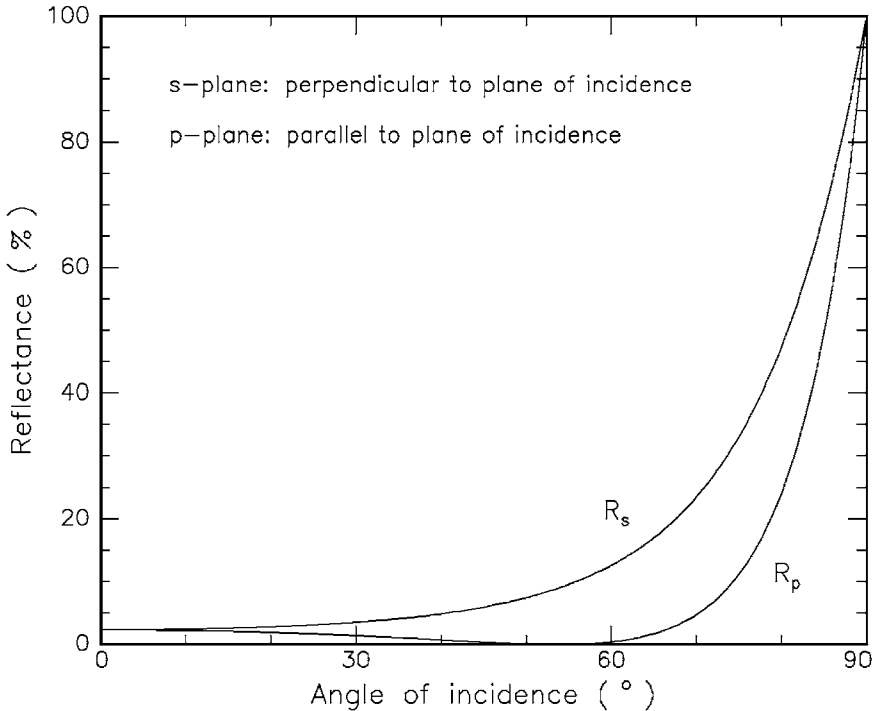


Fig. 2.3. Reflectances in s- and p-plane for water ($n = 1.33$)

For water, the indices of refraction and the corresponding reflectances at different wavelengths are listed in Table 2.1. Two strong absorption bands occur at about 2.9 μm and 6.0 μm . They result from vibrational and rotational oscillations of the water molecule. The major aspects of absorption will be addressed in the next section.

Table 2.1. Indices of refraction and reflectances of water. Data according to Hale and Querry (1973)

Wavelength λ (μm)	Index of refraction n	Reflectance R
0.2	1.396	0.027
0.3	1.349	0.022
0.4	1.339	0.021
0.5	1.335	0.021
0.6	1.332	0.020
0.7	1.331	0.020
0.8	1.329	0.020
0.9	1.328	0.020
1.0	1.327	0.020
1.6	1.317	0.019
2.0	1.306	0.018
2.6	1.242	0.012
2.7	1.188	0.007
2.8	1.142	0.004
2.9	1.201	0.008
3.0	1.371	0.024
3.1	1.467	0.036
3.2	1.478	0.037
3.3	1.450	0.034
3.4	1.420	0.030
3.5	1.400	0.028
4.0	1.351	0.022
5.0	1.325	0.020
6.0	1.265	0.014
7.0	1.317	0.019
8.0	1.291	0.016
9.0	1.262	0.013
10.0	1.218	0.010

Even if the dependence of the index of refraction on wavelength is rather weak in the visible spectrum, it should be taken into account when striving for predictable results. In general, indices of refraction for various kinds of tissue are difficult to measure due to absorption and scattering. Reflection from these tissues must be obtained empirically. In most cases, the corresponding indices of the refraction of water are rough estimates only.

2.2 Absorption

During *absorption*, the intensity of an incident electromagnetic wave is attenuated in passing through a medium. The *absorbance* of a medium is defined as the ratio of absorbed and incident intensities. Absorption is due to a partial conversion of light energy into heat motion or certain vibrations of molecules of the absorbing material. A perfectly *transparent* medium permits the passage of light without any absorption, i.e. the total radiant energy entering into and emerging from such a medium is the same. Among biological tissues, cornea and lens can be considered as being highly transparent for visible light. In contrast, media in which incident radiation is reduced practically to zero are called *opaque*.

The terms “transparent” and “opaque” are relative, since they certainly are wavelength-dependent. Cornea and lens, for instance, mainly consist of water which shows a strong absorption at wavelengths in the infrared spectrum. Hence, these tissues appear opaque in this spectral region. Actually, no medium is known to be either transparent or opaque to all wavelengths of the electromagnetic spectrum.

A substance is said to show *general absorption* if it reduces the intensity of all wavelengths in the considered spectrum by a similar fraction. In the case of visible light, such substances will thus appear grey to our eye. *Selective absorption*, on the other hand, is the absorption of certain wavelengths in preference to others. The existence of colors actually originates from selective absorption. Usually, *body colors* and *surface colors* are distinguished. Body color is generated by light which penetrates a certain distance into the substance. By backscattering, it is then deviated and escapes backwards from the surface but only after being partially absorbed at selected wavelengths. In contrast, surface color originates from reflection at the surface itself. It mainly depends on the reflectances which are related to the wavelength of incident radiation by (2.12).

The ability of a medium to absorb electromagnetic radiation depends on a number of factors, mainly the electronic constitution of its atoms and molecules, the wavelength of radiation, the thickness of the absorbing layer, and internal parameters such as the temperature or concentration of absorbing agents. Two laws are frequently applied which describe the effect of either thickness or concentration on absorption, respectively. They are commonly called *Lambert’s law* and *Beer’s law*, and are expressed by

$$I(z) = I_0 \exp(-\alpha z) , \quad (2.13)$$

and

$$I(z) = I_0 \exp(-k'cz) , \quad (2.14)$$

where z denotes the optical axis, $I(z)$ is the intensity at a distance z , I_0 is the incident intensity, α is the absorption coefficient of the medium, c is the

concentration of absorbing agents, and k' depends on internal parameters other than concentration. Since both laws describe the same behavior of absorption, they are also known as the *Lambert–Beer law*. From (2.13), we obtain

$$z = \frac{1}{\alpha} \ln \frac{I_0}{I(z)} . \quad (2.15)$$

The inverse of the absorption coefficient α is also referred to as the absorption length L , i.e.

$$L = \frac{1}{\alpha} . \quad (2.16)$$

The absorption length measures the distance z in which the intensity $I(z)$ has dropped to $1/e$ of its incident value I_0 .

In biological tissues, absorption is mainly caused by either water molecules or macromolecules such as proteins and pigments. Whereas absorption in the IR region of the spectrum can be primarily attributed to water molecules, proteins as well as pigments mainly absorb in the UV and visible range of the spectrum. Proteins, in particular, have an absorption peak at approximately 280 nm according to Boulnois (1986). The discussion of the absorption spectrum of water – the main constituent of most tissues – will be deferred to Sect. 3.2 when addressing thermal interactions.

In Fig. 2.4, absorption spectra of two elementary biological absorbers are shown. They belong to melanin and hemoglobin (HbO_2), respectively. Melanin is the basic pigment of skin and is by far the most important epidermal chromophore. Its absorption coefficient monotonically increases across the visible spectrum toward the UV. Hemoglobin is predominant in vascularized tissue. It has relative absorption peaks around 280 nm, 420 nm, 540 nm, and 580 nm, and then exhibits a cut-off at approximately 600 nm. A general feature of most biomolecules is their complex band structure between 400 nm and 600 nm. Since neither macromolecules nor water strongly absorb in the near IR, a “therapeutic window” is delineated between roughly 600 nm and 1200 nm. In this spectral range, radiation penetrates biological tissues at a lower loss, thus enabling treatment of deeper tissue structures.

The absorption spectra of three typical tissues are presented in Fig. 2.5. They are obtained from the skin, aortic wall, and cornea, respectively. Among these, skin is the highest absorber, whereas the cornea is almost perfectly transparent¹ in the visible region of the spectrum. Because of the uniqueness of the absorption spectra, each of them can be regarded as a fingerprint of the corresponding tissue. Of course, slight deviations from these spectra can occur due to the inhomogeneity of most tissues.

¹ Actually, it is amazing how nature was able to create tissue with such transparency. The latter is due to the extremely regular structure of collagen fibrils inside the cornea and its high water content.

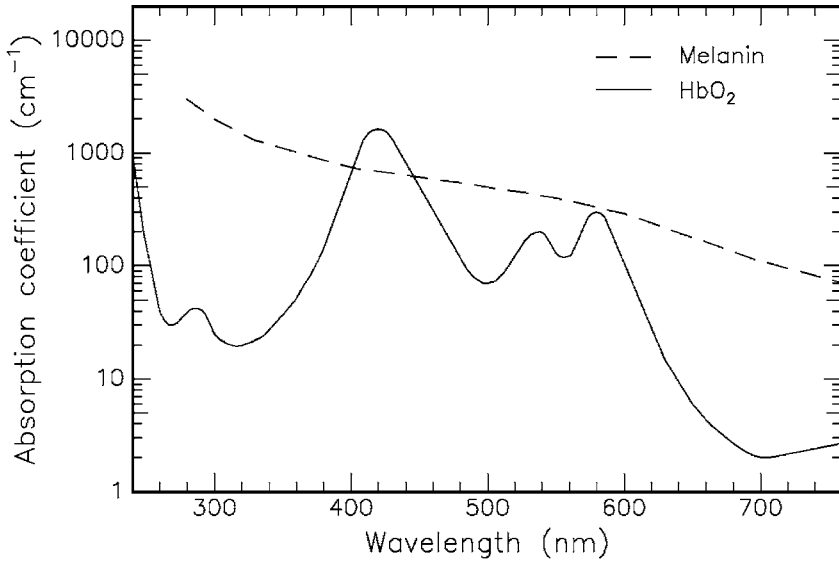


Fig. 2.4. Absorption spectra of melanin in skin and hemoglobin (HbO_2) in blood. Relative absorption peaks of hemoglobin are at 280 nm, 420 nm, 540 nm, and 580 nm. Data according to Boulnois (1986)

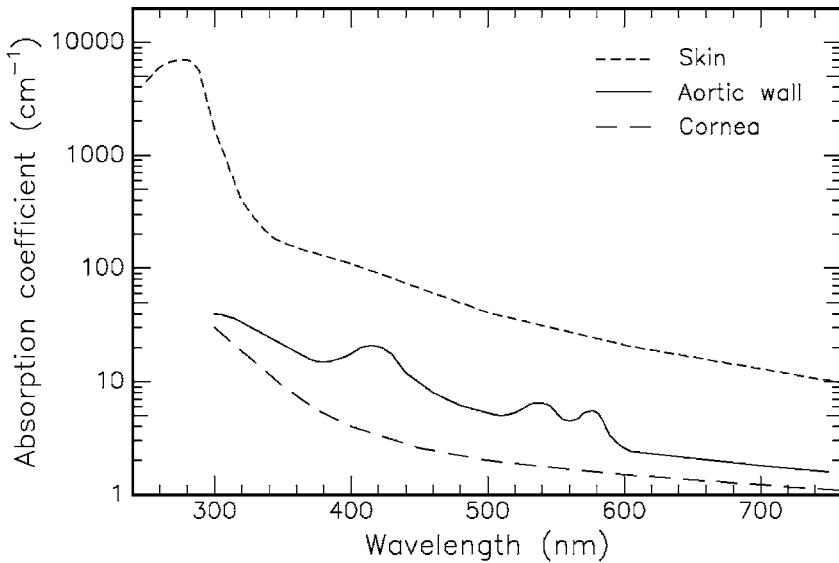


Fig. 2.5. Absorption spectra of skin, aortic wall, and cornea. In the visible range, the absorption of skin is 20–30 times higher than the absorption of corneal tissue. The absorption spectrum of aortic wall exhibits similar peaks as hemoglobin. Data according to Parrish and Anderson (1983), Keijzer et al. (1989), and Eichler and Seiler (1991)

When comparing Figs. 2.4 and 2.5, we find that the absorption spectra of the aortic wall and hemoglobin are quite similar. This observation can be explained by the fact that hemoglobin – as already previously stated – is predominant in vascularized tissue. Thus, it becomes evident that the same absorption peaks must be present in both spectra. Since the green and yellow wavelengths of krypton ion lasers at 531 nm and 568 nm, respectively, almost perfectly match the absorption peaks of hemoglobin, these lasers can be used for the coagulation of blood and blood vessels. For certain clinical applications, dye lasers may be an alternative choice, since their tunability can be advantageously used to match particular absorption bands of specific proteins and pigments.

Not only the absorption of biological tissue, though, is important for medical laser surgery. In certain laser applications, e.g. sclerostomies, special dyes and inks are frequently applied prior to laser exposure. By this means, the original absorption coefficient of the specific tissue is increased, leading to a higher efficiency of the laser treatment. Moreover, adjacent tissue is less damaged due to the enhanced absorption. For further details on sclerostomy, the reader is referred to Sect. 4.1.

In Table 2.2, the effects of some selected dyes on the damage threshold are demonstrated in the case of scleral tissue. The dyes were applied to the sclera by means of electrophoresis, i.e. an electric current was used to direct the dye into the tissue. Afterwards, the samples were exposed to picosecond pulses from a Nd:YLF laser to achieve optical breakdown (see Sect. 3.4). The absolute and relative threshold values of pulse energy are listed for each dye. Obviously, the threshold for the occurrence of optical breakdown can be decreased by a factor of two when choosing the correct dye. Other dyes evoked only a slight decrease in threshold or no effect at all. In general, the application of dyes should be handled very carefully, since some of them might induce toxic side effects.

Table 2.2. Effect of selected dyes and inks on damage threshold of scleral tissue. Damage was induced by a Nd:YLF laser (pulse duration: 30 ps, focal spot size: 30 μm). Unpublished data

Dye	Damage threshold (μJ)	Relative threshold
None	87	100 %
Erythrosine	87	100 %
Nigrosine	87	100 %
Reactive black	82	94 %
Brilliant black	81	93 %
Amido black	75	86 %
Methylene blue	62	71 %
Tatrazine	62	71 %
Bismarck brown	56	64 %
India ink	48	55 %

2.3 Scattering

When elastically bound charged particles are exposed to electromagnetic waves, the particles are set into motion by the electric field. If the frequency of the wave equals the natural frequency of free vibrations of a particle, resonance occurs being accompanied by a considerable amount of absorption. *Scattering*, on the other hand, takes place at frequencies not corresponding to those natural frequencies of particles. The resulting oscillation is determined by forced vibration. In general, this vibration will have the same frequency and direction as that of the electric force in the incident wave. Its amplitude, however, is much smaller than in the case of resonance. Also, the phase of the forced vibration differs from the incident wave, causing photons to slow down when penetrating into a denser medium. Hence, scattering can be regarded as the basic origin of dispersion.

Elastic and *inelastic scattering* are distinguished, depending on whether part of the incident photon energy is converted during the process of scattering. In the following paragraphs, we will first consider elastic scattering, where incident and scattered photons have the same energy. A special kind of elastic scattering is *Rayleigh scattering*. Its only restriction is that the scattering particles be smaller than the wavelength of incident radiation. In particular, we will find a relationship between scattered intensity and index of refraction, and that scattering is inversely proportional to the fourth power of wavelength. The latter statement is also known as *Rayleigh's law* and shall be derived in the following paragraphs.

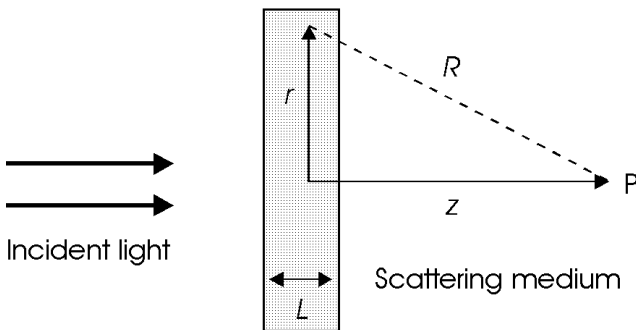


Fig. 2.6. Geometry of Rayleigh scattering

In Fig. 2.6, a simple geometry of Rayleigh scattering is shown. A plane electromagnetic wave is incident on a thin scattering medium with a total thickness L . At a particular time, the electric field of the incident wave can be expressed by

$$E(z) = E_0 \exp(ikz) ,$$

where E_0 is the amplitude of the incident electric field, k is the amount of the propagation vector, and z denotes the optical axis. In a first approximation, we assume that the wave reaching some point P on the optical axis will essentially be the original wave, plus a small contribution due to scattering. The loss in intensity due to scattering is described by a similar relation as absorption, i.e.

$$I(z) = I_0 \exp(-\alpha_s z) , \quad (2.17)$$

where α_s is the scattering coefficient. Differentiation of (2.17) with respect to z leads to

$$dI = -\alpha_s I dz .$$

The intensity scattered by a thin medium of a thickness L as shown in Fig. 2.6 is thus proportional to α_s and L :

$$I_s \sim \alpha_s L . \quad (2.18)$$

Let us now assume that there are NL atoms per unit area of the scattering medium. Herein, the parameter N shall denote the density of scattering atoms. Then, the intensity scattered by one of these atoms can be described by the relation

$$I_1 \sim \frac{\alpha_s L}{NL} = \frac{\alpha_s}{N} .$$

Thus, the amplitude of the corresponding electric field is

$$E_1 \sim \sqrt{\frac{\alpha_s}{N}} .$$

Due to the interference of all scattered waves, the total scattered amplitude can be expressed by

$$E_s \sim NL \sqrt{\frac{\alpha_s}{N}} = L\sqrt{\alpha_s N} .$$

The complex amplitude at a distance z on the optical axis is obtained by adding the amplitudes of all scattered spherical waves to the amplitude of the incident plane wave, i.e.

$$E(z) = E_0 \left(e^{ikz} + L\sqrt{\alpha_s N} \int_0^\infty \frac{e^{ikR}}{R} 2\pi r dr \right) , \quad (2.19)$$

with $R^2 = z^2 + r^2$.

At a given z , we thus obtain

$$r dr = R dR ,$$

which reduces (2.19) to

$$E(z) = E_0 \left(e^{ikz} + L\sqrt{\alpha_s N} 2\pi \int_z^\infty e^{ikR} dR \right) . \quad (2.20)$$

Since wave trains always have a finite length, scattering from $R \rightarrow \infty$ can be neglected. Hence, (2.20) turns into

$$E(z) = E_0 \left(e^{ikz} - L\sqrt{\alpha_s N} \frac{2\pi}{ik} e^{ikz} \right) ,$$

and when inserting the wavelength $\lambda = 2\pi/k$

$$E(z) = E_0 e^{ikz} \left(1 + i\lambda L\sqrt{\alpha_s N} \right) . \quad (2.21)$$

According to our assumption, the contribution of scattering – i.e. the second term in parentheses in (2.21) – is small compared to the first. Hence, they can be regarded as the first two terms of an expansion of

$$E(z) = E_0 \exp \left[i \left(kz + \lambda L\sqrt{\alpha_s N} \right) \right] .$$

Therefore, the phase of the incident wave is altered by the amount $\lambda L\sqrt{\alpha_s N}$ due to scattering. This value must be equal to the well-known expression of phase retardation given by

$$\Delta\phi = \frac{2\pi}{\lambda} (n - 1)L ,$$

which occurs when light enters from free space into a medium with refractive index n . Hence,

$$\begin{aligned} \lambda L\sqrt{\alpha_s N} &= \frac{2\pi}{\lambda} (n - 1)L , \\ n - 1 &= \frac{\lambda^2}{2\pi} \sqrt{\alpha_s N} . \end{aligned} \quad (2.22)$$

From (2.18) and (2.22), we finally obtain *Rayleigh's law* of scattering when neglecting the wavelength-dependence of n , i.e.

$$I_s \sim \frac{1}{\lambda^4} . \quad (2.23)$$

If the scattering angle θ is taken into account, a more detailed analysis yields

$$I_s(\theta) \sim \frac{1 + \cos^2(\theta)}{\lambda^4} , \quad (2.24)$$

where $\theta = 0$ denotes forward scattering. Rayleigh's law is illustrated in Fig. 2.7. Within the visible spectrum, scattering is already significantly reduced when comparing blue and red light.

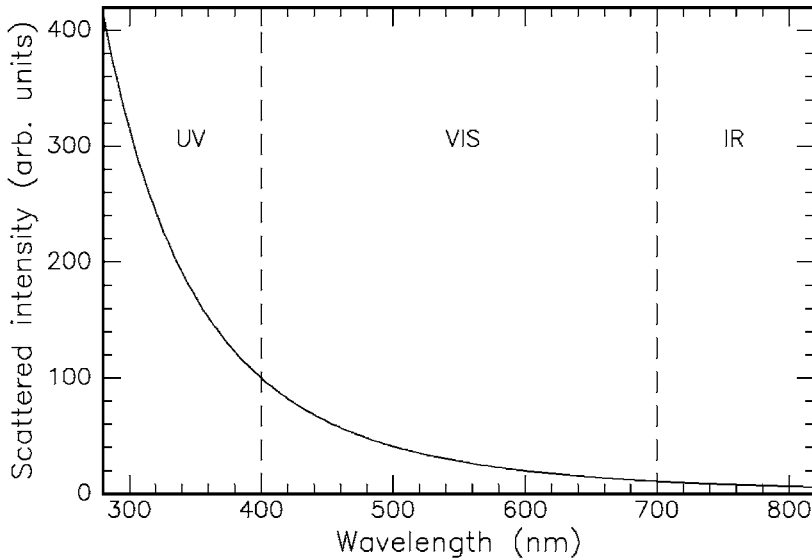


Fig. 2.7. Rayleigh’s law of scattering for near UV, visible, and near IR light

Rayleigh scattering is elastic scattering, i.e. scattered light has the same values of k and λ as incident light. One important type of inelastic scattering is known as *Brillouin scattering*. It arises from acoustic waves propagating through a medium, thereby inducing inhomogeneities of the refractive index. Brillouin scattering of light to higher (or lower) frequencies occurs, because scattering particles are moving toward (or away from) the light source. It can thus be regarded as an optical *Doppler effect* in which the frequency of photons is shifted up or down. In laser–tissue interactions, Brillouin scattering becomes significant only during the generation of shock waves as will be discussed in Sect. 3.5.

In our derivation of Rayleigh’s law, absorption has been neglected. Therefore, (2.22)–(2.24) are valid only for wavelengths far away from any absorption bands. Simultaneous absorption and scattering will be discussed in Sect. 2.4. Moreover, we did not take the spatial extent of scattering particles into account. If this extent becomes comparable to the wavelength of the incident radiation such as in blood cells, Rayleigh scattering no longer applies and another type of scattering called *Mie scattering* occurs. The theory of Mie scattering is rather complex and shall thus not be repeated here. However, it is emphasized that Mie scattering and Rayleigh scattering differ in two important respects. First, Mie scattering shows a weaker dependence on wavelength ($\sim \lambda^{-x}$ with $0.4 \leq x \leq 0.5$) compared to Rayleigh scattering ($\sim \lambda^{-4}$). Second, Mie scattering preferably takes place in the forward direction, whereas Rayleigh scattering is proportional to $1 + \cos^2(\theta)$ according to (2.24), i.e. forward and backward scattered intensities are the same.

In most biological tissues, it was found by Wilson and Adam (1983), Jacques et al. (1987b), and Parsa et al. (1989) that photons are preferably scattered in the forward direction. This phenomenon cannot be explained by Rayleigh scattering. On the other hand, the observed wavelength-dependence is somewhat stronger than predicted by Mie scattering. Thus, neither Rayleigh scattering nor Mie scattering completely describe scattering in tissues. Therefore, it is very convenient to define a *probability function* $p(\theta)$ of a photon to be scattered by an angle θ which can be fitted to experimental data. If $p(\theta)$ does not depend on θ , we speak of *isotropic scattering*. Otherwise, *anisotropic scattering* occurs.

A measure of the anisotropy of scattering is given by the coefficient of anisotropy g , where $g = 1$ denotes purely forward scattering, $g = -1$ purely backward scattering, and $g = 0$ isotropic scattering. In polar coordinates, the coefficient g is defined by

$$g = \frac{\int_{4\pi} p(\theta) \cos \theta \, d\omega}{\int_{4\pi} p(\theta) \, d\omega}, \quad (2.25)$$

where $p(\theta)$ is a probability function and $d\omega = \sin \theta \, d\theta \, d\phi$ is the elementary solid angle. By definition, the coefficient of anisotropy g represents the average value of the cosine of the scattering angle θ . As a good approximation, it can be assumed that g ranges from 0.7 to 0.99 for most biological tissues. Hence, the corresponding scattering angles are most frequently between 8° and 45° . The important term in (2.25) is the probability function $p(\theta)$. It is also called the *phase function* and is usually normalized by

$$\frac{1}{4\pi} \int_{4\pi} p(\theta) \, d\omega = 1. \quad (2.26)$$

Several theoretical phase functions $p(\theta)$ have been proposed and are known as *Heney-Greenstein*, *Rayleigh-Gans*, *δ -Eddington*, and *Reynolds* functions². Among these, the first is best in accordance with experimental observations. It was introduced by Heney and Greenstein (1941) and is given by

$$p(\theta) = \frac{1 - g^2}{(1 + g^2 - 2g \cos \theta)^{3/2}}. \quad (2.27)$$

This phase function is mathematically very convenient to handle, since it is equivalent to the representation

$$p(\theta) = \sum_{i=0}^{\infty} (2i + 1) g^i P_i(\cos \theta), \quad (2.28)$$

² Detailed information on these phase functions is provided in the reports by Heney and Greenstein (1941), van de Hulst (1957), Joseph et al. (1976), and Reynolds and McCormick (1980).

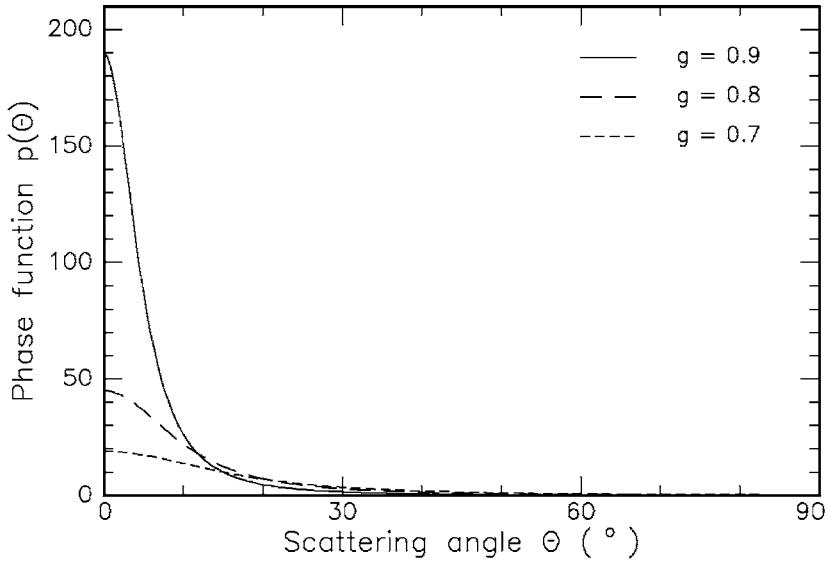


Fig. 2.8. Henyey–Greenstein function for different coefficients of anisotropy ranging from $g = 0.7$ to $g = 0.9$

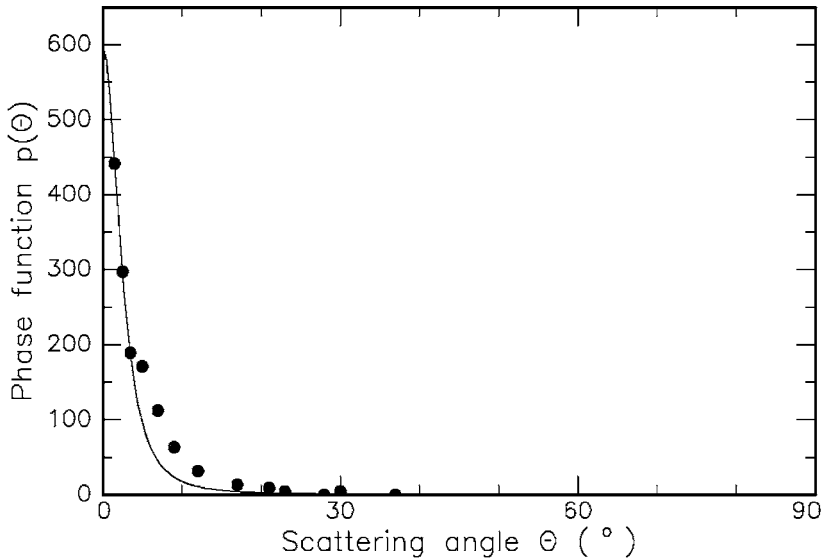


Fig. 2.9. Phase function for an $80\ \mu\text{m}$ thick sample of aortic wall. The data are fitted to a composite function consisting of an isotropic term u and the anisotropic Henyey–Greenstein function (fit parameters: $g = 0.945$, $u = 0.071$). Data according to Yoon et al. (1987)

where P_i are the Legendre polynomials. In some cases, though, a composite function of an isotropic term u and the Henyey–Greenstein function does fit better to experimental data. According to Yoon et al. (1987), this modified function can be expressed by

$$p(\theta) = \frac{1}{4\pi} \frac{u + (1-u)(1-g^2)}{(1+g^2 - 2g \cos \theta)^{3/2}} . \quad (2.29)$$

In Fig. 2.8, the Henyey–Greenstein phase function is graphically shown for different values of g . Obviously, it describes the dominant process of scattering in the forward direction very well. In Fig. 2.9, experimental data are plotted for an 80 μm sample of aortic tissue. The data are fitted to the modified Henyey–Greenstein function as determined by (2.29) with the parameters $g = 0.945$ and $u = 0.071$.

2.4 Turbid Media

In the previous two sections, we have considered the occurrences of either absorption or scattering. In most tissues, though, both of them will be present simultaneously. Such media are called *turbid media*. Their total attenuation coefficient can be expressed by

$$\alpha_t = \alpha + \alpha_s . \quad (2.30)$$

In turbid media, the mean free optical path of incident photons is thus determined by

$$L_t = \frac{1}{\alpha_t} = \frac{1}{\alpha + \alpha_s} . \quad (2.31)$$

Only in some cases, either α or α_s may be negligible with respect to each other, but it is important to realize the existence of both processes and the fact that usually both are operating. Also, it is very convenient to define an additional parameter, the *optical albedo* a , by

$$a = \frac{\alpha_s}{\alpha_t} = \frac{\alpha_s}{\alpha + \alpha_s} . \quad (2.32)$$

For $a = 0$, attenuation is exclusively due to absorption, whereas in the case of $a = 1$ only scattering occurs. For $a = 1/2$, (2.32) can be turned into the equality $\alpha = \alpha_s$, i.e. the coefficients of absorption and scattering are of the same magnitude. In general, both effects will take place but they will occur in variable ratios.

In Fig. 2.10, the albedo is shown as a function of the scattering coefficient. Three different absorption coefficients are assumed which are typical for biological tissue. In addition, the value $a = 1/2$ is indicated. For $\alpha_s \gg \alpha$, the albedo asymptotically approaches unity.

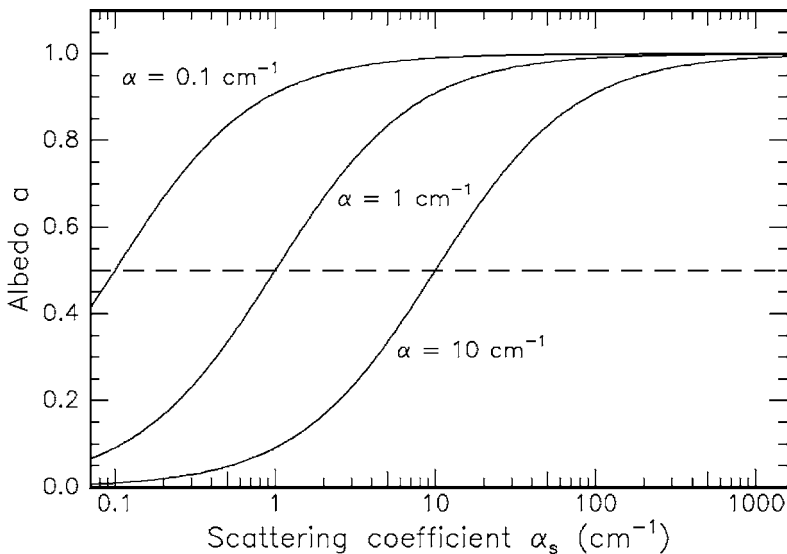


Fig. 2.10. Optical albedo as a function of scattering coefficient (absorption coefficient: as labeled). The albedo $a = 1/2$ is indicated

When dealing with turbid media, another useful parameter is the *optical depth* d which is defined by

$$d = \int_0^s \alpha_t ds' , \tag{2.33}$$

where ds' denotes a segment of the optical path, and s is the total length of the optical path. In the case of homogeneous attenuation, i.e. a constant attenuation coefficient α_t , (2.33) turns into

$$d = \alpha_t s .$$

The advantage of using albedo a and optical depth d – instead of absorption coefficient α and scattering coefficient α_s – is that the former are dimensionless parameters. The information contained in the pair a and d , though, is the same as in the pair α and α_s .

When considering turbid media, the normalization of the phase function as given by (2.26) must be altered to

$$\frac{1}{4\pi} \int_{4\pi} p(\theta) d\omega = a ,$$

since the probability function should approach zero at negligible scattering. Hence, (2.27) and (2.28) are no longer valid and must be replaced by

$$p(\theta) = a \frac{1 - g^2}{(1 + g^2 - 2g \cos \theta)^{3/2}} ,$$

and

$$p(\theta) = a \sum_{i=0}^{\infty} (2i + 1) g^i P_i(\cos \theta) .$$

In the literature, reduced scattering and attenuation coefficients are often dealt with and are given by

$$\alpha_s' = \alpha_s (1 - g) , \quad (2.34)$$

and

$$\alpha_t' = \alpha + \alpha_s' , \quad (2.35)$$

since forward scattering alone, i.e. $g = 1$, would not lead to an attenuation of intensity. These definitions will turn out to be very useful, especially when discussing the diffusion approximation in the next section.

2.5 Photon Transport Theory

A mathematical description of the absorption and scattering characteristics of light can be performed in two different ways: analytical theory or transport theory. The first is based on the physics of *Maxwell's equations* and is, at least in principle, the most fundamental approach. However, its applicability is limited due to the complexities involved when deriving exact analytical solutions. Transport theory, on the other hand, directly addresses the transport of photons through absorbing and scattering media without taking Maxwell's equations into account. It is of a heuristic character and lacks the strictness of analytical theories. Nevertheless, transport theory has been used extensively when dealing with laser–tissue interactions, and experimental evidence is given that its predictions are satisfactory in many cases. Therefore, this section is confined to the transport theory of light.

In our presentation, we will follow the excellent review of transport theory given by Ishimaru (1989). The fundamental quantity in transport theory is called the *radiance*³ $J(\mathbf{r}, \mathbf{s})$ and is expressed in units of $\text{W cm}^{-2} \text{sr}^{-1}$. It denotes the power flux density in a specific direction \mathbf{s} within a unit solid angle $d\omega$. The governing differential equation for radiance is called the *radiative transport equation* and is given by

$$\frac{dJ(\mathbf{r}, \mathbf{s})}{ds} = -\alpha_t J(\mathbf{r}, \mathbf{s}) + \frac{\alpha_s}{4\pi} \int_{4\pi} p(\mathbf{s}, \mathbf{s}') J(\mathbf{r}, \mathbf{s}') d\omega' , \quad (2.36)$$

³ Note that our definition of *radiance* differs from *intensity* by the extra unit sr^{-1} . We are thus using two different symbols J and I , respectively. This mathematically inconvenient distinction becomes necessary, since scattered photons may proceed into any solid angle.

where $p(\mathbf{s}, \mathbf{s}')$ is the phase function of a photon to be scattered from direction \mathbf{s}' into \mathbf{s} , ds is an infinitesimal path length, and $d\omega'$ is the elementary solid angle about the direction \mathbf{s}' . If scattering is symmetric about the optical axis, we may set $p(\mathbf{s}, \mathbf{s}') = p(\theta)$ with θ being the scattering angle as defined in Sect. 2.3.

When performing measurements of optical properties, the observable quantity is the *intensity* which is derived from radiance by integration over the solid angle

$$I(\mathbf{r}) = \int_{4\pi} J(\mathbf{r}, \mathbf{s}) d\omega . \quad (2.37)$$

On the other hand, radiance may be expressed in terms of intensity by

$$J(\mathbf{r}, \mathbf{s}) = I(\mathbf{r}) \delta(\omega - \omega_s) , \quad (2.38)$$

where $\delta(\omega - \omega_s)$ is a solid angle delta function pointing into the direction given by \mathbf{s} .

When a laser beam is incident on a turbid medium, the radiance inside the medium can be divided into a coherent and a diffuse term according to the relation

$$J = J_c + J_d .$$

The coherent radiance is reduced by attenuation due to absorption and scattering of the direct beam. It can thus be calculated from

$$\frac{dJ_c}{ds} = -\alpha_t J_c ,$$

with the solution

$$J_c = I_0 \delta(\omega - \omega_s) \exp(-d) ,$$

where I_0 is the incident intensity, and the dimensionless parameter d is the optical depth defined by (2.33). Hence, the coherent intensity in turbid media is characterized by an exponential decay.

The main problem with which transport theory has to deal is the evaluation of the diffuse radiance, since scattered photons do not follow a determined path. Hence, adequate approximations and statistical approaches must be chosen, mainly depending on the value of the albedo, i.e. whether either absorption or scattering is the dominant process of attenuation. These methods are referred to as *first-order scattering*, *Kubelka-Munk theory*, *diffusion approximation*, *Monte Carlo simulations*, or *inverse adding-doubling*. In the following paragraphs, they will be discussed in this order. Each method is based on certain assumptions regarding initial and boundary conditions. In general, the complexity of either approach is closely related to its accuracy but also to the calculation time needed.

First-Order Scattering. Only if the diffuse radiance is considerably smaller than the coherent radiance can an analytical solution be given by assuming that

$$J_c + J_d \simeq J_c .$$

This case is called *first-order scattering*, since scattered light can be treated in a similar manner as absorbed light. The intensity at a distance z from the tissue surface is thus given by Lambert's law

$$I(z) = I_0 \exp[-(\alpha + \alpha_s)z] ,$$

where z denotes the axis of the incident beam. Hence, first-order scattering is limited to plane incident waves, and multiple scattering is not taken into account. It is thus a very simple solution and might be useful for a few practical problems only, i.e. if $d \ll 1$ or $a \ll 0.5$. However, in the therapeutic window between 600 nm and 1200 nm, where most tissues are highly transparent, the albedo is close to unity. For these wavelengths, the first-order solution is often not applicable.

Kubelka–Munk Theory. A more useful model which is still restricted to linear geometries has been developed by Kubelka and Munk (1931). Since its parameters are often used in medical physics, the basic idea of this theory shall be described. In contrast to first-order scattering, the main assumption is that the radiance be diffuse, i.e.

$$J_c = 0 .$$

In Fig. 2.11, a geometry is shown which illustrates that two diffuse fluxes inside the tissue can be distinguished: a flux J_1 in the direction of the incident radiation and a backscattered flux J_2 in the opposite direction. Two Kubelka–Munk coefficients, A_{KM} and S_{KM} , are defined for the absorption and scattering of diffuse radiation, respectively⁴. With these parameters, two differential equations can be formed:

$$\frac{dJ_1}{dz} = -S_{KM}J_1 - A_{KM}J_1 + S_{KM}J_2 , \quad (2.39)$$

$$\frac{dJ_2}{dz} = -S_{KM}J_2 - A_{KM}J_2 + S_{KM}J_1 , \quad (2.40)$$

where z denotes the mean direction of incident radiation. Each of these equations states that radiance in either direction encounters two losses due to absorption and scattering and one gain due to scattering of photons from the opposite direction. The general solutions to (2.39) and (2.40) can be expressed by

⁴ The coefficients A_{KM} and S_{KM} must be distinguished from α and α_s , since the latter are defined for coherent radiation only.

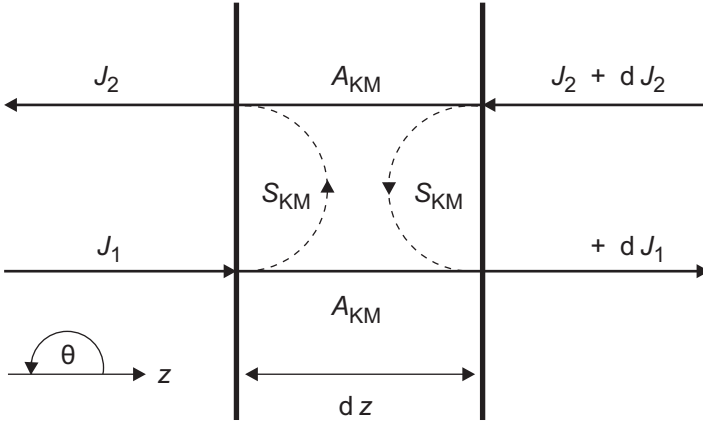


Fig. 2.11. Geometry of two fluxes in Kubelka–Munk theory

$$J_1(z) = c_{11} \exp(-\gamma z) + c_{12} \exp(+\gamma z) ,$$

$$J_2(z) = c_{21} \exp(-\gamma z) + c_{22} \exp(+\gamma z) ,$$

with

$$\gamma = \sqrt{A_{KM}^2 + 2A_{KM}S_{KM}} .$$

The major problem of Kubelka–Munk theory is the description of A_{KM} and S_{KM} in terms of α and α_s . When considering dl as an infinitesimal path length of a scattered photon and dz as an infinitesimal path length of a coherent photon, we may write for the average values

$$\alpha \langle dl \rangle = \alpha (b \langle dz \rangle) = (\alpha b) \langle dz \rangle = A_{KM} \langle dz \rangle , \tag{2.41}$$

with some numerical factor $b > 1$. When also taking the geometry shown in Fig. 2.12 into account, we obtain

$$\frac{\langle dl \rangle}{\langle dz \rangle} = \frac{\int_{-1}^{+1} \frac{1}{|\cos \theta|} J(z) |\cos \theta| d(\cos \theta)}{\int_{-1}^{+1} J(z) |\cos \theta| d(\cos \theta)} ,$$

and, since J does not depend on θ according to our assumption of purely diffuse scattering,

$$\frac{\langle dl \rangle}{\langle dz \rangle} = \frac{\int_{-1}^{+1} d(\cos \theta)}{\int_{-1}^{+1} |\cos \theta| d(\cos \theta)} = 2 . \tag{2.42}$$

Combining (2.41) and (2.42) leads to

$$A_{KM} = 2\alpha .$$

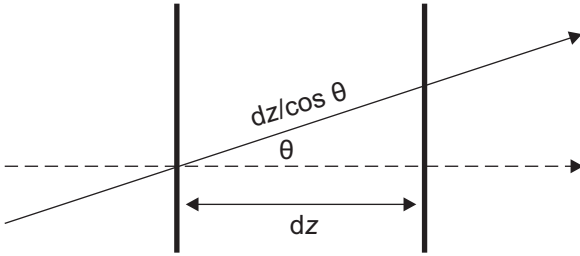


Fig. 2.12. Path length in a thin layer at scattering angle θ

Because only backscattering is assumed as pointed out in Fig. 2.11, the corresponding relation for S_{KM} is given by

$$S_{KM} = \alpha_s .$$

The Kubelka–Munk theory is a special case of the so-called *many flux theory*, where the transport equation is converted into a matrix differential equation by considering the radiance at many discrete angles. A detailed description of the many flux theory is found in the book by Ishimaru (1978). Beside the two fluxes proposed by Kubelka and Munk, other quantities of fluxes were also considered, as for instance seven fluxes by Yoon et al. (1987) or even twenty-two fluxes by Mudgett and Richards (1971). In general, though, all these many flux theories are restricted to a one-dimensional geometry and to the assumption that the incident light be already diffuse. Another disadvantage is the necessity of extensive computer calculations.

Diffusion Approximation. For albedos $a \gg 0.5$, i.e. if scattering overwhelms absorption, the diffuse part of (2.37) tends to be almost isotropic. According to Ishimaru (1989), we may then expand the diffuse radiance J_d in a series by

$$J_d = \frac{1}{4\pi} (I_d + 3\mathbf{F}_d \mathbf{s} + \dots) , \quad (2.43)$$

where I_d is the diffuse intensity, and the vector flux \mathbf{F}_d is determined by

$$\mathbf{F}_d(\mathbf{r}) = \int_{4\pi} J_d(\mathbf{r}, \mathbf{s}) \mathbf{s} \, d\omega .$$

The first two terms of the expansion expressed by (2.43) constitute the diffusion approximation. The diffuse intensity I_d itself satisfies the following diffusion equation

$$(\nabla^2 - \kappa^2) I_d(\mathbf{r}) = -Q(\mathbf{r}) , \quad (2.44)$$

where κ^2 is the diffusion parameter, and Q represents the source of scattered photons. It was shown by Ishimaru (1978) that

$$\begin{aligned}\kappa^2 &= 3\alpha [\alpha + \alpha_s (1 - g)] , \\ Q &= 3\alpha_s(\alpha_t + g\alpha) F_0 \exp(-d) ,\end{aligned}$$

with the incident flux amplitude F_0 and the optical depth d as determined by (2.33). According to our previous definition of reduced coefficients in (2.34) and (2.35), we thus have

$$\kappa^2 = 3\alpha\alpha_t' .$$

The diffusion equation (2.44) suggests the introduction of an effective diffusion length L_{eff} and an effective attenuation coefficient α_{eff} of diffuse light which can be defined by

$$\begin{aligned}L_{\text{eff}} &= \frac{1}{\kappa} = \frac{1}{\sqrt{3\alpha\alpha_t'}} , \\ \alpha_{\text{eff}} &= \frac{1}{L_{\text{eff}}} = \sqrt{3\alpha\alpha_t'} .\end{aligned}$$

In general, the diffusion approximation thus states that

$$I = I_c + I_d = A \exp(-\alpha_t z) + B \exp(-\alpha_{\text{eff}} z) , \quad (2.45)$$

with $A + B = I_0$. There exist different sets of values for α , α_s , and g which provide similar radiances in diffusion approximation calculations. They can be expressed in terms of each other by so-called *similarity relations* given by

$$\begin{aligned}\tilde{\alpha} &= \alpha , \\ \tilde{\alpha}_s (1 - \tilde{g}) &= \alpha_s (1 - g) ,\end{aligned}$$

where tildes indicate transformed parameters. One motive for applying similarity relations is the transformation of anisotropic scattering into isotropic scattering by using

$$\begin{aligned}\tilde{g} &= 0 , \\ \tilde{\alpha} &= \alpha , \\ \tilde{\alpha}_s &= \alpha_s (1 - g) = \alpha_s' .\end{aligned}$$

By this transformation, computer calculations are significantly facilitated, since only absorption coefficient and reduced scattering coefficients are needed for the characterization of optical tissue properties.

In Fig. 2.13, the dependence of the diffuse radiance on optical depth is illustrated in the case of isotropic scattering ($g = 0$) and different albedos ($0 < a < 1$). For $a = 0$, attenuation follows Lambert's law of absorption. For $a = 1$, the radiance obviously approaches an asymptotic value. It is also interesting to note that just beneath the surface of the scattering medium the diffuse intensity exceeds the incident intensity, since backscattered photons from deeper layers must be added to the incident intensity.

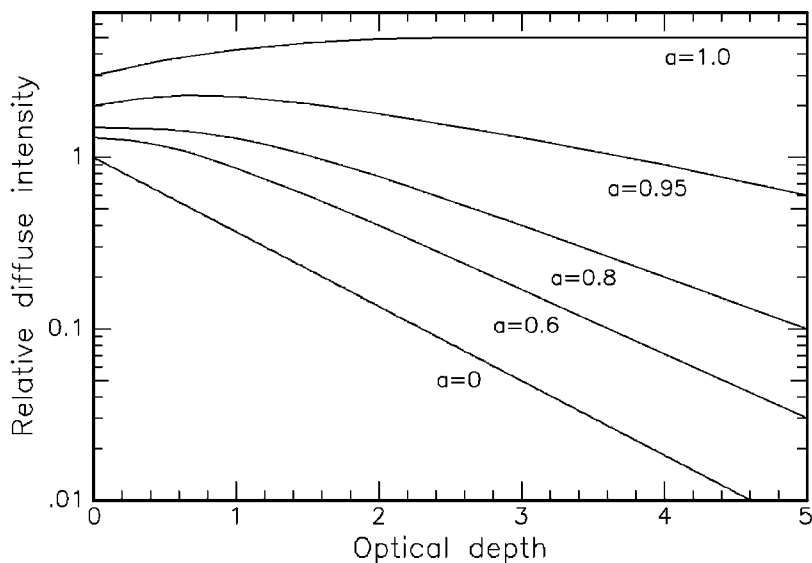


Fig. 2.13. Diffuse intensity as a function of optical depth, assuming the validity of the diffusion approximation and isotropic scattering. The ordinate expresses diffuse intensity in units of incident intensity. Data according to van Gemert et al. (1990)

Monte Carlo Simulations. A numerical approach to the transport equation (2.36) is based on Monte Carlo simulations. The Monte Carlo method essentially runs a computer simulation of the random walk of a number N of photons. It is thus a statistical approach. Since the accuracy of results based on statistics is proportional to \sqrt{N} , a large number of photons has to be taken into account to yield a valuable approximation. Therefore, the whole procedure is rather time-consuming and can be efficiently performed only on large computers. The Monte Carlo method was first proposed by Metropolis and Ulam (1949). It has meanwhile advanced to a powerful tool in many disciplines. Here, we will first point out the basic idea and then briefly discuss each step of the simulation.

The principal idea of Monte Carlo simulations applied to absorption and scattering phenomena is to follow the optical path of a photon through the turbid medium. The distance between two collisions is selected from a logarithmic distribution, using a random number generated by the computer. Absorption is accounted for by implementing a weight to each photon and permanently reducing this weight during propagation. If scattering is to occur, a new direction of propagation is chosen according to a given phase function and another random number. The whole procedure continues until the photon escapes from the considered volume or its weight reaches a given cutoff value. According to Meier et al. (1978) and Groenhuis et al. (1983), Monte Carlo simulations of absorption and scattering consist of five principal

steps: *source photon generation, pathway generation, absorption, elimination, and detection.*

- 1. Source photon generation. Photons are generated at a surface of the considered medium. Their spatial and angular distribution can be fitted to a given light source, e.g. a Gaussian beam.
- 2. Pathway generation. After generating a photon, the distance to the first collision is determined. Absorbing and scattering particles in the turbid medium are supposed to be randomly distributed. Thus, the mean free path is $1/\varrho\sigma_s$, where ϱ is the density of particles and σ_s is their scattering cross-section⁵. A random number $0 < \xi_1 < 1$ is generated by the computer, and the distance $L(\xi_1)$ to the next collision is calculated from

$$L(\xi_1) = - \frac{\ln \xi_1}{\varrho\sigma_s} .$$

Since

$$\int_0^1 \ln \xi_1 \, d\xi_1 = -1 ,$$

the average value of $L(\xi_1)$ is indeed $1/\varrho\sigma_s$. Hence, a scattering point has been obtained. The scattering angle is determined by a second random number ξ_2 in accordance with a certain phase function, e.g. the Henyey–Greenstein function. The corresponding azimuth angle Φ is chosen as

$$\Phi = 2\pi \xi_3 ,$$

where ξ_3 is a third random number between 0 and 1.

- 3. Absorption. To account for absorption, a weight is attributed to each photon. When entering the turbid medium, the weight of the photon is unity. Due to absorption – in a more accurate program also due to reflection – the weight is reduced by $\exp[-\alpha L(\xi_1)]$, where α is the absorption coefficient. As an alternative to implementing a weight, a fourth random number ξ_4 between 0 and 1 can be drawn. Then, instead of assuming only scattering events in Step 2, scattering takes place if $\xi_4 < a$, where a is the albedo. For $\xi_4 > a$, on the other hand, the photon is absorbed which then is equivalent to Step 4.
- 4. Elimination. This step only applies if a weight has been attributed to each photon (see Step 3.). When this weight reaches a certain cutoff value, the photon is eliminated. Then, a new photon is launched, and the program proceeds with Step 1.
- 5. Detection. After having repeated Steps 1–4 for a sufficient number of photons, a map of pathways is calculated and stored in the computer. Thus, statistical statements can be made about the fraction of incident photons being absorbed by the medium as well as the spatial and angular distribution of photons having escaped from it.

⁵ Absorption will be taken into account by Step 3.

It has already been mentioned that the accuracy of Monte Carlo simulations increases with the larger numbers of photons to be considered. Due to the necessity of extensive computer calculations, though, this is a very time-consuming process. Recently, a novel approach has been introduced by Graaff et al. (1993a) in what they called *condensed Monte Carlo simulations*. The results of earlier calculations can be stored and used again if needed for the same phase function but for different values of the absorption coefficient and the albedo. When applying this alternative technique, a considerable amount of computing time can be saved.

Inverse Adding–Doubling Method. Another numerical approach to the transport equation is called *inverse adding–doubling* which was recently introduced by Prahl et al. (1993). The term “inverse” implies a reversal of the usual process of calculating reflectance and transmittance from optical properties. The term “adding–doubling” refers to earlier techniques established by van de Hulst (1962) and Plass et al. (1973). The doubling method assumes that reflection and transmission of light incident at a certain angle is known for one layer of a tissue slab. The same properties for a layer twice as thick is found by dividing it into two equal slabs and adding the reflection and transmission contributions from either slab. Thus, reflection and transmission for an arbitrary slab of tissue can be calculated by starting with a thin slab with known properties, e.g. as obtained by absorption and single scattering measurements, and doubling it until the desired thickness is achieved. The adding method extends the doubling method to dissimilar slabs of tissue. With this supplement, layered tissues with different optical properties can be simulated, as well.

So far, we have always assumed that the radiance J is a scalar and polarization effects are negligible. In the 1980s, several extensive studies were done on transport theory pointing out the importance of additional polarizing effects. A good summary is given in the paper by Ishimaru and Yeh (1984). Herein, the radiance is replaced by a four-dimensional *Stokes vector*, and the phase function by a 4×4 *Müller matrix*. The Stokes vector accounts for all states of polarization. The Müller matrix describes the probability of a photon to be scattered into a certain direction at a given polarization. The transport equation then becomes a matrix integro-differential equation and is called a *vector transport equation*.

In this section, we have discussed different methods for solving the transport equation. Among them, the most important are the Kubelka–Munk theory, the diffusion approximation, and Monte Carlo simulations. In a short summary, we will now compare either method with each other. The Kubelka–Munk theory can deal with diffuse radiation only and is limited to those cases where scattering overwhelms absorption. Another disadvantage of the Kubelka–Munk theory is that it can be applied to one-dimensional geometries only. The diffusion approximation, on the other hand, is not restricted

to diffuse radiation but is also limited to predominant scattering. In the latter case, though, it can be regarded as a powerful tool. Monte Carlo simulations, finally, provide the most accurate solutions, since a variety of input parameters may be considered in specially developed computer programs. Moreover, two-dimensional and three-dimensional geometries can be evaluated, even though they often require long computation times.

In Fig. 2.14, the intensity distributions inside a turbid medium calculated with either method are compared with each other. Because isotropic scattering is assumed, an analytical solution can also be considered which is labeled “transport theory”. Two different albedos, $a = 0.9$ and $a = 0.99$, are taken into account. Hence, the coefficient of scattering surpasses the coefficient of absorption by a factor of 9 or 99, respectively. The accordance of all four approaches is fairly good. The Kubelka–Munk theory usually yields higher values, whereas diffusion approximation and Monte Carlo simulation frequently underestimate the intensity.

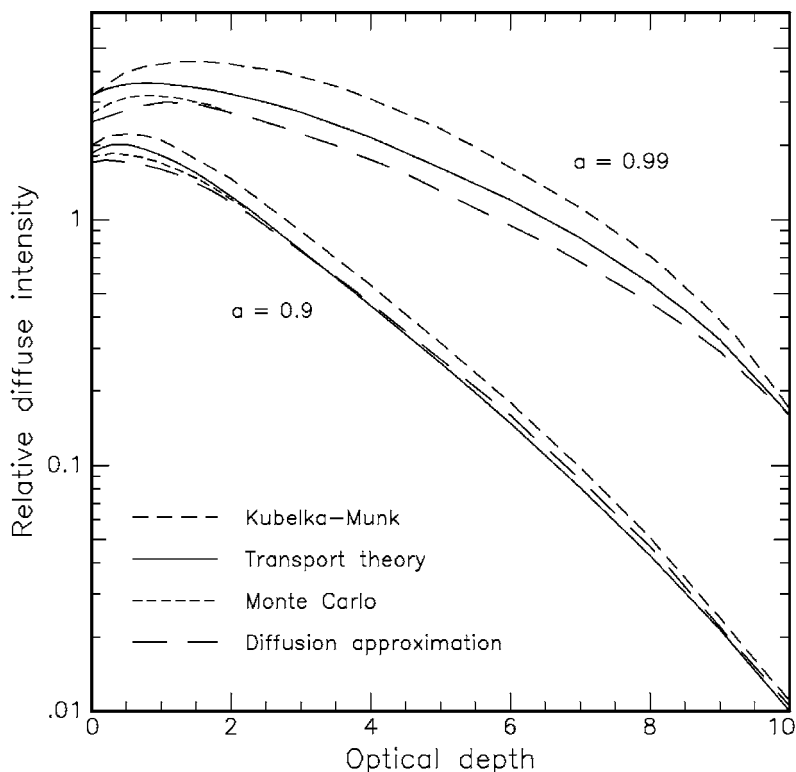


Fig. 2.14. Comparison of different methods for calculating the diffuse intensity as a function of optical depth. The ordinate expresses diffuse intensity in units of incident intensity. Isotropic scattering is assumed. Data according to Wilson and Patterson (1986)

2.6 Measurement of Optical Tissue Properties

In general, there exist several methods for the measurement of optical tissue properties. They focus on different quantities such as transmitted, reflected, and scattered intensities. The absorbance itself is difficult to determine, since photons absorbed by the tissue can no longer be used for detection. Therefore, the absorbed intensity is usually obtained when subtracting transmitted, reflected, and scattered intensities from the incident intensity. Depending on the experimental method, either only the total attenuation coefficient or the coefficients of both absorption and scattering can be evaluated. If the angular dependence of the scattered intensity is measured by rotating the corresponding detector, the coefficient of anisotropy can be obtained, as well.

In Fig. 2.15a–c, three commonly used arrangements are illustrated. The simplest setup for measuring total attenuation is shown in Fig. 2.15a. By means of a beamsplitter, typically 50% of the laser radiation is directed on one detector serving as a reference signal. The other 50% is applied to the tissue sample. A second detector behind the sample and on the optical axis of the beam measures the transmitted intensity. By subtracting this intensity from the intensity measured with the reference detector, the attenuation coefficient⁶ of the tissue can be obtained. The reader is reminded that total attenuation is due to both absorption and scattering. Thus, with this measurement no distinction can be made between these two processes.

In Fig. 2.15b, a setup for the evaluation of the absorbance is shown. Its basic component is called an *integrating sphere* and was discussed in theoretical studies by Jacquez and Kuppenheim (1955), Miller and Sant (1958), and Goebel (1967). The sphere has a highly reflecting coating. An integrated detector only measures light that has not been absorbed by a sample placed inside the sphere. Usually, the experiment consists of two measurements: one with and the other without the sample. The difference in both detected intensities is the amount absorbed by the sample. Thus, when taking the geometrical dimensions of the sample into account, its absorption coefficient can be obtained. Frequently, a baffle is positioned between sample and detector to prevent specular reflection from being detected.

A third experiment is illustrated in Fig. 2.15c. Here, the angular dependence of scattering can be measured by moving the detector on a 360° rotary stage around the sample. From the detected signals, the corresponding phase function of scattering is obtained. By fitting this result to a given function, e.g. the Henyey–Greenstein phase function, the coefficient of anisotropy can also be evaluated.

⁶ Actually, this method does not lead to the same attenuation coefficient as defined by (2.30), since reflection on the tissue surface should also be taken into account. Specular reflection can be measured by placing a third detector opposite to the beamsplitter. Diffuse reflection can be evaluated only when using two integrating spheres as will be discussed below.

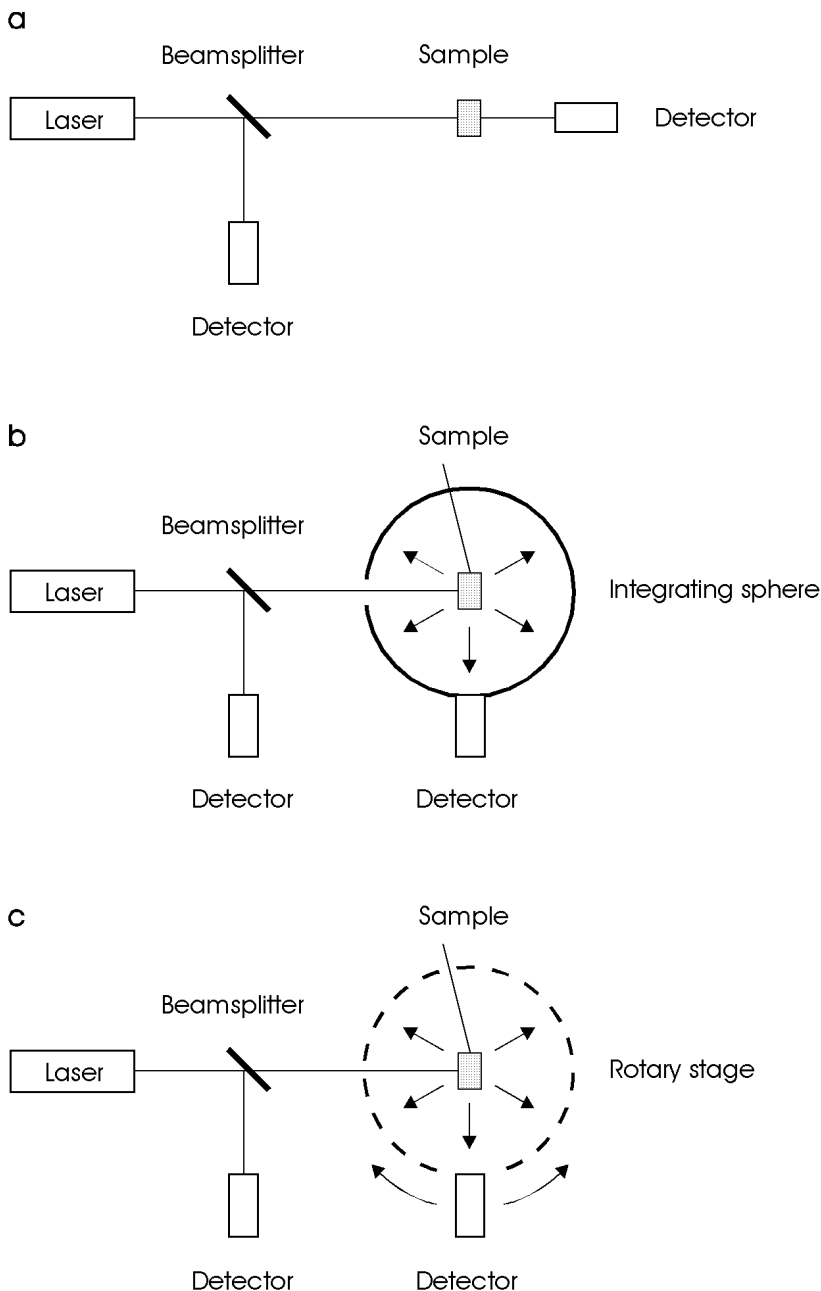


Fig. 2.15. (a) Experimental setup for measuring total attenuation. (b) Experimental setup for measuring absorption. (c) Experimental setup for measuring the angular dependence of scattering

The main disadvantage of the techniques shown in Fig. 2.15a–c is that they cannot be performed simultaneously. However, it is well known that the optical properties of biological tissue are altered during heating which is often associated with exposure to laser radiation. Hence, it is more accurate to measure these properties in the same experimental arrangement and at the same time. One commonly used setup satisfying this requirement is the double-integrating sphere geometry shown in Fig. 2.16. It was first applied to the measurement of optical tissue properties by Derbyshire et al. (1990) and Rol et al. (1990), and has meanwhile turned into an unsurpassed diagnostic tool.

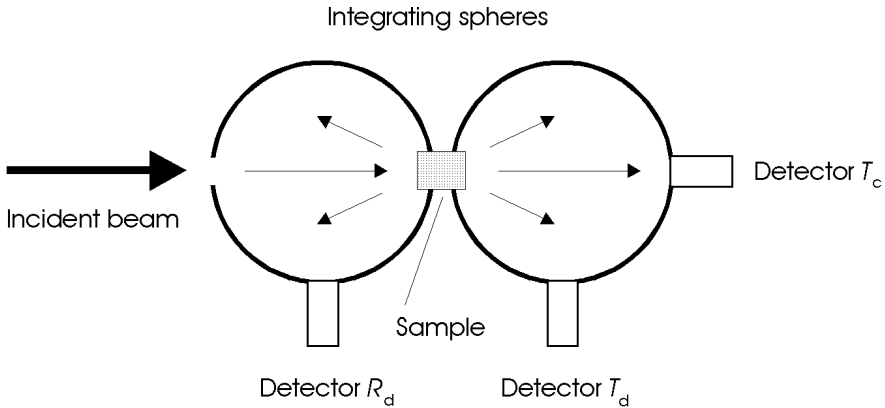


Fig. 2.16. Double-integrating sphere geometry for the simultaneous measurement of different optical tissue properties. The detectors measure the transmitted coherent intensity (T_c), the transmitted diffuse intensity (T_d), and the reflected diffuse intensity (R_d)

The double-integrating sphere geometry incorporates two more or less identical spheres which are located in front and behind the sample to be investigated. One sphere integrates all radiation which is either reflected or scattered backwards from the sample. Transmitted and forward scattered radiation is absorbed in the second sphere. With three detectors, all required measurements can be performed simultaneously. In Fig. 2.16, these detectors are labeled T_c for coherent transmittance, T_d for diffuse transmittance, and R_d for diffuse reflectance, respectively. Specular reflection can again be avoided by placing baffles between the sample and each detector. However, a small fraction of light in either sphere might penetrate again through the sample, thereby reaching the other sphere. The possibility of such an effect was first recognized by Pickering et al. (1992) who then developed an improved model by taking the multiple exchange of light between both spheres into account. First results regarding optical tissue properties with this more accurate theory were published by Pickering et al. (1993).

Since the Kubelka–Munk theory is one of the most frequently used methods to obtain data on optical tissue properties, we shall briefly discuss how the Kubelka–Munk coefficients introduced in Sect. 2.5 relate to measured values of diffuse reflectance and transmission. According to Kottler (1960), these expressions are given by

$$R_d = \frac{\sinh(S_{KM}yD)}{x \cosh(S_{KM}yD) + y \sinh(S_{KM}yD)}, \quad (2.46)$$

$$T_d = \frac{y}{x \cosh(S_{KM}yD) + y \sinh(S_{KM}yD)}, \quad (2.47)$$

where D is the optical thickness of the slab to be considered, and S_{KM} is the Kubelka–Munk coefficient for scattering. The parameters x and y can be expressed in terms of

$$x = \frac{1 + R_d^2 - T_d^2}{2R_d}, \quad (2.48)$$

$$y = \sqrt{x^2 - 1}. \quad (2.49)$$

According to Kottler (1960), the convenience of applying the Kubelka–Munk method arises from the fact that scattering and absorption coefficients may be directly calculated from measured reflection and transmission coefficients, i.e. by means of

$$S_{KM} = \frac{1}{yD} \ln \left[\frac{1 - R_d(x - y)}{T_d} \right], \quad (2.50)$$

$$A_{KM} = (x - 1) S_{KM}. \quad (2.51)$$

The simplicity of the Kubelka–Munk model has made it a popular method for measuring optical properties of matter. In general, the model is based on the propagation of a uniform and diffuse radiance in a one-dimensional geometry. This is equivalent to the requirement of a forward and backward peaked phase function. Unfortunately, though, the assumptions of a purely diffuse radiance and a one-dimensional geometry are not satisfied by biological tissues. Thus, several attempts have been made to extend the Kubelka–Munk theory to partially collimated radiance, e.g. by Kottler (1960) and van Gemert et al. (1987), and to the case of anisotropic scattering, e.g. by Meador and Weaver (1979) and Jacques and Prahl (1987a). Despite these improvements, this method remains a rather simple approximation for the propagation of laser light in biological tissues.

Nearly all optical properties can be separated into either transport coefficients (α , α_s , g) or Kubelka–Munk coefficients (A_{KM} , S_{KM}), depending on the theory used to obtain them. It is not surprising that transport properties are derived from theories based on the transport equation, i.e. (2.36), whereas Kubelka–Munk properties are calculated from (2.50) and (2.51).

Before providing a detailed list of optical tissue parameters, it should be noted that absorption and scattering coefficients may change during laser exposure. When discussing thermal effects in Sect. 3.2, we will find that carbonization, in particular, leads to increased absorption. However, the occurrence of carbonization is usually avoided during any kind of clinical surgery. Scattering, on the other hand, is already affected at lower temperatures, e.g. when tissue is coagulated⁷. In Fig. 2.17, the absorption and scattering coefficients are shown for white matter of human brain as calculated by Roggan et al. (1995a) using the Kubelka–Munk theory. Coagulation was achieved by keeping the tissue in a bath of hot water at approximately 75°C.

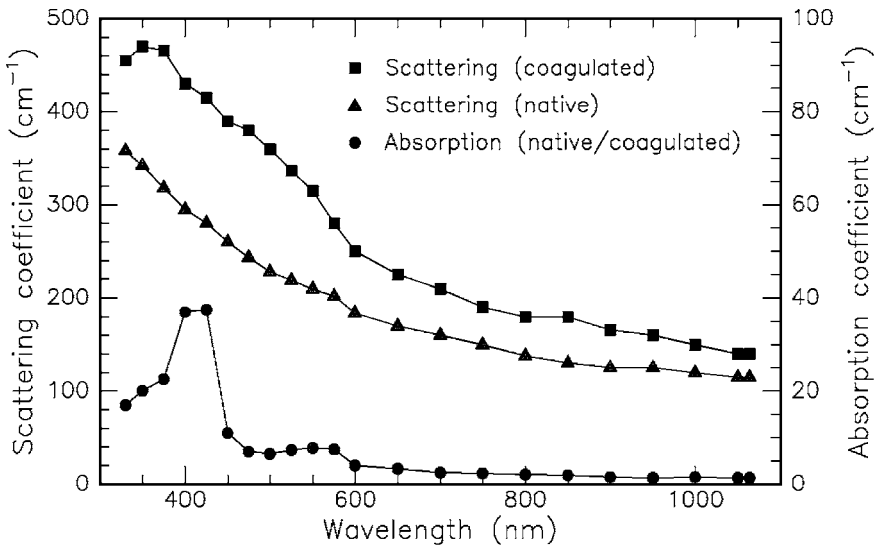


Fig. 2.17. Optical properties of white matter of human brain in its native and coagulated state. Data according to Roggan et al. (1995a)

We have now discussed different theoretical approaches and experimental arrangements for determining optical tissue properties. It is important to realize that both theory and experiment are necessary in order to yield valuable results. During the past decade, several research groups have been investigating all kinds of biological tissue. A short summary of the most significant results is given in Table 2.3. Type of tissue, laser wavelength, absorption coefficient, scattering coefficient, attenuation coefficient, coefficient of anisotropy, reference, and the applied theoretical method are listed. Additional data can be found in a review paper published by Cheong et al. (1990).

⁷ Coagulation is a thermal effect which is very useful for many types of surgery, especially in laser-induced interstitial thermotherapy (LITT), ophthalmology, and angioplasty. Further information is given in the Sects. 3.2, 4.1, and 4.6.

Table 2.3. Optical properties of human tissues in vitro

Tissue	λ (nm)	α (cm^{-1})	α_s (cm^{-1})	α_t (cm^{-1})	g	Reference
Aorta advent.	476	18.1	267	285	0.74	Keijzer et al. (1989) ^c
Aorta advent.	580	11.3	217	228	0.77	Keijzer et al. (1989) ^c
Aorta advent.	600	6.1	211	217	0.78	Keijzer et al. (1989) ^c
Aorta advent.	633	5.8	195	201	0.81	Keijzer et al. (1989) ^c
Aorta intima	476	14.8	237	252	0.81	Keijzer et al. (1989) ^c
Aorta intima	580	8.9	183	192	0.81	Keijzer et al. (1989) ^c
Aorta intima	600	4.0	178	182	0.81	Keijzer et al. (1989) ^c
Aorta intima	633	3.6	171	175	0.85	Keijzer et al. (1989) ^c
Aorta media	476	7.3	410	417	0.89	Keijzer et al. (1989) ^c
Aorta media	580	4.8	331	336	0.90	Keijzer et al. (1989) ^c
Aorta media	600	2.5	323	326	0.89	Keijzer et al. (1989) ^c
Aorta media	633	2.3	310	312	0.90	Keijzer et al. (1989) ^c
Bladder	633	1.4	88.0	89.4	0.96	Cheong et al. (1987) ^b
Bladder	633	1.4	29.3	30.7	0.91	Splinter et al. (1989) ^b
Blood	665	1.3	1246	1247	0.99	Reynolds et al. (1976) ^a
Blood	685	2.65	1413	1416	0.99	Pedersen et al. (1976) ^c
Blood	960	2.84	505	508	0.99	Reynolds et al. (1976) ^a
Bone (skull)	488	1.4	200	201	0.87	Roggan et al. (1995a) ^d
Bone (skull)	514	1.3	190	191	0.87	Roggan et al. (1995a) ^d
Bone (skull)	1064	0.5	120	121	0.90	Roggan et al. (1995a) ^d
Brain (white)	633	1.58	51.0	52.6	0.96	Splinter et al. (1989) ^b
Brain (white)	850	0.8	140	141	0.95	Roggan et al. (1995a) ^d
Brain (white)	1064	0.4	110	110	0.95	Roggan et al. (1995a) ^d
Brain (grey)	633	2.63	60.2	62.8	0.88	Splinter et al. (1989) ^b
Breast	635	<0.2	395	395	–	Marchesini et al. (1989) ^a
Gallbladder	633	4.0	182	186	0.94	Maitland et al. (1993) ^c
Liver	515	18.9	285	304	–	Marchesini et al. (1989) ^a
Liver	635	2.3	313	315	0.68	Marchesini et al. (1989) ^a
Liver	850	0.3	200	200	0.95	Roggan et al. (1995a) ^d
Liver	1064	0.3	150	150	0.93	Roggan et al. (1995a) ^d
Lung	515	25.5	356	382	–	Marchesini et al. (1989) ^a
Lung	635	8.1	324	332	0.75	Marchesini et al. (1989) ^a
Muscle	515	11.2	530	541	–	Marchesini et al. (1989) ^a
Myocardium	1064	0.4	175	175	0.97	Splinter et al. (1993) ^d
Prostate	850	0.6	130	131	0.96	Roggan et al. (1995a) ^d
Prostate	1064	0.4	110	110	0.96	Roggan et al. (1995a) ^d
Skin (white)	633	2.7	187	190	0.81	Jacques et al. (1987b) ^c
Skin (white)	700	2.7	237	240	0.91	Graaff et al. (1993b) ^d
Skin (dark)	700	8.1	229	237	0.91	Graaff et al. (1993b) ^d
Uterus	635	0.35	394	394	0.69	Marchesini et al. (1989) ^a

^a Lambert's law^b Kubelka–Munk or 3-flux theory^c Diffusion approximation^d Monte Carlo simulations

Finally, the reader is reminded that biological tissue is something very inhomogeneous and fragile. The inhomogeneity makes it difficult to transfer experimental data from one sample to another. Usually, it is taken into account by applying generous error bars. Throughout this book, however, error bars are often neglected to facilitate readability of the figures. Fragility, on the other hand, is something the experimenter is confronted with. It was pointed out by Graaff et al. (1993b) that optical properties determined *in vitro* may differ extremely from those valid *in vivo*. There are several reasons to be considered. First of all, living tissue does not have the same morphologic structure as excised tissue. One typical example is corneal tissue which turns into a turbid material within a few hours after dissection. Secondly, alterations are induced by unavoidable deformation and handling of the tissue such as drying, freezing, or just soaking in saline. According to Cilesiz and Welch (1993), dehydration especially leads to a gross effect on the optical properties of tissue⁸. During all these processes, scattering is extremely enhanced. Therefore, published data are valid only for the documented type of tissue preparation and should not be taken for granted. When needing data for certain clinical applications, a careful analysis of the specific arrangement should be performed instead of blindly relying on measurements reported elsewhere.

2.7 Questions to Chapter 2

Q2.1. A laser beam is refracted on its transition from air to corneal tissue. The angle of incidence is θ . Which angle θ'' is a potential angle of refraction?
A: $\theta'' < \theta$. B: $\theta'' = \theta$. C: $\theta'' > \theta$.

Q2.2. A biological tissue has the optical albedo $a = 0.9$. Its coefficients of absorption and scattering are α and α_s , respectively. Which is correct?
A: $\alpha = 0.9\alpha_s$. B: $\alpha = 9\alpha_s$. C: $\alpha_s = 9\alpha$.

Q2.3. The diffusion approximation may be applied to a biological tissue with an optical albedo
A: $a = 0.05$. B: $a = 0.5$. C: $a = 0.95$.

Q2.4. Lambert's law describes the loss in intensity due to
A: absorption. B: scattering. C: total attenuation.

Q2.5. If g is the coefficient of anisotropy, then isotropic scattering is characterized by
A: $g = 0$. B: $g = 0.5$. C: $g = 1$.

Q2.6. The index of refraction is approximately 1.5 for most glasses at visible wavelengths. How much light is lost due to reflection, when a red laser beam accidentally exits a laboratory through an observation window?

Q2.7. A 1 mm thick optical filter has an absorption coefficient of 10 cm^{-1} for a He-Ne laser at a wavelength of 633 nm. A collinear 5 mW beam is attenuated

⁸ Theoretical and experimental results regarding the optical response of laser-irradiated tissue are summarized in the excellent book edited by Welch and van Gemert (1995).

by the filter with the beam propagation being perpendicular to the filter surface. What is the intensity of the attenuated laser beam when assuming that attenuation is due to absorption only?

Q2.8. Compare the intensities of scattered light in Rayleigh scattering for a 1 W Nd:YAG laser at a wavelength of 1064 nm and a frequency-doubled 1 W Nd:YAG laser at a wavelength of 532 nm.

Q2.9. The aortic wall has an absorption coefficient of 2.3 cm^{-1} and a scattering coefficient of 310 cm^{-1} for a He-Ne laser at a wavelength of 633 nm. What is the optical albedo of the tissue?

Q2.10. When cooking an egg “sunny side up” in a pan, the egg white turns from transparent to white at a temperature of approximately 60°C . Why?

3. Interaction Mechanisms

The variety of interaction mechanisms that may occur when applying laser light to biological tissue is manifold. Specific tissue characteristics as well as laser parameters contribute to this diversity. Most important among optical tissue properties are the coefficients of reflection, absorption, and scattering which were discussed in detail in the preceding chapter. Together, they determine the total transmission of the tissue at a certain wavelength. Thermal tissue properties – such as heat conduction and heat capacity – will be added in this chapter. On the other hand, the following parameters are given by the laser radiation itself: wavelength, exposure time, applied energy, focal spot size, energy density, and power density¹. Among these, the exposure time is a very crucial parameter when selecting a certain type of interaction, as we will find later on.

During the first decades after the invention of the laser by Maiman (1960), many studies were conducted investigating potential interaction effects by using all types of laser systems and tissue targets. Although the number of possible combinations for the experimental parameters is unlimited, mainly five categories of interaction types are classified today. These are *photochemical interactions*, *thermal interactions*, *photoablation*, *plasma-induced ablation*, and *photodisruption*. Each of these interaction mechanisms will be thoroughly discussed in this chapter. In particular, the physical principles governing these interactions are reviewed. Emphasis is placed on microscopic mechanisms controlling various processes of laser energy conversion. Each type of interaction will be introduced by common macroscopic observations including typical experimental data and/or histology of tissue samples after laser exposure. At the end of each discussion, a comprehensive summary of the specific interaction mechanism is given.

Before going into detail, an interesting result shall be stated. All these seemingly different interaction types share a single common datum: the characteristic energy density ranges from approximately 1 J/cm² to 1000 J/cm².

¹ In the literature, the terms used for radiometric parameters such as fluence, irradiance, intensity, and energy dose are often somewhat confusing. Throughout this book, the following agreements are met: *power* is expressed in units of W, *energy* in units of J, the synonyms *power density*, *intensity*, and *irradiance* in units of W/cm², the synonyms *energy density*, *fluence*, and *radiant exposure* in units of J/cm², and *energy dose* in units of J/cm³ (see also the Appendix).

This is surprising, since the power density itself varies over 15 orders of magnitude! Thus, a single parameter distinguishes and primarily controls these processes: the duration of laser exposure which is mainly identical with the interaction time itself.

A double-logarithmic map with the five basic interaction types is shown in Fig. 3.1 as found in several experiments. The ordinate expresses the applied power density or irradiance in W/cm^2 . The abscissa represents the exposure time in seconds. Two diagonals show constant energy fluences at $1 \text{ J}/\text{cm}^2$ and $1000 \text{ J}/\text{cm}^2$, respectively. According to this chart, the time scale can be roughly divided into five sections: continuous wave or exposure times $> 1 \text{ s}$ for *photochemical interactions*, 1 min down to $1 \mu\text{s}$ for *thermal interactions*, $1 \mu\text{s}$ down to 1 ns for *photoablation*, and $< 1 \text{ ns}$ for *plasma-induced ablation* and *photodisruption*. The difference between the latter two is attributed to different energy densities. They will be addressed separately in Sects. 3.4 and 3.5, since one of them is solely based on ionization, whereas the other is an associated but primarily mechanical effect.

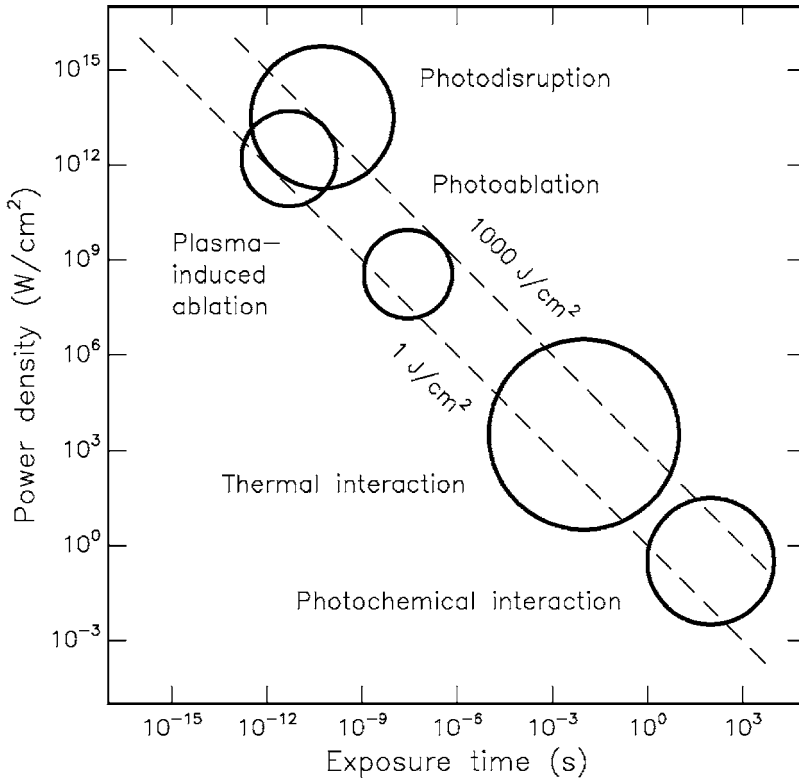


Fig. 3.1. Map of laser-tissue interactions. The circles give only a rough estimate of the associated laser parameters. Modified from Boulnois (1986)

Obviously, Fig. 3.1 proves the statement from above that the total energy density relevant for medical laser applications ranges from about 1 J/cm^2 to 1000 J/cm^2 . The reciprocal correlation between power density and exposure time clearly demonstrates that roughly the same energy density is required for any intended type of interaction. Thus, the exposure time appears to be the main parameter responsible for the variety of interaction mechanisms.

Adjacent interaction types cannot always be strictly separated. As shown in the following sections, thermal effects may also play an important role during photochemical interaction. And even ultrashort laser pulses with pulse durations shorter than 100 ps – each of them having no thermal effect – may add up to a measurable increase in temperature if applied at repetition rates higher than about 10–20 Hz, depending on the laser. These two examples reveal our need for a better understanding of each laser–tissue interaction. This task, of course, is aggravated due to the inhomogeneity of most tissues which cannot be altered. However, the basic physics involved in each interaction becomes accessible if enough data are collected to fit unknown parameters.

3.1 Photochemical Interaction

The group of photochemical interactions stems from empirical observations that light can induce chemical effects and reactions within macromolecules or tissues. One of the most popular examples was created by evolution itself: the energy release due to photosynthesis. In the field of medical laser physics, photochemical interaction mechanisms play a significant role during *photodynamic therapy (PDT)*. Frequently, *biostimulation* is also attributed to photochemical interactions, although this is not scientifically ascertained. After a detailed description of the physical background, both of these methods will be discussed in this section.

Photochemical interactions take place at very low power densities (typically 1 W/cm^2) and long exposure times ranging from seconds to continuous wave. Careful selection of laser parameters yields a radiation distribution inside the tissue that is determined by scattering. In most cases, wavelengths in the visible range (e.g. Rhodamine dye lasers at 630 nm) are used because of their efficiency and their high optical penetration depths. The latter are of importance if deeper tissue structures are to be reached.

During PDT, spectrally adapted chromophores are injected into the body. Monochromatic irradiation may then trigger selective photochemical reactions, resulting in certain biological transformations. A chromophore compound which is capable of causing light-induced reactions in other non-absorbing molecules is called a *photosensitizer*. After resonant excitation by laser irradiation, the photosensitizer performs several simultaneous or sequential decays which result in intramolecular transfer reactions. At the end of these diverse reaction channels, highly cytotoxic reactands are released causing an irreversible oxidation of essential cell structures. Thus, the main

idea of photochemical treatment is to use a chromophore receptor acting as a catalyst. Its excited states are able to store energy transferred from resonant absorption, and their deactivation leads to toxic compounds leaving the photosensitizer in its original state. Therefore, this type of interaction is also called *photosensitized oxidation*.

Most photosensitizers belong to the group of organic dyes. Their electronic states are characterized by singlet states (total electron spin momentum $s=0$) and triplet states ($s=1$). Furthermore, each electronic state is subdivided into a band of vibrational states. Intersystem crossing is permitted but is associated with an increased lifetime.

Potential reaction kinetics of the photosensitizer are listed in Table 3.1. The reaction types can be characterized by either *excitation*, *decays*, *Type I* or *Type II reactions*, and *carotenoid protection*.

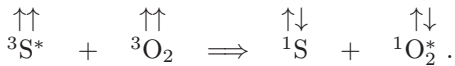
Table 3.1. Kinetics of photosensitization (S: photosensitizer, RH: substrate with H-bond, CAR: carotenoid). Modified from Boulnois (1986)

<i>Excitation</i>	
• Singlet state absorption	${}^1S + h\nu \Rightarrow {}^1S^*$
<i>Decays</i>	
• Radiative singlet decay	${}^1S^* \Rightarrow {}^1S + h\nu'$ (<i>fluorescence</i>)
• Nonradiative singlet decay	${}^1S^* \Rightarrow {}^1S$
• Intersystem crossing	${}^1S^* \Rightarrow {}^3S^*$
• Radiative triplet decay	${}^3S^* \Rightarrow {}^1S + h\nu''$ (<i>phosphorescence</i>)
• Nonradiative triplet decay	${}^3S^* \Rightarrow {}^1S$
<i>Type I reactions</i>	
• Hydrogen transfer	${}^3S^* + RH \Rightarrow SH^\bullet + R^\bullet$
• Electron transfer	${}^3S^* + RH \Rightarrow S^{\bullet-} + RH^{\bullet+}$
• Formation of hydrogen dioxide	$SH^\bullet + {}^3O_2 \Rightarrow {}^1S + HO_2^\bullet$
• Formation of superoxide anion	$S^{\bullet-} + {}^3O_2 \Rightarrow {}^1S + O_2^{\bullet-}$
<i>Type II reactions</i>	
• Intramolecular exchange	${}^3S^* + {}^3O_2 \Rightarrow {}^1S + {}^1O_2^*$
• Cellular oxidation	${}^1O_2^* + \text{cell} \Rightarrow \text{cell}_{ox}$
<i>Carotenoid protection</i>	
• Singlet oxygen extinction	${}^1O_2^* + {}^1CAR \Rightarrow {}^3O_2 + {}^3CAR^*$
• Deactivation	${}^3CAR^* \Rightarrow {}^1CAR + \text{heat}$

After the absorption of laser photons, the photosensitizer is first transferred to an excited singlet state ${}^1S^*$. Then, three potential decay channels are available: nonradiative and radiative singlet decay to the singlet ground state, and intersystem crossing to an excited triplet state. The latter, finally, may also promote to the singlet ground state by either nonradiative

or radiative triplet decay. The radiative singlet and triplet decays are called *fluorescence* and *phosphorescence*, respectively. Typical lifetimes of fluorescence are of the order of nanoseconds, whereas phosphorescence may last up to a few milliseconds or seconds. According to Foote (1968), two alternative reaction mechanisms exist for the decay of the excited triplet state which are called *Type I* and *Type II* reactions (see Table 3.1). They are characterized by either the generation of free radicals (Type I) or the transfer of excitation energy to oxygen molecules (Type II).

During Type I reactions, the triplet state next interacts with a target molecule, other than oxygen, resulting in the release of free neutral or ionized radicals. Further reaction with triplet oxygen may lead to the formation of hydrogen dioxide or superoxide anions. In Type II reactions, the triplet state of the photosensitizer directly interacts with molecular triplet oxygen $^3\text{O}_2$ which is then transferred to an excited singlet state $^1\text{O}_2^*$. During this reaction, the electronic spins are flipped in the following manner:



Excited singlet oxygen $^1\text{O}_2^*$ is very reactive, thus leading to cellular oxidation and necrosis. For instance, Weishaupt et al. (1986) identified singlet oxygen as the toxic agent in photoactivation of tumor cells. To avoid additional oxidation of healthy cells, carotin is injected after laser exposure which then promotes the toxic singlet oxygen to harmless triplet oxygen. Usually, Type I and Type II reactions take place at the same time. Which mechanism is favored mainly depends on the concentration of available triplet oxygen and appropriate target molecules.

3.1.1 Photodynamic Therapy (PDT)

Since the beginning of the 20th century, certain dyes have been known to induce photosensitizing effects as reported by von Tappeiner (1900). The first intended therapeutic application of dyes in combination with light was proposed by von Tappeiner and Jesionek (1903). Later, it was observed by Auler and Banzer (1942) that certain porphyrins have a long clearance period in tumor cells. If these dyes could somehow be transferred to a toxic state, e.g. by laser light, tumor cells could be preferentially treated. Kelly and Snell (1976) have reported on the first endoscopic application of a photosensitizer in the case of human bladder carcinoma. Today, the idea of photodynamic therapy has become one of the major pillars in the modern treatment of cancer.

Photodynamic therapy is performed as follows: first, a photosensitizer, e.g. hematoporphyrin derivative (HpD), is injected into a vein of the patient. In the case of HpD, 2.5–5 mg per kg body weight are applied. Within the next few hours, HpD is distributed among all soft tissues except the brain. The basic characteristic of a photosensitizer is that it remains inactive until irradiated. After 48–72 hours, most of it is cleared from healthy tissue. However,

its concentration in tumor cells has not decreased much even after a period of 7–10 days. Thus, HpD does not accumulate in tumor cells immediately after injection, but these cells show a longer storage ability (*affinity*) for HpD. The initial concentration is the same as in healthy cells, but the clearance is faster in the latter cells. After about three days, the concentration of HpD in tumor cells is about thirty times higher than in healthy cells.

Laser irradiation usually takes place after the third day and up to the seventh day after injection if several treatments are necessary. Within this period, tumor cells are still very sensitive and selective necrosis of tumor cells is enabled. However, many healthy tissues may retain certain constituents of HpD and are thus photosensitized, as well. Cellular effects of HpD were studied in detail by Moan and Christensen (1981) and Berns et al. (1982). The general procedure of photodynamic therapy is illustrated in Fig. 3.2.

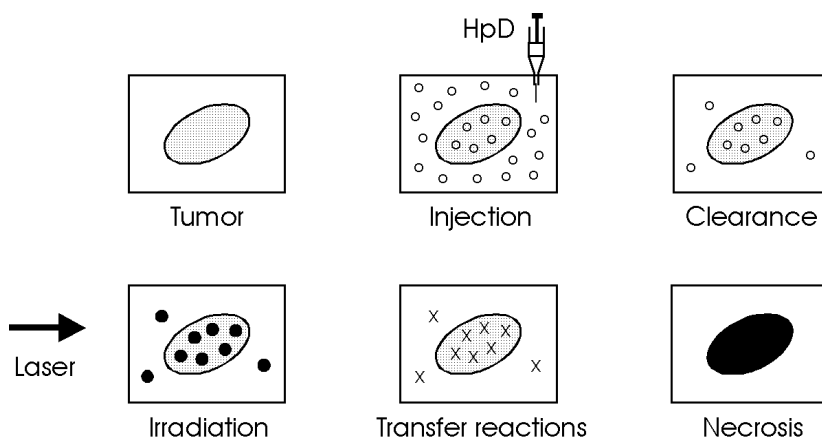


Fig. 3.2. Scheme of photodynamic therapy

Tumor treatment is the principal but not the only application field of photodynamic therapy. Malik et al. (1990) have observed bactericidal effects of laser-activated porphyrins. And recently, Wilson et al. (1993) have investigated the effect of different photosensitizers on *streptococcus sanguis*, a common bacterium of dental plaques. Some of their results are summarized in Figs. 3.3a–b. Obviously, only the combined action of photosensitizer and laser exposure significantly reduces the fraction of surviving bacteria.

One of the most commonly used photosensitizers in photodynamic therapy is a hematoporphyrin derivative called HpD. It is derived from calf blood and is a complex collection of different porphyrins, mainly

- dihematoporphyrin,
- hydroxyethylvinyl-deuteroporphyrin,
- protoporphyrin.

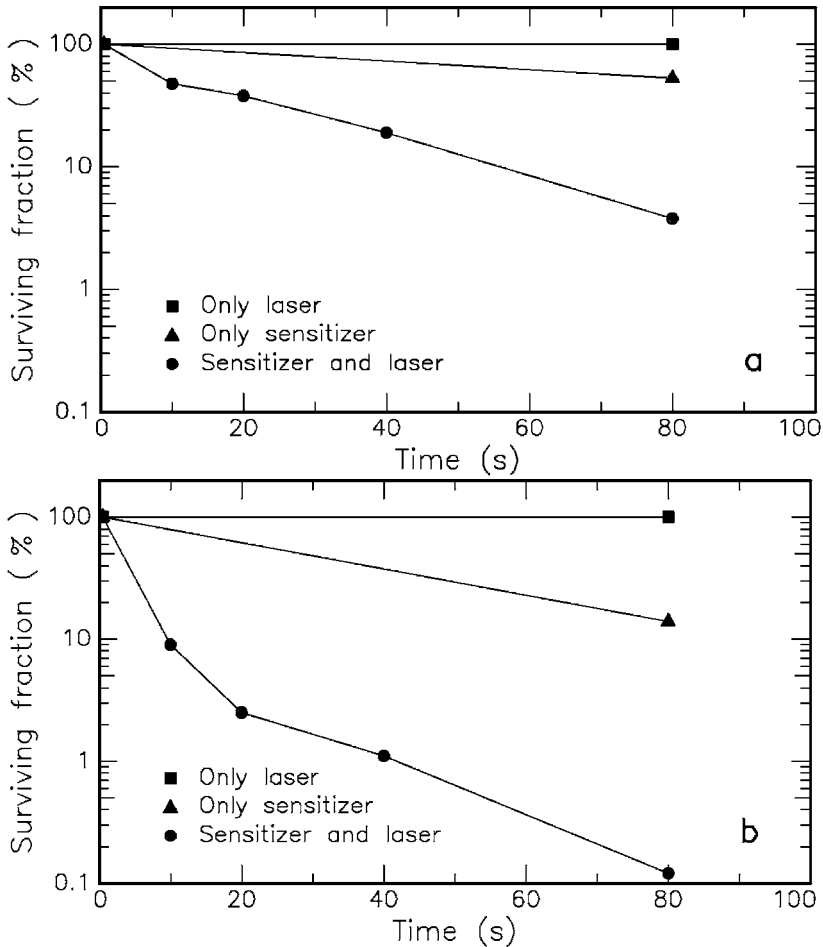


Fig. 3.3. (a) Effect of methylene blue and/or helium–neon laser (power: 7.3 mW) on the viability of streptococcus sanguis. (b) Effect of hematoporphyrin ester and/or helium–neon laser (power: 7.3 mW) on the viability of streptococcus sanguis. Data according to Wilson et al. (1993)

Among those substances, dihematoporphyrin is the active constituent in providing the photosensitizing effect. Medical application of HpD was first performed and reported by Lipson and Baldes (1961). Proprietary names for HpD include Photofrin I and Photofrin II. Both of these agents are complex chemical mixtures with the latter being enriched in the tumor-localizing fraction during PDT.

The chemical structure of dihematoporphyrin is shown in Fig. 3.4. It consists of two porphyrin rings connected by a C–O–C chain. According to Dolphin (1979), porphyrins are characterized by a high thermal stability and

a dark color (from Greek: *πορφυρα* = purple). The absorption and fluorescence spectra of HpD are shown in Fig. 3.5, whereas Fig. 3.6 illustrates the corresponding energy level diagram. The strong absorption at 350–400 nm originates from the broad excitation band 1S_2 of the dye. The relative low absorption at approximately 620–630 nm is used for clinical purposes. At this wavelength, deeper structures can be reached compared to using UV light due to the lower absorption coefficient of most tissues in the red spectrum. Detailed studies on porphyrin photosensitizers are found in the book edited by Kessel and Dougherty (1983).

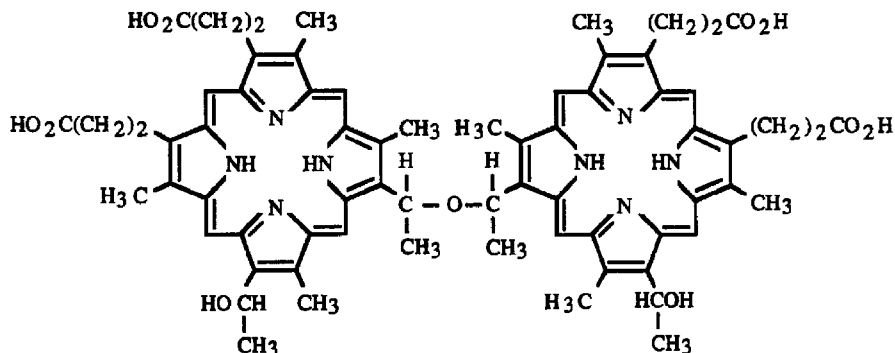


Fig. 3.4. Chemical structure of the active substance dihematoporphyrin which consists of two symmetric porphyrin rings

Primarily, the fluorescence spectrum of HpD is characterized by two peaks at 620 nm and 680 nm. They stem from the transitions $^1S_{1,0} \rightarrow ^1S_{0,0}$ and $^1S_{1,0} \rightarrow ^1S_{0,1}$, respectively. As in all macromolecules, the ground and the excited electronic states are further split into several vibrational states. After excitation, the macromolecule first relaxes to the lowest vibrational state belonging to the same excited electronic state. From there, it reaches the ground state by emitting fluorescence radiation.

The dependence of fluorescence on the concentration level of HpD is of considerable interest. It was found by Kinoshita (1988) that the emission peak at 620 nm decreases toward higher concentrations of HpD. This effect is explained by self-absorption which becomes a dominant process at concentrations higher than about 10^{-3} mol/l. Therefore, the comparison of relative fluorescence intensities is an indicator for the concentration level of HpD and, thus, for the distinction of tumor cells from healthy cells.

An even more powerful technique is given by *time-resolved fluorescence*. It was observed by Yamashita (1984) that the duration of the fluorescence decay of HpD also depends on its respective concentration level. The lowest investigated concentration of 8.4×10^{-6} mol/l yields a fluorescence decay time in the nanosecond range, whereas higher concentrations such as 8.4×10^{-3} mol/l are characterized by decays as short as a few hundred picoseconds. The time-

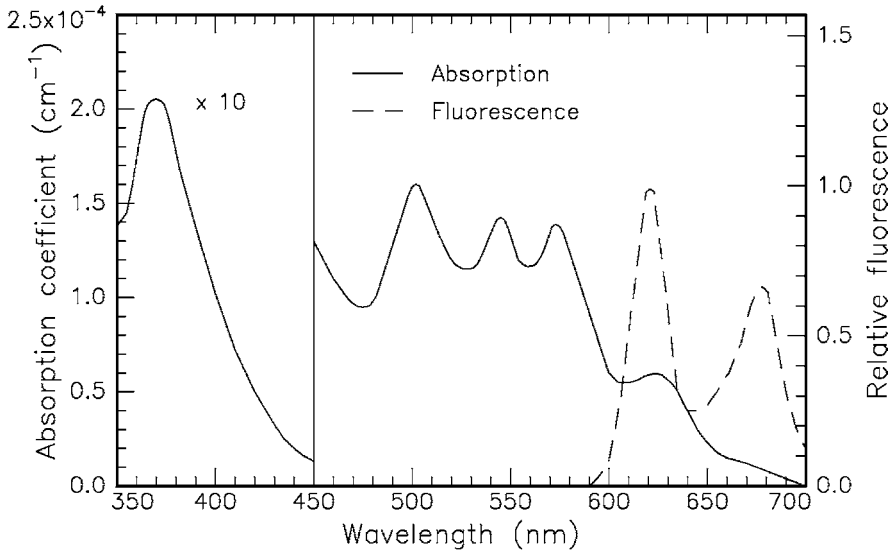


Fig. 3.5. Absorption and fluorescence spectra of hematoporphyrin derivative (HpD) dissolved in phosphate-buffered saline solution (PBS). Data according to Yamashita (1984)

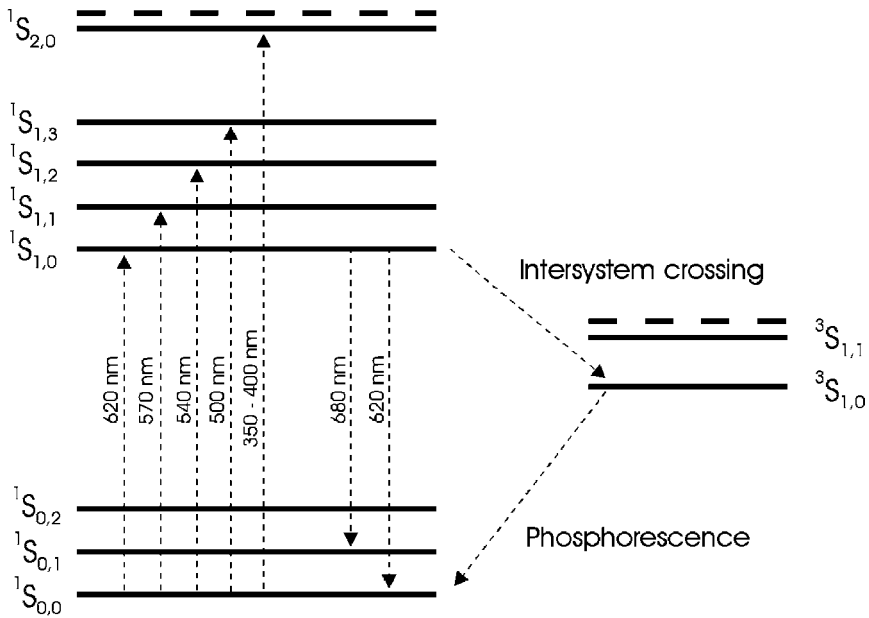


Fig. 3.6. Energy level diagram of HpD. Singlet (1S) and triplet (3S) states are shown. Dashed lines indicate higher excited states

resolved fluorescence signals are summarized in Fig. 3.7. Tumor diagnosis can thus be established by time-gated detection of the fluorescence. For instance, Fig. 3.8 illustrates the decay in fluorescence intensity of healthy cells with respect to tumor cells as found by Kinoshita (1988). Since clearance of HpD is faster in healthy cells, the corresponding decay duration is significantly longer than in tumor cells. According to Unsöld et al. (1987), the simultaneous diagnosis and therapy of tumors with photosensitizers is one of the key advantages of PDT. Extensive *in vivo* studies of time-resolved fluorescence have been performed by Schneckenburger et al. (1993).

Meanwhile, the results of several experiments and clinical applications have been collected. It was found that other photosensitizers might even be more useful than HpD. The major disadvantage of HpD is the fact that the patient needs to remain in a dark room during the first weeks of therapy. This is necessary, because HpD is distributed all over the body, and sun light or artificial light would kill healthy tissue cells, as well. According to Kessel (1987), the primary adverse reaction of photodynamic therapy relates to the photosensitization of skin. Other disadvantages of HpD are:

- since HpD absorbs very poorly in the red and near infrared spectrum, only tumors very close to the surface can be treated,
- its concentration gradient among tumor and healthy cells could be steeper,
- the production of HpD from calf blood is very expensive.

However, the initial isolation in the period between injection of HpD and laser irradiation remains and is one of the biggest problems for patients. This context also explains the injection of carotenoids immediately after laser irradiation. These agents act as a protection system on a molecular basis, because they reverse the production of singlet oxygen by means of a triplet carotenoid state (compare Table 3.1). The protective property of carotenoids has been successfully tested by Mathews-Roth (1982).

Currently, further photosensitive compounds of a so-called second generation are under investigation concerning their applicability for PDT. These are, for instance, certain groups of phthalocyanins, naphthalocyanins and phorbides (reduced porphyrins) as reported by Spikes (1986), Firey and Rodgers (1987), and Röder et al. (1990). Hopefully, a dye will soon be found that is more efficient than HpD and overcomes its major disadvantage, the need for carotenoid protection. One potential candidate is meso-tetra-hydroxyphenylchlorin (mTHPC), a chemically well-defined substance compared to HpD. In order to achieve a similar extent of tumor necrosis, it was reported by Gossner et al. (1994) that in the case of mTHPC only one fifth of the light energy is needed compared to HpD. Another interesting substance is 5-aminolaevulinic acid (ALA) which itself is not even a photosensitizer but a precursor of the endogeneous synthesis of porphyrins. According to Loh et al. (1993), it can be orally administered rather than being injected like most of the porphyrins.

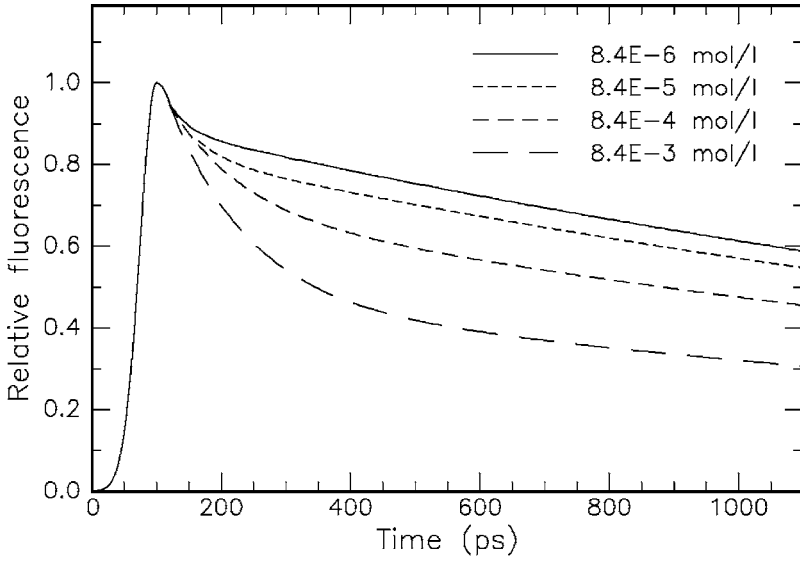


Fig. 3.7. Time-resolved fluorescence signals of HpD dissolved in phosphate-buffered saline solution (PBS). Concentrations of HpD as labeled. The corresponding decay durations of the fluorescence vary between approximately 350 ps and 2 ns. Data according to Yamashita (1984)

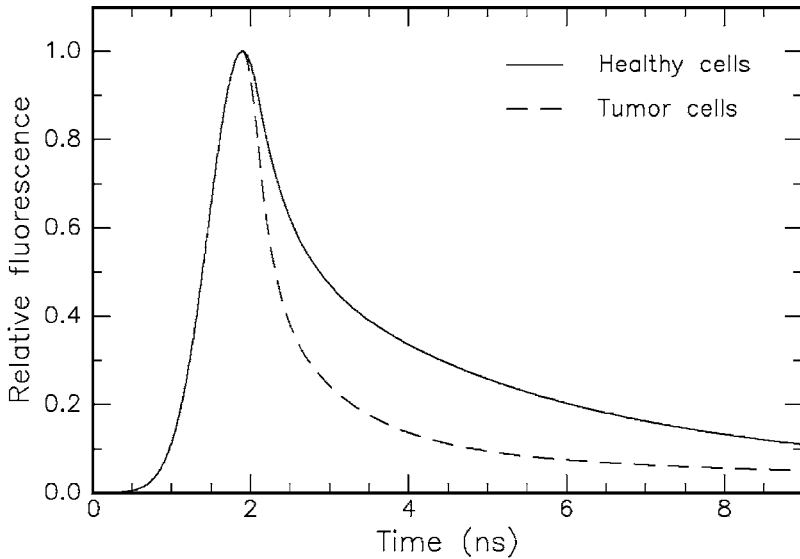


Fig. 3.8. Time-resolved HpD fluorescence of healthy cells versus tumor cells. The approximate decay durations are 2.5 ns and 1.0 ns, respectively. Data according to Kinoshita (1988)

Gossner et al. (1994) have compared the skin sensibility after application of DHE (dihematoporphyrin ester), mTHPC, and ALA. The results are graphically summarized in Fig. 3.9. The sensibility is measured in terms of a commonly used index of skin edema. It is interesting to observe that ALA induces least toxic skin damage. An increased sensibility is detectable only during the first two days after application. Although mTHPC is associated with the highest sensibility during the first week, only a slightly higher sensibility remains after the second week. This negative side effect during the first week is acceptable, though, since mTHPC is highly efficient in achieving tumor necrosis according to Gossner et al. (1994). The sensibility after application of DHE gradually decreases within the first four weeks and is still significantly enhanced at the end of this period. Thus, patients treated with DHE will have to remain in dark rooms for at least four weeks.

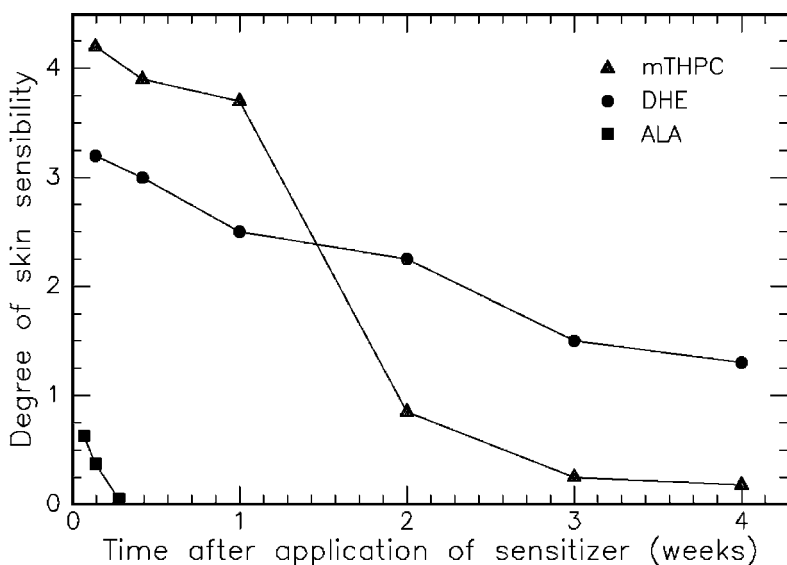


Fig. 3.9. Degree of skin sensibility after application of various photosensitizers as a function of time. Data according to Gossner et al. (1994)

The field of photodynamic tumor therapy has just begun to develop. Although much effort has already been made concerning treatment with HpD, a lot more research still needs to be done. Alternative photosensitizers such as mTHPC and ALA should be investigated in a large group of patients to further improve this type of treatment. Careful conclusions should then be drawn regarding their efficiency, indications, and potential contraindications. Finally, an approved committee has to compare all results with those obtained with other minimally invasive methods of tumor treatment such as exposure to ionizing radiation.

3.1.2 Biostimulation

Biostimulation is believed to occur at very low irradiances and to belong to the group of photochemical interactions. Unfortunately, the term *biostimulation* has not been scientifically very well defined, so far. The potential effects of extremely low laser powers (1–5 mW) on biological tissue have been a subject of controversy, since they were first claimed by the Hungarian surgeon Mester at the end of the 1960s. Wound healing and anti-inflammatory properties by red or near infrared light sources such as helium–neon lasers or diode lasers were reported. Typical energy fluences lie in the range 1–10 J/cm². In several cases, observers have noticed improvements for the patients. But in a few studies only, results could be verified by independent research groups. Moreover, contradictory results were obtained in many experiments.

The most significant studies concerning biostimulation are summarized in Table 3.2. They demonstrate the variety of potential application fields. However, often only very few patients were treated, and no clinical protocols were established. Furthermore, the success is rather doubtful, since in many of these diseases 50% of the patients are spontaneously cured even without treatment. According to Wilder-Smith (1988), the distinction from an ordinary placebo effect is thus rather difficult to perform.

Table 3.2. Biostimulative effects investigated by different studies

Observation	Target	Laser type	Reference
Hair growth	Skin	Ruby	Mester et al. (1968)
Wound healing	Skin	Ruby	Mester et al. (1969)
			Mester et al. (1971)
		He-Ne	Brunner et al. (1984)
No wound healing	Skin	He-Ne	Lyons et al. (1987)
			Hunter et al. (1984)
		Argon ion	Strube et al. (1988)
Stimulated collagen synthesis	Fibroblasts	Nd:YAG	Jongsma et al. (1983)
		He-Ne	McCaughan et al. (1985)
			Castro et al. (1983)
Suppressed collagen synthesis	Fibroblasts	Nd:YAG	Kubasova et al. (1984)
			Abergel et al. (1984)
Increased growth	Cells	Diode	Dyson and Young (1986)
		He-Cd	Lin and Chan (1984)
		He-Ne	Quickenden et al. (1993)
Suppressed growth	Cells	Diode	Kovacs et al. (1974)
			Cho and Cho (1986)
Vascularization	Oral soft tissue	Diode	Carrillo et al. (1990)
Pain relief	Teeth	He-Ne	Taube et al. (1990)
		Diode	Lundeberg et al. (1987)
No pain relief	Teeth	He-Ne	Roynesdal et al. (1993)
		Diode	

According to Karu (1987), local wound healing effects with helium–neon or diode lasers may be explained by the action of low-intensity light on cell proliferation. In the area of such injuries, conditions are usually created preventing proliferation such as low oxygen concentration or pH. The exposure to red or near infrared light might thus serve as a stimulus to increase cell proliferation. When irradiating fresh wounds, though, the effect of biostimulation is found to be minimal or even nonexistent. This observation is probably due to the fact that cell proliferation is very active in fresh wounds, and regeneration is not significantly altered by laser irradiation.

One remaining open question is, which of the characteristics of laser radiation – coherence, narrow bandwidth, polarization – is of primary importance for biostimulation? Or, in other words, does it necessarily have to be a laser or would an incoherent light source serve as well? Hence, biostimulation is still a research field with a lot of speculation involved. Usually, the controversy stems from our inability to specify the photochemical channels of potential reactions. Detailed investigations in this area and reproducible experimental results are badly needed.

3.1.3 Summary of Photochemical Interaction

- *Main idea:* using a photosensitizer acting as catalyst (only in photodynamic therapy)
- *Observations:* no macroscopic observations
- *Typical lasers:* red dye lasers, diode lasers
- *Typical pulse durations:* 1 s . . . CW
- *Typical power densities:* 0.01 . . . 50 W/cm²
- *Special applications:* photodynamic therapy, biostimulation

3.2 Thermal Interaction

The term *thermal interaction* stands for a large group of interaction types, where the increase in local temperature is the significant parameter change. Thermal effects can be induced by either CW or pulsed laser radiation. While photochemical processes are often governed by a specific reaction pathway, thermal effects generally tend to be nonspecific according to Parrish and Deutsch (1984). However, depending on the duration and peak value of the tissue temperature achieved, different effects like *coagulation*, *vaporization*, *carbonization*, and *melting* may be distinguished. In the following paragraphs, these effects shall first be visualized by selected photographs taken with either light microscopy or scanning electron microscopy (SEM). Afterwards, detailed models of heat generation, heat transport, and associated heat effects are given. Finally, the principles of laser-induced interstitial thermotherapy – a recently established treatment technique – are discussed.

Coagulation. The histologic appearance of coagulated tissue is illustrated in Figs. 3.10a–b. In one case, a sample of uterine tissue was coagulated using a CW Nd:YAG laser. In a histologic section, the coagulated area can be easily detected when staining the tissue with hematoxylin and eosin. Coagulated tissue appears significantly darker than other tissue. In the second photograph, 120 pulses from an Er:YAG laser were applied to an excised cornea. Again, the tissue was stained with hematoxylin and eosin. During the process of coagulation, temperatures reach at least 60°C, and coagulated tissue becomes necrotic as will be discussed in this section.

Vaporization. Another example of an important thermal effect is shown in Figs. 3.11a–b. A tooth was exposed to 20 pulses from an Er:YAG laser. During the ablation process, complete layers of tooth substance were removed leaving stair-like structures. This observation is attributed to the existence of so-called *striae of Retzius* which are layers with a high content of water molecules. Water strongly absorbs the Er:YAG wavelength at 2.94 μm as shown below, thus leading to vaporization within these layers. The induced increase in pressure – water tries to expand in volume as it vaporizes – leads to localized microexplosions with results as demonstrated in the enlargement in Fig. 3.11b. In the literature, vaporization is sometimes also referred to as a *thermomechanical effect* due to the pressure build-up involved. The resulting ablation is called *thermal decomposition* and must be distinguished from *photoablation* which will be described in Sect. 3.3.

Carbonization. In Fig. 3.12a, a sample of skin is shown which was exposed to a CW CO₂ laser for the purpose of treating metastases. In this case, however, too much energy was applied and carbonization occurred. Thus, the local temperature of the exposed tissue had been drastically increased. At temperatures above approximately 100°C, the tissue starts to carbonize, i.e. carbon is released, leading to a blackening in color. A similar effect is seen in Fig. 3.12b, where a tooth was exposed to a CW CO₂ laser. For medical laser applications, carbonization should be avoided in any case, since tissue already becomes necrotic at lower temperatures. Thus, carbonization only reduces visibility during surgery.

Melting. Finally, Figs. 3.13a–b show the surface of a tooth after exposure to 100 pulses from a Ho:YAG laser. In Fig. 3.13a, several cracks can be seen leaving the application spot radially. They originate from thermal stress induced by a local temperature gradient across the tooth surface. The edge of the interaction zone is shown in an enlargement in Fig. 3.13b. Melted and afterwards down-cooled tooth substance as well as gas bubbles are observed similar to solidified lava. The temperature must have reached a few hundred degrees Celsius to melt the tooth substance which mainly consists of hydroxyapatite, a chemical compound of calcium and phosphate as will be discussed in Sect. 4.2. Obviously, the pulse duration of a few microseconds is still long enough to enable a sufficient increase in temperature, since the applied repetition rate of 1 Hz is extremely low.

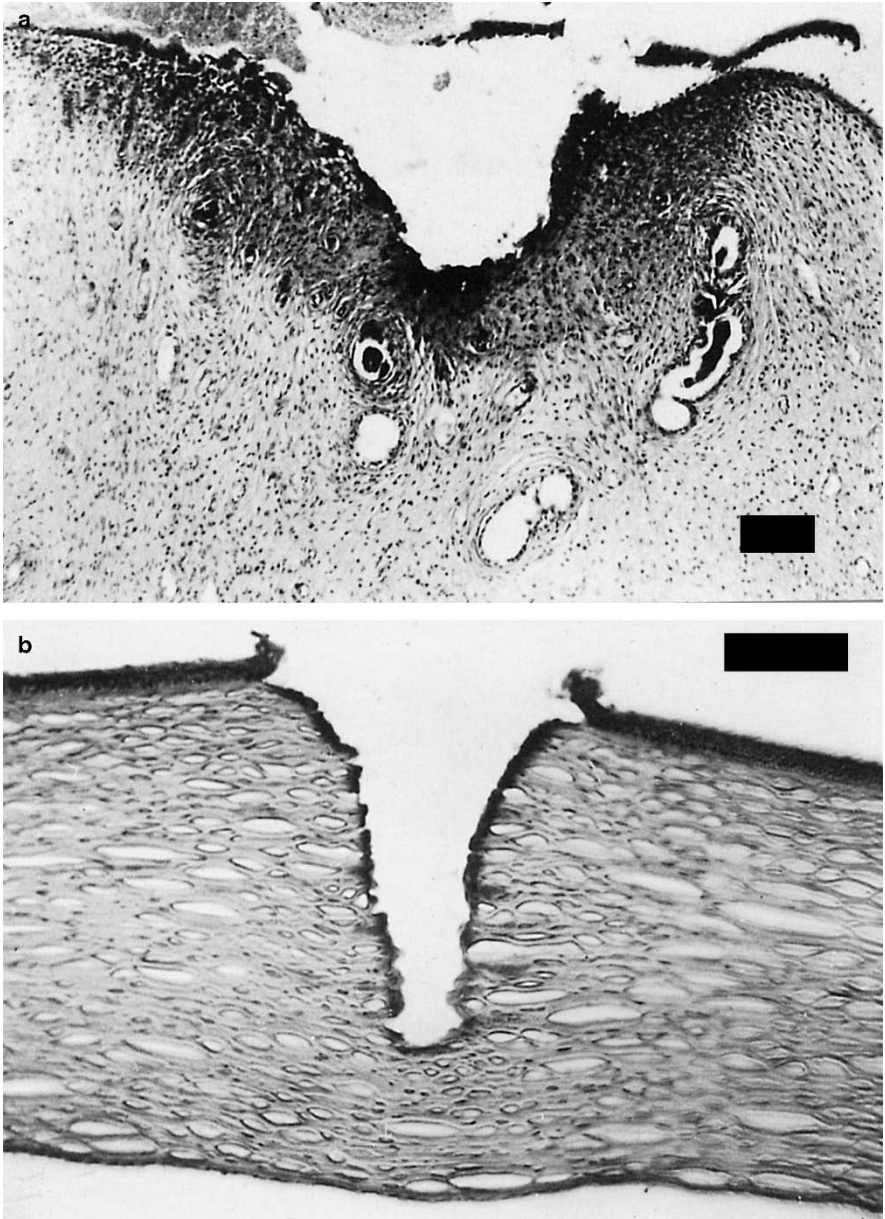


Fig. 3.10. (a) Uterine tissue of a wistar rat coagulated with a CW Nd:YAG laser (power: 10 W, bar: 80 μm). Photograph kindly provided by Dr. Kurek (Heidelberg). (b) Human cornea coagulated with 120 pulses from an Er:YAG laser (pulse duration: 90 μs , pulse energy: 5 mJ, repetition rate: 1 Hz, bar: 100 μm)

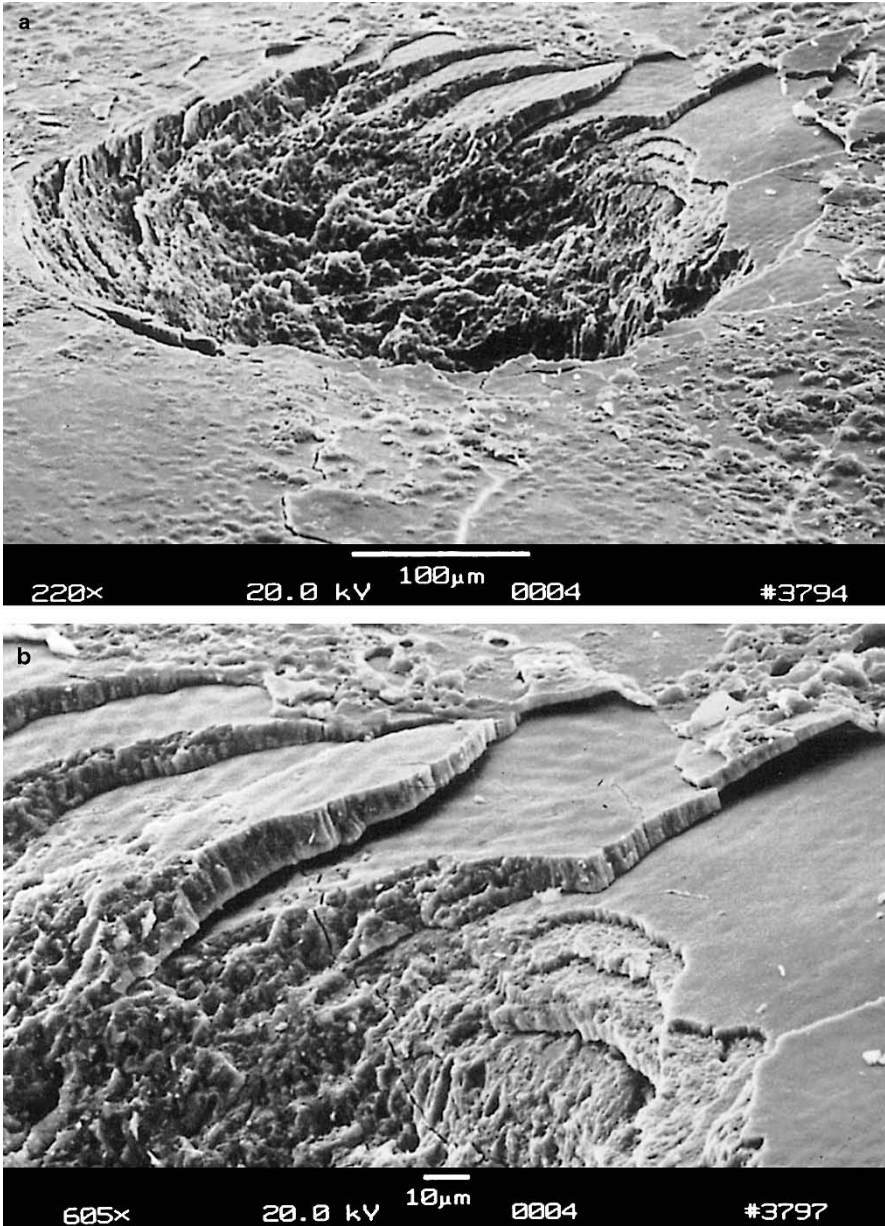


Fig. 3.11. (a) Human tooth vaporized with 20 pulses from an Er:YAG laser (pulse duration: 90 μ s, pulse energy: 100 mJ, repetition rate: 1 Hz). (b) Enlargement showing the edge of ablation

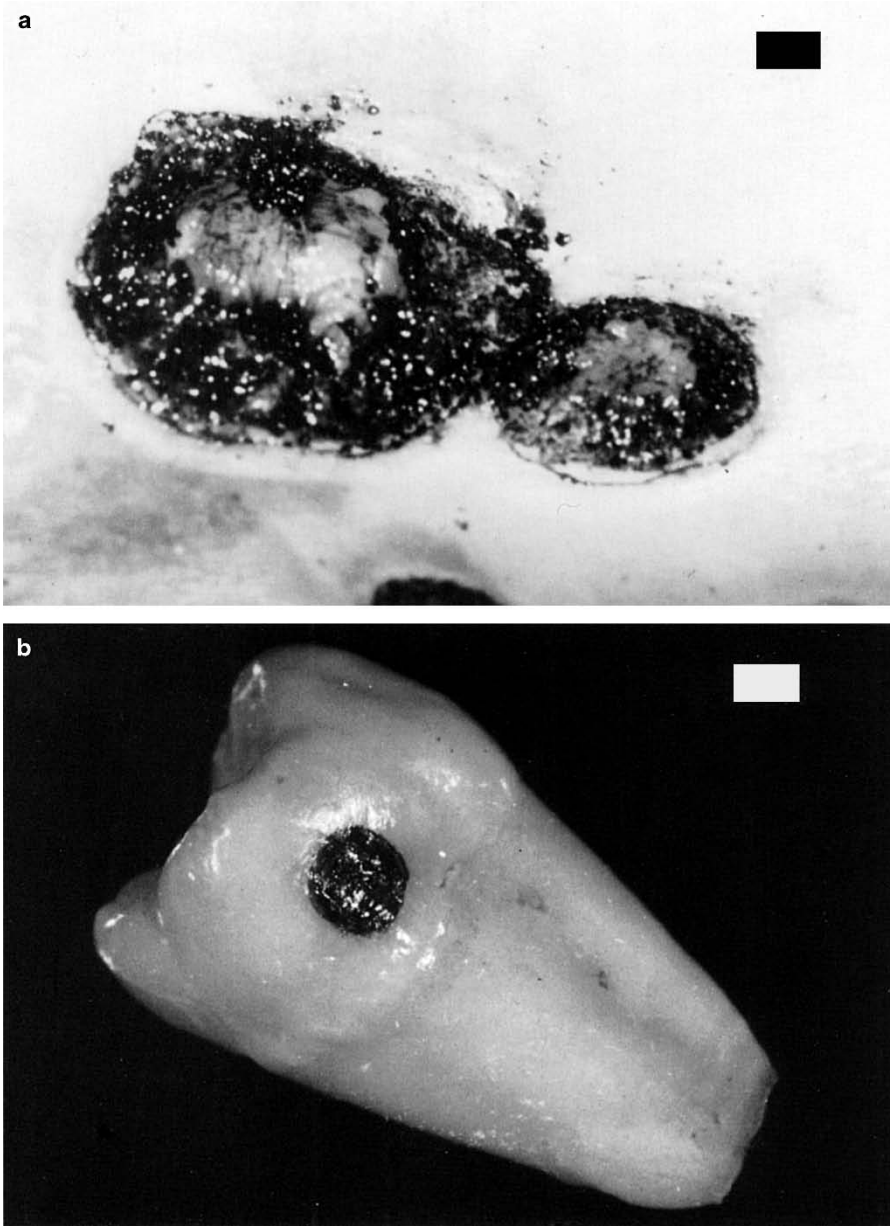


Fig. 3.12. (a) Tumor metastases on human skin carbonized with a CW CO₂ laser (power: 40 W, bar: 1 mm). Photograph kindly provided by Dr. Kurek (Heidelberg).
(b) Human tooth carbonized with a CW CO₂ laser (power: 1 W, bar: 1 mm)

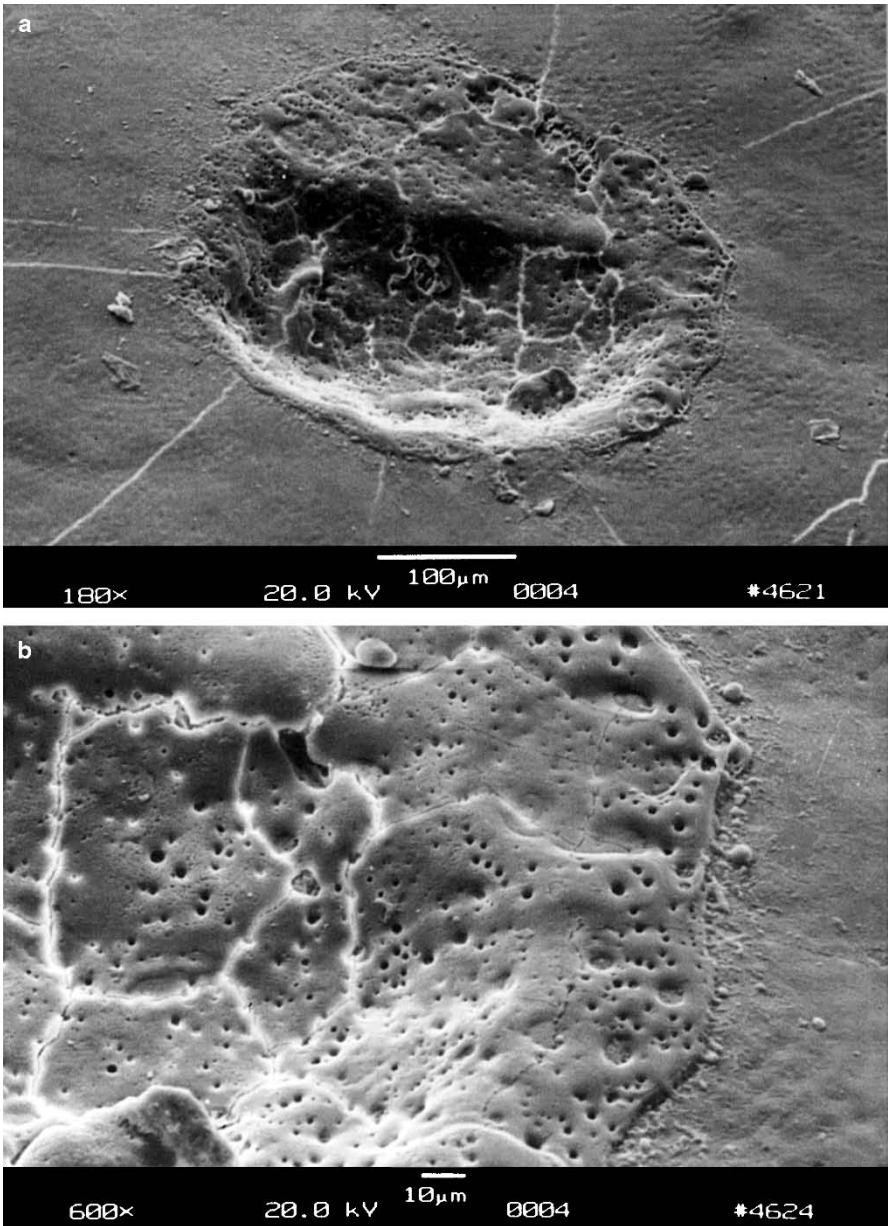


Fig. 3.13. (a) Human tooth melted with 100 pulses from a Ho:YAG laser (pulse duration: $3.8 \mu\text{s}$, pulse energy: 18 mJ, repetition rate: 1 Hz). (b) Enlargement showing the edge of the melted zone

Temperature certainly is the governing parameter of all thermal laser-tissue interactions. And, for the purpose of predicting the thermal response, a model for the temperature distribution inside the tissue must be derived. Before we start working on this task, let us first look at the basics of what happens during thermal interaction.

At the microscopic level, thermal effects have their origin in bulk absorption occurring in molecular vibration-rotation bands followed by nonradiative decay. The reaction with a target molecule A can be considered as a two-step process. First, absorption of a photon with an energy $h\nu$ promotes the molecule to an excited state A^* ; and second, inelastic collisions with some partner M of the surrounding medium lead to a deactivation of A^* and a simultaneous increase in the kinetic energy of M. Therefore, the temperature rise microscopically originates from the transfer of photon energy to kinetic energy. This two-step process can be written as

- absorption: $A + h\nu \longrightarrow A^*$,
- deactivation: $A^* + M(E_{\text{kin}}) \longrightarrow A + M(E_{\text{kin}} + \Delta E_{\text{kin}})$.

How efficient is this two-step process? To answer this question, we have to consider both steps separately. First, absorption is facilitated due to the extremely large number of accessible vibrational states of most biomolecules. Second, the channels available for deactivation and thermal decay are also numerous, because typical energies of laser photons (Er:YAG laser: 0.35 eV, Nd:YAG laser: 1.2 eV, ArF laser: 6.4 eV) exceed by far the kinetic energy of a molecule at room temperature which is only about 0.025 eV. Thus, both of these steps are highly efficient provided the duration of laser exposure is properly selected.

The spatial extent and degree of tissue damage primarily depend on magnitude, exposure time, and placement of deposited heat inside the tissue. The deposition of laser energy, however, is not only a function of *laser parameters* such as wavelength, power density, exposure time, spot size, and repetition rate. It also strongly depends on *optical tissue properties* like absorption and scattering coefficients. For the description of storage and transfer of heat, *thermal tissue properties* are of primary importance such as heat capacity and thermal conductivity.

In biological tissue, absorption is mainly due to the presence of free water molecules, proteins, pigments, and other macromolecules as discussed in Sect. 2.3. It is governed by Lambert's law which we already encountered in (2.13). The absorption coefficient strongly depends on the wavelength of the incident laser radiation. In thermal interactions, absorption by water molecules plays a significant role. Therefore, the absorption spectrum of water – one important constituent of most tissues – is plotted in Fig. 3.14. In the visible range, the absorption coefficient of water is extremely small. In this section of the spectrum and in the UV, absorption in tissue is higher than shown in Fig. 3.14, depending on the relative content of macromolecules such as melanin and hemoglobin. Toward the IR range of the spectrum, however,

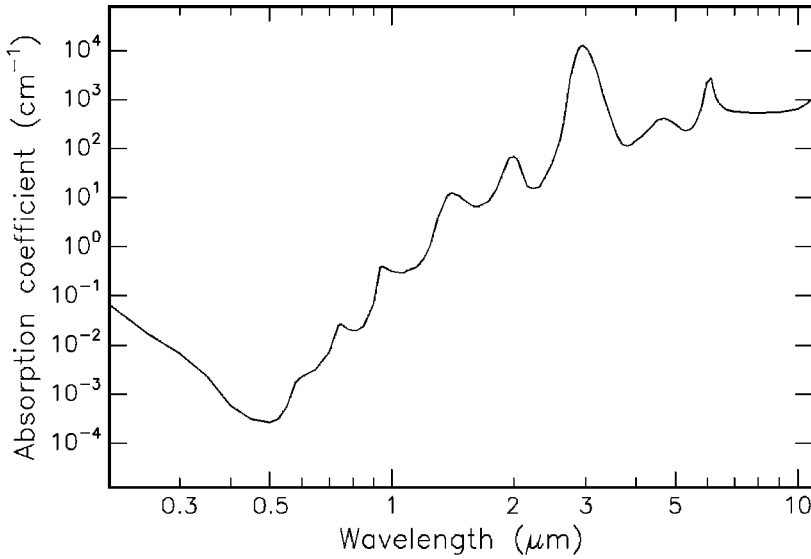


Fig. 3.14. Absorption of water. Data calculated from Hale and Query (1973)

water molecules are the dominant absorbers, since their absorption coefficient then increases by several orders of magnitude. Typical absorption coefficients α and the corresponding absorption lengths L for the most important laser wavelengths are summarized in Table 3.3. It should be borne in mind that the total attenuation in the UV is strongly enhanced by Rayleigh scattering as discussed in Sect. 2.3.

Table 3.3. Absorption coefficients α and absorption lengths L of water at different wavelengths. Data calculated from Hale and Query (1973)

Wavelength (nm)	Laser type	α (cm ⁻¹)	L (cm)
193	ArF	0.1	10
248	KrF	0.018	55
308	XeCl	0.0058	170
351	XeF	0.0023	430
514	Argon ion	0.00029	3400
633	He-Ne	0.0029	340
694	Ruby	0.0056	180
800	Diode	0.020	50
1053	Nd:YLF	0.57	1.7
1064	Nd:YAG	0.61	1.6
2120	Ho:YAG	36	0.028
2940	Er:YAG	12 000	0.00008
10600	CO ₂	860	0.001

The absorption peak at about $3\ \mu\text{m}$ – as shown in Fig. 3.14 – is of considerable interest. It originates from symmetric and asymmetric vibrational modes of water molecules as illustrated in Fig. 3.15. According to Pohl (1976), the resonance frequencies of these vibrational modes are $1.08 \times 10^{14}\ \text{Hz}$ and $1.13 \times 10^{14}\ \text{Hz}$, respectively. These correspond to a wavelength close to $3\ \mu\text{m}$, thereby explaining the high absorption peak at this wavelength. Thus, the family of Er^{3+} doped lasers (Er:YAG at $2.94\ \mu\text{m}$, Er:YLF at $2.8\ \mu\text{m}$, and Er:YSGG at $2.79\ \mu\text{m}$) is a typical representative of thermally acting lasers. A similar argument applies for the wavelength of the Ho:YAG laser at $2.12\ \mu\text{m}$ which also matches an absorption peak of water.

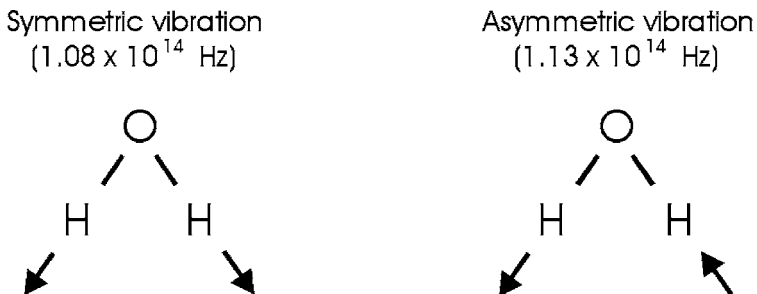


Fig. 3.15. Vibrational oscillations of water molecules

So far, we have encountered the basic origins of thermal effects, and we will now proceed to setting up a model explaining the basic physics involved. In order to derive a model which describes thermal effects quantitatively, several input parameters have to be taken into account. They are summarized in a flow chart as shown in Fig. 3.16.

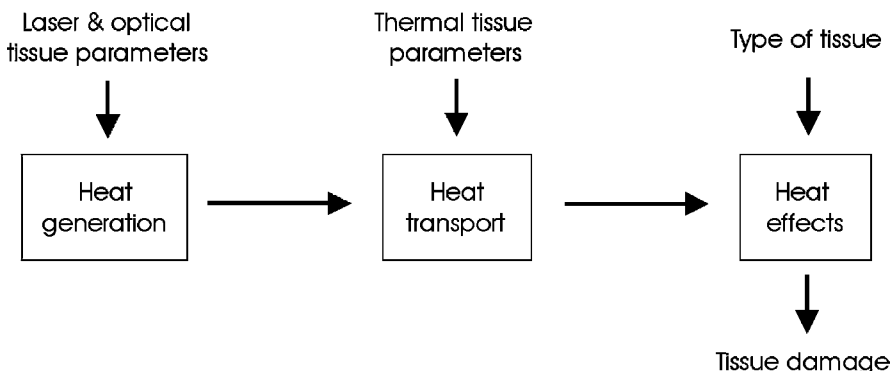


Fig. 3.16. Flow chart with important parameters for modeling thermal interaction

Heat generation is determined by laser parameters and optical tissue properties – primarily irradiance, exposure time, and the absorption coefficient – with the absorption coefficient itself being a function of the laser wavelength. *Heat transport* is solely characterized by thermal tissue properties such as heat conductivity and heat capacity. *Heat effects*, finally, depend on the type of tissue and the temperature achieved inside the tissue.

We assume that a slab of tissue is exposed in air to a Gaussian-shaped laser beam as illustrated in Fig. 3.17. For the sake of simplicity, a cylindrical geometry is chosen with z denoting the optical axis, and r the distance from this axis. Then, the amplitude of the electric field and the corresponding intensity inside the tissue are given by

$$\mathbf{E}(r, z, t) = \mathbf{E}_0 \exp\left(-\frac{r^2}{w^2} - \frac{\alpha z}{2}\right) \exp\left(-\frac{4t^2}{\tau^2}\right), \quad (3.1)$$

$$I(r, z, t) = I_0 \exp\left(-\frac{2r^2}{w^2} - \alpha z\right) \exp\left(-\frac{8t^2}{\tau^2}\right), \quad (3.2)$$

where \mathbf{E}_0 and I_0 are the incident values of electric field and intensity, respectively, w is the beam waist, α is the absorption coefficient, and τ is the pulse duration. From (3.2), we obtain that either at $r = w$ or at $t = \tau/2$ the intensity is cut down to $1/e^2$ of its incident value. The incident values \mathbf{E}_0 and I_0 are related to each other by the basic electrodynamic equation

$$I_0 = \frac{1}{2} \varepsilon_0 c \mathbf{E}_0^2,$$

where ε_0 is the dielectric constant, and c is the speed of light. Scattering inside the tissue is neglected in a first approximation. Calculations taking scattering effects into account will be found at the end of this section.

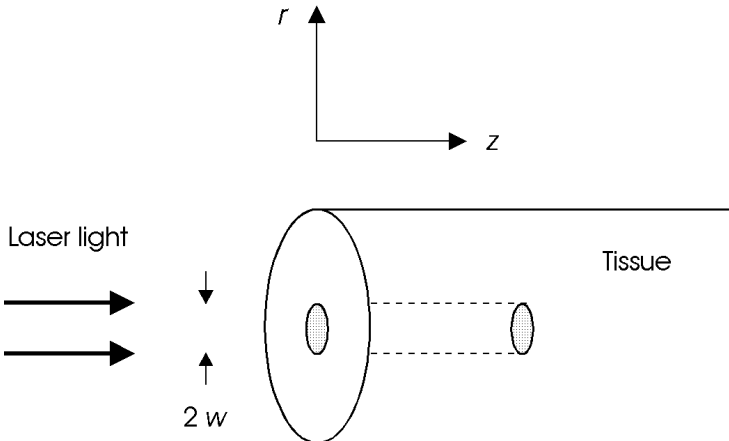


Fig. 3.17. Geometry of tissue irradiation

3.2.1 Heat Generation

By means of the two-step process as described above, heat is generated inside the tissue during laser exposure. Deposition of heat in tissue is due only to light that is absorbed in the tissue. For a light flux in the z -direction in a nonscattering medium, the local heat deposition per unit area and time in a thickness Δz is given by

$$S(r, z, t) = \frac{I(r, z, t) - I(r, z + \Delta z, t)}{\Delta z} \quad \text{in units of } \frac{\text{W}}{\text{cm}^3} .$$

And, as Δz approaches zero,

$$S(r, z, t) = - \frac{\partial I(r, z, t)}{\partial z} .$$

Therefore, under all circumstances, heat deposition is determined by

$$S(r, z, t) = \alpha I(r, z, t) . \quad (3.3)$$

Thus, the heat source $S(r, z, t)$ inside the exposed tissue is a function of the absorption coefficient α and the local intensity $I(r, z, t)$. Since α is strongly wavelength-dependent, the same applies for S . If phase transitions (vaporization, melting) or tissue alterations (coagulation, carbonization) do not occur, an alteration in heat content dQ induces a linear change in temperature dT according to a basic law of thermodynamics

$$dQ = m c dT , \quad (3.4)$$

where m is the tissue mass, and c is the specific heat capacity expressed in units of $\text{kJ kg}^{-1} \text{K}^{-1}$. According to Takata et al. (1977), for most tissues, a good approximation is given by

$$c = \left(1.55 + 2.8 \frac{\rho_w}{\rho} \right) \frac{\text{kJ}}{\text{kg K}} ,$$

where ρ is the tissue density expressed in units of kg/m^3 , and ρ_w is its water content expressed in units of kg/m^3 . In the case of water, i.e. $\rho_w = \rho$, the last relation reduces to

$$c = 4.35 \frac{\text{kJ}}{\text{kg K}} \quad \text{at } T = 37^\circ\text{C} .$$

3.2.2 Heat Transport

Within a closed physical system, the relationship between temperature and heat content is described by (3.4). In real laser-tissue interactions, however, there are losses of heat to be taken into account, as well. They are based on either *heat conduction*, *heat convection*, or *heat radiation*. Usually, the latter two can be neglected for most types of laser applications. One typical example

of heat convection in tissue is heat transfer due to blood flow. The perfusion rates of some human organs are summarized in Table 3.4. Due to the low perfusivity of most tissues, however, heat convection is negligible in a first approximation. Only during long exposures and in special cases such as laser-induced interstitial thermotherapy (LITT) does it play a significant role and should be considered by adding a negative heat loss S_{loss} to the source term S . Heat radiation is described by the *Stefan–Boltzmann law* which states that the radiated power is related to the fourth power of temperature. Due to the moderate temperatures achieved in most laser–tissue interactions, heat radiation can thus often be neglected.

Table 3.4. Blood perfusion rates of some selected human organs. Data according to Svaasand (1985)

Tissue	Perfusion rate (ml min ⁻¹ g ⁻¹)
Fat	0.012–0.015
Muscle	0.02–0.07
Skin	0.15–0.5
Brain	0.46–1.0
Kidney	≈ 3.4
Thyroid gland	≈ 4.0

Heat conduction, though, is a considerable heat loss term and is the primary mechanism by which heat is transferred to unexposed tissue structures. The heat flow \mathbf{j}_Q is proportional to the temperature gradient according to the general diffusion equation²

$$\mathbf{j}_Q = -k \nabla T . \quad (3.5)$$

Herein, the constant k is called *heat conductivity* and is expressed in units of W m⁻¹ K⁻¹. According to Takata et al. (1977), k can be approximated by

$$k = \left(0.06 + 0.57 \frac{\varrho_w}{\varrho} \right) \frac{\text{W}}{\text{m K}} .$$

In the case of water, i.e. $\varrho_w = \varrho$, the last relation reduces to

$$k = 0.63 \frac{\text{W}}{\text{m K}} \quad \text{at } T = 37^\circ\text{C} .$$

The dynamics of the temperature behavior of a certain tissue type can also be expressed by a combination of the two parameters k and c . It is called *temperature conductivity* and is defined by

² This equation is the analog to the electrodynamic equation $\mathbf{j} = -\sigma \nabla \phi$, where \mathbf{j} is the electric current density, σ is the electric conductivity, and ϕ is the electric potential.

$$\kappa = \frac{k}{\rho c} \quad \text{in units of } \frac{\text{m}^2}{\text{s}} . \quad (3.6)$$

The value of κ is approximately the same for liquid water and most tissues – about $1.4 \times 10^{-7} \text{ m}^2/\text{s}$ according to Boulnois (1986) – since a decrease in heat conductivity due to a lower water content is usually compensated by a parallel decrease in heat capacity.

With these mathematical prerequisites, we are able to derive the general heat conduction equation. Our starting point is the *equation of continuity* which states that the temporal change in heat content per unit volume³, \dot{q} , is determined by the divergence of the heat flow \mathbf{j}_Q :

$$\text{div } \mathbf{j}_Q = -\dot{q} . \quad (3.7)$$

Inserting (3.7) into (3.4) leads to

$$\dot{T} = \frac{1}{mc} \dot{Q} = \frac{1}{\rho c} \frac{\dot{Q}}{V} = \frac{1}{\rho c} \dot{q} = -\frac{1}{\rho c} \text{div } \mathbf{j}_Q . \quad (3.8)$$

The other important basic equation is the diffusion equation, i.e. (3.5). Its combination with (3.8) yields

$$\dot{T} = \kappa \Delta T , \quad (3.9)$$

where Δ is the *Laplace operator*. This is the homogeneous *heat conduction equation* with the temperature conductivity as defined by (3.6). With an additional heat source S like the absorption of laser radiation, (3.8) and (3.9) turn into the inhomogeneous equations

$$\dot{T} = -\frac{1}{\rho c} (\text{div } \mathbf{j}_Q - S) , \quad (3.10)$$

$$\dot{T} = \kappa \Delta T + \frac{1}{\rho c} S . \quad (3.11)$$

Next, we want to solve the homogeneous part of the heat conduction equation, i.e. (3.9). It describes the decrease in temperature after laser exposure due to heat diffusion. In cylindrical coordinates, (3.9) can be expressed by

$$\dot{T} = \kappa \left(\frac{\partial^2}{\partial r^2} + \frac{1}{r} \frac{\partial}{\partial r} + \frac{\partial^2}{\partial z^2} \right) T , \quad (3.12)$$

with the general solution

$$T(r, z, t) = T_0 + \frac{\chi_0}{(4\pi\kappa t)^{3/2}} \exp\left(-\frac{r^2 + z^2}{4\kappa t}\right) , \quad (3.13)$$

³ Note that q in (3.7) is expressed in units of J/cm^3 , while Q is in units of J . We thus obtain according to *Gauss' theorem*: $\int dV \text{div } \mathbf{j}_Q = \oint d\mathbf{f} \mathbf{j}_Q = -\dot{Q}$.

where T_0 is the initial temperature, and χ_0 is an integration constant. The proof is straightforward. We simply assume that (3.13) represents a correct solution to (3.12) and find

$$\begin{aligned}\dot{T} &= -\frac{3}{2} \frac{T - T_0}{t} + \frac{r^2 + z^2}{4\kappa t^2} (T - T_0), \\ \frac{\partial^2}{\partial r^2} T &= \frac{\partial}{\partial r} \left(-2r \frac{T - T_0}{4\kappa t} \right) = -\frac{T - T_0}{2\kappa t} + 4r^2 \frac{T - T_0}{16\kappa^2 t^2}, \\ \frac{1}{r} \frac{\partial}{\partial r} T &= -\frac{T - T_0}{2\kappa t}, \\ \frac{\partial^2}{\partial z^2} T &= \frac{\partial}{\partial z} \left(-2z \frac{T - T_0}{4\kappa t} \right) = -\frac{T - T_0}{2\kappa t} + 4z^2 \frac{T - T_0}{16\kappa^2 t^2}.\end{aligned}$$

Hence,

$$\begin{aligned}\kappa \Delta T &= -\frac{T - T_0}{2t} + r^2 \frac{T - T_0}{4\kappa t^2} - \frac{T - T_0}{2t} - \frac{T - T_0}{2t} + z^2 \frac{T - T_0}{4\kappa t^2}, \\ \kappa \Delta T &= -\frac{3}{2} \frac{T - T_0}{t} + \frac{r^2 + z^2}{4\kappa t^2} (T - T_0) = \dot{T}, \quad \text{q.e.d.}\end{aligned}$$

The solution to the inhomogeneous heat conduction equation, (3.11) strongly depends on the temporal and spatial dependences of $S(r, z, t)$. Usually, it is numerically evaluated assuming appropriate initial value and boundary conditions. Nevertheless, an analytical solution can be derived if the heat source function $S(r, z, t)$ is approximated by a delta-function

$$S(r, z, t) = S_0 \delta(r - r_0) \delta(z - z_0) \delta(t - t_0).$$

For the sake of simplicity, we assume that the heat conduction parameters are isotropic⁴. Thus,

$$S(z, t) = S_0 \delta(z - z_0) \delta(t - t_0).$$

In this case, the solution can be expressed by a one-dimensional *Green's function* which is given by

$$G(z - z_0, t - t_0) = \frac{1}{\sqrt{4\pi\kappa(t - t_0)}} \exp \left[-\frac{(z - z_0)^2}{4\kappa(t - t_0)} \right]. \quad (3.14)$$

By means of this function, the general solution for a spatially and temporally changing irradiation is determined by

$$T(z, t) = \frac{1}{\rho c} \int_0^t \int_{-\infty}^{+\infty} S(z', t') G(z - z', t - t') dz' dt'. \quad (3.15)$$

⁴ A valuable theoretical approach to the three-dimensional and time-dependent problem is found in the paper by Halldorsson and Langerholm (1978).

The spatial extent of heat transfer is described by the time-dependent *thermal penetration depth*

$$z_{\text{therm}}(t) = \sqrt{4\kappa t} . \quad (3.16)$$

The term “penetration depth” originates from the argument of the exponential function in (3.14), since (3.16) turns into

$$\frac{z_{\text{therm}}^2(t)}{4\kappa t} = 1 .$$

Thus, $z_{\text{therm}}(t)$ is the distance in which the temperature has decreased to $1/e$ of its peak value. In Table 3.5, the relationship expressed by (3.16) is evaluated for water ($\kappa = 1.4 \times 10^{-7} \text{ m}^2/\text{s}$). We keep in mind that heat diffuses in water to approximately $0.7 \mu\text{m}$ within $1 \mu\text{s}$.

Table 3.5. Thermal penetration depths of water

Time t	Thermal penetration depth $z_{\text{therm}}(t)$
1 μs	0.7 μm
10 μs	2.2 μm
100 μs	7 μm
1 ms	22 μm
10 ms	70 μm
100 ms	0.22 mm
1 s	0.7 mm

For thermal decomposition of tissues, it is important to adjust the duration of the laser pulse in order to minimize thermal damage to adjacent structures. By this means, the least possible necrosis is obtained. The scaling parameter for this time-dependent problem is the so-called *thermal relaxation time* according to Hayes and Wolbarsht (1968) and Wolbarsht (1971). It is obtained by equating the optical penetration depth L as defined by (2.16) to the thermal penetration depth z_{therm} , hence

$$L = \sqrt{4\kappa\tau_{\text{therm}}} , \quad (3.17)$$

where τ_{therm} is the thermal relaxation time. One might argue the significance of τ_{therm} , because it is a theoretically constructed parameter. During thermal decomposition, however, τ_{therm} becomes very important, since it measures the thermal susceptibility of the tissue. This shall be explained by the following consideration: for laser pulse durations $\tau < \tau_{\text{therm}}$, heat does not even diffuse to the distance given by the optical penetration depth L . Hence, thermal damage of nondecomposed tissue is negligible. For $\tau > \tau_{\text{therm}}$, heat can diffuse to a multiple of the optical penetration depth, i.e. thermal damage of tissue adjacent to the decomposed volume is possible.

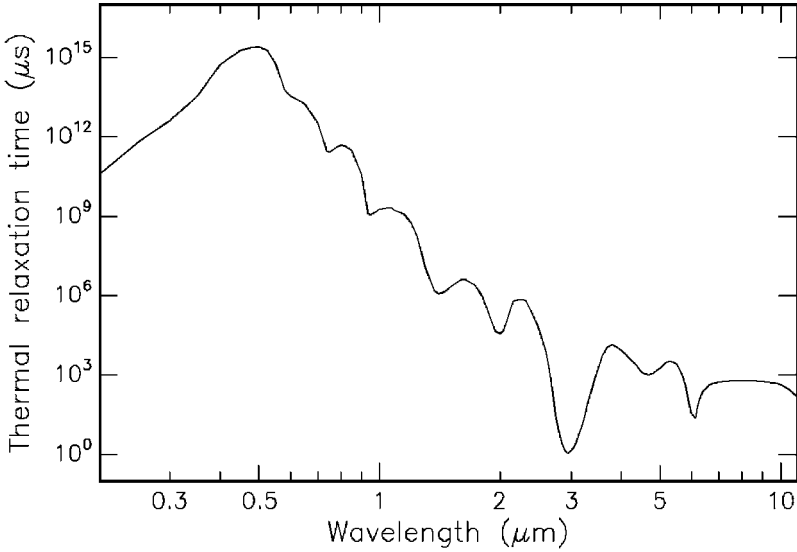


Fig. 3.18. Thermal relaxation times of water

Because of (3.17), the wavelength-dependence of L^2 is transferred to τ_{therm} . In Fig. 3.18, thermal relaxation times of water are shown as calculated from Fig. 3.14 and (3.17). We find that the shortest thermal relaxation time of approximately $1 \mu\text{s}$ occurs at the absorption peak of water near $3 \mu\text{m}$. We may thus conclude that laser pulse durations $\tau < 1 \mu\text{s}$ are usually⁵ not associated with thermal damage. This statement is also referred to as the “ $1 \mu\text{s}$ rule”.

- *Case I:* $\tau < 1 \mu\text{s}$. For nano- or picosecond pulses, heat diffusion during the laser pulse is negligible. If, in addition, we make the simplifying assumption that the intensity is constant during the laser pulse, we obtain from (3.3) that

$$S = \alpha I_0 .$$

For a quantitative relationship $T(t)$ at the tissue surface ($r = z = 0$), we may write

$$T = \left\{ \begin{array}{ll} T_0 + \frac{\alpha I_0}{\rho c} t & \text{for } 0 \leq t \leq \tau \\ T_0 + T_{\text{max}} \left(\frac{\tau}{t}\right)^{3/2} & \text{for } t > \tau \end{array} \right\} , \quad (3.18)$$

where T_{max} is the maximum increase in temperature given by

$$T_{\text{max}} = \frac{\alpha I_0}{\rho c} \tau \quad \text{at } t = \tau .$$

⁵ Laser pulses shorter than $1 \mu\text{s}$ can also lead to thermal effects if they are applied at a high repetition rate as discussed later in this section.

In Fig. 3.19, the temporal evolution of temperature in the pigment epithelium of the retina is shown according to (3.18). By neglecting heat diffusion during the short laser pulse, the temperature first increases linearly with respect to time. After the laser pulse, i.e. $t > \tau$, it decreases according to $t^{-3/2}$ as determined by the solution to the homogeneous heat conduction equation. The thermally damaged zone is shorter than the optical absorption length. Thus, thermal damage to adjacent tissue can be kept small if a wavelength is selected that is strongly absorbed by the tissue. In the case of tissues with a high water content, Er:YAG and Er:YSGG lasers are potential candidates for this task. However, only a few groups like Andreeva et al. (1986), Eichler et al. (1992), and Pelz et al. (1994) have reported on mode locking of these lasers. But their operation is not yet stable enough for clinical applications. Alternatives might soon arise due to recent advances in the development of tunable IR lasers such as the optical parametric oscillator (OPO) and the free electron laser (FEL).

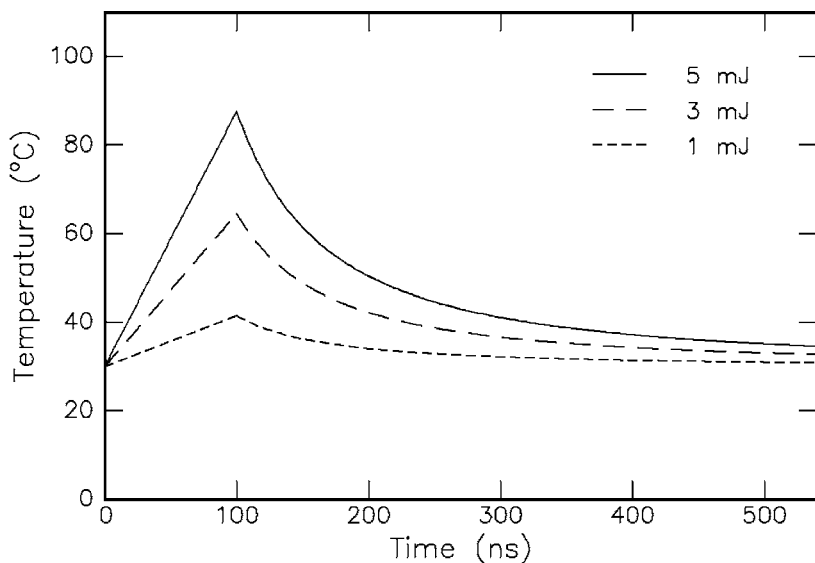


Fig. 3.19. Temporal evolution of temperature in the pigment epithelium of the retina during and after exposure to a short laser pulse ($\tau = 100$ ns, beam diameter: 2 mm, pulse energy: as labeled, $T_0 = 30^\circ\text{C}$, $\alpha = 1587\text{ cm}^{-1}$, $\rho = 1.35\text{ g cm}^{-3}$, and $c = 2.55\text{ J g}^{-1}\text{ K}^{-1}$). Tissue parameters according to Hayes and Wolbarsht (1968) and Weinberg et al. (1984)

- *Case II:* $\tau > 1\ \mu\text{s}$. For pulse durations during which heat diffusion is considerable, the thermally damaged zone is significantly broadened. In this case, the solution to the inhomogeneous heat conduction equation cannot be given analytically but must be derived numerically, for instance by using the methods of *finite differences* and *recursion algorithms*. This procedure

becomes necessary because heat diffusion during the laser pulse can no longer be neglected. Thus, for this period of time, temperature does not linearly increase as assumed in (3.18) and Fig. 3.19. Detailed simulations were performed by Weinberg et al. (1984) and Roggan and Müller (1993). One example is found in Fig. 3.24 during the discussion of laser-induced interstitial thermotherapy.

A high repetition rate ν_{rep} of the laser pulses can evoke an additional increase in temperature if the rate of heat transport is less than the rate of heat generation. The dependence of temperature on repetition rate of the laser pulses was modeled by van Gemert and Welch (1989). The significance of the repetition rate becomes evident when looking at Figs. 3.20a–b. In this case, 1000 pulses from a picosecond Nd:YLF laser were focused on the same spot of a human tooth at a repetition rate of 1 kHz. Although, usually such short pulses do not evoke any thermal effect as discussed above, radial cracking and melting obviously occurred at the surface of the tooth. In particular, the enlargement shown in Fig. 3.20b demonstrates that the chemical compounds of the tooth had melted and recrystallized in a cubic structure. Thus, the temperature achieved must have reached a few hundred °C due to insufficient heat transport.

In order to get a basic feeling for typical laser parameters, the following very simple calculations might be very useful. We assume that a pulse energy of $3 \mu\text{J}$ is absorbed within a tissue volume of $1000 \mu\text{m}^3$ which contains 80% water. The amount of water in the specified volume is equal to $8 \times 10^{-10} \text{ cm}^{-3}$ or $8 \times 10^{-10} \text{ g}$, respectively. There are now three steps to be taken into account when aiming for a rough approximation of the final temperature. First, energy is needed to heat the tissue up to 100°C . Second, energy is transferred to vaporization heat. And third, the remaining energy leads to a further increase in temperature of the water vapor.

– Step 1: $37^\circ\text{C} \rightarrow 100^\circ\text{C}$ (assumed body temperature: 37°C)

$$Q_1 = mc\Delta T = 8 \times 10^{-10} \text{ g } 4.3 \frac{\text{kJ}}{\text{kg } ^\circ\text{C}} 63^\circ\text{C} = 2.2 \times 10^{-7} \text{ J.}$$

– Step 2: Vaporization at 100°C

$$Q_2 = mQ_{\text{vap}} = 8 \times 10^{-10} \text{ g } 2253 \frac{\text{kJ}}{\text{kg}} = 1.8 \times 10^{-6} \text{ J.}$$

– Step 3: $100^\circ\text{C} \rightarrow T_{\text{fin}}$

$$Q_3 = 3 \mu\text{J} - Q_1 - Q_2 = 0.98 \mu\text{J},$$

$$T_{\text{fin}} = 100^\circ\text{C} + \frac{Q_3}{mc} = 100^\circ\text{C} + \frac{0.98 \mu\text{J}}{8 \times 10^{-10} \text{ g } 4.3 \text{ kJ } (\text{kg } ^\circ\text{C})^{-1}} \simeq 385^\circ\text{C}.$$

Thus, the resulting temperature is approximately 385°C .

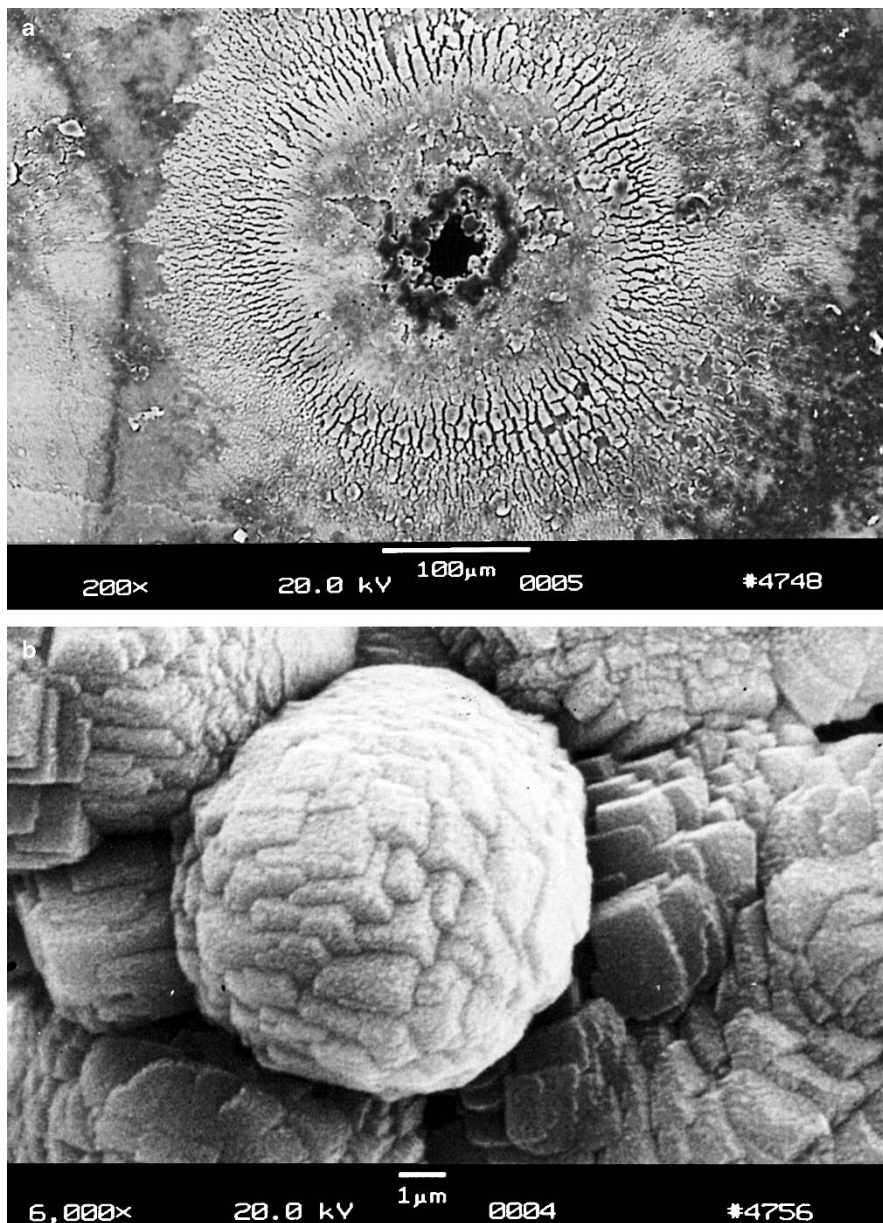


Fig. 3.20. (a) Hole in tooth created by focusing 1000 pulses from a Nd:YLF laser on the same spot (pulse duration: 30 ps, pulse energy: 1 mJ, repetition rate: 1 kHz). (b) Enlargement showing cubic recrystallization in form of plasma sublimations. Reproduced from Niemz (1994a). © 1994 Springer-Verlag

3.2.3 Heat Effects

The model developed above usually predicts the spatial and temporal distribution of temperature inside tissue very well if an appropriate initial value and boundary conditions are chosen. This, however, is not always an easy task. In general, though, approximate values of achievable temperatures can often be estimated. Therefore, the last topic in our model of thermal interaction deals with biological effects related to different temperatures inside the tissue. As already stated at the beginning of this section, these can be manifold, depending on the type of tissue and laser parameters chosen. The most important and significant tissue alterations will be reviewed here.

Assuming a body temperature of 37°C , no measurable effects are observed for the next 5°C above this. The first mechanism by which tissue is thermally affected can be attributed to conformational changes of molecules. These effects, accompanied by bond destruction and membrane alterations, are summarized in the single term *hyperthermia* ranging from approximately 42 – 50°C . If such a hyperthermia lasts for several minutes, a significant percentage of the tissue will already undergo necrosis as described below by *Arrhenius' equation*. Beyond 50°C , a measurable reduction in enzyme activity is observed, resulting in reduced energy transfer within the cell and immobility of the cell. Furthermore, certain repair mechanisms of the cell are disabled. Thereby, the fraction of surviving cells is further reduced.

At 60°C , denaturation of proteins and collagen occurs which leads to coagulation of tissue and necrosis of cells. The corresponding macroscopic response is visible paling of the tissue. Several treatment techniques such as laser-induced interstitial thermotherapy (LITT) aim at temperatures just above 60°C . At even higher temperatures ($> 80^{\circ}\text{C}$), the membrane permeability is drastically increased, thereby destroying the otherwise maintained equilibrium of chemical concentrations.

At 100°C , water molecules contained in most tissues start to vaporize. The large vaporization heat of water (2253 kJ/kg) is advantageous, since the vapor generated carries away excess heat and helps to prevent any further increase in the temperature of adjacent tissue. Due to the large increase in volume during this phase transition, gas bubbles are formed inducing mechanical ruptures and thermal decomposition of tissue fragments.

Only if all water molecules have been vaporized, and laser exposure is still continuing, does the increase in temperature proceed. At temperatures exceeding 100°C , carbonization takes place which is observable by the blackening of adjacent tissue and the escape of smoke. To avoid carbonization, the tissue is usually cooled with either water or gas. Finally, beyond 300°C , melting can occur, depending on the target material.

All these steps are summarized in Table 3.6, where the local temperature and the associated tissue effects are listed. For illustrating photographs, the reader is referred to Figs. 3.10–3.13 and Fig. 3.20.

Table 3.6. Thermal effects of laser radiation

Temperature	Biological effect
37°C	Normal
45°C	Hyperthermia
50°C	Reduction in enzyme activity, cell immobility
60°C	Denaturation of proteins and collagen, coagulation
80°C	Permeabilization of membranes
100°C	Vaporization, thermal decomposition (ablation)
> 100°C	Carbonization
> 300°C	Melting

In general, the exact temperature for the onset of cell necrosis is rather difficult to determine. As a matter of fact, it was observed that not only the temperature achieved but also the temporal duration of this temperature plays a significant role for the induction of irreversible damage. It is illustrated in Fig. 3.21 how the critical temperature and the corresponding temporal duration relate to each other if irreversible damage is meant to occur. The curve is derived from several empirical observations. In the example selected in Fig. 3.21, a temperature of 60°C lasting for at least 6 s will lead to irreversible damage.

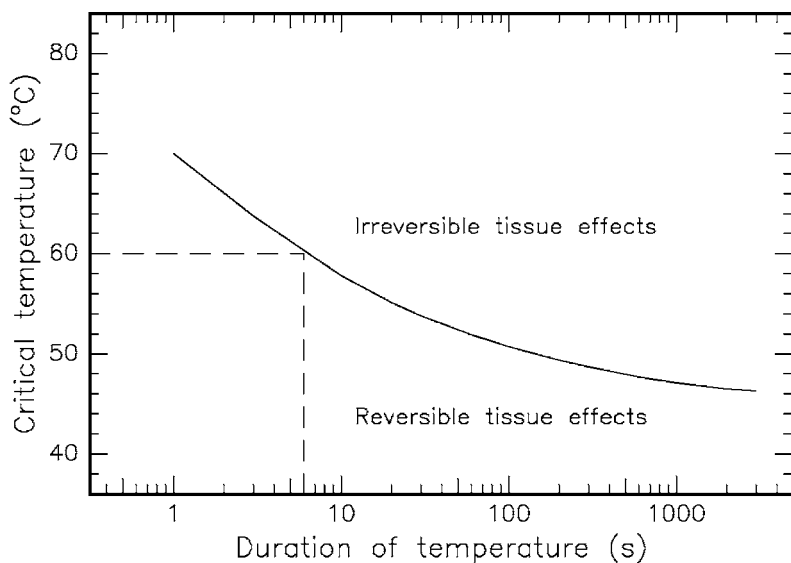


Fig. 3.21. Critical temperatures for the occurrence of cell necrosis. Data according to Henriques (1947) and Eichler and Seiler (1991)

Areas in which the temperature reaches values higher than 60°C are coagulated, and irradiated tissue cells become necrotic. Areas with maximum temperatures less than 60°C are treated hyperthermically only, and the probability of cells staying alive depends on the duration and temporal evolution of the temperature obtained. For a quantitative approximation of the remaining active molecules and cells at a certain temperature level, *Arrhenius' equation* is very useful:

$$\ln \frac{C(t)}{C_0} = -A \int_0^t \exp\left(-\frac{\Delta E}{RT(t')}\right) dt' \equiv -\Omega, \quad (3.19)$$

where C_0 is the initial concentration of molecules or cells, $C(t)$ is the concentration at a time t , A is Arrhenius' constant, R is the universal gas constant, and ΔE and Ω are specific tissue properties. According to Welch (1984), the coefficient A can be approximated by

$$A \simeq \frac{kT}{h} \exp \frac{\Delta S}{R},$$

where ΔS is the activation entropy, k is Boltzmann's constant, and h is Planck's constant. But, according to Johnson et al. (1974), this relation has no simple significance.

The local degree of tissue damage is determined by the damage integral given in (3.19). The damage degree is defined as the fraction of deactivated molecules or cells given by

$$D_d(t) = \frac{C_0 - C(t)}{C_0} = 1 - \exp(-\Omega).$$

Thus, by inserting an appropriate value of the tissue constant Ω , we are able to calculate the probable damage degree $D_d(t)$ as a function of time t . This was performed by Weinberg et al. (1984) in the case of retinal tissue.

Unfortunately, experimental data for the two parameters A and ΔE are very difficult to obtain due to the inhomogeneity of most tissues and the uncertainty in measuring the surviving fraction. However, in Table 3.7 some values of various tissues are listed as found in different studies.

Table 3.7. Arrhenius' constants of different tissues

Tissue	$A(s^{-1})$	ΔE (J/mol)	Reference
Retina	1.0×10^{44}	2.9×10^5	Vassiliadis et al. (1971) Weinberg et al. (1984)
Retina ($T < 50^{\circ}\text{C}$)	4.3×10^{64}	4.2×10^5	Takata et al. (1977)
Retina ($T > 50^{\circ}\text{C}$)	9.3×10^{104}	6.7×10^5	Takata et al. (1977)
Skin	3.1×10^{98}	6.3×10^5	Henriques (1947)
Liver	1.0×10^{70}	4.0×10^5	Roggan and Müller (1993)

Laser radiation acts thermally if power densities $\geq 10 \text{ W/cm}^2$ are applied from either CW radiation or pulse durations exceeding approximately $1 \mu\text{s}$. Typical lasers for coagulation are Nd:YAG lasers or diode lasers. CO_2 lasers are very suitable for vaporization and the precise thermal cutting of tissue. Carbonization and melting can occur with almost any type of laser if sufficient power densities and exposure durations are provided.

Frequently, not only one but several thermal effects are induced in biological tissue, depending on the laser parameters. These effects might even range from carbonization at the tissue surface to hyperthermia a few millimeters inside the tissue. In most applications, though, only one specific effect is aimed at. Therefore, careful evaluation of the required laser parameters is essential. Reversible and irreversible tissue damage can be distinguished. Carbonization, vaporization, and coagulation certainly are irreversible processes, because they induce irreparable damage. Hyperthermia, though, can turn out to be either a reversible or an irreversible process, depending on the type of tissue and laser parameters. Since the critical temperature for cell necrosis is determined by the exposure time as shown in Fig. 3.21, no well-defined temperature can be declared which distinguishes reversible from irreversible effects. Thus, exposure energy, exposure volume, and exposure duration together determine the degree and extent of tissue damage. The coincidence of several thermal processes is illustrated in Fig. 3.22. The location and spatial extent of each thermal effect depend on the locally achieved temperature during and after laser exposure.

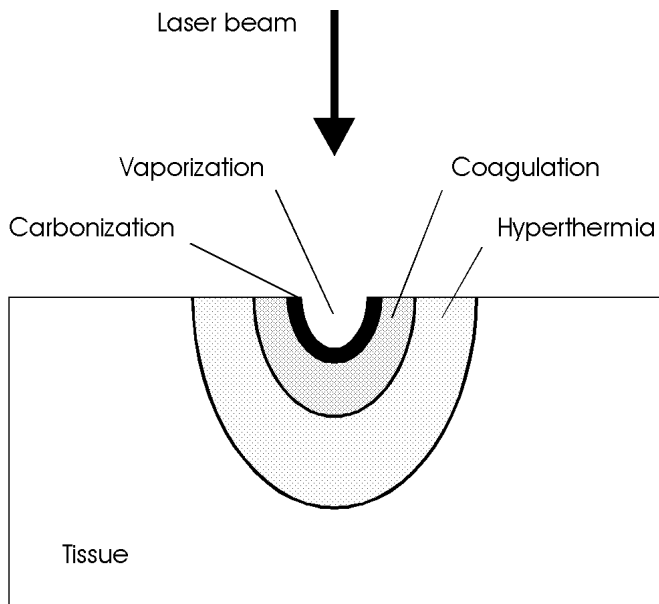


Fig. 3.22. Location of thermal effects inside biological tissue

3.2.4 Laser-Induced Interstitial Thermotherapy (LITT)

The possibility of localized tissue coagulation has formed the basis of a novel tumor treatment technique called *laser-induced interstitial thermotherapy*. It was recently introduced to the treatment of various types of tumors such as in retina, brain, prostate, liver, or uterus, and has already become a well established tool in minimally invasive surgery (MIS). Detailed descriptions and first clinical results are found in the papers by Svaasand et al. (1989), Ascher et al. (1991), Muschter et al. (1992), Roggan and Müller (1993), and Wallwiener et al. (1994), respectively. The most significant applications of LITT reside in the disciplines of gynecology and urology, e.g. the treatment of malignant tumors in the uterus and the treatment of benign prostatic hyperplasia (BPH) as described in Sects. 4.3 and 4.4.

The principal idea of LITT is to position an appropriate laser applicator inside the tissue to be coagulated, e.g. a tumor, and to achieve necrosis by heating cells above 60°C. As stated in Table 3.6, denaturation of proteins and coagulation occur at these temperatures. Due to the associated coagulation of blood vessels, severe hemorrhages are less likely to occur than in conventional surgery. This is of particular importance in the case of tumors, because they usually are highly vascularized. Either Nd:YAG lasers at 1064 nm or different types of diode lasers at 800–900 nm are applied, since light deeply penetrates into tissue at these wavelengths. Thus, large volumes can be treated with temperature gradients not as steep as those associated with conventional thermotherapies based on heat conduction only. Typical parameters of the procedure are 1–5 W of CW laser power for a period of several minutes and coagulation volumes with diameters of up to 40 mm.

In order to achieve a safe LITT procedure, knowledge of the final damage zone is essential. Especially in neurosurgery, it is very important to prevent injury from adjacent healthy tissue and sensitive structures. The spatial extent of the damage zone primarily depends on laser power, laser exposure, geometry of the laser applicator, and on thermal and optical tissue properties. Since the optical penetration depth of laser light in the near infrared is very high, deeper zones are reached more easily by the mechanism of light scattering rather than by heat conduction. Therefore, laser applicators emitting their radiation through a scattering surface are favored compared to focusing optics. Actually, first applications of LITT had been performed using bare fibers which were directly guided into the tissue. The main disadvantage was the high power density at the end surface of the fiber, leading to immediate carbonization of adjacent tissue. Recently improved applicators scatter laser light isotropically into all spatial directions by means of a frosted (rough) surface as described by Roggan et al. (1995c).

The basic setup for LITT is illustrated in Fig. 3.23. The laser applicator usually consists of a flexible fiber and a transparent catheter through which the fiber is moved into the tissue. Frequently, fibers with typical diameters of 400 μm are chosen. In order to ensure isotropic scattering at the interface

of the applicator and tissue, the surface of the fiber is etched by a special technique after removing the cladding. Continuous emitting surfaces with active lengths up to 20 mm can be manufactured. Depending on size and geometry of the treated volume, though, fibers with different active lengths should be available during surgery. Laser light is emitted from the distal end of the fiber on an active length which is approximately half the tumor size. The specially designed catheter protects the sensitive fiber from mechanical stress. Optional cooling of the catheter may help to prevent thermal damage to the fiber tip at even higher power densities. Only then can large tissue volumes be safely coagulated at a rather moderate gradient of temperature.

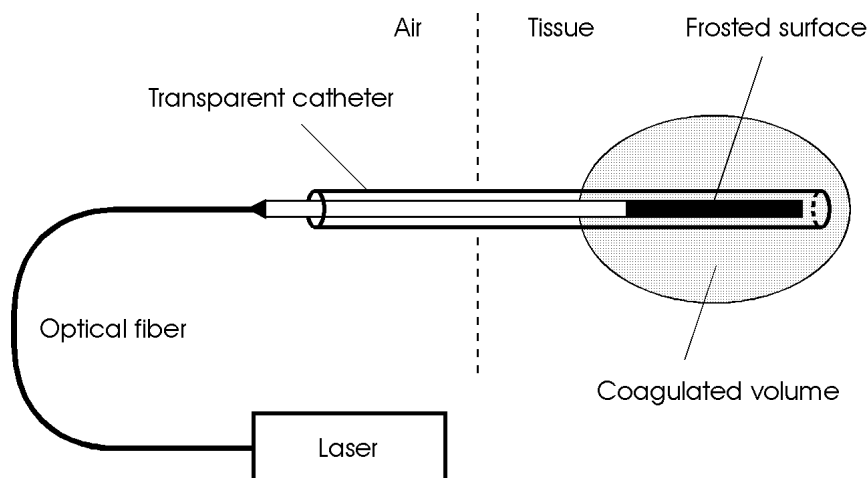


Fig. 3.23. Experimental setup for laser-induced interstitial thermotherapy. Laser radiation is applied to the tissue through an optical fiber. The fiber is placed inside the tissue by means of a specially designed, transparent catheter. Tissue necrosis occurs in selected coagulated volumes only

At the start of a LITT procedure, the catheter is placed inside the tumor assisted by qualified monitoring. According to Roggan et al. (1994), Eyrich et al. (2000), and Wacker et al. (2001), either ultrasound or magnetic resonance imaging (MRI) can be used for this purpose⁶. The fiber is then carefully guided through the catheter without actually being in contact with the tissue. In an accidental break of the fiber, glass splinters will remain inside the catheter without injuring the patient. After laser exposure, the fiber is either completely pulled back or only by its active length if several treatments are to be performed. Finally, i.e. if no further irradiation is required, the fiber is withdrawn. And, after a short period of temperature equalization,

⁶ In MRI-controlled LITT treatments, a special marker is mounted at the distal end of the fiber which facilitates its localization.

the protecting catheter may be removed. The same target may be treated several times by LITT to increase the spatial extent of tissue necrosis. For large lesions, the distance between adjacent puncturing canals should not exceed 1.5 mm to ensure an overlap of the coagulated tissue volumes.

The whole procedure can be performed either intraoperatively or percutaneously. In both cases, it should be preceded by suitable irradiation planning to obtain best surgical results. This can be achieved with appropriate computer simulations by considering a variety of input parameters. Most important among these are the position, extent, and topology of the diseased volume as well as optical and thermal tissue parameters, and the rate of blood perfusion. A choice of laser power and exposure duration should then be provided by the program. Detailed computer simulations for the laser treatment of liver tissue are illustrated in Figs. 3.24 and 3.25. They were obtained by applying the method of finite differences to the inhomogeneous heat conduction equation (3.11). This is performed by dividing the tissue into consecutive shells and using a mathematical algorithm which takes into account the heat conduction from adjacent layers only. After a few recursions of this algorithm, a steady-state solution is obtained expressing the desired temperature distribution. Further details on the simulation technique can be found in the paper by Roggan and Müller (1993). From Fig. 3.24, we conclude that adequate computer simulations fit very well to measured data, whereas Fig. 3.25 proves that cooled laser applicators enable the coagulation of larger tissue volumes at comparable peak temperatures.

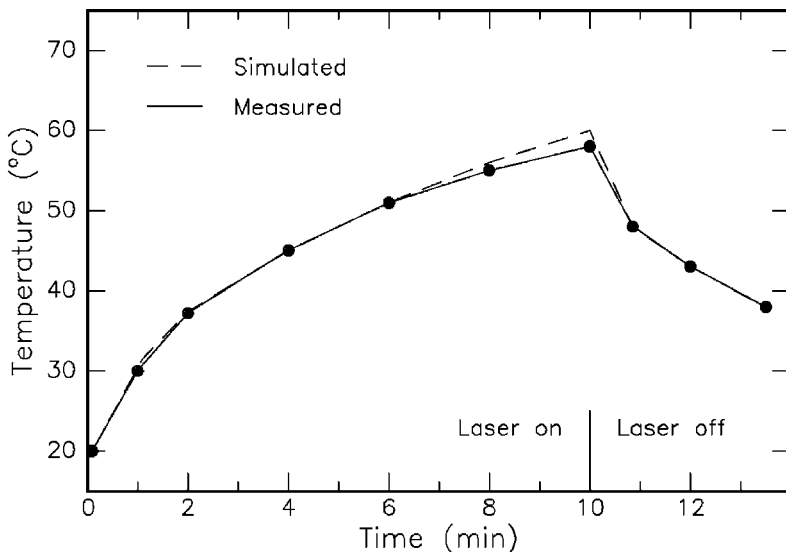


Fig. 3.24. Computer simulation and experimental results of LITT for liver tissue (laser power: 4 W, surface of applicator: 125 mm²). The switch-off time of the laser is indicated. Data according to Roggan and Müller (1993)

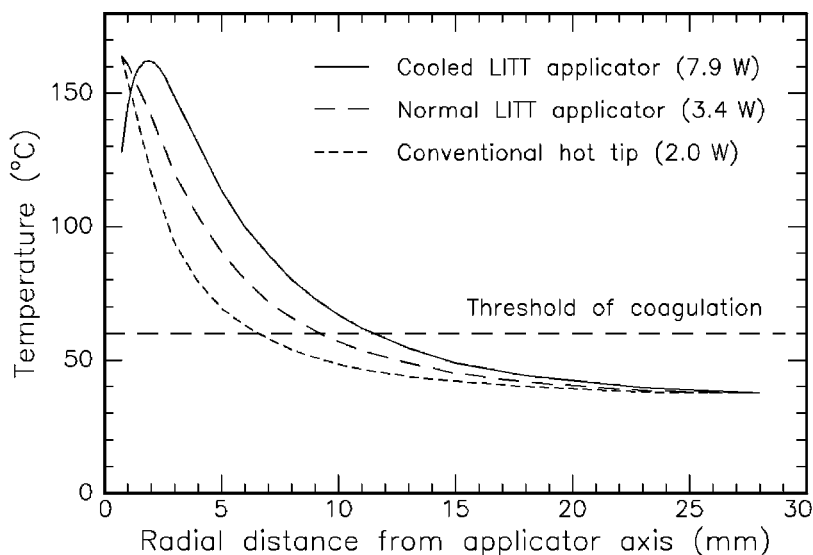


Fig. 3.25. Comparison of the calculated final temperature distributions for different types of thermotherapies (conventional hot tip, LITT without fiber cooling, LITT with fiber cooling). In the case of fiber cooling, the peak temperature does not occur at the applicator surface which is located at the *left* end of all curves. Data according to Roggan and Müller (1993)

The propagation of laser light in biological tissue and its transformation to thermal energy due to absorption is governed by the optical properties of the tissue. In the model of thermal interaction as described above, only absorption was taken into account. During LITT, scattering also plays a significant role for reasons just stated. Especially during the process of coagulation, the optical properties of tissue are changed, leading to higher scattering but nearly the same absorption. Usually, this effect is observable by a change in color of the irradiated volume, resulting in a reduced penetration depth. In Fig. 3.26, a sample of liver tissue is shown which was irradiated by using a standard LITT applicator as described above. The coagulated zone around the fiber is clearly visible.

For the treatment of very large tissue volumes with diameters of up to a few centimeters the application of several fibers is strongly recommended according to Klingenberg et al. (2000). The laser output is distributed among several fibers by optical beamsplitters as illustrated in Fig. 3.27. Each beamsplitter separates the incident laser beam into two laser beams with equal power. Using a total of three optical beamsplitters, a single input beam can be divided into four output beams. Focusing lenses are used to couple the laser power out of the input fiber and into the output fibers. Further adjustment of the laser power within each output beam can be achieved by implementation of optical filters.



Fig. 3.26. Liver tissue after exposure to a Nd:YAG laser, using a standard LITT fiber applicator (laser power: 5.5 W, exposure duration: 10 min). The coagulated volume visibly pales. Photograph kindly provided by Dr. Roggan (Berlin)

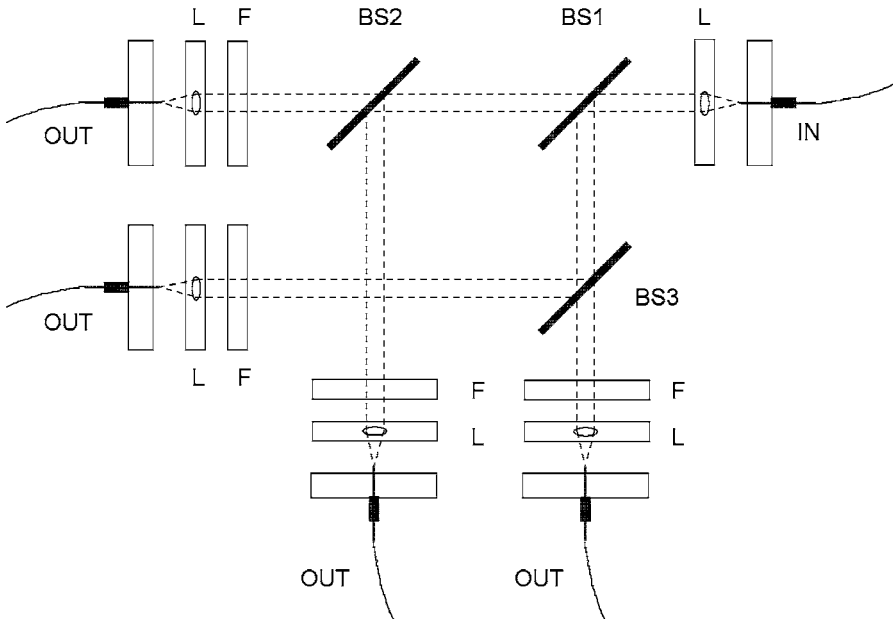


Fig. 3.27. LITT with four output fibers (BS: beamsplitter, F: filter, L: lens)

Depending on number and arrangement of the fibers, different geometries can be obtained for the coagulation of tissue. As shown in Fig. 3.28, the surgeon may choose among either spherical, ellipsoidal, or trapezoidal lesions. He can thus adjust the coagulated volume to the geometry of a tumor. Some indications, e.g. in brain surgery, require the treatment of tumors closely located to vital structures. In these cases, it is extremely important to avoid the coagulation of these organs at risk. This task can be achieved by applying trapezoidal lesions. Detailed discussion on this topic and the advantages of a multi-fiber treatment is provided by Klingenberg et al. (2000).

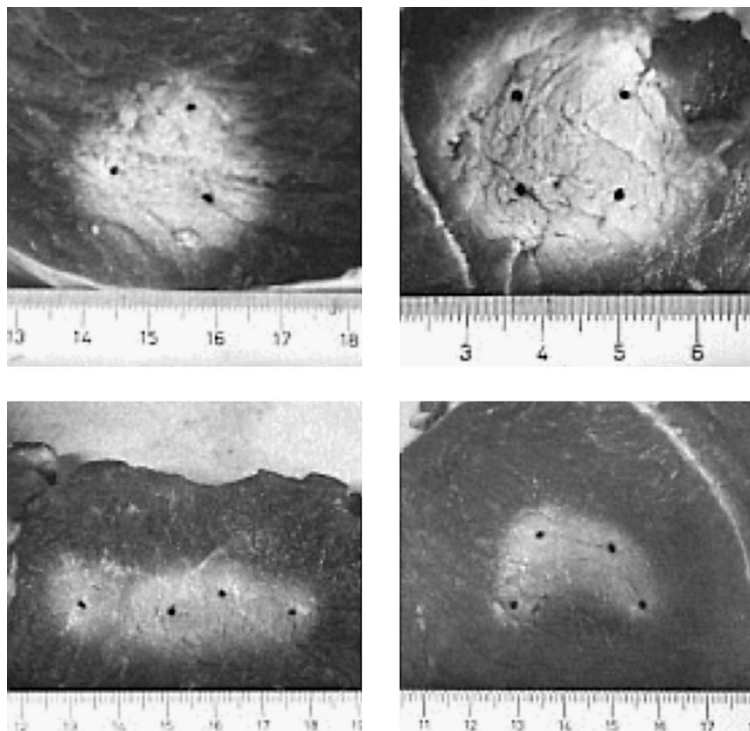


Fig. 3.28. Coagulations achieved in muscle tissue with several fibers (Nd:YAG laser, 4 W per fiber)

In general, two kinds of LITT applicators are distinguished: surface scatterers and volume scatterers. In surface scatterers, light is scattered only at the very surface of the applicator leading to a less homogeneous scattering profile as shown in Fig. 3.29. In volume scatterers, light is scattered by tiny scattering centers distributed throughout the whole volume of the applicator. Raw quartz is one of the basic materials used for volume scatterers. In raw quartz, the scattering centers consist of tiny gas bubbles.

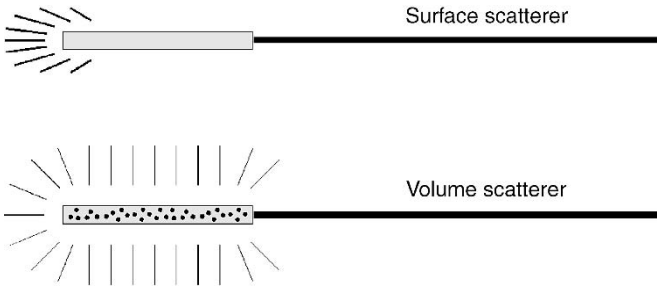


Fig. 3.29. Scattering profiles of surface scatterer and volume scatterer, respectively

As stated above, scattering is the dominant mechanism by which light is homogeneously distributed inside the tissue. In Sect. 2.5, we have already become acquainted with the *transport equation* of radiation, (2.36), which takes scattering effects into account. It was mentioned that exact analytical solutions to this integro-differential equation do not exist. However, five approaches have been made to solve the equation:

- first-order scattering,
- Kubelka–Munk theory,
- diffusion approximation,
- Monte Carlo simulations,
- inverse adding–doubling.

In principle, the same five approaches can be chosen when trying to estimate the temperature field within laser-irradiated tissue. Detailed computer calculations based on Monte Carlo simulations are found in the paper by Roggan and Müller (1995b). For a further characterization of each method, the reader is referred to Sect. 2.5.

3.2.5 Summary of Thermal Interaction

- *Main idea:* achieving a certain temperature which leads to the desired thermal effect
- *Observations:* either coagulation, vaporization, carbonization or melting
- *Typical lasers:* CO₂, Nd:YAG, Er:YAG, Ho:YAG, argon ion and diode lasers
- *Typical pulse durations:* 1 μ s ... 1 min
- *Typical power densities:* 10 ... 10⁶ W/cm²
- *Special applications:* coagulation, vaporization, melting, thermal decomposition, treatment of retinal detachment, laser-induced interstitial thermotherapy

3.3 Photoablation

In Fig. 3.30, the cross-section of a cornea is shown which was exposed to an ArF excimer laser. The removal of tissue was performed in a very clean and exact fashion without any appearance of thermal damage such as coagulation or vaporization. Instead, evidence is given that the tissue was very precisely “etched”. This kind of UV light-induced ablation is called *photoablation* and will be discussed in this section.

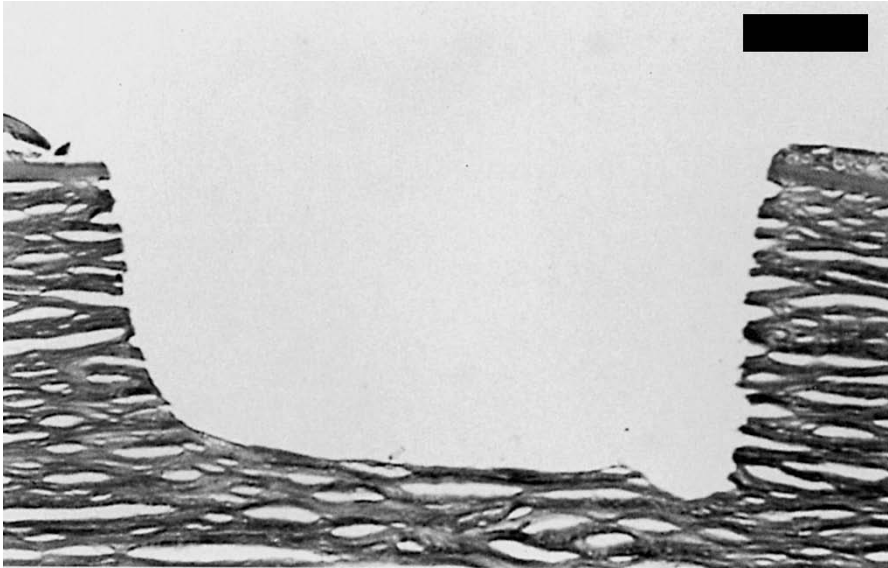


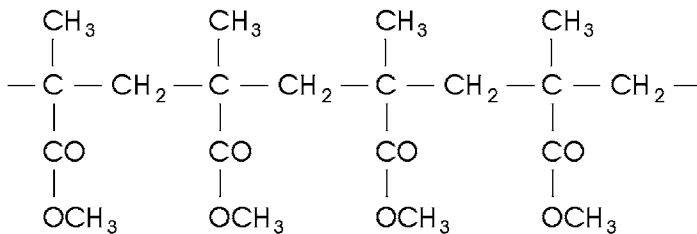
Fig. 3.30. Photoablation of corneal tissue achieved with an ArF excimer laser (pulse duration: 14 ns, energy density: 180 mJ/cm^2 , bar: $100 \mu\text{m}$). Photograph kindly provided by Dr. Bende (Tübingen)

Photoablation was first discovered by Srinivasan and Mayne-Banton (1982). They identified it as *ablative photodecomposition*, meaning that material is decomposed when exposed to high intense laser irradiation. Typical threshold values of this type of interaction are 10^7 – 10^8 W/cm^2 at laser pulse durations in the nanosecond range. The ablation depth, i.e. the depth of tissue removal per pulse, is determined by the pulse energy up to a certain saturation limit. The geometry of the ablation pattern itself is defined by the spatial parameters of the laser beam. The main advantages of this ablation technique lie in the precision of the etching process as demonstrated in Fig. 3.30, its excellent predictability, and the lack of thermal damage to adjacent tissue.

First studies regarding ablative photodecomposition were performed with polymethyl-metacrylate (PMMA), polyimide, Teflon, and other synthetic organic polymers⁷. Soon after, biological tissues were also ablated. Today, photoablation is one of the most successful techniques for refractive corneal surgery, where the refractive power of the cornea is altered in myopia, hyperopia, or astigmatism (see Sect. 4.1). In this section, for the sake of simplicity, we will follow the explanations given by Garrison and Srinivasan (1985) in the case of synthetic polymer targets. Due to the homogeneity of these materials, their behavior under certain experimental conditions is easier to understand. Thus, experimental data on the ablative process are very reliable and theoretical modeling is strongly facilitated. However, most of the theory applies for the more inhomogeneous biological tissues, as well.

Organic polymers are made up of large molecules consisting of more than 10^3 atoms, mainly carbon, hydrogen, oxygen, and nitrogen. A smaller molecular unit of up to 50 atoms is called a *monomer*. It is repeated several times along a well-defined axis to form the polymer chain. In Figs. 3.31a–b, the basic chemical structures of the most popular polymers – PMMA and polyimide – are illustrated.

a



b

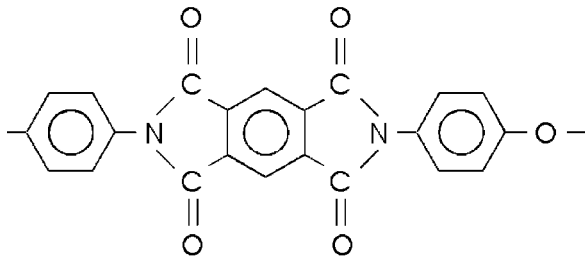


Fig. 3.31. (a) Chemical structure of four monomers of PMMA. (b) Chemical structure of one monomer of polyimide

⁷ In the field of material processing, especially in the manufacture of miniaturized surface structures, photoablation by means of excimer lasers has meanwhile become a well-established technique.

For PMMA, the temporal progress of photoablation was modeled by Garrison and Srinivasan (1985) using *Newton's equation* of motion. The polymer is described by structureless monomer units held together by strong attractive forces. The interaction with laser radiation is simulated by allowing each monomer unit to undergo excitation directly from an attractive to a repulsive state. This promotion is associated with a change in volume occupied by each monomer, leading to a transfer of momentum and, thus, to the process of ablation. For the sake of simplicity, a face-centered cubic (fcc) crystalline array is assumed. With a density of 1.22 g/cm^3 and a monomer mass of 100 amu, a lattice constant of 0.81 nm is calculated. The main attractive forces holding the monomer units together are the two carbon-carbon bonds along the chain. The strength of such a C-C bond is approximately 3.6 eV (see Table 3.8). The basic repulsive term is proportional to $1/r^{12}$, where r denotes a mean distance of two monomers. With these assumptions, the process of photoablation was simulated as shown in Fig. 3.32.

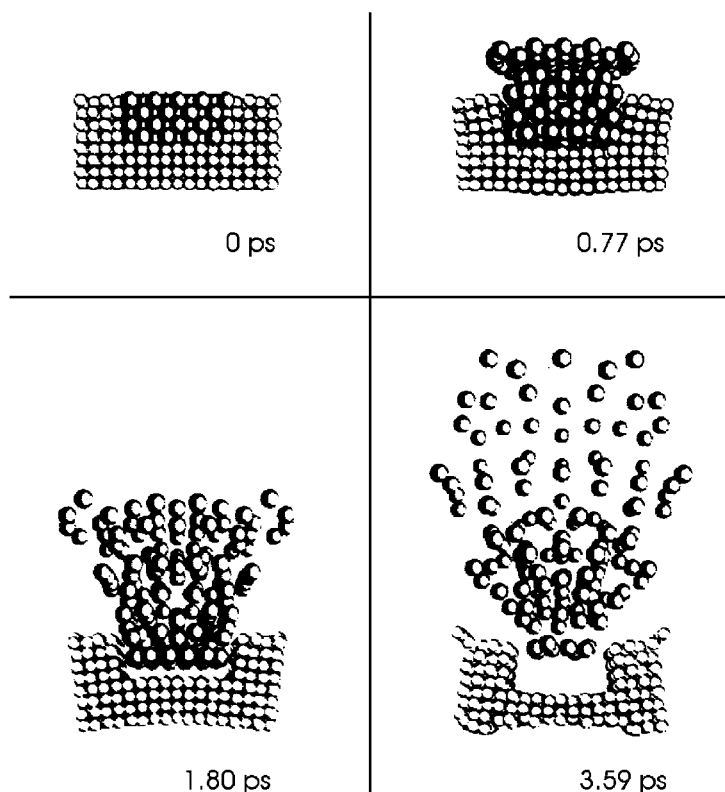


Fig. 3.32. Computer simulation of photoablation showing the movement of PMMA monomers as a function of time. Reproduced from Garrison and Srinivasan (1985) by permission. © 1985 American Institute of Physics

The character of the bonds within an organic polymer is primarily covalent. In order to obtain a physical explanation of the photoablation process, let us assume that two atoms A and B are bound by a common electron. The corresponding energy level diagram of the ground and several excited states is shown in Fig. 3.33. Due to the macromolecular structure, each electronic level is split into further vibrational states. Absorption of a photon may promote the two atoms to an excited state $(AB)^*$. Usually, the excitation is achieved by satisfying the *Franck-Condon principle*. It states that the radial distance of the two nuclei of the atoms A and B will not be affected during the process of excitation due to the small electron mass. Thus, transitions characterized by a vertical line in the energy level diagram are favored as indicated in Fig. 3.33. The probability of such a transition is increased if the maxima of the corresponding *Schrödinger functions* of the initial and final states coincide at the same radial distance.

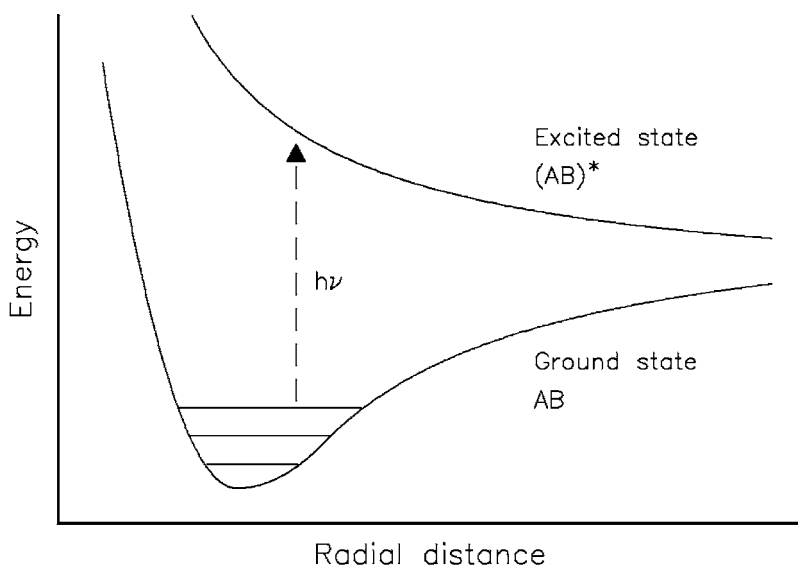


Fig. 3.33. Energy level diagram for photoablation

If a UV photon is absorbed, the energy gain is usually high enough to access an electronic state which exceeds the bond energy. In this case, the two atoms A and B may dissociate at the very next vibration. Thus, photoablation can be summarized as a two-step process:

- excitation: $AB + h\nu \rightarrow (AB)^*$,
- dissociation: $(AB)^* \rightarrow A + B + E_{\text{kin}}$.

The dissociation energies of some typical chemical bonds are listed in Table 3.8. Moreover, the wavelengths and the corresponding photon energies of selected laser systems are given in Table 3.9. When comparing both tables,

Table 3.8. Dissociation energies of selected chemical bonds. Data according to Pauling (1962)

Type of bond	Dissociation energy (eV)
C=O	7.1
C=C	6.4
O-H	4.8
N-H	4.1
C-O	3.6
C-C	3.6
S-H	3.5
C-N	3.0
C-S	2.7

Table 3.9. Wavelengths and photon energies of selected laser systems

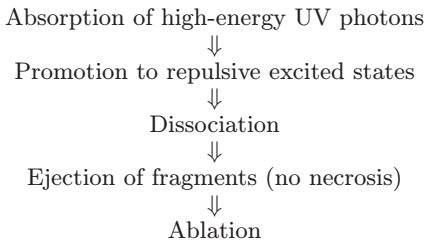
Laser type	Wavelength (nm)	Photon energy (eV)
ArF	193	6.4
KrF	248	5.0
Nd:YLF (4ω)	263	4.7
XeCl	308	4.0
XeF	351	3.5
Argon ion	514	2.4
Nd:YLF (2ω)	526.5	2.4
He-Ne	633	2.0
Diode	800	1.6
Nd:YLF	1053	1.2
Nd:YAG	1064	1.2
Ho:YAG	2120	0.6
Er:YAG	2940	0.4
CO ₂	10600	0.1

we find that only photons from UV lasers – typically excimer lasers – provide an energy sufficient for dissociating such bonds. Therefore, the interaction mechanism of photoablation is limited to the application of UV light.

The ejected photoproducts of excimer laser ablation have been analyzed in several studies, e.g. by Srinivasan and Mayne-Banton (1982) and Brannon et al. (1985). Usually, a mixture of single atoms (C, N, H, O), molecules (C₂, CN, CH, CO), and stable fragments (MMA-monomer, HCN, benzene) were detected. It is interesting to add that the product composition was found to be wavelength-dependent. Srinivasan et al. (1986b) found that radiation at 248 nm generates fragments of a higher molecular weight than does 193 nm radiation. Thus, the corresponding etched surface at 248 nm is rougher and less predictable than at 193 nm.

Moreover, it was observed that a certain threshold intensity must be applied to achieve photoablation. Above this intensity, a well-defined depth is ablated, depending on the absorption coefficient and the incident intensity. At the same time, an audible report is heard and visible fluorescence is observed at the impact site. If the incident intensity is moderate and such that the ablation depth is smaller than the corresponding optical absorption length, subsequent pulses will enter partially irradiated tissue as well as unexposed tissue underlying it. Therefore, only the first few pulses are unique. After these, a linear relation between the number of applied pulses and the total etch depth is obtained. In practice, the etch depths are averaged over several pulses and noted as ablation depth per pulse. This value is reproducible within an uncertainty of about 10% for most materials which is an excellent value when taking all the inhomogeneities of tissue into account. The physical principles of photoablation are summarized in Table 3.10.

Table 3.10. Principles of photoablation



We stated above that photoablation is a process which is restricted to the application of UV light. However, it is not limited to excimer lasers, since generating higher harmonics of other laser types can result in UV radiation, as well. The 4th harmonic of a solid-state laser, for instance, also induces photoablation as reported by Niemz et al. (1994b). In Figs. 3.34a–b and 3.35a–b, a sample of corneal tissue is shown which was partially exposed to either the second or the fourth harmonic of a Nd:YLF laser. In both cases, the pulse duration at the fundamental wavelength was set to 30 ps. The higher harmonics were induced by means of two BBO crystals. The pulse energies were approximately 150 μJ in the green and 20 μJ in the UV, respectively. The laser beam was scanned over the surface within a $1 \times 1 \text{ mm}^2$ pattern. Whereas distinct impact sites of the focused laser beam are clearly visible in the section exposed to the second harmonic, a clean and homogeneous layer is ablated with the fourth harmonic. Only the latter belongs to the group of photoablation, whereas the other effect is attributed to plasma-induced ablation which will be discussed in Sect. 3.4.

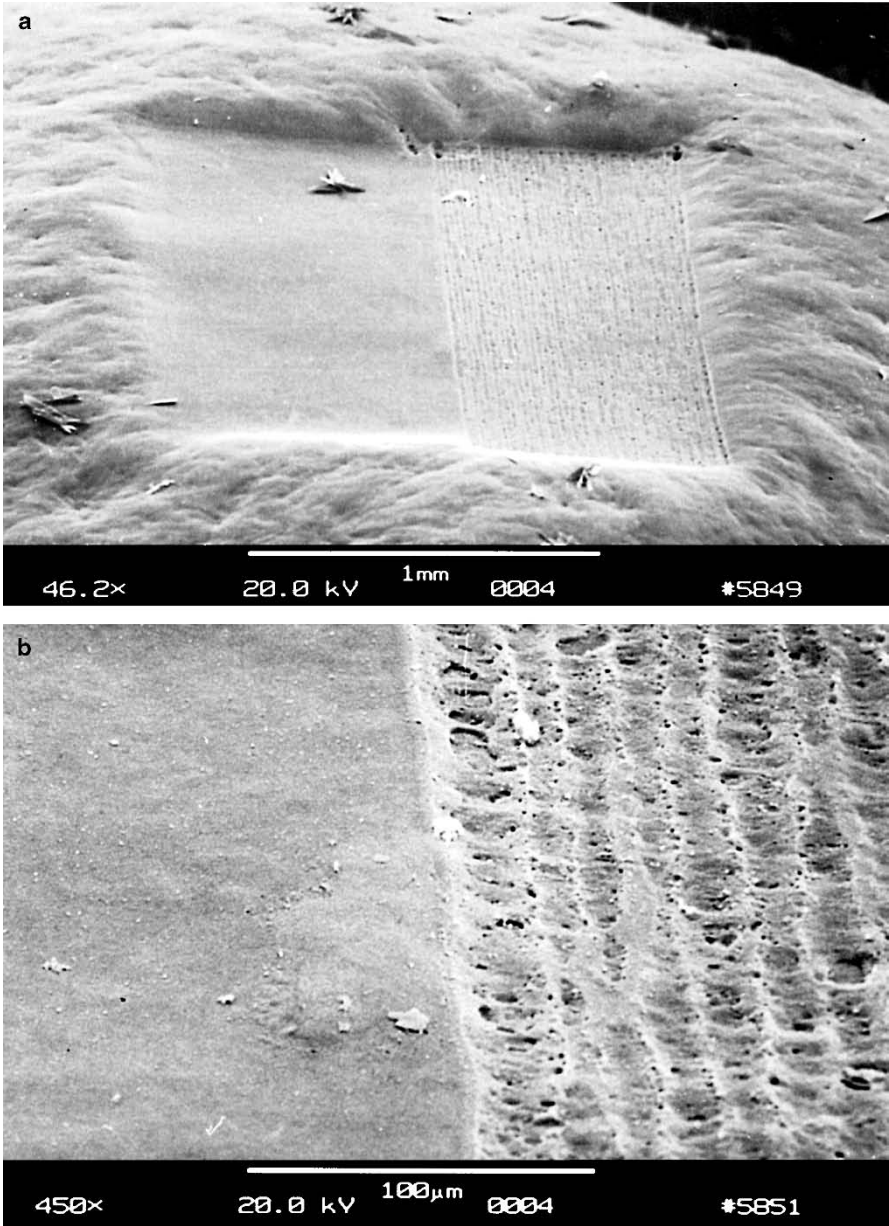


Fig. 3.34. (a) Human cornea exposed to the second (*right*) and fourth (*left*) harmonics of a Nd:YLF laser, respectively (pulse duration: 30 ps). (b) Enlargement of the boundary with the adjacent zones

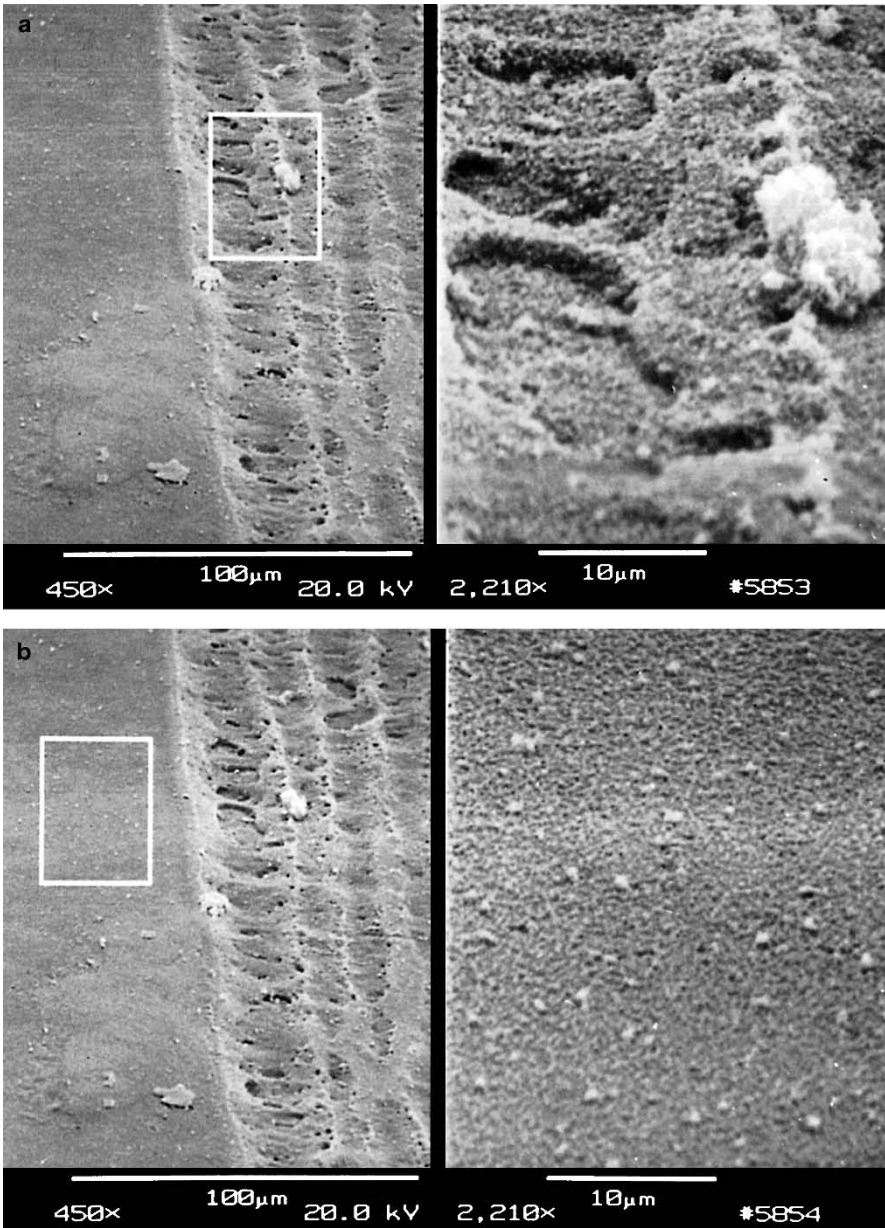


Fig. 3.35. (a) Human cornea exposed to the second and fourth harmonics of a Nd:YLF laser, respectively (*left*). Enlargement of area exposed to the second harmonic (*right*). (b) Same view (*left*). Enlargement of area exposed to the fourth harmonic (*right*)

3.3.1 Model of Photoablation

In order to come up with a model which describes the dependence of ablated depth on incident laser intensity, most research groups – such as Srinivasan and Mayne-Banton (1982), Andrew et al. (1983), Deutsch and Geis (1983), Garrison and Srinivasan (1985) – based their assumptions on the validity of Lambert's law of light absorption given by⁸

$$I(z) = I_0 \exp(-\alpha z) , \quad (3.20)$$

where z denotes the optical axis, I_0 is the incident laser intensity, and α is the absorption coefficient of the tissue. To evaluate the decrease in intensity, (3.20) has to be differentiated with respect to z which leads to

$$-\frac{\partial I}{\partial z} = \alpha I(z) . \quad (3.21)$$

Photoablation will take place only as long as the left side in (3.21) does not drop below a certain threshold value αI_{ph} , i.e.

$$\alpha I(z) \geq \alpha I_{\text{ph}} ,$$

where I_{ph} is the threshold intensity of photoablation. This condition requires that a certain amount of energy must be absorbed per unit volume and time to achieve photoablation. The threshold intensity I_{ph} is determined by the minimal number of bonds that have to be dissociated to yield decomposition. We thus obtain

$$I_0 \exp(-\alpha z) \geq I_{\text{ph}} .$$

The ablation depth d , i.e. the depth at which $I(z) = I_{\text{ph}}$, should then be

$$d = \frac{1}{\alpha} \ln \frac{I_0}{I_{\text{ph}}} \simeq \frac{2.3}{\alpha} \log_{10} \frac{I_0}{I_{\text{ph}}} . \quad (3.22)$$

This simple model describes photoablation very well, except for the threshold I_{ph} at the onset of photoablation and the threshold I_{pl} at the onset of plasma generation. The ablation curve of rabbit cornea is shown in Fig. 3.36 in a single-logarithmic plot. Usually, the ablation depth per pulse is given as a function of the incident energy density E_0 , where $E_0 = I_0 \tau$ and τ is the pulse duration. The logarithmic dependence, i.e. the central and linear part in Fig. 3.36, is in good agreement with theoretical predictions based on (3.22). This section of the ablation curve is observed in almost any kind of tissue. However, the threshold I_{ph} is not as sharp as predicted by (3.22), i.e. the slope of the curve approaches zero when intercepting with the abscissa. This result most probably stems from the inhomogeneity in fragment

⁸ For a complete mathematical description of photoablation, the temporal shape of the applied laser pulses should also be taken into account. Further details are found in the paper by Srinivasan (1986a).

sizes. The threshold varies around an average value $\langle I_{\text{ph}} \rangle$ according to the size of the ablated fragment. Imagine that such a fragment was bound to several molecules prior to ablation. As soon as a certain ratio of dissociated molecules is reached, the fragment will be released. Because larger fragments have a smaller “surface” compared to their “volume”, the threshold I_{ph} will decrease with increasing size of the ablated fragment. Consequently, averaging of various fragment sizes leads to a smooth intercept with the abscissa.

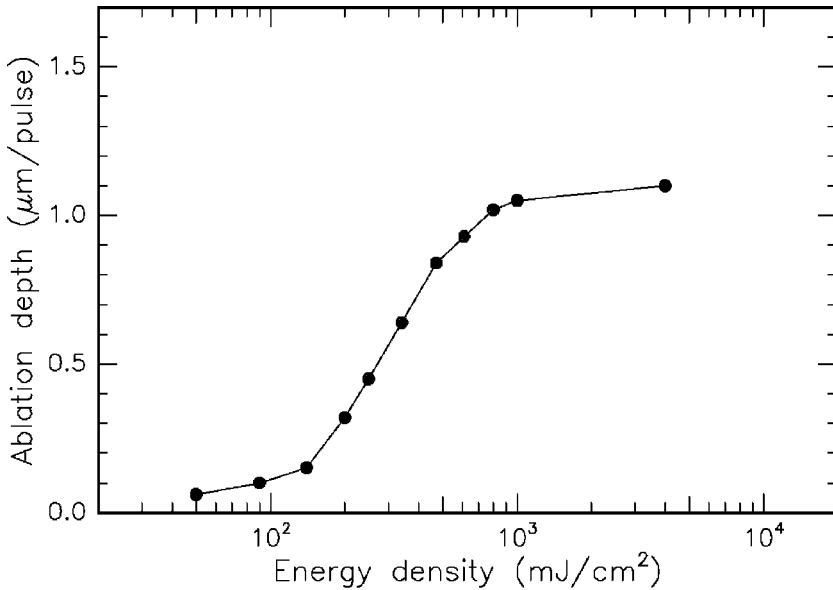


Fig. 3.36. Ablation curve of rabbit cornea obtained with an ArF excimer laser (pulse duration: 14 ns). Data according to Fantès and Waring (1989)

Above a second threshold I_{pl} – the threshold of plasma generation – the ablation depth per pulse obviously saturates as shown in Fig. 3.36. This effect stems from a well-known phenomenon called *plasma shielding*. Once a plasma is ignited at high power densities due to the generation of a high electric field, most of the succeeding laser radiation is absorbed by the plasma, thereby heating it up and leading to additional thermal effects. All abundant energy thus dissipates to heat and does not contribute to a further increase in ablation depth. Therefore, the ablation curve saturates at high energy densities. The absorption coefficient α_{pl} of the induced plasma is significantly higher than the original absorption coefficient α of the tissue as will be evaluated in Sect. 3.4. Hence, (3.20)–(3.22) are no longer valid. For a detailed discussion of plasma parameters and plasma shielding, the reader is referred to Sect. 3.4.

In the 1980s, the question was raised whether photoablation is based on a photochemical or a photothermal process. This discussion has led to

much controversy. Andrew et al. (1983) and Brannon et al. (1985) claimed UV ablation to be exclusively of thermal character, whereas Garrison and Srinivasan (1985) tended to attribute it to photochemical effects. Today, it is well accepted that photoablation – or the synonym ablative photodecomposition in the sense of UV ablation – shall be considered as an interaction mechanism of its own that can certainly be distinguished from pure photochemical and thermal processes described in Sects. 3.1 and 3.2. However, due to the dissociation of molecules during photoablation, a chemical transition is involved which could also justify misleading terms like “photochemical ablation”. But, with respect to the historical sequence, the term “photochemical” should be reserved for pulse interactions with photosensitizers at long pulse durations. And only an ablation caused by UV photons should be regarded as photoablation⁹.

In order to distinguish *photoablation* or *ablative photodecomposition* from *thermal interaction*, we take a closer look once more at the energy level diagram shown in Fig. 3.33. In the case of photoablation, we concluded that the energy of a single UV photon is sufficient to dissociate the former bound molecule AB. In thermal interactions, the situation is completely different. The photon energy is not high enough for the molecule to reach a repulsive state. The molecule is promoted only to a vibrational state within the ground level or to a rather low electronic state including any of its vibrational states. By means of nonradiative relaxation, the absorbed energy then dissipates to heat, and the molecule returns to its ground state. Hence, the crucial parameter for differentiating these two mechanisms – photoablation and thermal interaction – is the photon energy or laser wavelength. Only if $h\nu > 3.6\text{ eV}$, or in other measures $\lambda < 350\text{ nm}$, is the single photon dissociation of C–C bonds enabled. Of course, several photons with $h\nu < 3.5\text{ eV}$ can be absorbed. Then, these photons add up in energy and may thus lead to a dissociated state, as well. However, during the time needed for such a multiphoton absorption process, other tissue areas become vibrationally excited, hence leading to a global increase in temperature and an observable thermal effect (usually either vaporization or melting). If this effect is associated with ablation, the whole process is called *thermal decomposition* and has to be distinguished from pure *ablative photodecomposition*. These statements hold true, unless ultrashort pulses with a pulse duration shorter than 100 ps are used at pulse energies high enough to induce a localized microplasma. Then, even VIS- and IR-lasers can interact nonthermally. But the discussion of this mechanism shall be deferred to Sect. 3.4.

In reality, pure photoablation is only observed for the 193 nm wavelength of the ArF excimer laser. Higher wavelengths are usually associated with a more or less apparent *thermal component*. Sutcliffe and Srinivasan (1986)

⁹ Actually, the term “photoablation” itself is not well defined. It only states that an ablation occurs which is caused by photons, but it does not imply any further details. Photoablation in the common sense, though, is a very precise ablation caused by UV photons.

even postulated that the thermal component of the radiation from a XeCl excimer laser at 308 nm is 100 % thermal if its radiation is incident on PMMA. In Fig. 3.37, the thermal components of three excimer lasers are compared with each other. Obviously, each laser induces thermal effects at low energy densities. In the cases of the ArF laser and the KrF laser, the slope of the curve strongly decreases above a certain threshold, i.e. the threshold of photoablation. Radiation from the XeCl laser, on the other hand, continues to act thermally even at higher energy densities.

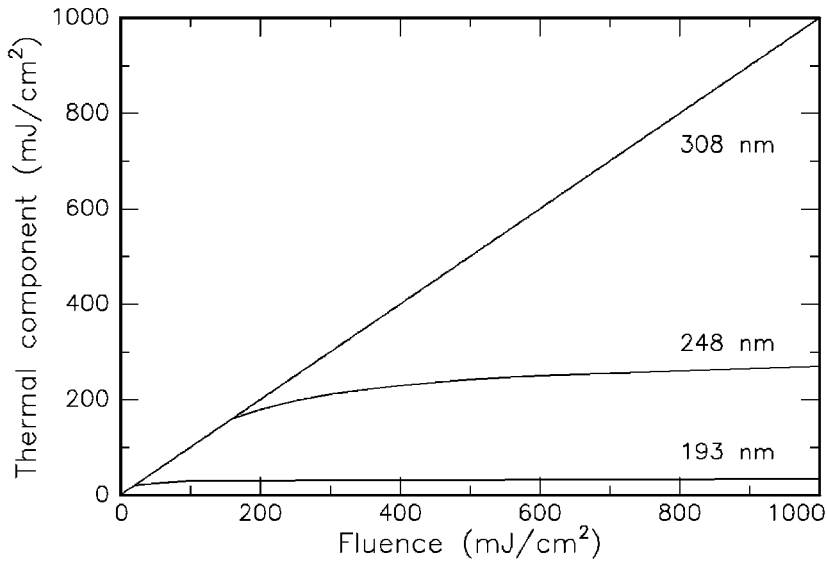


Fig. 3.37. Thermal component of UV radiation from three different excimer lasers (ArF laser at 193 nm, KrF laser at 248 nm, and XeCl laser at 308 nm) in PMMA. Data according to Sutcliffe and Srinivasan (1986)

The data presented in Fig. 3.37 are only valid for the target material PMMA. They cannot be generalized to any biological tissue, since the absorption characteristics of PMMA and biological tissue are quite different. However, the bottom line of the above observation – i.e. that the significance of the thermal component increases with higher wavelengths – will be true in biological tissue, as well. Therefore, we can conclude that ArF excimer lasers are probably the best choice when aiming at photoablation. XeCl laser could be used for thermal decomposition, although CW lasers might do a similar job. KrF lasers offer both photoablative and thermal decomposition but are less useful in medical applications as we will discuss next.

3.3.2 Cytotoxicity of UV Radiation

It has been argued that the application of UV radiation for photoablative purposes might induce mutagenic – and thus cytotoxic – effects within cells. This statement has to be taken seriously, since laser surgery, of course, should not evoke new maladies when eliminating others. It is a fact that DNA strongly absorbs UV radiation, especially at approximately 240–260 nm. And it is also well known that this radiation can cause mutagenic alterations of cells, e.g. exchanges of sister chromatids.

The effect of UV radiation on cells and biological tissue is initiated by photochemical reactions of chromophores contained by them. Absorption of UV photons by DNA causes alterations in the chemical structure of the DNA molecule. The major chemical change is the formation of a dimer from two adjacent pyrimidine bases. Other products are also synthesized in the DNA that may have biological consequences. Cells are frequently able to repair dimers before any adverse responses occur. This is an indispensable mechanism of protection, since the DNA contains important genetic information. Thus, if these photoproducts are not repaired, erroneous information may be passed on to progeny cells when the cell divides. This event, finally, leads to the process of mutagenesis.

Several studies have been done in order to evaluate potential hazards from UV laser radiation. Usually, the effects of one or two excimer lasers were compared to each other and to low-pressure Hg lamps. With these, most of the UV spectrum is covered. In Table 3.11, the wavelengths of commonly used UV sources are listed.

Table 3.11. Sources of UV radiation

Light source	Wavelength (nm)
ArF laser	193
KrF laser	248
Hg lamp	254
Nd:YLF laser (4ω)	263
Nd:YAG laser (4ω)	266
XeCl laser	308
XeF laser	351

Cytotoxic effects of UV radiation have been investigated by several groups, among them especially by Green et al. (1987), Kochevar (1989), and Rasmussen et al. (1989). In general, it can be concluded that the relative ability of excimer laser radiation to cause DNA defects decreases in the order of 248 nm > 193 nm > 308 nm. Only in some cases was radiation at 193 nm found to be less cytotoxic than at 308 nm. In Fig. 3.38, the surviving fraction of Chinese hamster ovary (CHO) cells after exposure to three different light sources is shown as a function of incident energy density. Whereas the Hg

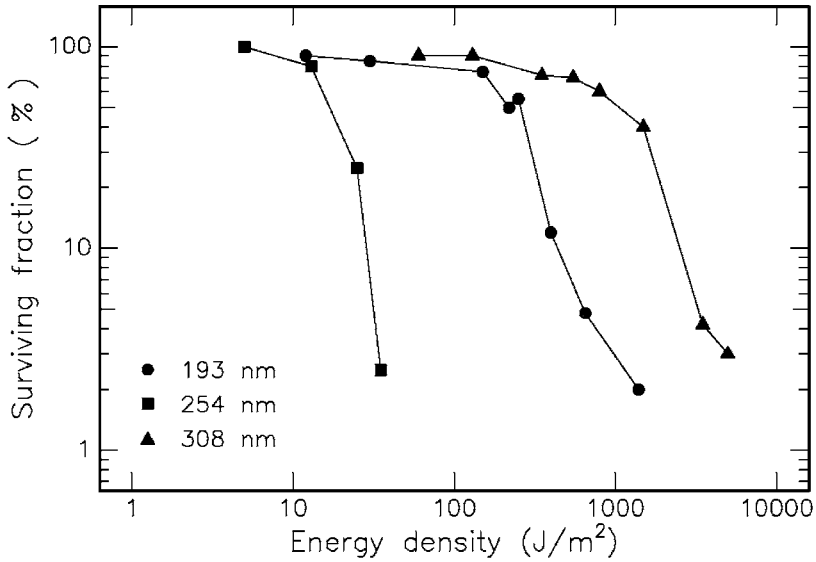


Fig. 3.38. Surviving fraction of Chinese hamster ovary (CHO) cells after UV irradiation. Light sources: ArF laser (193 nm), Hg lamp (254 nm), and XeCl laser (308 nm). Data according to Rasmussen et al. (1989)

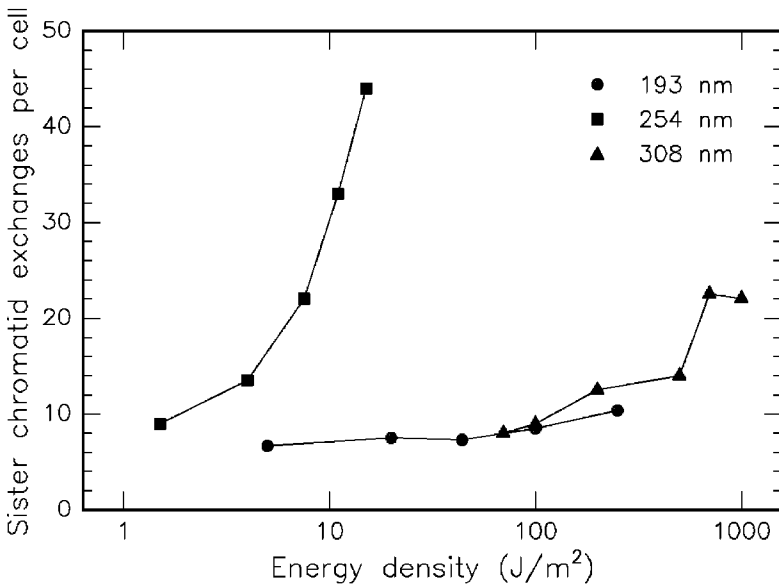


Fig. 3.39. Sister chromatid exchanges per cell after UV irradiation. Light sources: ArF laser (193 nm), Hg lamp (254 nm), and XeCl laser (308 nm). Data according to Rasmussen et al. (1989)

lamp induces measurable damage at 15 J/m^2 , it takes a few hundred J/m^2 of excimer laser radiation to cause a similar effect. When comparing the ArF laser at 193 nm and the XeCl laser at 308 nm, the latter is less cytotoxic.

In the same study, the exchange of sister chromatids was measured. These can either be repaired by the cell or, in severe cases, lead to irreversible defects. In the latter case, either cell necrosis or uncontrolled cell proliferation, i.e. certain types of cancer, can occur. The extent of sister chromatid exchange was investigated for the same UV sources and is shown in Fig. 3.39. All three radiations caused an increase in the incidence of sister chromatid exchange but with different effectiveness. The required energy density at 254 nm, for instance, is much less than at 193 nm or 308 nm. Moreover, the slope of the curve at 254 nm is much steeper than the others. Thus, another proof is given that radiation from a Hg lamp can be considered as being more mutagenic than ArF or XeCl lasers. This is the main reason why there are no significant medical applications for KrF lasers, since its wavelength at 248 nm almost coincides with that of Hg lamps.

We conclude that radiation from excimer lasers is less mutagenic than UV light from Hg lamps. This observation can probably be explained by the existence of proteins in the cell matrix which strongly absorb radiation at 193 nm, before it reaches the cell nucleus containing the DNA. According to Green et al. (1987), about 60% of incident radiation is already absorbed by only $1 \mu\text{m}$ of cytoplasm. Hence, the sensitive DNA inside the nucleus is shielded by the surrounding cytoplasm. However, potential risks should never be ignored when using ArF or XeCl lasers. Actually, a few altered cells might be enough to induce cancer in tissue. And, according to Rasmussen et al. (1989), there is some preliminary evidence that fluorescence emission around 250 nm occurs following absorption at 193 nm.

In general, the difficulty in judging the severity of mutagenic effects is due to the long follow-up periods during which maladies can develop. For instance, a haze inside the cornea is frequently observed within a few years after refractive corneal surgery has been performed with excimer lasers. The origin of this haze is yet unknown. It might well be attributed to cell alterations, even if corneal tumors do not occur.

3.3.3 Summary of Photoablation

- *Main idea:* direct breaking of molecular bonds by high-energy UV photons
- *Observations:* very clean ablation, associated with audible report and visible fluorescence
- *Typical lasers:* excimer lasers, e.g. ArF, KrF, XeCl, XeF
- *Typical pulse durations:* 10 ... 100 ns
- *Typical power densities:* $10^7 \dots 10^{10} \text{ W/cm}^2$
- *Special applications:* refractive corneal surgery

3.4 Plasma-Induced Ablation

When obtaining power densities exceeding 10^{11} W/cm² in solids and fluids – or 10^{14} W/cm² in air – a phenomenon called *optical breakdown* occurs. This effect is demonstrated in Fig. 3.40. One 30 ps laser pulse from a mode locked and amplified Nd:YLF laser was focused on an extracted human tooth. A bright plasma spark is clearly visible which is pointing toward the laser source. If several laser pulses are applied, a typical sparking noise at the repetition rate of the pulses is heard.



Fig. 3.40. Laser-induced plasma sparking on tooth surface caused by a single pulse from a Nd:YLF laser (pulse duration: 30 ps, pulse energy: 1 mJ, focal spot size: 30 μ m, bar: 1 mm). With these parameters, a power density of about 5×10^{12} W/cm² is obtained

By means of plasma-induced ablation, very clean and well-defined removal of tissue without evidence of thermal or mechanical damage can be achieved when choosing appropriate laser parameters. The effects of plasma-induced ablation on both soft and hard tissues are demonstrated in Figs. 3.41a–b. In one case, a sample of corneal tissue was ablated with a picosecond Nd:YLF

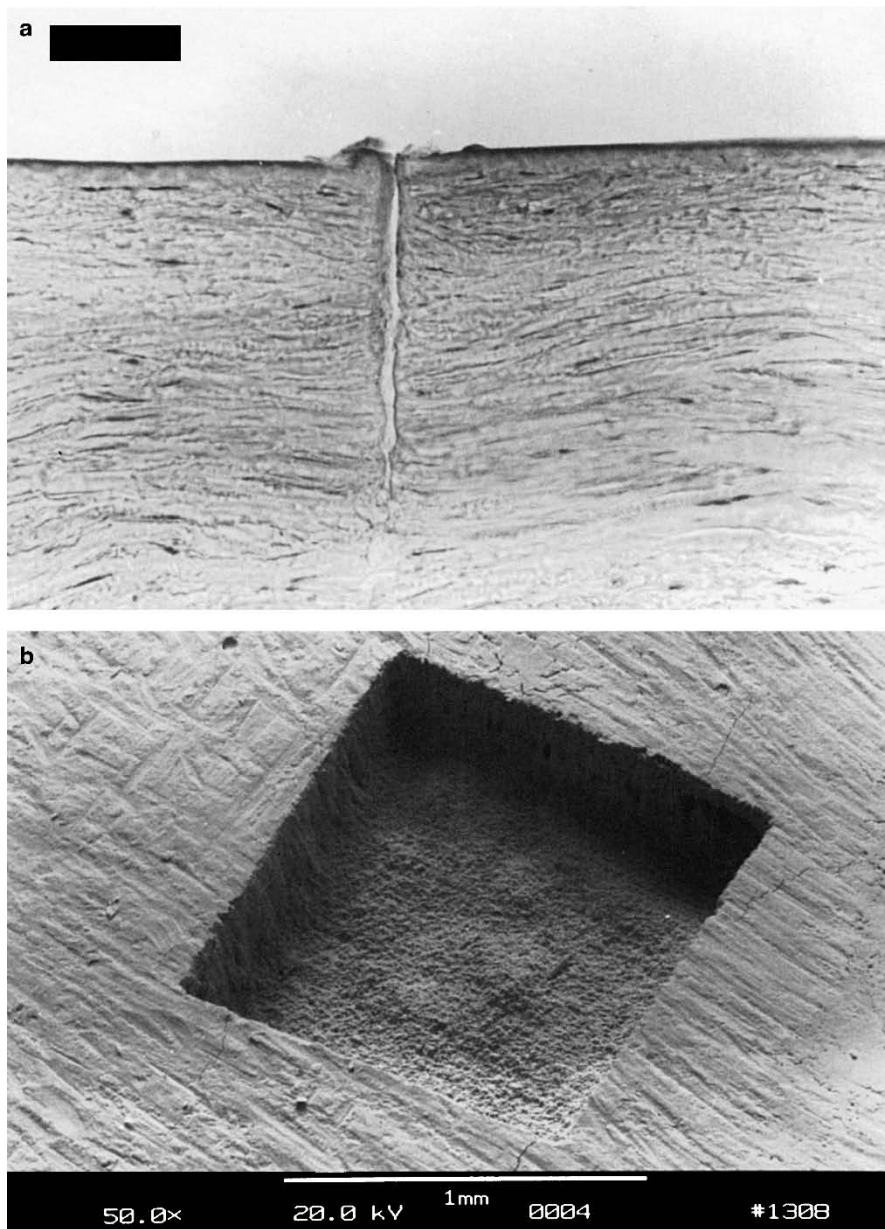


Fig. 3.41. (a) Excision in a human cornea achieved with a picosecond Nd:YLF laser (pulse duration: 30 ps, pulse energy: 200 μ J, bar: 50 μ m). (b) Human tooth exposed to 16 000 pulses from a picosecond Nd:YLF laser (pulse duration: 30 ps, pulse energy: 1 mJ, pattern size: 1 \times 1 mm²). Superficial cracking occurred as an artefact during the preparation for electron microscopy

laser by applying the pulses in a straight line pattern. The cross-sectional view shows a very precise excision without mechanical ruptures. In the other case, pulses from the same Nd:YLF laser were scanned over the surface of a tooth in a $1 \times 1 \text{ mm}^2$ square pattern. In particular, the fairly smooth bottom of the cavity and the steep side walls are very significant. Further details on potential applications are given in Sects. 4.1 and 4.2.

Sometimes, *plasma-induced ablation* is also referred to as *plasma-mediated ablation*. It was recently investigated and discussed by Teng et al. (1987), Stern et al. (1989), and Niemz et al. (1991). Both synonyms express a generally well accepted interpretation that this kind of ablation is primarily caused by plasma ionization itself. This is in contrast to a more mechanical process called *photodisruption* which will be described in Sect. 3.5. The most important parameter of plasma-induced ablation¹⁰ is the local electric field strength \mathbf{E} which determines when optical breakdown is achieved. If \mathbf{E} exceeds a certain threshold value, i.e. if the applied electric field forces the ionization of molecules and atoms, breakdown occurs. The electric field strength itself is related to the local power density I by the basic electrodynamic equation

$$I(r, z, t) = \frac{1}{2} \varepsilon_0 c \mathbf{E}^2, \quad (3.23)$$

where ε_0 is the dielectric constant, and c is the speed of light. For picosecond pulses, typical threshold intensities of optical breakdown are 10^{11} W/cm^2 . Hence, the corresponding electric field amounts to approximately 10^7 V/cm . This value is comparable to the average atomic or intramolecular *Coulomb* electric fields, thus providing the necessary condition for plasma ionization. Within a few hundred picoseconds, a very large free electron density with typical values of $10^{18}/\text{cm}^3$ is created in the focal volume of the laser beam. In general, plasma generation due to an intense electric field is called *dielectric breakdown*. The term *optical breakdown* especially emphasizes that UV, visible, and IR light are strongly absorbed by the plasma. The physical principles of breakdown have been investigated in several theoretical studies, e.g. by Seitz (1949), Molchanov (1970), Yablonovitch and Bloembergen (1972), Bloembergen (1974), Epifanov (1981), and Sacchi (1991).

Fradin et al. (1973b) have measured the intensity of ruby laser pulses transmitted through NaCl. They used a TEM₀₀ mode ruby laser with pulse energies of 0.3 mJ and pulse durations of 15 ns which was focused with a lens of 14 mm focal length. In Figs. 3.42a–c, the transmitted intensities are shown as a function of time. Obviously, the shape of the transmitted pulse is not altered in Fig. 3.42a, whereas the rear part of the pulse is strongly absorbed in Figs. 3.42b–c. Fradin et al. (1973b) concluded that the intensity as in Fig. 3.42a was just below the threshold of optical breakdown, while it was above in Fig. 3.42b, thereby damaging the NaCl sample. In Fig. 3.42c, breakdown was achieved at the very peak of the laser pulse.

¹⁰ Throughout this book we will use the term *plasma-induced ablation* rather than *plasma-mediated ablation*, since the first term emphasizes its primary cause.

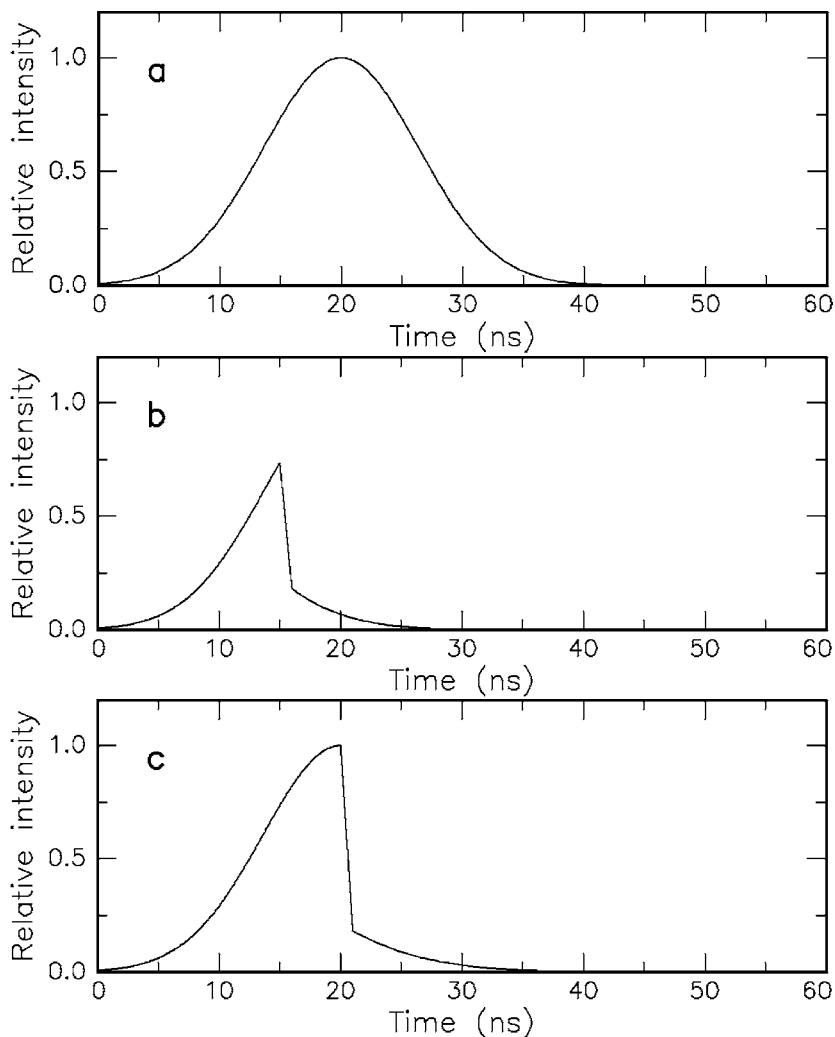


Fig. 3.42. (a–c) Ruby laser pulses transmitted through NaCl. Data according to Fradin et al. (1973b)

The initiation of plasma generation can be two-fold and was described in detail by Puliafito and Steinert (1984). It was observed that either Q-switched pulses in the nanosecond range or mode locked laser pulses in the picosecond or femtosecond range can induce a localized microplasma. In Q-switched pulses, the initial process for the generation of free electrons is supposed to be *thermionic emission*, i.e. the release of electrons due to thermal ionization as shown in Fig. 3.43. In mode locked pulses, *multi-photon ionization* may occur due to the high electric field induced by the intense

laser pulse. In general, the term multi-photon ionization denotes processes in which coherent absorption of several photons provides the energy needed for ionization. Due to the requirement of coherence, multi-photon ionization is achievable only during high peak intensities as in picosecond or femtosecond laser pulses. Plasma energies and plasma temperatures, though, are usually higher in Q-switched laser pulses because of the associated increase in threshold energy of plasma formation. Thus, optical breakdown achieved with nanosecond pulses is often accompanied by nonionizing side effects and will be deferred to Sect. 3.5.

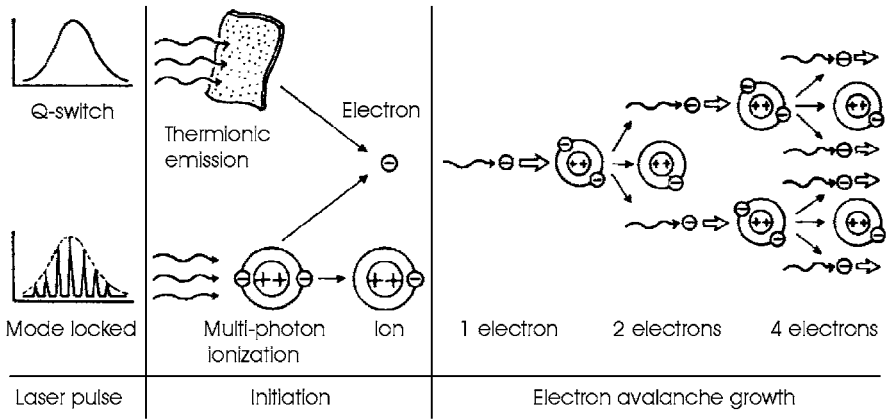
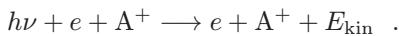


Fig. 3.43. Initiation of ionization with subsequent electron avalanche. Reproduced from Puliافتo and Steinert (1984) by permission. © 1984 IEEE

In either case, however, a few “lucky” electrons initiate an avalanche effect, leading to the accumulation of free electrons and ions. A free electron absorbs a photon and accelerates. The accelerated electron collides with another atom and ionizes it, resulting in two free electrons, each of them with less individual kinetic energy than the initial electron. Again, these free electrons may absorb incoming photons, accelerate, strike other atoms, release two more electrons, and so forth. The basic process of photon absorption and electron acceleration taking place in the presence of an atom is called *inverse Bremsstrahlung*¹¹. It is based on a free-free absorption, i.e. a transition, where a free electron is present in the initial and final states. In order to fulfill the conservation laws of energy and momentum, this event must necessarily take place in the electric field of an ion A^+ or a neutral atom. The process is schematically written as



¹¹ In ordinary *Bremsstrahlung*, the opposite effect occurs, i.e. electrons are accelerated in the electromagnetic field of an atom, thereby emitting radiation.

In particular, the important feature of optical breakdown is that it renders possible an energy deposition not only in pigmented tissue but also in nominally weakly absorbing media. This is due to the increased absorption coefficient of the induced plasma. Thereby, the field of potential medical laser applications is considerably widened. Especially in ophthalmology, transparent tissues – like cornea and lens – become potential targets of laser surgery. It is also worthwhile noting that during the process there is no restriction of the photon energy involved. The electron may increase its kinetic energy by means of absorbing any amount of energy, thus leading to a very short risetime of the free electron density of the order of picoseconds. In order to achieve optical breakdown, though, the irradiance must be intense enough to cause rapid ionization so that losses do not quench the electron avalanche. According to Smith and Haught (1966), inelastic collisions and diffusion of free electrons from the focal volume are the main loss mechanisms during avalanche ionization.

As already emphasized, the electric field strength \mathbf{E} is the crucial parameter for the onset of plasma-induced ablation. In the following paragraphs, a model of plasma-induced ablation is developed which is based on fundamental relations of electrodynamics and plasma physics. It derives a general expression for the dielectric factor ε and culminates in a relation for the absorption coefficient α_{pl} of the plasma. For visible and near infrared laser wavelengths, the original absorption coefficient α of most tissues is quite low compared to using UV light. However, calculations derived from the following model will prove that $\alpha_{\text{pl}} \gg \alpha$, thus leading to enhanced absorption and efficient ablation.

3.4.1 Model of Plasma-Induced Ablation

Our model is based on *Maxwell's equations* of electrodynamics relating the electric and magnetic field strengths \mathbf{E} and \mathbf{H} to the electromagnetic inductions \mathbf{D} and \mathbf{B} , respectively. In order to account for free electrons and currents associated with plasma formation, the inhomogeneous version of Maxwell's equations is considered. In their differential form, these equations are given by

$$\text{rot}\mathbf{E} = - \frac{\partial\mathbf{B}}{\partial t} , \quad (3.24)$$

$$\text{rot}\mathbf{H} = \frac{\partial\mathbf{D}}{\partial t} + \mathbf{j}_f , \quad (3.25)$$

$$\text{div}\mathbf{D} = \varrho_f , \quad (3.26)$$

$$\text{div}\mathbf{B} = 0 , \quad (3.27)$$

where ϱ_f denotes the density of all free electric charges, and \mathbf{j}_f the density of all free electric currents of the plasma.

The laser beam itself is approximated by a plane electromagnetic wave

$$\mathbf{E}(\mathbf{r}, t) = \mathbf{E}_0 \exp[i(\omega t - \mathbf{k}\mathbf{r})] , \quad (3.28)$$

$$\mathbf{H}(\mathbf{r}, t) = \mathbf{H}_0 \exp[i(\omega t - \mathbf{k}\mathbf{r})] , \quad (3.29)$$

where \mathbf{k} is the propagation vector of the electromagnetic wave. Assuming the relative magnetic permeability of the tissue to be $\mu = 1$, the electromagnetic inductions can be expressed by

$$\mathbf{B} = \mu_0 \mathbf{H} , \quad (3.30)$$

$$\mathbf{D} = \varepsilon \varepsilon_0 \mathbf{E} , \quad (3.31)$$

where μ_0 and ε_0 are the electromagnetic constants, and ε is the dielectric factor of the plasma. Inserting (3.28)–(3.31) into the first two of Maxwell's equations leads to

$$\mathbf{k} \times \mathbf{E} = \omega \mu_0 \mathbf{H} ,$$

$$\mathbf{k} \times \mathbf{H} = -\omega \varepsilon \varepsilon_0 \mathbf{E} + i \mathbf{j}_f = -\omega \varepsilon \varepsilon_0 \mathbf{E} + i \sigma \mathbf{E} ,$$

where σ is the electric conductivity of the plasma. Hence,

$$\mathbf{k} \times (\mathbf{k} \times \mathbf{E}) = -\omega^2 \varepsilon \mu_0 \varepsilon_0 \mathbf{E} + i \omega \mu_0 \sigma \mathbf{E} ,$$

$$\mathbf{k} \times (\mathbf{k} \times \mathbf{E}) = \left(-\frac{\omega^2}{c^2} \varepsilon + i \frac{\omega \sigma}{c^2 \varepsilon_0} \right) \mathbf{E} , \quad (3.32)$$

where $c = \sqrt{1/\varepsilon_0 \mu_0}$ is the speed of light. In electrodynamics, (3.32) is also referred to as the *telegraph equation*. Since electromagnetic waves are transversal, i.e. $\mathbf{k}\mathbf{E} = 0$, the amount $k = |\mathbf{k}|$ can be expressed by

$$k^2 = \frac{\omega^2}{c^2} \varepsilon' , \quad (3.33)$$

with the complex dielectric factor

$$\varepsilon' = \varepsilon - i \frac{\sigma}{\omega \varepsilon_0} . \quad (3.34)$$

In the case of negligible absorption, (3.33) reduces to the simple relation of dispersion

$$k = \frac{\omega}{c} n , \quad (3.35)$$

where n is the index of refraction. However, since the plasma absorbs incident radiation, (3.35) is replaced by

$$k = \frac{\omega}{c} (n + i\tilde{\alpha}) , \quad (3.36)$$

where $\tilde{\alpha}$ is the index of absorption. Combining (3.33) and (3.36) leads to the general expression

$$\varepsilon' = (n + i\tilde{\alpha})^2 . \quad (3.37)$$

Moreover, the following two relations are derived from (3.36)

$$n = \frac{c}{\omega} \operatorname{Re}(k) ,$$

$$\tilde{\alpha} = \frac{c}{\omega} \operatorname{Im}(k) .$$

The absorption coefficient α – which is not to be mistaken for $\tilde{\alpha}$ – was defined in the previous section by (3.20). Together with (3.23) and (3.28), we thus obtain

$$\alpha_{\text{pl}} = -2 \operatorname{Im}(k) = -\frac{2\omega}{c} \tilde{\alpha}_{\text{pl}} ,$$

which expresses the plasma absorption coefficient α_{pl} and the index of plasma absorption $\tilde{\alpha}_{\text{pl}}$ in terms of each other. We may separate (3.37) into

$$\operatorname{Re}(\varepsilon') = n^2 - \tilde{\alpha}_{\text{pl}}^2 ,$$

$$\operatorname{Im}(\varepsilon') = 2n\tilde{\alpha}_{\text{pl}} \implies \tilde{\alpha}_{\text{pl}} = \frac{1}{2n} \operatorname{Im}(\varepsilon') .$$

Hence,

$$\alpha_{\text{pl}} = -\frac{\omega}{nc} \operatorname{Im}(\varepsilon') , \quad (3.38)$$

stating that the existence of an imaginary part of ε' evokes absorption.

Next, we will consider the equation of motion of a plasma electron. It is given by

$$m_e \frac{\partial \mathbf{v}_e}{\partial t} = -e\mathbf{E} - \nu_{\text{ei}} m_e \mathbf{v}_e , \quad (3.39)$$

where m_e is the electron mass, \mathbf{v}_e is the electron velocity, e is the electron charge, and ν_{ei} is the mean collision rate of free electrons and ions. Assuming that the plasma electrons are performing oscillations induced by the incident electromagnetic field at its frequency ω , we obtain

$$i\omega m_e \mathbf{v}_e = -e\mathbf{E} - \nu_{\text{ei}} m_e \mathbf{v}_e ,$$

$$\mathbf{v}_e = -\frac{e}{m_e(\nu_{\text{ei}} + i\omega)} \mathbf{E} . \quad (3.40)$$

Together with the basic relation

$$\mathbf{j}_f = -N e \mathbf{v}_e ,$$

where N is the density of free electrons, (3.40) turns into

$$\begin{aligned} \mathbf{j}_f &= \frac{Ne^2}{m_e(\nu_{ei} + i\omega)} \mathbf{E} , \\ \sigma &= \frac{Ne^2}{m_e(\nu_{ei} + i\omega)} . \end{aligned} \quad (3.41)$$

Inserting (3.41) into (3.34) leads to

$$\begin{aligned} \varepsilon' &= \varepsilon - i \frac{1}{\omega\varepsilon_0} \frac{Ne^2}{m_e(\nu_{ei} + i\omega)} = \varepsilon - i \frac{\omega_{pl}^2}{\omega(\nu_{ei} + i\omega)} , \\ \varepsilon' &= \varepsilon - \frac{\omega^2\omega_{pl}^2}{\omega^2\nu_{ei}^2 + \omega^4} - i \frac{\omega\nu_{ei}\omega_{pl}^2}{\omega^2\nu_{ei}^2 + \omega^4} , \end{aligned} \quad (3.42)$$

where ω_{pl} is the *plasma frequency* defined by

$$\omega_{pl}^2 = \frac{Ne^2}{\varepsilon_0 m_e} . \quad (3.43)$$

From (3.38) and (3.42), the plasma absorption coefficient is derived as

$$\alpha_{pl} = \frac{\omega}{nc} \frac{\omega\nu_{ei}\omega_{pl}^2}{\omega^2\nu_{ei}^2 + \omega^4} = \frac{\nu_{ei}}{nc} \frac{\omega_{pl}^2}{\omega^2 + \nu_{ei}^2} . \quad (3.44)$$

In cold laser plasmas, i.e. $\nu_{ei} \ll \omega$, (3.44) can be simplified to

$$\alpha_{pl} = \frac{\nu_{ei}}{nc} \frac{\omega_{pl}^2}{\omega^2} . \quad (3.45)$$

Therefore, plasma absorption is enhanced in the IR region of the spectrum. And, since $\omega_{pl}^2 \sim N$ and $\nu_{ei} \sim N$, we obtain the important relation

$$\alpha_{pl} \sim N^2 ,$$

stating that the absorption is a nonlinear function of the free electron density and, thus, of the absorbed energy itself.

In Fig. 3.44, typical absorption coefficients α_{pl} for various incident power densities have been collected. The plasma was induced in a cuvette filled with distilled water by picosecond pulses from a Nd:YLF laser at a wavelength of 1.053 μm . The absorption coefficient has already gained two to three orders of magnitude if the incident energy density is twice the threshold value of plasma generation. In the example shown in Fig. 3.44, the absorption coefficient increases from 0.1 cm^{-1} at low fluences to 100 cm^{-1} at approximately 23 J/cm^2 . Therefore, the induced plasma serves as a shield for succeeding laser photons. This phenomenon is referred to as the *plasma shielding effect*. At higher pulse energies, its significance even increases and will be discussed in Sect. 3.5. Primarily, the enhanced absorption of the plasma is caused by the high density of free electrons capable of absorbing laser photons. Thus, by means of plasma generation, a very efficient type of ablation is created.

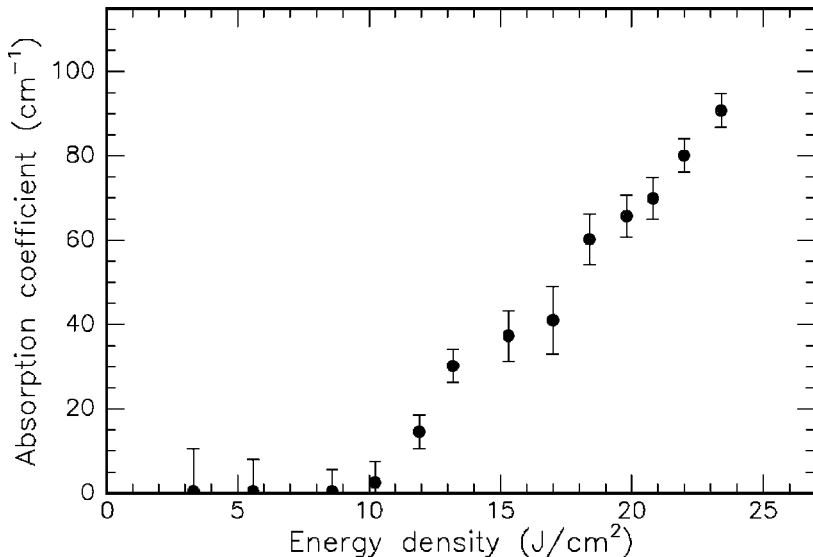


Fig. 3.44. Absorption of laser plasmas induced in distilled water by a Nd:YLF laser (wavelength: 1.053 μm , pulse duration: 30 ps). Unpublished data

The condition for plasma growth and sustainment is that losses – such as inelastic collisions and free electron diffusion – do not quench the avalanche process. As the free electron density N increases, photon scattering is enhanced. Consequently, laser photons are not only absorbed but also scattered by the plasma. The critical density N_{crit} at which a net amount of energy is not converted any further to plasma energy is obtained when the plasma frequency becomes equal to the frequency of the incident electromagnetic wave¹². Mathematically, this condition is written as $\omega_{\text{pl}} = \omega$ and, when inserting (3.43),

$$N_{\text{crit}} = \frac{\varepsilon_0 m_e}{e^2} \omega^2 . \quad (3.46)$$

For visible laser radiation, i.e. $\omega \simeq 10^{15}$ Hz, the electron density may thus reach values of up to a few $10^{20}/\text{cm}^3$.

In the remaining part of this section, we will evaluate the threshold dependence of optical breakdown on pulse duration of the laser. In several studies – as discussed below – a square root dependence of the threshold power density on pulse duration was observed when using picosecond or nanosecond laser pulses. This relationship, however, was only known as an *empirical scaling law* as stated by Koechner (1992). On the following pages, a novel model is developed which illuminates its theoretical background.

¹² Plasma oscillations are characterized by density-dependent eigenfrequencies. The highest amplitude occurs at resonance, i.e. at $\omega_{\text{pl}} = \omega$. At $\omega_{\text{pl}} > \omega$, the plasma oscillation is decelerated due to the phase shift of the external force.

The temporal behavior of the free electron density $N(t)$ is described by

$$\frac{\partial N}{\partial t} = [\beta - \gamma N(t)] N(t) - \delta N(t) , \quad (3.47)$$

with the rate parameters β for *avalanche ionization*, γ for *inelastic collision*, and δ for *electron diffusion*. Avalanche ionization is a two-step process. First, electrons gain energy in the electromagnetic field of the laser pulse, then further electrons are dissociated by subsequent collisions with either atoms or ions. According to Smith and Haught (1966), inelastic collisions and diffusion of free electrons from the focal volume are the main loss mechanisms during avalanche ionization. They are accounted for in (3.47) by negative signs. The avalanche parameter β primarily depends on the incident intensity $I(t)$. A *reduced avalanche rate* can be defined by

$$\beta' = \beta - \gamma N(t) ,$$

which takes into consideration that some of the collisions are inelastic, i.e. no additional electrons are released but kinetic energy is transferred to the collision partners. This energy is lost for further avalanche processes and thus reduces the effective rate parameter β' . The rate parameter γ is multiplied by $N(t)$, since the cross-section for the occurrence of inelastic collisions scales linearly with $N(t)$. By substituting $u(t) = 1/N(t)$, (3.47) turns into

$$\frac{\partial u}{\partial t} + (\beta - \delta) u(t) - \gamma = 0 .$$

This differential equation has the following general solution

$$u(t) = c(t) \exp \left[- \int_0^t (\beta - \delta) dt' \right] , \quad (3.48)$$

with

$$c(t) = c_0 + \gamma \int_0^t \exp \left[\int_0^{t'} (\beta - \delta) dt'' \right] dt' .$$

The initial condition is expressed by $u(0) = 1/N_0$. Hence, it follows that $c_0 = 1/N_0$, where N_0 is the initial electron density. After resubstituting $N(t)$ in (3.48), the following general solution is derived

$$N(t) = \frac{\exp \int_0^t (\beta - \delta) dt'}{\frac{1}{N_0} + \gamma \int_0^t \exp \left[\int_0^{t'} (\beta - \delta) dt'' \right] dt'} . \quad (3.49)$$

We will now assume a laser pulse with duration τ and constant intensity I_0 . According to Molchanov (1970), the parameter β can be approximated by

$$\beta = \left\{ \begin{array}{ll} \eta I_0 & \text{for } 0 \leq t \leq \tau \\ 0 & \text{else} \end{array} \right\} , \quad (3.50)$$

where η is called the *ionization probability* and is expressed in units of $(\text{J}/\text{cm}^2)^{-1}$. In our model, multi-photon processes are not taken into account. It is rather assumed that the initial electrons for the avalanche are provided by thermal ionization as stated by Bloembergen (1974) who estimated an initial electron density of $N_0 \simeq 10^8\text{--}10^{10} \text{ cm}^{-3}$ and a breakdown density of $N_{\text{th}} \simeq 10^{18} \text{ cm}^{-3}$.

– *Case I:* ($0 \leq t \leq \tau$). By making the simplifying assumptions that the parameters η and δ are not time-dependent, (3.49) reduces to

$$N(t) = N_0 \frac{e^{(\beta-\delta)t}}{1 + \frac{\gamma N_0}{\beta-\delta} [e^{(\beta-\delta)t} - 1]} .$$

According to Bloembergen (1974), a certain threshold ratio s can be defined for the occurrence of optical breakdown

$$s = \ln \frac{N_{\text{th}}(t)}{N_0} = \ln \frac{e^{(\beta-\delta)t}}{1 + \frac{\gamma N_0}{\beta-\delta} [e^{(\beta-\delta)t} - 1]} .$$

When assuming $\beta \gg \delta$, we obtain

$$s = (\beta - \delta)t - \ln \left[1 + \frac{\gamma N_0}{\beta - \delta} e^{(\beta-\delta)t} \right] . \quad (3.51)$$

It is now supposed that optical breakdown occurs near the end of the laser pulse, i.e. at $t = \tau$, and that the free electron density saturates at this threshold condition. Hence,

$$\begin{aligned} \left. \frac{\partial N}{\partial t} \right|_{t=\tau} &= \beta N_\tau - \gamma N_\tau^2 - \delta N_\tau \simeq 0 \quad \text{with} \quad N_\tau = N(\tau) , \\ \frac{\gamma N_\tau}{\beta - \delta} &\simeq 1 , \\ 1 + \frac{\gamma N_0}{\beta - \delta} e^{(\beta-\delta)\tau} &\simeq 1 + \frac{\gamma N_0}{\beta - \delta} e^{\beta\tau} \simeq 1 + \frac{\gamma N_\tau}{\beta - \delta} \simeq 2 . \end{aligned} \quad (3.52)$$

Therefore, (3.51) reduces to

$$s = (\beta - \delta)\tau - \ln \left(1 + \frac{\gamma N_\tau}{\beta - \delta} \right) . \quad (3.53)$$

Because of (3.52), the logarithm in (3.53) is evaluated in a series at the argument “2” up to the second term

$$s = (\beta - \delta)\tau - \ln 2 - \frac{1}{2} \left[\left(1 + \frac{\gamma N_\tau}{\beta - \delta} \right) - 2 \right] ,$$

with the general solution

$$\beta - \delta = \frac{s + \ln 2 - 0.5}{2\tau} + \sqrt{\left(\frac{s + \ln 2 - 0.5}{2\tau} \right)^2 + \frac{\gamma N_\tau}{2\tau}} .$$

The rate parameters for inelastic collision and diffusion are defined by $\gamma = (N_\tau \tau_c)^{-1}$ and $\delta = \tau_d^{-1}$, where τ_c and τ_d are the respective mean time constants. Then, together with (3.50), the following two relations are obtained for the threshold parameters of plasma generation

$$\eta E_{\text{th}} = \frac{s}{2} + \sqrt{\left(\frac{s}{2}\right)^2 + \frac{\tau}{2\tau_c}} + \frac{\tau}{\tau_d}, \quad (3.54)$$

$$\eta I_{\text{th}} = \frac{s}{2\tau} + \sqrt{\left(\frac{s}{2\tau}\right)^2 + \frac{1}{2\tau\tau_c}} + \frac{1}{\tau_d}, \quad (3.55)$$

where E_{th} and I_{th} are the threshold values of incident energy density and intensity, respectively. The term $(\ln 2 - 0.5)$ has been neglected, because Bloembergen (1974) estimated a typical ratio of $s = \ln(N_{\text{th}}/N_0) \simeq 18$, where N_{th} is the electron density at the threshold of optical breakdown.

– *Case II: ($t > \tau$)*. The integration in (3.49) is performed by means of

$$N(t) = \frac{\exp\left[\int_0^\tau(\beta - \delta) dt' + \int_\tau^t(\beta - \delta) dt'\right]}{\frac{1}{N_0} + \gamma \int_0^\tau \exp\left[\int_0^{t'}(\beta - \delta) dt''\right] dt' + \gamma \int_\tau^t \exp\left[\int_0^{t'}(\beta - \delta) dt''\right] dt'}. \quad (3.56)$$

Keeping in mind that $\beta = 0$ for any $t' > \tau$, (3.56) can be written as

$$N(t) = N_0 \frac{e^{(\beta - \delta)\tau} e^{-\delta(t - \tau)}}{1 + \gamma N_0 \int_0^\tau e^{(\beta - \delta)t'} dt' + \gamma N_0 \int_\tau^t e^{(\beta - \delta)\tau - \delta(t' - \tau)} dt'}. \quad (3.57)$$

with the final solution

$$N(t) = N_0 \frac{e^{\beta\tau - \delta t}}{1 + \frac{\gamma N_0}{\beta - \delta} [e^{(\beta - \delta)\tau} - 1] - \frac{\gamma N_0}{\delta} e^{\beta\tau} (e^{-\delta t} - e^{-\delta\tau})}. \quad (3.58)$$

The last equation generally describes the decrease in electron density after the laser pulse due to collision and diffusion processes.

In Figs. 3.45 and 3.46, the threshold dependences of incident energy density and intensity on pulse duration are illustrated, respectively, assuming $\tau_c = 1$ fs according to Bloembergen (1974) and $\tau_d = 500$ ps according to Zysset et al. (1989). It is supposed that the electron diffusion time is of the order of plasma lifetimes achieved with picosecond pulses. With these values, numerical evaluation of (3.54) and (3.55) yields that $E_{\text{th}} \sim \tau^x$ and $I_{\text{th}} \sim \tau^{x-1}$ with

$$\begin{aligned} x < 0.1 & \quad \text{for } \tau < 100 \text{ fs}, \\ x = 0.4 \dots 0.6 & \quad \text{for } 4 \text{ ps} < \tau < 8 \text{ } \mu\text{s}, \\ x > 0.8 & \quad \text{for } \tau > 300 \text{ } \mu\text{s}. \end{aligned}$$

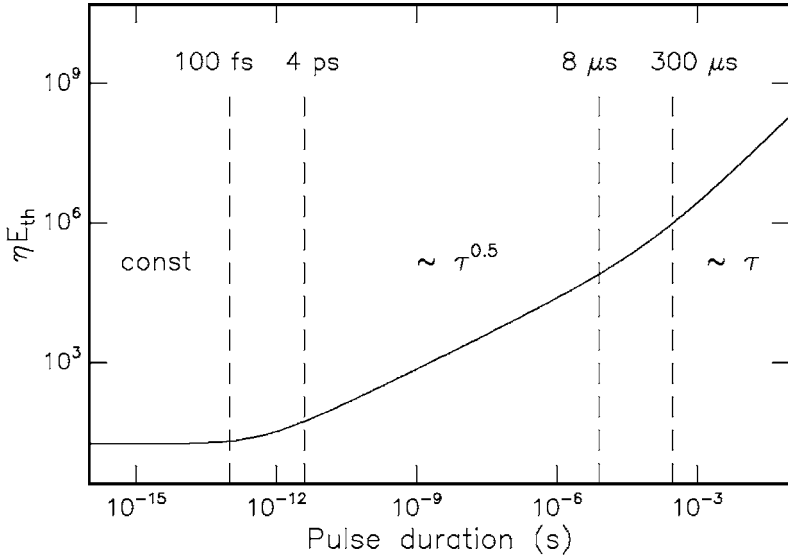


Fig. 3.45. Threshold dependence of incident energy density on laser pulse duration. A square root dependence is postulated for pulse durations between 4 ps and 8 μ s. The parameter η is tissue-dependent and is expressed in units of $(J/cm^2)^{-1}$

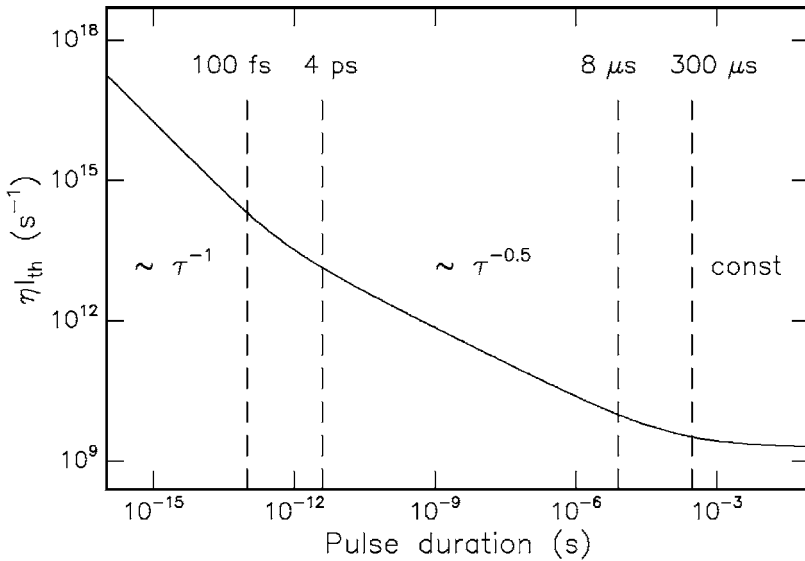


Fig. 3.46. Threshold dependence of incident intensity on laser pulse duration. An inverse square root dependence is postulated for pulse durations between 4 ps and 8 μ s. The parameter η is tissue-dependent and is expressed in units of $(J/cm^2)^{-1}$

Primarily, the two limits within the three time domains are determined by the time constants of inelastic collision and diffusion modified by the empirical threshold parameter s . There remains, of course, an uncertainty in the absolute value of these time constants. This uncertainty is thus carried forward to the domain limits, i.e. insertion of longer time constants would shift the two limits to longer pulse durations, as well.

Indeed, the results of a series of experiments indicate a relationship of the form $E_{\text{th}} \sim \sqrt{\tau}$ for pulse durations in the picosecond and nanosecond range. These studies have been made with a variety of anorganic target materials such as NaCl and SiO₂ as performed by Fradin et al. (1973a), Bloembergen (1974), Vaidyanthan et al. (1980), van Stryland et al. (1981), Taylor et al. (1987), and Du et al. (1994). A similar threshold dependence was obtained for various biological tissues as investigated by Stern et al. (1989), Niemz et al. (1993a), and Vogel et al. (1994b).

In Table 3.12, the exponent in the relationship $E_{\text{th}} \sim \tau^x$ is listed for various targets and pulse durations. They are calculated from threshold data which were published by different authors. Obviously, most of the values fit very well to the postulated relationship $E_{\text{th}} \sim \sqrt{\tau}$, i.e. $x \simeq 0.5$, except the data obtained by Zysset et al. (1989). The latter discrepancy might be caused by performing the experiments at extremely small focal spot sizes and the associated errors in threshold determination.

Table 3.12. Exponents in the relationship $E_{\text{th}} \sim \tau^x$ as calculated from published threshold data. Pulse durations shorter than 1 ps were not considered to remain in the time domain of the square root dependence

Target	Reference	Considered pulse durations	x
H ₂ O (distilled)	Docchio et al. (1986)	30 ps – 7 ns	0.49
	Zysset et al. (1989)	40 ps – 10 ns	0.71
	Vogel et al. (1994a)	30 ps – 6 ns	0.54
Cornea	Stern et al. (1989)	1 ps – 8 ns	0.44
	Niemz et al. (1993a)	1 ps – 200 ps	0.52
	Vogel et al. (1994b)	30 ps – 6 ns	0.47
Lens	Vogel et al. (1994b)	30 ps – 6 ns	0.46
Vitreous	Vogel et al. (1994b)	30 ps – 6 ns	0.48
Tooth	unpublished	1.5 ps – 30 ps	0.46

In Figs. 3.47a–b, the threshold dependence of the incident energy density is illustrated in corneal tissue and teeth. The data were obtained with two different laser systems, a Nd:YLF laser and a Rhodamine 590 dye laser, respectively. The dye laser was necessary to provide pulse durations in the femtosecond range. From the slope of each curve, the corresponding exponents $x = 0.52$ and $x = 0.46$ are calculated, respectively. At the shortest pulse durations, both curves tend to decrease in slope.

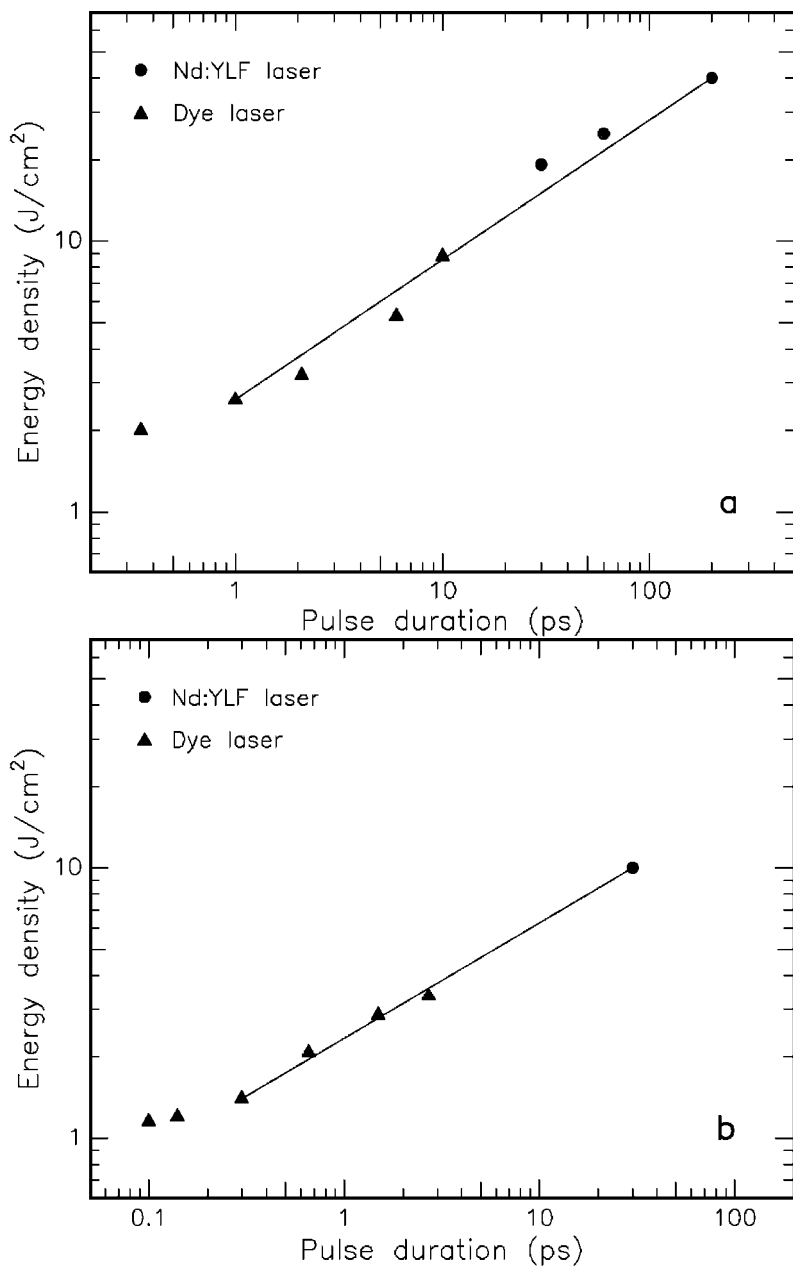


Fig. 3.47. (a) Threshold dependence of incident energy density on laser pulse duration for corneal tissue. Measured with a Nd:YLF laser and a Rhodamine 590 dye laser, respectively. The slope of the linear section is 0.52. Data according to Niemz et al. (1993). **(b)** Same dependence for teeth. The slope of the linear section is 0.46. Unpublished data

The ionization probability η was defined by (3.50). It is a tissue-dependent parameter and must thus be evaluated from experimental data. Its significance becomes evident when comparing different media with each other. In Table 3.13, some values of η are listed as calculated from published threshold data and (3.54). Obviously, the ionization probabilities of cornea and tooth are significantly higher than the corresponding values of water, lens, or vitreous. The accordance of values from different authors and experimental conditions is fairly good.

Table 3.13. Ionization probabilities of various targets as calculated from published threshold data

Target	Reference	Pulse duration	η (J/cm ²) ⁻¹
H ₂ O (distilled)	Docchio et al. (1986)	30 ps	6.0
		7 ns	6.4
	Zysset et al. (1989)	40 ps	2.2
		10 ns	0.71
	Vogel et al. (1994a)	30 ps	1.3
6 ns		0.95	
Cornea	Stern et al. (1989)	1 ps	16.2
		30 ps	12.9
	Niemz et al. (1993a)	10 ps	8.0
		30 ps	6.6
		60 ps	7.3
	Vogel et al. (1994b)	200 ps	8.1
		30 ps	8.8
Lens	Vogel et al. (1994b)	6 ns	9.7
		30 ps	2.7
Vitreous	Vogel et al. (1994b)	6 ns	3.1
		30 ps	3.8
Tooth	unpublished	6 ns	3.9
		1.5 ps	14.0
		30 ps	13.2

According to (3.58), the temporal evolution of the free electron density after the laser pulse can be approximated by

$$N(t) \simeq N_{\max} \exp(-\delta t) = N_{\max} \exp\left(-\frac{t}{\tau_d}\right).$$

For the same $\tau_d = 500$ ps as chosen above and a typical laser pulse duration of 1 ns, the temporal decrease in electron density is illustrated in Fig. 3.48. In theory, the lifetime of the plasma is thus a few nanoseconds. Time-resolved measurements of the plasma were performed by Docchio et al. (1988a-b) and Zysset et al. (1989). The photon emission of a plasma induced by a 30 ps pulse from a Nd:YLF laser is captured in Fig. 3.49. The upper and lower traces represent laser pulse and plasma emission, respectively. Both signals

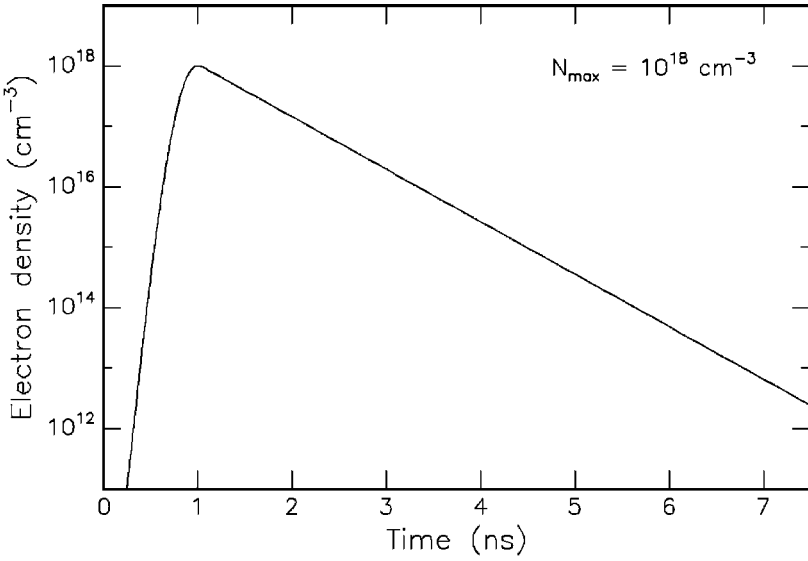


Fig. 3.48. Temporal evolution of free electron density in a laser-induced plasma. The simulation is based on a laser pulse duration of 1 ns, i.e. the maximum value N_{max} of the electron density is reached after 1 ns

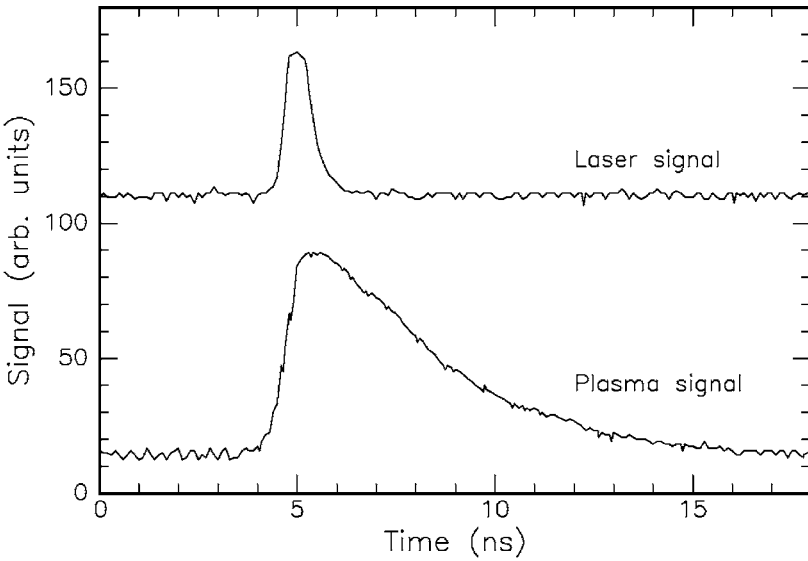


Fig. 3.49. Temporal traces of a Nd:YLF laser pulse (pulse duration: 30 ps, pulse energy: $500 \mu\text{J}$) and plasma emission. The plasma signal was detected with a photodiode at a risetime of approximately 1 ns

were detected with a photodiode at a risetime of 1 ns. Even though the laser signal is broadened in time, the lifetime of the plasma can be determined to be approximately 3 ns.

The model presented above finally explains the observed square root dependence for the time domain $4 \text{ ps} < \tau < 8 \text{ }\mu\text{s}$. It also indicates that femtosecond pulses are not associated with a lower threshold energy compared to picosecond pulses, thus providing no significant advantage to several medical laser applications.

3.4.2 Analysis of Plasma Parameters

The interaction type of plasma-induced ablation can be used for diagnostic purposes, as well. By means of a spectroscopic analysis of the induced plasma spark, the free electron density and the temperature of the plasma can be evaluated. Moreover, detailed information on the chemical consistency of the target can be obtained, thereby allowing certain conclusions to be drawn regarding the state of health of the investigated tissue volume.

One example for the analysis of laser-induced plasmas is the simultaneous caries diagnosis and therapy developed by Niemz (1994a) which is based on the detection of tooth demineralization and is enabled by the evaluation of plasma spectra. A typical setup for such an experiment is shown in Fig. 3.50. Optical breakdown is induced on the tooth surface by a picosecond Nd:YLF laser. Then, the plasma is imaged on the entrance pupil of a spectrometer and analyzed. Finally, the data are fed into a computer and processed.

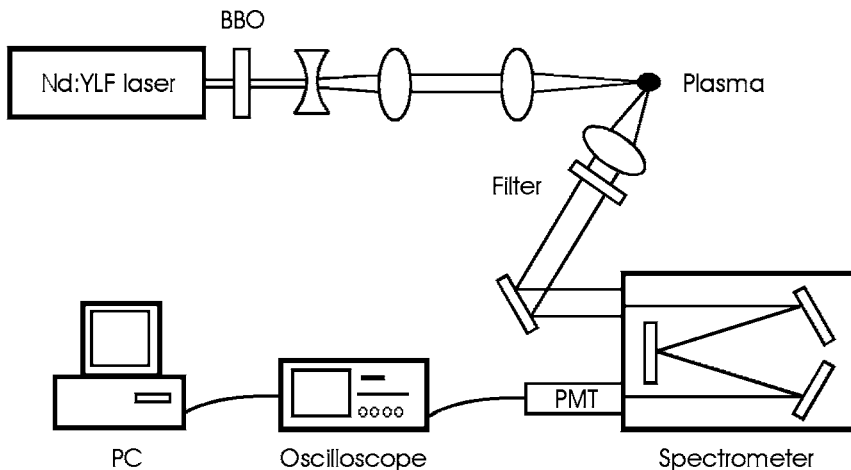


Fig. 3.50. Experimental setup for a computer-controlled spectroscopic analysis of laser-induced plasmas

Two typical plasma spectra are shown in Figs. 3.51a–b, one of which was obtained from healthy tooth substance, the other from carious substance. Calcium in neutral and singly ionized states and the major doublet of neutral sodium is found in the spectra according to emission wavelengths listed by Weast (1981). They are the minerals occurring most in dental hydroxyapatite with the chemical formula $\text{Ca}_{10}(\text{PO}_4)_6(\text{OH})_2$. Phosphorus is also expected, but neither of its strongest emission lines at 602.4 nm and 603.4 nm is observed. This result most probably stems from the fact that the plasma temperature is not high enough to transfer phosphate to its atomic constituents, i.e. phosphorus and oxygen. The two lines between 390 nm and 400 nm probably result from neutral calcium (394.8 nm, 397.3 nm) and the major emission of singly ionized calcium (393.3 nm, 396.8 nm). One strong peak can be seen at about 526.5 nm that partly arises from a multiplet of calcium lines and from external second-harmonic generation (SHG). A few percent of the incident laser beam are converted to the second harmonic by means of a BBO crystal as seen in Fig. 3.50. Therefore, in the spectra, this peak is labeled “Ca & 2ω ”. SHG at the tooth surface is also conceivable, but its amplitude is expected to be surpassed by the calcium multiplet. The detected signal at 526.5 nm is normalized to unity. This normalization is useful when comparing spectra of healthy and carious teeth. The latter spectra show a strong decrease for all mineral lines due to the demineralization process induced by caries. Slight deviations in the ratio of calcium and sodium intensities might be observed because of different demineralization stages.

The normalization realized in this study is correct only if the diffuse reflectivities of healthy and carious teeth are the same for the second harmonic at 526.5 nm. This was tested by filtering out the fundamental wavelength, thereby preventing plasma generation, and measuring the reflected signal while moving different areas of the tooth through the focus. No significant difference in the intensities was observed. However, since the intensities of the calcium multiplet at 526.5 nm are also decreased in carious teeth, the ratio of SHG photons contributing to the normalization signal at 526.5 nm varies. Therefore, a direct comparison of absolute intensities cannot be derived from these spectra. For further details on the subject of simultaneous caries diagnosis and therapy, the reader is referred to Sect. 4.2.

An exact evaluation of the plasma temperature is difficult due to the short lifetime of the plasma. Temporal measurements are required to understand the dynamic behavior of the plasma temperature and the free electron density. However, by comparing the intensities of two different calcium lines, an estimate of a mean plasma temperature can be given. According to Lochte-Holtgreven (1968), the following relation applies for two spectral lines of the same atomic species in the same ionization stage

$$\frac{I_1}{I_2} = \frac{A_1 g_1 \lambda_2}{A_2 g_2 \lambda_1} \exp\left(-\frac{E_1 - E_2}{kT}\right), \quad (3.59)$$

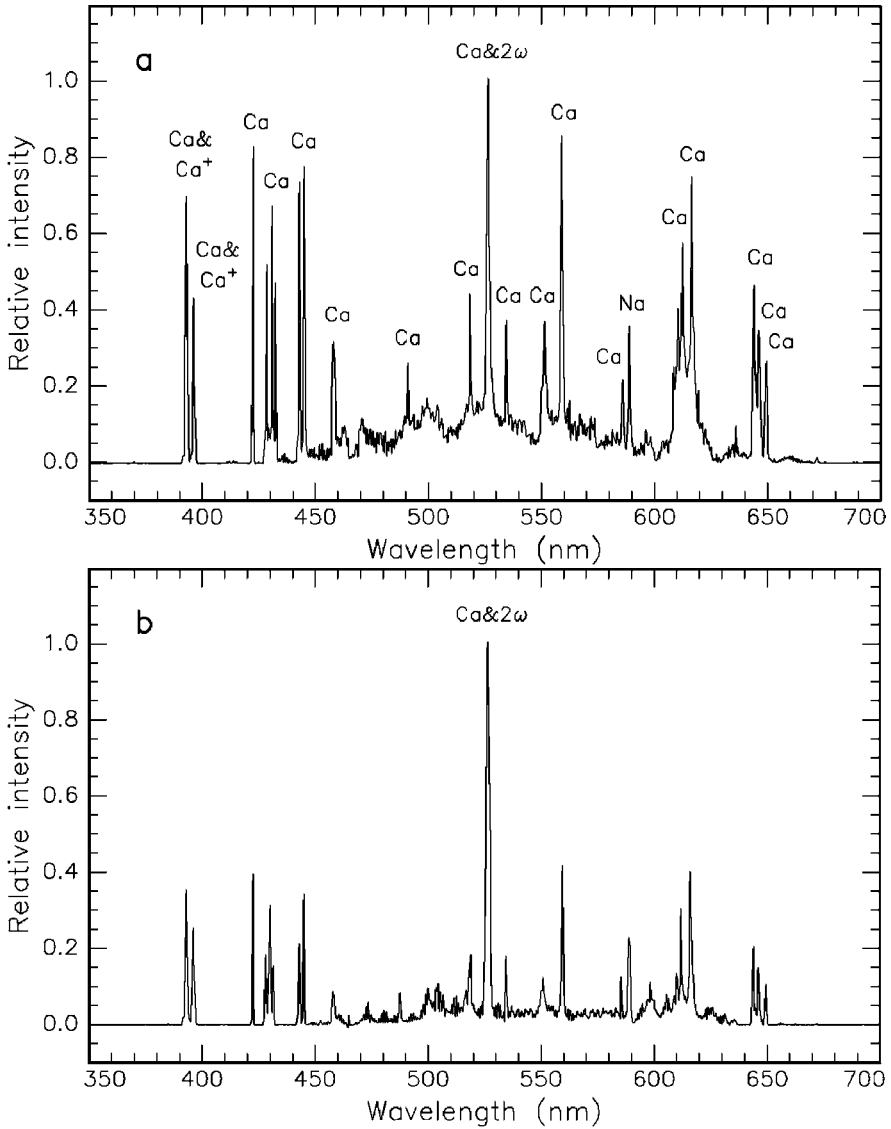


Fig. 3.51. (a) Spectrum of plasma on healthy tooth substance induced by a Nd:YLF laser (pulse duration: 30 ps, pulse energy: 500 μ J). Lines of neutral calcium (Ca), singly ionized calcium (Ca^+), and neutral sodium (Na) are seen. The signal at 526.5 nm partly originates from calcium and from second harmonic generation (SHG) of the laser beam. (b) Spectrum of laser-induced plasma on carious tooth substance. Due to the process of demineralization, the intensity of all mineral lines is reduced. Data according to Niemz (1994a)

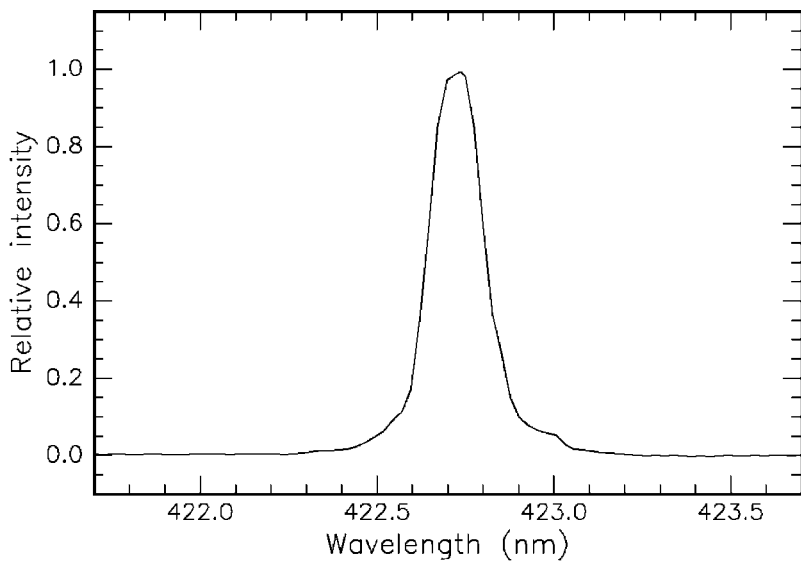


Fig. 3.52. Calcium line at 422.7 nm of a plasma on healthy tooth substance. The plasma was induced by a Nd:YLF laser (pulse duration: 30 ps, pulse energy: 500 μJ). Unpublished data

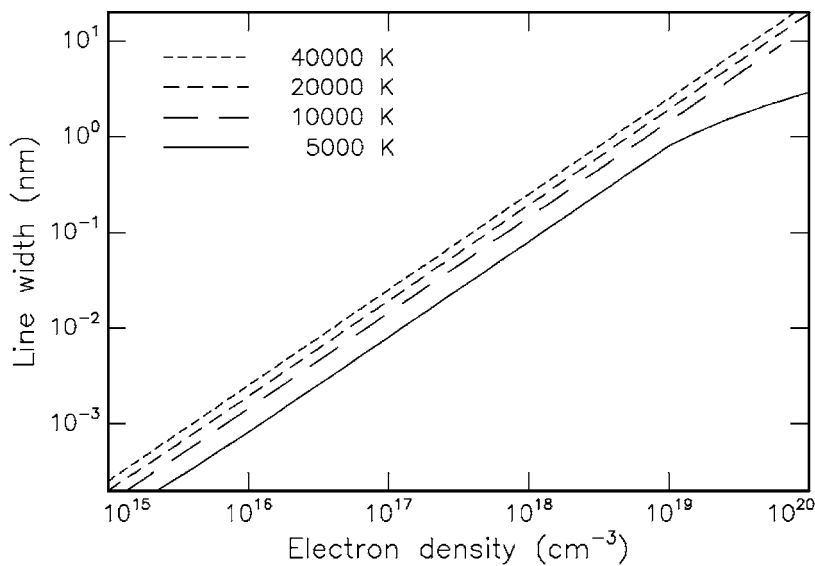


Fig. 3.53. Dependence of spectral width on plasma density and temperature according to Saha's equation (plasma temperature: as labeled). Given values apply for the calcium line at 422.7 nm. Unpublished data

where I is the detected intensity, A is the transition probability, g is the statistical weight of the upper energy level, λ is the detected wavelength, E is the upper energy level, k is Boltzmann's constant, and T is the plasma temperature. By differentiating (3.59), we obtain

$$\frac{\Delta T}{T} = \frac{kT}{E_1 - E_2} \frac{\Delta(I_1/I_2)}{I_1/I_2}. \quad (3.60)$$

Hence, the accuracy of temperature determination can be improved by choosing two upper energy levels far apart from each other. The accuracy of the measured intensities is better for singlets. Because of these two reasons, it is convenient to compare the intensities at the two calcium wavelengths of $\lambda_1 = 422.7$ nm and $\lambda_2 = 585.7$ nm. According to Weast (1981), the corresponding parameters are

$$\begin{aligned} A_1 &= 2.18 \times 10^8 \text{ s}^{-1}, & g_1 &= 3, & E_1 &= 2.94 \text{ eV}, \\ A_2 &= 0.66 \times 10^8 \text{ s}^{-1}, & g_2 &= 5, & E_2 &= 5.05 \text{ eV}. \end{aligned}$$

On average, the intensity ratio of the spectra shown in Figs. 3.51a–b is about $I_1/I_2 \simeq 4$. Thus, the mean plasma temperature corresponding to these spectra is about 5 eV or 60 000 K which is in good agreement with theoretical predictions by Mulser et al. (1973). This plasma temperature is not to be mistaken for the local tissue temperature, since it represents the kinetic energy of plasma electrons only.

In order to evaluate the free electron density of the plasma, the spectral widths of singlet lines need to be measured. These experiments were performed by Niemi (1994a) and yielded typical spectral widths of 0.15 nm for the calcium line at 422.7 nm as shown in Fig. 3.52. From these, the free electron density can be determined by applying *Saha's equation* of plasma physics. The derivation and significance of Saha's equation is discussed in detail by Griem (1964). Its physical interpretation is summarized in Fig. 3.53, where the spectral width at a given wavelength – in this case the calcium line at 422.7 nm – is plotted as a function of electron density and plasma temperature. In the example shown, a measured spectral width of 0.15 nm corresponds to a free electron density of approximately $10^{18}/\text{cm}^3$. Moreover, Fig. 3.53 illustrates that the free electron density shows a rather weak dependence on plasma temperature.

3.4.3 Summary of Plasma-Induced Ablation

- *Main idea:* ablation by ionizing plasma formation
- *Observations:* very clean ablation, associated with audible report and blueish plasma sparking
- *Typical lasers:* Nd:YAG, Nd:YLF, Ti:Sapphire
- *Typical pulse durations:* 100 fs . . . 500 ps
- *Typical power densities:* 10^{11} . . . 10^{13} W/cm²
- *Special applications:* refractive corneal surgery, caries therapy

3.5 Photodisruption

The physical effects associated with optical breakdown are *plasma formation* and *shock wave generation*. If breakdown occurs inside soft tissues or fluids, *cavitation* and *jet formation* may additionally take place. The meaning of these terms will be discussed in this section. The ablative process due to plasma ionization has already been described in Sect. 3.4. However, when discussing plasma-induced ablation, we neglected any secondary effects of the plasma. At higher pulse energies – and thus higher plasma energies – shock waves and other mechanical side effects become more significant and might even determine the global effect upon the tissue. Primarily, this is due to the fact that mechanical effects scale linearly with the absorbed energy. Then, because of the mechanical impact, the term *disruption* (from Latin: *ruptus* = ruptured) is more appropriate.

The effect of rupturing becomes evident when looking at Figs. 3.54a–b. These two photographs show a 90 μm thick glass plate on which picosecond pulses from a Nd:YLF laser were focused. Since glass is a simple detector for shocks – it splinters above a certain threshold value – the mechanical impact on the anterior and posterior surfaces are easily seen.

Cavitation is an effect that occurs when focusing the laser beam not on the surface of a tissue but into the tissue. For instance, a cavitation within a human cornea is seen in Fig. 3.55. It was generated by focusing a single picosecond pulse from a Nd:YLF laser underneath the epithelium. Immediately after laser exposure, the tissue was fixated to prevent the cavitation bubble from collapsing. The cross-section of the cavitation is elongated on an axis determined by the orientation of the collagen fibrils, because shear forces can readily split the tissue in this direction. Cavitation bubbles consist of gaseous vapors – mainly water vapor and carbon oxides – which eventually diffuse again into the surrounding tissue.

Photodisruption has become a well-established tool of minimally invasive surgery (MIS), since it was introduced by Krasnov (1973) and then further investigated by Aron-Rosa et al. (1980) and Fankhauser et al. (1981). Two of the most important applications of photodisruptive interaction are posterior capsulotomy of the lens – frequently being necessary after cataract surgery – and laser-induced lithotripsy of urinary calculi.

During photodisruption, the tissue is split by mechanical forces. Whereas plasma-induced ablation is spatially confined to the breakdown region, shock wave and cavitation effects propagate into adjacent tissue, thus limiting the localizability of the interaction zone. For pulse durations in the nanosecond range, the spatial extent of the mechanical effects is already of the order of millimeters even at the very threshold of breakdown. Actually, purely plasma-induced ablation is not observed for nanosecond pulses, because the threshold energy density of optical breakdown is higher compared to picosecond pulses as shown in Fig. 3.45, and the pressure gradient scales with plasma energy. Hence, for nanosecond pulses, optical breakdown is always associated with

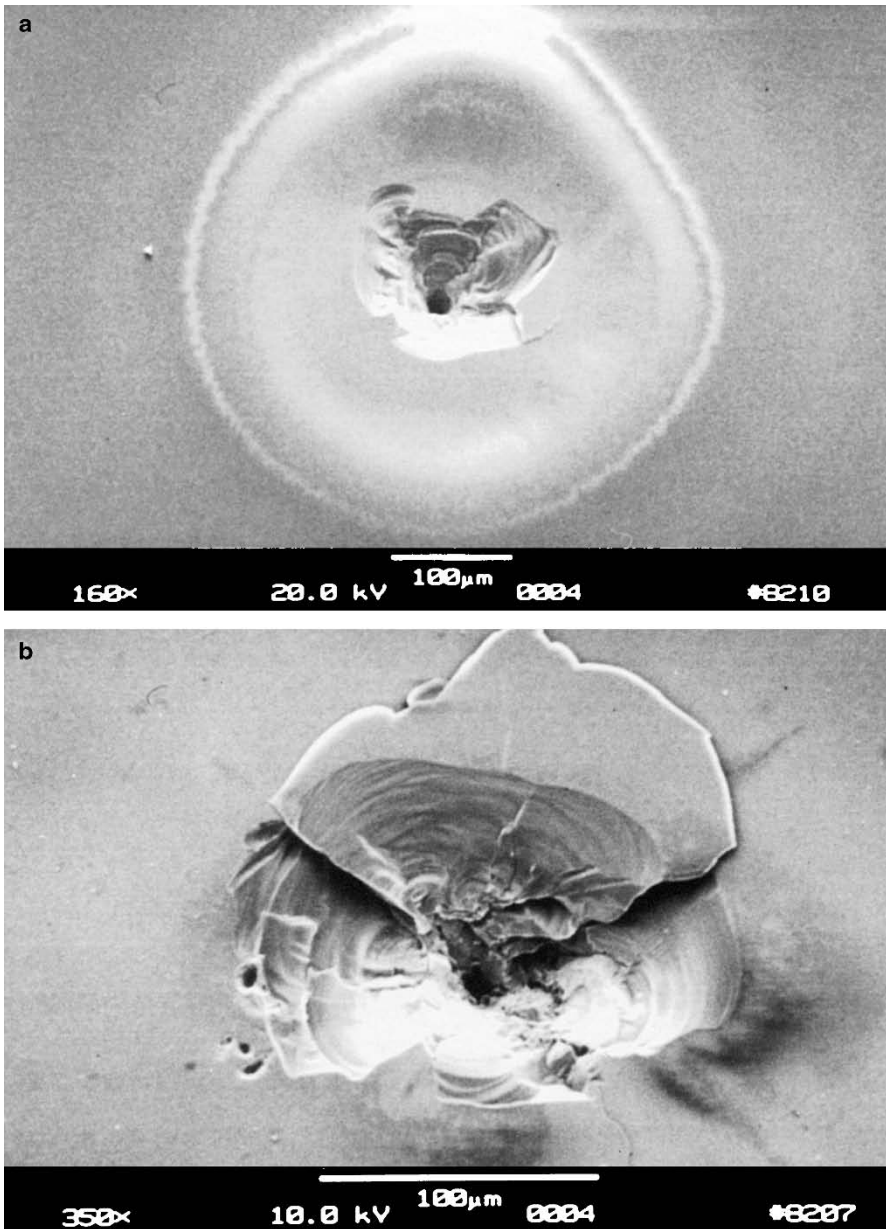


Fig. 3.54. (a) Anterior surface of a 90 μm thick glass plate exposed to ten pulses from a Nd:YLF laser (pulse duration: 30 ps, pulse energy: 1 mJ, focal spot size: 30 μm). (b) Posterior surface of a glass plate after a similar experiment. Reproduced from Niemz (1994a). © 1994 Springer-Verlag

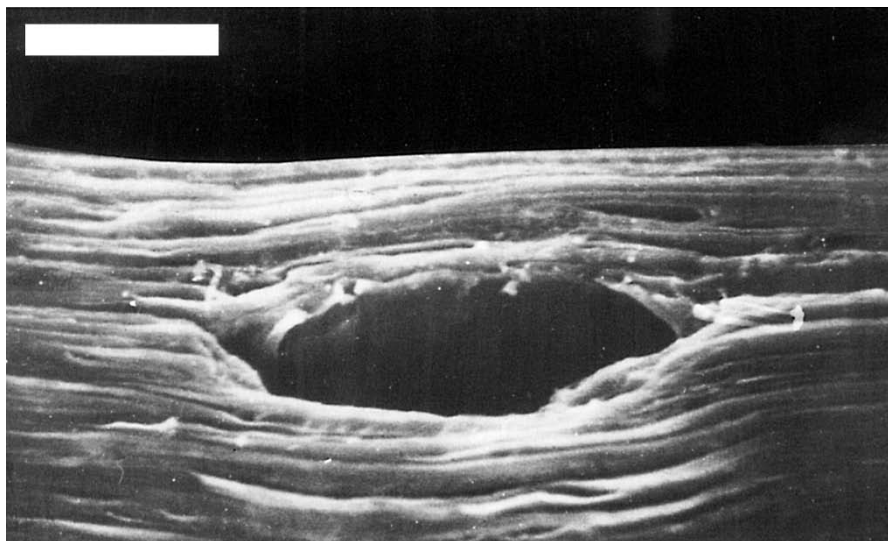


Fig. 3.55. Cavitation bubble within a human cornea induced by a single pulse from a Nd:YLF laser (pulse duration: 30 ps, pulse energy: 1 mJ, bar: 30 μm)

shock wave formation even at the very threshold. Since adjacent tissue can be damaged by disruptive forces, the presence of these effects is often an undesired but associated symptom. In contrast, picosecond or femtosecond pulses permit the generation of high peak intensities with considerably lower pulse energies. With these extremely short pulse durations, optical breakdown may still be achieved while significantly reducing plasma energy and, thus, disruptive effects. Moreover, spatial confinement and predictability of the laser–tissue interaction is strongly enhanced.

Since both interaction mechanisms – plasma-induced ablation as well as photodisruption – rely on plasma generation, it is not always easy to distinguish between these two processes. Actually, in the 1970s and 1980s, all tissue effects evoked by ultrashort laser pulses were attributed to photodisruption. It was only because of recent research that a differentiation between ablations solely due to ionization and ablations owing to mechanical forces seems justified. For instance, it was found by Niemz (1994a) that, in the case of picosecond pulses, ablation without mechanical side effects takes place at incident power densities of a few times the plasma threshold. Based on these findings and the theory describing the dependence of threshold parameters (see Figs. 3.45 and 3.46 in Sect. 3.4), approximate thresholds of both interaction types are listed in Table 3.14. The data represent estimated values for corneal tissue, assuming a mean ionization probability of about $\eta = 10 (\text{J}/\text{cm}^2)^{-1}$ as obtained from Table 3.13.

Table 3.14. Estimated parameters for the onset of plasma-induced ablation and photodisruption in corneal tissue

Pulse duration	Onset of plasma-induced ablation Energy density (J/cm ²)	Onset of photodisruption Energy density (J/cm ²)
100 fs	2.0	50
1 ps	3.3	50
10 ps	8.0	50
100 ps	23	50
1 ns	–	72
10 ns	–	230
100 ns	–	730

	Power density (W/cm ²)	Power density (W/cm ²)
100 fs	2.0×10^{13}	5.0×10^{14}
1 ps	3.3×10^{12}	5.0×10^{13}
10 ps	8.0×10^{11}	5.0×10^{12}
100 ps	2.3×10^{11}	5.0×10^{11}
1 ns	–	7.2×10^{10}
10 ns	–	2.3×10^{10}
100 ns	–	7.3×10^9

The values listed in Table 3.14 are graphically presented in Fig. 3.56. Obviously, plasma-induced ablation is limited to a rather narrow range of pulse durations up to approximately 500 ps. At longer pulse durations, the energy density necessary for achieving breakdown already induces significant mechanical side effects.

In general, photodisruption may be regarded as a multi-cause mechanical effect starting with optical breakdown. The primary mechanisms are shock wave generation and cavitation, completed by jet formation if cavitations collapse in fluids and near a solid boundary. In Fig. 3.57, a schematic sequence of these processes is illustrated indicating their relations to each other. Moreover, the distinction between photodisruption and plasma-induced ablation is emphasized.

The four effects – plasma formation, shock wave generation, cavitation, and jet formation – all take place at a different time scale. This is schematically illustrated in Fig. 3.58. Plasma formation begins during the laser pulse and lasts for a few nanoseconds afterwards as already mentioned when discussing Fig. 3.49. This basically is the time needed by the free electrons to diffuse into the surrounding medium. Shock wave generation is associated with the expansion of the plasma and, thus, already starts during plasma formation. However, the shock wave then propagates into adjacent tissue and leaves the focal volume. Approximately 30–50 ns later, it has slowed down to an ordinary acoustic wave. Cavitation, finally, is a macroscopic effect start-

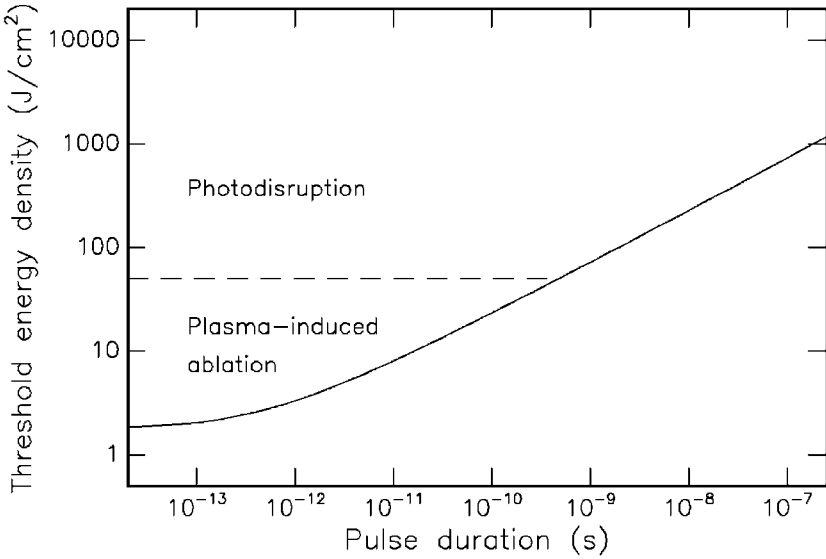


Fig. 3.56. Distinction of plasma-induced ablation and photodisruption according to applied energy density

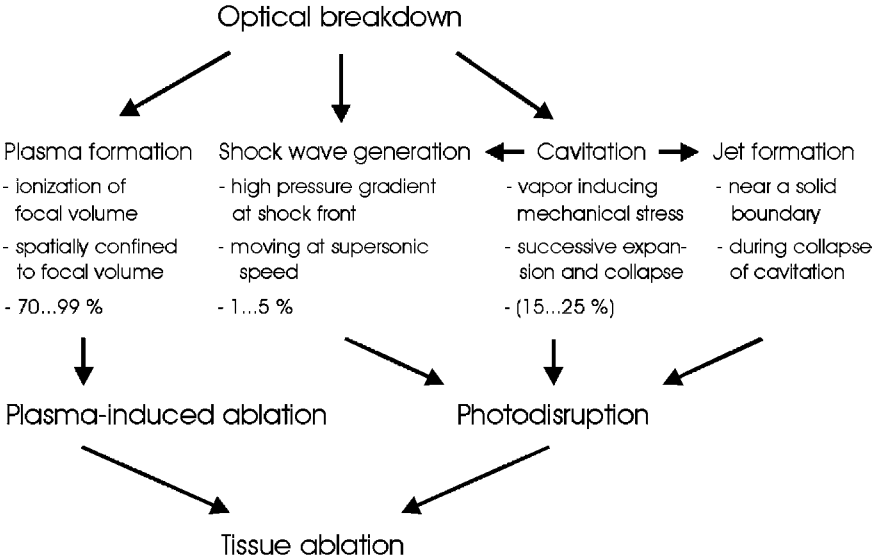


Fig. 3.57. Scheme of the physical processes associated with optical breakdown. Percentages given are rough estimates of the approximate energy transferred to each effect (incident pulse energy: 100 %). Cavitation occurs in soft tissues and fluids only. In fluids, part of the cavitation energy might be converted to jet formation

ing roughly 50–150 ns after the laser pulse. The time delay is caused by the material during the process of vaporization. Usually, the cavitation bubble performs several oscillations of expansion and collapses within a period of a few hundred microseconds as will be shown below. Since the pressure inside the bubble again increases during collapse, each rebound of the cavitation bubble is accompanied by another shock wave. Furthermore, every collapse can induce a jet formation if the bubble is generated in the vicinity of a solid boundary. Each of the effects contributing to photodisruption will be discussed in detail in the following paragraphs, because they all have their own physical significance.

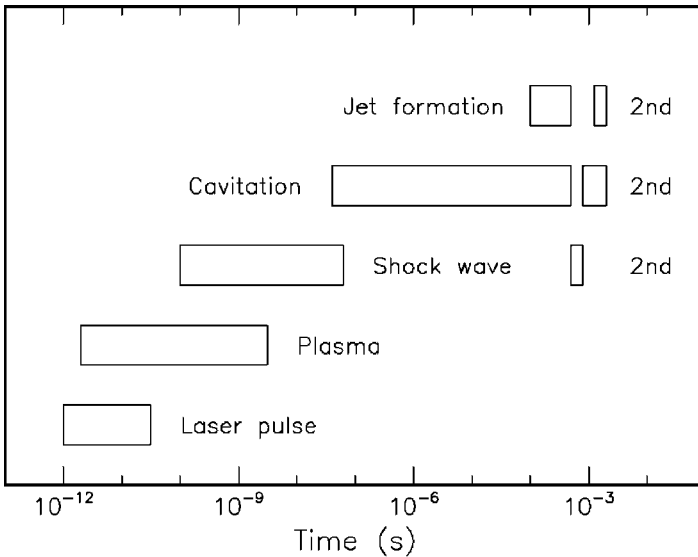


Fig. 3.58. Approximate time scale for all processes contributing to photodisruption. Assumed is a 30 ps laser pulse. The first and second occurrences of shock wave, cavitation and jet formation are indicated

3.5.1 Plasma Formation

The principles of laser-induced plasma formation have already been considered in Sect. 3.4. It should be emphasized, however, that the amount of energy absorbed during photodisruption is typically two or more orders of magnitude higher than during plasma-induced ablation. This is an immediate consequence of the different energy densities associated with either process as already emphasized in Fig. 3.1. Thus, the free electron density and the plasma temperature are also higher than for purely plasma-induced ablation. Therefore, in photodisruptive laser–tissue interactions, the following three effects are enabled or become more significant:

- plasma shielding,
- Brillouin scattering,
- multiple plasma generation.

Once formed, the plasma absorbs and scatters further incident light. This property “shields” underlying structures which are also in the beam path. The importance of the *plasma shielding* effect for medical laser applications was first recognized by Steinert et al. (1983) and Puliafito and Steinert (1984). In ophthalmology, the retina is considerably protected by this plasma shield during laser surgery of the lens or the vitreous. In Fig. 3.44, we have already encountered an increased absorption coefficient of the plasma. However, with the conditions of plasma-induced ablation, a significant amount of laser energy is still transmitted by the plasma. During photodisruptive interactions, thus at denser plasmas, the absorption coefficient is even enhanced, and the plasma serves as a very effective shield.

In *Brillouin scattering*, incident light is scattered by thermally excited acoustic waves and shifted in frequency corresponding to potential phonon frequencies of the material. During the heating process of the plasma, acoustic waves are generated which lead to Brillouin scattering. When applying even higher irradiances, the laser light itself may create alterations in optical density by which, in turn, it is scattered. Accordingly, this effect is called *stimulated Brillouin scattering*. It was described in detail by Ready (1971).

Finally, at the very high electric field strengths achieved during photodisruption, *multiple plasma generation* is enabled. Whereas close to the ablation threshold only one spark is induced at the very focus, several plasmas can be ignited at higher pulse energies. In the latter case, only the first section of the laser pulse will induce a plasma at the focal spot. Then, as the fluence increases during the pulse, succeeding radiation may also generate optical breakdown before reaching the smallest beam waist. Thus, a cascade of plasmas is initiated pointing from the focal spot into the direction of the laser source. This effect is schematically illustrated in Fig. 3.59.

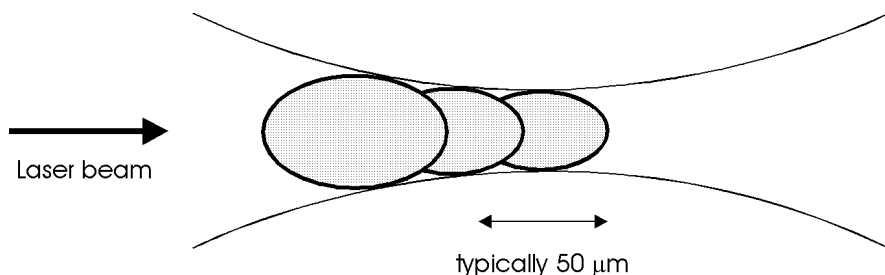


Fig. 3.59. Cascade of laser-induced plasmas. A Gaussian-shaped laser beam is incident from the left

Plasma formation in distilled water has been extensively studied by Docchio et al. (1986), Zysset et al. (1989), and Vogel et al. (1994a). Some of their results were presented in Sect. 3.4 when discussing the threshold behavior of laser-induced optical breakdown. Moreover, Vogel et al. (1994a) have determined plasma sizes with time-resolved photography. They have observed that the length of plasmas is strongly related to the pulse duration. Their measurements are summarized in Fig. 3.60.

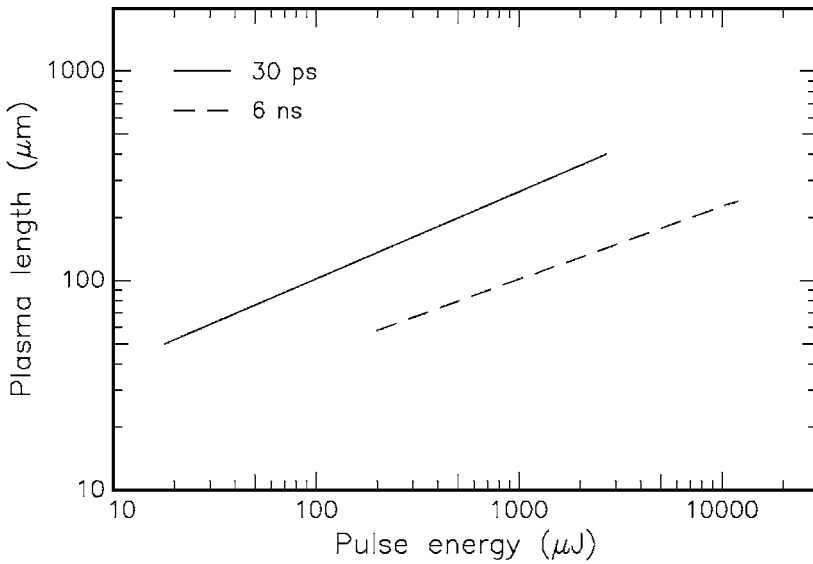


Fig. 3.60. Plasma length as a function of incident pulse energy. Measured with a Nd:YAG laser (pulse duration: as labeled, focal spot diameter: $4\ \mu\text{m}$) in distilled water. Data according to Vogel et al. (1994a)

Obviously, plasmas induced by 30 ps pulses are approximately 2.5 times as long as plasmas induced by 6 ns pulses of the same energy. Only at the respective thresholds of breakdown are the latter slightly longer. These different plasma lengths – and thus volumes – result in a considerably lower energy density of plasmas induced by picosecond pulses. Indeed, Vogel et al. (1994a) have observed a significant difference in the corresponding intensities of visible plasma fluorescence. Moreover, the plasma volume determines the fraction of incident energy to be converted to shock waves or cavitations. If the plasma volume is larger – like in plasmas induced by picosecond pulses – more energy is required for ionization and vaporization of matter. Hence, this amount of energy can no longer contribute to the generation of potential shock waves or cavitations. Therefore, we can conclude that plasmas induced by picosecond pulses are less likely to cause mechanical tissue damage than plasmas from nanosecond pulses.

The overall sequence of plasma formation is summarized in Table 3.15. In order to distinguish the physical parameters of plasma-induced ablation and photodisruption, two typical pulse durations of 10 ps and 100 ns are considered. These correspond to typical values of mode locked or Q-switched pulses, respectively. Energy densities and power densities at the threshold of plasma formation apply for corneal tissue and are taken from Table 3.14. Associated electric field strengths are calculated using (3.23). The critical electron density at the plasma threshold is derived from (3.46). It is not directly related to the pulse duration of the laser but does depend on its wavelength. In Sect. 3.4, we estimated typical densities of $10^{18}/\text{cm}^3$ for visible laser radiation. For the process of photodisruption, higher electron densities were obtained by Boulnois (1986). Finally, the absorption coefficient of the plasma is given by (3.45). It is also wavelength-dependent and determines the extent of the plasma shielding effect. In the case of plasma-induced ablation, some measured absorption coefficients are listed in Fig. 3.44. Although these data apply for water only, similar values can be assumed for corneal tissue because of its high water content. During photodisruption, higher absorption coefficients are accessible due to the increased electron density.

Table 3.15. Physical parameters of plasma formation in corneal tissue

Pulse duration	10 ps	100 ns
↓		
Energy density	8.0 J/cm ²	730 J/cm ²
↓		
Power density	8.0×10^{11} W/cm ²	7.3×10^9 W/cm ²
↓		
Electric field strength	2.5×10^7 V/cm	2.3×10^6 V/cm
↓		
Electron density of plasma	10^{18} – 10^{19} /cm ³	10^{18} – 10^{20} /cm ³
↓		
Nonlinear absorption of plasma (Plasma shielding)	1–100/cm	1–10 000/cm

The values listed in Table 3.15 provide a good estimate of the physical parameters associated with optical breakdown. In a first approximation, they apply for other targets, as well. In order to achieve a similar plasma electron density, roughly 100 times the energy density is needed when applying 100 ns pulses rather than 10 ps pulses. Therefore, provided the same focus size is chosen, plasmas induced by nanosecond pulses contain significantly more energy. This additional amount of energy must somehow dissipate into the surrounding medium. It is partly converted to the generation of shock waves, cavitation, and jet formation as will be discussed next.

3.5.2 Shock Wave Generation

As discussed in Sect. 3.4, laser-induced optical breakdown is accompanied by a sudden adiabatic rise in plasma temperature to values of up to a few 10 000 K. Primarily, this temperature can be attributed to the kinetic energy of free electrons. Due to their high kinetic energy, the plasma electrons are not confined to the focal volume of the laser beam but rather diffuse into the surrounding medium. When the inert ions follow at a certain time delay, mass is moved which is the basic origin of shock wave generation. This shock wave soon separates from the boundary of the plasma. It initially moves at hypersonic speed and eventually slows down to the speed of sound. In Fig. 3.61, the geometry of shock wave generation is illustrated.

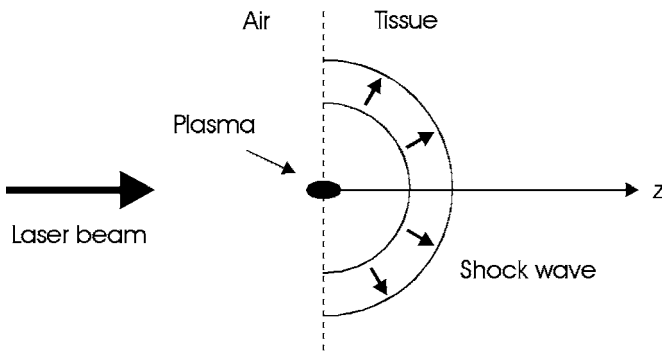


Fig. 3.61. Geometry of shock wave generation

Laser-induced shock waves in water were first investigated by Carome et al. (1966), Bell and Landt (1967), and Felix and Ellis (1971). Shock waves differ from sonic acoustic waves by their speed. Whereas the speed of sound in water, for instance, is 1483 m/s at 37°C, laser-induced shock waves typically reach speeds of up to 5000 m/s at the very focus. Both hypersonic shock waves and sonic acoustic waves are referred to as *acoustic transients*. In order to derive a relation describing the pressure gradient at the shock front, let us consider a slab of tissue with a cross-section A_0 which is passed through by a shock front at a speed u_s as seen in Fig. 3.62. During a time interval of dt , the shock front moves a distance of dx_s , thus

$$u_s = \frac{dx_s}{dt} .$$

The pressure inside the medium and its density are p_0 and ϱ_0 , respectively. The shock front induces a sudden increase in local pressure from p_0 to p_1 and of the density from ϱ_0 to ϱ_1 . The conservation of mass demands compensation by other particles intruding from the left side in Fig. 3.62. These particles move at a particle speed u_p which is usually lower than u_s . During a time

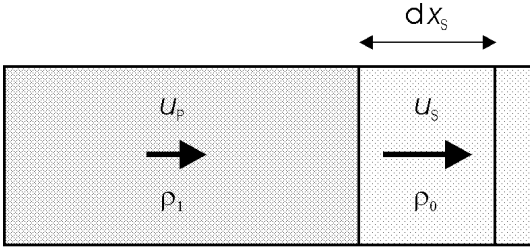


Fig. 3.62. Geometry of shock front moving through a slab of tissue

interval dt , a mass of $(\varrho_1 - \varrho_0)A_0dx_s$ must be provided. This is achieved at the particle speed u_p from a zone with a higher¹³ density ϱ_1 :

$$u_p \varrho_1 A_0 dt = (\varrho_1 - \varrho_0) A_0 dx_s .$$

Hence,

$$u_p = \frac{\varrho_1 - \varrho_0}{\varrho_1} u_s . \tag{3.61}$$

Beside the conservation of mass, the conservation of momentum must also be fulfilled. A mass $A_0 \varrho_1 dx_s$ begins to move at a speed u_p and thus receives a momentum $A_0 \varrho_1 u_p dx_s$. This momentum is provided by two means:

- The mass $A_0 \varrho_1 u_p dt$ intrudes at a speed u_p , thereby supplying a momentum of $A_0 \varrho_1 u_p^2 dt$.
- The shock front induces an increase in pressure from p_0 to p_1 . This pressure gradient induces a mechanical force $A_0(p_1 - p_0)$ which generates a momentum $A_0(p_1 - p_0)dt$ during the time interval dt .

The conservation law of momentum thus asks for

$$A_0 \varrho_1 u_p dx_s = A_0 \varrho_1 u_p^2 dt + A_0(p_1 - p_0)dt , \tag{3.62}$$

or

$$p_1 - p_0 = \varrho_1 u_p u_s - \varrho_1 u_p^2 . \tag{3.63}$$

Inserting (3.61) into (3.63) leads to a pressure increase

$$p_1 - p_0 = \varrho_0 u_p u_s . \tag{3.64}$$

An empirical relationship between the shock speed u_s and particle speed u_p was first determined by Rice and Walsh (1957). For water at high pressures exceeding 20 kbar, the following expression applies:

¹³ In our model, the shock front has just passed the left area in Fig. 3.62, thus leaving a higher density ϱ_1 behind.

$$u_s = 1.483 + 25.306 \log_{10} \left(1 + \frac{u_p}{5.19} \right), \quad (3.65)$$

where u_p and u_s must be inserted in units of km/s. For pressures lower than 20 kbar, an approximation was given by Doukas et al. (1991), i.e.

$$u_s = a + bu_p, \quad (3.66)$$

where a is the speed of sound and b is a dimensionless constant. In the case of water, $b = 2.07$ was estimated by Zweig and Deutsch (1992). Assuming a spherical shock wave with radius r , the conservation of momentum (3.62) leads to

$$4\pi r^2 \rho_1 u_p u_s \Delta t = c_0,$$

where Δt is the risetime of the shock front, and c_0 is a constant denoting the overall momentum. Replacing u_p within the last equation by an expression obtained from (3.66) yields

$$u_s(u_s - a) = \frac{c_1}{r^2},$$

with

$$c_1 = \frac{b}{4\pi \rho_1 \Delta t} c_0,$$

and the final solution

$$u_s(r) = \frac{a}{2} + \sqrt{\frac{a^2}{4} + \frac{c_1}{r^2}}. \quad (3.67)$$

The parameter c_1 can be empirically obtained. The particle speed is derived from (3.66)

$$u_p(r) = -\frac{a}{2b} + \frac{1}{b} \sqrt{\frac{a^2}{4} + \frac{c_1}{r^2}}. \quad (3.68)$$

Finally, the resulting pressure is obtained by inserting the expressions for particle speed u_p and shock speed u_s into (3.64), i.e.

$$p_1(r) = p_0(r) + \frac{\rho_0 c_1}{b} \frac{1}{r^2}. \quad (3.69)$$

From (3.64) and (3.65), we can also derive two relationships of the form

$$u_s = u_s(p_1),$$

$$u_p = u_p(p_1),$$

respectively. In the case of water, they are graphically presented in Fig. 3.63. At $p_1 = 0$ kbar, the shock speed u_s approaches 1483 km/s, whereas the particle speed u_p remains at 0 km/s. However, these relationships can also be

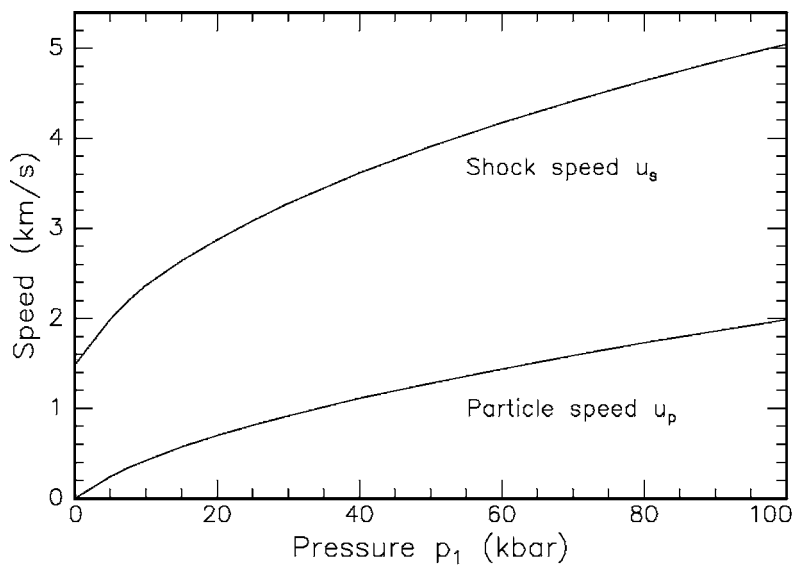


Fig. 3.63. Shock velocities and particle velocities in water as a function of shock wave pressure. Data according to Rice and Walsh (1957)

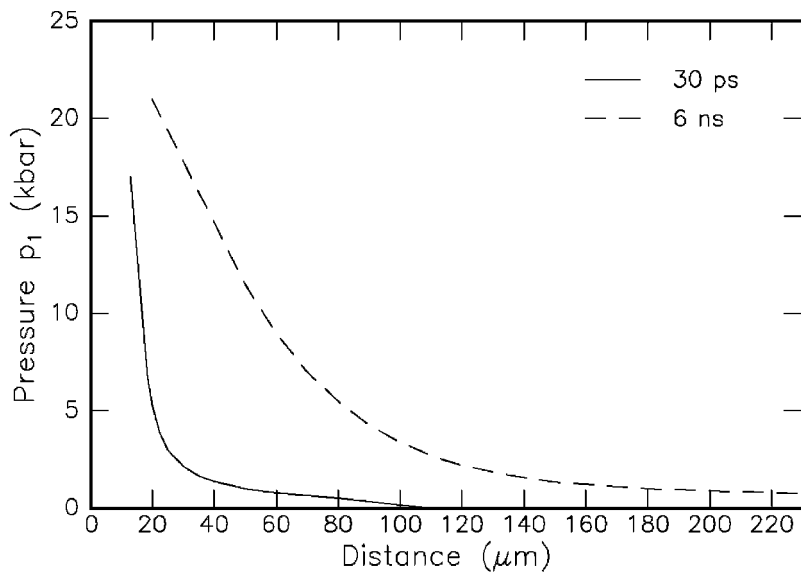


Fig. 3.64. Calculated shock wave pressures after optical breakdown in water. Breakdown was caused by pulses from a Nd:YAG laser (pulse duration: 30 ps, pulse energy: 50 μJ) and a Nd:YAG laser (pulse duration: 6 ns, pulse energy: 1 mJ), respectively. On the abscissa, the distance from the center of emission is given. Data according to Vogel et al. (1994a)

used to calculate the shock wave pressure p_1 as a function of shock speed u_s . By this means, shock wave pressures – which are usually very difficult to determine – can be derived from measured shock speeds.

Such calculations were performed by Vogel et al. (1994a) for shock waves induced by picosecond and nanosecond pulses. Their results are summarized in Fig. 3.64 where the shock wave pressure is shown in various distances from the center of emission. The initial pressure at the boundary of the laser plasma was 17 kbar for 50 μJ pulses with a duration of 30 ps, whereas it was 21 kbar for 1 mJ pulses with a duration of 6 ns. Although these values are quite similar, the pressure decay is significantly steeper for those shock waves which were induced by the picosecond pulses. In a distance of approximately 50 μm from the center of the shock wave emission, their pressure has already dropped to 1 kbar, whereas this takes a distance of roughly 200 μm when applying nanosecond pulses.

Moreover, it was observed by Vogel et al. (1994a) that the width of shock waves is smaller in the case of the picosecond pulses. They evaluated approximate widths of 3 μm and 10 μm for shock waves induced by either 30 ps or 6 ns pulses, respectively. Thus, the energies contained in these shock waves are not the same, because this energy is roughly given by

$$E_s \simeq (p_1 - p_0) A_s \Delta r, \quad (3.70)$$

with shock wave pressure p_1 , shock wave surface area A_s , and shock wave width Δr . Due to different plasma lengths as shown in Fig. 3.60, we obtain initial values of $A_s \simeq 100 \mu\text{m}^2$ for 30 ps pulses and $A_s \simeq 2500 \mu\text{m}^2$ for 6 ns pulses when assuming a focal spot diameter of 4 μm . From (3.70), we then find that $E_s \simeq 0.5 \mu\text{J}$ for 30 ps pulses and $E_s \simeq 50 \mu\text{J}$ for 6 ns pulses. Thus, only 1–5 % of the incident pulse energy is converted to shock wave energy, and shock waves from picosecond pulses are significantly weaker than those induced by nanosecond pulses with comparable peak pressures. From the corresponding particle speeds, Vogel et al. (1994a) have calculated a tissue displacement of approximately 1.2 μm for 30 ps pulses and a displacement of roughly 4 μm for 6 ns pulses. These rather small displacements can cause mechanical damage on a subcellular level only, but they might induce functional changes within cells.

Primarily, there exist two types of experiments which are performed to investigate the dynamics of shock wave phenomena: optical and mechanical measurements. During optical measurements, the shock wave is detected with a weaker probe beam after being generated by the main laser beam. In some setups, an external helium–neon laser or dye laser is used as a probe beam. In other cases, the probe beam is extracted from the main beam by means of a beamsplitter and directed through an optical delay. A decrease in probe beam intensity is detected with a fast photodiode as long as the shock wave passes through the focus of the probe beam. By moving the focus of the probe beam with respect to the site of plasma generation, the propagation of the

shock wave can be monitored on a fast digital oscilloscope. Fast photodiodes even enable a temporal analysis of the risetime of the shock front. Mechanical measurements rely on piezoelectric transducers transforming the shock wave pressure to a voltage signal. One commonly used detecting material is a thin foil made of polyvinylidene difluoride (PVDF) which is gold coated on both sides for measuring the induced voltage by attaching two thin wires. The corresponding pressure is monitored on a fast digital oscilloscope. Both types of experiments are illustrated in Figs. 3.65 and 3.66.

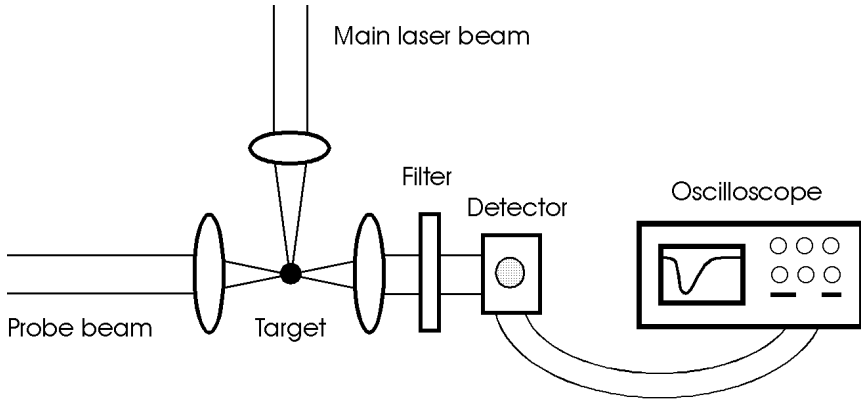


Fig. 3.65. Probe beam experiment for the detection of shock waves. A laser-induced shock wave deflects a second laser beam at the target. A fast photodiode measures the decrease in intensity of the probe beam

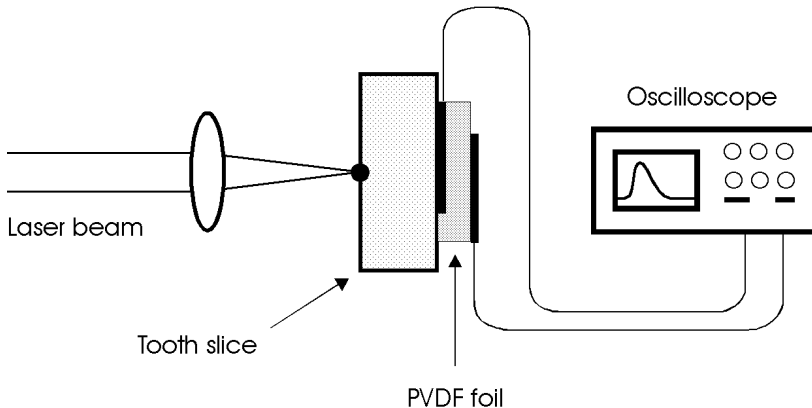


Fig. 3.66. PVDF experiment for the detection of shock waves. A laser-induced shock wave hits a piezoelectric transducer which converts pressure into a voltage signal. The voltage is measured with a digital oscilloscope

In Figs. 3.67 and 3.68, typical results are shown concerning the detection of acoustic transients. In Fig. 3.67, a shock wave was generated when inducing a plasma inside water by a 30 ps pulse from a Nd:YLF laser. A helium–neon laser served as a probe beam being focused at the depth of interest and detected with a fast photodiode. The probe beam is deflected as the shock wave passes through the focus of the probe beam, resulting in a decrease in detected intensity. A steep shock front is seen lasting for approximately 10 ns. After another 30 ns, the shock wave has completely passed. During its overall duration of roughly 40 ns, the shock wave can hardly cause any gross tissue displacement. Thus, further evidence is given that shock wave damage is limited to a subcellular level.

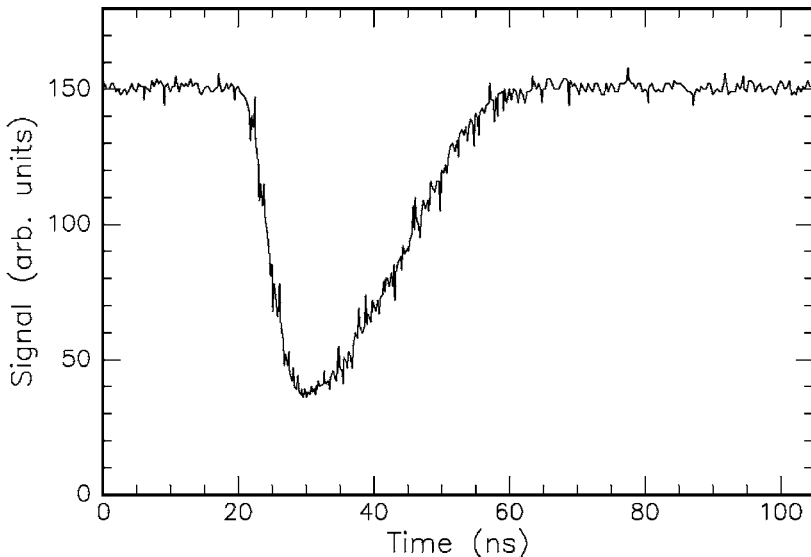


Fig. 3.67. Signal from a helium–neon laser serving as a detector for a shock wave generated in water by a Nd:YLF laser (pulse duration: 30 ps, pulse energy: 1 mJ)

In Fig. 3.68, on the other hand, the voltage signal from a PVDF transducer is shown. In this case, a plasma was induced at the surface of a tooth slice with a thickness of 0.5 mm. The detected PVDF signal arrives approximately 130 ns after the incident laser pulse, thus corresponding to a velocity of about 3800 m/s which is the speed of sound in teeth. The acoustic transient is reflected at the opposite surface of the tooth slice and is again detected after about $2 \times 130 \text{ ns} = 260 \text{ ns}$. Taking the round trip through the tooth slice into account, this time delay is related to the same speed of sound.

Since the shock wave loses energy when propagating through a medium, it eventually slows down until it finally moves at the speed of sound. With probe beam experiments as discussed above, traces of the shock wave at different

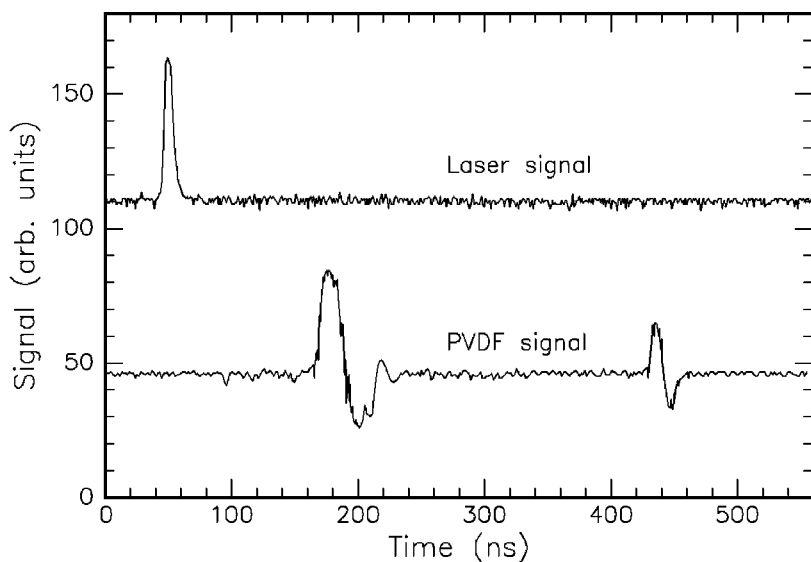


Fig. 3.68. Temporal traces of a Nd:YLF laser pulse (pulse duration: 30 ps, pulse energy: 500 μJ) and acoustic transient induced in a 0.5 mm thick tooth slice. The shock wave is detected with a PVDF transducer

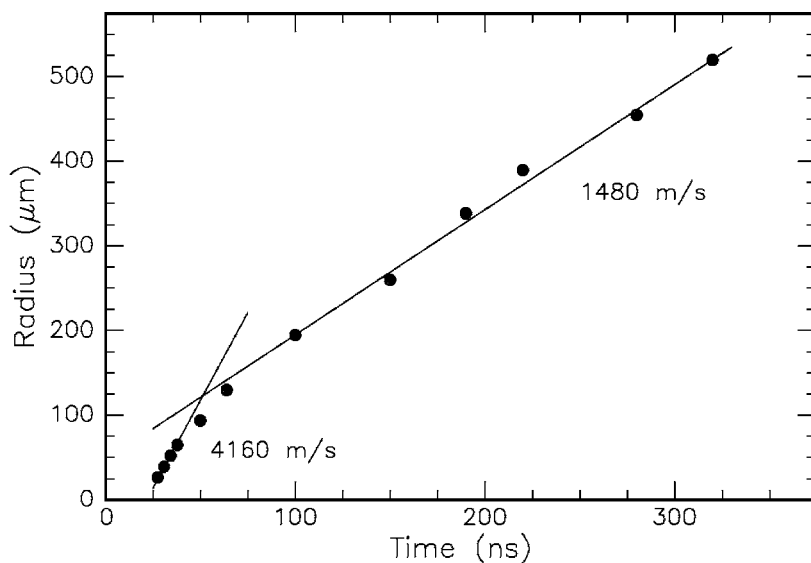


Fig. 3.69. Temporal evolution of a shock front induced in water by a Nd:YLF laser (pulse duration: 30 ps, pulse energy: 1 mJ). The shock speed decreases from 4160 m/s to 1480 m/s. Unpublished data

distances from its origin can be measured by moving the focus of the probe beam away from the plasma site. Typical results for such an experiment are shown in Fig. 3.69. From these data, a shock speed of approximately 4160 m/s is calculated for the first 30 ns. According to Fig. 3.63, this value corresponds to a shock wave pressure of approximately 60 kbar. The shock wave then slows down to about 1480 m/s – the speed of sound in water – after another 30 ns. Therefore, the spatial extent of shock waves is limited to approximately 0.2 mm. Similar results were reported by Puliafito and Steinert (1984) and Teng et al. (1987).

3.5.3 Cavitation

Historically, interest in the dynamics of cavitation bubbles started to rise after realizing their destructive effect on solid surfaces such as ship propellers and other hydraulic equipment. Laser-induced cavitations occur if plasmas are generated inside soft tissues or fluids. By means of the high plasma temperature, the focal volume is vaporized. Thereby, work is done against the outer pressure of the surrounding medium, and kinetic energy is converted to potential energy being stored in the expanded cavitation bubble. Within less than a millisecond, the bubble implodes again as a result of the outer static pressure, whereby the bubble content – typically water vapor and carbon oxides – is strongly compressed. Thus, pressure and temperature rise again to values similar to those achieved during optical breakdown, leading to a rebound of the bubble. Consequently, a second transient is emitted, and the whole sequence may repeat a few times, until all energy is dissipated and all gases are solved by surrounding fluids.

Cavitation bubbles have long been studied by a variety of techniques. The high-speed photographic technique was pioneered by Lauterborn (1972). It is very helpful in visualizing the temporal behavior of the cavitation bubble. High-speed photography is performed at framing rates with up to one million frames per second. A typical sequence of growth and collapse of a cavitation bubble is shown in Fig. 3.70. The bubble appears dark in front of a bright background, because it is illuminated from behind and the light was deflected by its wall. Through the center of the bubble, the illuminating light is transmitted without deflection. In the case shown, a Q-switched ruby laser with pulse energies ranging from 100 mJ to 400 mJ was used to induce the cavitation bubble. Its maximum diameter reaches a value of 2.05 mm at a time delay of approximately 300 μ s. The end of the first and second collapse is seen in the eighth and thirteenth frames, respectively.

A theory of the collapse of spherical cavitation bubbles was first given by Rayleigh (1917). He derived the relationship

$$r_{\max} = \frac{t_c}{0.915 \sqrt{\rho/(p_{\text{stat}} - p_{\text{vap}})}}, \quad (3.71)$$

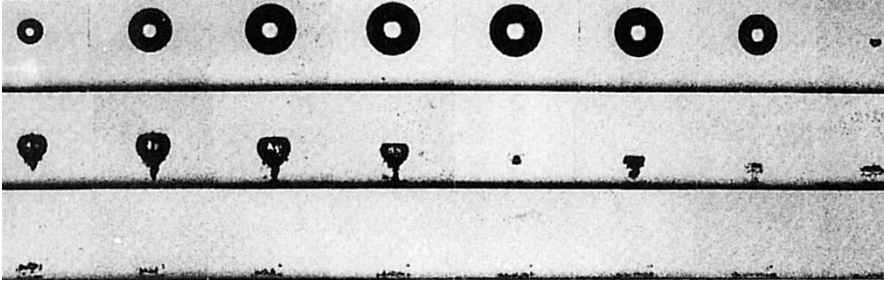


Fig. 3.70. Dynamics of cavitation bubble captured with high-speed photography. Pictures taken at 20 000 frames per second (frame size: 7.3 mm \times 5.6 mm). Reproduced from Vogel et al. (1989) by permission. © 1989 Cambridge University Press

where r_{\max} is the maximum radius of cavitation, t_c is the duration of the collapse, ρ is the density of the fluid, p_{stat} is the static pressure, and p_{vap} is the vapor pressure of the fluid. Thus, the time needed for each collapse is proportional to its maximum radius. The latter, on the other hand, is directly related to the bubble energy E_b by means of

$$E_b = \frac{4}{3} \pi (p_{\text{stat}} - p_{\text{vap}}) r_{\max}^3, \quad (3.72)$$

according to Rayleigh (1917). This equation states that the bubble energy is given by the product of its maximum volume and the corresponding pressure gradient. The bubble energy is thus readily determined when all kinetic energy has turned into potential energy.

The temporal oscillation of the cavitation bubble can be captured in probe beam experiments as shown in Fig. 3.71. Three complete oscillations are seen. The period of subsequent oscillations decreases in the same manner as their amplitude as already postulated by (3.71). In order to evaluate the dependence of the radius of cavitation on incident pulse energy, probe beam experiments have been performed similar to those discussed for shock wave detection. In Fig. 3.72, some data for picosecond and nanosecond pulses were collected by Zysset et al. (1989). Except for the lowest energy value, their measurements fit well to a straight line with a slope of 1/3. Because of the double-logarithmic scale of the plot, the relation given above by (3.72) is thus experimentally confirmed.

The conversion of incident energy to cavitation bubble energy is summarized in Figs. 3.73a–b. From the slopes, a conversion factor of approximately 19% is obtained for picosecond pulses, whereas it is roughly 24% when applying nanosecond pulses. Moreover, it was observed by Vogel et al. (1989) that the average energy loss of the cavitation bubbles during their first cycle is approximately 84%. The major part of this loss is attributed to the emission of sound. These results were confirmed in theoretical work performed by Ebeling (1978) and Fujikawa and Akamatsu (1980). From (3.72), it can

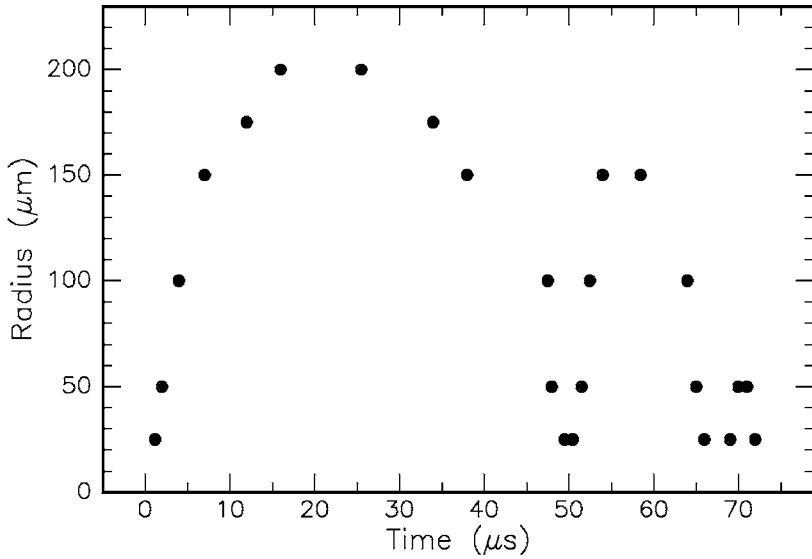


Fig. 3.71. Detection of cavitation bubble by means of a probe beam experiment with a helium–neon laser. Three complete oscillations of a cavitation bubble are observed which was induced in water by a Nd:YLF laser (pulse duration: 30 ps). Unpublished data

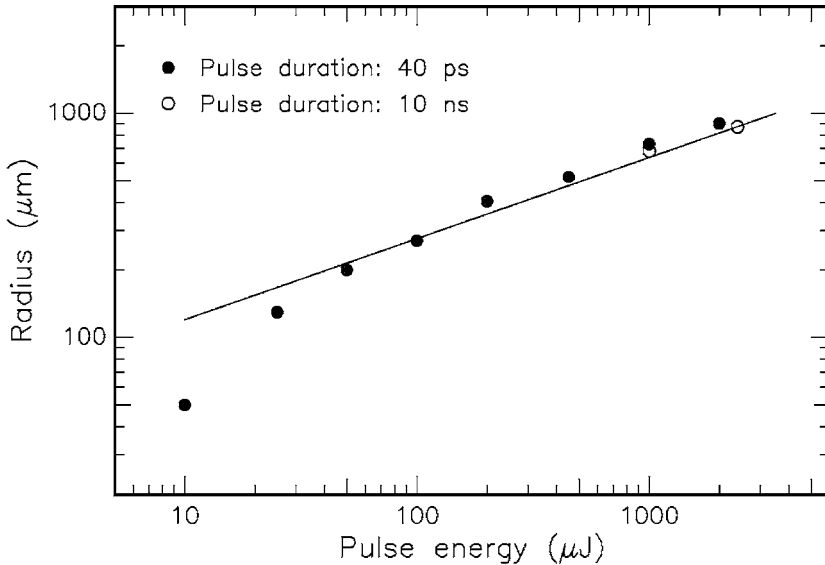


Fig. 3.72. Maximum radius of cavitation bubble as a function of incident pulse energy. Cavitations were induced in water by a Nd:YAG laser (pulse duration: as labeled). Data according to Zysset et al. (1989)

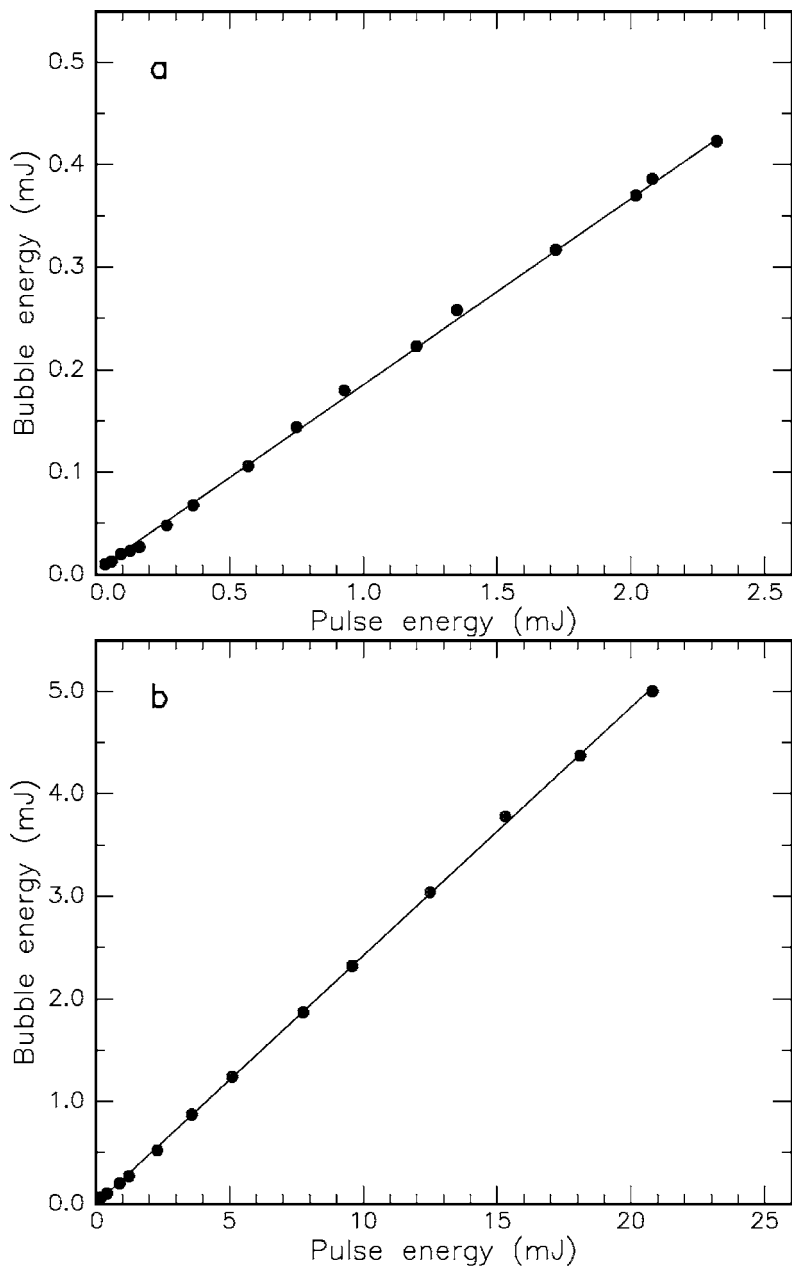


Fig. 3.73. (a) Cavitation bubble energy as a function of incident pulse energy from a Nd:YAG laser (pulse duration: 30 ps). The slope of the fitted line is 0.19. (b) Cavitation bubble energy as a function of incident pulse energy from a Nd:YAG laser (pulse duration: 6 ns). The slope of the fitted line is 0.24. Data according to Vogel et al. (1994a)

also be concluded that bubble-induced damage – i.e. the linear extent of the damage zone – scales with the cube root of the contained energy. This is of importance when determining the primary cause of tissue damage. It was observed by Vogel et al. (1990) that tissue damage also scales with the cube root of pulse energy. Thus, cavitations are more likely to induce damage than shock waves, since shock wave damage should be related to \sqrt{E} as can be derived from (3.70) when inserting $A_s \sim r^2$.

It has been emphasized above that damage of tissue due to shock waves is limited to a subcellular level due to their short displacement lengths of approximately 1–4 μm . Since the diameter of cavitation bubbles may reach up to a few millimeters, macroscopic photodisruptive effects inside tissues are believed to primarily originate from the combined action of cavitation and jet formation which will be discussed next.

3.5.4 Jet Formation

As recently stated by Tomita and Shima (1986), the impingement of a high-speed liquid jet developing during the collapse of a cavitation bubble may lead to severe damage and erosion of solids. Jet formation was first investigated and described by Lauterborn (1974) and Lauterborn and Bolle (1975) when producing single cavitation bubbles by focusing Q-switched laser pulses into fluids. When cavitation bubbles collapse in the vicinity of a solid boundary, a high-speed liquid jet directed toward the wall is produced. If the bubble is in direct contact with the solid boundary during its collapse, the jet can cause high-impact pressure against the wall. Thus, bubbles attached to solids have the largest damage potential.

Jet formation has been thoroughly studied by means of high-speed photography as introduced above. The temporal behavior of cavitation and jet formation is shown in Fig. 3.74. A cavitation bubble was generated near a solid boundary – a brass block located at the bottom of each frame and visible by a dark stripe – and captured with high-speed photography. Jet formation toward the brass block is observed during the collapse of the bubble. Jet velocities of up to 156 m/s were reported by Vogel et al. (1989). The water hammer pressure corresponding to such a velocity is approximately 2 kbar. If the distance between the cavitation bubble and solid boundary is further decreased as seen in the bottom sequence of Fig. 3.74, a counterjet is formed which points away from the solid boundary.

What is the origin of jet formation, and why does it only occur near a solid boundary? To answer these questions, let us take a closer look at the collapse of a cavitation bubble. When the bubble collapses due to external pressure, the surrounding fluid is accelerated toward the center of the bubble. However, at the side pointing to the boundary there is less fluid available. Hence, the collapse takes place more slowly at this side of the bubble. This effect ultimately leads to an asymmetric collapse. At the faster collapsing side, fluid particles gain additional kinetic energy, since the decelerating force – i.e. the

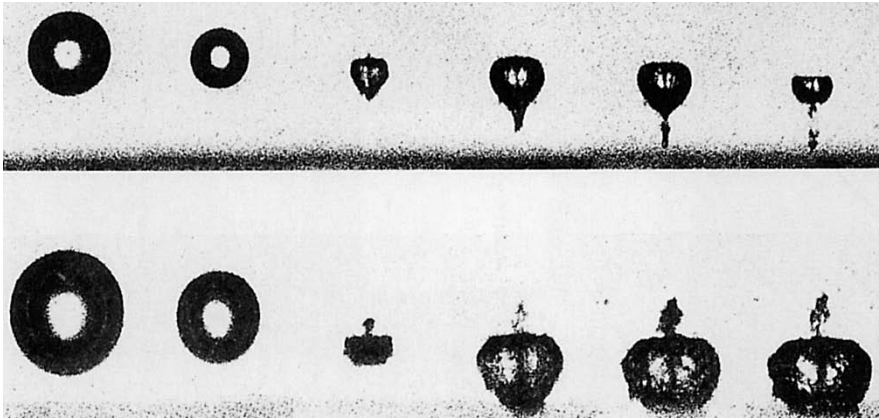


Fig. 3.74. Bubble collapse with jet formation (*top*). Pictures taken at 20 000 frames per second (frame size: 7.3 mm × 5.6 mm). Bubble collapse with counterjet formation (*bottom*). Reproduced from Vogel et al. (1989) by permission. © 1989 Cambridge University Press

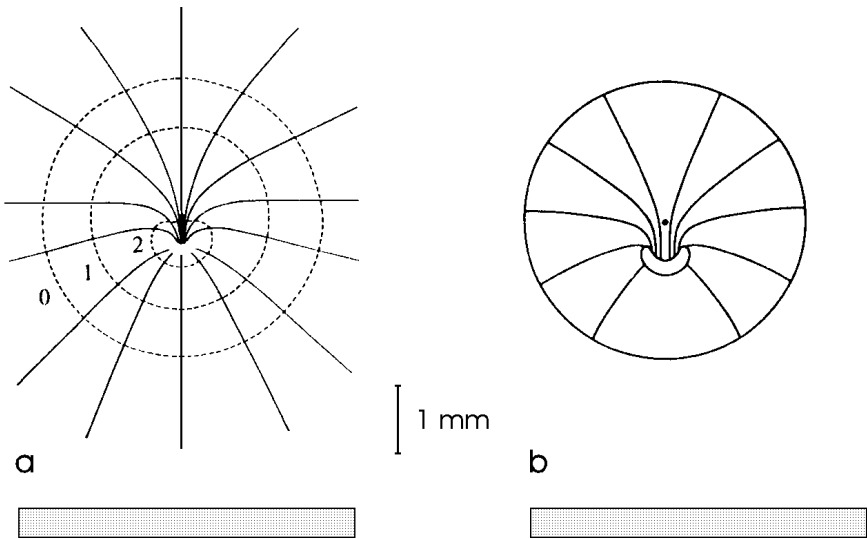


Fig. 3.75. (a) Experimentally obtained pathline portrait of the flow around a collapsing cavitation bubble near a solid wall. Bubble shape 0 represents the bubble at maximum expansion, whereas shapes 1 and 2 correspond to later stages during the collapse. (b) Calculated pathline portrait from Kucera and Blake (1988) for several points on the wall of the collapsing bubble. Reproduced from Vogel and Lauterborn (1988) by permission. © 1988 Optical Society of America

force by the slower collapsing opposite wall – is delayed. This explains why jet formation occurs toward the solid boundary. If the jet is relatively slow, the velocity of the central part of the slower collapsing side might even be higher than the jet itself. This is conceivable, because that side of the bubble is accelerated until the very end of the collapse. In this case, a counterjet is formed pointing in the opposite direction. Pathline portraits of the flow around collapsing bubbles have been experimentally and theoretically determined by Vogel and Lauterborn (1988) and Kucera and Blake (1988), respectively. In Figs. 3.75a–b, two of them are shown which offer a good visualization of the fluid flow during the collapse.

The damaging effect of jet formation is extremely enhanced if a gas bubble remaining from an earlier laser pulse is hit by acoustic transients generated by subsequent pulses. According to Vogel et al. (1990), the damage range induced by a 4 mJ pulse can reach diameters of up to 2–3.5 mm if gas bubbles are attached to the corneal tissue. Very small gas bubbles, however, quickly dissolve due to their small volume and strong surface tension. Therefore, these microbubbles should not cause any problem in achieving a certain predictable effect if the repetition rate of the laser pulses is adequately chosen.

3.5.5 Summary of Photodisruption

- *Main idea:* fragmentation and cutting of tissue by mechanical forces
- *Observations:* plasma sparking, generation of shock waves, cavitation, jet formation
- *Typical lasers:* solid-state lasers, e.g. Nd:YAG, Nd:YLF, Ti:Sapphire
- *Typical pulse durations:* 100 fs . . . 100 ns
- *Typical power densities:* 10^{11} . . . 10^{16} W/cm²
- *Special applications:* lens fragmentation, lithotripsy

3.6 Questions to Chapter 3

Q3.1. Which energy density is typical for a laser–tissue interaction?

A: 1 J/m². B: 1 mJ/cm². C: 1 J/cm².

Q3.2. Which is toxic to a biological cell?

A: carotenoid. B: excited singlet oxygen. C: photosensitizer.

Q3.3. Coagulation occurs at approximately

A: 60°C. B: 80°C. C: 100°C.

Q3.4. UV photons have an energy

A: < 0.3 eV. B: < 3 eV. C: > 3 eV.

Q3.5. In a plasma with electron density N , the coefficient of absorption is

A: $\sim \sqrt{N}$. B: $\sim N$. C: $\sim N^2$.

Q3.6. Why should there be an appropriate time gap in photodynamic therapy between application of a photosensitizer and laser exposition?

Q3.7. Two different laser pulses from a Nd:YAG laser are used to irradiate living liver tissue: a 100 mJ pulse at a pulse duration of 1 ms and a 100 pJ pulse at a pulse duration of 1 ps. Both laser pulses have an average power of 100 W and are focused to a spot of 1 mm in diameter. How will the tissue react in either case?

Q3.8. Why can a frequency-quadrupoled Nd:YAG laser at a wavelength of 266 nm induce photoablation, while a frequency-doubled Nd:YAG laser at a wavelength of 532 nm cannot?

Q3.9. Which three processes determine the temporal behavior of the free electron density in a plasma?

Q3.10. What is the basic physical mechanism that plasma-induced ablation and photodisruption have in common, and which laser parameter has to be altered to switch from one type of interaction to the other?

4. Medical Applications of Lasers

In this chapter, we will discuss principal applications of lasers in modern medicine. Due to the present boom in developing new laser techniques and due to the limitations given by the dimensions of this book, not all disciplines and procedures can be taken into account. The main intention is thus to focus on the most significant applications and to evoke a basic feeling for using certain techniques. The examples are chosen to emphasize substantial ideas and to assist the reader in grasping some technical solutions. Potential difficulties and complications arising from either method are addressed, as well. However, we should always keep in mind that any kind of laser therapy will not be indicated if alternative methods are available which offer a better rate of success, are less dangerous to the patient, and/or easier to perform.

Because of the historic sequence, the first section will be concerned with laser applications in *ophthalmology*. Even today, the majority of medical lasers sold is applied in this field. *Dentistry* was the second clinical discipline to which lasers were introduced. However, although considerable research has been done, the results were not quite as promising in most cases, and the discussion on the usefulness of dental lasers still proceeds. Today, the major effort of clinical laser research is focusing on various kinds of tumor treatments such as photodynamic therapy (PDT) and laser-induced interstitial thermotherapy (LITT). These play a significant role in many other medical disciplines like *gynecology*, *urology*, and *neurosurgery*. Due to recent advancements in instrumentation for minimally invasive surgery (MIS), e.g. the development of miniature catheters and endoscopes, novel techniques are under present investigation in *angioplasty* and *cardiology*. Very interesting laser applications were found in *dermatology* and *orthopedics*. And, recently, successful laser treatments have been reported in *gastroenterology*, *otorhinolaryngology*, and *pulmology* as discussed at the end of this chapter.

Thus, it can be concluded that – at the present time – laser medicine is a rapidly growing field of both research and application. This is not at all astonishing, since neither the development of novel laser systems nor the design of appropriate application units have yet come to stagnation. Moreover, laser medicine is not restricted to one or a few disciplines. Instead, it has meanwhile been introduced to almost all of them, and it is expected that additional clinical applications will be developed in the near future.

4.1 Lasers in Ophthalmology

In ophthalmology, various types of lasers are being applied today for either diagnostic or therapeutic purposes. In diagnostics, lasers are advantageous if conventional incoherent light sources fail. One major diagnostic tool is confocal laser microscopy which allows the detection of early stages of retinal alterations. By this means, retinal detachment and also glaucoma¹ can be recognized in time to increase the probability of successful treatment. In this book, however, our interest focuses on therapeutic laser applications. The first indications for laser treatment were given by detachments of the retina. Meanwhile, this kind of surgery has turned into a well-established tool and only represents a minor part of today's ophthalmic laser procedures. Others are, for instance, treatment of glaucoma and cataract. And, recently, refractive corneal surgery has become a major field of research, too.

The targets of all therapeutic laser treatments of the eye can be classified into front and rear segments. The front segments consist of the *cornea*, *sclera*, *trabeculum*, *iris*, and *lens*. The rear segments are given by the *vitreous body* and *retina*. A schematic illustration of a human eye is shown in Fig. 4.1. In the following paragraphs, we will discuss various treatments of these segments according to the historic sequence, i.e. from the rear to the front.

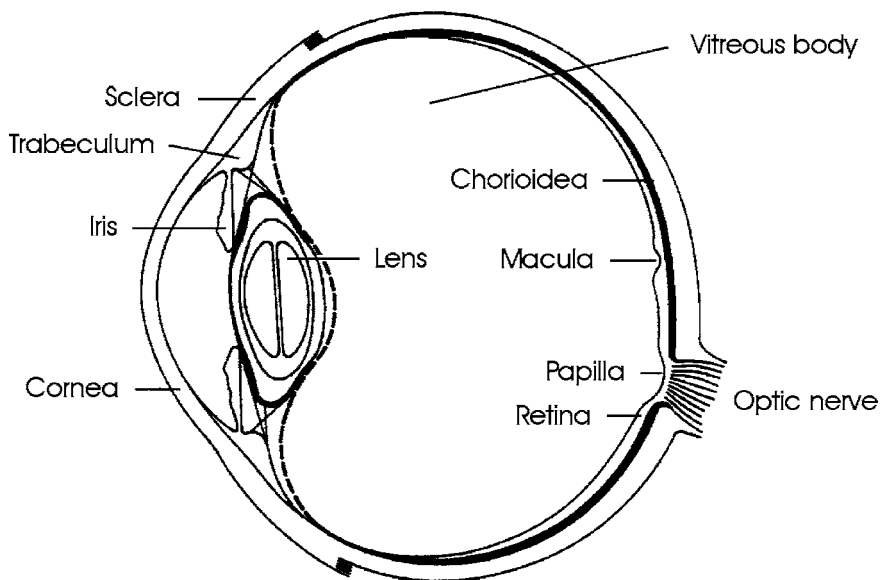


Fig. 4.1. Scheme of a human eye

¹ Since glaucoma is usually associated with a degeneration of the optical nerve fibers, it can be detected by measuring either the thickness of these fibers or alterations of the optic disc. Further details are given by Bille et al. (1990).

Retina

The retina is a part of the central nervous system. Its function is to convert an optical image focused on it into nerve impulses of the optic nerve emerging from it. The retina is a thin and rather transparent membrane which is permeated with blood vessels. According to Le Grand and El Hage (1980), the thickness of the retina varies from 0.5 mm near the papilla to 0.1 mm at the macula². Anatomically, the retina is subdivided into several different layers, each of them having their own distinct function: pigment epithelium, receptor layer, external limiting membrane, cell layer, nerve fiber layer, and internal limiting membrane. A schematic cross-section of a human retina is shown in Fig. 4.2.

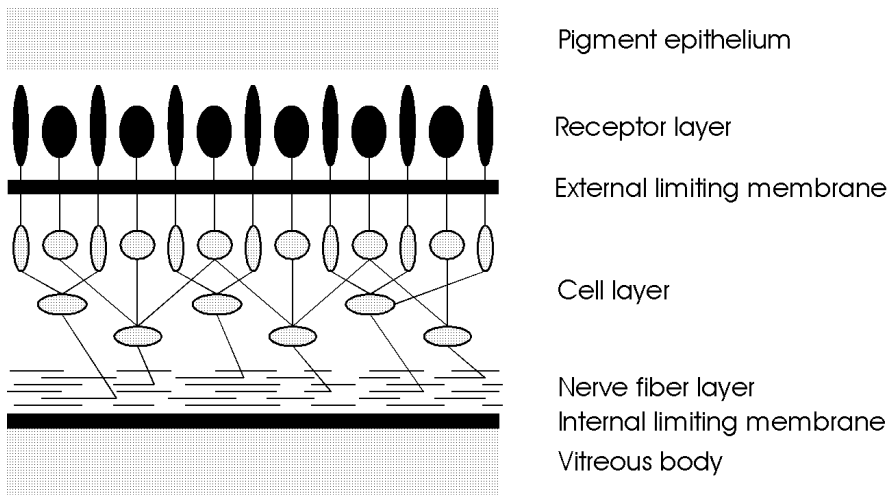


Fig. 4.2. Cross-section of a human retina

The *pigment epithelium* is strongly attached to the chorioidea. The *receptor layer* consists of two types of cells – rods and cones. Rods are used in dim light and are primarily located around the macula. Cones are receiving colors in good light and are found especially in the fovea. Obviously, light has to pass through virtually the whole retina beyond the *external limiting membrane*, before it can stimulate any receptor cells. This structural arrangement is known as the “reversed retina” and can be explained by the fact that the retina is an invagination of the embryonic cerebral wall. The *cell layer* is made up of horizontal cells, bipolar cells, amacrine cells, and ganglion cells.

² The *papilla* is a certain location where the optic nerve exits the retina. The *macula* is the region with the highest density of color receptors. An image formed on the *fovea*, the central section of the macula, is characterized by best vision. Thus, macula and fovea are the most important segments of the retina.

The main function of these cells is to serve as a first network with corresponding receptive fields. Finally, the *nerve fiber layer* contains the axons of the ganglion cells, whereas the *internal limiting membrane* forms a boundary between the retina and vitreous body.

The ophthalmologist Meyer-Schwickerath (1949) was the first to investigate the coagulation of the retina with sunlight for therapeutic purposes. Because of the inconvenient circumstances of this kind of surgery, e.g. the necessity of sunshine, he continued his studies with his famous xenon photo-coagulator as reported in 1956. Shortly after the invention of the laser by Maiman (1960), first experimental studies with the ruby laser were performed by Zaret et al. (1961). The first reports on the treatment of patients were given by Campbell et al. (1963) and Zweng et al. (1964). They discovered that the ruby laser was a very suitable tool when welding detached segments of the retina to the chorioidea located underneath. However, it also became evident that the ruby laser was not able to close open blood vessels or stop bleeding. It was soon found that the argon ion laser is better suited for this aim. Its green and blue wavelengths are strongly absorbed by the hemoglobin of blood – in contrast to the red light from a ruby laser – which finally leads to the coagulation of blood and blood vessels. At typical exposure durations ranging from 0.1 s to a few seconds, applied laser powers of 0.1–1 W, and spot diameters of approximately 200–1000 μm , almost all incident laser energy is converted to heat. Thus, coagulation of retinal tissue is achieved by means of thermal interaction. As discussed in Sect. 3.2, proteins are denaturated and enzymes are inactivated, thereby initiating the process of congealment.

The surgeon conducts the laser coagulation through a slit lamp and a contact glass. He approaches the necessary laser power from below threshold until the focused area just turns greyish. Coagulation of the macula is strictly forbidden, since it would be associated with a severe loss in vision. The temperatures achieved should generally remain below 80°C to prevent unnecessary vaporization and carbonization. A good localization of blood vessels, i.e. by confocal laser microscopy, and a precise application of the desired energy dose are mandatory when striving for satisfactory results.

At the beginning of the 1970s, the krypton ion laser became very significant for ophthalmic applications. Its red and yellow wavelengths at 647 nm and 568 nm, respectively, turned out to be very useful when trying to restrict the interaction zone to either the pigment epithelium or the chorioidea. Detailed histologic studies on this phenomenon were conducted by Marshall and Bird (1979). It was found that the red line is preferably absorbed by the chorioidea, whereas the yellow line is strongly absorbed by the pigment epithelium and also by the xanthophyll contained in the macula. Recently, McHugh et al. (1988) proposed the application of diode lasers, since their invisible emission at a wavelength of approximately 800 nm does not dazzle the patient's eye.

There exist six major indications for laser treatment of the retina:

- retinal holes,
- retinal detachment,
- diabetic retinopathy,
- central vein occlusion,
- senile macula degeneration,
- retinal tumors (retinoblastoma).

In the case of *retinal holes*, proper laser treatment prevents their further enlargement which could otherwise lead to retinal detachment. Laser surgery is performed by welding the retina to the underlying chorioidea within a narrow ring-shaped zone around the hole as shown in Fig. 4.3a. The attachment of the coagulated tissue is so strong that further tearing is usually suppressed. If necessary, however, the procedure can be repeated several times without severe complications.

Retinal detachment is often a consequence of undetected retinal holes or tears. It mainly occurs in myopic patients, since the vitreous body then induces an increased tensile stress to the retina. Moderate detachments are treated in a similar mode as retinal holes. In the case of a severe detachment, the treatment aims at saving the fovea or at least a small segment of the macula. This procedure is called panretinal coagulation and is illustrated in Fig. 4.3b. Unfortunately, laser treatment of retinal detachment is often associated with the formation of new membranes in the vitreous body, the retina, or beneath the retina. These complications are summarized by the clinical term *proliferative retinopathy*. A useful therapeutic technique for the dissection of such membranes was given by Machemer and Laqua (1978).

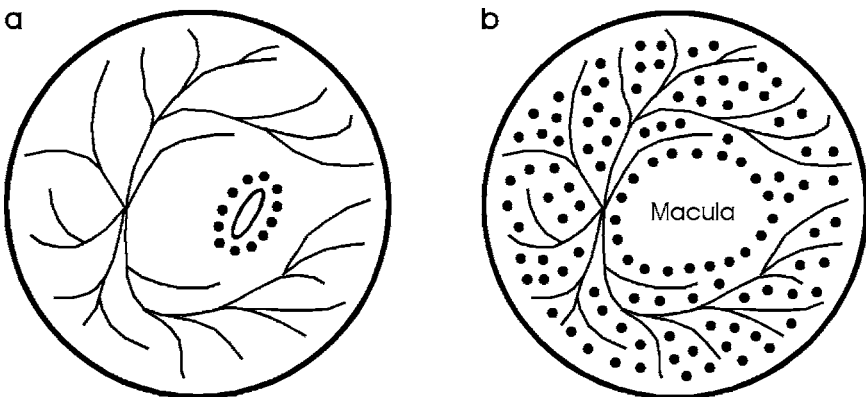


Fig. 4.3. (a) Placement of coagulation spots in the case of retinal holes or moderate detachments. (b) Placement of coagulation spots during panretinal coagulation

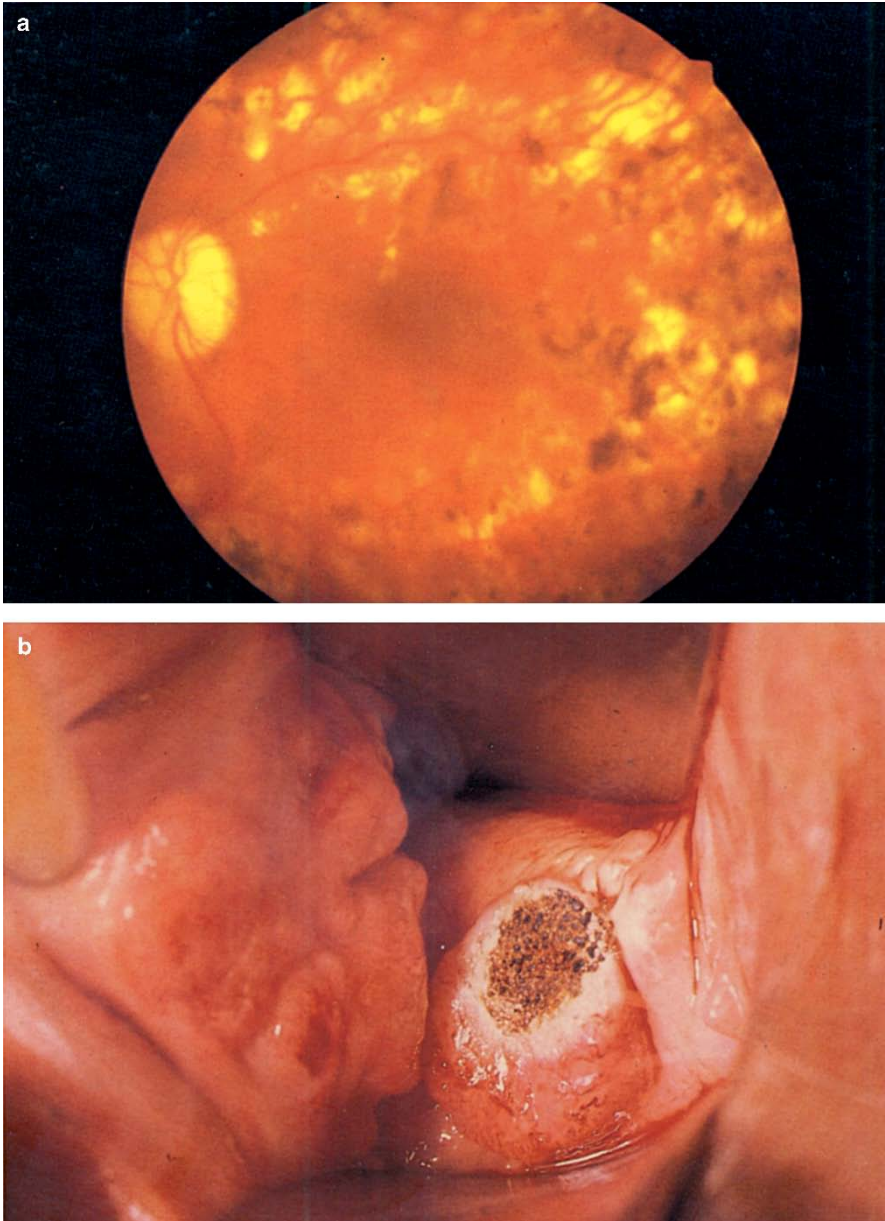


Fig. 4.4. (a) Panretinal coagulation in a diabetes patient performed with an argon ion laser (power: 200 mW). (b) Vaporization of cervical tissue with a CO₂ laser (power: 10 W). Photographs kindly provided by Dr. Burk (Heidelberg) and Dr. Kurek (Heidelberg)

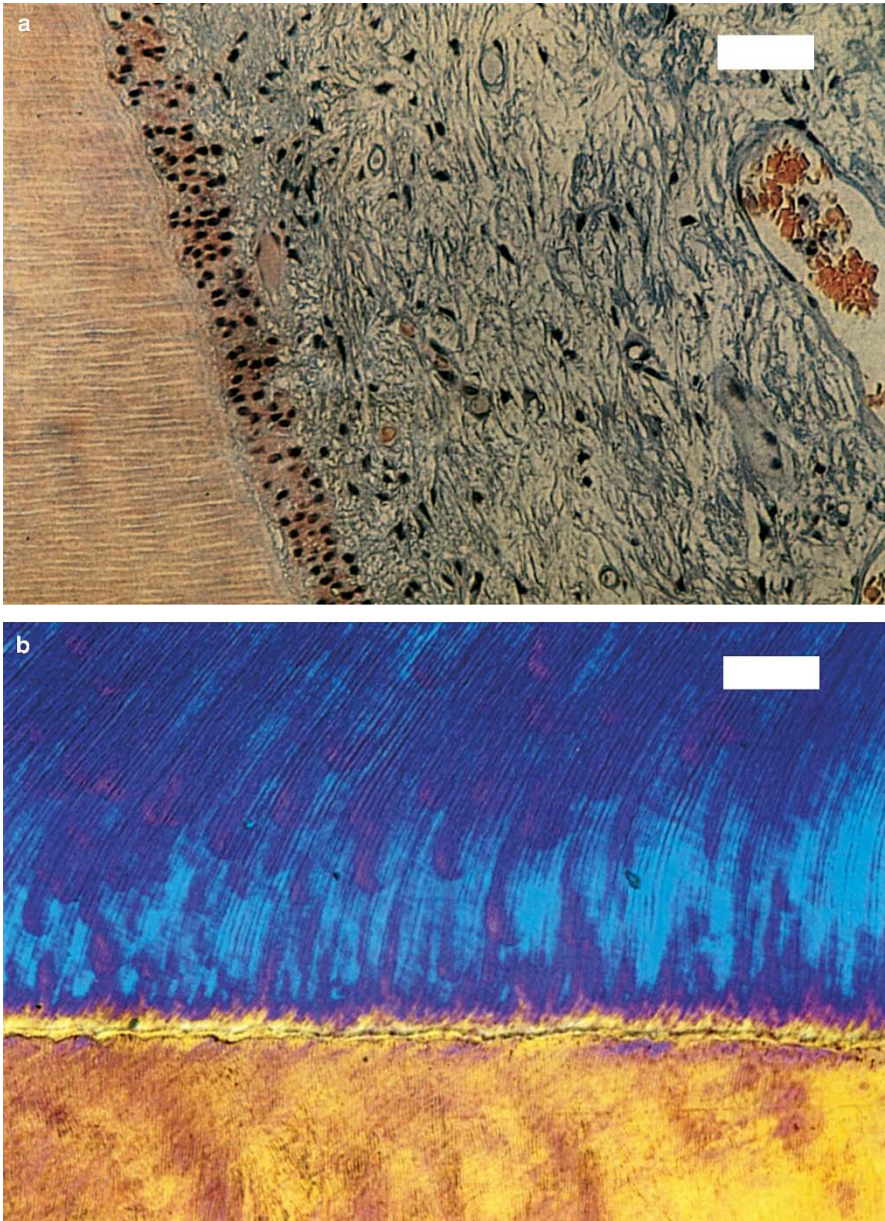


Fig. 4.5. (a) Histologic section of a human tooth after exposure to 16 000 pulses from a Nd:YLF laser (pulse duration: 30 ps, pulse energy: 500 μ J, bar: 50 μ m). The junction of dentin (*left*) and pulp (*right*) is shown which was located next to the application site. (b) Polarized microscopy of a human tooth slice after exposure to 16 000 pulses from the same laser (bar: 50 μ m). The junction of dentin (*top*) and enamel (*bottom*) is shown which was located next to the application site

When a patient is suffering from *diabetic retinopathy*, the concentration of oxygen in the blood is strongly reduced due to disturbances in the body. Because of the lack in oxygen, new blood vessels are formed which is called *neovascularization*. Hemorrhages inside the vitreous body might then lead to severe losses in vision. In order to prevent complete blindness, the whole retina is coagulated except the fovea itself, i.e. a panretinal coagulation is performed as in the case of a severe retinal detachment. By this means, it is assured that the progress of neovascularization is stopped and that at least the fovea does receive enough oxygen. The physiological mechanism of this often successful treatment is not completely understood. Probably, a significant percentage of the receptors which are consuming most of the oxygen provided is turned off. During the treatment, between 1000 and 3000 laser spots should be placed next to each other according to Schulenburg et al. (1979) and Hövener (1980). One section of a panretinal coagulation performed in a diabetes patient is captured in Fig. 4.4a.

Central vein occlusion occurs in the eyes of older patients and is usually restricted to one eye only. As an immediate consequence, retinal veins become dilated and severe edema are formed in the region of the macula. Multiple hemorrhages are associated with a strong decrease in vision. To prevent the occurrence of a secondary glaucoma, the procedure of panretinal coagulation is often performed as stated by Laatikainen et al. (1977).

Senile macula degeneration was recently increased among older patients. According to Bird (1974), it is caused by neovascular membranes being formed in the chorioidea. Subretinal fluids emerging from these membranes might lead to severe edema in the region of the macula. Further neovascularization can be prevented by coagulation with the green line of the argon ion laser or the red line of the krypton laser, respectively. These wavelengths are preferably absorbed by subretinal tissues in the pigment epithelium or the chorioidea but not by xanthophyll contained by the macula itself.

Finally, laser treatment of *retinoblastoma* has also been investigated, e.g. by Svaasand et al. (1989). Destruction of the tumor is obtained by converting laser energy to heat. In the case of malignant tumors, however, mechanical excisions or implants of radioactive substances are favored.

Vitreous Body

The vitreous body is a transparent gel that has a little greater consistency than the white of a raw egg. Its water content varies from 98% to 99.7% according to Le Grand and El Hage (1980), and it contains 7 g/l NaCl and 0.5 g/l soluble proteins. The vitreous body of a child is very homogeneous, whereas internal structures frequently appear in the vitreous body of an adult. Many of these inhomogeneities do not really impair the degree of vision. Most of the floating particles can be resorbed by biological mechanisms. Major pathologic alterations, however, are given by the formation of new membranes and neovascularizations extending from the retina into the

vitreous body. Their occurrence has already been described when discussing retinal detachment and diabetic retinopathy. It shall be added that only thermally acting lasers should be used for treatment due to the direct vicinity of the retina. Short pulsed lasers evoking photodisruptive effects may only be used for lens surgery and the front segments of the eye.

Lens

The lens grows during the entire human life forming an onion-like structure of adjacent shells. As a result of its continuous development and the associated decrease in water content, the lens interior progressively hardens with age. The bulk of the lens is formed by transparent lens fibers which originate from the anterior lens epithelium. The lens interior is enclosed by a homogeneous elastic membrane called the *capsule*. The capsule is connected to the *ciliary muscle* which is essential for the eye to accommodate. In a cataract, the transparency of the lens is strongly decreasing. The opaqueness is caused by either age, disease, UV radiation, food deficiencies, or trauma. The changes in the lens that lead to the formation of a cataract are not completely understood. They are somehow related to common observations of reduced amounts of potassium and soluble lens proteins which are associated with increased concentrations of calcium and insoluble lens proteins.

Beside retinal coagulation, cataract surgery of the lens is the other major laser treatment in ophthalmology. In order to achieve acceptable vision, the lens interior must be extracted. Conventional methods rely on fragmentation of the lens by phaco-emulsification followed by aspiration of the fragments. Afterwards, either an artificial lens made of silicon is inserted or the patient must wear special cataract glasses. This treatment has been proposed and documented by Kelman (1967). The posterior lens capsule is retained to prevent a collapse of the vitreous body and subsequent retinal detachment. However, new lens fibers frequently emerge from this posterior capsule forming a scattering membrane. This membrane must be removed during a second invasive surgery.

Posterior capsulotomy with a Nd:YAG laser, on the other hand, is characterized by the advantages of being both noninvasive and feasible during ambulant treatment. It was described in detail by Aron-Rosa et al. (1980) and Terry et al. (1983). Usually, a helium–neon laser is used as an aiming beam. The surgeon first focuses this laser on the posterior capsule and then adds the cutting Nd:YAG laser beam as shown in Fig. 4.6 by pressing a footpedal. Typically, pulse durations of 30 ns, pulse energies of up to 5 mJ, and focus diameters of 50–100 μm are used. With these laser parameters, local power densities exceeding 10^{10} W/cm^2 are achieved, leading to the phenomenon of optical breakdown as described in Sect. 3.4. After having placed several line cuts, the posterior membrane opens like a zipper as illustrated in Fig. 4.7. The whole procedure can be controlled through a slit lamp. The surgeon's eye is protected by a specially coated beamsplitter.

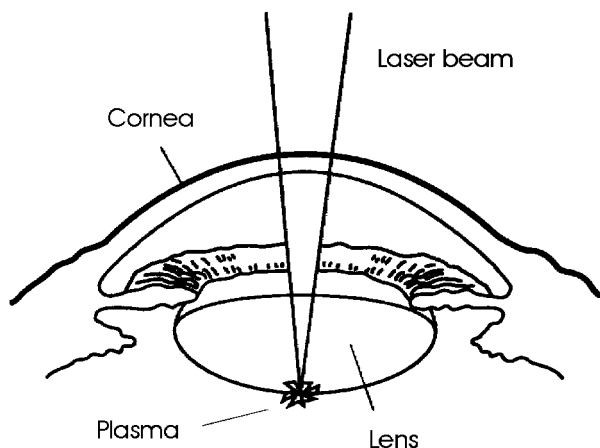


Fig. 4.6. Scheme of laser-performed posterior capsulotomy



Fig. 4.7. Lens before, during, and after posterior capsulotomy

Another laser treatment of the lens is the fragmentation of its interior rather than using ultrasonic exclusively³. For this kind of treatment, picosecond laser pulses are advantageous, because they are associated with a lower threshold energy for the occurrence of optical breakdown if compared with nanosecond pulses. Thus, more energy can be converted to the ionizing process itself. In Fig. 4.8, the fragmentation of a human lens is shown which was obtained by using a picosecond Nd:YLF laser. The surgeon steadily moves the focus of the laser beam without injuring the capsule. During this treatment, it is important to choose a pulse energy well above the threshold of optical breakdown, because otherwise all laser energy will be absorbed by the retina and other tissues lying underneath.

³ Laser fragmentation can significantly reduce the amount of necessary phaco time.

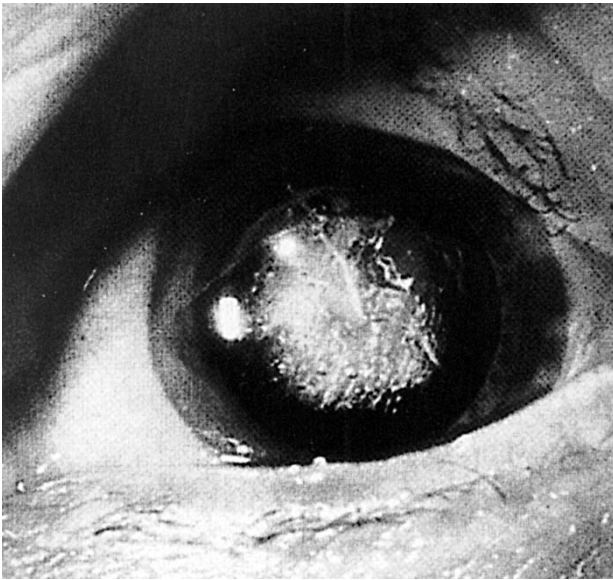


Fig. 4.8. Fragmentation of a human lens using a picosecond Nd:YLF laser (pulse duration: 30 ps, pulse energy: 1 mJ)

Iris

The iris is a tissue which is pierced by a variable circular opening called the *pupil*. Its diameter can vary from 1.5 mm to 8 mm, depending on brightness. In moderate light, the pupil diameter measures approximately 4 mm. The bulk of the iris consists of collagen fibers and pigment cells. The size of the pupil is determined by the action of two smooth muscles – the *sphincter pupillae* and the *dilatator pupillae* – which are responsible for contraction and dilatation, respectively.

In an acute block glaucoma, the drainage of aqueous humor from the rear to the front chamber is obstructed. Hence, the pressure in the rear chamber increases and shifts the iris forward. This dislocation of the iris induces a closed chamber angle which justifies the clinical term *closed-angle glaucoma*. Thereby, aqueous humor is prevented from entering the trabeculum and the canal of Schlemm. The inner eye pressure increases to values far above 20 mm Hg, thus inducing strong headaches, severe edema, degeneration of retinal nerve fibers, and a sudden loss in vision. A generally well-established procedure is called *laser iridotomy*. It provides a high immediate success rate but does not guarantee lasting cure. During this treatment, the iris is perforated as shown in Fig. 4.9 to obtain an additional passage for the aqueous humor to reach the front chamber and the trabeculum.

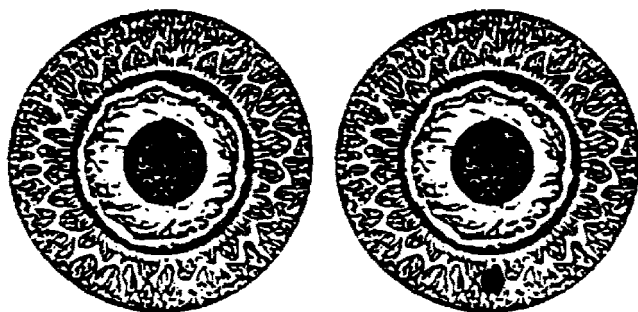


Fig. 4.9. Iris before and after laser treatment

Laser iridotomy can be performed with either argon ion lasers or pulsed neodymium lasers. Prior to laser exposure, the iris is medically narrowed. If applying the argon ion laser, typical exposure durations of 0.1–0.2 s, laser powers ranging from 700–1500 mW, and spot diameters of 50 μm are chosen according to Pollack and Patz (1976), and Schwartz and Spaeth (1980). Iridotomies induced by the argon ion laser are very successful if the iris is dark and strongly pigmented. For bright irises, neodymium lasers with pulse durations in the nanosecond or picosecond range and pulse energies up to a few millijoules are better suited. Detailed data of the procedure are given in the book by Steinert and Puliafito (1985). Perforations around the 12 o'clock position should be avoided because of rising gas bubbles disturbing the surgeon's vision. Therefore, iridotomies are usually placed between the 3 o'clock and 9 o'clock positions. The use of a proper contact glass was recommended by Roussel and Fankhauser (1983).

Laser iridotomy is a minor surgical treatment which can be performed ambulant. Only in rare cases, complications such as severe hemorrhages or infections are induced. Prior to performing iridotomies, however, medicinal treatment is provided to set an upper limit for the eye pressure.

Trabeculum

Another type of glaucoma is called *open-angle glaucoma*. It is not induced by a dislocation of the iris but a malfunction of the trabecular meshwork. The drainage of aqueous humor can be improved by a treatment called *laser trabeculotomy* during which the trabeculum is carefully perforated. First results with ruby and argon ion lasers were published by Krasnov (1973) and Worthen and Wickham (1974), respectively. Two years later, it was reported by Ticho and Zauberman (1976) that in some cases a decrease in eye pressure was obtained just by shrinking the tissue of the trabeculum instead of perforating it. These observations have been the origin for another treatment technique called *trabeculoplasty* which was described in detail by Wise and Witter (1979).

During trabeculoplasty, approximately 100 pulses from an argon ion laser are applied to the surface of the trabeculum. Focusing of the laser beam is facilitated by specially designed contact glasses. Typical focus diameters are 50–100 μm . The drop in eye pressure is assumed to arise from thermal interaction, since the heat deposited by the argon ion laser causes a shrinkage of the exposed trabecular meshwork. By this means, tensile forces are induced capable of enlarging intermediate fluid canals located in between exposed tissue areas. Moreover, these forces could possibly even widen the canal of Schlemm. Thus, the drainage of aqueous humor is improved and the eye pressure is kept at a moderate level.

Today, clinical data of follow-up periods as long as ten years are available. According to Wise (1987), trabeculoplasty has meanwhile developed to a standard type of modern laser surgery. Especially in primarily chronic glaucoma with eye pressures below 35 mm Hg, the therapy is very successful. It was pointed out, though, that ruptures of the meshwork itself should be avoided in any case.

Sclera

Among laser treatments of the sclera, external and internal sclerostomies are distinguished. In either case, surgery aims at achieving a continuous channel from the front chamber to the fluid beneath the conjunctiva. Again, this type of filtration treatment is indicated in the case of an open-angle glaucoma⁴.

External sclerostomies start from the anterior sclera, thereby injuring the conjunctiva. First laser sclerostomies in glaucomatous eyes were performed by Beckman et al. (1971) using a thermally acting CO₂ laser. The main disadvantage of this method is the need for dissection of a conjunctival flap which frequently causes severe inflammation. Moreover, the low absorption of scleral tissue at visible and near infrared wavelengths makes it extremely difficult to apply neodymium lasers or other pulsed laser systems. A solution to this problem was offered by L'Esperance (1983) when using exogeneous dyes to artificially increase the absorption coefficient. By dyeing the sclera with sterile india ink at the superior limbus, some fraction of the ink also diffused deeper into the sclera. Then, when focusing an argon ion laser beam on the trabecular meshwork, L'Esperance was able to cut through the trabeculum and the sclera starting from the interior. This was the first internal sclerostomy ever performed. More recently, pulsed Nd:YAG lasers have been used to improve filtration with the method of *internal sclerostomy*. With a specially designed gonioscope, the incident laser beam is redirected into an acute angle inside the eye. Scleral perforation starts just next to the trabeculum and ends beneath the conjunctiva. A schematic illustration of the surgical procedure is shown in Fig. 4.10.

⁴ If even this procedure does not stabilize the eye pressure, the ciliary body itself must be coagulated which is the production site of the aqueous humor.

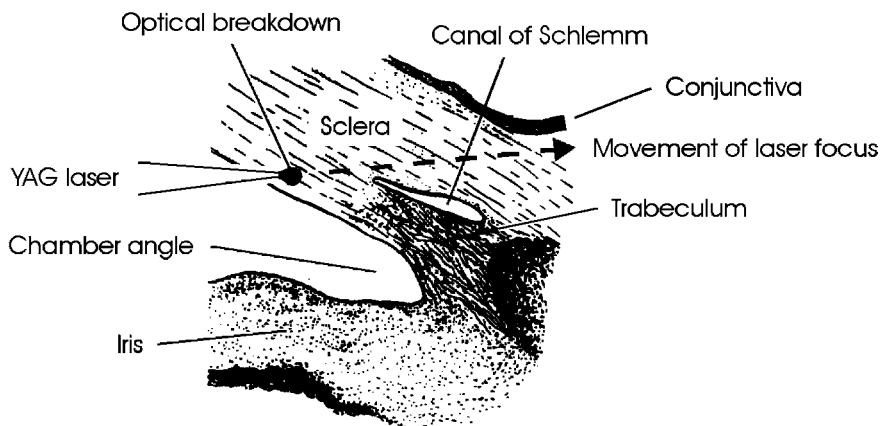


Fig. 4.10. Scheme of internal sclerostomy

First experimental and histologic results on Nd:YAG laser sclerostomy were described by March et al. (1984) and March et al. (1985). They found that approximately 250–500 pulses with pulse durations of 12 ns each and energies ranging from 16 mJ to 53 mJ were required to achieve a complete perforation of the sclera. With these laser parameters, thermal damage to adjacent tissue was limited to a few hundred μm . A few years later, visible dye lasers were also applied by again making use of different inks. The diffusion of these inks into the tissue can be accelerated by means of electrophoresis as reported by Latina et al. (1988) and Latina et al. (1990).

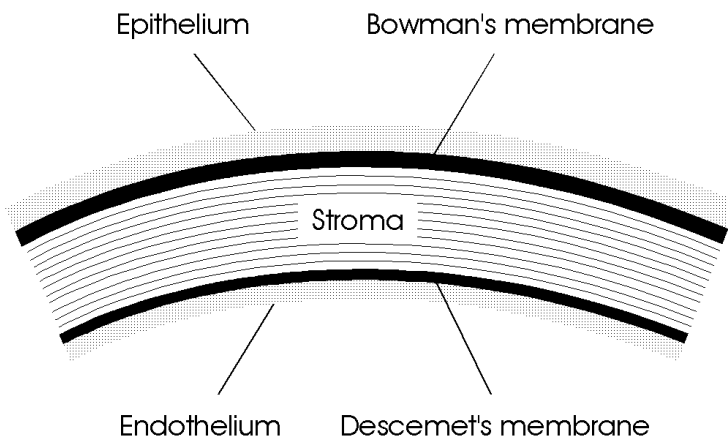
Cornea

Cornea and lens together account for the total refraction of the eye. However, since the anterior surface of the cornea is exposed to air with an index of refraction close to unity, refraction at the anterior surface of the cornea represents the major part. A list of refractive properties of the human eye was first provided by Gullstrand at the beginning of this century. A theoretical analysis of the refractive properties is found in the book by Le Grand and El Hage (1980). Both sets of data are given in Table 4.1 together with a third column called the *simplified eye*. In the simplified eye, the same principal planes and focal distances are assumed as for the theoretical eye. However, a round value of 8 mm is chosen for the radius of curvature of the anterior corneal surface. And, because also assuming the same indices of refraction for the cornea and aqueous humor, refraction at the posterior corneal surface is neglected. From these data, it can be concluded that the power of the cornea is approximately 42 diopters, whereas the total power of the eye is roughly 59 diopters. Therefore, about 70 % of the overall refraction arises from the cornea.

Table 4.1. Parameters of the unaccommodated human eye. Data according to Le Grand and El Hage (1980)

	Gullstrand eye	Theoretical eye	Simplified eye
<i>Index of refraction</i>			
Cornea	1.376	1.377	1.336
Aqueous humor	1.336	1.337	1.336
Lens	1.408	1.420	1.421
Vitreous body	1.336	1.336	1.336
<i>Radius of curvature (mm)</i>			
Cornea (ant. surface)	7.7	7.8	8.0
Cornea (post. surface)	6.8	6.5	—
Lens (ant. surface)	10.0	10.2	10.2
Lens (post. surface)	-6.0	-6.0	-6.0
<i>Power (diopters)</i>			
Cornea	43.05	42.36	42.0
Lens	19.11	21.78	22.44
Total eye	58.64	59.94	59.64

The transparency of corneal tissue in the spectral region from 400 nm to 1200 nm can be attributed to its extremely regular microscopic structure as will be discussed below. The optical zone of the human cornea has typical diameters ranging from 2 mm to 4 mm and is controlled by the iris. The overall thickness of the cornea varies between 500 μm at the center of the optical axis and 700 μm at the periphery. Corneal tissue is avascular and basically consists of five distinct layers: epithelium, Bowman's membrane, stroma, Descemet's membrane, and endothelium. A schematic cross-section of the human cornea is shown in Fig. 4.11.

**Fig. 4.11.** Cross-section of a human cornea

According to Le Grand and El Hage (1980), the *epithelium* is made up of two to three layers of flat cells which – in combination with tear fluid – provide the smooth surface of the cornea. These cells are the only corneal cells capable of regenerating. *Bowman's membrane* consists of densely packed collagen fibers. All these fibers are oriented in planes parallel to the corneal surface, resulting in extremely high transparency. Due to its high density, Bowman's membrane is primarily responsible for the mechanical stability of the cornea. Almost 90% of the corneal thickness belongs to the *stroma*. It has a structure similar to Bowman's membrane but at a lower density. Since the stroma contributes the major part of the cornea, refractive corneal surgery relies on removing stromal tissue. *Descemet's membrane* protects the cornea from its posterior side. And, finally, the *endothelium* consists of two layers of hexagonally oriented cells. Their main function is to prevent fluid of the front chamber from diffusing into the cornea.

In general, two types of corneal surgeries are distinguished: removal of any pathologic conditions and refractive corneal surgery. The first group includes treatments of irregularly shaped corneas, e.g. keratoconus, externally induced corneal injuries, and corneal transplantations. Prior to laser surgery, all these treatments had to be performed with mechanical scalpels. Today, ophthalmic lasers – among these especially the ArF excimer laser – offer a noninvasive and painless surgery. Successful circular trephinations and smoothing of irregular surfaces were, for instance, reported by Loertscher et al. (1987) and Lang et al. (1989). Very clean corneal excisions can also be obtained when using short pulsed neodymium lasers as shown in Figs. 4.12 and 4.13. The dependence of the ablation depth on pulse energy is illustrated in Figs. 4.14 and 4.15.

The other group of corneal surgeries aims at an alteration of its refractive power. Although most cases of wrongsightedness cannot be attributed to a pathologic condition of the cornea⁵, it is the corneal power which is the easiest to change. First successful studies on refractive corneal surgery were reported by Fjodorov and Durnev (1979) using a diamond knife. The whole procedure is called *radial keratotomy* (from Greek: *κερας* = cornea, *τομαειν* = to be cut). By placing radial incisions into the peripheral cornea, tensile forces are rearranged which leads to a flattening of the central anterior surface, i.e. a decrease in refractive power. Radial keratotomy has meanwhile been investigated by a variety of surgeons. Several profound reviews are available today, e.g. by Bores (1983), Sawelson and Marks (1985), and Arrowsmith and Marks (1988).

In the beginning of the 1980s, a novel method was developed which is actually removing part of the tissue with a laser. Thus, excisions are performed instead of incisions. This surgical technique is therefore called *radial keratectomy (RK)* (from Greek: *εκτομαειν* = to be cut out). Actually, the con-

⁵ In most myopias, the bulbus is too long. Senile hyperopia is due to a decrease in lens accommodability. Only astigmatism is frequently caused by the cornea itself.

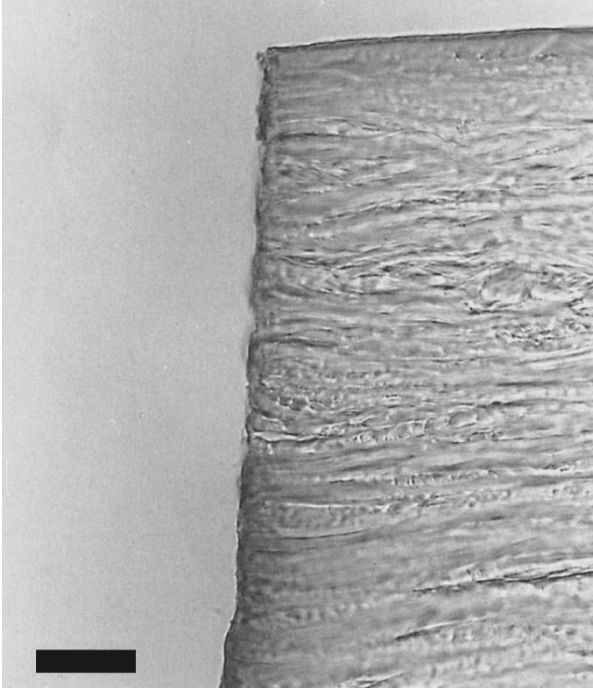


Fig. 4.12. Magnification (light microscopy) of a corneal excision achieved with a Nd:YLF laser (pulse duration: 30 ps, bar: 10 μm , original surface: *horizontal*, laser excision: *vertical*)

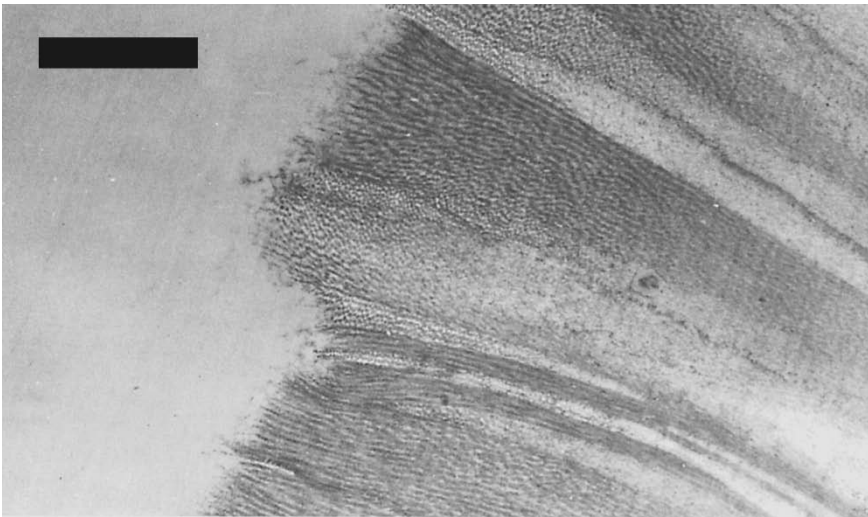


Fig. 4.13. High magnification (transmission electron microscopy) of a corneal excision achieved with a Nd:YLF laser (pulse duration: 30 ps, bar: 1 μm)

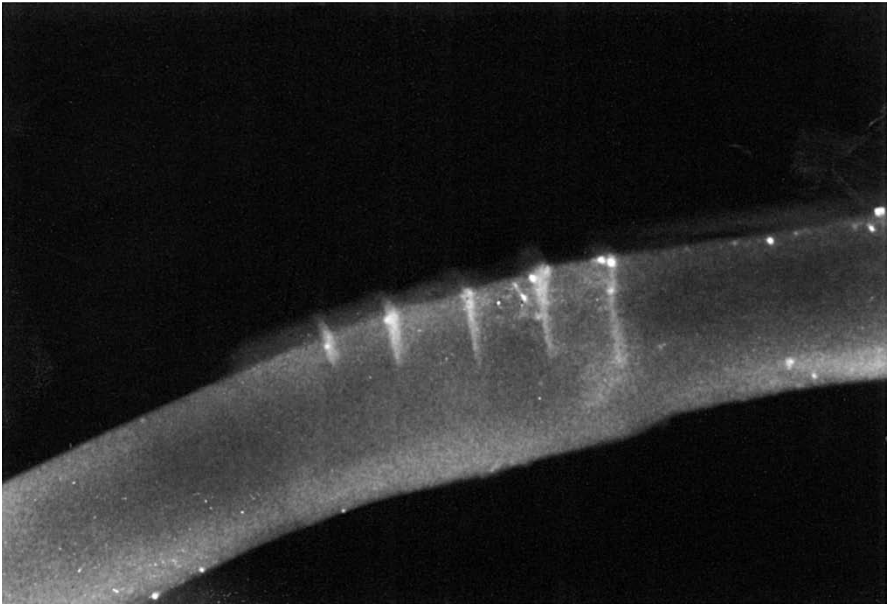


Fig. 4.14. Corneal excisions achieved with a Nd:YLF laser at different pulse energies (from *left to right*: 30 μJ , 50 μJ , 70 μJ , 90 μJ , and 110 μJ)

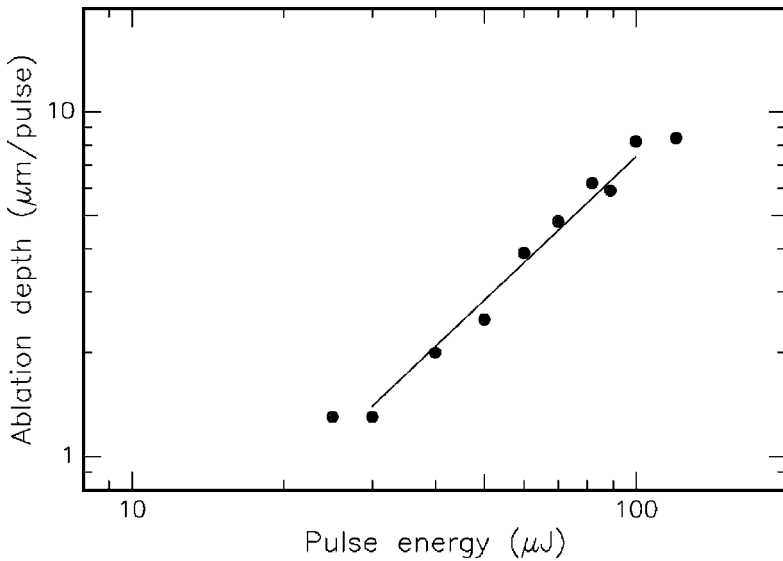


Fig. 4.15. Ablation curve of corneal stroma obtained with a Nd:YLF laser (pulse duration: 30 ps, focal spot size: 15 μm). Data according to Niemz et al. (1991)

cept of reshaping the curvature of the cornea with a laser beam was initially proposed by Keates et al. (1981). However, his original concept of applying the CO₂ laser failed, and Trokel et al. (1983) first achieved a successful keratectomy with an ArF excimer laser. Shortly afterwards, other groups also published their results, e.g. Cotlair et al. (1985), Marshall et al. (1985), and Puliafito et al. (1985). All these researchers focused on radial excisions for the purpose of correcting myopia. Moreover, astigmatism can be corrected by placing transverse excisions as reported by Seiler et al. (1988). Since excisions need to be of the order of 90% of the corneal thickness – otherwise no significant alteration of refractive power is observed – the initial rate of corneal perforation was quite high. Today, however, perforation is usually avoidable due to improved application systems and more accurate preoperative measurements of corneal parameters. Detailed computer simulations were described by Hanna et al. (1989a).

More recently, another laser technique called *keratomileusis* (from Greek: *λυειν* = to detach) or *photorefractive keratectomy (PRK)* has been proposed by Marshall et al. (1986). They recognized the superior quality of excimer laser ablations and investigated the direct carving of the cornea to change its optical power. During this treatment, large area ablations are performed around the optical axis rather than linear excisions in the periphery. The major advantage of keratomileusis over radial keratectomy is the ability to achieve direct optical correction rather than depending on indirect biomechanical effects of peripheral excisions. However, the basic hopes for minimal wound healing without opacification and for rapidly obtained stable refraction have not yet been supported by clinical experience. Corneal wound healing does occur in most cases, and it may take up to several months until refraction is stabilized. Radial keratectomy and keratomileusis are compared in a schematic drawing shown in Fig. 4.16.

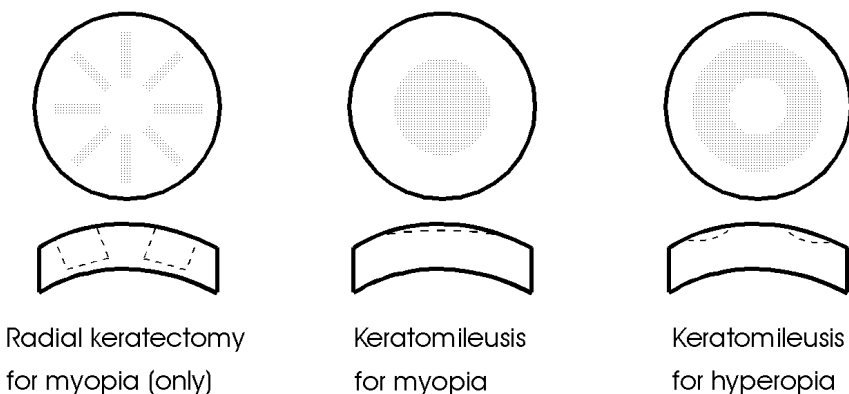


Fig. 4.16. Schemes of radial keratectomy and keratomileusis for the correction of myopia and hyperopia, respectively. Anterior view and cross-section of the cornea are shown. Dotted areas and dashed lines refer to the postoperative state

In the following paragraphs, a geometrically derived instruction is given of how the reshaping of a myopic eye has to be done. In Fig. 4.17, the pre- and postoperative anterior surfaces of the cornea are shown together with other geometrical parameters. The optical axis and an arbitrary perpendicular to it are labeled x and y , respectively. The curvature of the cornea is given by R , and the indices “i” and “f” refer to the initial and final states of the cornea, respectively.

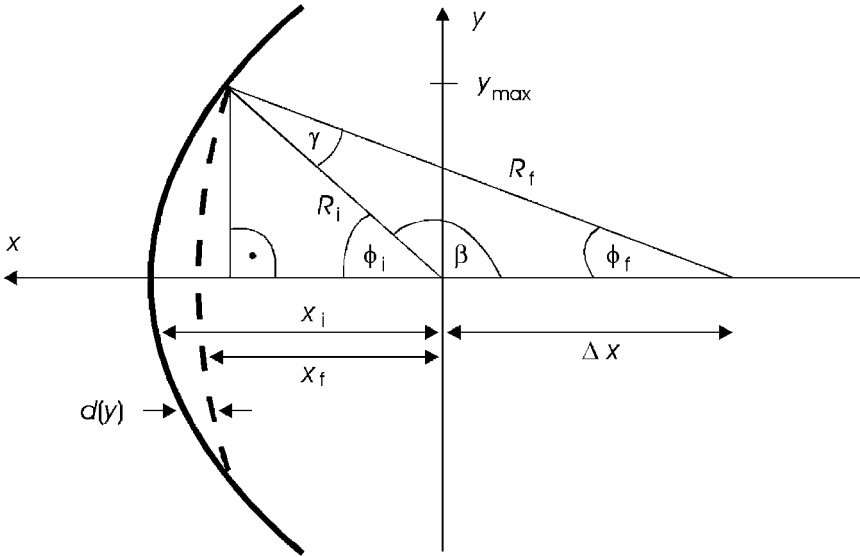


Fig. 4.17. Geometry of performing keratomileusis in a myopic eye. The pre- and postoperative anterior surfaces of the cornea are drawn as a solid curve and a dashed curve, respectively. The alteration in curvature is exaggerated

The equations for the initial and final anterior surfaces of the cornea are given by

$$x_i^2 + y^2 = R_i^2, \tag{4.1}$$

$$(x_f + \Delta x)^2 + y^2 = R_f^2, \tag{4.2}$$

where (x_i, y) and (x_f, y) are the coordinates of the initial and final surfaces, respectively, and Δx is the shift in the centers of curvature as shown in Fig. 4.17. We thus obtain for the depth of ablation

$$d(y) = x_i - x_f = \sqrt{R_i^2 - y^2} - \sqrt{R_f^2 - y^2} + \Delta x. \tag{4.3}$$

The shift Δx can be calculated from the sines of the angles β and γ and is expressed by

$$\frac{\Delta x}{\sin \gamma} = \frac{R_f}{\sin \beta} . \quad (4.4)$$

When using the following geometrical relations

$$\sin \beta = \sin (180^\circ - \phi_i) = \sin \phi_i ,$$

$$\gamma = \phi_i - \phi_f ,$$

(4.4) can be turned into

$$\Delta x = R_f \frac{\sin (\phi_i - \phi_f)}{\sin \phi_i} . \quad (4.5)$$

Furthermore, we deduce from Fig. 4.17 the two expressions

$$\sin \phi_i = \frac{y_{\max}}{R_i} ,$$

$$\sin \phi_f = \frac{y_{\max}}{R_f} ,$$

where y_{\max} is the maximum radius of the optical zone to be altered. Hence, substituting ϕ_i and ϕ_f in (4.5) leads to

$$\Delta x = \frac{R_i R_f}{y_{\max}} \sin \left(\arcsin \frac{y_{\max}}{R_i} - \arcsin \frac{y_{\max}}{R_f} \right) . \quad (4.6)$$

From (4.3) and (4.6), we obtain

$$d(y) = \sqrt{R_i^2 - y^2} - \sqrt{R_f^2 - y^2} + \frac{R_i R_f}{y_{\max}} \sin \left(\arcsin \frac{y_{\max}}{R_i} - \arcsin \frac{y_{\max}}{R_f} \right) .$$

The highest ablation depth must be obtained at $y = 0$ with

$$d(0) = R_i - R_f + \frac{R_i R_f}{y_{\max}} \sin \left(\arcsin \frac{y_{\max}}{R_i} - \arcsin \frac{y_{\max}}{R_f} \right) . \quad (4.7)$$

In (4.7), the depth $d(0)$ is given which the surgeon has to remove at the vertex of the optical axis. The unknown parameter R_f is readily obtained from the basic law of a curved refracting surface

$$\Delta D = (n_c - 1) \left(\frac{1}{R_i} - \frac{1}{R_f} \right) , \quad (4.8)$$

where ΔD is the degree of myopia expressed in units of diopters, and n_c is the refractive index of the cornea. For an attempted correction of ΔD ranging from 1 diopter to 10 diopters, the required values of R_f and $d(0)$ are listed in Table 4.2, assuming $R_i = 7.8$ mm, $n_c = 1.377$, and $y_{\max} = 2.5$ mm. From these data, it can be concluded that for myopias up to 5 diopters less than one tenth of the corneal thickness needs to be ablated.

Table 4.2. Theoretical values of keratomileusis in the case of myopia. Actual data might slightly differ due to a rearrangement in mechanical stress. Assumed is an optical zone of 5 mm, i.e. $y_{\max} = 2.5$ mm

ΔD (diopters)	R_f (mm)	$d(0)$ (μm)
1	7.965	9.0
2	8.137	17.9
3	8.316	26.8
4	8.504	35.7
5	8.700	44.6
6	8.906	53.4
7	9.121	62.2
8	9.347	71.0
9	9.585	79.7
10	9.835	88.4

A similar calculation applies for the correction of hyperopic eyes. However, since a peripheral ring-shaped zone needs to be ablated, the diameter of the optical zone is usually extended to 7–8 mm. It should be added that astigmatism can also be corrected by means of keratomileusis. This is achieved by simply aiming at two different values of R_f in two planes located perpendicularly to the optical axis.

In the 1980s, i.e. during the early stage of performing keratomileusis, this novel technique was further improved and corticosteroids were infrequently used. Early experiences were reported by Aron-Rosa et al. (1987) and Taylor et al. (1989). Normal reepithelialization as well as mild subepithelial haze were observed. McDonald et al. (1990) demonstrated the ability to achieve a measurable myopic refractive correction. However, they also reported on an initial regression and a poor predictability of the refractive effect. Wilson (1990) distinguished between preoperative myopias with less and more than 5.5 diopters. From his clinical observations, he concluded that good predictions can be made in the first case only. Some of his results are shown in Figs. 4.18a–b. Similar statements regarding predictability were published by Seiler and Genth (1994).

Meanwhile, several variations of PRK are being studied all over the world. The ArF excimer laser is well suited for this type of surgery because of its ablation characteristics. As we have already encountered when discussing Fig. 3.36, one pulse from this laser typically ablates 0.1–1 μm of corneal tissue which corresponds to 0.01–0.1 diopters. Usually, energy densities of 1–5 J/cm² are applied in order to be less dependent on energy fluctuations, since the ablation curve shown in Fig. 3.36 approaches a saturation limit. Then, the correction of one diopter is achieved with approximately 10 pulses which takes about one second at a repetition rate of 10 Hz. Although most researchers agree that the ArF laser is well suited for PRK, the choice of a proper delivery system is being controversially discussed. Most common are

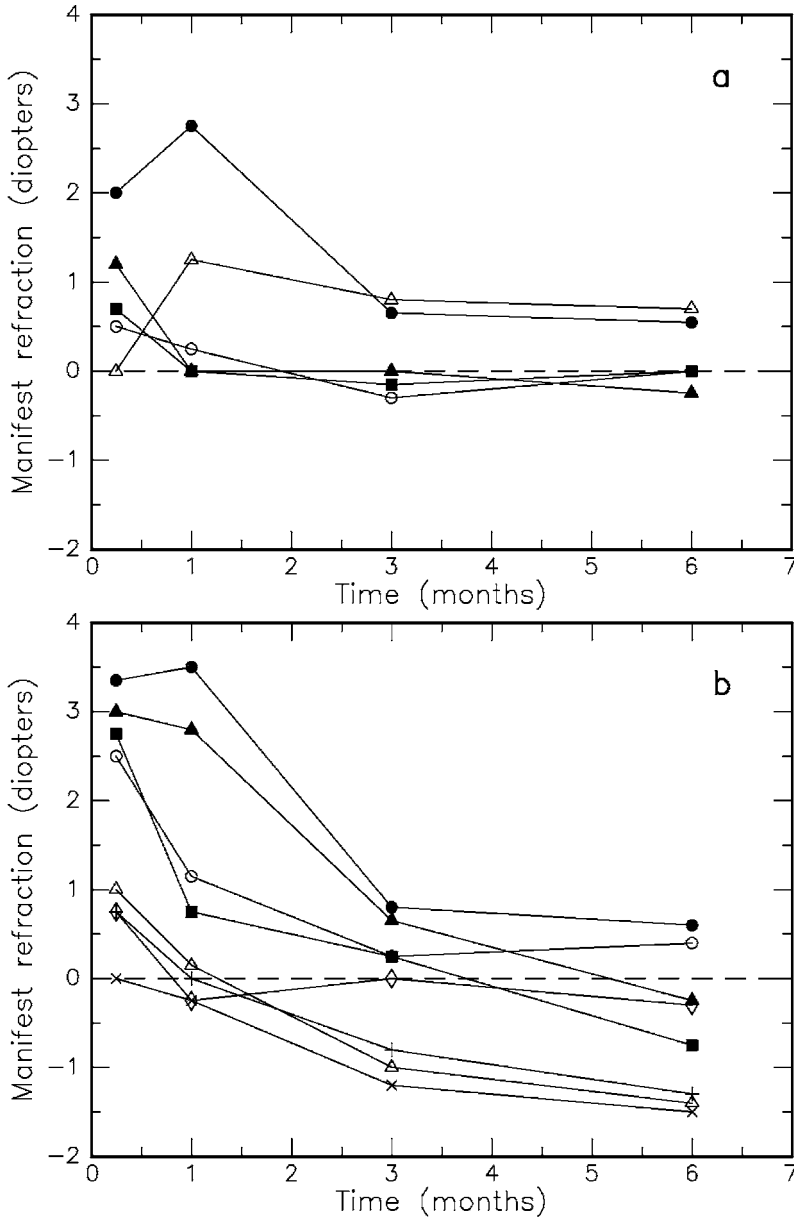


Fig. 4.18. (a) Results of ArF excimer laser keratomileusis performed in five cases of myopia with attempted corrections less than 5.5 diopters. (b) Results of ArF excimer laser keratomileusis performed in eight cases of myopia with attempted corrections more than 5.5 diopters. During a follow-up period of six months, eyes with more than 5.5 diopters of preoperative myopia appear to be less stable than eyes with less than 5.5 diopters. Emmetropia is indicated by a dashed line. Data according to Wilson (1990)

the methods of using a scanning slit as described by Hanna et al. (1988) and Hanna et al. (1989b), or a rotating disk mask with different apertures as used by L'Esperance et al. (1989). In the first case, the cornea is exposed to radiation from an ArF laser through a movable slit. If the slit is wider near its center, i.e. if more tissue is removed from the central cornea, it can be used for correcting myopic eyes. If the slit is wider near its ends, it is designed for treating hyperopia. The rotating disk mask, on the other hand, consists of several apertures with different diameters which are concentrically located on a wheel. The patient's eye is irradiated through one aperture at a time. In between, the wheel is turned to the next aperture. By this means, it is assured that the overall exposure gradually decreases from the center to the periphery of the cornea. Thus, more tissue is removed from central areas, i.e. myopia is corrected. Hyperopias cannot be treated using the rotating disk. Either method is illustrated in Figs. 4.19a–c.

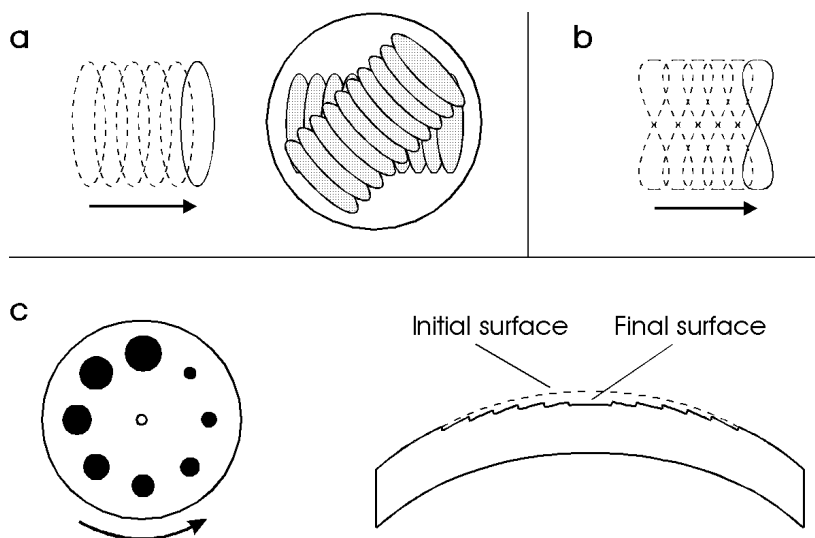


Fig. 4.19. (a) Scanning slit for correction of myopia and anterior view of cornea. (b) Scanning slit for correction of hyperopia. (c) Rotating disk mask for correction of myopia. Initial and final surfaces are shown in a corneal cross-section

In Fig. 4.20a, a photograph is shown which demonstrates the removal of corneal tissue after performance of keratomileusis. In order to visualize the stair-like ablations, a large difference in aperture diameters was chosen. The view of a treated eye through a slit lamp is captured in Fig. 4.20b. With this device, the patient's eye is illuminated by a slit which is positioned at an angle to the optical axis. From its image on the cornea, information on the corneal thickness can be derived. In the example shown in Fig. 4.20b, the cornea appears thinner at its center. Thus, a myopic eye was treated.

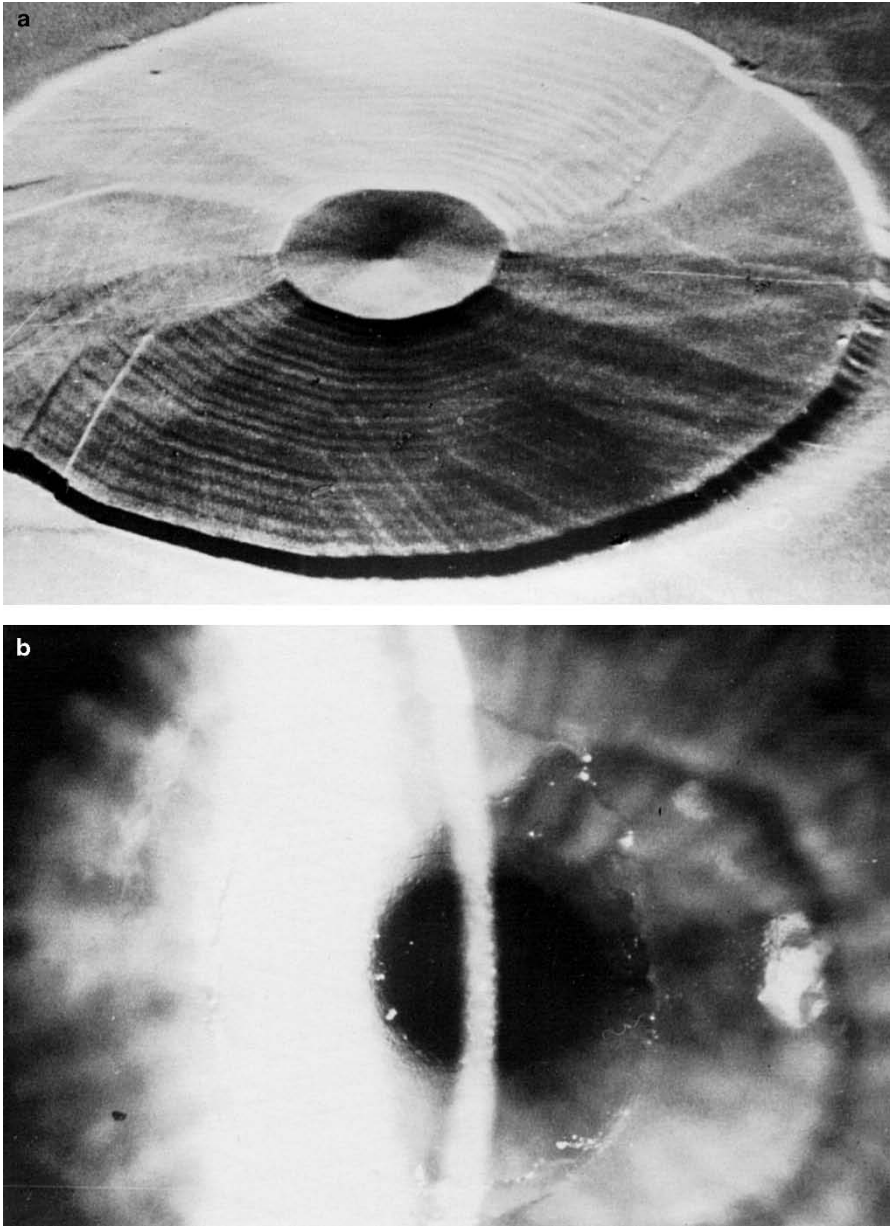


Fig. 4.20. (a) Stair-like ablations of corneal tissue after performance of keratomileusis with an ArF laser. (b) View of a treated eye through a slit lamp. Photographs kindly provided by Dr. Bende (Tübingen)

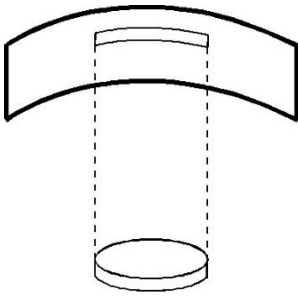
In a large group of keratomileusis treatments, good optical correction is obtained after approximately six months. Despite several improvements, however, two major disadvantages still remain:

- regression of the initially achieved refractive power,
- appearance of a subepithelial haze after the regression period.

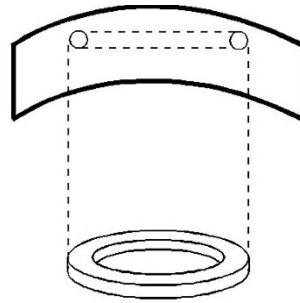
The existence of a regression effect becomes obvious when looking at Figs. 4.18a–b. Within the first three months after PRK, a regression of up to three diopters has been observed. It is probably due to the processes of corneal wound healing and reepithelialization. Therefore, the patient's eye is usually transferred to a hyperopic state immediately after surgery. It is hoped that refraction stabilizes at emmetropy after the period of regression. This procedure, of course, requires a lot of patience since the patient has to use several pairs of glasses during the first months after surgery. Subepithelial haze has not been found in all patients but is a frequent consequence. It disturbs vision especially in darkness when the pupil widens. The primary cause of this haze is yet unknown. It might arise from a rearrangement of collagen fibers inside Bowman's membrane and the stroma. However, haze could also be induced by the toxic UV radiation. As stated in Sect. 3.3, cytotoxicity and mutagenicity cannot be excluded for the ArF laser wavelength at 193 nm. It is generally believed that corneal tumors do not occur. Cytotoxic effects, though, might cause a reduction in corneal transparency.

Infrared lasers have also been proposed for refractive corneal surgery, especially erbium, holmium, and neodymium lasers. When using erbium and holmium lasers, thermal degradation of corneal tissue is attempted, leading to a shrinkage of the involved collagen fibers. By this means, tensile stress is induced inside the cornea evoking a change in refractive power. Actually, this method is based on earlier studies performed by Gasset and Kaufman (1975) who used conventional heat sources in the treatment of severe keratoconus. Since thermal effects are associated with opacification, the laser energy is usually applied to a peripheral ring of the cornea. With this method, corrections of hyperopia were observed as reported by Householder et al. (1989) and Brinkmann et al. (1994).

An interesting and challenging technique for refractive corneal surgery has emerged at the beginning of the 1990s. It is called *intraströmål ablation*, and its basic principle is illustrated in Fig. 4.21. By means of focusing a laser beam inside the cornea, either a continuous disk-shaped or a ring-shaped cavity is generated, depending on the type of correction needed. When the gaseous vapor inside these cavities has diffused into the surrounding medium, the cavity collapses. It is expected that the removal of stromal tissue then induces a stable change in curvature of the anterior corneal surface. The main advantage of this technique is that the original layers of epithelium and Bowman's membrane are not injured. Thus, the stability of the cornea is less affected, and corneal haze is less likely to occur.



Intrastromal ablation
for myopia



Intrastromal ablation
for hyperopia

Fig. 4.21. Schemes of intrastromal ablation

Intrastromal ablations were first reported by Höh (1990) when focusing a Q-switched Nd:YAG laser beam inside the stroma. A more detailed study followed soon after by Niemz et al. (1993a) using picosecond pulses from a two-stage Nd:YLF laser system. It was shown for the first time that a continuous intrastromal cavity can be achieved which is located approximately $150\ \mu\text{m}$ beneath the epithelium. A typical example of such a laser-induced cavity inside the stroma of a human cornea is shown in Fig. 4.22. This photograph was obtained with a scanning electron microscope. Due to shrinking processes during the preparation, the cavity appears closer to the epithelium than $150\ \mu\text{m}$. The collapse of an intrastromal cavity is captured in Fig. 4.23 which was taken with a transmission electron microscope. In this case, fixation took place one hour after laser exposure. Two vacuoles are still visible which have not yet collapsed. According to Vogel et al. (1994b), endothelial damage does not occur if the focus of the laser beam is placed at least $150\ \mu\text{m}$ away from the endothelium.

Meanwhile, preliminary intrastromal ablations have been performed which lead to alterations in refractive power of up to 5 diopters. In addition, extensive theoretical models have been proposed for this kind of surgery, e.g. by Hennighausen and Bille (1995). Using the algorithm of *finite elements*, certain predictions can be made concerning any changes in refraction. The method of finite elements is a very powerful tool of modern engineering science. Reshaping of the cornea by mechanical alterations is a typical problem of a special branch called *biomechanics* or *bioengineering*. Mechanical properties of the cornea have been reported by Jue and Maurice (1989). Its governing equations have been discussed by Fung (1981).

When applying the method of finite elements, the object, e.g. the cornea, is subdivided into a certain number of finite elements. The size of these elements is chosen such that each of them can be characterized by constant

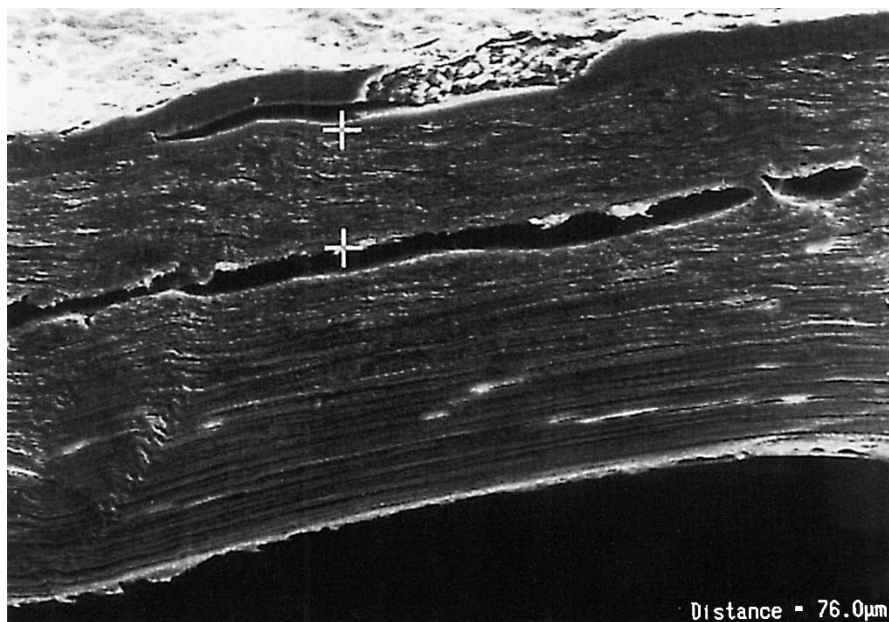


Fig. 4.22. Intrastromal cavity achieved with a Nd:YLF laser (pulse duration: 30 ps, pulse energy: 140 μJ)



Fig. 4.23. Collapse of an intrastromal cavity achieved with a Nd:YLF laser (pulse duration: 30 ps, pulse energy: 100 μJ). The two vacuoles which have not yet collapsed measure about 20 μm

physical parameters. The advantage of this procedure is that all governing equations are readily solved within each element. Then, by implementing proper boundary conditions, each element is related to its adjacent elements which finally leads to a physical description of the whole object. Any alteration of a single element consequently influences other elements, as well. In our example shown in Fig. 4.24, two intrastromal elements within the optical zone are removed. Using iterative calculations on fast processing computers, the deformed postoperative state of the cornea is simulated. In order to obtain reliable results, such a model should comprise the following properties of the cornea:

- anisotropy,
- incompressibility,
- nonlinear stress–strain behavior⁶,
- nonuniform initial stress distribution.

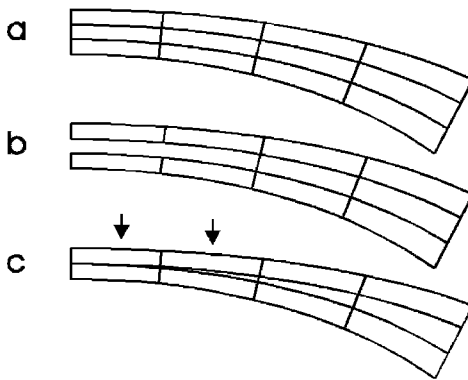


Fig. 4.24. (a–c) Simulation of an intrastromal ablation by twelve finite elements. One half of the corneal cross-section is shown. (a) Preoperative state. (b) Intrastromal ablation (immediate postoperative state). (c) Steady postoperative state

Today, the standard technique for refractive corneal surgery beside PRK is called *laser in situ keratomileusis (LASIK)*. This kind of treatment basically consists of three steps shown in Fig. 4.25: cutting a flap into the anterior section of the cornea with a surgical knife or a femtosecond laser, removing intrastromal tissue with an ArF laser or a femtosecond laser according to Table 4.2, and pulling the flap down again with surgical tweezers. No sewing is necessary after the treatment, since the flap immediately sticks again to the tissue underneath due to adhesive forces. The removed tissue volume causes a similar change in refraction as in the case of the intrastromal ablations described above, but LASIK provides the high precision achievable with ArF or femtosecond lasers.

⁶ Most biological tissues do not obey *Hooke's law* of elasticity.

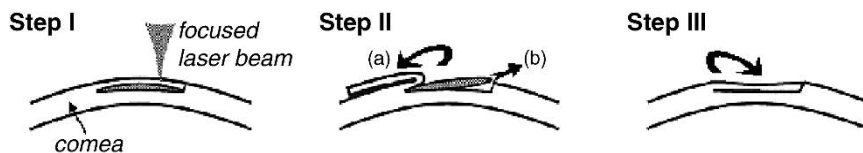


Fig. 4.25. LASIK technique based on three steps: cutting a flap into the anterior section of the cornea, removing intrastromal tissue, and pulling the flap down again

In Fig. 4.26, a high-magnification photograph of LASIK treatment is shown. With a Nd:Glass femtosecond laser, a flap was cut into the cornea and pulled upward. Furthermore, a disc-shaped volume of intrastromal tissue was excised and put aside. This fascinating photograph proves the high accuracy associated with this technique. Since LASIK has just recently been developed, of course, not much data are available so far. However, as progress with excimer laser surgery has demonstrated, research in this field continues to grow rapidly. Details are given by Pallikaris and Siganos (1994), Knorz et al. (1996), Farah et al. (1998), Patel et al. (2000), Lipshitz et al. (2001), and Rosen (2001). A reasonable judgement of this alternative for refractive corneal surgery should be possible in the near future.

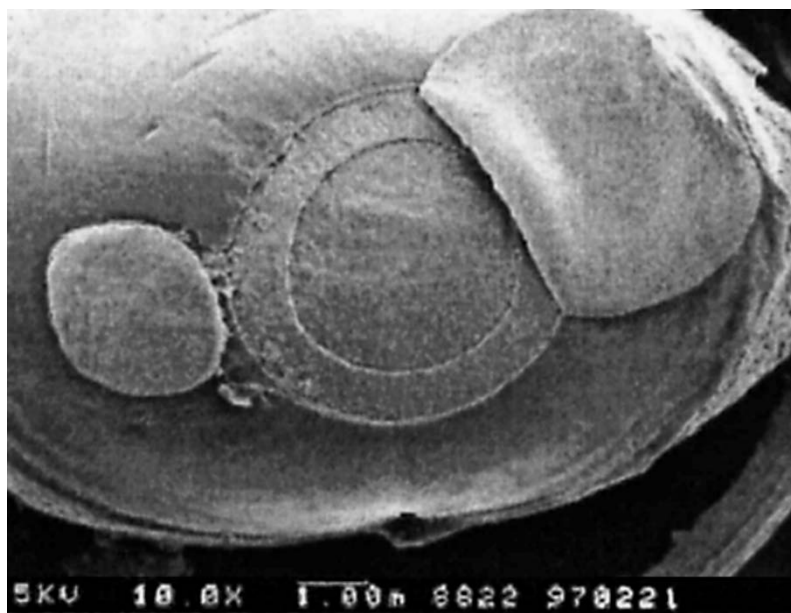


Fig. 4.26. High-magnification photograph of LASIK treatment performed with a Nd:Glass laser (pulse duration: 500 fs, pulse energy: 3 μ J)

4.2 Lasers in Dentistry

Although dentistry was the second medical discipline where lasers were applied, it basically remained a field of research. Especially in caries therapy – the most frequent dental surgery – conventional mechanical drills are still superior compared to most types of lasers, particularly CW or long-pulse lasers. Only laser systems capable of providing ultrashort pulses might be an alternative to mechanical drills as was recently shown by Niemz et al. (1993b) and Pioch et al. (1994). However, many clinical studies and extensive engineering effort still remain to be done in order to achieve satisfactory results. We should keep in mind that mechanical drills have improved over several decades until the present stage was reached, and that the development of suitable application units for laser radiation also takes time. Other topics of interest in dentistry include laser treatment of soft tissue as well as laser-welding of dental bridges and dentures. In some of these areas, research has been very successful. In this section, laser treatment of hard tooth substances, soft dental tissues, and filling materials will be addressed.

The Human Tooth

Before going into the details of laser dentistry, a brief summary of the anatomy of the human tooth as well as its physiology and pathology shall be given. In principle, the human tooth consists of mainly three distinct segments called enamel, dentin, and pulp. A schematic cross-section of a human tooth is shown in Fig. 4.27.

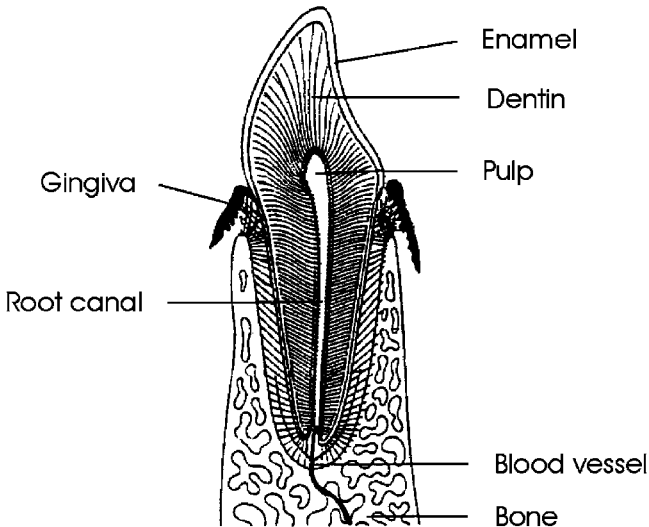


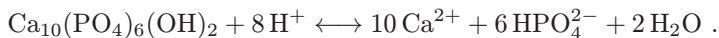
Fig. 4.27. Cross-section of a human tooth

The *enamel* is the hardest substance of the human body. It is made of approximately 95 % (by weight) hydroxyapatite, 4 % water, and 1 % organic matter. Hydroxyapatite is a mineralized compound with the chemical formula $\text{Ca}_{10}(\text{PO}_4)_6(\text{OH})_2$. Its substructure consists of tiny crystallites which form so-called *enamel prisms* with diameters ranging from 4 μm to 6 μm . The crystal lattice itself is intruded by several impurities, especially Cl^- , F^- , Na^+ , K^+ , and Mg^{2+} .

The *dentin*, on the other hand, is much softer. Only 70 % of its volume consists of hydroxyapatite, whereas 20 % is organic matter – mainly collagen fibers – and 10 % is water. The internal structure of dentin is characterized by small tubuli which measure up to a few millimeters in length, and between 100 nm and 3 μm in diameter. These tubuli are essential for the growth of the tooth.

The *pulp*, finally, is not mineralized at all. It contains the supplying blood vessels, nerve fibers, and different types of cells, particularly odontoblasts and fibroblasts. Odontoblasts are in charge of producing the dentin, whereas fibroblasts contribute to both stability and regulation mechanisms. The pulp is connected to peripheral blood vessels by a small channel called the *root canal*. The tooth itself is embedded into soft tissue called the *gingiva* which keeps the tooth in place and prevents bacteria from attacking the root.

The most frequent pathologic condition of teeth is called *decay* or *caries*. Its origin lies in both cariogenic nourishment and insufficient oral hygiene. Microorganisms multiply at the tooth surface and form a layer of *plaque*. These microorganisms produce lactic and acetic acid, thereby reducing the pH down to values of approximately 3.5. The pH and the solubility of hydroxyapatite are strongly related by



By means of this reaction, the enamel can be demineralized within a few days only. Calcium bound to the hydroxyapatite is ionized and washed out by saliva. This process turns the hard enamel into a very porous and permeable structure as shown in Fig. 4.28. Usually, this kind of decay is associated with a darkening in color. Sometimes, however, carious lesions appear bright at the surface and are thus difficult to detect. At an advanced stage, the dentin is demineralized, as well. In this case, microorganisms can even infect the pulp and its interior which often induces severe pain. Then, at the latest, must the dentist remove all infected substance and refill the tooth with suitable alloys, gold, ceramics, or composites. Among alloys, amalgam has been a very popular choice of the past. Recently, though, a new controversy has arisen concerning the toxicity of this filling material, since it contains a significant amount of mercury.

The removal of infected substance is usually accomplished with conventional mechanical drills. These drills do evoke additional pain for two reasons. First, tooth nerves are very sensitive to induced vibrations. Second,

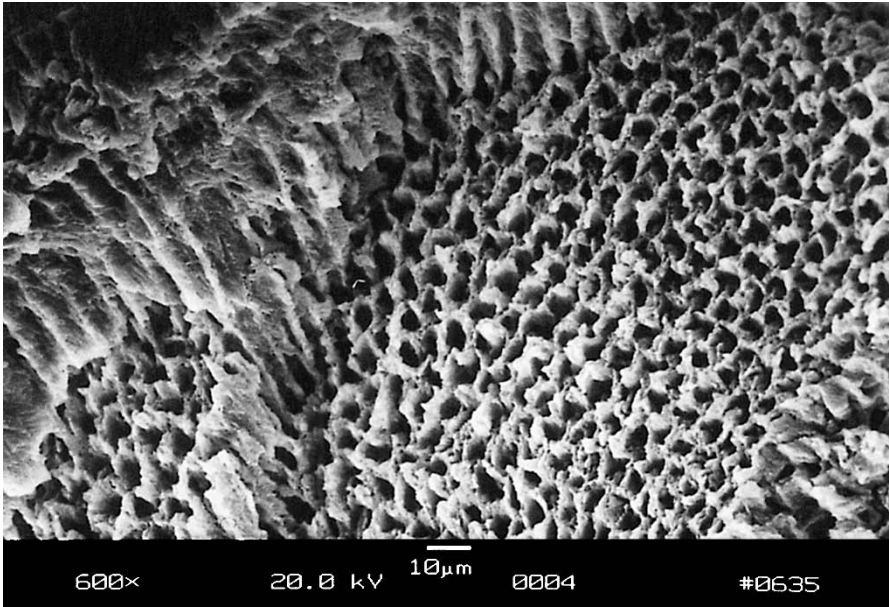


Fig. 4.28. High-magnification photograph of caries taken with a scanning electron microscope. Reproduced from Niemz (1994a). © 1994 Springer-Verlag

tooth nerves also detect sudden increases in temperature which are induced by friction during the drilling process. Pain relief without injection of an anaesthetic was the basic ulterior motive when looking for laser applications in caries therapy. However, it turned out that not all types of lasers fulfill this task. Although vibrations are avoided due to the contactless technique, thermal side effects are not always eliminated when using lasers. CW and long-pulse lasers, in particular, induce extremely high temperatures in the pulp as shown in Figs. 4.29a–b. Even air cooling does not reduce this temperature to a tolerable value. Thermal damage is negligible only when using ultrashort pulses according to the statements given in Sect. 3.2.

Meanwhile, other advantages are being discussed which could even be more significant than just pain relief⁷. Very important among these are the so-called conditioning of dental substance and a possibly more precise procedure of caries removal. Conditioning provides additional protection of the tooth by means of sealing its surface. Thereby, the occurrence of caries can be significantly delayed. Improved control of caries removal, e.g. by a spectroscopic analysis of laser-induced plasmas as shown in Figs. 3.51a–b, could minimize the amount of healthy substance to be removed. Then, indications for expensive dental crowns or bridges are effectively reduced.

⁷ It should be kept in mind that pain relief alone would not justify the application of more expensive machines.

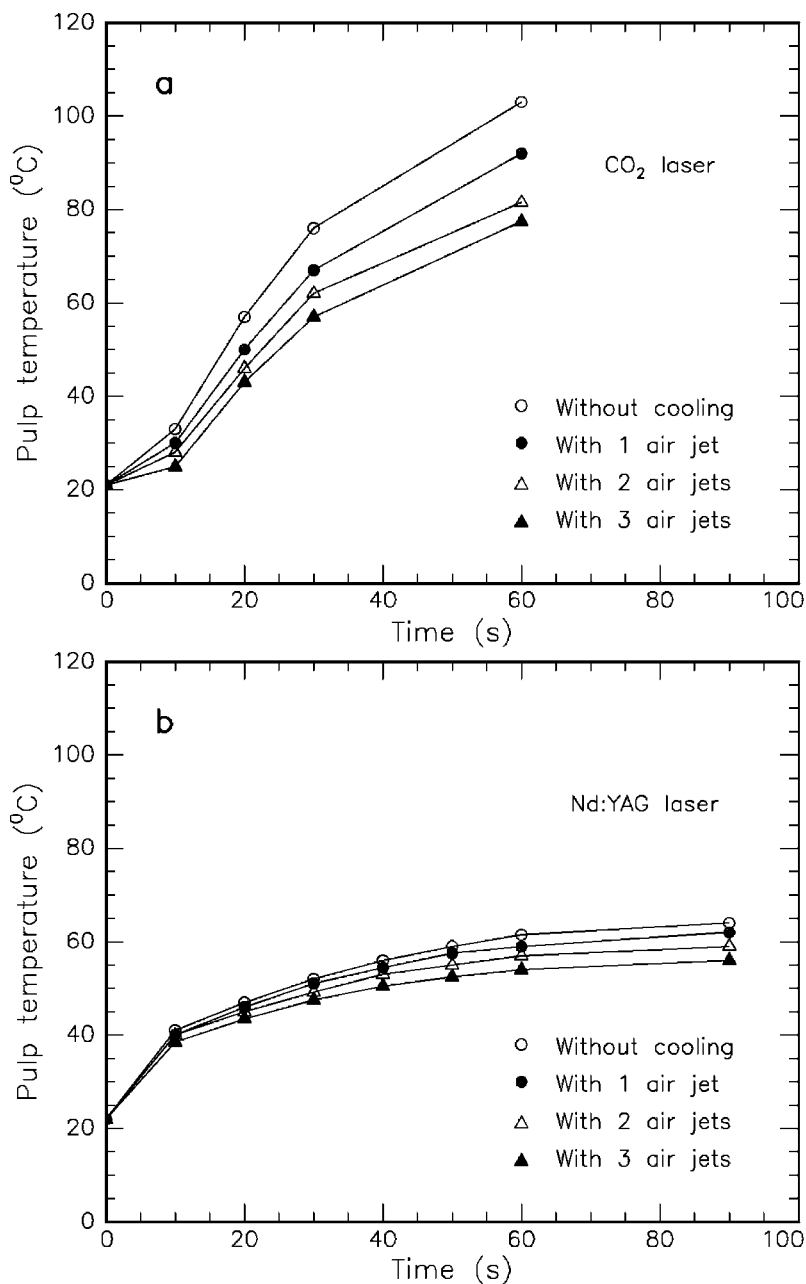


Fig. 4.29. (a) Mean temperatures in the pulp during exposure to a CW CO₂ laser (power: 5 W) without and with air cooling, respectively. (b) Mean temperatures in the pulp during exposure to a CW Nd:YAG laser (power: 4 W) without and with air cooling, respectively. Data according to Frentzen and Koort (1992)

Laser Treatment of Hard Tooth Substance

First experiments with teeth using the laser as a surgical tool were performed by Goldman et al. (1964) and Stern and Sognaes (1964). Both of these groups used a pulsed ruby laser at a wavelength of $694\ \mu\text{m}$. This laser induced severe thermal side effects such as irreversible injury of nerve fibers and tooth cracking. Thus, it is not very surprising that these initial studies never gained clinical relevance. A few years later, a CO_2 laser system was investigated by Stern et al. (1972). However, the results did not improve very much compared with the ruby laser. These observations are due to the fact that both ruby and CO_2 lasers are typical representatives of thermally acting lasers. Thus, it was straightforward to conclude with Stern (1974) that without being able to eliminate these thermal effects, lasers would never turn into a suitable tool for the preparation of teeth.

Meanwhile, several experiments have been conducted using alternative laser systems. At the end of the 1980s, the Er:YAG laser was introduced to dental applications by Hibst and Keller (1989), Keller and Hibst (1989), and Kayano et al. (1989). The wavelength of the Er:YAG laser at $2.94\ \mu\text{m}$ matches the resonance frequency of the vibrational oscillations of water molecules contained in the teeth as described in Sect. 3.2. Thereby, the absorption of the Er:YAG radiation is strongly enhanced, resulting in a high efficiency. However, the sudden vaporization of water is associated with a pressure gradient. Small microexplosions are responsible for the break-up of the hydroxyapatite structure. High-magnification photographs of a human tooth after Er:YAG laser exposure were shown in Sect. 3.2 in Figs. 3.11a–b. The coincidence of thermal (e.g. vaporization) and mechanical (e.g. pressure gradient) ablation effects has led to the term “thermomechanical interaction” as used by Frentzen and Koort (1991).

Initially, Er:YAG lasers seemed to be very promising because of their high efficiency in ablating dental substances. Meanwhile, though, some indication has been given that microcracks can be induced by Er:YAG laser radiation. It was found by Niemz et al. (1993b) and Frentzen et al. (1994) – using scanning electron microscopy and dye penetration tests – that these fissures can extend up to $300\ \mu\text{m}$ in depth. They could thus easily serve as an origin for the development of new decay. External cooling of the tooth might help to reduce the occurrence of cracking but further research needs to be performed prior to clinical applications.

Even worse results were found with the Ho:YAG laser as reported by Niemz et al. (1993b). High-magnification photographs of a human tooth after laser exposure were shown in Figs. 3.13a–b. Severe thermal effects including melting of tooth substance were observed. Moreover, cracks up to $3\ \text{mm}$ in depth were measured when performing dye penetration tests.

Dye penetration tests are suitable experiments for the detection of laser-induced tooth fissures. After laser exposure, the tooth is stained with a dye, e.g. neofuchsin solution, for several hours. Afterwards, the tooth is sliced

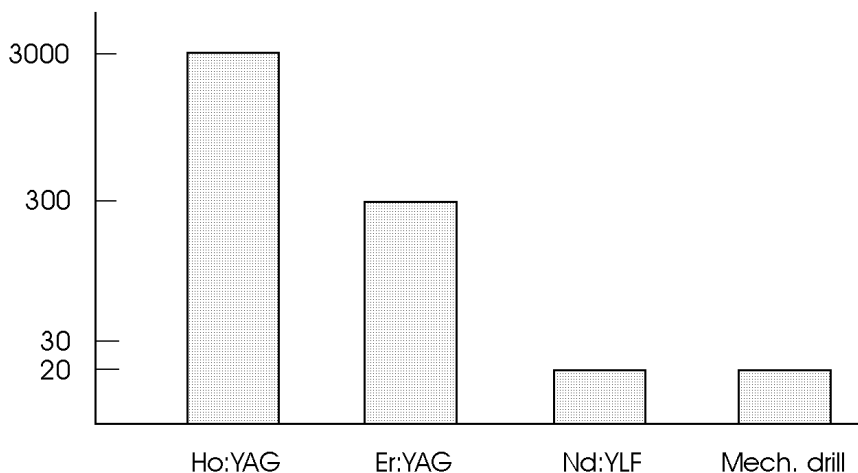
Dye penetration (μm)

Fig. 4.30. Results of dye penetration tests for three different solid-state lasers and the mechanical drill. Listed are the maximum penetration depths inside the enamel of human teeth. Pulse durations: 250 μs (Ho:YAG), 90 μs (Er:YAG), and 30 ps (Nd:YLF). Data according to Niemz (1993b)

using a microtome, and the maximum penetration depth of the dye is determined. The results of some representative measurements are summarized in Fig. 4.30. Obviously, tooth fissures induced by Ho:YAG and Er:YAG lasers must be considered as a severe side effect.

Another laser type – the ArF excimer laser – was investigated by Frentzen et al. (1989) and Liesenhoff et al. (1989) regarding its usefulness in dentistry. Indeed, initial experiments proved that only very slight thermal effects were induced which was attributed to the shorter pulse duration of approximately 15 ns and the gentle interaction mechanism of photoablation. However, the ablation rate achieved with this laser, i.e. the ablated volume per unit time, is too low for clinical applications. Although very successful in refractive corneal surgery because of its high precision, it is exactly this accuracy with ablation depths less than 1 μm per pulse and the rather moderate repetition rates which pull the ablation rate down. This ineffectiveness and the general risks of UV radiation are the major disadvantages concerning the use of the ArF laser in dentistry.

A second UV laser – the frequency-doubled Alexandrite laser at 377 nm – was studied by Steiger et al. (1993) and Rechmann et al. (1993). It was observed that this laser offers a better selectivity for carious dentin than the Er:YAG laser, i.e. the required fluence at the ablation threshold of healthy dentin is higher when using the Alexandrite laser, whereas the thresholds for carious dentin are about the same.

Recently, a novel approach to laser caries therapy has been made by Niemz et al. (1993b) and Pioch et al. (1994) when using picosecond pulses from a Nd:YLF laser system. Although, at the early stage of experiments, uncertainty predominated concerning potential shock wave effects, it has meanwhile been verified by five independent tests that mechanical impacts are negligible. These consist of *scanning electron microscopy*, *dye penetration tests*, *hardness tests*, *histology*, and *polarized microscopy*. Latest results have been published by Niemz (1995b).

Scanning Electron Microscopy. In Figs. 4.31a–b, two SEM are shown demonstrating the ability of a picosecond Nd:YLF laser to produce extremely precise tetragonal cavities in teeth. The cavities are located in healthy and carious enamel, respectively. Both of them have lateral dimensions of $1 \times 1 \text{ mm}^2$ and a depth of approximately $400 \mu\text{m}$. They were created by distributing 1 mJ laser pulses onto 40 lines over the tooth surface with 400 lasered spots per line, and repeating this procedure ten times for the cavity shown in Fig. 4.31a and only once for the cavity in Fig. 4.31b. Thus, a total number of 160 000 laser shots was necessary for the cavity in healthy enamel, and only one tenth of this number was needed to achieve a similar depth in carious enamel. This observation already indicates that the ablation rate of demineralized enamel is about ten times higher than that of healthy enamel, i.e. the Nd:YLF laser provides a caries-selective ablation.

In Figs. 4.32a–b, the cavity wall and bottom are shown, respectively. The cavity wall is extremely steep and is characterized by a sealed glass-like structure. This is of great significance for the prevention of further decay. The roughness of the cavity bottom is of the order of $10\text{--}20 \mu\text{m}$ and thus facilitates the adhesion of most filling materials. The scanning ablation becomes more evident when using fewer pulses to produce a shallow cavity as shown in Fig. 4.33a. In this case, a circular ablation pattern with 2500 pulses was selected. In Fig. 4.33b, the effect of a conventional drill on the cavity wall is demonstrated. Deep grooves and crumbled edges are clearly visible.

Dye Penetration Tests. The results of dye penetration tests after exposure to a picosecond Nd:YLF laser have already been presented in Fig. 4.30. Laser-induced fissures typically remained below $20 \mu\text{m}$. This value is of the same order as fissure depths obtained with the mechanical drill. One potential cause for the extremely small dye penetration might be the sealing effect demonstrated in Fig. 4.32a.

Hardness Tests. One obvious test for the potential influence of shock waves is the measurement of hardness of a tooth before and after laser exposure. In hardness tests according to Vickers, the impact of a diamond tip into a tooth surface is determined. Softer material is characterized by a deeper impact of the diamond tip – and thus a larger impact diameter. The hardness itself is defined as

$$H_V = 1.8544 \frac{K}{D^2},$$

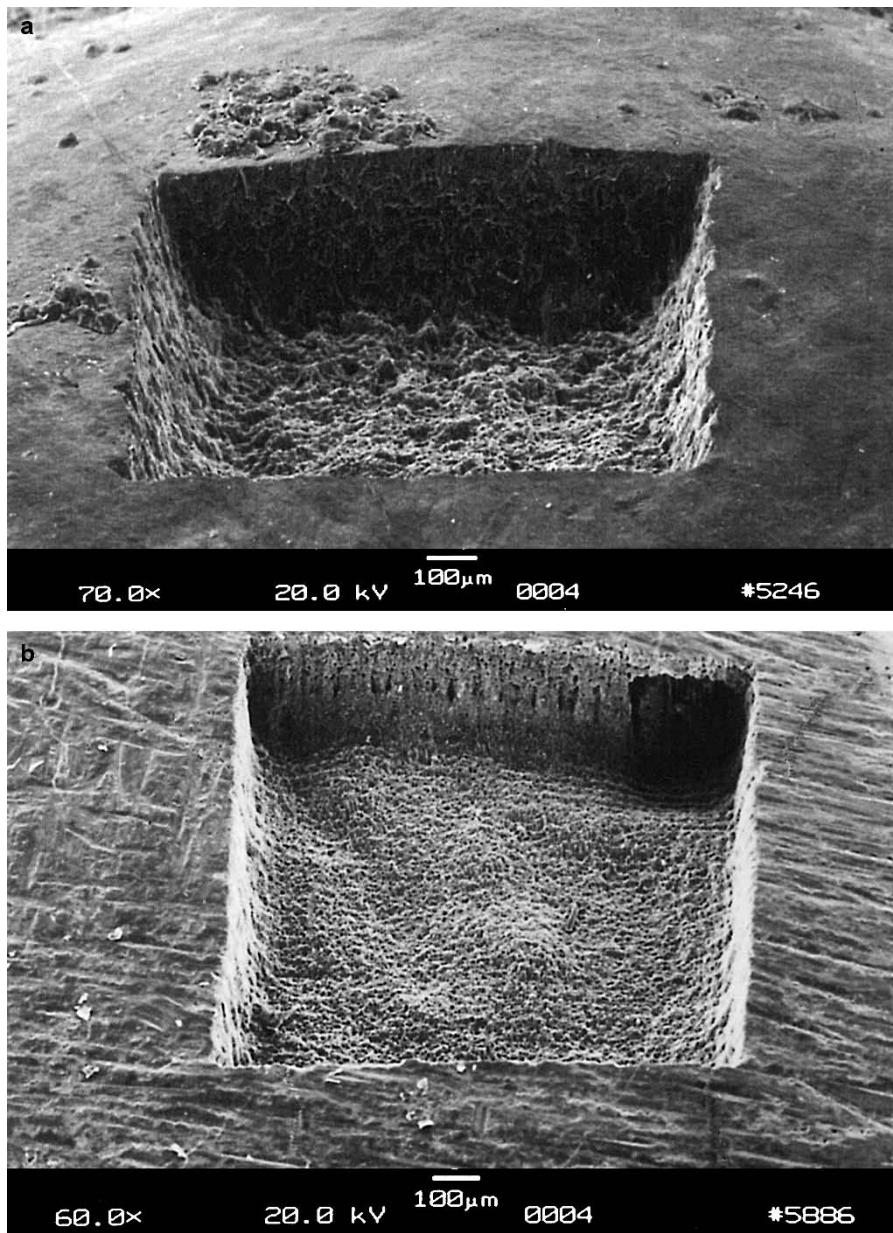


Fig. 4.31. (a) Cavity in healthy enamel achieved with 160 000 pulses from a Nd:YLF laser (pulse duration: 30 ps, pulse energy: 1 mJ). (b) Cavity in carious enamel achieved with 16 000 pulses from a Nd:YLF laser (pulse duration: 30 ps, pulse energy: 1 mJ)

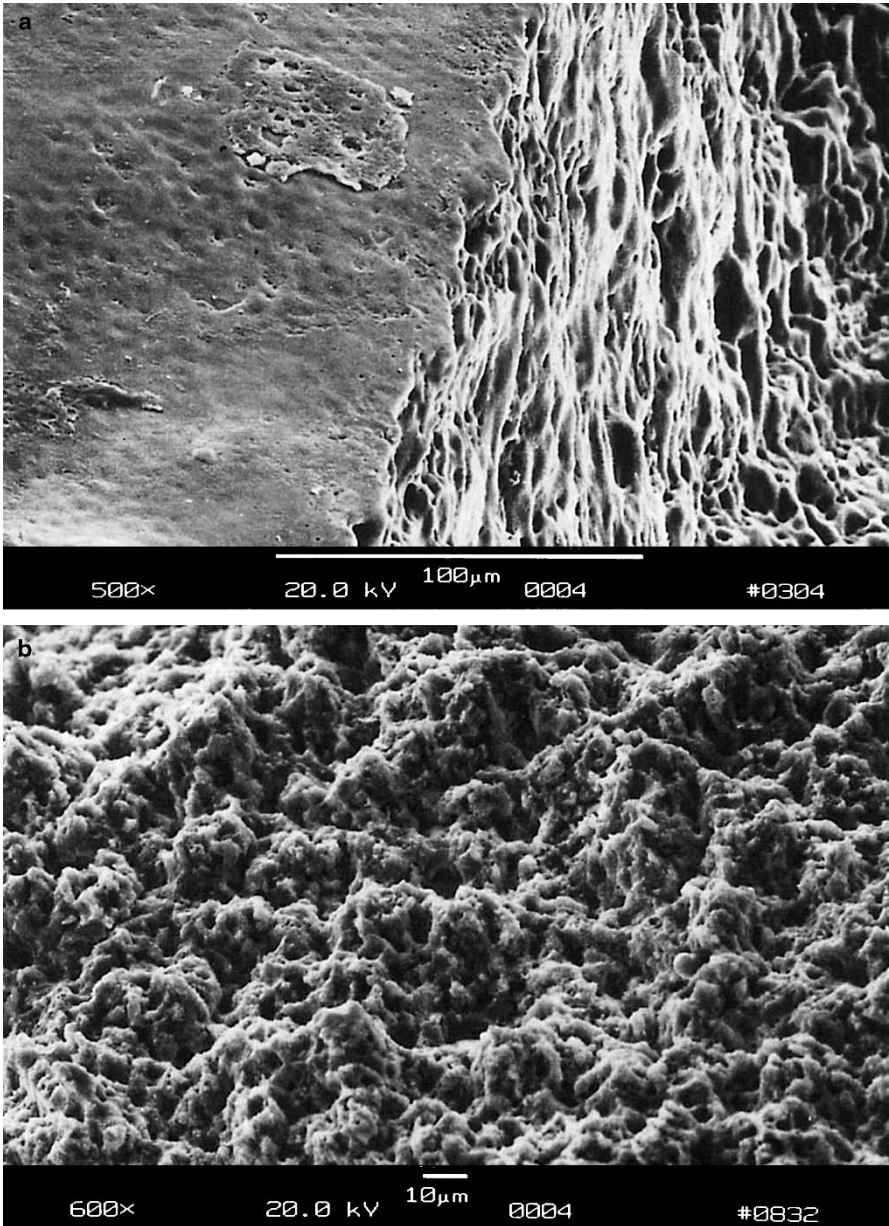


Fig. 4.32. (a) Cavity wall in healthy enamel achieved with a Nd:YLF laser (pulse duration: 30 ps, pulse energy: 1 mJ). (b) Cavity bottom in healthy enamel achieved with a Nd:YLF laser (pulse duration: 30 ps, pulse energy: 1 mJ)

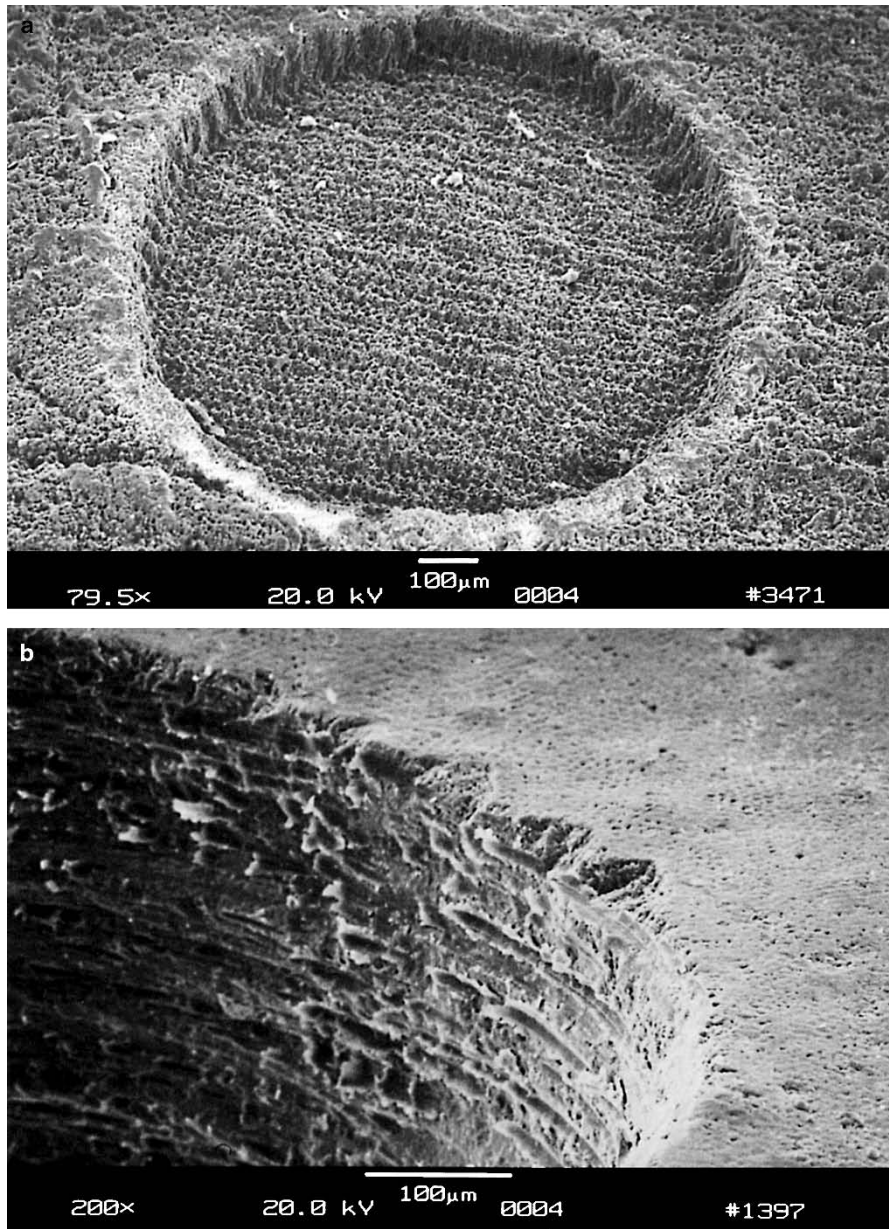


Fig. 4.33. (a) Cavity in carious enamel achieved with 2 500 pulses from a Nd:YLF laser (pulse duration: 30 ps, pulse energy: 1 mJ). (b) Cavity wall achieved with a conventional diamond drill

where $K = 5.0 \times 10^4$ N, and D is the impact of a diamond tip cut at an angle of 136° and expressed in millimeters. The results of hardness tests after exposure to picosecond Nd:YLF pulses are presented in Table 4.3. According to Niemz (1995c), no significant alteration in hardness is observed in exposed and unexposed enamel. As expected, though, dentin appears much softer due to its lower content of hydroxyapatite.

Table 4.3. Mean hardness values of teeth before and after exposure to a Nd:YLF laser (pulse duration: 30 ps, pulse energy: 1 mJ)

	D (mm)	H_V (N/mm ²)
Exposed enamel	5.9	2660
Unexposed enamel	5.8	2760
Unexposed dentin	11.5	700

Histology. The most important touchstone for the introduction of a new therapeutic technique is the biological response of the tissue, i.e. the survival of cells. Histologic sections enable specific statements concerning the condition of cells due to highly sophisticated staining techniques. In Fig. 4.5a (page 157), the dentin–pulp junction of a human tooth is shown. It was located underneath a 1×1 mm² area exposed to 16 000 pulses from a Nd:YLF laser. Along the junction, several odontoblasts are clearly visible. They have not intruded into the dentin and have a similar appearance as in unexposed teeth. Thus, potential shock waves do not have a detectable impact on the pulp – not even on a cellular level.

Polarized Microscopy. Polarized microscopy is an efficient tool for detecting alterations in optical density which might arise from the exposure to shock waves. If these shock waves are reflected, e.g. at the enamel–dentin junction, such alterations might even be enhanced and should thus become evident. For polarized microscopy, exposed teeth are dehydrated in an upgraded series of ethanol. Afterwards, they are kept in fluid methacrylate for at least three days. Within the following period of seven days, polymerization takes place in a heat chamber set to 43°C . Then, the embedded samples are cut into 100 μm thick slices using a saw microtome. Finally, the slices are polished and examined with a polarized light microscope. In Fig. 4.5b (page 157), the enamel–dentin junction of a human tooth is shown. It was located underneath a 1×1 mm² area exposed to 16 000 pulses from a Nd:YLF laser. In the top and bottom parts of the picture, dentin tubuli and enamel prisms are found, respectively. Due to the different optical densities of dentin and enamel, these two structures appear blue and yellow in the corresponding color photograph. However, no substantial alteration in color is observed within either the dentin or the enamel. Hence, no evidence of an altered optical density due to laser-induced shock waves is given.

From the results of the above tests, i.e. the negligibility of mechanical effects, it can be concluded that the cavities shown in Figs. 4.31a–b were produced by means of plasma-induced ablation as discussed in Sect. 3.4. The main reason for these observations is that the applied pulse energies were just slightly above the threshold energy of optical breakdown. In Fig. 4.34, the ablation curves of healthy enamel, healthy dentin, and carious enamel are given, respectively. In healthy enamel, plasma sparking was already visible at approximately 0.2 mJ. Then, when taking the corresponding focal spot size of 30 μm into account, the ablation threshold is determined to be about 30 J/cm². For carious enamel, plasma generation started at roughly 0.1 mJ, i.e. at a threshold density of 15 J/cm². In the range of pulse energies investigated, all three ablation curves are mainly linear. Linear regression analysis yields that the corresponding slopes in Fig. 4.34 are 1 $\mu\text{m}/0.2 \text{ mJ}$, 3 $\mu\text{m}/0.2 \text{ mJ}$, and 8 $\mu\text{m}/0.2 \text{ mJ}$, respectively. Thus, the ablation efficiency increases from healthy enamel and healthy dentin to carious enamel. From the ablation volumes, we derive that – at the given laser parameters – approximately 1.5 mm³ of carious enamel can be ablated per minute. To cope with conventional mechanical drills, a ten times higher ablation efficiency would be desirable. It can be achieved by increasing both the pulse energy and repetition rate. Then, the Nd:YLF picosecond laser might represent a considerable alternative in the preparation of hard tooth substances. The potential realization of such a clinical laser system is currently being evaluated.

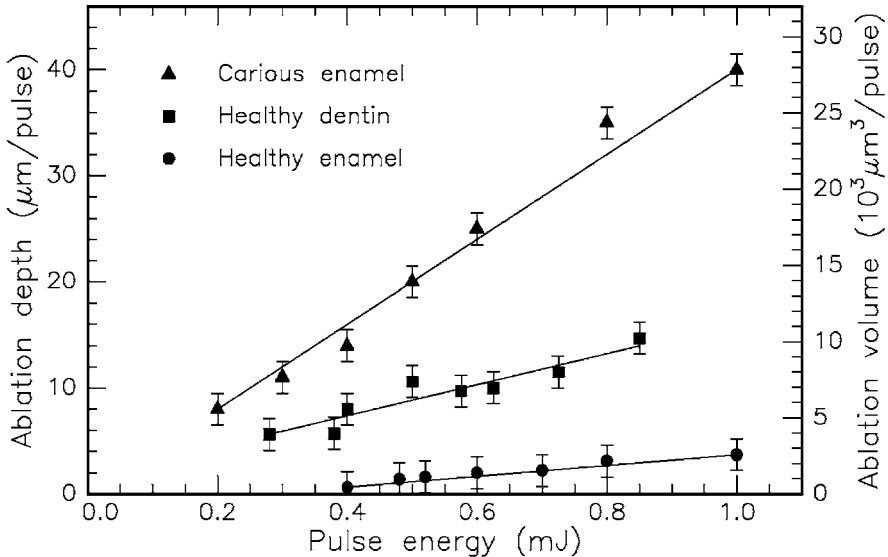


Fig. 4.34. Ablation curves of carious enamel, healthy dentin, and healthy enamel, respectively, obtained with a Nd:YLF laser (pulse duration: 30 ps, focal spot size: 30 μm). Data according to Niemz (1994a) and unpublished data

The results with the Nd:YLF picosecond laser described above have proven that ultrashort laser pulses are a considerable alternative to the mechanical drill for the removal of caries. Due to the recent progress in the generation of even shorter laser pulses, femtosecond lasers have become very promising tools, as well. First experiments with these ultrashort pulse durations have been reported by Niemz (1998). The cavity shown in Fig. 4.35 was achieved with 660 000 pulses from a Ti:Sapphire femtosecond laser at a pulse duration of 700 fs. The geometrical accuracy of the cavity and its steep walls are fascinating.

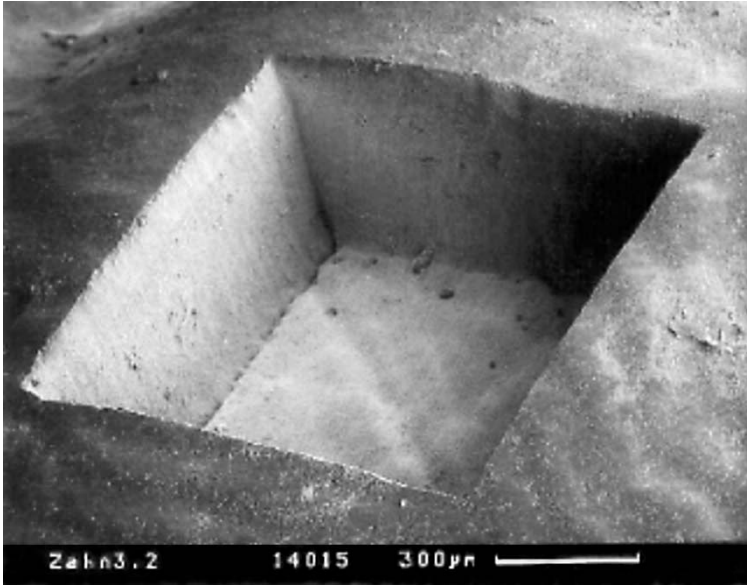


Fig. 4.35. Cavity in healthy enamel achieved with a Ti:Sapphire laser (pulse duration: 700 fs, pulse energy: 100 μ J). Photograph kindly provided by Dipl.-Ing. Bauer (Hannover), Dr. Kasenbacher (Traunstein), and Dr. Nolte (Jena)

In Fig. 4.36, a similar cavity was produced with the same laser but at a larger spacing of adjacent laser pulses. The impacts of individual line scans are clearly visible at the bottom of the cavity. The cavity itself is very clean and of superior quality, if compared to results achievable with conventional diamond drills. Finally, Fig. 4.37 demonstrates the extremely high precision provided by femtosecond lasers. In between exposed areas, unexposed bars remain with a width of less than 10 μ m. No mechanical drill is able to achieve similar results. Furthermore, Fig. 4.37 provides the ultimate proof that mechanical shock waves are negligible when applying femtosecond laser pulses at a suitable energy.

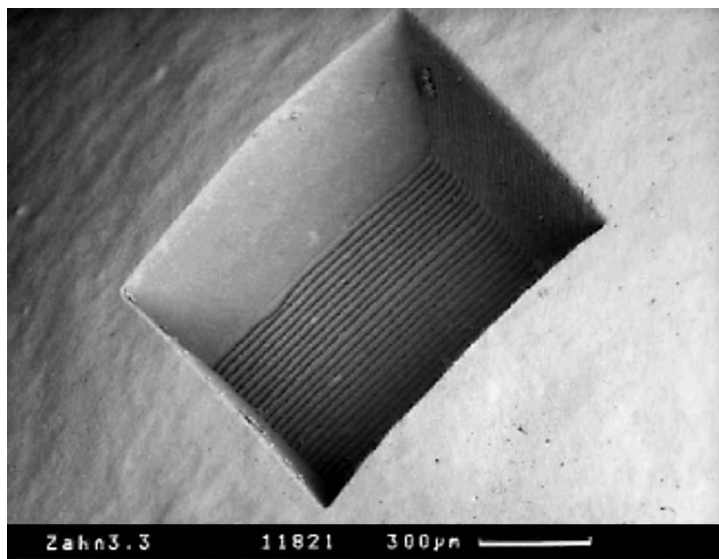


Fig. 4.36. Cavity in healthy enamel achieved with a Ti:Sapphire laser (pulse duration: 700 fs, pulse energy: 100 μ J). Photograph kindly provided by Dipl.-Ing. Bauer (Hannover), Dr. Kasenbacher (Traunstein), and Dr. Nolte (Jena)

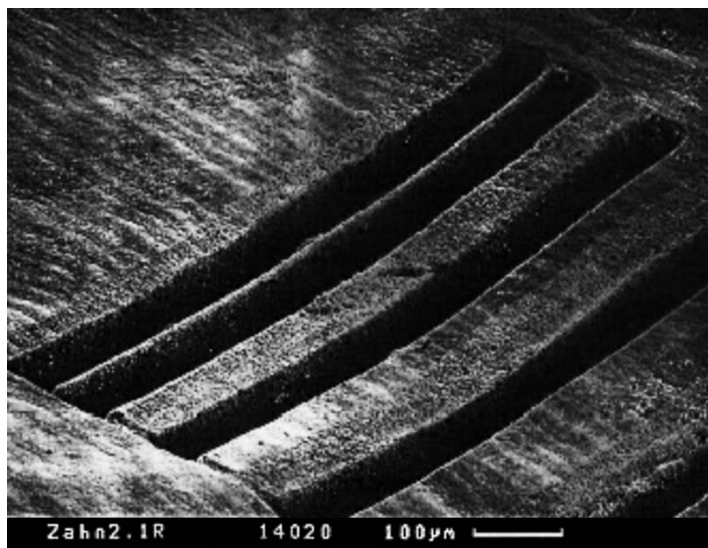


Fig. 4.37. Cavities in healthy enamel achieved with a Ti:Sapphire laser (pulse duration: 700 fs, pulse energy: 100 μ J). Photograph kindly provided by Dipl.-Ing. Bauer (Hannover), Dr. Kasenbacher (Traunstein), and Dr. Nolte (Jena)

One very important issue associated with dental laser systems is the temperature increase inside the pulp where odontoblasts, blood vessels, and tooth nerves are located. Only increments below 5°C are tolerable, otherwise thermal side effects might occur as discussed in Sect. 3.2. Moreover, the feeling of pain is induced at pulp temperatures which exceed approximately 45°C . It is thus very important to remain below these temperatures when striving for clinical applicability. In Fig. 4.38, the temperature increments induced by a picosecond Nd:YLF laser at a repetition rate of 1 kHz are summarized. For this experiment, human teeth were cut into 1 mm thick slices. On one surface of these slices, the laser beam was scanned over a $1 \times 1 \text{ mm}^2$ area, while the temperature was measured at the opposite surface by means of a thermocouple. The observed temperature increments depend on the number of consecutive pulses as well as on the total duration of exposure. We have already stated in Sect. 3.2 that high repetition rates can also induce an increase in temperature even when using picosecond pulses. Hence, a higher temperature is obtained when applying 30 instead of only 10 consecutive pulses before moving the focal spot to the next position. The total duration of exposure also affects the final temperature, although the increase during the first minute is most significant. From these results, we can conclude that up to approximately 10 consecutive pulses may be applied to a tooth at a repetition rate of 1 kHz if the temperature in the pulp shall not increase by more than 5°C .

Temperature increase ($^{\circ}\text{C}$)

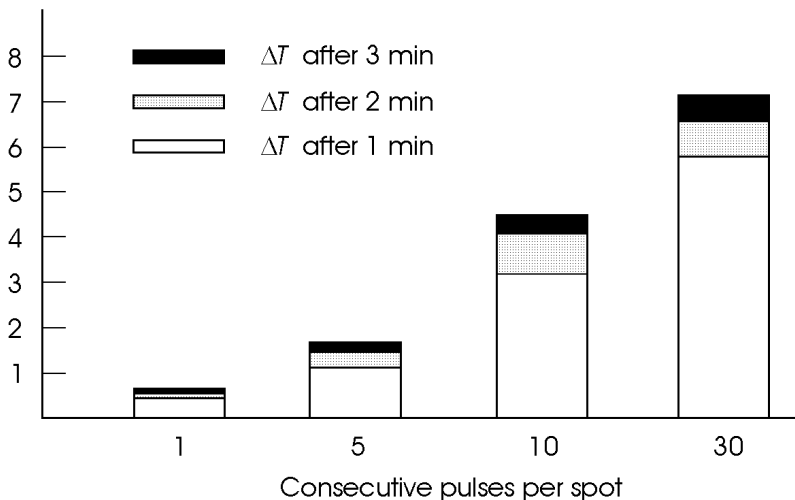


Fig. 4.38. Increase in temperature in a distance of 1 mm from cavities achieved with a Nd:YLF laser (pulse duration: 30 ps, pulse energy: 1 mJ, repetition rate: 1 kHz). Unpublished data

A novel dental application of lasers has recently been proposed by Niemz (1995d). Using a confocal laser scanning microscope, the space to be occupied by dental fillings can be very precisely determined. The confocal principle requires that only light reflected within the focal plane is detected. Thereby, very high axial resolutions can be obtained compared to conventional microscopy. With the confocal microscope, several layers of the cavity to be filled are scanned. From the reflected intensities, a three-dimensional plot of the cavity is calculated as shown in Fig. 4.39a. These data can be inverted to form a direct pattern for the milling of inlays or crowns with a CNC-machine as demonstrated in Fig. 4.39b.

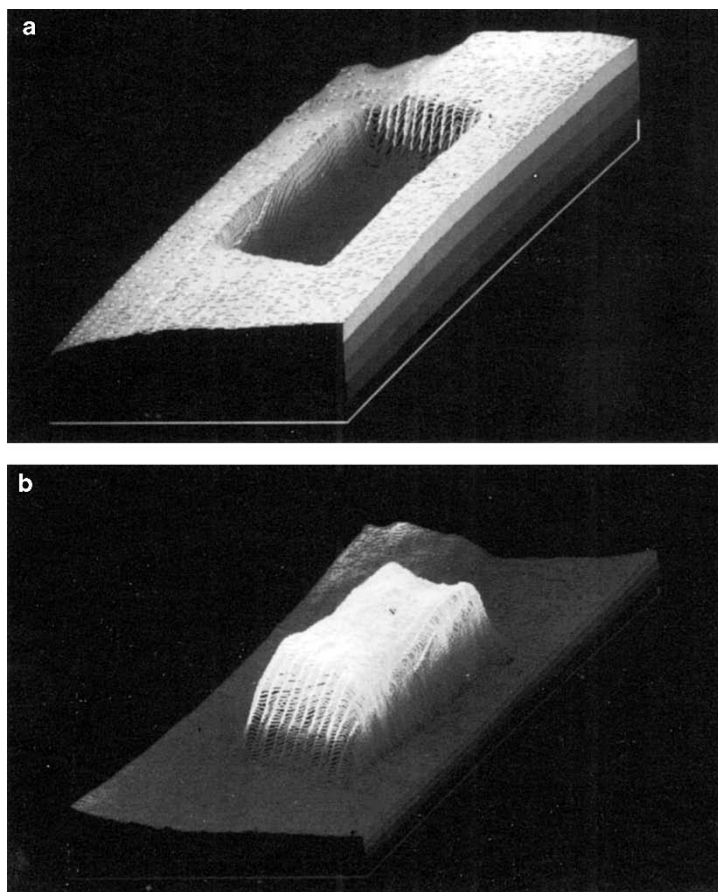


Fig. 4.39. (a) Three-dimensional plot of a laser-induced cavity captured with a confocal laser scanning microscope. The cavity was achieved with a Nd:YLF laser (pulse duration: 30 ps). (b) Inverted image of the same cavity as calculated with a computer. Reproduced from Niemz et al. (1995d). © 1995 Springer-Verlag

Laser Treatment of Soft Dental Tissue

Several studies have been reported on the use of a CO₂ laser in the management of malignant, premalignant, and benign lesions of the oral mucosa, e.g. by Strong et al. (1979), Horch and Gerlach (1982), Frame et al. (1984), and Frame (1985). Since the oral environment is very moist, radiation from the CO₂ laser is predestined for such purposes because of its high absorption. When treating a soft tissue lesion inside the mouth, the surgeon has a choice of two techniques – either excision or vaporization. It is usually preferable to excise the lesion because this provides histologic evidence of its complete removal and confirmation of the preceding diagnosis. During vaporization, a risk always remains that not all altered tissue is eliminated. Hence, if a pathologic lesion is vaporized, a biopsy should be obtained from the adjacent tissue after the treatment.

The CO₂ laser is particularly useful for small mucosal lesions. Most of them can be vaporized at a power of 5–10 W in pulsed or CW mode. After laser treatment, the wound is sterile and only minimal inflammatory reactions of the surrounding tissue occur. One major advantage is that there is no need to suture the wound, since small blood vessels are coagulated and bleeding is thus stopped. The wound edges can even be smoothed with a defocused beam. Wound healing usually occurs within a period of two weeks, and the process of reepithelialization is complete after about 4–6 weeks. Frame (1985) states that patients tolerate the procedure well and initially complain of little pain. However, the treated area may become uncomfortable for approximately 2–3 weeks.

Cases of leukoplakia are difficult to treat by conventional surgery, since they are frequently widespread inside the mouth. The lesion is usually outlined with a focused CO₂ laser beam for easy visualization. Afterwards, it is vaporized with a defocused beam at a power of about 15–20 W. According to Horch (1992), laser-treated leukoplakias heal very well, and there is only little evidence of recurrence. Even leukoplakias on the tongue and lips can be treated without losses in performance of these organs.

Malignant lesions require a higher laser power of approximately 20–30 W to deal with the bulk of the tumor. Lanzafame et al. (1986) state that the recurrence of local tumors is reduced when using the CO₂ laser rather than a mechanical scalpel. The thermal effect of the radiation is made responsible for this observation. However, it is questionable whether laser treatments of malignant oral tumors are successful during a longer follow-up period, since metastases have often already spread to other parts of the body. In these cases, laser application is restricted to a palliative treatment. A specimen, for biopsy can also be excised with a CO₂ laser as one would do with a conventional scalpel. More recently, Patel (1988) reported on the application of a Nd:YAG laser in the treatment of oral cancer. However, in the treatment of soft dental tissues, this laser has not gained clinical relevance so far.

Lasers in Endodontics

Endodontics is concerned with the treatment of infections of the root canal. These arise from either a breakthrough of decay into the pulp or from plaque accumulation beneath the gingiva and subsequent bacterial attacks of the root. In either case, once the pulp or the root canal are infected by bacteria, the only treatment is to sterilize both pulp and root, thereby taking into account the associated death of the tooth. However, even a dead tooth may reside in place for years.

The mechanical removal of bacteria, plaque, infected root cementum, and inflamed soft tissues is regarded as an essential part of systematic periodontal treatment. The excavation of the root itself is a very complicated and time-consuming procedure, since roots are very thin and special tools are required. The procedure can be supported by antimicrobial chemicals to ensure sterility which is a mandatory condition for success of the treatment. Along with the rapid development of medical laser systems, it has been discussed whether lasers could improve conventional techniques of endodontics, especially in removal of plaques and sterilization. First experimental results using CO₂ and Nd:YAG lasers in endodontics were published by Weichmann and Johnson (1971) and Weichmann et al. (1972). By means of melting the dentin next to the root, the canal wall appears to be sealed and thus less permeable for bacteria. Indeed, Melcer et al. (1987) and Frentzen and Koort (1990) stated that lasers may have a sterilizing effect. Sievers et al. (1993) observed very clean surfaces of the root canal after application of an ArF excimer laser. However, both the CO₂ laser and the ArF laser will not gain clinical relevance in endodontics, since their radiation cannot be applied through flexible fibers. Even other laser systems will not be applicable exclusively, since suitable fiber diameters of 400 μm are still too large for unprepared roots. Thinner fibers are very likely to break inside the root causing severe complications and additional mechanical operation.

Laser Treatment of Filling Materials

In dental practice, not only tooth substance needs to be ablated but also old fillings have to be removed, e.g. when a secondary decay is located underneath. For the removal of metallic fillings, infrared lasers cannot be used, since the reflectivity of these materials is too high in that spectral range. Amalgam should never be ablated with lasers at all. In Figs. 4.40a–b, two samples of amalgam are shown which were exposed to a Nd:YLF laser and an Er:YAG laser, respectively. During irradiation, the amalgam has melted and a significant amount of mercury has been released which is extremely toxic for both patient and dentist. For other filling materials, e.g. composites, little data are available. Hibst and Keller (1991) have shown that the Er:YAG laser removes certain kinds of composites very efficiently. However, it is quite uncertain whether lasers will ever be clinically used for such purposes.

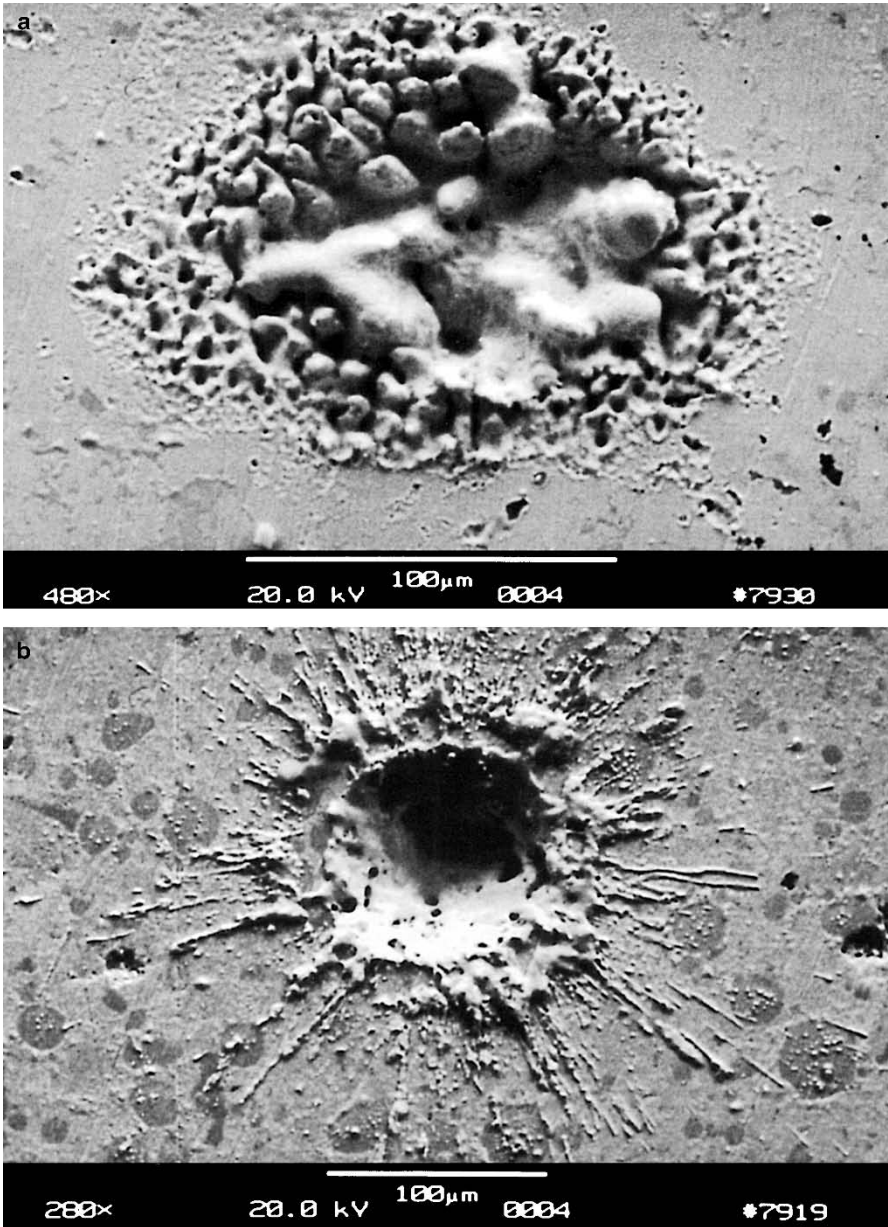


Fig. 4.40. (a) Removal of amalgam with a Nd:YLF laser (pulse duration: 30 ps, pulse energy: 0.5 mJ). (b) Removal of amalgam with an Er:YAG laser (pulse duration: 90 μ s, pulse energy: 100 mJ)

Another very interesting topic in dental technology is laser-welding of dental bridges and dentures. It can be regarded as an alternative to conventional soldering. During soldering, the parts to be joined are not melted themselves but are attached by melting an additional substance which, in general, is meant to form an alloy between them. Laser-welding, on the other hand, attaches two parts to each other by means of transferring them to a plastic or fluid state. This is achieved with high power densities in the range 10^2 – 10^9 W/cm². According to van Benthem (1992), CO₂ lasers and Nd:YAG lasers are preferably used. Since the reflectivity of metals is very high in the infrared spectrum, it must be assured that either a laser plasma is induced at the surface of the target or that the target is coated with a highly absorbing layer prior to laser exposure. Dobberstein et al. (1991) state that some laser-welded alloys are characterized by a higher tear threshold than soldered samples as shown in Fig. 4.41. However, van Benthem (1992) argues that such behavior cannot be observed in all alloys, but tear thresholds in laser-welded alloys can definitely reach the same values as the original cast. According to his studies, the major advantages of laser-welding are: higher resistance against corrosion, the ability to weld different metals, the ability to weld coated alloys, and lower heat load. Moreover, the reproducibility of laser-welded alloys is significantly higher than during soldering. For further results, the interested reader should consult the excellent review given by van Benthem (1992).

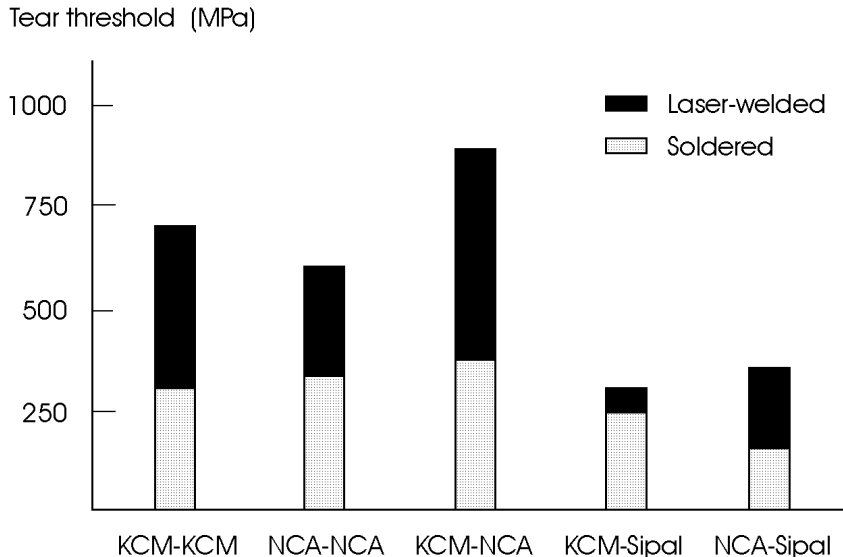


Fig. 4.41. Tear thresholds of laser-welded and soldered dental alloys (KCM: cobalt-based alloy, NCA: nickel-based alloy, Sipal: silver-palladium-based alloy). Data according to Dobberstein et al. (1991)

4.3 Lasers in Gynecology

Beside ophthalmology, gynecology is one of the most significant disciplines for laser applications. This is mainly due to the high success rate of about 93–97% in treating *cervical intraepithelial neoplasia (CIN)*, i.e. uncommon growth of new cervical tissue, with the CO₂ laser. CIN is the most frequent alteration of the *cervix* and should be treated as soon as possible. Otherwise, cervical cancer is very likely to develop. The cervix represents the connective channel between the *vagina* and *uterus*. The locations of the cervix and adjacent organs are illustrated in Fig. 4.42.

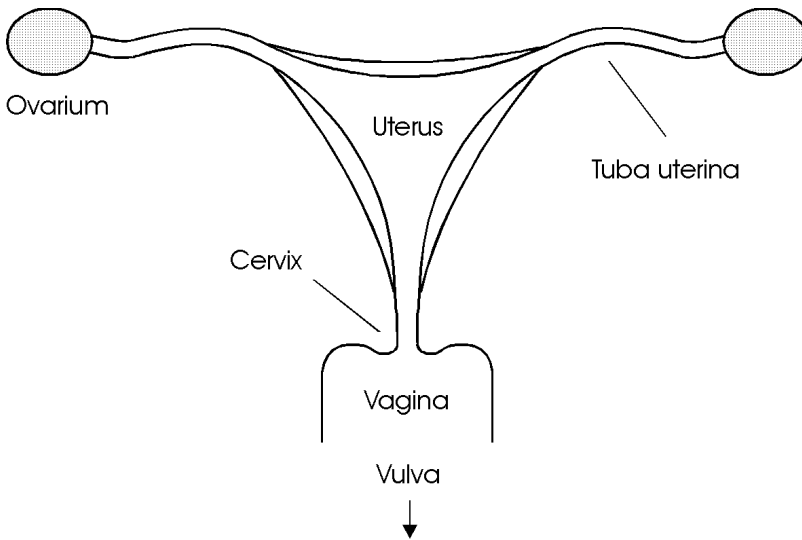


Fig. 4.42. Scheme of female reproduction organs

The CO₂ laser is the standard laser in gynecology. Beside treating CIN, it is applied in vulvar intraepithelial neoplasia (VIN) and vaginal intraepithelial neoplasia (VAIN). Depending on the type of treatment, CO₂ lasers can be operated in three different modes – CW radiation, chopped pulse, and superpulse – as shown in Fig. 4.43. Chopped pulses with durations in the millisecond range are obtained from CW lasers when using rotating apertures. Superpulses are achieved by modulation of the high voltage discharge. Thereby, pulse durations less than 1 ms can be generated. The peak power is inversely related to the pulse duration. The mean powers of CW radiation and chopped pulses are nearly the same, whereas it decreases in the case of superpulses. As discussed in Sect. 3.2, shorter pulse durations are associated with a reduction of thermal effects. Hence, by choosing an appropriate mode of the laser, the best surgical result can be obtained.

Peak power (W)

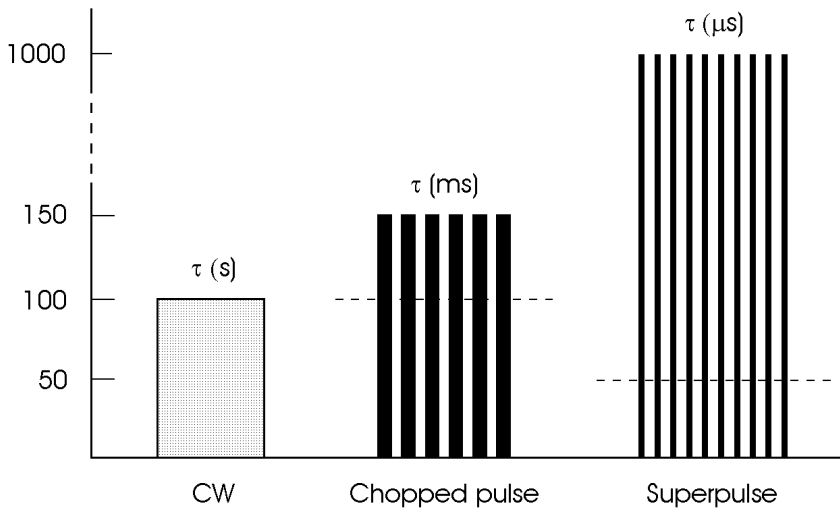


Fig. 4.43. CW, chopped pulse, and superpulse modes of a CO₂ laser. Dashed lines denote mean powers

Beside selecting the temporal mode, the surgeon has to decide whether he applies a focused or defocused mode as shown in Fig. 4.44. Only in tightly focused mode are deep excisions achieved. In partially focused mode, less depth but a larger surface is vaporized. In defocused mode, the power density decreases below the threshold of vaporization, and tissue is coagulated only.

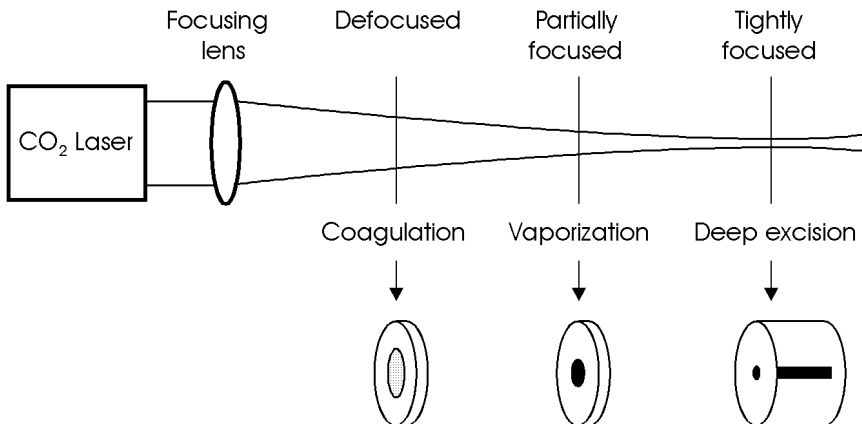


Fig. 4.44. Coagulation, vaporization, and excision modes of a CO₂ laser, depending on a defocused, partially focused, or tightly focused beam

In gynecology, there exist several indications for laser treatment:

- vulvar intraepithelial neoplasia (VIN),
- vaginal intraepithelial neoplasia (VAIN),
- cervical intraepithelial neoplasia (CIN),
- endometriosis,
- obstruction of the uterine tube,
- sterilization,
- twin-twin transfusion syndrome.

Vulvar Intraepithelial Neoplasia (VIN). As already mentioned above, neoplasia generally describes uncommon growth of new tissue. In the case of VIN, intraepithelial tissue of the vulva is significantly proliferated. After histologic examination, the altered tissue is usually vaporized with a CW CO₂ laser in a partially focused mode. According to Baggish and Dorsey (1981), typical power densities of 100 W/cm² are applied to achieve vaporization depths of about 3–4 mm. In the event of bleeding, the laser beam is immediately switched to a defocused mode.

Vaginal Intraepithelial Neoplasia (VAIN). VAIN is a similar diagnosis as VIN, except that it occurs inside the vagina. Initial studies using the CO₂ laser were reported by Staff et al. (1977). Due to the thinner and more sensitive vaginal tissue, slightly lower power densities are applied. The use of a proper surgical microscope is indicated.

Cervical Intraepithelial Neoplasia (CIN). The tissue at risk for the development of cervical cancer is the columnar epithelium which is located in the transformation zone. This type of epithelium can migrate up and down the endocervical channel. Therefore, it is very important to determine its exact location prior to any treatment. This is usually achieved with a colposcope which essentially is an endoscope specially designed for gynecologic purposes. The extent of columnar epithelium is relatively constant. Thus, the more it is exposed at the ectocervix, the less likely is the existence of diseased tissue inside the channel. In order to exclude any potential inflammation, a biopsy specimen is obtained and a second or third control examination is performed after 3–6 months. According to the histologic evaluation of the biopsy, three grades of CIN (I–III) and cervical carcinoma are distinguished, depending on the progress of neoplasia. If the biopsy reveals the presence of cervical carcinoma, a complete resection of the cervix is indicated. At a late stage of cancer, adjacent organs such as the uterus or vagina might have to be removed, as well.

In the case of CIN I, the columnar epithelium is usually located at the ectocervix as shown in Fig. 4.45a. The ablated epithelium is vaporized in a similar fashion as in VIN or VAIN. According to Wright et al. (1983), the procedure should aim at a treated depth of approximately 6 mm. Fast movements of the laser beam cause a more homogeneous distribution of heat and thus reduce the probability of carbonization. Scanning mirror devices are

available to assist the surgeon in steadily moving the beam. In Fig. 4.4b (page 156), a vaporization of cervical tissue is shown as achieved with a CO₂ laser at a power of 10 W. Escape of smoke is usually inevitable during surgery, but can be managed with specially designed suction tubes.

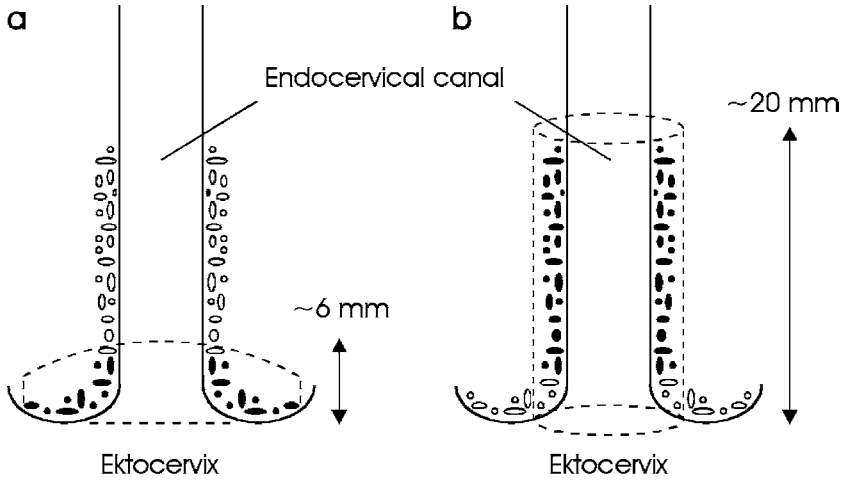


Fig. 4.45. (a) CO₂ laser treatment in the case of CIN I. Diseased epithelium is illustrated by filled ovals. Dashed lines indicate the dome-shaped volume to be vaporized. (b) CO₂ laser treatment in the case of CIN II or CIN III. Dashed lines indicate the cylindrical volume to be excised

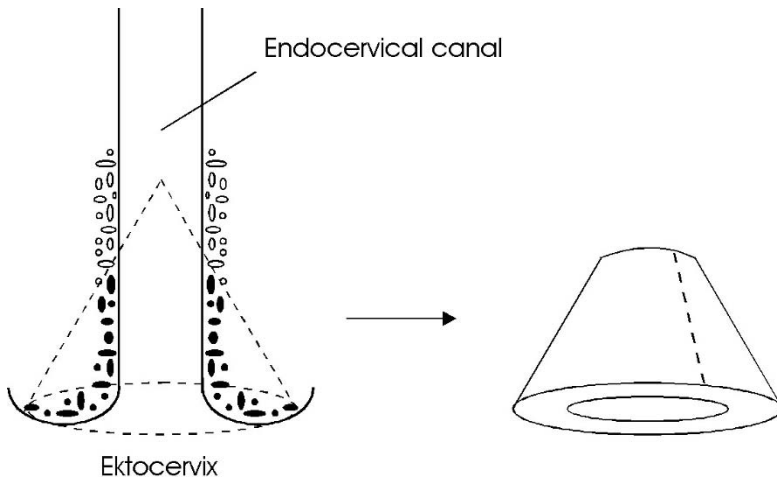


Fig. 4.46. Alternative CO₂ laser treatment in the case of CIN II or CIN III. Diseased epithelium is illustrated by filled ovals. Dashed lines indicate the cone-shaped volume to be excised (*left*). The excised cone is unzipped for histologic examination (*right*)

If CIN II or CIN III is diagnosed, parts of the cervix must be removed to reduce the probability of recurrence. Two different treatment techniques were proposed by Dorsey and Diggs (1979) and Wright et al. (1983). Either surgery is performed only after careful evaluation of the obtained biopsy and determination of the cervical length with a micrometer probe. Dorsey and Diggs (1979) suggest excising a cone-shaped volume out of the cervix with a focused CO₂ laser as demonstrated in Fig. 4.46. The angle of the cone can be adjusted to individual extents of neoplasia. The procedure itself is called *laser conization*. The excised cone is then unzipped for histologic examination as shown in Fig. 4.46. By this means, it can be determined whether all altered tissue has been removed.

An alternative method was proposed by Wright et al. (1983) which is illustrated in Fig. 4.45b. Instead of a cone-shaped volume, a cylindrical volume is removed. The vertical cylindrical excisions are achieved with a focused CW CO₂ laser, whereas the horizontal excision inside the cervix is performed with either a mechanical scalpel or the same CO₂ laser in superpulse mode. After excision of the complete cylinder, the remaining surface is coagulated by defocusing the CW laser beam to achieve local hemostasis. According to Heckmann (1992), cylindrical excisions are better adjusted to individual cases than cone-shaped excisions. In either case, most of the cervical tissue regenerates after being removed. A ten-year review on the treatment of CIN with the CO₂ laser was published by Baggish et al. (1989). In Table 4.4, typical cure rates after one laser treatment are summarized.

Table 4.4. Results of CIN treatment with the CO₂ laser. Data according to Baggish et al. (1989)

	Vaporization	Conization
Number of patients	3070 (100 %)	954 (100 %)
Cured	2881 (93.8 %)	925 (97.0 %)
Persistent	189 (6.2 %)	29 (3.0 %)

According to Wright et al. (1983), laser surgery is an excellent modality for treating CIN when compared to conventional techniques, e.g. cryotherapy. Recently, however, it has been demonstrated by Baggish et al. (1992) that high-frequency electric currents can do the same job as CO₂ lasers. When using thin loops of 10–15 mm in height, similar thermal damage was observed as with a 40 W CO₂ laser. Profound studies with low voltage loop diathermy have already been reported by Prendeville et al. (1986) for the purpose of taking cervical biopsies. Since electrically induced excisions are faster and less expensive equipment is required, they probably represent the preferred choice in the near future. This is one of the few applications, where lasers can – and should – be replaced by simpler surgical tools.

Endometriosis. The cyclic growth of uterine-like mucosa outside the uterus is called *endometriosis*. It appears as dark burns, deep nodules, or vesicles. Endometriosis can be either coagulated, vaporized, or excised. In the 1980s, Keye and Dixon (1983) reported on the use of an argon ion laser in coagulating endometriosis. Further studies soon followed by Feste (1985) and Lomano (1985) using CO₂ and Nd:YAG lasers, respectively. However, treatment of endometriosis with the Nd:YAG laser involves the risk of injuring deeper structures because of the low absorption coefficient at this wavelength. Nevertheless, this laser is being clinically applied in cases of endometriosis which are associated with infertility, and reasonable success rates have been reported, e.g. by Corson et al. (1989) and Shirk (1989). Deeply located endometriosis is usually excised rather than vaporized. A scalpel is still necessary to cut off the distal end.

Obstruction of the Uterine Tube. Tubal obstructions can be caused by either adhesions, proliferated growth of tissue, or tubal pregnancies. In the case of adhesions, *salpingolysis* is performed, i.e. the recanalization of the *salpinx* (from Greek: σαλπινγξ = trumpet). By means of CO₂ or Nd:YAG laser radiation, the adhesions are vaporized to obtain a free tubal lumen. Care should be taken not to traumatize the endothelium of the tube, since this can cause troublesome bleeding as well as damage to the tube. In the presence of proliferated growth of tissue, additional openings of the tube can be generated in a treatment called *salpingostomy*. Tubal pregnancies can usually be managed by either salpingostomy or *salpingectomy*. Salpingectomy denotes the complete removal of one tube. Successful laser treatment of tubal pregnancies was reported by Huber et al. (1989).

Sterilization. A sure way to achieve sterilization is to artificially occlude both uterine tubes. This is performed by either suturing the tube or by coagulating it with a Nd:YAG laser. According to Bailer (1983), safe sterilization is obtained when coagulating both tubes on a length of about 1 cm.

Twin-Twin Transfusion Syndrome. This syndrome is caused by a misplaced shunt vessel between the twins. It usually leads to an unbalanced blood supply and is often lethal to both twins. In pilot studies, De Lia et al. (1995) and Ville et al. (1995) have just recently demonstrated that occlusion of this vessel by means of coagulation with a Nd:YAG laser is technically feasible.

Gynecology comprises a wide range of potential laser applications. An excellent review is found in the book by Bastert and Wallwiener (1992). Several minimally invasive techniques have already been described above, but others are yet to be developed. Very promising is the recently established method of laser-induced interstitial thermotherapy (LITT) which can be used to coagulate malformations inside the uterus by means of thin optical fibers. Initial studies have already been reported by Wallwiener et al. (1994). Thus, lasers might turn into irreplaceable gynecologic tools, especially in the presence of pregnancies where conventional surgery is often lethal to the fetus.

4.4 Lasers in Urology

The workhorse lasers of urology are primarily CO₂, argon ion, Nd:YAG, and dye lasers. CO₂ lasers are best in precise cutting of tissue as already discussed in Sect. 3.2. Argon ion lasers and Nd:YAG lasers are used for the coagulation of highly vascularized tumors or malformations. Among these two lasers, the Nd:YAG laser is preferably applied for the coagulation of large tissue volumes because its radiation deeply penetrates into tissues. Moreover, Q-switched Nd:YAG lasers which interact in the photodisruptive mode have become a standard tool in lithotripsy beside ultrasound fragmentation. Dye lasers have not been investigated until recently in lithotripsy and in photodynamic therapy.

After the development of the first fiberoptic endoscope by Nath et al. (1973), Staehler et al. (1976) performed initial experimental studies with the argon ion laser in urology. Meanwhile, the indications for urologic laser treatments have significantly increased. They extend from the *external genital*, the *lower urinary tract (urethra)*, the *bladder*, the *upper urinary tract (ureter)*, all the way up to the *kidneys* as shown in Fig. 4.47. In addition, very promising results have already been achieved in treating benign hyperplasia of the *prostate* which embraces the urethra. Various laser therapies for all these different organs require specific strategies and parameters. They shall now be discussed in the above order.

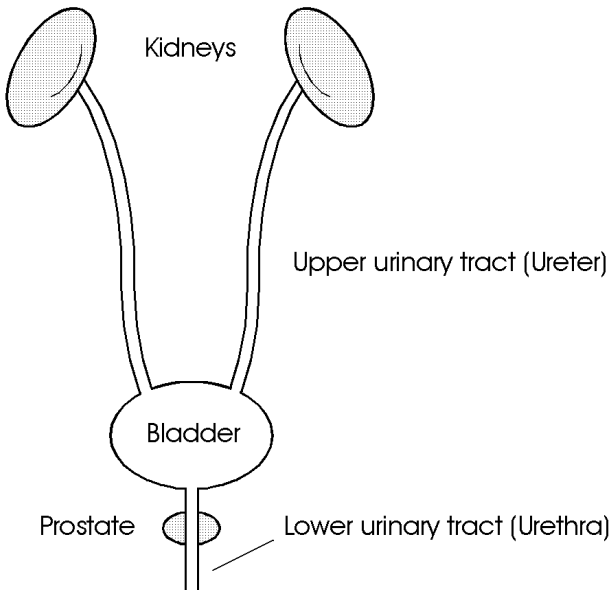


Fig. 4.47. Scheme of male urinary tract

The most frequent malformations of the external genital are called *condylomata acuminata*. These benign warts must be treated as early as possible, because they tend to be very infectious and degenerating. After circumcision and application of 4% acetic acid to suspected areas, they are coagulated with either Nd:YAG or CO₂ lasers. Occasional recurrences cannot be excluded, especially in the treatment of intraurethral condylomata. With both laser types, however, the rate of recurrence is less than 10% as reported by Baggish (1980) and Rosemberg (1983). Hemangiomas of the external genital should be treated with radiation from Nd:YAG lasers because of its higher penetration depth. Hofstetter and Pensel (1993) stated that additional cooling of the tissue surface may even improve the procedure. Carcinoma of the external genital are best treated with a Nd:YAG laser if they are at an early stage. This significantly reduces the risk of having to perform a partial amputation. According to Eichler and Seiler (1991), powers of 40 W and focal spot sizes of 600 μm are usually applied. At an advanced stage, the tumor is first mechanically extirpated. Afterwards, the remaining tissue surface should be additionally coagulated.

Frequent diseases of the lower urinary tract are stenoses induced by either inflammation, tumor growth, or unknown origins. In these cases, *urethrotomy* by endoscopic control is usually performed as proposed by Sachse (1974). During this conventional technique, stenotic material is removed with a cold scalpel. Unfortunately, restenoses often occur due to scarring of the tissue. Further urethrotomies are not of great help, since they only enhance additional scarring. The first recanalizations of urethral stenoses with an argon ion laser were performed by Rothauge (1980). However, the results obtained were not as promising as initially expected. Then, no further progress was made until Wieland et al. (1993) recently published first results using a Ho:YAG laser. Meanwhile, follow-up periods of 20 months after Ho:YAG laser treatment were reported by Nicolai et al. (1995). They concluded that this technique is a considerable alternative to mechanical urethrotomy in virgin stenoses as well as restenoses. The probability for the occurrence of laser-induced restenoses is approximately 10% only. In Figs. 4.48a–b, the effects of the Ho:YAG laser on the urethra and ureter are shown, respectively. In both samples, thirty pulses with an energy of 370 mJ and an approximate duration of 1 ms were applied.

Tumors of the bladder are very difficult to treat, since they tend to recur after therapy. It is yet unknown whether this is due to metastasation induced either prior to or by the treatment. Unfortunately, bladder tumors also easily break through the bladder wall. Thus, a treatment is successful only if it completely removes the tumor, does not perforate the bladder wall, and does not damage the adjacent intestine. Frank et al. (1982) have compared the effects of CO₂, Nd:YAG, and argon ion lasers on bladder tissue. Among these, the Nd:YAG laser has proven to be best suited in coagulating bladder tumors. Argon ion lasers are applicable only in superficial bladder tumors.

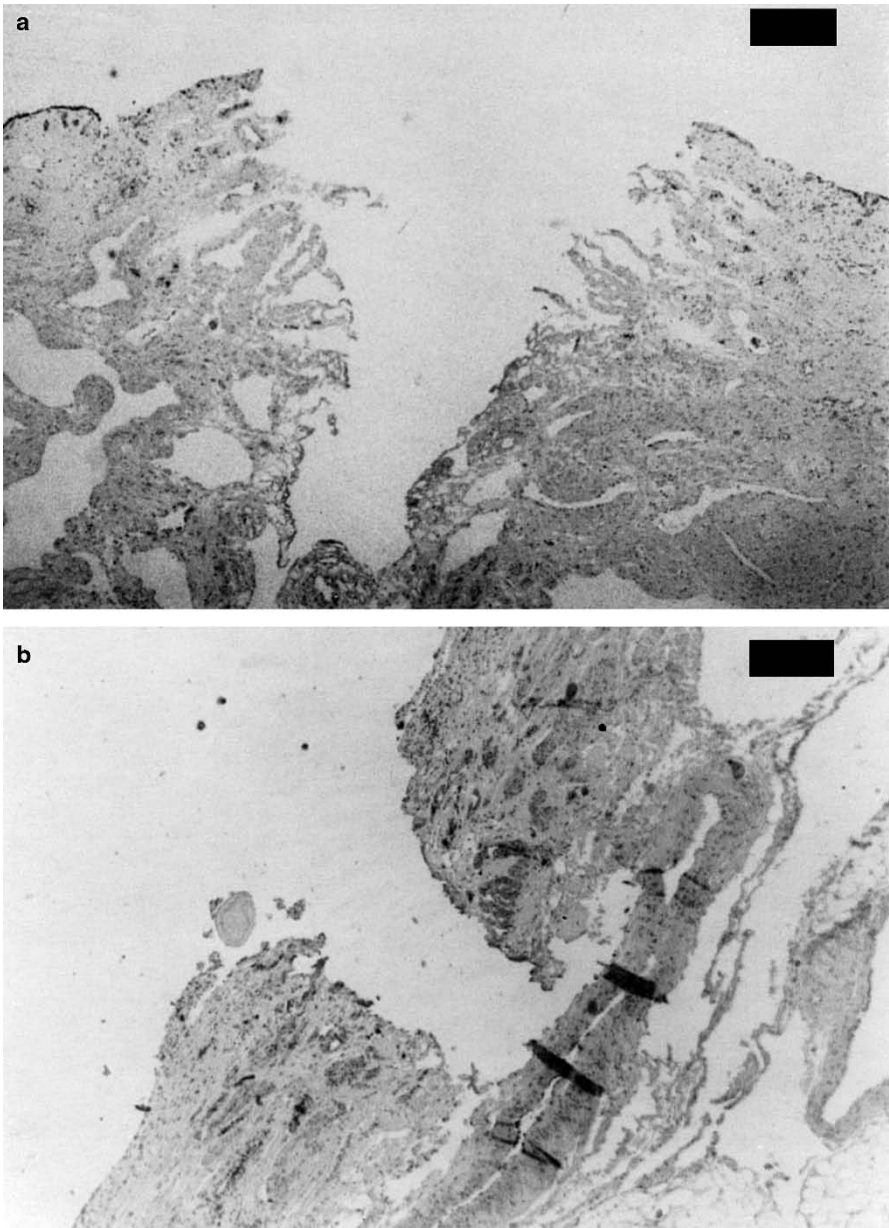


Fig. 4.48. (a) Effect of thirty pulses from a Ho:YAG laser (pulse duration: 1 ms, pulse energy: 370 mJ, bar: 250 μm) on the urethra. (b) Effect of thirty pulses from a Ho:YAG laser (pulse duration: 1 ms, pulse energy: 370 mJ, bar: 250 μm) on the ureter. Photographs kindly provided by Dr. Nicolai (Regensburg)

According to Hofstetter et al. (1980), the rate of recurrence after laser treatment is approximately 1–5%, whereas it ranges from 40–60% if conventional transurethral resection (TUR) is performed. Even advanced tumors can be efficiently removed with Nd:YAG lasers, since the hemostatic treatment guarantees best vision. Pensel (1986) suggests the application of 30–40 W of laser power and a working distance between 1 mm and 2 mm. The tumor should be irradiated until it visibly pales. Afterwards, coagulated necrotic tissue is mechanically removed. For safety reasons, the remaining tissue surface should be coagulated, as well.

It was emphasized by Hofstetter and Pensel (1993) that tumors can still be graded and staged by biopsies after coagulation. Usually, control biopsies should be obtained within the next 3–6 months. The laser treatment itself is extremely safe, since perforations of the bladder wall are very unlikely, and the function of the bladder remains unaffected. All transurethral treatments are performed with a rigid cystoscope and a flexible fiber. In most cases, local anesthetization is sufficient.

Recently, photodynamic therapy (PDT) has gained increasing significance in the treatment of bladder tumors. First endoscopic applications of HpD have already been investigated by Kelly and Snell (1976). Several clinical reports on PDT are available, e.g. by Benson (1985), Nseyo et al. (1985), and Shumaker and Hetzel (1987). A complete treatment system including in vivo monitoring and dose control was described by Marynissen et al. (1989). A list of potential complications arising when using dihematoporphyrin ether was given by Harty et al. (1989). Today, photodynamic therapy is considered as a useful supplement to other techniques, since it enables the resection of tumors which are not visible otherwise. The ability of simultaneous diagnosis – by means of laser-induced fluorescence – and the treatment of tumors is thus one of the key advantages of photodynamic therapy. So far, red dye lasers at 630 nm and energy densities between 10–50 J/cm² are usually applied. In most cases, laser treatment is still restricted to superficial tumors due to the limited penetration depth at the specific wavelength. However, the recent discovery of novel photosensitizers like 5-aminolaevulinic acid (ALA) – as already discussed in Sect. 3.1 – will certainly improve photodynamic therapy in urology during the next few years.

Lithotripsy of urinary calculi is often based on ultrasound techniques. However, not all calculi are equally indicated for such an external therapy. In particular, those calculi which are stuck inside the ureter are in an extremely inconvenient location. In these cases, laser-induced lithotripsy offers the advantage of directly applying energy to the vicinity of the calculus by means of a flexible fiber. First experiments regarding laser lithotripsy have already been performed by Mulvaney and Beck (1968) using a ruby laser. From today's perspective, though, it is quite obvious that these initial studies had to be restricted to basic research, since they were associated with severe thermal side effects. Watson et al. (1983) first proposed the application of a Q-

switched Nd:YAG laser. Shortly after, pulsed dye lasers were investigated by Watson et al. (1987). With the decrease in pulse durations, additional complications arose concerning induced damage of the fiber. Extensive calculations of the limits of fiber transmission were published by Hering (1987). The advantages of different approaches like bare fibers or focusing fiber tips were studied by Dörschel et al. (1987) and Hofmann and Hartung (1987). Furthermore, a review of 20 years of laser lithotripsy experience was given by Dretler (1988).

Today, dye lasers and Nd:YAG lasers are preferably used for lithotripsy of urinary calculi inside the ureter. A detailed description of the procedure was given by Hofstetter et al. (1986). Typically, pulse energies of 50–200 mJ and pulse durations between 10 ns and 1 μ s are applied. The diameter of the optical fiber varies between 200 μ m and 600 μ m. With these parameters, optical breakdown is achieved close to the target. As described in Sect. 3.5, plasma formation at high pulse energies is associated with shock waves, cavitations, and jets. This photodisruptive interaction finally leads to the fragmentation of urinary calculi.

Since the 1980s, research in urology has increasingly focused on various treatments of the prostate. This very sensitive organ embraces the urethra. Diseases of the prostate, e.g. benign hyperplasias or carcinoma, thus often tend to handicap the discharge of urine. A profound analysis of the development of benign prostatic hyperplasia (BPH) was given by Berry et al. (1984). Several conventional therapies are available, e.g. the initial application of phytopharmaka or transurethral resection in severe cases. Other techniques such as cryotherapy or photodynamic therapy have also been investigated, e.g. by Bonney et al. (1982) and Camps et al. (1985). A complete list of potential treatment methods was provided by Mebust (1993). During the first few years, research was restricted to the treatment of prostatic carcinoma. Böwering et al. (1979) were the first to investigate the effect of Nd:YAG laser radiation on tumors of the prostate. Shortly after, several detailed reports followed, e.g. by Sander et al. (1982) and Beisland and Strandén (1984). The latter study pointed out the extreme importance of temperature monitoring of the adjacent rectum. Extensive clinical results were reported by McNicholas et al. (1988). Usually, indication for laser treatment is given only if the tumor cannot be completely resected otherwise.

At the beginning of the 1990s, the demand for minimally invasive techniques significantly increased. In the treatment of BPH, two milestones were achieved with the development of improved surgical techniques called *transurethral ultrasound-guided laser-induced prostatectomy (TULIP)* and *laser-induced interstitial thermotherapy (LITT)*. The idea of TULIP was proposed by Roth and Aretz (1991) and Johnson et al. (1992). Detailed clinical results were published by McCullough et al. (1993). The key element of TULIP is to position a 90° prism inside the urethra by ultrasound control. Thereby, the precision in aiming at the target is strongly enhanced.

In other studies, Siegel et al. (1991) have shown that hyperthermia alone, i.e. temperatures up to 45°C , is not sufficient in treating BPH. This has led to the idea of LITT as already described in Sect. 3.2. During LITT, the tissue is completely coagulated, i.e. temperatures above 60°C are obtained. The technical realization of suitable ITT fibers was discussed by Hessel and Frank (1990). In urology, initial experimental results with LITT were published by McNicholas et al. (1991) and Muschter et al. (1992). With typical laser powers of 1–5 W, coagulation volumes with diameters of up to 40 mm are achieved. Meanwhile, Muschter et al. (1994) have reported on clinical studies with approximately 200 patients. Roggan et al. (1994) have determined the optical parameters of prostatic tissue for diode lasers at 850 nm and Nd:YAG lasers at 1064 nm, respectively. Their data are found in Table 2.3. Moreover, they observed that the scattering coefficient of prostatic tissue increases during coagulation by an approximate factor of two. With these data and appropriate computer simulations, they were able to optimize the parameters for an efficient procedure.

In Fig. 4.49, the most significant postoperative results of LITT in the treatment of BPH are summarized. According to Muschter et al. (1993), the peak urinary flow rate increased from 6.6 ml/s to 15.2 ml/s two months after treatment, whereas the residual urinary volume decreased from 206 ml to 38 ml. The mean weight of the prostate dropped from 63 g to 44 g during the same period. These data are based on mean values obtained from 15 patients. Severe complications were not observed. From these results, it can be concluded that LITT is an excellent therapy for BPH.

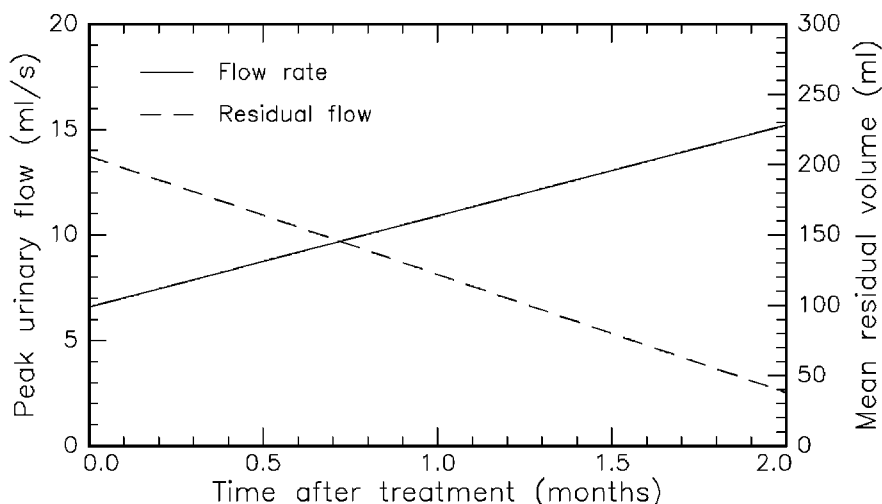


Fig. 4.49. Peak urinary flow and mean residual urinary volume after LITT of benign prostatic hyperplasia. The data represent mean values from 15 patients. Data according to Muschter et al. (1993)

4.5 Lasers in Neurosurgery

Neurosurgery deals with diseases of the central nervous system (CNS), i.e. the brain and the spine. Surgery of brain tumors is very difficult, since extremely localized operations are necessary due to the complicated structure and fragility of the brain. Moreover, the tumor itself is often not easily accessible, and very important vital centers are situated beside it. Therefore, it is not surprising that a considerable amount of research funds is currently being spent in this field, especially since any kind of brain tumor – even benign tumors – are extremely life-threatening. This is because space inside the skull is very limited. Hence, growth of new tissue increases the pressure inside the brain which leads to mechanical damage of other neurons. A schematic cross-section of the brain is shown in Fig. 4.50.

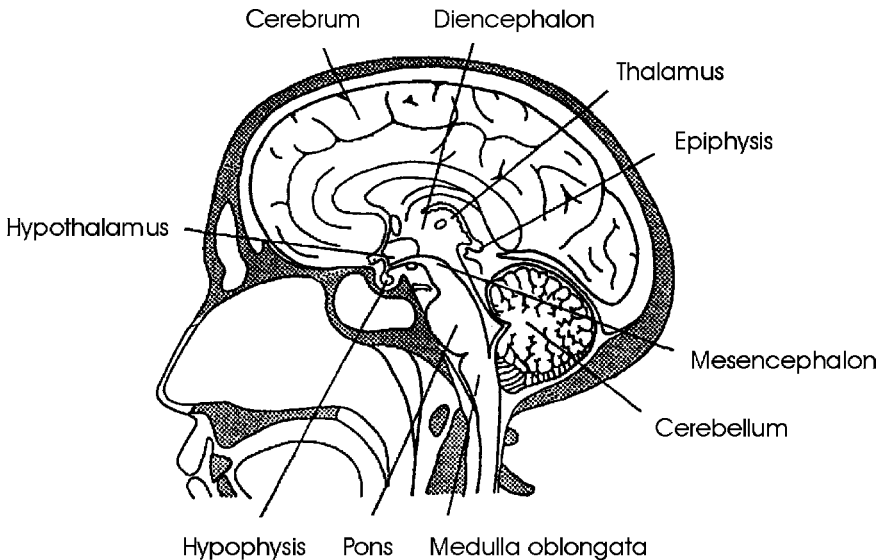


Fig. 4.50. Scheme of a human brain

The major parts of the brain are the cerebrum, diencephalon, cerebellum, and brainstem. The diencephalon can be further divided into the hypothalamus, hypophysis, thalamus, and epiphysis, whereas the brainstem consists of the mesencephalon, pons, and medulla oblongata. Usually, tumors of the brainstem are highly malignant and, unfortunately, they reside in an inaccessible location. In general, brain tissue can be divided into *gray matter* and *white matter* which are made up of cell nuclei and axons, respectively. Blood perfusion of gray and white matter differs remarkably. The corresponding ratio is about five to one.

The application of lasers in neurosurgery has been extremely slow compared with other medical fields, e.g. ophthalmology. This was mainly due to two reasons. First, studies by Rosomoff and Carroll (1966) revealed that the ruby laser was not of great help in neurosurgery. Second, initial experiments with the CO₂ laser were performed at too high energy levels, e.g. by Stellar et al. (1970), which was dangerous and completely unnecessary. It then took some time until Ascher (1979), Beck (1980), and Jain (1983) reawakened interest in neurosurgical lasers, especially moderate CO₂ lasers and Nd:YAG lasers. The principal advantages of lasers in neurosurgery are evident. Lasers are able to cut, vaporize, and coagulate tissue without mechanical contact. This is of great significance when dealing with very sensitive tissues. Simultaneous coagulation of blood vessels eliminates dangerous hemorrhages which are extremely life-threatening when occurring inside the brain. Moreover, the area of operation is sterilized as lasing takes place, thereby reducing the probability of potential infections.

According to Ascher and Heppner (1984) and Stellar (1984), the main advantage of the CO₂ laser is that its radiation at a wavelength of 10.6 μm is strongly absorbed by brain tissue. By this means, very precise cuts can be performed. However, CO₂ lasers are not appropriate for the coagulation of all blood vessels. In particular, arteries and veins with diameters > 0.5 mm tend to bleed after being hit by the laser beam. Nd:YAG lasers, on the other hand, are effective in coagulating blood vessels as stated by Fasano et al. (1982) and Wharen and Anderson (1984b). Ulrich et al. (1986) even observed very good results on both ablation and coagulation when combining a Nd:YAG laser emitting at 1.319 μm and a 200 μm fiber. The biological response of brain tissue to radiation from Nd:YAG lasers was extensively studied by Wharen and Anderson (1984a). A preliminary report on the clinical use of a Nd:YAG laser was given by Ascher et al. (1991). Moreover, neurosurgical applications of argon ion lasers had been investigated by Fasano (1981) and Boggan et al. (1982), but they seem to be rather limited, since radiation from these lasers is strongly scattered inside brain tissue.

The main problem with CW lasers is that they do not remove brain tumors but only coagulate them. Necrotic tissue remains inside the brain and can thus lead to the occurrence of severe edema. Moreover, adjacent healthy tissue might be damaged due to heat diffusion, as well. Recently, two alternative lasers have been investigated concerning their applicability to neurosurgery: Er:YAG and Nd:YLF lasers. Cubeddu et al. (1994) and Fischer et al. (1994) have studied the ablation of brain tissue using free-running and Q-switched Er:YAG lasers. They observed limited thermal alterations of adjacent tissue. However, mechanical damage was very pronounced. Since the Er:YAG laser emits at a wavelength of 2.94 μm, its radiation is strongly absorbed in water as already discussed in Sect. 3.2. Thus, soft brain tissue – having a high water content – is suddenly vaporized which leads to vacuoles inside the tissue with diameters ranging up to a few millimeters. In Fig. 4.51a, mechanical damage

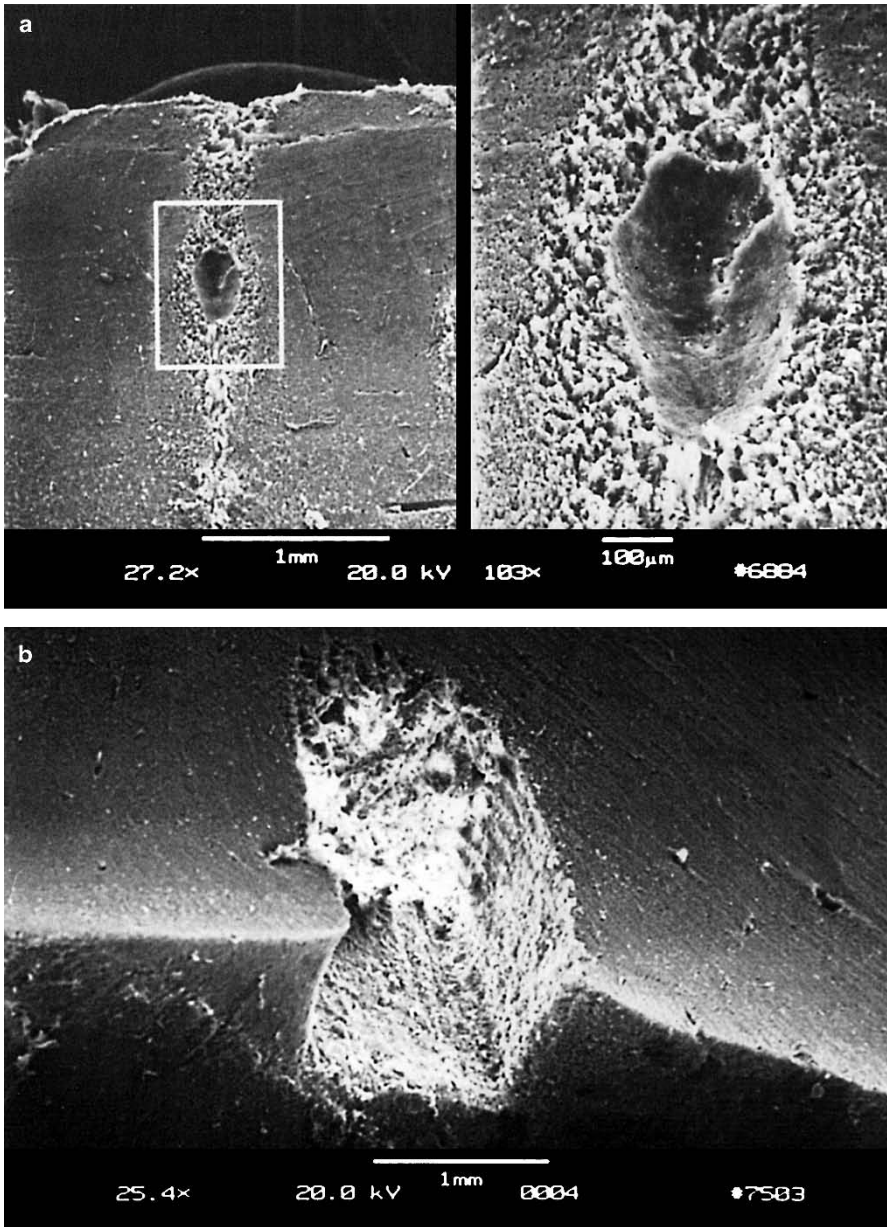


Fig. 4.51. (a) Brain tissue after exposure to an Er:YAG laser (pulse duration: 90 μ s, pulse energy: 60 mJ). Mechanical damage is evident. (b) Voluminous ablation of brain tissue achieved with the same laser. Reproduced from Fischer et al. (1994) by permission. © 1994 Springer-Verlag

up to a depth of at least 1.5 mm is clearly visible. Therefore, it is not very helpful that even large volumes of brain tissue can be ablated with Er:YAG lasers as shown in Fig. 4.51b.

The ablation of brain tissue with a picosecond Nd:YLF laser system was investigated by Fischer et al. (1994). In Fig. 4.52, the ablation depths of white and gray brain matter are given, respectively. Obviously, there is no significant difference in ablating either substance. It is interesting to observe, though, that there is no saturation in ablation depth even at energy densities as high as 125 J/cm^2 . Thus, higher laser powers will probably enable ablation depths $> 200 \mu\text{m}$. Fischer et al. (1994) state that the corresponding ablation threshold is at approximately 20 J/cm^2 .

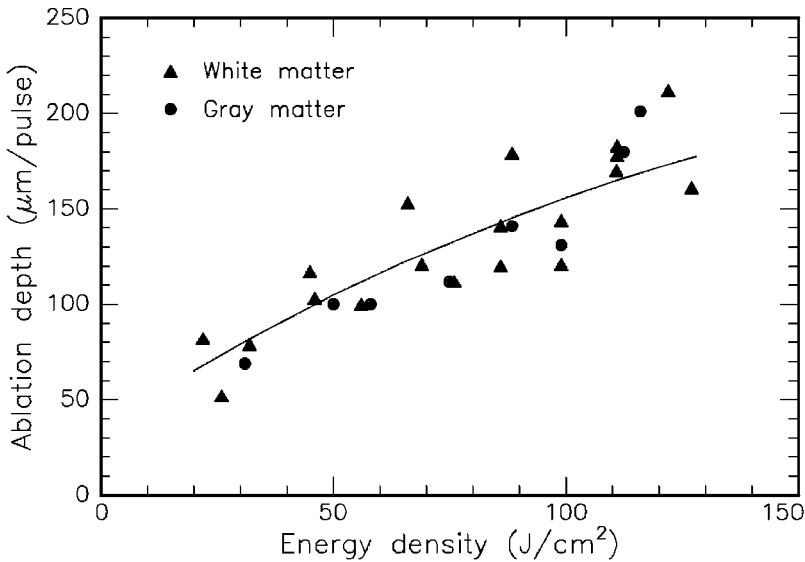


Fig. 4.52. Ablation curve of white and gray brain matter obtained with a Nd:YLF laser (pulse duration: 30 ps, focal spot size: $30 \mu\text{m}$). Data according to Fischer et al. (1994)

Two samples of brain tissue which were exposed to the Nd:YLF laser are shown in Figs. 4.53a–b. A rectangular ablation geometry was achieved by scanning the laser beam. The lesion in Fig. 4.53a is characterized by steep walls and is approximately $600 \mu\text{m}$ deep. In Fig. 4.53b, a histologic section of an ablation edge is shown as obtained with the Nd:YLF laser. The tissue was stained with cluever barrera to visualize any thermal effects. There is no evidence of either thermal or mechanical damage to adjacent tissue. Hence, removal of tissue can be attributed to the process of plasma-induced ablation as described in Sect. 3.4. Nonthermal ablation of tissue is a mandatory requirement for precise functional surgery of the brain.

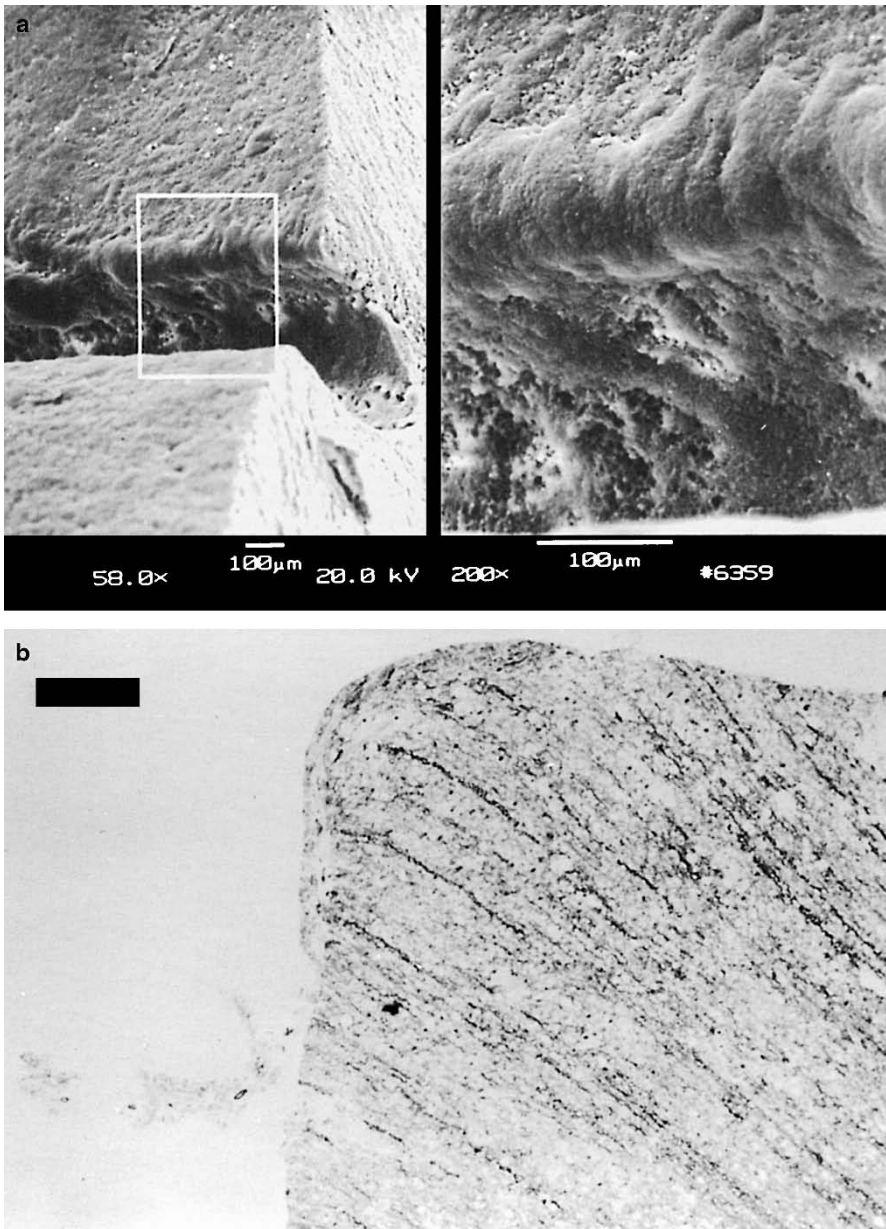


Fig. 4.53. (a) Brain tissue after exposure to a picosecond Nd:YLF laser (pulse duration: 30 ps, pulse energy: 0.5 mJ). (b) Histologic section of brain tissue after exposure to the same laser (bar: 50 µm). Reproduced from Fischer et al. (1994) by permission. © 1994 Springer-Verlag

A very precise technique is called *stereotactic neurosurgery* which was described in detail by Kelly et al. (1982). It requires a so-called stereotactic head ring made of steel or carbon fibers which is tightly fastened to the patient's skull by several screws. This ring defines a coordinate system which serves as a valuable means of orientation during surgery. The head ring appears on CT or magnetic resonance images (MRI) and thus determines the coordinates of the tumor. Various kinds of aiming devices can be mounted to the ring allowing for precise operation in all three dimensions. The main goal of stereotactic neurosurgery is to plan a suitable penetration channel in advance of surgery, set its coordinates with respect to the head ring, and then keep this channel during surgery. By this procedure, the risk of hitting a vital center within the brain can be significantly reduced, and the success of a treatment becomes more predictable.

The concept of stereotactic laser-neurosurgery according to Bille et al. (1993) is illustrated in Fig. 4.54. By means of a stereotactic head ring, a laser probe is inserted into the brain. CT and NMR data are used to correctly position the distal end of the probe inside the tumor. A schematic drawing of the laser probe is given in Fig. 4.55. It basically consists of a conical tube which contains a rotating mirror at its distal end, a movable focusing lens, and additional channels for aspiration and rinsing. Aspiration is necessary to maintain a constant pressure at the site of operation. The laser probe is rinsed to remove debris from the rotating mirror and to increase the efficiency of the ablation process. The rotating mirror deflects the laser beam perpendicularly to the axis of rotation. Tissue is thus ablated in cylindrical layers as shown in Fig. 4.55. Furthermore, it is planned to integrate a confocal laser scanning microscope into this system for the automatic detection of blood vessels as illustrated in Fig. 4.56.

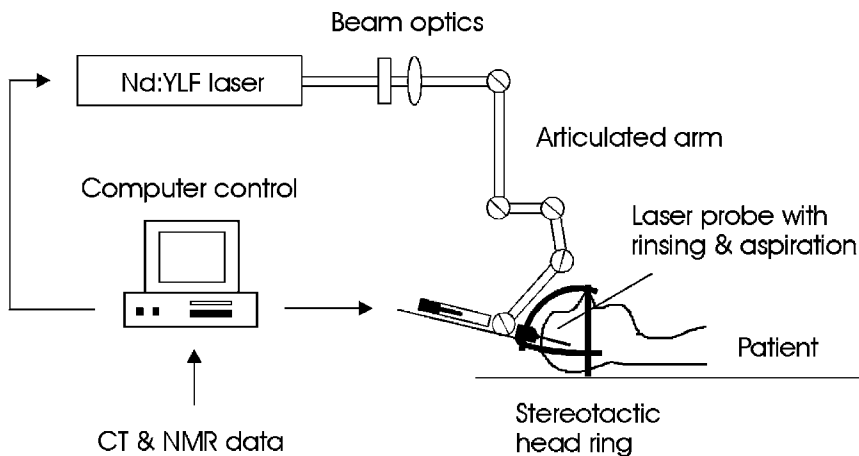


Fig. 4.54. Concept of stereotactic laser-neurosurgery

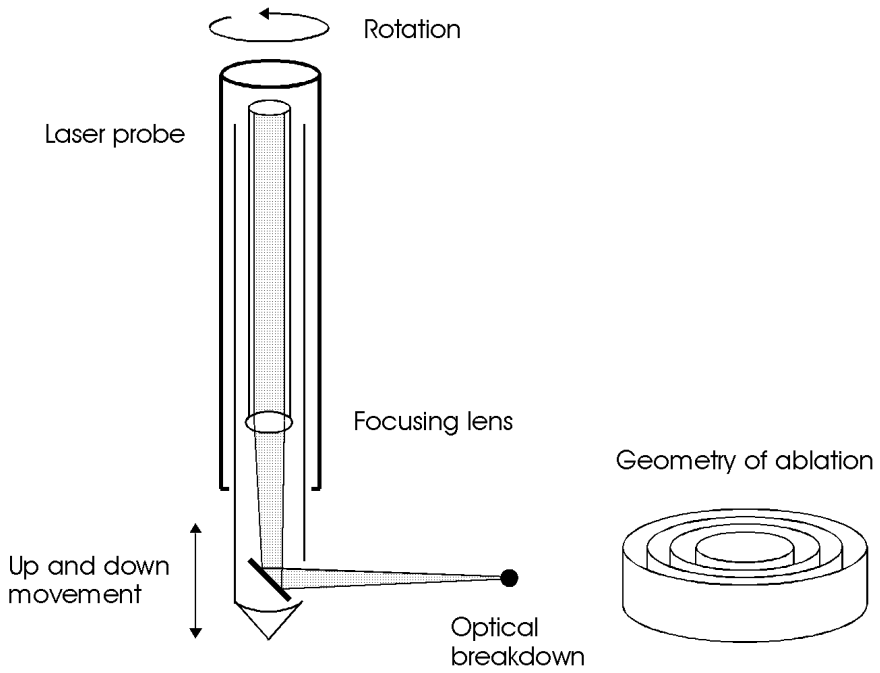


Fig. 4.55. Schematic drawing of laser probe

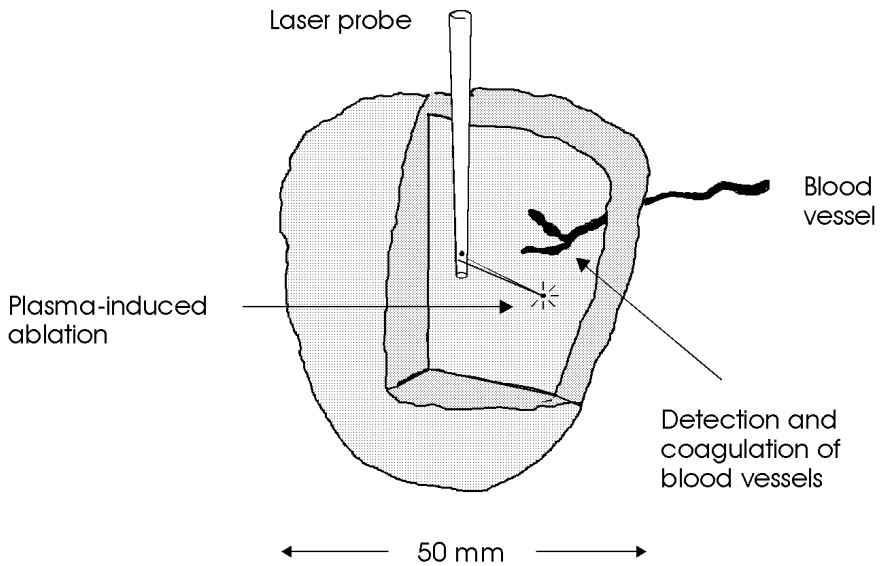


Fig. 4.56. Topology of tumor ablation

It should be mentioned that stereotactic neurosurgery is already a well-established clinical discipline. Stereotactic techniques are not only applied in combination with lasers but with alternative therapies, e.g. insertion of radioactive seeds (^{60}Co or ^{125}I) and high-frequency coagulation, as well. In general, any of these procedures alone might not lead to a complete necrosis of all tumor cells. In these cases, however, the stereotactic concept provides a useful combination of several treatment techniques by simply exchanging the surgical equipment mounted to the head ring of the patient. The principal advantages of stereotactic surgery, of course, are its high precision – within tenths of a millimeter – in aiming at the tumor and the ability to manage surgery with a tiny hole in the skull of less than 1 cm in diameter⁸. Stereotactic surgery thus certainly belongs to the favored treatments of minimally invasive surgery (MIS).

An exciting technique of sutureless microvascular anastomosis using the Nd:YAG laser was developed by Jain (1980). It is performed in some cases of cerebrovascular occlusive disease. During anastomosis, a branch of the superficial temporal artery is connected to a cortical branch of the middle cerebral artery. Typical laser parameters are powers of 18 W, focal spot sizes of 0.3 mm, and single exposure durations of 0.1 s. This method is considerably faster than conventional suture techniques, it does not induce damage to the endothelium of the vessel, and it can be performed on relatively small and/or deeply located blood vessels, as well. The mechanism of vessel welding is not completely understood but is believed to rely on heat-induced alterations in collagen of the vessel. First clinical results had already been reported by Jain (1984a), but a high rate of associated complications soon slowed down the initial euphoria. Later, Neblett et al. (1986) and Ulrich et al. (1988) combined the application of a Nd:YAG laser with conventional techniques of anastomosis, and they achieved more promising results. In blood vessels with diameters of 0.8–1.2 mm, neither short-term nor long-term complications occurred.

Spinal surgery is the other principal field of neurosurgical treatments. According to Jain (1984b), the CO_2 laser has proven to be useful in treating tumors of the spinal cord. Such tumors can be coagulated without severe complications. Ascher and Heppner (1984) have reported on the successful dissection of intramedullary gliomas of the spinal cord with a pulsed CO_2 laser. Moreover, some basic procedures concerning pain relief of the spinal cord can be performed with this laser. Spinal laser surgery is still in its infancy, and considerable progress is expected within the next few years when miniaturized surgical instruments become available, e.g. in the technique of laser-assisted nerve repair as already proposed by Bailes et al. (1989). The combination of highly sophisticated endoscopes and appropriate laser systems might then turn into a powerful joint venture.

⁸ Conventional craniotomies usually require openings in the skull of at least 5 cm in diameter.

4.6 Lasers in Angioplasty and Cardiology

Angioplasty is concerned with the treatment of blood vessels which are narrowed by atherosclerosis⁹. The obstructions stem from the formation of an anorganic plaque inside the vessels which reduces or even completely suppresses the blood flow. The degree of a so-called *stenosis* is determined by

$$\% \text{ stenosis} = 100 \frac{\text{intimal area}}{\text{intimal area} + \text{lumen area}},$$

where the areas are obtained from a cross-sectional view of the vessel, the intima is the interior wall of the vessel, and the lumen is the space available for blood flow.

The promotion factors of plaques are not completely understood. The formation of a plaque might be favored at sites of a local vessel injury where cells capable of repairing the vessel wall tend to gather. If some of the secreted products of these cells are not carried away, a plaque is formed. After the cells have died, primarily anorganic concretions with a high content of calcium are left behind.

The non-surgical treatment of atherosclerosis was introduced by Dotter and Judkins (1964) when performing angioplasty of femoral arterial stenoses with a specially designed dilatation catheter. In the 1970s, Grüntzig (1978) and Grüntzig et al. (1979) modified this technique to enable its application in coronary arteries, i.e. the blood vessels supplying the heart itself. Atherosclerotic plaques inside these vessels are extremely life-threatening, since their obstruction necessarily induces myocardial infarction. *Percutaneous transluminal coronary angioplasty (PTCA)* has since been used in many patients with angina or acute myocardial infarction, and a large variety of balloon catheters is available today. In general, the method of PTCA has been widely accepted, and several reviews have already been published, e.g. by Grüntzig and Meier (1983) and Landau et al. (1994).

The main mechanisms by which PTCA increases the size of the vessel lumen are cracking, splitting, and disruption of the atherosclerotic plaque. Resorption of plaque material is also initiated by simply pushing it into the vessel wall. All these effects are evoked by inflation of a balloon placed inside the blood vessel. According to Waller (1983), balloon inflation may be deleterious, however, causing plaque hemorrhage, extensive dissection of the vessel wall, and thrombus formation. Therefore, the treatment needs to be performed extremely carefully and by X-ray control. Aspirin and heparin are usually administered to reduce the incidence of thrombosis.

Although PTCA is generally safe, some short-term and long-term complications do occur. Among the first, arterial dissection and intracoronary thrombosis are most severe. On the other hand, a recurrence of the original stenosis may take place even months after the treatment. This process of

⁹ The term *arteriosclerosis* applies in arteries only.

so-called *restenosis* has been extensively studied by Lange et al. (1993) who also considered it as the “Achilles’ heel” of coronary angioplasty. Serruys et al. (1988) reported on the occurrence of restenoses in 30% of patients treated with PTCA. Restenoses are believed to be initiated by accidental injury of the vessel wall, resulting in the subsequent release of thrombogenic, vasoactive, and mitogenic factors. Endothelial damage, in particular, leads to the activation of macrophages and smooth muscle cells as stated by Austin et al. (1985). Thereby, growth factors are released which in turn may promote their own synthesis. Thus, a self-perpetuating process is initiated which is associated with a thickening of the intima, i.e. the interior part of the vessel wall. Finally, the vessel is obstructed again. Since the occurrence of these restenoses is not predictable, extensive follow-up studies are usually performed. According to Hombach et al. (1995), there is a slight decrease in the probability of restenoses when implanting specially designed mechanical stents inside the vessel wall immediately after balloon dilatation.

Beside PTCA, other surgical treatments are available in cases of coronary arteriosclerosis. These are *bypass surgery*, *atherectomy*, and *high-frequency rotational coronary angioplasty (HFRCA)*. Among these, only bypass surgery is performed during complete anesthetization. It is a very complicated type of surgery, since the chest must be opened and the heart beat is interrupted. Atherectomy is a more rigorous version of PTCA, where the plaque is additionally planed away by means of mechanical abrasion. Finally, in HFRCA, a miniaturized mechanical drill called a rotablator is used for vessel recanalization as described by Tierstein et al. (1991).

First experiments regarding laser angioplasty were performed by Macruz et al. (1980), Lee et al. (1981), Abela et al. (1982), and Choy et al. (1982). While these in vitro studies left no doubt that laser light could ablate atherosclerotic plaque, it was quite uncertain whether such a treatment could be transferred to in vivo surgery. Choy et al. (1984) and Ginsburg et al. (1985) were the first to try clinical laser angioplasties. Laser light was applied to the plaque by means of optical fibers. However, only thermally acting lasers – i.e. argon ion, CO₂, and Nd:YAG lasers – were investigated at that time which induced severe thermal injuries such as extensive coagulation, necrosis of vascular tissue, and perforation of the vessel wall. In addition, mechanical perforations often occurred due to the bare distal end of the optical fibers. All these complications turned out to be extremely critical when applying laser angioplasty to coronary arteries as initially suggested by Selzer et al. (1985) and Sanborn et al. (1986).

It was Hussein (1986) who developed a novel tip design, the so-called *hot tip*. It consists of a simple metal cap which completely encloses the distal end of the fiber, thereby converting all laser energy to heat by means of absorption. Instead of using a tightly focused laser beam, plaques are removed by homogeneously distributed heat as shown in Fig. 4.57. Usually, CW argon ion lasers and Nd:YAG lasers are applied, although any kind of laser radiation

could be used which is absorbed by the metal cap. Detailed measurements of the temperature distribution associated with various parameters were performed by Labs et al. (1987). According to Cumberland et al. (1986), the concept of using a hot tip diminishes the incidence of thermal perforations to a degree that makes it acceptable for many cases of peripheral angioplasty. However, the method of thermal angioplasty has led to considerable controversy, as well. Other groups, e.g. Diethrich et al. (1988), observed the occurrence of so-called vasospasm – i.e. thermally induced shrinkage of the vessel wall – when using a hot tip applicator. In general, these vasospasms are not predictable, and they can induce severe secondary obstructions.

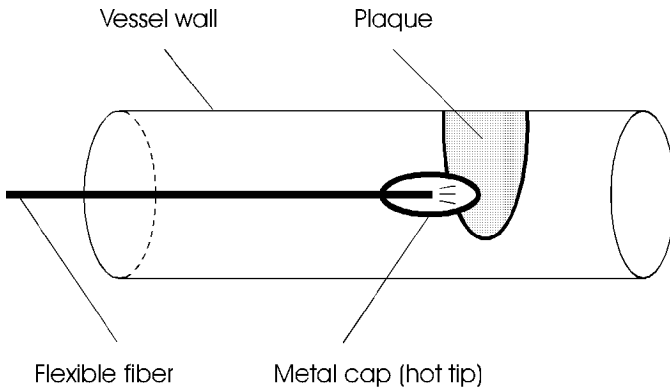


Fig. 4.57. Scheme of a laser-driven hot tip for vessel recanalization

The common denominator of the above concerns is that laser-induced thermal injury is a virtually unavoidable by-product of CW lasers. Basic improvement could not be achieved until moving from one laser-tissue interaction to another. As discussed in Sect. 3.2, only pulsed lasers with pulse durations shorter than $1\ \mu\text{s}$ provide nonthermal ablation.

Grundfest et al. (1985) first demonstrated that pulsed XeCl excimer lasers are capable of performing efficient plaque ablations with only minimal thermal injury of adjacent tissue. These studies were done shortly after the description of the photoablative interaction mechanism by Srinivasan and Mayne-Banton (1982). Thus, it was straightforward that researchers also focused on other applications for excimer laser radiation. Unfortunately, though, an unpredictable type of complication occurred as discussed below which soon slowed down initial enthusiasm. Karsch et al. (1989) were the first to report on clinical results of percutaneous coronary excimer laser angioplasty. In this study, thirty patients were treated with a 1.3 mm laser catheter consisting of twenty $100\ \mu\text{m}$ quartz fibers. These fibers were located concentrically around a 0.35 mm thick flexible guide wire as shown in Fig. 4.58.

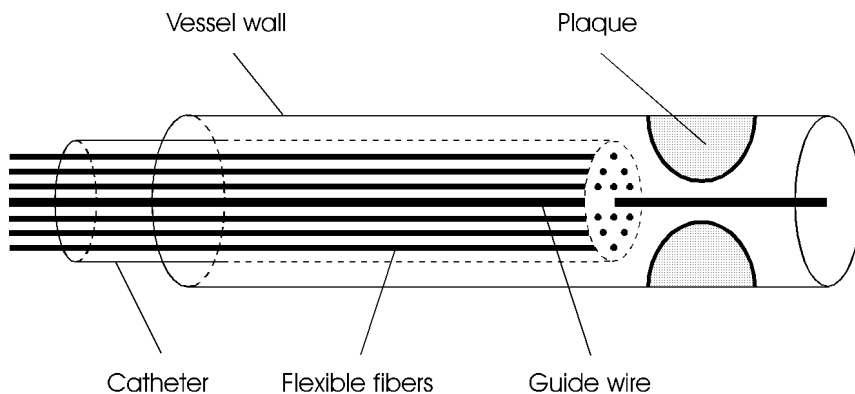


Fig. 4.58. Scheme of laser angioplasty for vessel recanalization

After moving the guide wire into the coronary artery, the catheter was guided into the correct position. The fibers were coupled to a XeCl excimer laser emitting at a wavelength of 308 nm and pulse durations of 60 ns. Typical energy densities of up to 5 J/cm^2 were applied. The mean percentage of stenosis fell from 85 % initially to 41 % immediately after laser treatment, and the primary success rate was as high as 90 %. In twenty patients, subsequent balloon dilatation was additionally performed. Perforations of the vessel wall did not occur in any of the patients. However, it was only shortly after when Karsch et al. (1991) published a second report admitting that one patient suddenly died two months after laser treatment. Postmortem histologic examination proved that a severe restenosis had occurred which had led to an acute myocardial infarction.

In Figs. 4.59a–b, two photographs are shown demonstrating the removal of atherosclerotic plaque with a XeCl excimer laser. For this ablation, Hanke et al. (1991) have applied pulse durations of 60 ns at a repetition rate of 20 Hz. An enlargement of the plaque itself is captured in Fig. 4.59a. On the right half of the picture shown in Fig. 4.59b, parts of the plaque have already been removed without injuring the vessel wall.

Today, it is well accepted that restenoses are extremely pronounced following excimer laser angioplasty. Their occurrence can be attributed to an enhanced proliferation of smooth muscle cells as has been demonstrated by Hanke et al. (1991). Most of these cells undergo DNA synthesis during two weeks after laser treatment, resulting in intimal thickening within the first four weeks. Obviously, the mechanism of photoablation is more stimulating than only mechanical cracking or abrasion. Thus, even though photoablation is a rather gentle technique for removing plaques, its long-term effects forbid its use for the purpose of vessel recanalization. Therefore, excimer laser angioplasty is generally being rejected today, and it is rather doubtful whether it will ever gain clinical relevance.

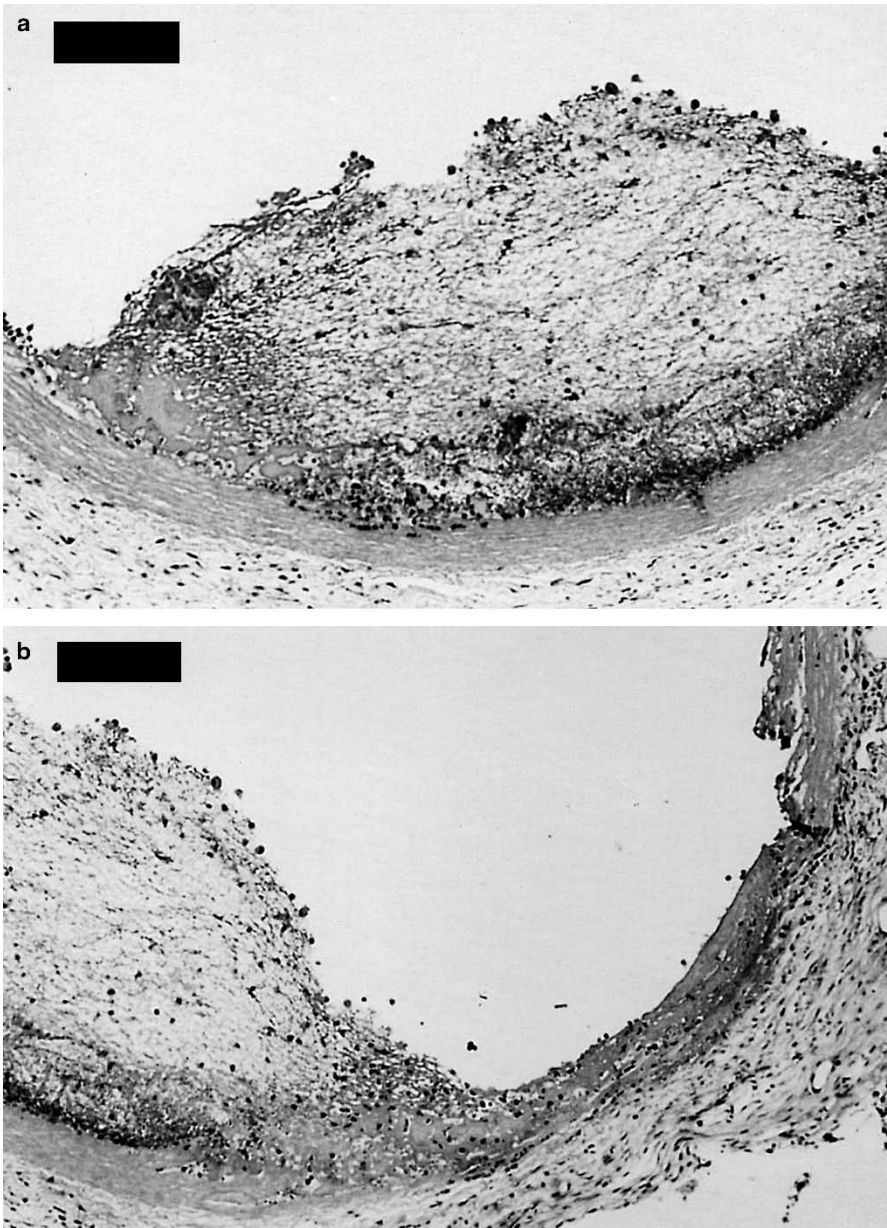


Fig. 4.59. (a) Histologic section of atherosclerotic plaque inside a blood vessel (bar: 150 μm). The vessel wall is located at the *bottom* of the picture. (b) Ablation of atherosclerotic plaque with a XeCl excimer laser (pulse duration: 60 ns, repetition rate: 20 Hz, bar: 150 μm , plaque: *left*, ablation: *right*). Photographs kindly provided by Dr. Hanke (Tübingen)

Meanwhile, other laser types have also been investigated concerning their application in angioplasty and cardiology. One of them is the Ho:YAG laser which has been studied in detail by Hassenstein et al. (1992). However, an extensive increase in intimal thickening was observed within the first six weeks after laser treatment. And, again, the proliferation of smooth muscle cells seems to be responsible for this effect. Thus, the clinical use of holmium laser angioplasty appears to be extremely limited.

More promising are CO₂ laser systems which can be used to create additional channels for the blood supply of the heart. These channels originate from the epicardium, i.e. the periphery of the heart, and remain open after laser treatment. This technique is called *transmyocardial laser revascularization (TMLR)* and was initially proposed by Mirohseini et al. (1982). Shortly after, first clinical experiences were reported by Mirohseini et al. (1986). Yano et al. (1993) have confirmed the effect of revascularization. Other investigators, though, could not verify their results, e.g. Whittaker et al. (1993). Recently, Horvath et al. (1995) were able to judge treatment effects by measuring the local contractility of the heart muscle. They concluded that acute infarcts treated by TMLR show improved contractility both in the short- and long-term. Moreover, they observed diminished areas of necrosis. However, further studies regarding blood flow and recovery need to be performed prior to the general acceptance of TMLR.

Even if therapeutic laser treatments of blood vessels should never become a safe procedure, laser diagnostics will always play a significant role in angioplasty and cardiology. Apart from X-ray and ultrasound angiography, Doppler angiography and laser endoscopy are very sensitive techniques. A typical example of a laser endoscope is shown in Fig. 4.60. Visible laser radiation is emitted from the distal end of a flexible fiber and illuminates the area of interest. Modern engineering science has meanwhile enabled the design of extremely miniaturized and highly sophisticated laser endoscopes.

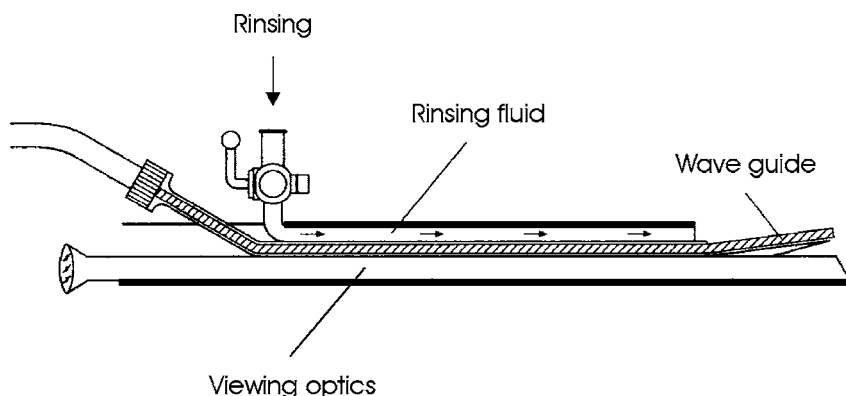


Fig. 4.60. Scheme of laser endoscope for angioplasty

4.7 Lasers in Dermatology

In dermatology, thermal effects of laser radiation are commonly used, especially coagulation and vaporization. Since the optical parameters of skin, i.e. absorption and scattering, are strongly wavelength-dependent, various kinds of tissue reaction can be evoked by different laser systems. In clinical practice, mainly five types of lasers are currently being used: argon ion lasers, dye lasers, CO₂ lasers, Nd:YAG lasers, and ruby lasers.

A schematic cross-section of the human skin is given in Fig. 4.61. The skin grossly consists of three layers: *epidermis*, *dermis*, and *subcutis*. The outer two layers – epidermis and dermis – together form the *cutis*. The epidermis contains so-called keratocytes and melanocytes which produce keratin and melanin, respectively. Both keratin and melanin are important protective proteins of the skin. Most of the dermis is a semi-solid mixture of collagen fibers, water, and a highly viscous gel called ground substance. The complex nature of the skin creates a remarkable tissue with a very high tensile strength which can resist external compression but remains pliable at the same time. Blood vessels, nerves, and receptors are primarily located within the subcutis and the dermis.

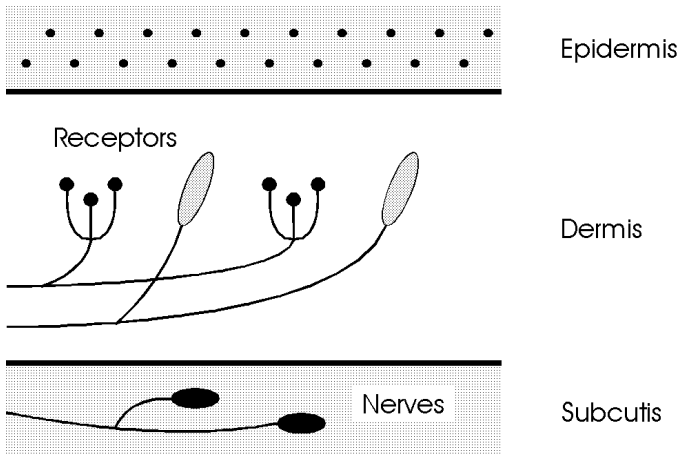


Fig. 4.61. Cross-section of human skin

On a microscopic scale, the air–skin interface is quite rough and therefore scatters incident radiation. Absorption of light by chromophores such as hemoglobin or melanin give skin its unique color. Optical scattering by collagen fibers in the ground substance largely determines which fraction of incident light penetrates into connective tissues. Detailed studies regarding the optical parameters of skin were performed by Graaff et al. (1993b).

Radiation from the argon ion laser is strongly absorbed by hemoglobin and melanin as already illustrated in Fig. 2.4. This laser is thus predestined for superficial treatments of highly vascularized skin. Apfelberg et al. (1978) and Apfelberg et al. (1979a) investigated laser-induced effects on various abnormalities of the skin. The most frequent indications for the application of argon ion lasers are given by port wine stains (*naevi flammei*). Earlier methods of treating these malformations – e.g. cryotherapy, X-ray, or chemical treatment – had failed, and patients were advised to accept their misery. The idea of removing port wine stains with argon ion lasers has led to the most significant progress of lasers in dermatology so far. The treatment itself requires a lot of patience, since several sessions are necessary over a period of up to a few years. The faster the treatment is to come to an end, the higher is the probability for the occurrence of scarring. However, “patient” patients are usually rewarded with an acceptable outcome. In Figs. 4.62a–b, two photographs of the pre- and postoperative states of a laser-treated port wine stain are shown.

Treatment of port wine stains with argon ion lasers is usually performed in several sessions. First, a small test area of approximately 4 mm^2 is irradiated. During this test, a suitable laser power is determined by gradually increasing it until the skin visibly pales. According to Dixon and Gilbertson (1986) and Philipp et al. (1992), laser powers of 2–5 W are applied during an exposure time of 0.02–0.1s. Immediately after laser exposure, inflammation of the skin frequently occurs. After four weeks, the test area is checked for recanalization and scarring. And after another four weeks, a second test area is treated. If both tests lead to acceptable results, the whole stain is exposed. Multiple exposures of the same area should be avoided in any case. Laser treatment may be repeated after a few years, but it is advisable to choose pulsed dye lasers for the second time. Haina et al. (1988) did not recommend treatment of patients up to 16 years of age, since otherwise severe scarring might occur. Laser radiation is usually applied by means of a flexible handpiece. In the treatment of facial stains, the eyes of both patient and surgeon must be properly protected. One disadvantage of treating port wine stains with argon ion lasers is that it is rather painful to the patient. Depending on the location and spatial extent of the stain, treatment is performed during either local or complete anesthetization.

Less painful and probably even more efficient is the treatment of port wine stains with dye lasers. Although quite expensive, these machines have recently gained increasing significance in dermatology, especially in the treatment of port wine stains and capillary hemangiomas. Detailed studies were reported by Morelli et al. (1986), Garden et al. (1988), and Tan et al. (1989). Frequently, Rhodamine dye lasers are used which emit radiation at wavelengths in the range 570–590 nm. Typical pulse durations of 0.5 ms and energy densities of $4\text{--}10\text{ J/cm}^2$ have been recommended. About 20–60s after laser exposure, the color of the treated skin turns red, and after another few



Fig. 4.62. (a) Preoperative state of a port wine stain. (b) Postoperative state of the same stain after several treatments with an argon ion laser (pulse duration: 0.3 s, power: 2.5 W, focal spot size: 2 mm). Photographs kindly provided by Dr. Seipp (Darmstadt)

minutes livid blue. Although pain is less pronounced as with argon ion lasers, patients frequently talk of triple pain perception: mechanical impact during the light flash, stabbing pain shortly afterwards, and finally a longer lasting heat wave within the skin. The irradiated area itself might be irritating for several days. One major advantage of treating port wine stains with dye lasers is that this procedure can be successfully performed among children as reported by Tan et al. (1989).

The basic mechanism by which pulsed laser radiation can cause selective damage to pigmented structures in vivo has been termed *selective photothermolysis* and was thoroughly described by Anderson and Parrish (1983). It requires the presence of highly absorbing particles, e.g. pigments of the skin. Extensive experimental and theoretical studies were recently performed by Kimel et al. (1994) and van Gemert et al. (1995). With their results, treatment of port wine stains will be further improved in the near future.

In dermatology, the CO₂ laser is used for tissue vaporization. Compared to the conventional scalpel, it offers the possibility of precise tissue removal without touching the tissue. Thus, feeling of pain is significantly reduced. External ulcers and refractory warts are common indications. In warts, however, deep lesions should be performed to reduce the probability of recurrence.

Recently, argon ion and CO₂ lasers have also gained attention in efficiently removing tattoos. Clinical studies were reported by Apfelberg et al. (1979b) and Reid and Muller (1980). Today, ruby lasers are commonly used for tattoo removal as stated by Scheibner et al. (1990) and Taylor et al. (1990). Indeed, good results can be obtained, although they do depend on the dyes used in the tattoo. It is extremely important that all dye particles are removed during the same session. In Figs. 4.63a–b, two photographs are shown which prove the efficiency of laser-induced tattoo removal.

Radiation from the Nd:YAG laser is significantly less scattered and absorbed in skin than radiation from the argon ion laser. The optical penetration depth of Nd:YAG laser radiation is thus much larger. According to Seipp et al. (1989), major indications for Nd:YAG laser treatments in dermatology are given by deeply located hemangiomas or semimalignant skin tumors. However, argon ion and CO₂ lasers should never be replaced by Nd:YAG lasers when treating skin surfaces.

Dermatology is one of the few medical disciplines where biostimulative effects of laser radiation have been reported. Positive stimulation on wound healing is one of the current topics of controversy as discussed in Sect. 3.1. A considerable number of papers has been published, but most of the results could not be reproduced, and initial claims could thus not be verified. Moreover, the principal mechanisms of biostimulation have not yet been understood. In general, one should be very careful when using laser radiation for such purposes, especially when applying so-called “soft lasers” with extremely low output powers which most probably do not evoke any effect at all other than additional expenses according to Alora and Anderson (2000).



Fig. 4.63. (a) Preoperative state of a tattoo. (b) Postoperative state of the same tattoo after six complete treatments with an argon ion laser (pulse duration: 0.3 s, power: 3 W, focal spot size: 0.5 mm). Photographs kindly provided by Dr. Seipp (Darmstadt)

4.8 Lasers in Orthopedics

Progress in surgical medicine is often related to an improved technique of performing *osteotomies*, i.e. bone excisions. Standard tools in orthopedics are saws, milling-machines and mechanical drills. All of them operate in contact mode and possibly induce severe mechanical vibrations and hemorrhage. It is thus straightforward to ask whether lasers might represent a considerable alternative in orthopedic surgery.

Bone fulfills three major functions: mechanical support of the body, protection of soft tissues, and supply of minerals and blood cells. The hardness of bone results from a complex structure of hydroxyapatite, water, soluble agents, collagen, and proteins. The chemical composition of bone is listed in Table 4.5. The high water content is responsible for strong absorption of infrared radiation. Therefore, CO₂, Er:YAG, and Ho:YAG lasers are predestined for the efficient treatment of bone.

Table 4.5. Mean composition of human bone

Matter	Percentage	Constituent
Anorganic	50–60 %	Hydroxyapatite
	15–20 %	Water
	5 %	Carbonates
	1 %	Phosphates
Organic	20 %	Collagen
	1–2 %	Proteins

In the 1970s, Moore (1973), Verschueren and Oldhoff (1975), and Clayman et al. (1978) reported on osteotomies performed with CO₂ lasers. Extensive studies on bone healing were published by Gertzbein et al. (1981) and Pao-Chang et al. (1981). All researchers agreed on a delayed healing process compared with conventional osteotomies. Thermal damage of the bone rim is exclusively made responsible for this time delay. Detailed data on the ablation characteristics were given by Kaplan and Giler (1984) and Forrer et al. (1993). The ablation curves of fresh and dried bone obtained with the CO₂ laser are illustrated in Fig. 4.64a. From the above, we could conclude that CO₂ lasers always evoke severe thermal side effects in bone. This statement, however, is not generally true. Forrer et al. (1993) have also demonstrated the potential of CO₂ lasers for bone ablation with very little thermal damage. When selecting the laser transition at 9.6 μm, a pulse duration of 1.8 μs, and an energy density of 15 J/cm², they found thermally altered damage zones of 10–15 μm only. In this case, both wavelength and pulse duration play a significant role. First, the absorbance of bone at 9.6 μm is higher than at 10.6 μm. Second, shorter pulse durations tend to be associated with less thermal damage as already discussed in Sect. 3.2.

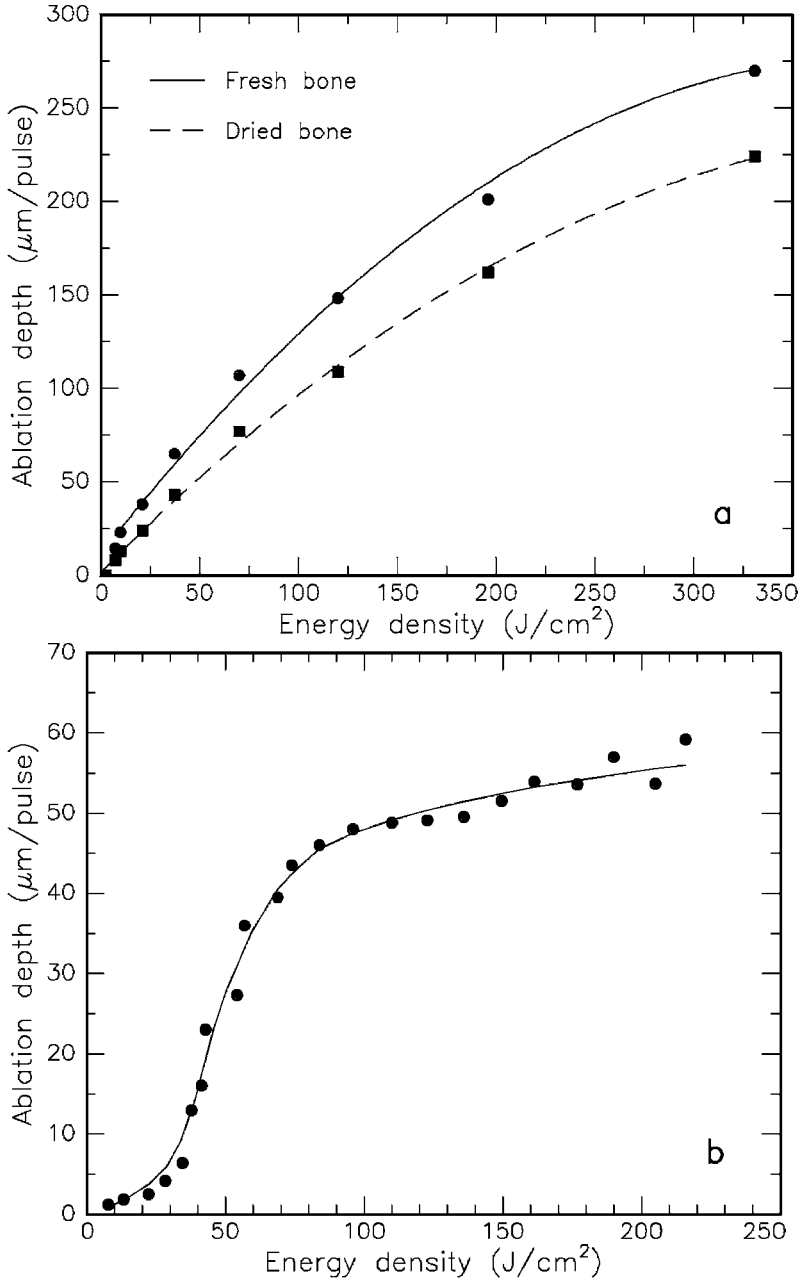


Fig. 4.64. (a) Ablation curves of fresh and dried bone obtained with a CO₂ laser (pulse duration: 250 μs , wavelength: 10.6 μm). Due to its higher water content, fresh bone is ablated more efficiently. Data according to Forrer et al. (1993). (b) Ablation curve of bone obtained with an Er:YAG laser (pulse duration: 180 μs , wavelength: 2.94 μm). Data according to Scholz and Grothves-Spork (1992)

In the 1980s, research focused on laser radiation at a wavelength of approximately $3\ \mu\text{m}$ which is strongly absorbed by water. For instance, Wolbarsht (1984) compared the effects induced by CO_2 lasers at $10.6\ \mu\text{m}$ and HF^* lasers¹⁰ at $2.9\ \mu\text{m}$ with each other. From his observations, he concluded that the latter wavelength is better suited for orthopedic applications. Similar results were published by Izatt et al. (1990). Unfortunately, though, HF^* lasers are very unwieldy machines. Walsh and Deutsch (1989), Nelson et al. (1989a), and Gonzales et al. (1990) reported on the application of compact Er:YAG lasers at a wavelength of $2.94\ \mu\text{m}$. They stated that this radiation efficiently ablates both bone and cartilage. The ablation curve of bone obtained with the Er:YAG laser is illustrated in Fig. 4.64b.

Another promising laser in orthopedics is the Ho:YAG laser which emits at a wavelength of $2.12\ \mu\text{m}$. Nuss et al. (1988), Charlton et al. (1990), and Stein et al. (1990) have investigated acute as well as chronic effects of bone ablation with this laser. Its major advantage is that its radiation can be efficiently transmitted through flexible fibers. However, thermal effects are significantly enhanced compared to those induced by Er:YAG lasers at a wavelength of $2.94\ \mu\text{m}$ as observed by Romano et al. (1994). They found that thermal damage is extremely pronounced when applying $250\ \mu\text{s}$ pulses from a Ho:YAG laser. At an incident energy density of $120\ \text{J}/\text{cm}^2$, a thermal damage zone of roughly $300\ \mu\text{m}$ is determined. On the other hand, pulses from an Er:YAG laser are associated with very little thermal damage. At an energy density of $35\ \text{J}/\text{cm}^2$, a damage zone of only $12\ \mu\text{m}$ is estimated. The corresponding histologic sections are shown in Fig. 4.65a–b. In the case of the Er:YAG laser, a lower energy density was chosen to obtain a similar ablation depth as with the Ho:YAG laser. One potential application field of erbium lasers is microsurgery of the stapes footplate in the inner ear. This treatment belongs to the discipline of otorhinolaryngology, and it will therefore be addressed in Sect. 4.10.

Due to their high precision in removing tissues, excimer lasers have also been proposed for the ablation of bone material, e.g. by Yow et al. (1989). However, it was soon observed that their efficiency is much too low to justify their clinical application. Moreover, osteotomies performed with XeCl lasers at $308\ \text{nm}$ are associated with severe thermal damage as reported by Nelson et al. (1989b). As in the case of CO_2 laser radiation, these thermal effects are believed to be responsible for the manifest delay in healing of the laser-induced bone excisions.

An interesting approach to determine laser effects on bone has recently been reported by Barton et al. (1995) and Christ et al. (1995). By using a confocal laser scanning microscope, they were able to analyze ablation rate and morphology as a function of incident pulse energy from a Ho:YAG laser. They concluded that scattering is a dominant factor in the interaction of Ho:YAG laser radiation and bone.

¹⁰ Hydrogen fluoride lasers.

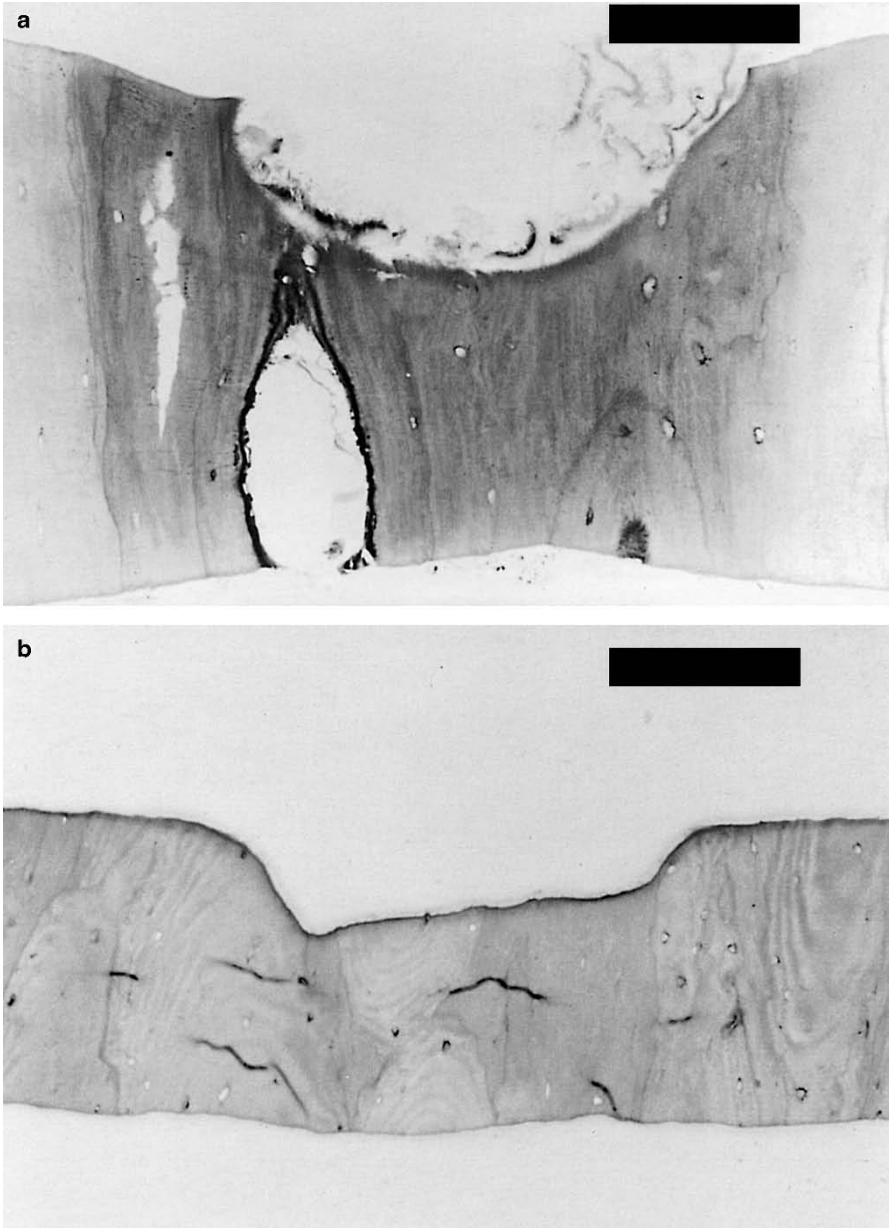


Fig. 4.65. (a) Histologic section of bone after exposure to a Ho:YAG laser (pulse duration: 250 μ s, energy density: 120 J/cm², bar: 100 μ m). (b) Histologic section of bone after exposure to an Er:YAG laser (pulse duration: 250 μ s, energy density: 35 J/cm², bar: 200 μ m). Photographs kindly provided by Dr. Romano (Bern)

Another discipline for laser applications within orthopedics is arthroscopy. Preliminary results regarding laser *meniscectomy*, i.e. the treatment of the meniscus, have already been reported by Glick (1981) and Whipple (1981) when using Nd:YAG and CO₂ lasers, respectively. At that time, though, suitable delivery systems were not available. Moreover, the CW mode of these lasers led to unacceptable thermal damage. Katsuyuki et al. (1983) and Bradrick et al. (1989) applied Nd:YAG lasers in arthroscopic treatment of the jaw joint. Significant improvements were not achieved until O'Brien and Miller (1990) made use of specially designed contact probes consisting of ceramics. Limbird (1990) pointed out the necessity of blood perfusion measurements after surgery. Major limitations for all infrared lasers in arthroscopic surgery arise from the optical delivery system. Transmission through flexible fibers can be regarded as a mandatory requirement for an efficient surgical procedure. Therefore, CO₂ lasers will never gain clinical relevance in arthroscopic treatments.

A new era of laser arthroscopy began with the application of holmium and erbium lasers. Trauner et al. (1990) reported promising results when using the Ho:YAG laser for the ablation of cartilage. Recently, Ith et al. (1994) have investigated the application of a fiber-delivered Er:YSGG laser emitting at a wavelength of 2.79 μm . The transmittance of novel zirconium fluoride (ZrF₄) fibers at this specific wavelength is satisfactory. Ith et al. (1994) have used fresh human meniscus from the knee joint which was obtained during surgery. They have observed a thermally damaged zone of 60 μm when exposing the tissue in air to five laser pulses at a pulse energy of 53 mJ and a pulse duration of 250 μs . On the other hand, when exposing the tissue through water at a slightly higher energy of 65 mJ, thermal damage extended to only 40 μm close to surface and was even negligible elsewhere. In either case – whether exposed in air or through water – a crater depth of roughly 1 mm was achieved. The surprising result of this study is that laser radiation at 2.79 μm can be effectively used for tissue ablation, although it should be strongly absorbed by surrounding water. Thus, Ith et al. (1994) concluded that light – after exiting the fiber – is guided through a water-vapor channel created by the leading part of the laser pulse. The period during which this channel is open was found to be dependent on the duration of the laser pulse. For pulse durations of 250–350 μs , most of the laser energy is transmitted through the water-vapor channel to the target.

The experimental results mentioned above encourage the application of holmium and erbium lasers in arthroscopic surgery. Nevertheless, further investigations need to be performed regarding both thermal and mechanical side effects associated with laser exposure. From today's perspective, though, it is already obvious that arthroscopy belongs to those medical disciplines where minimally invasive techniques based on laser radiation will turn into unrenounceable surgical tools.

4.9 Lasers in Gastroenterology

Gastrointestinal diseases primarily include ulcers and tumors of the *esophagus*, *stomach*, *liver*, *gallbladder*, and *intestine*. The intestine further consists of the *jejunum*, *ileum*, *colon*, and *rectum*. According to the position of these organs, the gastrointestinal tract is subdivided into an upper and a lower tract. Both tracts are schematically illustrated in Fig. 4.66. Most intestinal tumors are reported to occur inside the colon or the rectum.

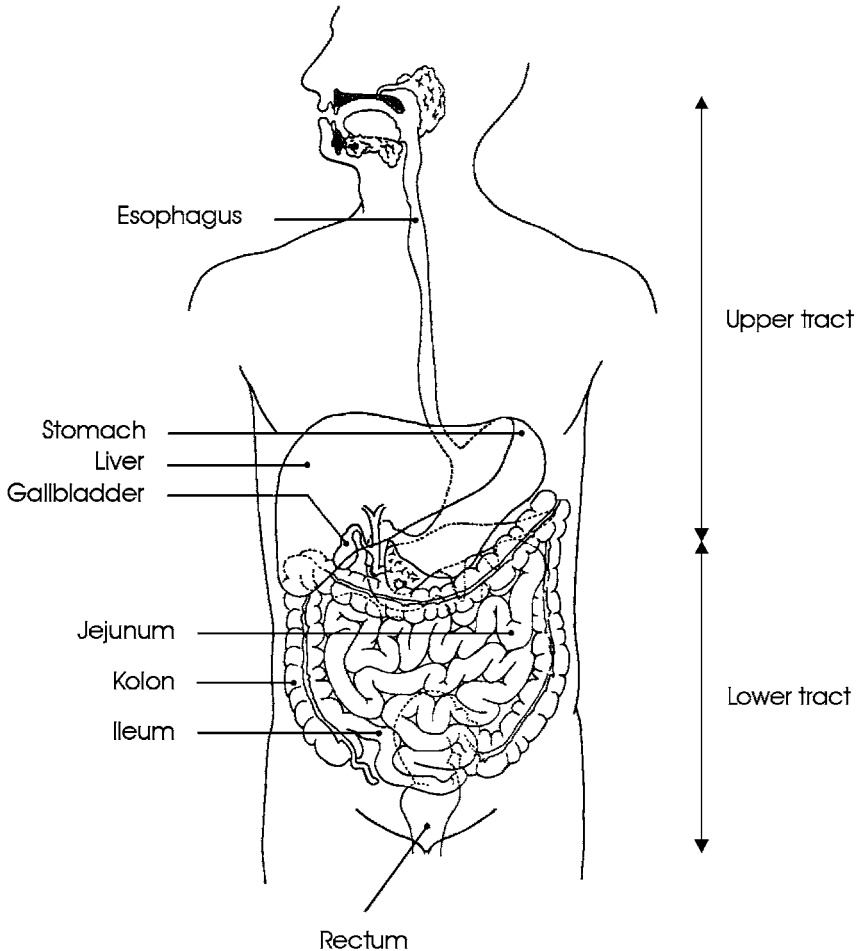


Fig. 4.66. Cross-section of the upper and lower gastrointestinal tracts. The upper tract includes esophagus, stomach, liver, and gallbladder, whereas the lower tract primarily consists of the intestine

In general, any kind of ulcer or tumor can be treated with lasers if it is accessible with endoscopic surgery. Ulcers and tumors tend to occupy additional space and are thus likely to induce severe stenoses. According to Sander et al. (1990), short and scarred stenoses of the lower tract are better suited for treatment than long and inflammable stenoses of the upper tract. If a tumor itself is no longer completely resectable due to its rather late detection – which unfortunately is quite often the case – laser application is restricted to a palliative treatment. The major concern of a palliative treatment is to provide an improved quality of the remaining life which also includes pain relief.

Gastroenterology is one of the major domains of the CW Nd:YAG laser. Only in photodynamic therapy are dye lasers applied. There exist mainly two indications for laser therapy: gastrointestinal hemorrhages and benign, malignant, or nonneoplastic¹¹ stenoses. Since the CW Nd:YAG laser is acting thermally, it can stop bleeding by means of coagulation. At higher power levels, i.e. in the vaporizing mode, it may serve in recanalization of stenoses. The application of other lasers was also investigated, e.g. the argon ion laser by Prauser et al. (1991), but was not associated with any significant advantages so far. The CO₂ laser is not suitable for clinical gastroenterology, since it is not transmitted through optical fibers which belong to the mandatory equipment of successful endoscopic surgery.

Stenoses of the esophagus are a common indication for laser treatment, since lasers can assist the surgeon in opening the stenosis. If even endoscopes cannot pass the stenosis, it must first be mechanically widened with specially designed dilators. Afterwards, the stenotic tissue may be coagulated using a Nd:YAG laser and a flexible fiber. Frequently, quartz fibers with a diameter of 600 μm are used. The fiber is protected by a Teflon tube with diameters of 1.8–2.5 mm. CO₂ gas is provided to cool the fiber tip and to keep debris away from the tissue. During coagulation, the tissue significantly shrinks, thereby reducing the occupied lumen inside the esophagus. If the stenosis was induced by a tumor, the fiber should be placed inside the tumor – by endoscopic control – and the tumor is coagulated starting from its interior. Induced bleeding can be stopped by a temporary increase in laser power. Dilatation of the stenosis and coagulation of the tumor are usually performed during the same session. Up to 30 kJ may be necessary during one treatment as stated by Semler (1989). Remaining necrotic tissue is usually repelled during the next few days, resulting in a further widening of the available lumen of the esophagus.

Unfortunately, restenoses of the esophagus frequently occur after a few weeks. According to Bader et al. (1986), they can be efficiently prevented by a second treatment called *afterloading*. This treatment involves a radioactive source, e.g. ¹⁹²Ir, which is placed inside the esophagus for a few minutes by means of a computer-controlled probe. Between three and five of these

¹¹ Stenoses which are not related to tumor formation are called *nonneoplastic*.

afterloading treatments are normally performed starting approximately two weeks after laser coagulation. In malignant esophagus tumors, the mean survival rate is extremely low, since most of them are diagnosed at a very late stage. Treatment can then only be of a palliative character according to Fleischer and Sivak (1985), and *esophagectomy*, i.e. the complete or partial removal of the esophagus, must be performed. Afterwards, an artificial tube can be implanted.

Laser treatments of tumors belonging to the lower gastrointestinal tract were described by Hohenberger et al. (1986) and Kiefhaber et al. (1987). The conventional technique is called *cryotherapy*, since it induces tumor necrosis by freezing the tissue to temperatures of approximately -180°C . In contrast to laser and afterloading therapy, it can be performed only during a complete anesthetization of the patient. Especially among older patients, this is one of the major disadvantages of cryotherapy. On the other hand, laser therapy is associated with an enhanced formation of edema. However, such edema can be treated with proper medicamentation.

Nonneoplastic stenoses of the lower gastrointestinal tract are treated by applying 80–100 W of laser power to an optical quartz fiber and slowly moving this fiber backwards out of the stenosis. Thereby, 1–2 mm deep grooves along the stenosis are induced according to Sander et al. (1990). After 3–5 days the grooves have dilated to a permeable path, and endoscopic passage is possible without mechanical pressure. In extended and inflamed stenoses, several treatments may be necessary.

The first laser therapy in gastroenterology was performed in the case of a massive hemorrhage by Kiefhaber et al. (1977). Since then, several extensive studies have been reported, e.g. by Rutgeerts et al. (1982), Macleod et al. (1983), and Swain et al. (1986). In general, it can be summarized that all localized and acute hemorrhages are suitable for laser coagulation. Inside the rectum and stomach, powers of 50–70 W and 70–100 W, respectively, are applied. After a complete clearance of the bleeding source, the tissue is coagulated from a distance of 5–10 mm by performing circularly shaped movements of the laser beam. There is no time limit for this procedure. The operation is stopped by releasing a footpedal if the desired effect is achieved. Patients are normally supervised by intensive care for at least three days following laser treatment.

An improved technique for the laser treatment of ulcers or hemorrhages was developed by Sander et al. (1988). It is based on a combination of laser beam and water jet. The laser beam is guided through a water jet to the site of application. First results reported by Sander et al. (1989) have shown that – using this technique – the percentage of successful hemostatic treatments could be raised from 82 % to 93 %. Moreover, fewer emergency surgeries needed to be performed and less mortality was observed. Sander et al. (1990) added that this technique has proven to be useful for other kinds of tissue coagulation, as well.

Despite early expectations concerning the potential of lasers in gastroenterology, e.g. by Fleischer et al. (1982), they could only partially be fulfilled so far. It is not obvious that the Nd:YAG laser at a wavelength of 1.064 μm provides the optimum radiation for gastrointestinal diseases. An extensive analysis of potential complications arising from the use of this laser was given by Mathus-Vliegen and Tytgat (1990). In the near future, alternative lasers with different wavelengths will certainly be investigated, as well. The surgical results obtained with these lasers must be compared to those achieved with the Nd:YAG laser. Most probably, not just one single laser will then prove to be best in the treatment of all diseases. There will rather be a variety of different lasers which – in combination with alternative treatments – should be used in specific cases.

One important branch of modern gastroenterologic treatment – which has not been addressed yet – is based on photodynamic therapy (PDT). The procedure of PDT has already been described in detail in Sect. 3.1. After injection of an appropriate photosensitizer and a time delay of approximately 48–72 hours, tumors of the gastrointestinal tract are exposed to a dye laser, e.g. a Rhodamine dye laser pumped with an argon ion laser. The clearance of the photosensitizer leads to a concentration gradient among benign and malignant tissue ranging from about 1:2 to 1:4. Meanwhile, several reports on PDT in gastroenterology have been published, e.g. by Barr et al. (1989), Barr et al. (1990), and Karanov et al. (1991). The success is inversely related to the tumor size at the time of treatment. According to Gossner and Ell (1993), tumors are curable only if their infiltration depths remain below 5–10 mm. Overholt et al. (1993) have shown that normal epithelium might then cover the interior of the esophagus again. The extent of a tumor is usually determined by ultrasound techniques. If a tumor is diagnosed at an early stage, more than 75 % of cases can be completely cured. In advanced cancer, the corresponding rate is less than 30 %. Tumors of the stomach are often more difficult to access for PDT due to wrinkles of the mucosa. Thus, treatments of the stomach are frequently associated with the application of higher energy doses. One major advantage of PDT is that fewer endoscopic sessions are usually required compared to treatments with the Nd:YAG laser. Hence, the overall duration of a PDT treatment is significantly shorter and easier to tolerate, as well.

In general, PDT is applied at early stages of cancer and in otherwise inoperable patients, e.g. if alternative methods are associated with a high risk for the patient. At advanced stages of esophagus cancer, PDT usually cannot provide a complete cure. However, it might significantly facilitate the act of swallowing. With the development of novel photosensitizers having a higher efficiency in the red and near infrared spectrum, additional applications of PDT might be indicated in the near future. Then, after careful evaluation of clinical studies, improved treatments characterized by even higher cure rates might be achievable.

4.10 Lasers in Otorhinolaryngology and Pulmology

Otorhinolaryngology is concerned with diseases of the *ear*, the *nose*, and the *throat*. So far, the most significant application of lasers in otorhinolaryngology aims at microsurgery of the *larynx*, e.g. in stenoses or laryngeal carcinoma. Stenoses of the larynx can be inherent or acquired. In either case, they are often associated with a severe impairment of the airway and should be treated immediately. Laryngeal carcinoma are the most frequent malignant tumors of the throat. The five major origins of these carcinoma are illustrated in Fig. 4.67. Diagnosis and treatment of laryngeal carcinoma are performed by means of a laryngoscope which consists of a rigid tube being connected to a surgical microscope. During treatment, the patient must be intubated as demonstrated in Fig. 4.68.

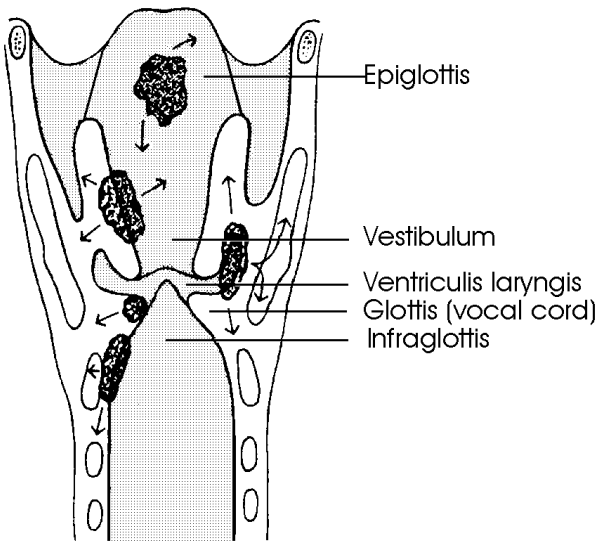


Fig. 4.67. Origins and directions of growth of laryngeal carcinoma

It has already been shown by Jako (1972) and Strong et al. (1976) that benign and malignant lesions of the glottis, i.e. the vocal cords, can be more safely removed with the CO₂ laser rather than mechanically. In laryngeal carcinoma, a complete resection is ascertained if histopathology proves the absence of tumor cells in adjacent tissue. If the tumor is already at an advanced stage, however, laser therapy aims at a palliative treatment only. Complications arise when the laser treatment requires complete anesthetization of the patient, since the associated gases are inflammable. For a proper operation of the intubation tube, different materials are currently being investigated. Among these, metal tubes probably provide highest security.

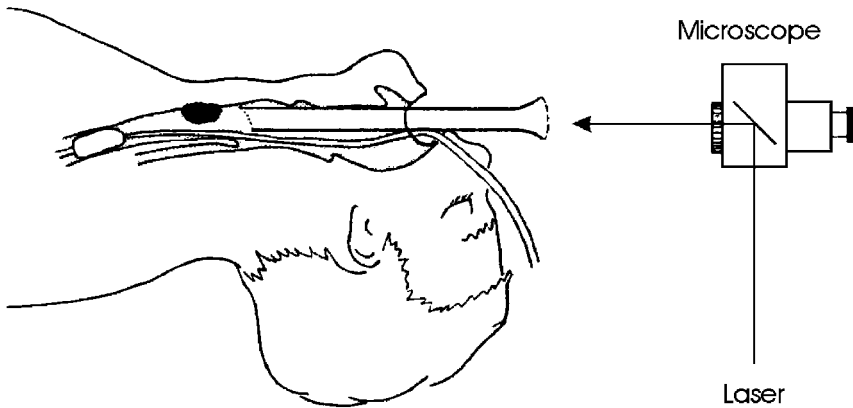


Fig. 4.68. Direct laryngoscopy with simultaneous intubation. Reproduced from Boenninghaus (1980) by permission. © 1980 Springer-Verlag

It was demonstrated by Holinger (1982) and Duncavage et al. (1985) that CO_2 lasers are superior to conventional therapy when treating laryngeal or subglottic stenoses. However, Steiner (1989) emphasizes that not all kinds of stenoses are equally indicated for laser treatment. In particular, large stenoses which extend over several centimeters in size should always be assigned to conventional surgery.

Major indications for laser treatment of the nose are highly vascularized tumors such as hemangiomas or premalignant alterations of the mucosa. The principal advantage of lasers is again their ability to simultaneously perform surgery and coagulate blood vessels. Lenz and Eichler (1984) and Parkin and Dixon (1985) have reported on argon ion laser treatments in vascular surgery of the nose. In proximal nose segments, Steiner (1989) suggests the application of a CO_2 laser which is connected to a surgical microscope. By means of tissue coagulation, even chronic nose-bleeding can be efficiently and safely treated.

Another very useful laser application in otolaryngology has been developed in the treatment of otosclerosis which is a bone disease of the inner ear. Otosclerosis usually affects the stapes shown in Fig. 4.69 and ultimately leads to its fixation. It is often associated with hearing impairment, because a movable stapes is necessary for the physiologic transport of sound to the cochlea. Two potential treatments are called *stapedectomy* and *stapedotomy*. In stapedectomy, the stapes footplate in the inner ear is mechanically removed and replaced by an artificial implant. In stapedotomy, a hole is drilled into the stapes to improve the propagation of sound to the oval window. Perforation of the stapes is achieved with either miniaturized mechanical drills or with suitable lasers and application units. Laser stapedotomy can be considered as a typical method of minimally invasive surgery (MIS).

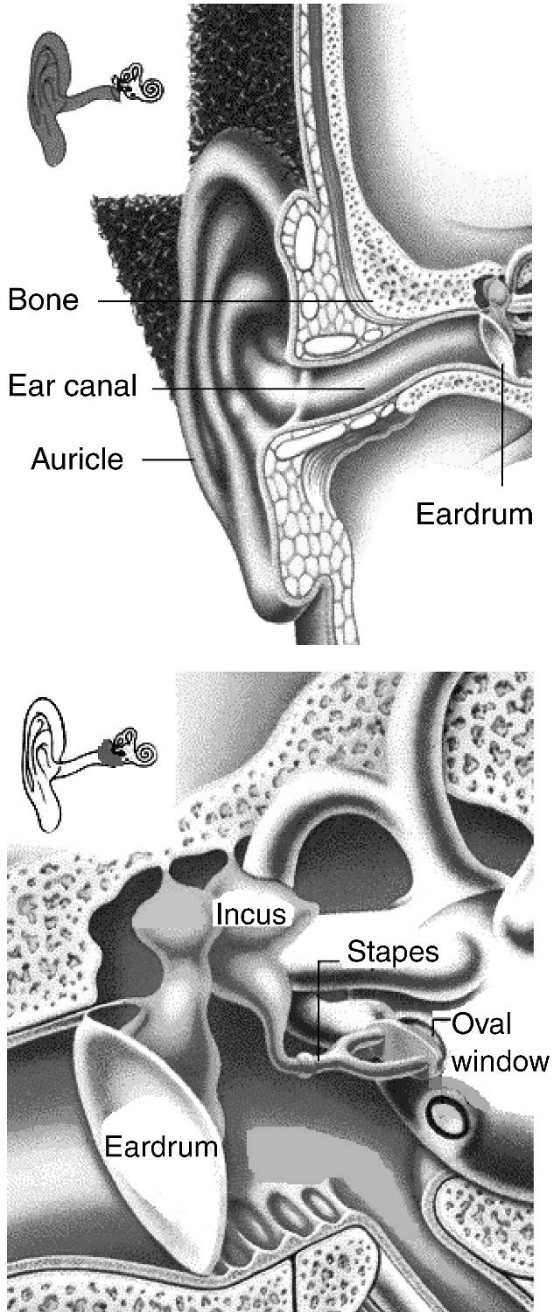


Fig. 4.69. Anatomy of outer and inner ear

Stapedotomy seems to be a predestined treatment for laser radiation, since it requires least mechanical damage. It is generally accepted that a noncontact method is certainly the best choice in preventing the inner ear structures from externally induced compression. Perkins (1980) and Gantz et al. (1982) performed the first stapedotomies with an argon ion laser. A few years later, Coker et al. (1986) investigated the application of a CO₂ laser for the same purpose. Finally, Lesinski and Palmer (1989) compared surgical results achieved with the CO₂ laser, argon ion laser, and a frequency-doubled Nd:YAG laser. The main disadvantage of radiation from the CO₂ laser is that it cannot be guided through optical fibers. On the other hand, radiation from argon ion or frequency-doubled Nd:YAG lasers is strongly absorbed only in highly pigmented tissue. The efficiency of these lasers in ablating cortical bone is thus rather weak. Due to the low absorption, their radiation might even induce severe lesions in adjacent tissue.

Recently, Frenz et al. (1994) and Pratisto et al. (1996) have studied stapedotomies performed with Er:YAG and Er:YSGG lasers, respectively. Radiation from erbium lasers combines the advantages of being strongly absorbed in bone and of being transmitted through zirconium fluoride (ZrF₄) fibers. In Figs. 4.70a–b, a perforation of the stapes is shown which was induced by only five pulses from an Er:YAG laser at a rather moderate fluence of only 10 J/cm². The edge of the perforation is very precise and does not indicate any mechanical damage. In Fig. 4.71, the ablation curve of cortical bone obtained with the Er:YSGG laser is shown. Due to the high ablation depths achieved with erbium lasers, only a few pulses are necessary to perforate the stapes. According to Pratisto et al. (1996), the ablation threshold was less than 5 J/cm².

Potential risks in laser-assisted stapedotomy evolve from either an excessive increase in temperature of the perilymph or too high pressures induced inside the cochlea of the inner ear. It was found by Frenz et al. (1994) that the temperature at the stapes increases by only less than 5°C if the power output of the Er:YAG laser is limited to 10 J/cm². In a specially designed ear model, the temperature increase in the perilymph was even negligible. The pressure inside the cochlea during the laser treatment is very important, since the ear is a very sensitive organ. Frenz et al. (1994) have measured pressure signals in their ear model using a PVDF foil as described in Sect. 3.5. The PVDF foil was located 3 mm below the exposed area. The corresponding pressure data are presented in Fig. 4.72. Frenz et al. (1994) have compared these data with maximum tolerable sound pressures as published by Pfander (1975). They stated that erbium lasers permit a safe pressure level if their fluence is limited to 10 J/cm².

We conclude that laser-assisted stapedotomy has meanwhile become a considerable alternative to mechanical drills. Erbium lasers, e.g. Er:YAG or Er:YSGG lasers, are capable of performing safe and very precise stapedotomies with negligible thermal damage.

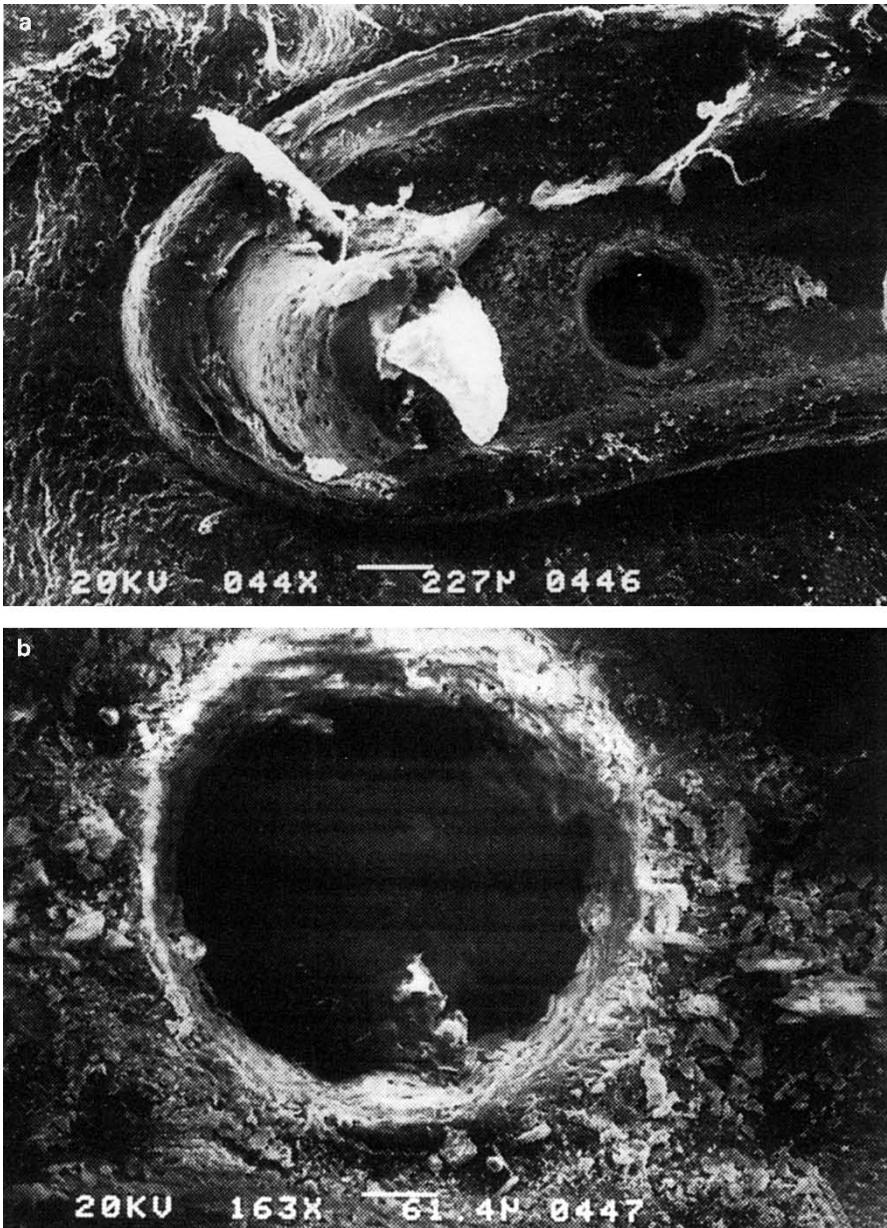


Fig. 4.70. (a) Stapedotomy performed with five pulses from an Er:YAG laser (pulse duration: 200 μ s, fluence: 10 J/cm²). (b) Enlargement of the perforation. Reproduced from Frenz et al. (1994) by permission. © 1994 Verlag Huber AG

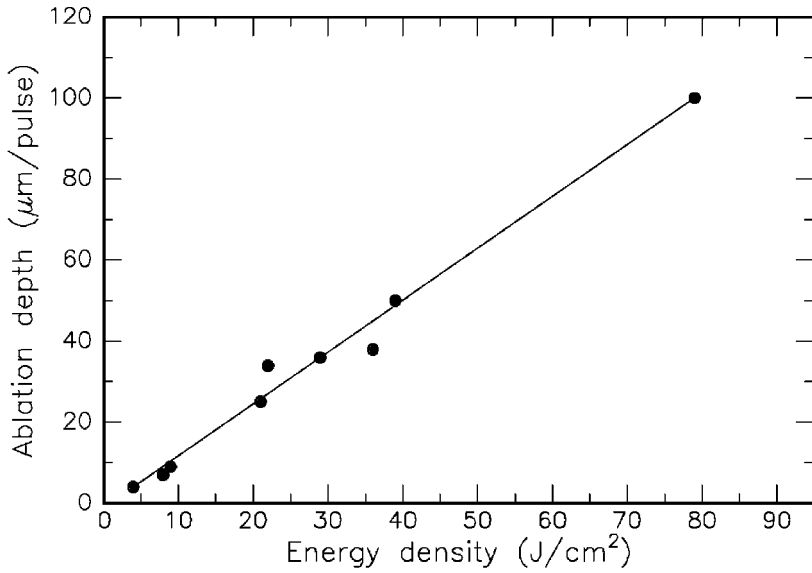


Fig. 4.71. Ablation curve of cortical bone obtained with an Er:YSGG laser (wave-length: 2.79 µm, pulse duration: 200 µs). Data according to Pratisto et al. (1996)

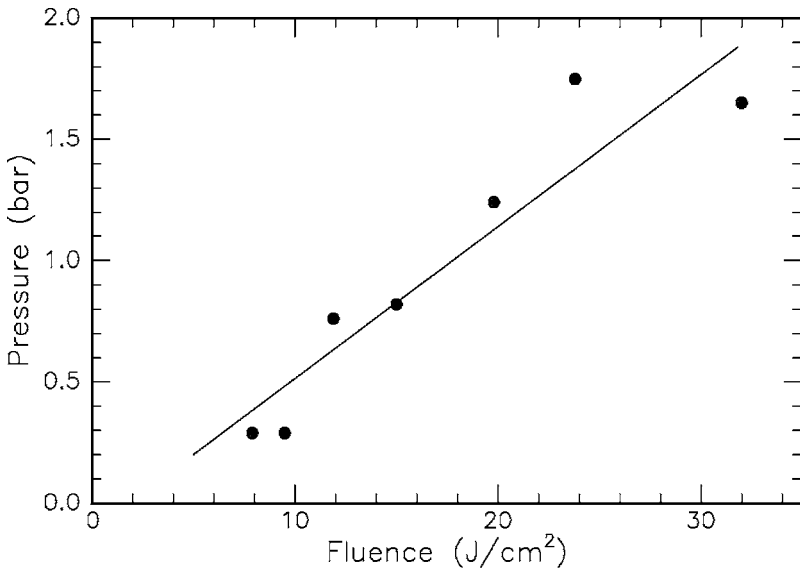


Fig. 4.72. Pressure in the perilymph of the inner ear during Er:YAG laser (wave-length: 2.94 µm, pulse duration: 200 µs) irradiation of the stapes footplate. Data according to Frenz et al. (1994)

Pulmology is concerned with diseases of the lung. In the western civilized world, tracheobronchial tumors are the primary cause of death due to cancer. According to Macha (1991), only less than 6–8 % of patients survive the next five years after diagnosis, because the tumor is often diagnosed at a rather late stage. The resection of tracheobronchial tumors is conventionally performed with a rigid bronchoscope. Severe and life-threatening hemorrhage is often inevitable. Beside mechanical removal, electrocoagulation and cryotherapy are performed. Dumon et al. (1982) and Hetzel et al. (1985) have investigated the application of a Nd:YAG laser and a flexible fiber in the treatment of tracheobronchial lesions. Since the Nd:YAG laser provides the surgeon with the ability of immediate coagulation, the occurrence of severe hemorrhage can be significantly reduced. Moreover, Macha et al. (1987) have proposed a combined therapy of a radioactive source, e.g. ^{192}Ir , and laser radiation to improve the surgical result.

In summary, the Nd:YAG laser is a valuable supplement in the therapy of tracheobronchial tumors, although it is usually limited to a palliative treatment. However, patients soon perceive pain relief during breathing. Further clinical studies with alternative lasers and sophisticated application units are badly needed. Preliminary results concerning photodynamic therapy in the treatment of lung cancer have already been published by Hayata et al. (1982). Meanwhile, this technique has been investigated in head and neck surgery, as well, e.g. by Feyh et al. (1990).

4.11 Questions to Chapter 4

Q4.1. During the treatment of hyperopia with PRK, the curvature of the anterior corneal surface must

A: be flattened. B: remain unchanged. C: be steepened.

Q4.2. Er:YAG lasers are not suitable for the treatment of caries because of
A: cytotoxicity. B: low efficiency. C: thermal effects.

Q4.3. Angioplasty with excimer lasers is likely to induce
A: atherosclerosis. B: restenoses. C: thermal injury.

Q4.4. In stapedotomy with Er:YAG lasers, the fluence should be limited to
A: 1 J/cm^2 . B: 10 J/cm^2 . C: 100 J/cm^2 .

Q4.5. The deepest layer of the skin is called
A: dermis. B: epidermis. C: subcutis.

Q4.6. Why is LASIK less sensitive to scattering effects than PRK?

Q4.7. Why is laser dentistry with picosecond or femtosecond pulses painfree?

Q4.8. What is the workhorse laser in gynecology?

Q4.9. How can BPH be treated optically?

Q4.10. What is the purpose of a stereotactic ring?

5. Laser Safety

Most parts of this chapter are adapted from the booklet “Laser Safety Guide” (Editor: D.H.Sliney, 9th edition, 1993) published by the *Laser Institute of America, Orlando, Florida, USA*. The permission obtained for reproduction is gratefully acknowledged.

5.1 Introduction

The increasingly widespread use of lasers requires more people to become familiar with the potential hazards associated with the misuse of this valuable new product of modern science. Applications exist in many technologies, including material processing, construction, medicine, communications, energy production, and national defense. Of recent importance from a safety consideration, however, is the introduction of laser devices into more consumer-oriented retail products, such as the laser scanning devices, office copy and printing machines, and audio/visual recording devices. Most devices in these markets emit relatively low energy levels and, consequently, are easily engineered for safe use.

5.2 Laser Hazards

The basic hazards from laser equipment can be categorized as follows:

Laser Radiation Hazards

Lasers emit beams of optical radiation. Optical radiation (ultraviolet, visible, and infrared) is termed *nonionizing* radiation to distinguish it from *ionizing* radiation such as X-rays and gamma rays which are known to cause different biological effects.

- Eye hazards: Corneal and retinal burns (or both), depending upon laser wavelength, are possible from acute exposure; and corneal or lenticular opacities (cataracts), or retinal injury may be possible from chronic exposure to excessive levels.
- Skin hazards: Skin burns are possible from acute exposure to high levels of optical radiation. At some specific ultraviolet wavelengths, skin carcinogenesis may occur.

Chemical Hazards

Some materials used in lasers (i.e. excimer, dye, and chemical lasers) may be hazardous and/or contain toxic substances. In addition, laser-induced reactions can release hazardous particulate and gaseous products.

Electrical Hazards

Lethal electrical hazards may be present in all lasers, particularly in high-power laser systems.

Other Secondary Hazards

These include:

- cryogenic coolant hazards,
- excessive noise from very high energy lasers,
- X radiation from faulty high-voltage (> 15 kV) power supplies,
- explosions from faulty optical pumps and lamps,
- fire hazards.

5.3 Eye Hazards

The ocular hazards represent a potential for injury to several different structures of the eye. This is generally dependent on which structure absorbs the most radiant energy per volume of tissue. Retinal effects are possible when the laser emission wavelength occurs in the visible and near infrared spectral regions ($0.4\ \mu\text{m}$ to $1.4\ \mu\text{m}$). Light directly from the laser or from a specular (mirror-like) reflection entering the eye at these wavelengths can be focused to an extremely small image on the retina. The incidental corneal irradiance and radiant exposure will be increased approximately 100 000 times at the retina due to the focusing effect of the cornea and lens.

Laser emissions in the ultraviolet and far infrared spectral regions (outside $0.4\ \mu\text{m}$ to $1.4\ \mu\text{m}$) produce ocular effects primarily at the cornea. However, laser radiation at certain wavelengths may reach the lens and cause damage to that structure.

Optical Radiation Hazards

Effects of optical radiation at various wavelengths on various structures of the eye are shown in Figs. 5.1a–c. Actinic-ultraviolet, at wavelengths of 180 nm to 315 nm, is absorbed at the cornea. These wavelengths are responsible for “welder’s flash” or *photokeratitis*. Near ultraviolet (UV-A) radiation between 315 nm and 400 nm is absorbed in the lens and may contribute to certain forms of *cataracts*.

Radiation at visible wavelengths, 400 nm to 780 nm, and near infrared wavelengths, 780 nm to 1400 nm, is transmitted through the ocular media with little loss of intensity and is focused to a spot on the retina 10 μm to 20 μm in diameter. Such focusing can cause intensities high enough to damage the retina. For this reason, laser radiation in the 400 nm to 1400 nm range is termed the *retinal hazard region*. Wavelengths between 400 nm and 550 nm are particularly hazardous for long-term retinal exposures or exposures lasting for minutes or hours. This is sometimes referred to as the *blue light hazard*.

Far infrared (IR-C) radiation with wavelengths of 3 μm to 1 mm is absorbed in the front surface of the eye. However, some middle infrared (IR-B) radiation between 1.4 μm and 3 μm penetrates deeper and may contribute to “glass-blower’s cataract”. Extensive exposure to near infrared (IR-A) radiation may also contribute to such cataracts.

The localization of injury is always the result of strong absorption in the specific tissue for the particular wavelength.

5.4 Skin Hazards

From a safety standpoint, skin effects have been usually considered of secondary importance. However, with the more widespread use of lasers emitting in the ultraviolet spectral region as well as higher power lasers, skin effects have assumed greater importance.

*Erythema*¹, *skin cancer*, and accelerated *skin aging* are possible in the 230 nm to 380 nm wavelength range (actinic ultraviolet). The most severe effects occur in the UV-B (280–315 nm). Increased *pigmentation* can result following chronic exposures in the 280 nm to 480 nm wavelength range. At high irradiances, these wavelengths also produce “long-wave” erythema of the skin. In addition, photosensitive reactions are possible in the 310 nm to 400 nm (near ultraviolet) and 400 nm to 600 nm (visible) wavelength regions. The most significant effects in the 700 nm to 1000 nm range (infrared) will be skin burns and excessive dry skin.

¹ Sunburn.

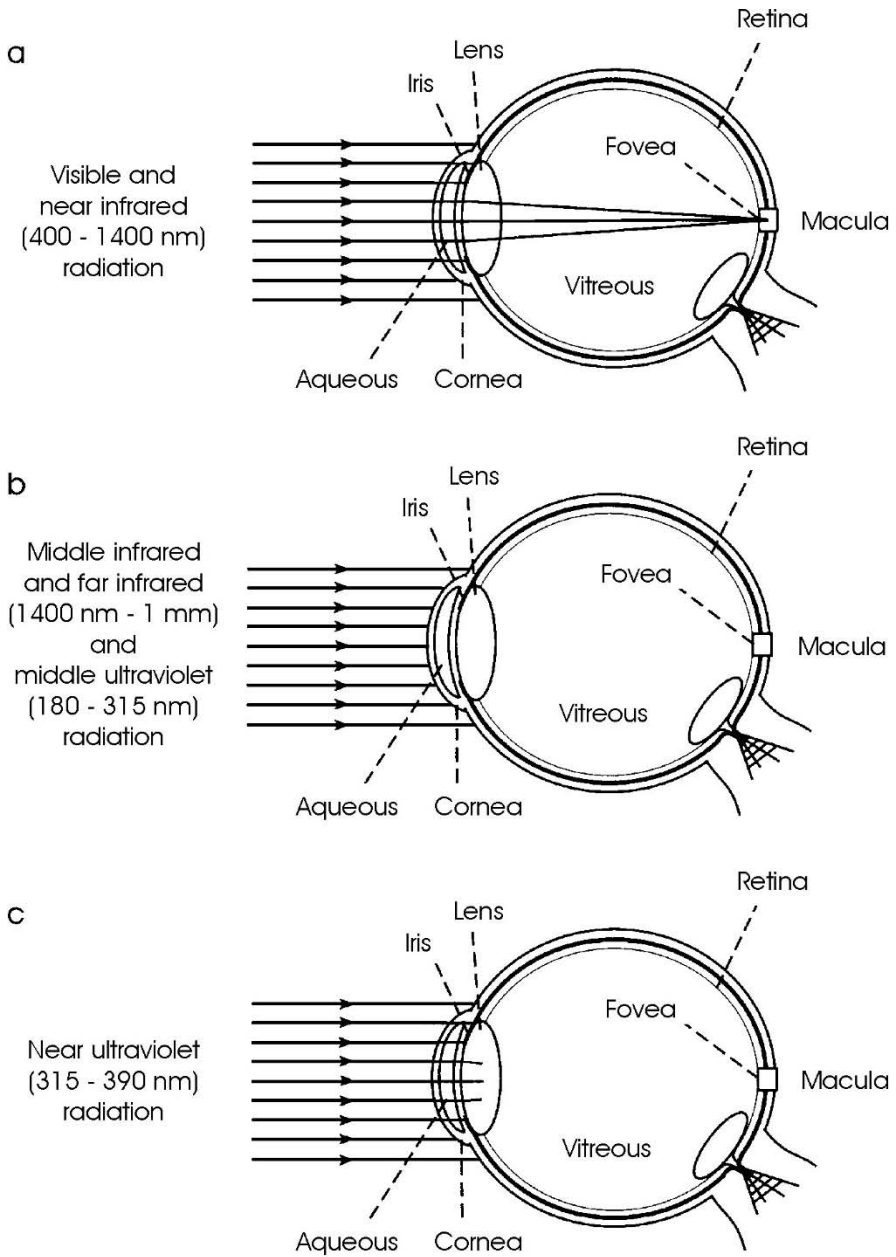


Fig. 5.1. (a) Absorption sites of visible and near infrared radiation. (b) Absorption sites of middle infrared, far infrared, and middle ultraviolet radiation. (c) Absorption sites of near ultraviolet radiation

5.5 Associated Hazards from High Power Lasers

Some applications of high-power lasers, especially in materials processing, can give rise to respiratory hazards. Laser welding, cutting, and drilling procedures can create potentially hazardous fumes and vapors. Fortunately, the same localized and general ventilation procedures developed for similar conventional operations apply to this type of laser application.

The most lethal hazards associated with the laser involves electricity. There have been several fatal accidents associated with lasers due to electrocution. These occurred when commonly accepted safety procedures were not followed when individuals were working with dangerous, high-voltage components of a laser system. Proper electrical hazards controls should be used at all times when working with laser systems.

Fire hazards may exist with some high-power laser devices, normally those with continuous wave (CW) lasers having an output power above 0.5 W. Another hazard sometimes associated with high-power laser systems involves the use of cryogenic coolants used in the laser system. Skin contact can cause burns, improper plumbing can cause explosions, and insufficient ventilation can result in the displacement of oxygen in the air by liquefied gas vaporizing (most commonly nitrogen). Cryogenic hazards are normally, but not exclusively, limited to research laboratories. Noise hazards are rarely present in laser operations.

5.6 Laser Safety Standards and Hazard Classification

The basic approach of virtually all laser safety standards has been to classify lasers by their hazard potential which is based upon their optical emission. The next step is to specify control measures which are commensurate with the relative hazard classification. In other words, the laser is classified based upon the hazard it presents, and for each classification a standard set of control measures applies. In this manner, unnecessary restrictions are not placed on the use of many lasers which are engineered to assure safety.

This philosophy has given rise to a number of specific classification schemes such as the one employed in the *American National Standards Institute's (ANSI) Z136.1 Safe Use of Lasers (1993)* standard. This standard was developed by the accredited standards committee Z136, and the Laser Institute of America is the secretariat. The standard has been used as a source by many organizations including the Occupational Health and Safety Agency (OSHA) and the American Conference of Governmental Industrial Hygienists (ACGIH) in developing their laser safety guidelines².

² Meanwhile, major parts of the ANSI classification scheme have been adapted by most European safety organizations, as well.

The ANSI scheme has four hazard classifications. The classification is based upon the beam output power or energy from the laser (emission) if it is used by itself. If the laser is a component within a laser system where the raw beam does not leave the enclosure, but instead a modified beam is emitted, the modified beam is normally used for classification. Basically, the classification scheme is used to describe the capability of the laser or laser system to produce injury to personnel. The higher the classification number, the greater is the potential hazard. Brief descriptions of each laser class are given as follows:

- *Class 1* denotes lasers or laser systems that do not, under normal operating conditions, pose a hazard.
- *Class 2* denotes low-power visible lasers or visible laser systems which, because of the normal human aversion response (i.e. blinking, eye movement, etc.), do not normally present a hazard, but may present some potential for hazard if viewed directly for extended periods of time (like many conventional light sources). Safety glasses are required for prolonged viewing only.
- *Class 3a* denotes the lowest class of lasers or laser systems that always require protective eyewear. These lasers would not injure the eye if viewed for only momentary periods (e.g. within the aversion response period of approximately 0.25 s) with the unaided eye, but may present a greater hazard if viewed using collecting optics or if viewed without the possibility of an aversion response (as for UV or IR radiation).
- *Class 3b* denotes lasers or laser systems that can produce a hazard if viewed directly. This includes intrabeam viewing of specular reflections. Normally, Class 3b lasers will not produce a hazardous diffuse reflection. Protective eyewear is always required.
- *Class 4* denotes lasers and laser systems that produce a hazard not only from direct or specular reflections, but may also produce hazardous diffuse reflections. Such lasers may produce significant skin hazards as well as fire hazards. Protective eyewear is always required.

Although the process of laser hazard evaluation does not rely entirely on the laser classification, the laser classification must be known. If the laser classification has not been provided by the manufacturer (as usually required by law), the class can be determined by measurement and/or calculation. A list of typical laser classifications is found in Table 5.1. Since the relative hazard of a laser may also vary depending upon use and/or environmental effects, measurements and/or calculations may be necessary to determine the degree of hazard in such cases.

Table 5.1. Typical classifications for selected CW and pulsed lasers, assuming that both skin and eye may be exposed (beam diameter: 1.0 mm)

Laser (CW)	Wavelength (nm)	Class 1 (W)	Class 2 (W)	Class 3b (W)	Class 4 (W)
Nd:YAG (4ω)	266	$\leq 9.6 \times 10^{-9}$	—	≤ 0.5	> 0.5
Argon ion	488/514	$\leq 0.4 \times 10^{-6}$	$\leq 10^{-3}$	≤ 0.5	> 0.5
Krypton ion	530	$\leq 0.4 \times 10^{-6}$	$\leq 10^{-3}$	≤ 0.5	> 0.5
Nd:YAG (2ω)	532	$\leq 0.4 \times 10^{-6}$	$\leq 10^{-3}$	≤ 0.5	> 0.5
Dye	400–550	$\leq 0.4 \times 10^{-6}$	$\leq 10^{-3}$	≤ 0.5	> 0.5
He-Ne	632	$\leq 7 \times 10^{-6}$	$\leq 10^{-3}$	≤ 0.5	> 0.5
Krypton ion	647	$\leq 11 \times 10^{-6}$	$\leq 10^{-3}$	≤ 0.5	> 0.5
Diode	670	$\leq 24 \times 10^{-6}$	$\leq 10^{-3}$	≤ 0.5	> 0.5
Diode	780	$\leq 0.18 \times 10^{-3}$	—	≤ 0.5	> 0.5
Diode	850	$\leq 0.25 \times 10^{-3}$	—	≤ 0.5	> 0.5
Diode	905	$\leq 0.32 \times 10^{-3}$	—	≤ 0.5	> 0.5
Nd:YAG	1064	$\leq 0.64 \times 10^{-3}$	—	≤ 0.5	> 0.5
Ho:YAG	2120	$\leq 9.6 \times 10^{-3}$	—	≤ 0.5	> 0.5
Er:YAG	2940	$\leq 9.6 \times 10^{-3}$	—	≤ 0.5	> 0.5
CO ₂	10600	$\leq 9.6 \times 10^{-3}$	—	≤ 0.5	> 0.5

Laser (pulsed)	Wavelength (nm)	Duration (s)	Class 1 (W)	Class 3b (W)	Class 4 (W)
ArF	193	20×10^{-9}	$\leq 23.7 \times 10^{-6}$	≤ 0.125	> 0.125
KrF	248	20×10^{-9}	$\leq 23.7 \times 10^{-6}$	≤ 0.125	> 0.125
Nd:YAG (4ω)	266	20×10^{-9}	$\leq 23.7 \times 10^{-6}$	≤ 0.125	> 0.125
XeCl	308	20×10^{-9}	$\leq 52.6 \times 10^{-6}$	≤ 0.125	> 0.125
XeF	351	20×10^{-9}	$\leq 52.6 \times 10^{-6}$	≤ 0.125	> 0.125
Dye	450–650	10^{-6}	$\leq 0.2 \times 10^{-6}$	≤ 0.03	> 0.03
Nd:YAG	532	20×10^{-9}	$\leq 0.2 \times 10^{-6}$	≤ 0.03	> 0.03
Ruby	694	10^{-3}	$\leq 4 \times 10^{-6}$	≤ 0.03	> 0.03
Ti:Sapphire	700–1000	6×10^{-6}	$\leq 0.19 \times 10^{-6}$	≤ 0.03	> 0.03
Alexandrite	720–800	0.1×10^{-3}	$\leq 0.76 \times 10^{-6}$	≤ 0.03	> 0.03
Nd:YAG	1064	20×10^{-9}	$\leq 2 \times 10^{-6}$	≤ 0.15	> 0.15
Ho:YAG	2120	0.25×10^{-3}	$\leq 9.7 \times 10^{-3}$	≤ 0.125	> 0.125
Er:YAG	2940	0.25×10^{-3}	$\leq 6.8 \times 10^{-3}$	≤ 0.125	> 0.125
CO ₂	10600	0.1×10^{-6}	$\leq 0.97 \times 10^{-3}$	≤ 0.125	> 0.125
CO ₂	10600	10^{-3}	$\leq 9.6 \times 10^{-3}$	≤ 0.125	> 0.125

The term *limiting aperture* is often used when discussing laser classification. Limiting aperture is defined as the maximum circular area over which irradiance and radiant exposure can be averaged. It is a function of wavelength region and use.

In the ANSI classification system, the user or the Laser Safety Officer uses his judgement to establish the longest reasonable possible exposure duration for a CW or repetitively pulsed laser. This is called the classification duration t_{\max} which cannot exceed an eight hour day equal to 3×10^4 seconds.

Very important is the so-called *MPE value* which denotes maximum permissible exposure. The MPE value depends on both exposure time and wavelength. In Fig. 5.2, some typical MPE values for maximum ocular exposure are graphically presented. The respective values for skin exposure are usually higher, since skin is not as sensitive as the retina. A comparison of ocular and skin exposure limits is provided in Table 5.2. For pulse durations shorter than 1 ns, the damage threshold of the energy density scales approximately with the square root of the pulse duration as discussed in Sect. 3.4. For instance, when evaluating an appropriate exposure limit for laser pulses with a duration of 10 ps, the energy densities listed for 1 ns pulses should be multiplied by a factor of $1/\sqrt{100} = 1/10$.

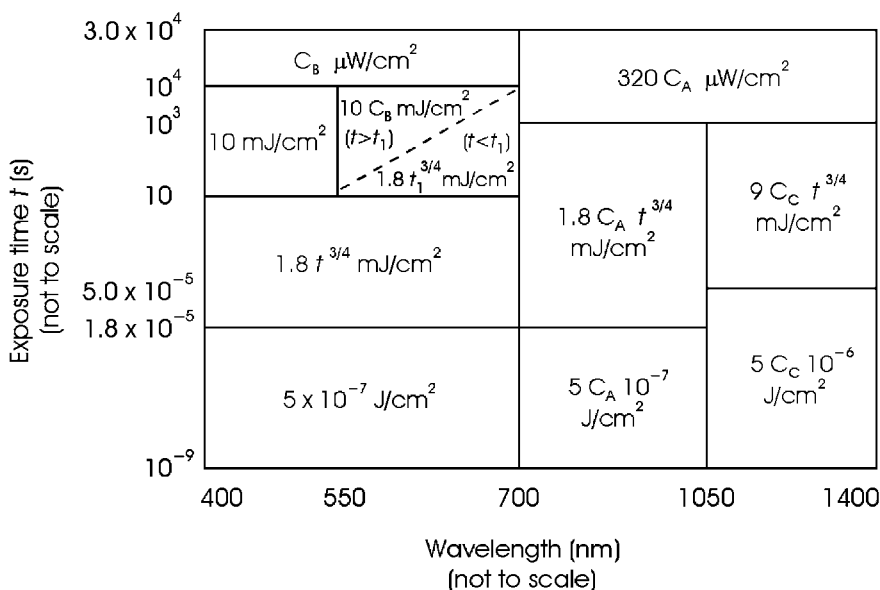


Fig. 5.2. Visible and near-IR MPE values for direct ocular exposure. Note that the correction factors (C) vary by wavelength. $C_A = 10^{2(\lambda - 0.700)}$ for 0.700–1.050 μm . $C_A = 5$ for 1.050–1.400 μm . $C_B = 1$ for 0.400–0.550 μm . $C_B = 10^{15(\lambda - 0.550)}$ for 0.550–0.700 μm . $t_1 = 10 \times 10^{20(\lambda - 0.550)}$ for 0.550–0.700 μm . $C_C = 1$ for 1.050–1.150 μm . $C_C = 10^{18(\lambda - 1.150)}$ for 1.150–1.200 μm . $C_C = 8$ for 1.200–1.400 μm

Table 5.2. Ocular and skin exposure limits of some representative lasers. Repetitive pulses at rates less than one pulse per second were assumed for any repetitive exposures. Higher repetition rates require more adjustment of the exposure limits. τ : pulse duration

Laser type	Wavelength (nm)	Ocular exposure limit ^a (MPE value)
Argon ion	488/514	0.5 $\mu\text{J}/\text{cm}^2$ for 1 ns to 18 μs 1.8 $\tau^{3/4}$ mJ/cm ² for 18 μs to 10 s 10 mJ/cm ² for 10 s to 10 000 s 1 $\mu\text{W}/\text{cm}^2$ for greater durations
He-Ne	632.8	0.5 $\mu\text{J}/\text{cm}^2$ for 1 ns to 18 μs 1.8 $\tau^{3/4}$ mJ/cm ² for 18 μs to 430 s 170 mJ/cm ² for 430 s to 10 000 s 17 $\mu\text{W}/\text{cm}^2$ for greater durations
Nd:YAG	1064	5 $\mu\text{J}/\text{cm}^2$ for 1 ns to 50 μs 9 $\tau^{3/4}$ mJ/cm ² for 50 μs to 1 000 s 1.6 mW/cm ² for greater durations
Diode	910	1.3 $\mu\text{J}/\text{cm}^2$ for 1 ns to 18 μs 4.5 $\tau^{3/4}$ mJ/cm ² for 18 μs to 1 000 s 0.8 mW/cm ² for greater durations
CO ₂	10600	10 mJ/cm ² for 1 ns to 100 ns 0.56 $\tau^{1/4}$ J/cm ² for 100 ns to 10 s 0.1 W/cm ² for greater durations
Laser type	Wavelength (nm)	Skin exposure limit ^b (MPE value)
Argon ion	488/514	0.02 J/cm ² for 1 ns to 100 ns 1.1 $\tau^{1/4}$ J/cm ² for 100 ns to 10 s 0.2 W/cm ² for greater durations
He-Ne	632.8	0.02 J/cm ² for 1 ns to 100 ns 1.1 $\tau^{1/4}$ J/cm ² for 100 ns to 10 s 0.2 W/cm ² for greater durations
Nd:YAG	1064	0.1 J/cm ² for 1 ns to 100 ns 5.5 $\tau^{1/4}$ J/cm ² for 100 ns to 10 s 1.0 W/cm ² for greater durations
Diode	910	0.05 J/cm ² for 1 ns to 100 ns 2.8 $\tau^{1/4}$ J/cm ² for 100 ns to 10 s 0.5 W/cm ² for greater durations
CO ₂	10600	10 mJ/cm ² for 1 ns to 100 ns 0.56 $\tau^{1/4}$ J/cm ² for 100 ns to 10 s 0.1 W/cm ² for greater durations

^a The exposure limit is averaged over a 7 mm aperture for wavelengths between 400 nm and 1400 nm, and over 1.0 mm for the CO₂ laser wavelength at 10.6 μm .

^b The exposure limit is defined for a 3.5 mm measuring aperture.

Any completely enclosed laser is classified as a Class 1 laser if emissions from the enclosure cannot exceed the MPE values under any conditions inherent in the laser design. During service procedures, however, the appropriate control measures are temporarily required for the class of laser contained within the enclosure. In the United States, a Federal government safety standard for laser products, which regulates laser manufacturers, was developed by the Center for Devices and Radiological Health (CDRH).

5.7 Viewing Laser Radiation

From a safety point of view, the laser can be considered as a highly collimated source of extremely intense monochromatic electromagnetic radiation. Due to these unique beam properties, most laser devices can be considered as a point source of great brightness. Conventional light sources or a diffuse reflection of a Class 2 or Class 3 laser beam are extended sources of very low brightness because the light radiates in all directions. This is of considerable consequence from a hazard point of view, since the eye will focus the rays (400–1400 nm) from a point source to a small spot on the retina while the rays from an extended source will be imaged, in general, over a much larger area. Only when one is relatively far away from a diffuse reflection (far enough that the eye can no longer resolve the image) will the diffuse reflection approximate a “point source”. Diffuse reflections are only of importance with extremely high-power Class 4 laser devices emitting visible and IR-A radiation between 400 nm and 1400 nm.

Different geometries of ocular exposure are demonstrated in Figs. 5.3–5.6. Intrabeam viewing of the direct (primary) laser beam is shown in Fig. 5.3. This type of viewing is most hazardous. Intrabeam viewing of a specularly reflected (secondary) beam from a flat surface is illustrated in Fig. 5.4. Specular reflections are most hazardous when the reflecting surface is either flat or concave. On the other hand, intrabeam viewing of a specularly reflected (secondary) beam from a convex surface is less hazardous, since the divergence of the beam has increased after reflection (see Fig. 5.5). Finally, Fig. 5.6 illustrates extended source viewing of a diffuse reflection. Usually, diffuse reflections are not hazardous except with very high power Class 4 lasers.

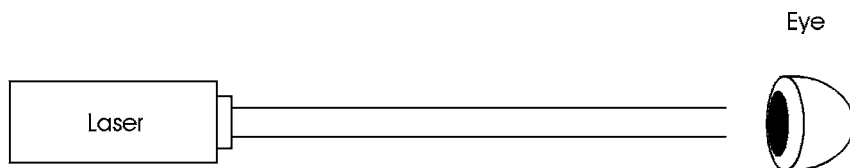


Fig. 5.3. Intrabeam viewing of a direct beam

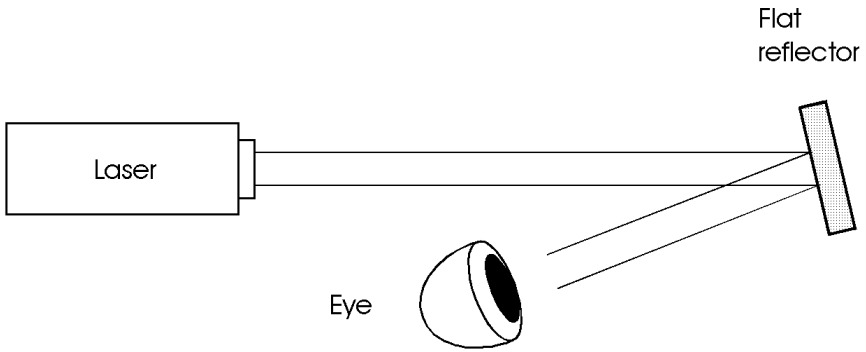


Fig. 5.4. Intrabeam viewing of a specularly reflected beam from a flat surface

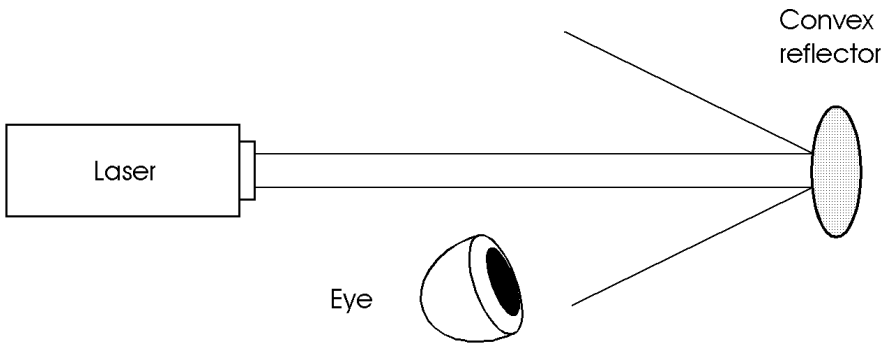


Fig. 5.5. Intrabeam viewing of a specularly reflected beam from a curved surface

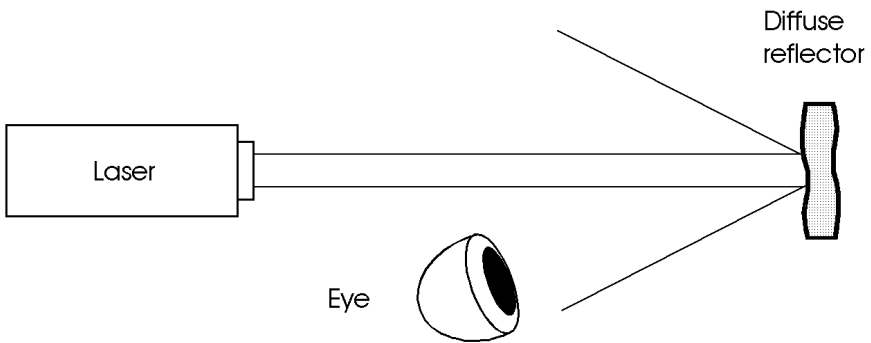


Fig. 5.6. Extended source viewing of a diffuse reflection

5.8 Eye Protection

Although engineering controls, such as enclosure of the laser beam, are far more preferable than the use of laser eye protection, there are instances when the use of laser eye protection is the most effective safety measure. It is important that the eye protection be clearly marked to insure that it is not used for protection against laser wavelengths for which it is not intended. If the eye protection is used outdoors it should employ curved-surface lenses to eliminate the additional hazard of generating collimated specular reflections. Table 5.3 provides a simplified approach for determining the optical density requirements for contemplated exposure conditions. A detailed discussion of safe eye protection was given by Sliney and Wolbarsht (1980).

Specifying Protective Filters

How does one properly specify protective eyewear? The optical density $OD(\lambda)$ of protective filters at a specific wavelength λ is given by the equation

$$OD(\lambda) = \log_{10} \frac{H_0}{MPE} ,$$

where H_0 is the anticipated worst case exposure (expressed usually in units of W/cm^2 for CW sources or J/cm^2 for pulsed sources). The MPE is expressed in units identical to those of H_0 .

As an example, consider a single-pulse Nd:YAG laser operating at a wavelength of 1064 nm with an emergent beam diameter of 2 mm and a beam divergence of 1.0 mrad. The output is a TEM_{00} pulse of 80 mJ delivered in a pulse duration of 15 ns. The MPE is $5 \times 10^{-6} J/cm^2$. The most likely exposure is intrabeam viewing of the raw beam, i.e. $H_{raw} \simeq 2.55 J/cm^2$ (the fluence of the 80 mJ pulse in the 2 mm beam diameter). Since ANSI values of the MPEs are determined using a limiting aperture of 7 mm (maximum pupil size), the value of H_0 for beams smaller than 7 mm should be calculated as though the beam were distributed over the limiting aperture (which is the worst case exposure, since larger beam diameters are focused to smaller spot sizes on the retina), thus

$$H_0 = \frac{80 \text{ mJ}}{\pi (0.35 \text{ cm})^2} \simeq 0.21 \text{ J/cm}^2 .$$

The required optical density would be

$$OD(\lambda) = \log_{10} \frac{0.21}{5 \times 10^{-6}} \simeq 4.6 \quad \text{at} \quad \lambda = 1064 \text{ nm} .$$

Thus, a direct exposure into the eye would require a filter density of nearly 5 to reduce the incident radiant exposure to the “safe” MPE level.

Table 5.3. Simplified method for selecting laser eye protection intrabeam viewing for wavelengths between 400 nm and 1400 nm. Data from American National Standards Institute's (ANSI) Z136.1 (1993)

Q-switched lasers (1 ns to 0.1 ms)		Non-Q-switched lasers (0.4 ms to 10 ms)		Attenuation	
Maximum output energy (J)	Maximum radiant exposure (J/cm ²)	Maximum output energy (J)	Maximum radiant exposure (J/cm ²)	Attenuation factor	OD
10	20	100	200	10 ⁸	8
1	2	10	20	10 ⁷	7
10 ⁻¹	2 × 10 ⁻¹	1	2	10 ⁶	6
10 ⁻²	2 × 10 ⁻²	10 ⁻¹	2 × 10 ⁻¹	10 ⁵	5
10 ⁻³	2 × 10 ⁻³	10 ⁻²	2 × 10 ⁻²	10 ⁴	4
10 ⁻⁴	2 × 10 ⁻⁴	10 ⁻³	2 × 10 ⁻³	10 ³	3
10 ⁻⁵	2 × 10 ⁻⁵	10 ⁻⁴	2 × 10 ⁻⁴	10 ²	2
10 ⁻⁶	2 × 10 ⁻⁶	10 ⁻⁵	2 × 10 ⁻⁵	10 ¹	1

CW lasers momentary (0.25 s to 10 s)		CW lasers long-term staring (greater than 3 hours)		Attenuation	
Maximum output power (W)	Maximum irradiance (W/cm ²)	Maximum output power (W)	Maximum irradiance (W/cm ²)	Attenuation factor	OD
NR	NR	NR	NR	NR	NR
NR	NR	NR	NR	NR	NR
NR	NR	1	2	10 ⁶	6
NR	NR	10 ⁻¹	2 × 10 ⁻¹	10 ⁵	5
10	20	10 ⁻²	2 × 10 ⁻²	10 ⁴	4
1	2	10 ⁻³	2 × 10 ⁻³	10 ³	3
10 ⁻¹	2 × 10 ⁻¹	10 ⁻⁴	2 × 10 ⁻⁴	10 ²	2
10 ⁻²	2 × 10 ⁻²	10 ⁻⁵	2 × 10 ⁻⁵	10 ¹	1

OD: optical density.

NR: not recommended.

5.9 Laser Beam Calculations

Only two laser beam calculations are provided in this section, since these are the most commonly encountered.

The emergent beam diameter is an important parameter in classifying a laser and in evaluating a hazard to the eye or skin. Most laser manufacturers specify output beam power or energy and generally provide the emergent beam diameter. It is often left to the user to calculate the output irradiance (intensity) in units of W/cm^2 and radiant exposure (fluence) in units of J/cm^2 for comparison with protection standards like the MPE values defined by ANSI.

The beam diameter specified by many laser manufacturers is the diameter of an aperture that will just accept 90% of the output energy of a pulsed laser or 87% of the output power of a CW laser having a Gaussian beam (also known as $1/e^2$ points). Regrettably for safety purposes it is necessary to calculate or measure *peak* radiant exposure or irradiance for a large beam diameter, or the fraction of power or energy passing through a specified “limiting aperture”.

For ocular exposure limits in the visible and near infrared (400–1400 nm) spectral region, the limiting aperture is 7 mm corresponding to the dilated pupil. For ultraviolet and most of the infrared spectral regions, this aperture is normally 1 mm or 3.5 mm. Only for the extreme infrared region (0.1–1.0 mm), a limiting aperture of 1 cm is assumed.

Using a laser power meter at two distances z_1 and z_2 with a fixed aperture, one can determine the change in beam radius w to calculate the beam divergence Φ by means of

$$\Phi = \frac{2w(z_2) - 2w(z_1)}{z_2 - z_1} = \frac{2\Delta w}{\Delta z},$$

where w and z are in units of cm, and Φ is in units of radians³.

The other beam calculation concerns the central-beam values of intensity and fluence, since they are usually the highest and thus determine potential hazards. Often, these values are not provided in the specification of a laser. However, if the laser has a Gaussian-shaped beam profile and emits in the fundamental TEM₀₀ mode, the corresponding central-beam values can be obtained from the beam radius $w_{1/e}$ specified at the $1/e$ points. This beam radius is defined as the radius of an aperture that will just accept 63% of the incident power, i.e. $1/e$ of the incident power is blocked.

³ More accurately, the beam radius of a Gaussian beam changes with distance according to a hyperbolic function rather than linearly. When the beam waist occurs at or near the exit port of the laser, the correct equation for the beam radius is $w(z) = \sqrt{w_0^2 + (\Phi/2)^2 z^2}$, where w_0 is the smallest beam waist. Only at distances far apart from the smallest beam waist may w_0 be omitted without loss of accuracy.

The relations for the central-beam intensity I_0 and fluence E_0 can then be expressed by

$$I_0 = \frac{P}{\pi w_{1/e}^2},$$

$$E_0 = \frac{Q}{\pi w_{1/e}^2},$$

where P is the radiant power in units of W, and Q is the radiant energy in units of J.

Often, the beam radius is specified at the $1/e^2$ points rather than at the $1/e$ points, so that the above relations would provide lower values than the central-beam values. In this case, the radius specified at the $1/e^2$ points should be divided by $\sqrt{2}$ to obtain the corresponding $1/e$ value, hence

$$w_{1/e} = \frac{w_{1/e^2}}{\sqrt{2}} \simeq 0.707 w_{1/e^2}.$$

5.10 Questions to Chapter 5

Q5.1. Which is the lowest laser class that always requires the use of safety glasses?

A: Class 2. B: Class 3a. C: Class 3b.

Q5.2. Which radiation is able to burn the fovea?

A: UV-B. B: VIS. C: IR-C.

Q5.3. Which radiation is able to cause skin cancer?

A: UV-B. B: VIS. C: IR-C.

Q5.4. Typical CW lasers in Class 4 have an output power

A: < 0.5 W. B: > 0.5 W. C: > 1 kW.

Q5.5. When comparing the MPE values for eyes and skin, then

A: $MPE_{\text{eye}} < MPE_{\text{skin}}$. B: $MPE_{\text{eye}} = MPE_{\text{skin}}$. C: $MPE_{\text{eye}} > MPE_{\text{skin}}$.

Q5.6. Which are the three basic hazards from laser equipment?

Q5.7. Why is a collinear, visible or near infrared laser beam most dangerous to our vision?

Q5.8. Why is there no ultraviolet or infrared Class 2 laser?

Q5.9. What laser class is a high power 100 W Nd:YAG laser at a wavelength of 1064 nm that is completely enclosed?

Q5.10. An ophthalmologist uses a 200 mW argon ion laser at a wavelength of 514 nm to perform a retinal coagulation. The procedure takes ten seconds. What is the optical density needed in his eyewear to protect his eyes from accidental damage (consider Fig. 5.2)?

A. Appendix

A.1 Medical Neodymium Laser System

Several of the tissue samples shown throughout this book were exposed to a picosecond Nd:YLF laser. Actually, Nd:YLF as well as Nd:YAG lasers are very versatile medical laser systems, since they can be used for inducing almost any type of laser–tissue interaction described in Chap. 3. Plasma-induced ablation and photodisruption are evoked by mode locking of these lasers. Photoablation occurs with their fourth harmonic, i.e. after two times frequency-doubling. Thermal effects are induced under either CW or Q-switched operation. Photochemical effects were also investigated as listed in Table 3.2. Moreover, both Nd:YLF and Nd:YAG lasers are solid-state lasers with several additional advantages for clinical applications, e.g.

- nontoxic laser media,
- low maintenance,
- compactness,
- operation in fundamental laser mode.

For the reasons just stated, a detailed description of the picosecond Nd:YLF laser system is given in this appendix. The other medical lasers mentioned in this book are described elsewhere.

The Nd:YLF laser system discussed below combines short pulse durations with moderate pulse energies and high repetition rates. It is designed as a two stage oscillator/regenerative amplifier combination to provide laser pulses with durations down to 30 ps and energies up to 1 mJ at a wavelength of 1053 nm. This arrangement was developed by Bado et al. (1987). First medical applications were reported by Niemz et al. (1991). A scheme of the complete laser system is shown in Fig. A.1.

The laser crystal in the oscillator is pumped with a temperature tuned 1 watt diode laser (DL) using beam shaping and collimating optics (CO). An acoustooptic mode locker (AOM) is placed near the flat 10 % output coupler (OC). For active amplitude modulation, an amplified 80 MHz RF signal is applied to this device generating a train of short laser pulses with typical durations of 25 ps each as illustrated in Fig. A.2. A real-time autocorrelation system allows for continuous supervision of the pulse width. To select the 1053 nm transition, a Brewster plate polarizer (BP) is added to the cavity.

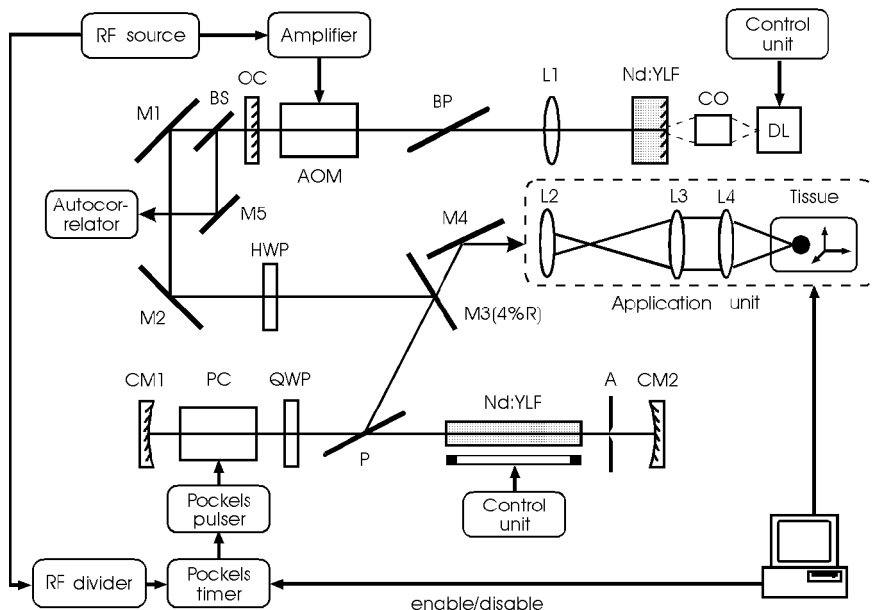


Fig. A.1. Complete picosecond Nd:YLF laser system consisting of laser oscillator (*top part*), regenerative amplifier (*bottom part*), and application unit. Layout according to Niemz (1994a) and Dr. Loesel (Heidelberg)

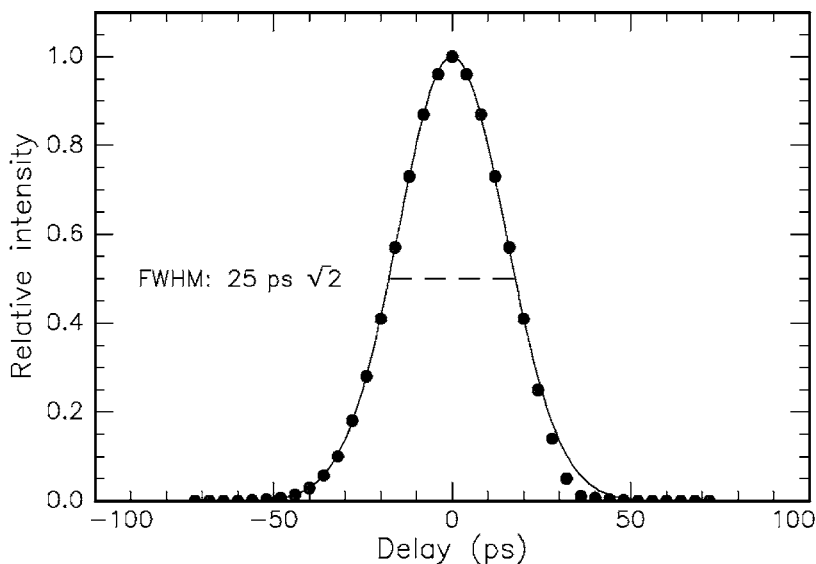


Fig. A.2. Autocorrelation trace and Gaussian fit of a 25 ps pulse

At the half-wave plate (HWP), the 160 MHz pulse train consisting of 0.2 nJ pulses experiences a 90° rotation of the polarization vector. Using a 4% reflecting mirror (M3) and a polarizing beamsplitter (P), the oscillator pulses are then injected into the regenerative amplifier unit. A 76 mm amplifier Nd:YLF rod is pumped with a single xenon lamp controlled by a standard power supply. The cavity employs two highly reflecting mirrors with a radius of curvature of 1 m each. Applying a 2 kV voltage signal at a repetition rate of up to 1 kHz to a LiNbO₃ Pockels cell (PC) provides half-wave retardation per round-trip. In combination with the double-pass half-wave retardation of the intracavity quarter-wave plate (QWP), a selected oscillator pulse is seeded and trapped in the amplifier unit. The driving of the Pockels cell is synchronized to the mode locking process by feeding the 80 MHz RF signal into a special divider and timer logic. After about 100 roundtrips in the cavity, the seeded pulse reaches its saturation limit. At maximum gain, the Pockels cell driver switches back to 0 V causing no retardation. The polarization vector is now rotated by 90° as the pulse double-passes the quarter-wave plate and the Pockels cell in the left part of the cavity. Consequently, the amplified pulse is then reflected at the polarizing beamsplitter and dumped out of the regenerative amplifier as shown in Fig. A.3. By this means, the pulse energy can be boosted up to 1 mJ corresponding to an amplification of 10^6 of the oscillator output energy. Installation of an aperture (A) restricts the laser operation to the fundamental TEM₀₀ mode.

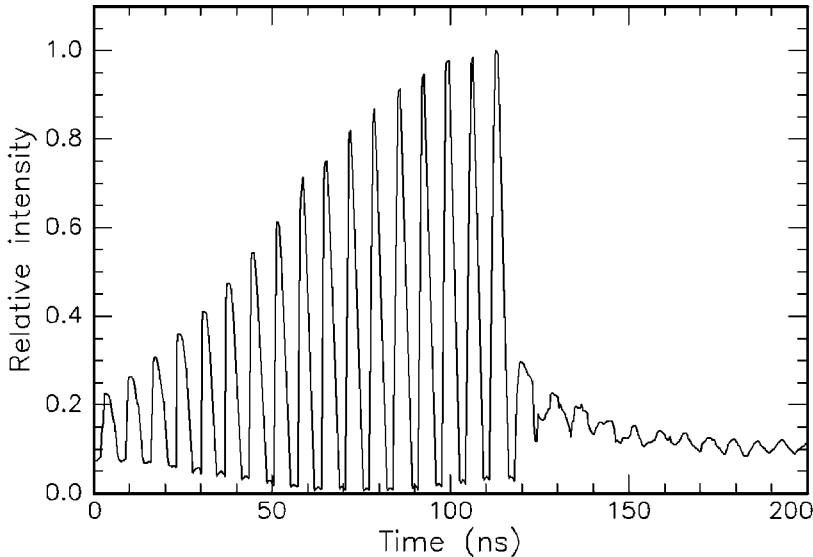


Fig. A.3. Amplification of a seeded pulse inside the regenerative amplifier unit. When reaching the limit of energy saturation, the pulse is dumped out of the cavity

After dumping the pulse out of the regenerative amplifier, mirror M3 is now transmitting 96 % of the amplified pulse energy. Using mirror M4, the pulse train is finally injected into a specially designed application unit as shown in Fig. A.1. Autocorrelation of the amplified pulses yields that their pulse duration slightly increases to about 30 ps due to dispersion inside the amplifier cavity. In Table A.1, the parameters of both laser oscillator and regenerative amplifier are listed.

Table A.1. Parameters of the picosecond Nd:YLF laser system. Data according to Niemz (1991)

Parameter	Laser oscillator	Regenerative amplifier
Wavelength	1053 nm	1053 nm
Pulse energy	0.2 nJ	1 mJ
Pulse duration	25 ps	30 ps
Repetition rate	160 MHz	1 kHz
Mean output power	32 mW	1 W

The application unit basically consists of delivering optics, focusing optics, and a computer controlled three-dimensional translation stage. After expanding the laser beam four times with the lenses L2 and L3, it is tightly focused on the tissue sample with lens L4. The diameter of the focus spot can be measured with the knife edge method. For a dumped beam diameter of 2 mm and a focal length of 50 mm of lens L4, a focal spot of approximately 30 μm is obtained. Stepping motors connected to the translation stage allow precise spot-to-spot movements of the tissue sample at an accuracy of 1 μm . A software package gives the user a choice of different ablation patterns. The motor control software also has the capability of enabling and disabling the dumping mechanism of the Nd:YLF amplifier, thus providing the ability of exact single-shot operation. The optical parameters of the application unit and the focus parameters are summarized in Table A.2.

Table A.2. Parameters of application unit and focus parameters

Parameter	Value
Beam diameter (amplifier output)	2 mm
Focal length of L2	50 mm
Focal length of L3	200 mm
Focal length of L4	50 mm
Diameter of focal spot	30 μm
Peak energy density	140 J/cm ²
Peak power density	4.7 $\times 10^{12}$ W/cm ²

The laser system shown in Fig. A.1 can also be operated using Nd:YAG crystals. Actually, Nd:YLF is a solid-state optical gain medium closely related to Nd:YAG, but without some of its undesirable features. Unlike Nd:YAG, it is only weakly affected by thermal birefringence as reported by Murray (1983). Hence, a simpler cavity design and a higher ratio of TEM₀₀ to multi-mode average power can be achieved according to Pollak et al. (1982). Nd:YLF also has a longer upper-level fluorescence lifetime compared to Nd:YAG which enables greater energy storage and thus higher peak pulse powers under Q-switched or mode locked operation. The physical parameters of both Nd:YLF and Nd:YAG are compared in Table A.3.

Table A.3. Comparison of Nd:YAG and Nd:YLF parameters. Data according to Koechner (1992), Murray (1983), and Dallas (1994)

Parameter	Nd:YAG	Nd:YLF
Chemical formula	Nd:Y ₃ Al ₅ O ₁₂	Nd:LiYF ₄
Wavelength	1064 nm	1053/1047 nm
Bandwidth	140 GHz	420 GHz
Pulse duration (theoretical limit)	7.1 ps	2.4 ps
Fluorescence lifetime	230 μs	480 μs
Cross section (stimulated emission)	$2.8 \times 10^{-19} \text{ cm}^2$	$1.2 - 1.8 \times 10^{-19} \text{ cm}^2$
Thermal conductivity (at 300 K)	$13 \text{ W m}^{-1} \text{ K}^{-1}$	$6 \text{ W m}^{-1} \text{ K}^{-1}$
Thermal lensing ^a	0.12 diopters	< 0.006 diopters

^a Measured at 633 nm for 10 mm rods pumped at 700 W average power.

A.2 Physical Constants and Parameters

In Table A.4, physical constants are listed as they appear in the book.

Table A.4. Physical constants

Quantity	Symbol	Value
Speed of light in vacuum	c	$2.9979 \times 10^8 \text{ m s}^{-1}$
Planck's constant	h	$6.6256 \times 10^{-34} \text{ J s}^{-1}$
Boltzmann's constant	k	$1.38 \times 10^{-23} \text{ J K}^{-1}$
Electron mass	m_e	$9.1091 \times 10^{-31} \text{ kg}$
Gas constant	R	$8.3143 \text{ J K}^{-1} \text{ mol}^{-1}$
Dielectric constant	ϵ_0	$8.854 \times 10^{-12} \text{ As V}^{-1} \text{ m}^{-1}$
Permeability constant	μ_0	$4\pi \cdot 10^{-7} \text{ Vs A}^{-1} \text{ m}^{-1}$

In the literature, the use of radiometric parameters is not always uniform. For the purpose of selecting the appropriate term, a list of all significant parameters and their units¹ is given in Table A.5. The other physical parameters used throughout this book are listed in Table A.6.

Table A.5. Radiometric parameters and units

Parameter	Symbol	Unit
Exposure time	τ	s
Beam radius	w	m
Beam divergence	Φ	–
Wavelength	λ	m
Electromagnetic frequency	ω	Hz
Propagation vector	\mathbf{k}	m^{-1}
Radiant power	P	W
Power density, intensity, irradiance	I	W cm^{-2}
Radiance	J	$\text{W cm}^{-2} \text{sr}^{-1}$
Vector flux	\mathbf{F}	W cm^{-2}
Heat source	S	W cm^{-3}
Radiant energy	Q	J
Energy density, fluence, radiant exposure	E	J cm^{-2}
Energy dose	q	J cm^{-3}
Maximum permissible exposure	MPE	J cm^{-2} or W cm^{-2}
Damage threshold (power density)	I_{th}	W cm^{-2}
Damage threshold (energy density)	E_{th}	J cm^{-2}
Reflectance, transmittance	R_i, T_i	–
Kubelka–Munk coefficients	$A_{\text{KM}}, S_{\text{KM}}$	cm^{-1}
Absorption length	L	cm
Absorption coefficient of tissue	α	cm^{-1}
Absorption coefficient of plasma	α_{pl}	cm^{-1}
Scattering coefficient of tissue	α_{s}	cm^{-1}
Attenuation coefficient of tissue	α_{t}	cm^{-1}
Index of absorption	$\tilde{\alpha}$	–
Albedo	a	–
Optical depth	d	–
Coefficient of anisotropy	g	–
Index of refraction	n	–
Scattering phase function	p	–

¹ While the meter is the preferred unit of length throughout the MKS system, the centimeter is the most commonly used unit of length for power densities, energy densities, and absorption coefficients when dealing with cm-sized tissues.

Table A.6. Nonradiometric parameters and units

Parameter	Symbol	Unit
Arrhenius' constant	A	s^{-1}
Transition probability	A_i	s^{-1}
Magnetic induction	\mathbf{B}	$Vs\ m^{-2}$
Specific heat capacity	c	$J\ kg^{-1}\ K^{-1}$
Ablation depth	d	m
Dielectric induction	\mathbf{D}	$As\ m^{-2}$
Electric field strength	\mathbf{E}	$V\ m^{-1}$
Energy level	E_i	eV
Statistical weight	g_i	–
Magnetic field strength	\mathbf{H}	$A\ m^{-1}$
Electric current	\mathbf{j}	$A\ m^{-2}$
Density of free electric currents	\mathbf{j}_f	$A\ m^{-2}$
Heat flow	\mathbf{j}_Q	$W\ m^{-2}$
Heat conductivity	k	$W\ m^{-1}\ K^{-1}$
Mass	m	kg
Density of free electrons	N	m^{-3}
Pressure	p_i	$N\ m^{-2}$
Heat content	Q	J
Direction vector	\mathbf{s}	–
Time	t	s
Temperature	T	K
Particle speed	u_p	$m\ s^{-1}$
Shock front speed	u_s	$m\ s^{-1}$
Speed of light in medium	v	$m\ s^{-1}$
Coordinates	x, y, z, r	m
Thermal penetration depth	z_{therm}	m
Rate parameter for avalanche ionization	β	s^{-1}
Rate parameter for inelastic collision	γ	$cm^3\ s^{-1}$
Rate parameter for electron diffusion	δ	s^{-1}
Dielectric factor	ϵ	–
Complex dielectric factor	ϵ'	–
Temperature conductivity	κ	$m^2\ s^{-1}$
Relative permeability	μ	–
Collision frequency (electron–ion)	ν_{ei}	Hz
Mass density	ρ	$kg\ m^{-3}$
Particle density	ρ	m^{-3}
Density of free electric charges	ρ_f	$As\ m^{-3}$
Electric conductivity	σ	$A\ V^{-1}\ m^{-1}$
Time constant of inelastic collision	τ_c	s
Time constant of diffusion	τ_d	s
Thermal relaxation time	τ_{therm}	s
Plasma frequency	ω_{pl}	Hz

B. Solutions

The solutions given here are not arranged by chapter. B2.1. is the solution to question Q2.1.

B2.1. A

B3.1. C

B4.1. C

B5.1. B

B2.2. C

B3.2. B

B4.2. C

B5.2. B

B2.3. C

B3.3. A

B4.3. B

B5.3. A

B2.4. A

B3.4. C

B4.4. B

B5.4. B

B2.5. A

B3.5. C

B4.5. C

B5.5. A

B2.6. $R_p \simeq R_s \simeq \left(\frac{1.5-1}{1.5+1}\right)^2 \simeq 4\%$. Since the laser beam is reflected at both glass surfaces, the total loss in intensity is approximately 8%.

B3.6. An appropriate time gap is needed for the photosensitizer to be mostly cleared from healthy tissue, while it is still present in tumor cells at a high concentration.

B4.6. Since the corneal surface after a LASIK treatment is the same natural surface as before the treatment, irritations due to scattering effects are significantly reduced.

B5.6. Laser radiation hazards, chemical hazards, and electrical hazards.

B2.7. $I(1\text{ mm}) = 5\text{ mW} \times \exp(-10\text{ cm}^{-1} \times 0.1\text{ cm}) \simeq 1.8\text{ mW}$.

B3.7. The 1 ms pulse will locally coagulate the tissue, while the 1 ps pulse will not induce a significant effect.

B4.7. Because thermal effects are negligible.

B5.7. Because only visible or near infrared wavelengths are transmitted to the retina, and because a collinear beam is focused to a tiny spot on the retina.

B2.8. $I_s(532 \text{ nm}) \simeq 16 I_s(1064 \text{ nm})$.

B3.8. Because only UV photons provide an energy sufficient for the photodissociation of molecular bonds, which is the basic mechanism of photoablation.

B4.8. The CO_2 laser.

B5.8. Visibility is a mandatory requirement of a Class 2 laser beam, because its definition is based on the normal human aversion response (blinking of the eye), which is available for visible laser beams only.

B2.9. $a = \frac{310 \text{ cm}^{-1}}{2.3 \text{ cm}^{-1} + 310 \text{ cm}^{-1}} \simeq 0.9926$.

B3.9. Avalanche ionization, inelastic collisions, and electron diffusion.

B4.9. By either transurethral ultrasound-guided laser-induced prostatectomy (TULIP), laser-induced interstitial thermotherapy (LITT), or photodynamic therapy (PDT).

B5.9. Class 1.

B2.10. At 60°C , the coagulation of egg white strongly increases its scattering coefficient, thus giving it a white appearance.

B3.10. Both types of interaction are based on the formation of a plasma. The laser pulse energy has to be increased to switch from plasma-induced ablation to photodisruption.

B4.10. A stereotactic ring defines a coordinate system which serves as a valuable means of orientation during surgery.

B5.10. From Fig. 5.2 we find that $\text{MPE} = 10 \text{ mJ/cm}^2$. Hence:

$$H_0 = \frac{200 \text{ mW} \cdot 10 \text{ s}}{\pi (0.35 \text{ cm})^2} \simeq 5200 \text{ mJ/cm}^2 \quad \text{and} \quad \text{OD} = \log_{10} \frac{5200 \text{ mJ/cm}^2}{10 \text{ mJ/cm}^2} \simeq 2.7.$$

Therefore, a filter with an optical density of 3 is required.

References

- Abela, G., Norman, S., Cohen, R., Feldman, R., Geiger, F., Conti, C.R. (1982): Effects of carbon dioxide, Nd-YAG and argon laser radiation on coronary atherosclerotic plaque. *Am. J. Cardiol.* **50**, 1129–1205
- Abergel, R.P., Meeker, C.A., Dwyer, R.M., Lesavoy, M.A. (1984): Nonthermal effects of Nd:YAG laser on biological functions of human skin fibroblast in culture. *Lasers Surg. Med.* **3**, 279–284
- Alora, M.B., Anderson, R.R. (2000): Recent developments in cutaneous lasers. *Lasers Surg. Med.* **26**, 108–118
- Anderson, R.R., Parrish, J.A. (1983): Selective photothermolysis: precise microsurgery by selective absorption of pulsed radiation. *Science* **220**, 524–527
- Andreeva, L.I., Vodop'yanov, K.L., Kaidalov, S.A., Kalinin, Y.M., Karasev, M.E., Kulevskii, L.A., Lukashov, A.V. (1986): Picosecond erbium-doped ErYAG laser ($\lambda = 2.94\mu$) with active mode locking. *Sov. J. Qu. Electron.* **16**, 326–333
- Andrew, J.E., Dyer, P.E., Forster, D., Key, P.H. (1983): Direct etching of polymeric materials using a XeCl laser. *Appl. Phys. Lett.* **43**, 717–719
- Apfelberg, D.B., Maser, M.R., Lash, H. (1978): Argon laser treatment of cutaneous vascular abnormalities: progress report. *Ann. Plast. Surg.* **1**, 14–18
- Apfelberg, D.B., Maser, M.R., Lash, H. (1979a): Extended clinical use of the argon laser for cutaneous lesions. *Arch. Dermatol.* **115**, 719–721
- Apfelberg, D.B., Maser, M.R., Lash, H. (1979b): Argon laser treatment of decorative tattoos. *Br. J. Plast. Surg.* **32**, 141–144
- Aron-Rosa, D., Aron, J., Griesemann, J., Thyzel, R. (1980): Use of the neodymium-YAG laser to open the posterior capsule after lens implant surgery: a preliminary report. *J. Am. Intraocul. Implant Soc.* **6**, 352–354
- Aron-Rosa, D.S., Boerner, C.F., Bath, P., Carre, F., Gross, M., Timsit, J.C., True, L., Hufnagel, T. (1987): Corneal wound healing after laser keratotomy in a human eye. *Am. J. Ophthalmol.* **103**, 454–464
- Arrowsmith, P.N., Marks, R.G. (1988): Four-year update on predictability of radial keratotomy. *J. Refract. Surg.* **4**, 37–45
- Ascher, P.W. (1979): Newest ultrastructural findings after the use of CO₂ laser on CNS tissue. *Acta Neurochirur.* **28**, 572–581
- Ascher, P.W., Heppner, F. (1984): CO₂-Laser in Neurosurgery. *Neurosurg. Rev.* **7**, 123–133
- Ascher, P.W., Justich, E., Schröttner, O. (1991): A new surgical but less invasive treatment of central brain tumours. Preliminary report. *Acta Neurochirur. Suppl.* **52**, 78–80
- Auler, H., Banzer, G. (1942): Untersuchungen über die Rolle der Porphyrine bei geschwulstkranken Menschen und Tieren. *Z. Krebsforsch.* **53**, 65–72
- Austin, G.E., Ratliff, N.B., Hollman, J., Tabei, S., Phillips, D.F. (1985): Intimal proliferation of smooth muscle cells as an explanation for recurrent coronary artery

- stenosis after percutaneous transluminal coronary angioplasty. *J. Am. Coll. Cardiol.* **6**, 369–375
- Bader, M., Dittler, H.J., Ultsch, B., Ries, G., Siewert, J.R. (1986): Palliative treatment of malignant stenoses of the upper gastrointestinal tract using a combination of laser and afterloading therapy. *Endoscopy* **18**, 27–31
- Bado, P., Bouvier, M., Coe, J.S. (1987): Nd:YLF mode-locked oscillator and regenerative amplifier. *Opt. Lett.* **12**, 319–321
- Baggish, M.S. (1980): Carbon dioxide laser treatment for condyloma accuminata venereal infections. *Obstet. Gynecol.* **55**, 711–715
- Baggish, M.S., Dorsey, J. (1981): CO₂-laser for the treatment of vulvar carcinoma in situ. *Obstet. Gynecol.* **57**, 371–375
- Baggish, M.S., Dorsey, J.H., Adelson, M. (1989): A ten-year experience treating cervical intraepithelial neoplasia with the carbon dioxide laser. *Am. J. Obstet. Gynecol.* **161**, 60–68
- Baggish, M.S., Barash, F., Noel, Y., Brooks, M. (1992): Comparison of thermal injury zones in loop electrical and laser cervical excisional conization. *Am. J. Obstet. Gynecol.* **166**, 545–548
- Bailer, P. (1983): Tubensterilisation durch Laser-Koagulation. *Fortschr. Med.* **43**, 1977
- Bailes, J.E., Cozzens, J.W., Hudson, A.R., Kline, D.G., Ciric, I., Gianaris, P., Bernstein, L.P., Hunter, D. (1989): Laser-assisted nerve repair in primates. *J. Neurosurg.* **71**, 266–272
- Barr, H., Bown, S.G., Krasner, N., Boulos, P.B. (1989): Photodynamic therapy for colorectal disease. *Int. J. Colorectal Dis.* **4**, 15–19
- Barr, H., Krasner, N., Boulos, P.B., Chatlani, P., Bown, S.G. (1990): Photodynamic therapy for colorectal cancer: a quantitative pilot study. *Br. J. Surg.* **77**, 93–96
- Barton, T.G., Christ, M., Foth, H.-J., Hörmann, K., Stasche, N. (1995): Ablation of hard tissue with the holmium laser investigated by a surface profile measurement system and a confocal laserscanning microscope. *Proc. SPIE* **2323**, 185–195
- Bastert, G., Wallwiener, D. (1992): Lasers in gynecology – possibilities and limitations. Springer-Verlag, Berlin, Heidelberg, New York
- Beck, O.J. (1980): The use of the Nd-YAG and the CO₂ laser in neurosurgery. *Neurosurg. Rev.* **3**, 261–266
- Beckman, H., Rota, A., Barraco, R., Sugar, H.S., Gaynes, E. (1971): Limbectomies, keratectomies and keratostomies performed with a rapid-pulsed carbon dioxide laser. *Am. J. Ophthalmol.* **72**, 1277–1283
- Beckman, H., Sugar, H.S.: Laser iridectomy therapy of glaucoma. *Arch. Ophthalmol.* **90**, 453–455
- Beisland, H.O., Strandén, E. (1984): Rectal temperature monitoring during neodymium-YAG laser irradiation for prostatic carcinoma. *Urol. Res.* **12**, 257–259
- Bell, C.E., Landt, J.A. (1967): Laser-induced high-pressure shock waves in water. *Appl. Phys. Lett.* **10**, 46–48
- Benson, R.C. (1985): Treatment of diffuse carcinoma in situ by whole bladder hematoporphyrin derivative photodynamic therapy. *J. Urol.* **134**, 675–678
- van Benthem, H. (1992): Laseranwendung in der zahnärztlichen Prothetik und der dentalen Technologie. In: *Laser in der Zahnmedizin* (Eds.: Vahl, J., van Benthem, H.). Quintessenz-Verlag, Berlin
- Berns, M.W., Dahlman, A., Johnson, F., Burns, R., Sperling, D., Guiltinan, M., Siemans, A., Walter, R., Wright, R., Hammer-Wilson, M., Wile, A. (1982): In vitro cellular effects of hematoporphyrin derivative. *Cancer Res.* **42**, 2325–2329
- Berry, S.J., Coffey, D.S., Walsh, P.C., Ewing, L.L. (1984): The development of human benign prostatic hyperplasia with age. *J. Urol.* **132**, 474–479

- Bille, J.F., Dreher, A.W., Zinser, G. (1990): Scanning laser tomography of the living human eye. In: Noninvasive diagnostic techniques in ophthalmology (Ed.: Masters, D.). Springer-Verlag, Berlin, Heidelberg, New York
- Bille, J.F., Schlegel, W., Sturm, V. (1993): Stereotaktische Laser-Neurochirurgie. *Physik in unserer Zeit* **24**, 280–286
- Bird, A.C. (1974): Recent advances in the treatment of senile disciform macular degeneration by photocoagulation. *Br. J. Ophthalmol.* **58**, 367–376
- Bloembergen, N. (1974): Laser-induced electric breakdown in solids. *IEEE J. Qu. Electron.* **QE-10**, 375–386
- Boenninghaus, H.-G. (1980): Hals-Nasen-Ohrenheilkunde. Springer-Verlag, Berlin, Heidelberg, New York
- Böwering, R., Hofstetter, A., Weinberg, W., Kronester, A., Keiditsch, E., Frank, F. (1979): Irradiation of prostatic carcinoma by neodymium-YAG-laser. In: Proc. 3rd Int. Congr. Laser Surgery, Graz (Eds.: Kaplan, I., Ascher, P.W.)
- Boggan, J.E., Edwards, M.S., Davis, R.L., Bolger, C.A., Martin, N. (1982): Comparison of the brain tissue response in rats to injury by argon and carbon dioxide lasers. *Neurosurgery* **11**, 609–616
- Bonney, W.W., Fallon, B., Gerber, W.L., Hawtrey, C.E., Loening, S.A., Narayana, A.S., Platz, C.E., Rose, E.F., Sall, J.C., Schmidt, J.D., Culp, D.A. (1982): Cryosurgery in prostatic cancer: survival. *Urology* **19**, 37–42
- Bores, L.D. (1983): Historical review and clinical results of radial keratotomy. *Int. Ophthalmol. Clin.* **23**, 93–118
- Boulnois, J.-L. (1986): Photophysical processes in recent medical laser developments: a review. *Lasers Med. Sci.* **1**, 47–66
- Boulton, M., Marshall, I. (1986): He-Ne-laser stimulation of human fibroblast proliferation and attachment in vitro. *Lasers Life Sci.* **2**, 125–134
- Bradrick, J.P., Eckhauser, M.L., Indresano, A.T. (1989): Morphologic and histologic changes in canine temporomandibular joint tissues following arthroscopic guided neodymium:YAG laser exposure. *J. Oral Maxillofac. Surg.* **47**, 1177–1181
- Brannon, J.H., Lamkard, J.R., Baise, A.I., Burns, F., Kaufman, J. (1985): Excimer laser etching of polyimide. *J. Appl. Phys.* **58**, 2036–2043
- Brinkmann, R., Koop, N., Dröge, G., Grotehusmann, U., Huber, A., Birngruber, R. (1994): Investigations on laser thermokeratoplasty. *Proc. SPIE* **2079**, 120–130
- Brunner, R., Landthaler, M., Haina, D., Waidelich, W., Braun-Falco, O. (1984): Experimentelle Untersuchungen zum Einfluß von Laserlicht niedriger Leistungsdichte auf die Epidermisregeneration. In: *Optoelektronik in der Medizin* (Ed.: Waidelich, W.), Springer-Verlag, Berlin, Heidelberg, New York
- Campbell, C.J., Rittler, M.C., Koester, C.J. (1963): The optical maser as a retinal coagulator: an evaluation. *Am. Acad. Ophthalmol. Otolaryngol.* **67**, 58
- Camps, J.L., Powers, S.K., Beckman, W.C., Brown, J.T., Weissmann, R.M. (1985): Photodynamic therapy of prostate cancer: an in vitro study. *J. Urol.* **134**, 1222–1226
- Carome, E.F., Moeller, C.E., Clark, N.A. (1966): Intense ruby-laser-induced acoustic impulse in liquids. *J. Acoust. Soc. Am.* **40**, 1462–1466
- Carrillo, J.S., Calatayud, J., Manso, F.J., Barberia, E., Martinez, J.M., Donado, M. (1990): A randomized double-blind clinical trial on effectiveness of helium-neon laser in the prevention of pain, swelling and trismus after removal of impacted third molars. *Int. Dent. J.* **40**, 31–36
- Castro, D.J., Abergel, R.P., Meeker, C., Dwyer, R.M., Lesavoy, M.A., Uitto, J. (1983): Effects of the Nd:YAG laser on DNA synthesis and collagen production in human skin fibroblast cultures. *Ann. Plast. Surg.* **11**, 214–222
- Charlton, A., Dickinson, M.R., King, T.A., Freemont, A.J. (1990): Erbium:YAG and holmium:YAG laser ablations of bones. *Lasers Med. Sci.* **5**, 365–373

- Cheong, W.-F., Motamedi, M., Welch, A.J. (1987): Optical modeling of laser photocoagulation of bladder tissue. *Lasers Surg. Med.* **7**, 72
- Cheong, W.-F., Prahl, S.A., Welch, A.J. (1990): A review of the optical properties of biological tissues. *IEEE J. Qu. Electron.* **QE-26**, 2166–2185
- Cho, B.-Y., Cho, J.O. (1986): Experimental study of the effect of the laser irradiation in treating oral soft tissue damage. *J. Dent. Res.* **65**, 600 (A34)
- Choy, D.S.J., Stertzer, S.H., Rotterdam, H.Z., Bruno, M.S. (1982): Laser coronary angioplasty; experience with 9 cadaver hearts. *Am. J. Cardiol.* **50**, 1209–1211
- Choy, D.S.J., Stertzer, S.H., Myler, R.K., Marco, J., Fournial, G. (1984): Human coronary laser recanalization. *Clin. Cardiol.* **7**, 377–381
- Christ, M., Barton, T.G., Hörmann, K., Foth, H.-J., Stasche, N. (1995): A new approach to determining laser effects on bone. *Proc. SPIE* **2327**, 394–401
- Cilesiz, I.F., Welch, A.J. (1993): Light dosimetry: effects of dehydration and thermal damage on the optical properties of the human aorta. *Appl. Opt.* **32**, 477–487
- Clayman, L., Fuller, T., Beckman, H. (1978): Healing of continuous-wave and rapid superpulsed carbon dioxide laser-induced bone defects. *J. Oral Maxillofac. Surg.* **36**, 932–937
- Coker, N.J., Ator, G.A., Jenklins, H.A., Neblett, C.R. (1986): Carbon dioxide laser stapedotomy: a histology study. *Am. J. Otolaryngol.* **7**, 253–257
- Corson, S.L., Unger, M., Kwa, D., Batzer, F.R., Gocial, B. (1989): Laparoscopic laser treatment of endometriosis with the Nd:YAG sapphire probe. *Am. J. Obstet. Gynecol.* **160**, 718–723
- Cotlair, A.M., Schubert, H.D., Mandek, E.R., Trokel, S.L. (1985): Excimer laser radial keratotomy. *Ophthalmology* **92**, 206–208
- Cubeddu, R., Sozzi, C., Taroni, P., Valentini, G., Bottirollo, G., Croce, A.C. (1994): Ablation of brain by Erbium laser: study of dynamic behavior and tissue damage. *Proc. SPIE* **2077**, 13–20
- Cumberland, D.C., Sanborn, T.A., Taylor, D.I., Moore, D.J., Welsh, C.L., Greenfield, A.J., Guben, J.K., Ryan, T.J. (1986): Percutaneous laser thermal angioplasty. *Lancet* **1**, 1457–1459
- Dallas, J.L. (1994): Frequency-modulation mode-locking performance for four Nd³⁺-doped laser crystals. *Appl. Opt.* **33**, 6373–6376
- De Lia, J.E., Kuhlmann, R.S., Harstad, T.W., Cruikshank, D.P. (1995): Fetoscopic laser ablation of placental vessels in severe previable twin-twin transfusion syndrome. *Am. J. Obstet. Gynecol.* **172**, 1202–1211
- Derbyshire, G.J., Bogen, D.K., Unger, M. (1990): Thermally induced optical property changes in myocardium at 1.06 μm . *Lasers Surg. Med.* **10**, 28–34
- Deutsch, T.F., Geis, M.W. (1983): Self-developing UV photoresist using excimer laser exposure. *J. Appl. Phys.* **54**, 7201–7204
- Diethrich, E.B., Timbadia, E., Bahadir, I., Coburn, K., Zenzen, S. (1988): Argon laser-assisted peripheral angioplasty. *Vasc. Surg.* **22**, 77–87
- Dixon, J.A., Gilbertson, J.J. (1986): Argon and neodymium YAG laser therapy of dark nodular port wine stains in older patients. *Lasers Surg. Med.* **6**, 5–11
- Dobberstein, H., Dobberstein, H., Zuhrt, R., Thierfelder, C., Ertl, T. (1991): Laserbearbeitung von Dentalkeramik und Dentallegierungen. In: *Angewandte Lasermedizin* (Eds.: Berlien, H.-P., Müller, G.). Ecomed-Verlag, Landsberg
- Docchio, F., Sacchi, C.A., Marshall, J. (1986): Experimental investigation of optical breakdown thresholds in ocular media under single pulse irradiation with different pulse durations. *Lasers Ophthalmol.* **1**, 83–93
- Docchio, F., Regondi, P., Capon, M.R.C., Mellerio, J. (1988a): Study of the temporal and spatial dynamics of plasmas induced in liquids by nanosecond Nd:YAG laser pulses. 1: Analysis of the plasma starting times. *Appl. Opt.* **27**, 3661–3668

- Docchio, F., Regondi, P., Capon, M.R.C., Mellerio, J. (1988b): Study of the temporal and spatial dynamics of plasmas induced in liquids by nanosecond Nd:YAG laser pulses. 2: Plasma luminescence and shielding. *Appl. Opt.* **27**, 3669–3674
- Dolphin, D. (1979): *The porphyrins I–VII*. Academic Press, New York
- Dörschel, K., Berlien, H.-P., Brodzinski, T., Helfmann, J., Müller, G.J., Scholz, C. (1988): Primary results in the laser lithotripsy using a frequency doubled Q-switched Nd:YAG laser. In: *Laser lithotripsy – clinical use and technical aspects* (Ed.: Steiner, R.). Springer-Verlag, Berlin, Heidelberg, New York
- Dorsey, J.H., Diggs, E.S. (1979): Microsurgical conization of the cervix by carbon dioxide laser. *Obstet. Gynecol.* **54**, 565–570
- Dotter, C.T., Judkins, M.P. (1964): Transluminal treatment of arteriosclerotic obstruction: description of a new technique and a preliminary report of its application. *Circulation* **30**, 654–670
- Doukas, A.G., Zweig, A.D., Frisoli, J.K., Birngruber, R., Deutsch, T.F. (1991): Non-invasive determination of shock wave pressure generated by optical breakdown. *Appl. Phys.* **B 53**, 237–245
- Dretler, S.P. (1988): Laser lithotripsy: a review of 20 years of research and clinical applications. *Lasers Surg. Med.* **8**, 341–356
- Du, D., Liu, X., Korn, G., Squier, J., Mourou, G. (1994): Laser-induced breakdown by impact ionization in SiO₂ with pulse widths from 7 ns to 150 fs. *Appl. Phys. Lett.* **64**, 3071–3073
- Dumon, J.F., Reboud, E., Garbe, L., Aucomte, F., Meric, B. (1982): Treatment of tracheobronchial lesions by laser photoresection. *Chest* **81**, 278–284
- Duncavage, J.A., Ossoff, R.H., Toohill, R.J. (1985): Carbon dioxide laser management of laryngeal stenosis. *Ann. Otol. Rhinol. Laryngol.* **94**, 565–569
- Dyson, M., Young, S. (1986): Effect of laser therapy on wound contraction and cellularity in mice. *Lasers Med. Sci.* **1**, 125–130
- Ebeling, K.J. (1978): Zum Verhalten kugelförmiger, lasererzeugter Kavitationsblasen in Wasser. *Acustica* **40**, 229–239
- Eichler, J., Seiler, T. (1991): *Lasertechnik in der Medizin*. Springer-Verlag, Berlin, Heidelberg, New York
- Eichler, H.J., Albertz, J., Below, F., Kummrow, A., Leitert, T., Kaminskii, A.A., Jakab, L. (1992): Acousto-optic mode locking of 3- μ m Er lasers. *Appl. Opt.* **31**, 4909–4911
- Epifanov, A.S. (1981): Theory of electron-avalanche ionization induced in solids by electromagnetic waves. *IEEE J. Qu. Electron.* **QE-17**, 2018–2022
- L'Esperance, F. (1983): *Laser trabeculosclerostomy in ophthalmic lasers: photocoagulation, photoradiation, and surgery*. C.V.Mosby Co., St. Louis
- L'Esperance, F.A., Warner, J.W., Telfair, W.B., Yoder, P.R., Martin, C.A. (1989): Excimer laser instrumentation and technique for human corneal surgery. *Arch. Ophthalmol.* **107**, 131–139
- Eyrich, G.K., Bruder, E., Hilfiker, P., Dubno, B., Quick, H.H., Patak, M.A., Gratz, K.W., Sailer, H.F. (2000): Temperature mapping of magnetic resonance-guided laser interstitial thermal therapy (LITT) in lymphangiomas of the head and neck. *Lasers Surg. Med.* **26**, 467–476
- Fankhauser, F., Roussel, P., Steffen, J., van der Zypen, E., Chrenkova, A. (1981): Clinical studies on the efficiency of high power laser radiation upon some structures of the anterior segment of the eye. *Int. Ophthalmol.* **3**, 129–139
- Fantes, F.E., Waring, G.O. (1989): Effect of excimer laser radiant exposure on uniformity of ablated corneal surface. *Lasers Surg. Med.* **9**, 533–542
- Farah, S.G., Azar, D.T., Gurdal, C., Wong, J. (1998): Laser in situ keratomileusis: literature review of a developing technique. *J. Cataract Refract. Surg.* **24**, 989–1006

- Fasano, V.A. (1981): Treatment of vascular malformations of the brain with laser source. *Lasers Surg. Med.* **1**, 347–356
- Fasano, V.A., Urciuoli, R., Ponzio, R.M. (1982): Photocoagulation of cerebral arteriovenous malformations and arterial aneurysms with Nd:YAG and argon laser. *Neurosurgery* **11**, 754–760
- Felix, M.P., Ellis, A.T. (1971): Laser-induced liquid breakdown – a step-by-step account. *Appl. Phys. Lett.* **19**, 484–486
- Feste, J.R. (1985): Laser laparoscopy: a new modality. *J. Reprod. Med.* **30**, 414–417
- Feyh, J., Goetz, A., Müller, W., Königsberger, R., Kastenbauer, E. (1990): Photodynamic therapy in head and neck surgery. *J. Photochem. Photobiol.* **7**, 353–358
- Firey, P.A., Rodgers, M.A.J. (1987): Photoproperties of a silicon naphthalocyanine: a potential photosensitizer for PDT. *Photochem. Photobiol.* **45**, 535–538
- Fischer, J.P., Dams, J., Götz, M.H., Kerker, E., Loesel, F.H., Messer, C.J., Niemz, M.H., Suhm, N., Bille, J.F. (1994): Plasma-mediated ablation of brain tissue with picosecond laser pulses. *Appl. Phys.* **B 58**, 493–499
- Fjodorov, S.N., Durnev, V.V. (1979): Operation of dosaged dissection of corneal circular ligament in cases of myopia of a mild degree. *Ann. Ophthalmol.* **11**, 1885–1890
- Fleischer, D., Kessler, F., Haye, O. (1982): Endoscopic Nd:YAG laser therapy for carcinoma of the esophagus: a new palliative approach. *Am. J. Surg.* **143**, 280–283
- Fleischer, D., Sivak, M.V. (1985): Endoscopic Nd:YAG laser therapy as palliation for esophagogastric cancer. *Gastroenterology* **89**, 827–831
- Foote, C.S. (1968): Mechanisms of photosensitized oxidation. *Science* **162**, 963–970
- Forrer, M., Frenz, M., Romano, V., Altermatt, H.J., Weber, H.P., Silenok, A., Istomyn, M., Konov, V.I. (1993): Bone-ablation mechanism using CO₂ lasers of different pulse duration and wavelength. *Appl. Phys.* **B 56**, 104–112
- Fradin, D.W., Bloembergen, N., Letellier, J.P. (1973a): Dependence of laser-induced breakdown field strength on pulse duration. *Appl. Phys. Lett.* **22**, 635–637
- Fradin, D.W., Yablonovitch, E., Bass, M. (1973b): Confirmation of an electron avalanche causing laser-induced bulk damage at 1.06 μm . *Appl. Opt.* **12**, 700–709
- Frame, J.W., Das Gupta, A.R., Dalton, G.A., Rhys Evans, P.H. (1984): Use of the carbon dioxide laser in the management of premalignant lesions of the oral mucosa. *J. Laryngol. Otol.* **98**, 1251–1260
- Frame, J.W. (1985): Carbon dioxide laser surgery for benign oral lesions. *Br. Dent. J.* **158**, 125–128
- Frank, F., Keiditsch, E., Hofstetter, A., Pensel, J., Rothenberger, K. (1982): Various effects of the CO₂-, the neodymium-YAG-, and the argon-laser irradiation on bladder tissue. *Lasers Surg. Med.* **2**, 89–96
- Frentzen, M., Koort, H.-J., Kermani, O., Dardenne, M.U. (1989): Bearbeitung von Zahnhartgeweben mit einem Excimer-Laser – eine in-vitro Studie. *Dtsch. Zahnärztl. Z.* **44**, 431–435
- Frentzen, M., Koort, H.-J. (1990): Lasers in dentistry. *Int. Dent. J.* **40**, 323–332
- Frentzen, M., Koort, H.-J. (1991): Lasertechnik in der Zahnheilkunde. *Dtsch. Zahnärztl. Z.* **46**, 443–454
- Frentzen, M., Koort, H.-J. (1992): Excimer Laser – Grundlagen und mögliche Anwendungen in der Zahnheilkunde. In: *Laser in der Zahnmedizin* (Eds.: Vahl, J., van Benthem, H.). Quintessenz-Verlag, Berlin, Chicago, London
- Frentzen, M., Winkelsträter, C., van Benthem, H., Koort, H.-J. (1994): Bearbeitung der Schmelzoberflächen mit gepulster Laserstrahlung. *Dtsch. Zahnärztl. Z.* **49**, 166–168

- Frenz, M., Romano, V., Pratisto, H., Weber, H.P., Altermatt, H.J., Delix, D., Grossenbacher, R. (1994): Stapedotomie: neue experimentelle Resultate mit dem Erbium-Laser. In: Aktuelle Probleme der Otorhinolaryngologie **ORL** **17** (Ed.: Sopko, J.). Verlag Huber AG, Bern
- Fujikawa, S., Akamatsu, T. (1980): Effects of the non-equilibrium condensation of vapour on the pressure wave produced by the collapse of a bubble in a liquid. *J. Fluid Mech.* **97**, 481–512
- Fung, Y.C. (1981): Biomechanics: mechanical properties of living tissue. Springer-Verlag, Berlin, Heidelberg, New York
- Gantz, B.J., Jenkins, H.A., Kishimoto, S., Fish, U. (1982): Argon laser stapedotomy. *Ann. Otol.* **91**, 25–26
- Garden, J.M., Polla, L.L., Tan, O.T. (1988): The treatment of port-wine stains by the pulsed dye laser. *Arch. Dermatol.* **124**, 889–896
- Garrison, B.J., Srinivasan, R. (1985): Laser ablation of organic polymers: microscopic models for photochemical and thermal processes. *J. Appl. Phys.* **57**, 2909–2914
- Gasset, A.R., Kaufman, H.E. (1975): Thermokeratoplasty in the treatment of keratoconus. *Am. J. Ophthalmol.* **79**, 226–232
- van Gemert, M.J.C., Welch, A.J., Star, W.M., Motamedi, M., Cheong, W.F. (1987): Tissue optics for a slab geometry in the diffusion approximation. *Lasers Med. Sci.* **2**, 295–302
- van Gemert, M.J.C., Welch, A.J. (1989): Time constants in thermal laser medicine. *Lasers Surg. Med.* **9**, 405–421
- van Gemert, M.J.C., Prah, S.A., Welch, A.S. (1990): Lichtausbreitung und Streuung in trüben Medien. In: *Angewandte Lasermedizin* (Eds.: Berlien, H.-P., Müller, G.), Ecomed-Verlag, Landsberg
- van Gemert, M.J.C., Welch, A.J., Pickering, J.W., Tan, O.T., Gijsbers, G.H. (1995): Wavelengths for laser treatment of port wine stains and telangiectasia. *Lasers Surg. Med.* **16**, 147–155
- Gertzbein, S.D., de Demeter, D., Cruickshank, B., Kapasouri, A. (1981): The effect of laser-osteotomy on bone healing. *Lasers Surg. Med.* **1**, 361–373
- Ginsburg, R., Wexler, L., Mitchell, R.S., Profitt, D. (1985): Percutaneous transluminal laser angioplasty for treatment of peripheral vascular disease. *Radiology* **156**, 619–624
- Glick, J. (1981): YAG-laser meniscectomy. *Proc. Triannual Meeting Int. Arthrosc. Assoc.*, Rio de Janeiro.
- Goebel, D.G. (1967): Generalized integrating-sphere theory. *Appl. Opt.* **6**, 125–128
- Goldman, L., Hornby, P., Mayer, R., Goldman, B. (1964): Impact of the laser on dental caries. *Nature* **203**, 417
- Gonzales, C., van de Merwe, W.P., Smith, M., Reinisch, L. (1990): Comparison of the erbium-yttrium aluminium garnet and carbon dioxide lasers for in vitro bone and cartilage ablation. *Laryngoscope* **100**, 14–17
- Gossner, L., Ell, C. (1993): Photodynamische Therapie in der Gastroenterologie. In: *Angewandte Lasermedizin* (Eds.: Berlien, H.-P., Müller, G.). Ecomed-Verlag, Landsberg
- Gossner, L., Borrmann, J., Ernst, H., Sroka, R., Hahn, E.G., Ell, C. (1994): Photodynamische Therapie. *Lasermedizin* **10**, 183–189
- Graaff, R., Koelink, M.H., de Mul, F.F.M., Zijlstra, W.G., Dassel, A.C.M., Aarnoudse, J.G. (1993a): Condensed Monte Carlo simulations for the description of light transport. *Appl. Opt.* **32**, 426–434
- Graaff, R., Dassel, A.C.M., Koelink, M.H., de Mul, F.F.M., Aarnoudse, J.G., Zijlstra, W.G. (1993b): Optical properties of human dermis in vitro and in vivo. *Appl. Opt.* **32**, 435–447

- Le Grand, Y., El Hage, S.G. (1980): *Physiological optics*. Springer-Verlag, Berlin, Heidelberg, New York
- Green, H., Boll, J., Parrish, J.A., Kochevar, I.E., Oseroff, A.R. (1987): Cytotoxicity and mutagenicity of low intensity, 248 and 193 nm excimer laser radiation in mammalian cells. *Canc. Res.* **47**, 410–413
- Griem, H.R. (1964): *Plasma spectroscopy*. McGraw-Hill, New York
- Groenhuis, R.A.J., Ferwerda, H.A., Ten Bosch, J.J. (1983): Scattering and absorption of turbid materials determined from reflection measurements. *Appl. Opt.* **22**, 2456–2462
- Grundfest, W.S., Litvack, F., Forrester, J.S., Goldenberg, T., Swan, H.J.C., Morgenstern, L., Fishbein, M., McDermid, S., Rider, D.M., Pacala, T.J., Laudenslager, J.B. (1985): Laser ablation of human atherosclerotic plaque without adjacent tissue injury. *J. Am. Coll. Cardiol.* **5**, 929–933
- Grüntzig, A. (1978): Transluminal dilatation of coronary-artery stenosis. *Lancet* **1**, 263
- Grüntzig, A.R., Senning, A., Siegenthaler, W.E. (1979): Nonoperative dilatation of coronary stenosis. *N. Engl. J. Med.* **301**, 61–68
- Grüntzig, A.R., Meier, B. (1983): Percutaneous transluminal coronary angioplasty. The first five years and the future. *Int. J. Cardiol.* **2**, 319–323
- Haina, D., Seipp, W., Landthaler, M., Waidelich, W. (1988): Improvement of therapy results in treatment of port wine stains with the argonlaser. *Proc. LASER'87*. Springer-Verlag, Berlin, Heidelberg, New York
- Hale, G.M., Querry, M.R. (1973): Optical constants of water in the 200-nm to 200- μ m wavelength region. *Appl. Opt.* **12**, 555–563
- Halldorsson, T., Langerholm, J. (1978): Thermodynamic analysis of laser irradiation of biological tissue. *Appl. Opt.* **17**, 3948–3958
- Hanke, H., Haase, K.K., Hanke, S., Oberhoff, M., Hassenstein, S., Betz, E., Karsch, K.R. (1991): Morphological changes and smooth muscle cell proliferation after experimental excimer laser treatment. *Circulation* **83**, 1380–1389
- Hanna, K.D., Chastang, J.C., Pouliquen, Y., Renard, G., Asfar, L., Waring, G.O. (1988): Excimer laser keratotomy for myopia with a rotating-slit delivery system. *Arch. Ophthalmol.* **106**, 245–250
- Hanna, K.D., Jouve, F.E., Waring, G.O. (1989a): Preliminary computer simulation of the effects of radial keratotomy. *Arch. Ophthalmol.* **107**, 911–918
- Hanna, K.D., Chastang, J.C., Asfar, L., Samson, J., Pouliquen, Y., Waring, G.O. (1989b): Scanning slit delivery system. *J. Cataract Refract. Surg.* **15**, 390–396
- Harty, J.I., Amin, M., Wieman, T.J., Tseng, M.T., Ackerman, D., Broghamer, W. (1989): Complications of whole bladder dihematoporphyrin ether photodynamic therapy. *J. Urol.* **141**, 1341–1346
- Hassenstein, S., Hanke, H., Kamenz, J., Oberhoff, M., Hanke, S., Rießen, R., Haase, K.K., Betz, E., Karsch, K.R. (1992): Vascular injury and time course of smooth muscle cell proliferation after experimental holmium laser angioplasty. *Circulation* **86**, 1575–1583
- Hayata, Y., Kato, H., Konaka, C., Ono, J., Takizawa, N. (1982): Hematoporphyrin derivative and laser photoradiation in the treatment of lung cancer. *Chest* **81**, 269–277
- Hayes, J.R., Wolbarsht, M.L. (1968): Thermal model for retinal damage induced by pulsed lasers. *Aerospace Med.* **39**, 474–480
- Heckmann, U. (1992): CO₂-laser excisional conization: five years experience treating cervical intraepithelial neoplasia. In: *Lasers in gynecology* (Eds.: Bastert, G., Wallwiener, D.). Springer-Verlag, Berlin, Heidelberg, New York

- Hennighausen, H., Bille, J.F. (1995): Computer simulation of corneal curvature change caused by intrastromal ablation using a pico-second lasersystem. *Proc. SPIE* **2330**, 5–13
- Henriques, F.C. (1947): Studies of thermal injury. V: The predictability and the significance of thermally induced rate processes leading to irreversible epidermal injury. *Am. J. Pathol.* **23**, 489–502
- Heney, L., Greenstein, J. (1941): Diffuse radiation in the galaxy. *Astrophys. J.* **93**, 70–83
- Hering, P. (1987): Limits of optical fiber systems for pulsed lasers. In: *Laser lithotripsy – clinical use and technical aspects* (Ed.: Steiner, R.). Springer-Verlag, Berlin, Heidelberg, New York
- Hessel, S., Frank, F. (1990): Technical prerequisites for the interstitial thermotherapy using the Nd:YAG laser. *Proc. SPIE* **1201**, 233–238
- Hetzel, M.R., Nixon, C., Edmondstone, W.M., Mitchell, D.M., Millard, F.J., Nanson, E.M., Woodcock, A.A., Bridges, C.E., Humberstone, A.M. (1985): Laser therapy in 100 tracheobronchial tumours. *Thorax* **40**, 341–345
- Hibst, R., Keller, U. (1989): Experimental studies of the application of the Er:YAG laser on dental hard substances: I. Measurement of the ablation rate. *Lasers Surg. Med.* **9**, 338–344
- Hibst, R., Keller, U. (1991): Removal of dental filling materials by Er:YAG laser radiation. *Proc. SPIE* **1200**, 120–126
- Hofmann, R., Hartung, R. (1987): Clinical experience with laser-induced shock wave lithotripsy. In: *Laser lithotripsy – clinical use and technical aspects* (Ed.: Steiner, R.). Springer-Verlag, Berlin, Heidelberg, New York
- Hofstetter, A., Böwering, R., Frank, F., Keiditsch, E., Pensel, J., Rothenberger, K.H., Staehler, G. (1980): Laserbehandlung von Blasen-tumoren. *Dtsch. Med. Wochenschr.* **105**, 1442–1444
- Hofstetter, A., Schmeller, N., Pensel, J., Arnholdt, H., Frank, F., Wondrazek, F. (1986): Harnstein-Lithotripsy mit laserinduzierten Stoßwellen. *Fortschr. Med.* **104**, 654–656
- Hofstetter, A., Pensel, J. (1993): Der Laser in der Urologie. In: *Angewandte Lasermedizin* (Eds.: Berlien, H.-P., Müller, G.). Ecomed-Verlag, Landsberg
- Höh, H. (1990): Neodymium:YAG laser keratotomy. A new method of refractive surgery. *Ann. Inst. Barraquer* **21**, 23–27
- Hohenberger, W., Altendorf, A., Hermanek, P., Gall, F.P. (1986): The laser in gastroenterology: malignant tumors in the lower gastrointestinal tract – therapeutic alternatives. *Endoscopy* **18**, 47–52
- Holinger, L.D. (1982): Treatment of severe subglottic stenosis without tracheotomy: a preliminary report. *Ann. Otol. Rhinol. Laryngol.* **91**, 407–412
- Hombach, V., Waltenberger, J., Voisard, R., Höher, M. (1995): Rezidivstenose nach Koronarangioplastie. *Z. Kardiol.* **84**, 5–21
- Horch, H.-H., Gerlach, K.L. (1982): CO₂ laser treatment of oral dysplastic precancerous lesions: a preliminary report. *Lasers Surg. Med.* **2**, 179–185
- Horch, H.-H. (1992): Laser in der Mund-Kiefer-Gesichts-Chirurgie. In: *Laser in der Zahnmedizin* (Eds.: Vahl, J., van Benthem, H.). Quintessenz-Verlag, Berlin, Chicago, London
- Horvath, K.A., Smith, W.J., Laurence, R.G., Schoen, F.J., Appleyard, R.F., Cohn, L.H. (1995): Recovery and viability of an acute myocardial infarct after transmyocardial laser revascularization. *J. Am. Coll. Cardiol.* **25**, 258–263
- Householder, J., Horwitz, L.S., Lowe, K., Murillo, A. (1989): Laser induced keratoplasty. *Proc. SPIE* **1066**, 18–23
- Höwener, G. (1980): Photokoagulation bei Retinopathia diabetica proliferans. *Klin. Mbl. Augenheilk.* **176**, 938–949

- Huber, J., Hosmann, J., Vytiska-Binstorfer, E. (1989): Laparoscopic surgery for tubal pregnancies utilizing laser. *Int. J. Gynecol. Obstet.* **29**, 153–157
- van de Hulst, H.C. (1957): *Light scattering by small particles*. Wiley & Sons, New York
- van de Hulst, H.C. (1962): A new look at multiple scattering. Tech. Report, NASA Institute for Space Studies, New York
- Hunter, J., Leonard, L., Wilson, R., Snider, G., Dixon, J. (1984): Effects of low energy laser on wound healing in a porcine model. *Lasers Surg. Med.* **3**, 285–290
- Hussein, H. (1986): A novel fiberoptic laserprobe for treatment of occlusive vessel disease. *Proc. SPIE* **605**, 59–66
- Ishimaru, A. (1978): *Wave propagation and scattering in random media*. Academic Press, New York
- Ishimaru, A., Yeh, C. (1984): Matrix representations of the vector-radiative transfer theory for randomly distributed non-spherical particles. *J. Opt. Soc. Am.* **A 1**, 359–364
- Ishimaru, A. (1989): Diffusion of light in turbid media. *Appl. Opt.* **28**, 2210–2215
- Ith, M., Pratisto, H., Altermatt, H.J., Frenz, M., Weber, H.P. (1994): Dynamics of laser-induced channel formation in water and influence of pulse duration on the ablation of biotissue under water with pulsed erbium-laser radiation. *Appl. Phys.* **B 59**, 621–629
- Izatt, J.A., Sankey, N.D., Partovi, F., Fitzmaurice, M., Rava, R.P., Itzkan, I., Feld, M.S. (1990): Ablation of calcified biological tissue using pulsed hydrogen fluoride laser radiation. *IEEE J. Qu. Electron.* **QE-26**, 2261–2270
- Jacques, S.L., Prahl, S.A. (1987a): Modeling optical and thermal distributions in tissue during laser irradiation. *Lasers Surg. Med.* **6**, 494–503
- Jacques, S.L., Alter, C.A., Prahl, S.A. (1987b): Angular dependence of HeNe laser light scattering by human dermis. *Lasers Life Sci.* **1**, 309–333
- Jacquez, J.A., Kuppenheim, H.F. (1955): Theory of the integrating sphere. *J. Opt. Soc. Am.* **45**, 460–470
- Jain, K.K. (1980): Sutureless microvascular anastomosis using a neodymium-yag laser. *J. Microsurg.* **1**, 436–439
- Jain, K.K. (1983): *Handbook of laser neurosurgery*. Charles Thomas Publications, Springfield
- Jain, K.K. (1984a): Sutureless extra-intracranial anastomosis by laser. *Lancet* **2**, 816–817
- Jain, K.K. (1984b): Current status of laser applications in neurosurgery. *IEEE J. Qu. Electron.* **QE-20**, 1401–1406
- Jako, G.J. (1972): Laser surgery of the vocal cords. An experimental study with carbon dioxide lasers on dogs. *Laryngoscope* **82**, 2204–2216
- Johnson, F.H., Eyring, H., Stover, B.J. (1974): *The theory of rate processes in biology and medicine*. Wiley & Sons, New York
- Johnson, D.E., Price, R.E., Cromeens, D.M. (1992): Pathologic changes occurring in the prostate following transurethral laser prostatectomy. *Lasers Surg. Med.* **12**, 254–263
- Jongsma, F., Bogaard, A., van Gemert, M., Hennig, J. (1983): Is closure of open skin wounds in rats accelerated by argon laser exposure? *Lasers Surg. Med.* **3**, 75–80
- Joseph, J.H., Wiscombe, W.J., Weinman, J.A. (1976): The delta-Eddington approximation for radiative flux transfer. *J. Atmos. Sci.* **33**, 2452–2459
- Jue, B., Maurice, D.M. (1989): The mechanical properties of the rabbit and human cornea. *J. Biomech.* **19**, 847–853
- Kaplan, I., Giler, S. (1984): *CO₂ laser surgery*. Springer-Verlag, Berlin, Heidelberg, New York

- Karanov, S., Shopova, M., Getov, H. (1991): Photodynamic therapy in gastrointestinal tumors. *Lasers Surg. Med.* **11**, 395–398
- Karsch, K.R., Haase, K.K., Mauser, M., Ickrath, O., Voelker, W., Duda, S., Seipel, L. (1989): Percutaneous coronary excimer laser angioplasty: initial clinical results. *Lancet* **2**, 647–650
- Karsch, K.R., Haase, K.K., Wehrmann, M., Hassenstein, S., Hanke, H. (1991): Smooth muscle cell proliferation and restenosis after stand alone coronary excimer laser angioplasty. *J. Am. Coll. Cardiol.* **17**, 991–994
- Karu, T.I. (1987): Photobiological fundamentals of low-power laser therapy. *IEEE J. Qu. Electron.* **QE-23**, 1703–1717
- Katsuyuki, A., Waseda, T., Ota, H., Azuma, T., Nagasawa, A. (1983): A preliminary study on clinical application of Nd:YAG laser to the face and head. *Lasers Surg. Med.* **3**, 231–239
- Kayano, T., Ochiai, S., Kiyono, K., Yamamoto, H., Nakajima, S., Mochizuki, T. (1989): Effects of Er:YAG laser irradiation on human extracted teeth. *J. Stomat. Soc. Jap.* **56**, 381–392
- Keates, R.H., Pedrotti, L.S., Weichel, H., Possel, W.H. (1981): Carbon dioxide laser beam control for corneal surgery. *Ophthalmic Surg.* **12**, 117–122
- Keijzer, M., Richards-Kortum, R.R., Jacques, S.L., Feld, M.S. (1989): Fluorescence spectroscopy of turbid media: autofluorescence of human aorta. *Appl. Opt.* **28**, 4286–4292
- Keller, U., Hibst, R. (1989): Experimental studies of the application of the Er:YAG laser on dental hard substances: II. Light microscopic and SEM investigations. *Lasers Surg. Med.* **9**, 345–351
- Kelly, J.F., Snell, M.E. (1976): Hematoporphyrin derivative: a possible aid in the diagnosis and therapy of carcinoma of the bladder. *J. Urol.* **115**, 150–151
- Kelly, P.J., Alker, G.J., Goerss, S. (1982): Computer assisted stereotactic laser microsurgery for the treatment of intracranial neoplasma. *Neurosurgery* **10**, 324–331
- Kelman, C.D. (1967): Phaco-emulsification and aspiration: a new technique of cataract extraction. *Am. J. Ophthalmol.* **64**, 23–35
- Kessel, D., Dougherty, T.J. (1983): Porphyrin photosensitization. Plenum Press, New York
- Kessel, D. (1987): Tumor localization and photosensitization by derivatives of hematoporphyrin: a review. *IEEE J. Qu. Electron.* **QE-23**, 1718–1720
- Keye, W.R., Dixon, J. (1983): Photocoagulation of endometriosis by the argon laser through the laparoscope. *Obstet. Gynecol.* **62**, 383–386
- Kiefhaber, P., Nath, G., Moritz, K. (1977): Endoscopical control of massive gastrointestinal haemorrhage by irradiation with a high-power neodymium-YAG laser. *Prog. Surg.* **15**, 140–155
- Kiefhaber, P., Huber, F., Kiefhaber, K. (1987): Palliative and preoperative endoscopic neodymium-YAG laser treatment of colorectal carcinoma. *Endoscopy* **19**, 43–46
- Kimel, S., Svaasand, L.O., Milner, T.E., Hammer-Wilson, M., Schell, M.J., Nelson, J.S., Berns, M.W. (1994): Laser photothermolysis of single blood vessels in the chick chorioallantoic membrane (CAM). *Proc. SPIE* **2077**, 216–226
- Kinoshita, S. (1988) Fluorescence of hematoporphyrin in living cells and in solution. *J. Photochem. Photobiol.* **B 2**, 195–208
- Klingenberg, M., Bohris, C., Niemz, M.H., Bille, J.F., Kurek, R., Wallwiener, D. (2000): Multifibre application in laser-induced interstitial thermotherapy under on-line MR control. *Lasers Med. Sci.* **15**, 6–14

- Knorz, M.C., Liermann, A., Seiberth, V., Steiner, H., Wiesinger, B. (1996): Laser in situ keratomileusis to correct myopia of -6.00 to -29.00 diopters. *J. Refract. Surg.* **12**, 575–584
- Kochevar, I.E. (1989): Cytotoxicity and mutagenicity of excimer laser radiation. *Lasers Surg. Med.* **9**, 440–445
- Koehner, W. (1992): Solid-state laser engineering. Springer-Verlag, Berlin, Heidelberg, New York
- Kottler, F. (1960): Turbid media with plane-parallel surfaces. *J. Opt. Soc. Am.* **50**, 483–490
- Kovacs, I.B., Mester, E., Görög, P. (1974): Stimulation of wound healing with laser beam in the rat. *Experientia* **30**, 1275–1276
- Krasnov, M.M. (1973): Laserpuncture of anterior chamber angle in glaucoma. *Am. J. Ophthalmol.* **75**, 674–678
- Kubasova, T., Kovacs, L., Somosy, Z., Unk, P., Kokai, A. (1984): Biological effect of He-Ne laser: investigations on functional and micromorphological alterations of cell membranes, in vitro. *Lasers Surg. Med.* **4**, 381–388
- Kubelka, P., Munk, F. (1931): Ein Beitrag zur Optik der Farbanstriche. *Z. Techn. Phys.* **12**, 593–601
- Kubelka, P. (1948): New contributions to the optics of intensely light-scattering materials. *J. Opt. Soc. Am.* **38**, 448–457
- Kucera, A., Blake, J.R. (1988): Computational modelling of cavitation bubbles near boundaries. In: Computational techniques and applications (Eds.: Noyce, J., Fletcher, C.) North-Holland, Amsterdam
- Laatikainen, L., Kohner, E.M., Khourey, D., Blach, R.K. (1977): Panretinal photocoagulation in central vein occlusion: a randomised controlled clinical study. *Br. J. Ophthalmol.* **61**, 741–753
- Labs, J.D., White, R.I., Anderson, J.H., Williams, G.M. (1987): Thermodynamic correlates of hot tip laser angioplasty. *Invest. Radiol.* **22**, 954–959
- Landau, C., Lange, R.A., Hillis, L.D. (1994): Percutaneous transluminal coronary angioplasty. *N. Engl. J. Med.* **330**, 981–993
- Lang, G.K., Schroder, E., Koch, J.W., Yanoff, M., Naumann, G.O.H. (1989): Excimer laser keratoplasty. Part I: basic concepts. *Ophthalmic Surg.* **20**, 262–265
- Lange, R.A., Willard, J.E., Hillis, L.D. (1993): Restenosis: the Achilles heel of coronary angioplasty. *Am. J. Med. Sci.* **306**, 265–275
- Lanzafame, R.J., Rogers, D.W., Naim, J.O., De France, C.A., Ochej, H., Hinshaw, J.R. (1986): Reduction of local tumor recurrence by excision with the CO₂ laser. *Lasers Surg. Med.* **6**, 439–441
- Latina, M., Goode, S., de Kater, A.W., Long, F.H., Deutsch, T.F., Epstein, D.L. (1988): Experimental ab interno sclerostomies using a pulsed-dye laser. *Lasers Surg. Med.* **8**, 233–240
- Latina, M.A., Dobrogowski, M., March, W.F., Birngruber, R. (1990): Laser sclerostomy by pulsed-dye laser and goniolens. *Lasers Surg. Med.* **10**, 1745–1750
- Lauterborn, W. (1972): High-speed photography of laser-induced breakdown in liquids. *Appl. Phys. Lett.* **21**, 27–29
- Lauterborn, W. (1974): Kavitation durch Laserlicht. *Acustica* **31**, 51–78
- Lauterborn, W., Bolle, H. (1975): Experimental investigations of cavitation-bubble collapse in the neighbourhood of a solid boundary. *J. Fluid Mech.* **72**, 391–399
- Lee, G., Ikeda, R.M., Kozina, J., Mason, D.T. (1981): Laser dissolution of atherosclerotic obstruction. *Am. Heart J.* **102**, 1074–1075
- Lenz, H., Eichler, J. (1984): Endonasale Chirurgie mit dem Argonlaser. *Laryng. Rhinol. Otol.* **63**, 534–540
- Lesinski, S.G., Palmer, A. (1989): Laser for otosclerosis: CO₂ vs. argon and KT-532. *Laryngoscope* **99**, 1–8

- Liesenhoff, T., Bende, T., Lenz, H., Seiler, T. (1989): Abtragen von Zahnhartsubstanzen mit Excimer-Laserstrahlen. *Dtsch. Zahnärztl. Z.* **44**, 426–430
- Limbird, T.J. (1990): Application of laser Doppler technology to meniscal injuries. *Clin. Orthop.* **252**, 88–91
- Lin, T., Chan, C. (1984): Effect of laser microbeam irradiation of the nucleus on the cleavage of mouse eggs in culture. *Rad. Res.* **98**, 549–560
- Lipshitz, I., Man, O., Shemesh, G., Lazar, M., Loewenstein, A. (2001): Laser in situ keratomileusis to correct hyperopic shift after radial keratotomy. *J. Cataract Refract. Surg.* **27**, 273–276
- Lipson, R., Baldes, E. (1961): Hematoporphyrin derivative: a new aid for endoscopic detection of malignant disease. *J. Thorac. Cardiovasc. Surg.* **42**, 623–629
- Lochte-Holtgreven, W. (1968): Plasma Diagnostics. North-Holland, Amsterdam
- Loertscher, H., Mandelbaum, S., Parel, J.M., Parrish, R.K. (1987): Noncontact trephination of the cornea using a pulsed hydrogen fluoride laser. *Am. J. Ophthalmol.* **104**, 471–475
- Loh, C.S., MacRobert, A.J., Bedwell, J., Regula, J., Krasner, N., Bown, S.G. (1993): Oral versus intravenous administration of 5-aminolaevulinic acid for photodynamic therapy. *Brit. J. Cancer* **68**, 41–51
- Lomano, J.M. (1985): Photocoagulation of early pelvic endometriosis with the Nd:YAG laser through the laparoscope. *J. Reprod. Med.* **30**, 77–81
- Lundberg, T., Hode, L., Zhou, J. (1987): A comparative study of the pain-relieving effect of laser treatment and acupuncture. *Acta Physiol. Scand.* **131**, 161–162
- Lyons, R.F., Abergel, R.P., White, R.A., Dwyer, R.M., Castel, J.C., Uitto, J. (1987): Biostimulation of wound healing in vivo by a helium-neon laser. *Ann. Plast. Surg.* **18**, 47–50
- Macha, H.-N., Koch, K., Stadler, M., Schumacher, W., Krumhaar, D. (1987): New technique for treating occlusive and stenosing tumours of the trachea and main bronchi: endobronchial irradiation by high dose iridium 192 combined with laser canalisation. *Thorax* **42**, 511–515
- Macha, H.-N. (1991): Die Möglichkeiten der Lasertherapie und ihre Kombination mit der endobronchialen Kleinraumbestrahlung zur Behandlung tracheobronchialer Tumoren. In: *Angewandte Lasermedizin* (Eds.: Berlien, H.-P., Müller, G.). Ecomed-Verlag, Landsberg
- Machemer, R., Laqua, H. (1978): A logical approach to the treatment of massive periretinal proliferation. *Ophthalmology* **85**, 584–593
- Macleod, I.A., Mills, P.R., MacKenzie, J.F., Joffe, S.N., Russell, R.I., Carter, D.C. (1983): Neodymium yttrium aluminium garnet laser photocoagulation for major haemorrhage from peptic ulcers and single vessels: a single blind controlled study. *Br. Med. J. Clin. Res.* **286**, 345–348
- Macruz, R., Martins, J.R.M., Tupinambas, A.S., Lopes, E.A., Vargas, H., Pena, A.F., Carvalho, V.B., Armelin, E., Delcourt, L.V. (1980): Possibilidades terapêuticas do raio laser em ateromas. *Arg. Bras. Cardiol.* **34**, 9
- Maiman, T. (1960): Optical and microwave-optical experiments in ruby. *Phys. Rev. Lett.* **4**, 564–566
- Maitland, D.J., Walsh, J.T., Prystowsky, J.B. (1993): Optical properties of human gallbladder tissue and bile. *Appl. Opt.* **32**, 586–590
- Malik, Z., Hanania, J., Nitzan, Y. (1990): Bactericidal effects of photoactivated porphyrins – an alternative approach to antimicrobial drugs. *J. Photochem. Photobiol.* **5**, 281–293
- March, W.F., Ghorezghiher, T., Koss, M.C., Nordquist, R.E. (1984): Experimental YAG laser sclerostomy. *Arch. Ophthalmol.* **102**, 1834–1836

- March, W.F., Gherezghiher, T., Koss, M.C., Shaver, R.P., Heath, W.D., Nordquist, R.D. (1985): Histologic study of a neodymium-YAG laser sclerostomy. *Arch. Ophthalmol.* **103**, 860–863
- Marchesini, R., Bertoni, A., Andreola, S., Melloni, E., Sichirollo, A.E. (1989): Extinction and absorption coefficients and scattering phase functions of human tissues in vitro. *Appl. Opt.* **28**, 2318–2324
- Marshall, J., Bird, A.C. (1979): A comparative histopathological study of argon and krypton laser irradiations of the human retina. *Br. J. Ophthalmol.* **63**, 657–668
- Marshall, J., Trokel, S., Rothery, S., Schubert, H. (1985): An ultrastructural study of corneal incisions induced by an excimer laser at 193 nm. *Ophthalmology* **92**, 749–758
- Marshall, J., Trokel, S., Rothery, S., Krueger, R.R. (1986): Photoablative reprofiling of the cornea using an excimer laser: photorefractive keratotomy. *Lasers Ophthalmol.* **1**, 21–48
- Marynissen, J.P.A., Jansen, H., Star, W.M. (1989): Treatment system for whole bladder wall photodynamic therapy with in vivo monitoring and control of light dose rate and dose. *J. Urol.* **142**, 1351–1355
- Mathews-Roth, M.M. (1982): Beta-carotenotherapy for erythropoietic protoporphyria and other photosensitivity diseases. In: *Science of Photomedicine* (Eds.: Regan, J.D., Parrish, J.A.), Plenum Press, New York
- Mathus-Vliegen, E.M.H., Tytgat, G.N.J. (1990): Analysis of failures and complications of neodymium:YAG laser photocoagulation in gastrointestinal tract tumors. *Endoscopy* **22**, 17–23
- McCaughan, J.S., Bethel, B.H., Johnston, T., Janssen, W. (1985): Effect of low-dose argonlaser irradiation on rate of wound closure. *Lasers Surg. Med.* **5**, 607–614
- McCullough, D.L., Roth, R.A., Babayan, R.K., Gordon, J.O., Reese, J.H., Crawford, E.D., Fuselier, H.A., Smith, J.A., Murchison, R.J., Kaye, K.W. (1993): Transurethral ultrasound-guided laser-induced prostatectomy: national human cooperative study results. *J. Urol.* **150**, 1607–1611
- McDonald, M.B., Frantz, J.M., Klyce, S.D., Beuerman, R.W., Varnell, R., Munnerlyn, C.R., Clapham, T.N., Salmeron, B., Kaufman, H.E. (1990): Central photorefractive keratectomy for myopia. The blind eye study. *Arch. Ophthalmol.* **108**, 799–808
- McHugh, J.D.A., Marshall, J., Capon, M., Tothery, S., Raven, A., Naylor, R.P. (1988): Transpupillary retinal photocoagulation in the eyes of rabbit and human using a diode laser. *Lasers Light Ophthalmol.* **2**, 125–143
- McNicholas, T.A., Carter, S.S.C., Wickham, J.E.A., O'Donoghue, E.P.N. (1988): YAG laser treatment of early carcinoma of the prostate. *Br. J. Urol.* **61**, 239–243
- McNicholas, T.A., Steger, A.C., Bown, S.G., O'Donoghue, N. (1991): Interstitial laser coagulation of the prostate: experimental studies. *Proc. SPIE* **1421**, 30–35
- Meador, W.E., Weaver, W.R. (1979): Diffusion approximation for large absorption in radiative transfer. *Appl. Opt.* **18**, 1204–1208
- Mebust, W.K. (1993): Benign prostatic hypertrophy: standards and guidelines. In: *Alternate methods in the treatment of benign prostatic hyperplasia* (Eds.: Romas, N.A., Vaughan, E.D.). Springer-Verlag, Berlin, Heidelberg, New York
- Meier, R.R., Lee, J.S., Anderson, D.E. (1978): Atmospheric scattering of middle UV radiation from an internal source. *Appl. Opt.* **17**, 3216–3225
- Melcer, J., Chaumette, M.T., Melcer, F. (1987): Dental pulp exposed to CO₂ laser beam. *Lasers Surg. Med.* **7**, 347–352
- Mester, E., Szende, B., Gärtner, P. (1968): Die Wirkung der Laserstrahlen auf den Haarwuchs der Maus. *Radiobiol. Radiother.* **9**, 621–626
- Mester, E., Gyenes, G., Tota, J.G. (1969): Experimentelle Untersuchungen über die Wirkung der Laserstrahlen auf die Wundheilung. *Z. Exp. Chirurg.* **2**, 94–101

- Mester, E., Spiry, T., Szende, B., Tota, J.G. (1971): Effect of laser rays on wound healing. *Am. J. Surg.* **122**, 532–535
- Metropolis, N., Ulam, S. (1949): The Monte Carlo method. *J. Am. Stat. Assoc.* **44**, 335–350
- Meyer-Schwickerath, G. (1949): Koagulation der Netzhaut mit Sonnenlicht. *Ber. Dtsch. Ophthalmol. Ges.* **55**, 256
- Meyer-Schwickerath, G. (1956): Erfahrungen mit der Lichtkoagulation der Netzhaut und der Iris. *Doc. Ophthalmol.* **10**, 91–131
- Miller, G.E., Sant, A.J. (1958): Incomplete integrating sphere. *J. Opt. Soc. Am.* **48**, 828–831
- Mirohseini, M., Muckerheide, M., Cayton, M.M. (1982): Transventricular revascularization by laser. *Lasers Surg. Med.* **2**, 187–198
- Mirohseini, M., Cayton, M.M., Shelgikar, S., Fisher, J.C. (1986): Clinical report: laser myocardial revascularization. *Lasers Surg. Med.* **6**, 459–461
- Moan, J., Christensen, T. (1981): Photodynamic effects on human cells exposed to light in the presence of hematoporphyrin. Localisation of the active dye. *Cancer Lett.* **11**, 209–214
- Molchanov, A.G. (1970): Avalanche ionization in transparent dielectrics induced by intense light pulses. *Sov. Phys. Solid State* **12**, 749
- Moore, J.H. (1973): Laser energy in orthopedic surgery. *Orthoped. Surg. Traumat. Excerpta Medica*, Amsterdam
- Morelli, J.G., Tan, O.T., Garden, J., Margolis, R., Seki, Y., Boll, J., Carney, J.M., Anderson, R.R., Furumoto, H., Parrish, J.A. (1986): Tunable dye laser (577 nm) treatment of port wine stains. *Lasers Surg. Med.* **6**, 94–99
- Mudgett, P.S., Richards, L.W. (1971): Multiple scattering calculations for technology. *Appl. Opt.* **10**, 1485–1502
- Mulser, P., Sigel, R., Witkowski, S. (1973): Plasma production by laser. *Phys. Lett.* **6 C**, 187–239
- Mulvaney, W.P., Beck, C.W. (1968): The laser beam in urology. *J. Urol.* **99**, 112
- Murray, J.E. (1983): Pulsed gain and thermal lensing of Nd:LiYF₄. *IEEE J. Qu. Electron.* **QE-19**, 488–491
- Muschter, R., Hofstetter, A., Hessel, S., Keiditsch, E., Rothenberger, K.-H., Scheede, P., Frank, F. (1992): Hi-tech of the prostate: interstitial laser coagulation of benign prostatic hypertrophy. *Proc. SPIE* **1643**, 25–34
- Muschter, R., Hessel, S., Hofstetter, A., Keiditsch, E., Rothenberger, K.-H., Schneede, P., Frank, F. (1993): Die interstitielle Laserkoagulation der benignen Prostatahyperplasie. *Urologe* **A 32**, 273–281
- Muschter, R., Hofstetter, A., Hessel, S. (1994): Laser induced thermotherapy of benign prostatic hyperplasia. *Min. Invas. Med.* **5**, 51–54
- Nath, G., Gorisch, W., Kiefhaber, P. (1973): First laser endoscopy via a fiber optic transmission system. *Endoscopy* **5**, 208
- Neblett, C.R., Morris, J.R., Thomson, S. (1986): Laser-assisted microsurgical anastomosis. *Neurosurgery* **19**, 914–934
- Nelson, J.S., Orenstein, A., Liaw, L.-H.L., Berns, M.W. (1989a): Mid-infrared erbium:YAG laser ablation of bone: the effect of laser osteotomy on bone healing. *Lasers Surg. Med.* **9**, 362–374
- Nelson, J.S., Orenstein, A., Liaw, L.-H.L., Zavar, R.B., Gianchandani, S., Berns, M.W. (1989b): Ultraviolet 308-nm excimer laser ablation of bone: an acute and chronic study. *Appl. Opt.* **28**, 2350–2357
- Nicolai, H., Semmelmann, M., Rößler, W., Wieland, W.F. (1995): Langzeitergebnisse in der Behandlung von Strikturen des unteren Harntraktes mit dem Holmium-YAG-Laser. *Proc. LASERmed'95*. Springer-Verlag, Berlin, Heidelberg, New York

- Niemz, M.H., Klancnik, E.G., Bille, J.F. (1991): Plasma-mediated ablation of corneal tissue at 1053 nm using a Nd:YLF oscillator/regenerative amplifier laser. *Lasers Surg. Med.* **11**, 426–431
- Niemz, M.H., Hoppeler, T.P., Juhasz, T., Bille, J.F. (1993a): Intrastromal ablations for refractive corneal surgery using picosecond infrared laser pulses. *Lasers Light Ophthalmol.* **5**, 149–155
- Niemz, M.H., Eisenmann, L., Pioch, T. (1993b): Vergleich von drei Lasersystemen zur Abtragung von Zahnschmelz. *Schweiz. Monatsschr. Zahnmed.* **103**, 1252–1256
- Niemz, M.H. (1994a): Investigation and spectral analysis of the plasma-induced ablation mechanism of dental hydroxyapatite. *Appl. Phys.* **B 58**, 273–281
- Niemz, M.H., Loesel, F.H., Fischer, M., Lappe, C., Bille, J.F. (1994b): Surface ablation of corneal tissue using UV, green and IR picosecond laser pulses. *Proc. SPIE* **2079**, 131–139
- Niemz, M.H. (1995a): Threshold dependence of laser-induced optical breakdown on pulse duration. *Appl. Phys. Lett.* **66**, 1181–1183
- Niemz, M.H. (1995b): Cavity preparation with the Nd:YLF picosecond laser. *J. Dent. Res.* **74**, 1194–1199
- Niemz, M.H. (1995c): Evaluation of physical parameters during the plasma-induced ablation of teeth. *Proc. SPIE* **2323**, 170–178
- Niemz, M.H., Herschel, A., Willms, L. (1995d): Application of a picosecond Nd:YLF laser in dentistry. *Proc. LASERmed'95*. Springer-Verlag, Berlin, Heidelberg, New York
- Niemz, M.H. (1998): Ultrashort laser pulses in dentistry – advantages and limitations. *Proc. SPIE* **3255**, 84–91
- Nseyo, U.O., Dougherty, T.J., Boyle, D.G., Potter, W.R., Wolf, R., Huben, R., Pontes, J.E. (1985): Whole bladder photodynamic therapy for transitional cell carcinoma of bladder. *Urology* **26**, 274–280
- Nuss, R.C., Fabian, R.L., Sarkar, R., Puliafito, C.A. (1988): Infrared laser bone ablation. *Lasers Surg. Med.* **8**, 381–392
- O'Brien, S.J., Miller, D.V. (1990): The contact neodymium-yttrium aluminium garnet laser. A new approach to arthroscopic laser surgery. *Clin. Orthop.* **252**, 310
- Overholt, B., Panjehpour, M., Tefftellar, E., Rose, M. (1993): Photodynamic therapy for treatment of early adenocarcinoma in Barrett's esophagus. *Gastrointest. Endosc.* **39**, 73–76
- Pallikaris, I.G., Siganos, D.S. (1994): Excimer laser in situ keratomileusis and photorefractive keratectomy for correction of high myopia. *J Refract. Corneal Surg.* **10**, 498–510
- Pao-Chang, M., Xiou-Qui, X., Hui, Z., Zheng, L., Rui-Peng, Z. (1981): Preliminary report on the application of CO₂ laser scalpel for operations on the maxillo-facial bones. *Lasers Surg. Med.* **1**, 375–384
- Parkin, J., Dixon, J. (1985): Argon laser treatment of head and neck vascular lesions. *Otolaryngol. Head Neck Surg.* **93**, 211–216
- Parrish, J., Anderson, R. (1983): Considerations of selectivity in laser therapy. In: *Cutaneous laser therapy* (Eds.: Arndt, K., Noc, J., Rosen, S.), Wiley & Sons, New York
- Parrish, J.A., Deutsch, T.F. (1984): Laser photomedicine. *IEEE J. Qu. Electron.* **QE-20**, 1386–1396
- Parsa, P., Jacques, S.L., Nishioka, N.S. (1989): Optical properties of rat liver between 350 and 2200 nm. *Appl. Opt.* **28**, 2325–2330

- Patel, D.D. (1988): Nd:YAG laser in oral cavity cancer report of 200 cases – minimum follow up of one year. In: *Laser-optoelectronics in medicine* (Ed.: Waidelich, W.). Springer-Verlag, Berlin, Heidelberg, New York
- Patel, N.P., Clinch, T.E., Weis, J.R., Ahn, C., Lundergan, M.K., Heidenreich, K. (2000): Comparison of visual results in initial and re-treatment laser in situ keratomileusis procedures for myopia and astigmatism. *Am. J. Ophthalmol.* **130**, 1–11
- Pauling, L. (1962): *Die Natur der chemischen Bindung*. Verlag Chemie, Weinheim
- Pedersen, G.D., McCormick, N.J., Reynolds, L.O. (1976): Transport calculations for light scattering in blood. *Biophys. J.* **16**, 199–207
- Pelz, B., Schott, M.K., Niemz, M.H. (1994): Electro-optic mode locking of an erbium:YAG laser with a rf resonance transformer. *Appl. Opt.* **33**, 364–367
- Pensel, J. (1986): Dosimetry of the neodymium-YAG-laser in urological applications. *Eur. Urol.* **12**, 17–20
- Perkins, R.C. (1980): Laser stapedotomy for otosclerosis. *Laryngoscope* **90**, 228–240
- Pfander, F. (1975): *Das Knalltrauma*. Springer-Verlag, Berlin, Heidelberg, New York
- Philipp, C., Poetke, M., Berlien, H.-P. (1992): Klinik und Technik der Laserbehandlung angeborener Gefäßerkrankungen. In: *Angewandte Lasermedizin* (Eds.: Berlien, H.-P., Müller, G.). Ecomed-Verlag, Landsberg
- Pickering, J.W., Moes, C.J., Sterenborg, H.J.C.M., Prah, S.A., van Gemert, M.J.C. (1992): Two integrating spheres with an intervening scattering sample. *J. Opt. Soc. Am.* **A 9**, 621–631
- Pickering, J.W., Prah, S.A., van Wieringen, N., Beek, J.F., Sterenborg, H.J.C.M., van Gemert, M.J.C. (1993): Double-integrating-sphere system for measuring the optical properties of tissue. *Appl. Opt.* **32**, 399–410
- Pioch, T., Niemz, M., Mindermann, A., Staehle, H.J. (1994): Schmelzablationen durch Laserimpulse im Pikosekundenbereich. *Dtsch. Zahnärztl. Z.* **49**, 163–165
- Plass, G.N., Kattawar, G.W., Catchings, F.E. (1973): Matrix operator theory of radiative transfer. 1: Rayleigh scattering. *Appl. Opt.* **12**, 314–329
- Pohl, R.W. (1976): *Optik und Atomphysik*. Springer-Verlag, Berlin, Heidelberg, New York
- Pollack, I.P., Patz, A. (1976): Argon laser iridotomies: an experimental and clinical study. *Ophthalmic. Surg.* **7**, 22–30
- Pollak, T.M., Wing, W.F., Gasso, R.J., Chicklis, E.P., Jenssen, J.P. (1982): Laser operation of Nd:YLF. *IEEE J. Qu. Electron.* **QE-18**, 159–162
- Prah, S.A., van Gemert, M.J.C., Welch, A.J. (1993): Determining the optical properties of turbid media by using the adding-doubling method. *Appl. Opt.* **32**, 559–568
- Pratisto, H., Frenz, M., Ith, M., Romano, V., Felix, D., Grossenbacher, R., Altermatt, H.J., Weber, H.P. (1996): Temperature and pressure effects during erbium laser stapedotomy. *Lasers Surg. Med.* **18**, to be published
- Prauser, R., Eitner, K., Donnerhacke, K.-H., Fritze, C., Schneider, A. (1991): Endoskopische Lasertherapie villöser and tubulovillöser Adenome des Rektosigmooids. In: *Angewandte Lasermedizin* (Eds.: Berlien, H.-P., Müller, G.). Ecomed-Verlag, Landsberg
- Prendeville, W., Davis, R., Berry, P.G. (1986): A low voltage diathermy loop for taking cervical biopsies: a qualitative comparison with punch biopsy forceps. *Br. J. Obstet. Gynaecol.* **93**, 773–776
- Puliafito, C.A., Steinert, R.F. (1984): Short-pulsed Nd:YAG laser microsurgery of the eye: biophysical considerations. *IEEE J. Qu. Electron.* **QE-20**, 1442–1448

- Puliafito, C.A., Steinert, R.F., Deutsch, T.F., Hillenkamp, F., Dehm, E.J., Adler, C.M. (1985): Excimer laser ablation of the cornea and lens: experimental studies. *Ophthalmology* **92**, 741–748
- Quickenden, T.I., Daniels, L.L. (1993): Attempted biostimulation of division in *saccharomyces cerevisiae* using red coherent light. *Photochem. Photobiol.* **57**, 272–278
- Rasmussen, R.E., Hammer-Wilson, M., Berns, M.W. (1989): Mutation and sister chromatid exchange induction in chinese hamster ovary (CHO) cells by pulsed excimer laser radiation at 193 nm and 308 nm and continuous UV radiation at 254 nm. *Photochem. Photobiol.* **49**, 413–418
- Rayleigh, Lord (1917): On the pressure developed in a liquid during the collapse of a spherical cavity. *Phil. Mag.* **34**, 94–98
- Ready, J.F. (1971): Effects of high-power laser radiation. Academic Press, New York, 279–283
- Rechmann, P., Hennig, T., von den Hoff, U., Kaufmann, R. (1993): Caries selective ablation: wavelength 377 nm versus 2.9 μm . *Proc. SPIE* **1880**, 235–239
- Reid, R., Muller, S. (1980): Tattoo removal by CO₂ laser dermabrasion. *Plast. Reconstr. Surg.* **65**, 717–728
- Reynolds, L.O., Johnson, C.C., Ishimaru, A. (1976): Diffuse reflectance from a finite blood medium: applications to the modeling of fiber optic catheters. *Appl. Opt.* **15**, 2059–2067
- Reynolds, L.O., McCormick, N.J. (1980): Approximate two-parameter phase function for light scattering. *J. Opt. Soc. Am.* **70**, 1206–1212
- Rice, M.H., Walsh, J.M. (1957): Equation of state of water to 250 kilobars. *J. Chem. Phys.* **26**, 824–830
- Röder, B., Näther, D., Lewald, T., Braune, M., Freyer, W., Nowak, C. (1990): Photophysical properties and photodynamic activity in vivo of some tetrapyrroles. *Biophys. Chem.* **35**, 303–312
- Roggan, A., Müller, G. (1993): Computer simulations for the irradiation planning of LITT. *Med. Tech.* **4**, 18–24
- Roggan, A., Handke, A., Miller, K., Müller, G. (1994): Laser induced interstitial thermotherapy of benign prostatic hyperplasia. *Min. Invas. Med.* **5**, 55–63
- Roggan, A., Albrecht, H., Dörschel, K., Minet, O., Müller, G. (1995a): Experimental set-up and Monte-Carlo model for the determination of optical tissue properties in the wavelength range 330–1100 nm. *Proc. SPIE* **2323**, 21–36
- Roggan, A., Müller, G. (1995b): 2D-computer simulations for real-time irradiation planning of laserinduced interstitial thermotherapy (LITT). *Proc. SPIE* **2327**, 242–252
- Roggan, A., Albrecht, D., Berlien, H.-P., Beuthan, J., Germer, C., Koch, H., Wodrich, W., Müller, G. (1995c): Development of an application-set for intraoperative and percutaneous laserinduced interstitial thermotherapy (LITT). *Proc. SPIE* **2327**, 253–260
- Rol, P., Nieder, P., Dürr, U., Henchoz, P.-D., Fankhauser, F. (1990): Experimental investigations on the light scattering properties of the human sclera. *Lasers Light Ophthalmol.* **3**, 201–212
- Romano, V., Rodriguez, R., Altermatt, H.J., Frenz, M., Weber, H.P. (1994): Bone microsurgery with IR-lasers: a comparative study of the thermal action at different wavelengths. *Proc. SPIE* **2077**, 87–97
- Rosenberg, S. (1983): The use of CO₂-laser in urology. *Lasers Surg. Med.* **3**, 152
- Rosen, E.S. (2001): What is LASIK? *J. Cataract Refract. Surg.* **27**, 339–340
- Rosomoff, H.L., Caroll, F. (1966): Reaction of neoplasm and brain to laser. *Arch. Neurol.* **1**, 143–148

- Roth, R.A., Aretz, H.T. (1991): Transurethral ultrasound-guided laser-induced prostatectomy (TULIP procedure): a canine prostate feasibility study. *J. Urol.* **146**, 1128–1135
- Rothauge, C.F. (1980): Urethrosopic recanalization of urethra stenosis using argon laser. *Urology* **16**, 158–161
- Roussel, R., Fankhauser, F. (1983): Contactglas for use with high powerlaser – geometrical and optical aspects. *Int. Ophthalmol.* **6**, 183–190
- Royneisdal, A.K., Bjornland, T., Barkvoll, P., Haanaes, H.R. (1993): The effect of soft-laser application on postoperative pain and swelling. A double-blind crossover study. *Int. J. Oral Maxillofac. Surg.* **22**, 242–245
- Rutgeerts, P., Vantrappen, G., Broeckaert, L., Janssens, J., Coremans, G., Geboes, K., Schurmans, P. (1982): Controlled trial of YAG laser treatment of upper digestive hemorrhage. *Gastroenterology* **83**, 410–416
- Sacchi, C.A. (1991): Laser-induced electric breakdown in water. *J. Opt. Soc. Am.* **B 8**, 337–345
- Sachse, H. (1974): Zur Behandlung der Harnröhrenstriktur: die transurethrale Schlitzung unter Sicht mit scharfem Messer. *Fortschr. Med.* **1992**, 12–15
- Sanborn, T.A., Faxon, D.P., Kellet, M.A., Ryan, T.J. (1986): Percutaneous coronary laser thermal angioplasty. *J. Am. Coll. Cardiol.* **8**, 1437–1440
- Sander, S., Beisland, H.O., Fossberg, E. (1982): Neodymium YAG laser in the treatment of prostatic cancer. *Urol. Res.* **10**, 85–86
- Sander, R., Poesl, H., Frank, F., Meister, P., Strobel, M., Spuhler, A. (1988): A Nd:YAG laser with a water-guided laser beam – a new transmission system. *Gastrointest. Endosc.* **34**, 336–338
- Sander, R., Poesl, H., Zuern, W., Spuhler, A., Braida, M. (1989): The water jet-guided Nd:YAG laser in the treatment of gastroduodenal ulcer with a visible vessel – a randomized, controlled and prospective study. *Endoscopy* **21**, 217–220
- Sander, R., Poesl, H., Spuhler, A. (1990): Lasertherapie von Blutungen und nicht neoplastischen Stenosen. In: *Angewandte Lasermedizin* (Eds.: Berlien, H.-P., Müller, G.). Ecomed-Verlag, Landsberg
- Sawelson, H.R., Marks, R.G. (1985): Two-year results of radial keratotomy. *Arch. Ophthalmol.* **103**, 505–510
- Scheibner, A., Kenny, G., White, W., Wheeland, R.G. (1990): A superior method of tattoo removal using the Q-switched ruby laser. *J. Dermatol. Surg. Oncol.* **16**, 1091–1098
- Schneckenburger, H., König, K., Kunzi-Rapp, K., Westphal-Frösch, C., Rück, A. (1993): Time-resolved in-vivo fluorescence of photosensitizing porphyrins. *J. Photochem. Photobiol.* **B 21**, 143–147
- Scholz, C., Grothves-Spork, M. (1992): Die Bearbeitung von Knochen mit dem Laser. In: *Angewandte Lasermedizin* (Eds.: Berlien, H.-P., Müller, G.). Ecomed-Verlag, Landsberg
- Schulenburg, W.E., Hamilton, A.M., Black, R.K. (1979): A comparative study of argon laser and krypton laser in the treatment of diabetic optic disc neovascularization. *Br. J. Ophthalmol.* **63**, 412–417
- Schwartz, L.W., Spaeth, G.L. (1980): Argon laser iridotomy in primary angle-closure or pupillary block glaucoma. *Lasers Surg. Med.* **1**, 153–164
- Seiler, T., Bende, T., Wollensak, J., Trokel, S. (1988): Excimer laser keratectomy for correction of astigmatism. *Am. J. Ophthalmol.* **105**, 117–124
- Seiler, T., Genth, U. (1994): Zum gegenwärtigen Stand der chirurgischen Myopie-Korrektur. *Dtsch. Ärztebl.* **91**, 3344–3350
- Seipp, W., Haina, D., Seipp, V. (1989): Laser in der Dermatologie. In: *Angewandte Lasermedizin* (Eds.: Berlien, H.-P., Müller, G.). Ecomed-Verlag, Landsberg

- Seitz, F. (1949): On the theory of electron multiplication in crystals. *Phys. Rev.* **76**, 1376–1393
- Selzer, P.M., Murphy-Chutorian, D., Ginsburg, R., Wexler, L. (1985): Optimizing strategies for laser angioplasty. *Invest. Radiol.* **20**, 860–866
- Semler, P. (1989): Tumortherapie im Gastrointestinaltrakt mit einer Kombination von Laserstrahl und Bestrahlung in "afterloading"-Technik. In: *Angewandte Lasermedizin* (Eds.: Berlien, H.-P., Müller, G.). Ecomed-Verlag, Landsberg
- Serruys, P.W., Luijten, H.E., Beat, K.J., Geuskens, R., de Feyter, P.J., van den Brand, M., Reiber, J.H.C., ten Katen, H.J., van Es, G.A., Hugenholtz, P.G. (1988): Incidence of restenosis after successful coronary angioplasty: a time-related phenomenon. *Circulation* **77**, 361–371
- Shirk, G.J. (1989): Use of the Nd:YAG laser for the treatment of endometriosis. *Am. J. Obstet. Gynecol.* **160**, 1344–1348
- Shumaker, B.P., Hetzel, F.W. (1987): Clinical laser photodynamic therapy in the treatment of bladder carcinoma. *Photochem. Photobiol.* **46**, 899–901
- Siegel, Y.I., Zaidel, L., Hammel, I., Korczak, D., Lindner, A. (1991): Histopathology of benign prostatic hyperplasia after failure of hyperthermia treatment. *Br. J. Urol.* **68**, 383–386
- Siegman, A.E. (1986): *Lasers*. University Science Books, Mill Valley, California
- Sievers, M., Frentzen, M., Kosina, A., Koort, H.-J. (1993): Scaling of root surfaces with lasers – an in vitro study. *Proc. SPIE* **2080**, 82–87
- Sliney, D.H., Wolbarsht, M.L. (1980): *Safety with lasers and other optical sources*. Plenum Pub. Corp., New York
- Smith, D.C., Haught, A.F. (1966): Energy-loss processes in optical-frequency gas breakdown. *Phys. Rev. Lett.* **16**, 1085–1088
- Smith, C., Johansen, E., Vangsnæs, T., Yamaguchi, K., McEleney, E. (1987): Does success of arthroscopic laser surgery in the knee joint warrant its extension to "non-knee" joints? *Proc. SPIE* **712**, 214–217
- Spikes, J.D. (1986): Phthalocyanines as photosensitizers in biological systems and for the PDT of tumors. *Photochem. Photobiol.* **43**, 691–699
- Splinter, R., Cheong, W.-F., van Gemert, M.J.C., Welch, A.J. (1989): In vitro optical properties of human and canine brain and urinary bladder tissues at 633 nm. *Lasers Surg. Med.* **9**, 37–41
- Splinter, R., Svenson, R.H., Littmann, L., Chuang, C.H., Tuntelder, J.R., Thompson, M., Tatsis, G.P., Keijzer, M. (1993): Computer simulated light distributions in myocardial tissues at the Nd-YAG wavelength of 1064 nm. *Lasers Med. Sci.* **8**, 15–21
- Srinivasan, R., Mayne-Banton, V. (1982): Self-developing photoetching of poly (ethylene terephthalate) films by far-ultraviolet excimer laser radiation. *Appl. Phys. Lett.* **41**, 576–578
- Srinivasan, R. (1986a): Ablation of polymers and biological tissue by ultraviolet lasers. *Science* **234**, 559–565
- Srinivasan, R., Braren, B., Dreyfus, R.W., Hadel, L., Seeger, D.E. (1986b): Mechanism of the ultraviolet laser ablation of polymethyl methacrylate at 193 and 248 nm: laser-induced fluorescence analysis, chemical analysis, and doping studies. *J. Opt. Soc. Am.* **B3**, 785–791
- Staehler, G., Hofstetter, A., Gorisch, W., Keiditsch, E., Müssiggang, M. (1976): Endoscopy in experimental urology using an argon-laser beam. *Endoscopy* **8**, 1–4
- Staff, A., Wilkinson, E.J., Mattingly, R.F. (1977): Laser treatment of cervical and vaginal neoplasia. *Am. J. Obstet. Gynecol.* **128**, 128–136
- Steiger, E., Maurer, N., Geisel, G. (1993): The frequency-doubled alexandrite laser: an alternative dental device. *Proc. SPIE* **1880**, 149–152

- Stein, E., Sedlacek, T., Fabian, R.L., Nishioka, N.S. (1990): Acute and chronic effects of bone ablation with a pulsed holmium laser. *Lasers Surg. Med.* **10**, 384–388
- Steiner, W. (1989): Die endoskopische Lasertherapie im oberen Aero-Digestivtrakt. In: *Angewandte Lasermedizin* (Eds.: Berlien, H.-P., Müller, G.). Ecomed-Verlag, Landsberg
- Steinert, R.F., Puliafito, C.A., Trokel, S. (1983): Plasma formation and shielding by three ophthalmic Nd-YAG lasers. *Am. J. Ophthalmol.* **90**, 973–991
- Steinert, R.F., Puliafito, C.A. (1985): *The Nd-YAG laser in ophthalmology*. W.B. Saunders Co., Philadelphia
- Stellar, S., Polanyi, T.G., Bredemeier, H.C. (1970): Experimental studies with the carbon dioxide laser as a neurosurgical instrument. *Med. Biol. Eng.* **8**, 549–558
- Stellar, S. (1984): Present status of laser neurosurgery. *Lasers Surg. Med.* **4**, 215–220
- Stern, R.H., Sognaes, R.F. (1964): Laser beam effect on dental hard tissues. *J. Dent. Res.* **43**, 873
- Stern, R.H., Vahl, J., Sognaes, R. (1972): Lased enamel: ultrastructural observations of pulsed carbon dioxide laser effects. *J. Dent. Res.* **51**, 455–460
- Stern, R.H. (1974): Dentistry and the laser. In: *Laser applications in medicine and biology* (Ed.: Wolbarsht, M.L.). Plenum Press, New York
- Stern, D., Schoenlein, R.W., Puliafito, C.A., Dobi, E.T., Birngruber, R., Fujimoto, J.G. (1989): Corneal ablation by nanosecond, picosecond and femtosecond lasers at 532 nm and 625 nm. *Arch. Ophthalmol.* **107**, 587–592
- Strong, M.S., Jako, G.J., Vaughan, C.W., Healy, G.B., Polanyi, T. (1976): The use of CO₂ laser in otolaryngology: a progress report. *Trans. Am. Acad. Ophthalmol. Otolaryngol.* **82**, 595–602
- Strong, M.S., Vaughan, C.W., Healy, G.B., Shapshay, S.M., Jako, G.J. (1979): Transoral management of localised carcinoma of the oral cavity using the CO₂ laser. *Laryngoscope* **89**, 897–905
- Strube, D., Haina, D., Landthaler, M., Braun-Falco, O., Waidelich, W. (1988): Störeffekte bei Tierversuchen zur Stimulation der Wundheilung mit Laserlicht. *Laser Med. Surg.* **4**, 15–20
- van Stryland, E.W., Soileau, M.J., Smirl, A.L., Williams, W.E. (1981): Pulse-width and focal-volume dependence of laser-induced breakdown. *Phys. Rev.* **B 23**, 2144–2151
- Sutcliffe, E., Srinivasan, R. (1986): Dynamics of UV laser ablation of organic polymer surfaces. *J. Appl. Phys.* **60**, 3315–3322
- Svaasand, L.O., Boerslid, T., Oeveraasen, M. (1985): Thermal and optical properties of living tissues. *Lasers Surg. Med.* **5**, 589–602
- Svaasand, L.O., Gomer, C.J., Profio, A.E. (1989): Laser-induced hyperthermia of ocular tumors. *Appl. Opt.* **28**, 2280–2287
- Swain, C.P., Kirkham, J.S., Salmon, P.S., Bown, S.G., Northfield, T.C. (1986): Controlled trial of Nd:YAG laser photocoagulation in bleeding peptic ulcers. *Lancet* **1**, 1113–1117
- Takata, A.N., Zaneveld, L., Richter, W. (1977): Laser-induced thermal damage in skin. *Aerospace Med., Rep.* SAM-TR-77-38
- Tan, O.T., Sherwood, K., Gilchrest, B.A. (1989): Treatment of children with port-wine stains using the flashlamp-pulsed tunable dye laser. *N. Engl. J. Med.* **320**, 416–421
- von Tappeiner, H. (1900): Über die Wirkung fluoreszierender Stoffe auf Infusorien nach Versuchen von O. Raab. *Münch. Med. Wochenschr.* **47**, 5–13
- von Tappeiner, H., Jesionek, A. (1903): Therapeutische Versuche mit fluoreszierenden Stoffen. *Münch. Med. Wochenschr.* **50**, 2042–2051

- Taube, S., Piironen, J., Ylipaavalniemi, P. (1990): Helium-neon laser therapy in the prevention of post-operative swelling and pain after wisdom tooth extraction. *Proc. Finn. Dent. Soc.* **86**, 23–27
- Taylor, R.S., Leopold, K.E., Mihailov, S. (1987): Damage measurements of fused silica fibres using long optical pulse XeCl lasers. *Opt. Commun.* **63**, 26–31
- Taylor, D.M., L'Esperance, F.A., Del Pero, R.A., Roberts, A.D., Gigstad, J.E., Klintworth, G., Martin, C.A., Warner, J. (1989): Human excimer laser lamellar keratectomy. *Ophthalmology* **96**, 654–664
- Taylor, C.R., Gange, R.W., Dover, J.S., Flotte, T.J., Gonzalez, E., Michaud, N., Anderson, R.R. (1990): Treatment of tattoos by Q-switched ruby laser. A dose-response study. *Arch. Dermatol.* **126**, 893–899
- Teng, P., Nishioka, N.S., Anderson, R.R., Deutsch, T.F. (1987): Acoustic studies of the role of immersion in plasma-mediated laser ablation. *IEEE J. Qu. Electron.* **QE-23**, 1845–1852
- Terry, A.C., Stark, W.J., Maumenee, H.E., Fagadau, W. (1983): Neodymium-Yag laser for posterior capsulotomy. *Am. J. Ophthalmol.* **96**, 716–720
- Ticho, U., Zauberman, H. (1976): Argon laser application to the angle structures in the glaucoma. *Arch. Ophthalmol.* **94**, 61–64
- Tierstein, P.S., Warth, D.C., Haq, N., Jenkins, M.S., McCowan, L.C., Aubanle-Reidel, P., Morris, N., Ginsburg, R. (1991): High speed rotational atherectomy for patients with diffuse coronary artery disease. *J. Am. Coll. Cardiol.* **18**, 1694–1701
- Tomita, Y., Shima, A. (1986): Mechanism of impulsive pressure generation and damage pit formation by bubble collapse. *J. Fluid Mech.* **169**, 535–564
- Trauner, K., Nishioka, N., Patel, D. (1990): Pulsed holmium:yttrium-aluminum-garnet (Ho:YAG) laser ablation of fibrocartilage and articular cartilage. *Am. J. Sports Med.* **18**, 316–320
- Trokkel, S.L., Srinivasan, R., Braren, B.A. (1983): Excimer laser surgery of the cornea. *Am. J. Ophthalmol.* **96**, 710–715
- Ulrich, F., Nicola, N., Bock, W.J. (1986): A micromanipulator to aid microsurgical removal of intracranial tumors with the Nd:YAG laser. *Lasers Med. Sci.* **1**, 131–133
- Ulrich, F., Dürselen, F., Schober, R. (1988): Long-term investigations of laser-assisted microvascular anastomoses with the 1.318 μm Nd:YAG-laser. *Lasers Surg. Med.* **8**, 104–107
- Unsöld, E., Baumgartner, R., Jocham, D., Stepp, H. (1987): Application of photosensitizers in diagnosis and therapy. *Lasers Surg. Med.* **3**, 210–214
- Vaidyanthan, A., Walker, T.W., Guenther, A.H. (1980): The relative roles of avalanche multiplication and multiphoton absorption in laser-induced damage of dielectrics. *IEEE J. Qu. Electron.* **QE-16**, 89–93
- Vassiliadis, A., Christian, H.C., Dedrick, K.G. (1971): Ocular laser threshold investigations. *Aerospace Med., Rep. F41609-70-C-0002*
- Verschuere, R.C.J., Oldhoff, J. (1975): The carbon-dioxide laser, a new surgical tool. *Arch. Chirur. Nederl.* **27**, 199–207
- Ville, Y., Hyett, J., Hecher, K., Nicolaidis, K. (1995): Preliminary experience with endoscopic laser surgery for severe twin-twin transfusion syndrome. *New Engl. J. Med.* **332**, 224–227
- Vogel, A., Lauterborn, W. (1988): Time resolved particle image velocimetry applied to the investigation of cavitation bubbles. *Appl. Opt.* **27**, 1869–1876
- Vogel, A., Lauterborn, W., Timm, R. (1989): Optical and acoustic investigation of the dynamics of laser-produced cavitation bubbles near a solid boundary. *J. Fluid Mech.* **206**, 299–338

- Vogel, A., Schweiger, P., Frieser, A., Asiyo, M.N., Birngruber, R. (1990): Intraocular Nd:YAG laser surgery: light-tissue interaction, damage range, and the reduction of collateral effects. *IEEE J. Qu. Electron.* **QE-26**, 2240–2260
- Vogel, A., Busch, S., Jungnickel, K., Birngruber, R. (1994a): Mechanisms of intraocular photodisruption with picosecond and nanosecond laser pulses. *Lasers Surg. Med.* **15**, 32–43
- Vogel, A., Capon, M.R.C., Asiyo-Vogel, M.N., Birngruber, R. (1994b): Intraocular photodisruption with picosecond and nanosecond laser pulses: tissue effects in cornea, lens, and retina. *Invest. Ophthalmol. Vis. Sci.* **35**, 3032–3044
- Wacker, F., Reither, K., Ritz, J., Roggan, A., Germer, C., Wolf, K. (2001): MR-guided interstitial laser-induced thermotherapy of hepatic metastasis combined with arterial blood flow reduction: technique and first clinical results in an open MR system. *J. Magn. Reson. Imaging* **13**, 31–36
- Waller, B.F. (1983): Early and late morphological changes in human coronary arteries after percutaneous transluminal coronary angioplasty. *Clin. Cardiol.* **6**, 363–372
- Wallwiener, D., Kurek, R., Pollmann, D., Kaufmann, M., Schmid, H., Bastert, G., Frank, F. (1994): Palliative therapy of gynecological malignancies by laserinduced interstitial thermotherapy. *Lasermedizin* **10**, 44–51
- Walsh, J.T., Deutsch, T.F. (1989): Er:YAG laser ablation of tissue: measurement of ablation rates. *Lasers Surg. Med.* **9**, 327–337
- Watson, G.M., Wickham, J.E.A., Mills, T.N., Bown, S.G., Swain, P., Salmon, P.R. (1983): Laser fragmentation of renal calculi. *Br. J. Urol.* **55**, 613–616
- Watson, G.M., Murray, S., Dretler, S.P., Parrish, J.A. (1987): The pulsed dye laser for fragmenting urinary calculi. *J. Urol.* **138**, 195–198
- Weast, R.C. (1981): *Handbook of chemistry and physics*. CRC Press, Boca Raton
- Weichmann, G., Johnson, J. (1971): Laser use in endodontics. A preliminary investigation. *Oral Surg.* **31**, 416–420
- Weichmann, G., Johnson, J., Nitta, L. (1972): Laser use in endodontics. Part II. *Oral Surg.* **34**, 828–830
- Weinberg, W.S., Birngruber, R., Lorenz, B. (1984): The change in light reflection of the retina during therapeutic laser-photocoagulation. *IEEE J. Qu. Electron.* **QE-20**, 1481–1489
- Weishaupt, K.R., Gomer, C.J., Dougherty, T.J. (1986): Identification of singlet oxygen as the toxic agent in photoactivation of a murine tumor. *Cancer Res.* **36**, 2326–2331
- Welch, A.J. (1984): The thermal response of laser irradiated tissue. *IEEE J. Qu. Electron.* **QE-20**, 1471–1481
- Welch, A.J., van Gemert, M.J.C. (1995): *Optical-thermal response of laser-irradiated tissue*. Plenum Press, New York, London
- Wharen, R.E., Anderson, R.E. (1984a): The Nd:YAG laser in neurosurgery. Part 1: Laboratory investigations – dose related biological response of neural tissue. *J. Neurosurg.* **60**, 531–539
- Wharen, R.E., Anderson, R.E. (1984b): The Nd:YAG laser in neurosurgery. Part 2: Clinical studies – an adjunctive measure for hemostasis in reactions of arteriovenous malformations. *J. Neurosurg.* **60**, 540–547
- Whipple, T.L. (1981): Applications of the CO₂ laser to arthroscopic meniscectomy in a gas medium. *Proc. Triannual Meeting Int. Arthrosc. Assoc.*, Rio de Janeiro.
- Whittaker, P., Kloner, R.A., Przyklenk, K. (1993): Laser-mediated transmural myocardial channels do not salvage acutely ischemic myocardium. *J. Am. Coll. Cardiol.* **22**, 302–309

- Wieland, W.F., Nicolai, H., Rössler, W., Hofstädter, F. (1993): Erste Erfahrungen mit dem Holmium-YAG-Laser bei der Behandlung von Harnröhrenstrikturen. Proc. LASERmed'93. Springer-Verlag, Berlin, Heidelberg, New York
- Wilder-Smith, P. (1988): The soft laser: therapeutic tool or popular placebo? Oral Surg. Oral Med. Oral Pathol. **66**, 654–658
- Wilson, B.C., Adam, G. (1983): A Monte Carlo model for the absorption and flux distributions of light in tissue. Med. Phys. **10**, 824–830
- Wilson, B.C., Patterson, M.S. (1986): The physics of photodynamic therapy. Phys. Med. Biol. **31**, 327–360
- Wilson, S.E. (1990): Excimer laser (193 nm) myopic keratomileusis in sighted and blind human eyes. Refract. Corneal Surg. **6**, 383–385
- Wilson, M., Dobson, J., Harvey, W. (1993): Sensitization of streptococcus sanguis to killing by light from a helium/neon laser. Lasers Med. Sci. **8**, 69–73
- Wise, J.B., Witter, S.L. (1979): Argon laser therapy for open-angle glaucoma. Arch. Ophthalmol. **97**, 319–322
- Wise, J.B. (1987): Ten years results of laser trabeculoplasty – does the laser avoid glaucoma surgery or merely defer it? Eye **1**, 45–50
- Wolbarsht, M.L. (1971): Laser applications in medicine and biology. Plenum Press, New York
- Wolbarsht, M.L. (1984): Laser surgery: CO₂ or HF. IEEE J. Qu. Electron. **QE-20**, 1427–1432
- Worthen, D.M., Wickham, M.G. (1974): Argon laser trabeculotomy. Trans. Am. Acad. Ophthalmol. Otolaryngol. **78**, 371–375
- Wright, V.C., Davies, E., Riopelle, M.A. (1983): Laser surgery for cervical intraepithelial neoplasia: principles and results. Am. J. Obstet. Gynecol. **145**, 181–184
- Yablonovitch, N., Bloembergen, N. (1972): Avalanche ionization and the limiting parameter of filaments induced by light pulses in transparent media. Phys. Rev. Lett. **29**, 907–910
- Yamashita, M. (1984): Picosecond time resolved fluorescence spectroscopy of HpD. IEEE J. Qu. Electron. **QE-20**, 1363–1369
- Yano, O.J., Bielefeld, M.R., Jeevanadam, V. (1993): Prevention of acute regional ischemia with endocardial laser channels. Ann. Thorac Surg. **56**, 46–53
- Yoon, G., Welch, A.J., Motamedi, M., van Gemert, M.C.J. (1987): Development and application of three-dimensional light distribution model for laser irradiated tissue. IEEE J. Qu. Electron. **QE-23**, 1721–1733
- Yow, L., Nelson, J.S., Berns, M.W. (1989): Ablation of bone and polymethylmethacrylate by an XeCl (308 nm) excimer laser. Lasers Surg. Med. **9**, 141–147
- Zaret, M.M., Breinin, G.M., Schmidt, H., Ripps, H., Siegel, I.M., Solon, L.R. (1961): Ocular lesions produced by an optical maser (laser). Science **134**, 1525
- Zhou, J., Taft, G., Huang, C.-P., Murnane, M.M., Kapteyn, H.C., Christov, I.P. (1994): Pulse evaluation in a broad-bandwidth Ti:sapphire laser. Opt. Lett. **19**, 1149–1151
- Zweig, A.D., Deutsch, T.F. (1992): Shock waves generated by XeCl excimer laser ablation of polyimide. Appl. Phys. **B 54**, 76–82
- Zweng, H.C., Flocks, M., Kapany, N.S., Silbertrust, N., Peppers, N.A. (1964): Experimental laser photocoagulation. Am. J. Ophthalmol. **58**, 353–362
- Zysset, B., Fujimoto, J.G., Deutsch, T.F. (1989): Time-resolved measurements of picosecond optical breakdown. Appl. Phys. **B 48**, 139–147

Index

- Ablation
 - pattern, 88, 268
 - photoablation, *see* Decomposition
 - plasma-induced, 103–125
 - plasma-mediated, 105
 - thermal, *see* Decomposition
- Absorbance, 15, 37
- Absorption
 - coefficient, 15, 37, 65, 96
 - index, 110
 - length, 16, 65
 - of dyes, 18
 - plasma, *see* Plasma
- Adding–doubling, 35, 87
- ALA, 54–56, 210
- Albedo, 25, 28, 32, 36
- Alexandrite laser, 3
- Amalgam, 182, 198–199
- Amido black, 18
- Amplifier
 - regenerative, 265–268
- Anastomosis, 220
- Angiography, 226
- Anisotropy
 - coefficient, 23, 37
- ANSI classification, *see* Laser
- Aorta, 16, 42
- ArF laser, 3, 65, 92, 98, 100–102
- Argon ion laser, 3, 57, 65, 92
- Arrhenius' constant, 79
- Arrhenius' equation, 77, 79
- Arteriosclerosis, 221
- Arthroscopy, 236
- Astigmatism, 166, 172
- Atherectomy, 222
- Atherosclerosis, 221
- Attenuation
 - coefficient, 25, 27, 32, 37
- Autocorrelation, 265
- Avalanche, *see* Electron
- Backscattering, 15
- Balloon dilatation, 221
- Bandwidth, 4–5, 58
- BBO, 93, 122
- Beer's law, 15
- Benign prostatic hyperplasia (BPH), 211–212
- Biostimulation, 57–58, 230
- Bismarck brown, 18
- Bladder, 42, 207–208, 210
- Blood, 42
 - coagulation, 81
 - perfusion, 69, 83
- Bone, 42, 232–234, 242–246
 - ablation, 233, 246
- Bowman's membrane, 165–166
- Brain, 42, 49, 69, 81, 213–220
 - ablation, 214–217
 - gray matter, 213
 - white matter, 213
- Brainstem, 213
- Breakdown, *see* Optical breakdown
- Breast, 42
- Bremsstrahlung, 107
 - inverse, 107
- Brewster angle, 12
- Brewster plate, 265
- Brilliant black, 18
- Brillouin scattering, *see* Scattering
- Bypass surgery, 222
- Cancer, 49, 102, 197, 201, 203, 240, 247
- Capsulotomy, 126
- Carbonization, 41, 58–59, 62, 77–78, 80–81
- Caries, 182–183
 - diagnosis, 121–123
 - therapy, 185–192
- Carotenoid protection, 48–49, 54
- Cartilage, 234, 236
- Catalyst, 48

- Cataract, 159–161, 250–251
- Catheter, 81–82
- Cavitation, 126–131, 143–147
- Cell
 - critical temperature, 78
 - immobility, 77–78
 - necrosis, *see* Necrosis
 - nucleus, 102
 - oxidation, 47–49
 - proliferation, 58, 102, 224
- Cerebellum, 213
- Cerebrovascular occlusive disease, 220
- Cerebrum, 213
- Cervical intraepithelial neoplasia (CIN), 201, 203–205
- Cervix, 201, 203–205
- Chorioidea, 152, 154
- Chromophore, 16, 47, 100
- Clearance, 49
- CO₂ laser, 3, 65, 80, 92
- Coagulation, 18, 41, 58–60, 77–82, 154, 202, 214
- Collagen, 16, 57, 126
 - denaturation, *see* Denaturation
- Collision
 - inelastic, 64, 108, 112–117
- Colon, 237
- Color
 - body, 15
 - surface, 15
- Computer simulation, 33, 83
- Condylomata acuminata, 208
- Confocal microscopy, 152, 196, 234
- Conization, 205
- Cornea, 108, 119, 129, 134, 152, 164–180
 - ablation, 60, 88, 94–95, 97, 117–118, 128, 168
 - absorption, 16
 - hazard, 250–251
 - refractive surgery, 89, 166–180
- Coulomb field, 105
- Counterjet, 147–149
- Cr:LiSAF laser, 5
- Craniotomy, 220
- Cryotherapy, 205, 211, 228, 239, 247
- Cutis, 227
- Cytotoxicity, 100–102

- Damage
 - degree, 79
 - irreversible, 78–80, 102
 - mechanical, 133, 141, 147–149
 - reversible, 80
 - thermal, 72–80, 82
- Decay
 - fluorescence, 52–55
 - non-radiative, 48, 64
 - radiative, 48
 - thermal, 64
 - tooth, *see* Caries
- Decomposition
 - energy diagram, 91
 - photoablative, 59, 88–99
 - thermal, 59, 72, 77–78, 98–99
- Dehydration, 43
- Denaturation, 77–78, 81
- Dental alloy, 200
- Dentin, 181–182, 192
- Depth
 - ablation, 88, 93, 96–97
 - optical, 26, 28
- Dermis, 227
- Descemet's membrane, 165–166
- DHE, 56
- Diabetic retinopathy, 156, 158
- Diagnosis
 - of caries, *see* Caries
 - of tumor, *see* Tumor
- Diathermy, 205
- Dielectric breakdown, 105
- Diencephalon, 213
- Diffusion
 - approximation, 31–32, 35, 87
 - electron, 108, 113–117
 - heat, *see* Heat
 - length, 32
- Diode laser, 3, 57, 65, 80–81, 92, 265
- Dispersion, 19, 109, 268
- Dissociation energy, 92
- DNA, 100, 102
- Doppler angiography, 226
- Doppler effect, 22
- Dumping, 267
- Dye laser, 3–4, 18, 47, 139
- Dye penetration test, 185–187

- Ear, 246
- Edema, 56
- Electrocoagulation, 247
- Electron
 - avalanche, 107, 113
 - diffusion, *see* Diffusion
- Electrophoresis, 18, 164
- Enamel, 181–182, 192
- Endodontics, 198

- Endometriosis, 206
 Endoscope, 226
 Enzyme activity, 77–78
 Eosin, 59
 Epidermis, 227
 Epiphysis, 213
 Er:YAG laser, 3, 65–66, 74, 92
 Er:YLF laser, 66
 Er:YSGG laser, 3, 66, 74
 Erythrosine, 18
 Esophagus, 237
 Excimer laser, 88, 92, 98–102
 Exposure limit
 – eye, 257
 – skin, 257
 Eye, 152
 – protection, 13, 261
- Fiber
 – bare, 81
 – frosted, 81–82
 Fibroblast, 57, 182
 Finite differences, 74, 83
 Finite elements, 177–179
 Fluorescence, 48–49, 52–55, 93, 102
 Flux theory, 29–31
 Fovea, 153
 Franck–Condon principle, 91
 Free electron laser, 3, 74
 Frequency-doubling, 93, 122, 265
 Fresnel’s laws, 9, 12
- Gallbladder, 42, 237
 Gaussian beam, 67, 262
 Gingiva, 181–182
 Glaucoma, 152, 161–163
 Glottis, 241
 Greens’ function, 71
- Half-wave plate, 267
 Hardness test, 187–191
 Heat
 – capacity, 68
 – conduction, 68–75
 – – equation, 70–71, 74, 83
 – conductivity, 69
 – convection, 68
 – diffusion, 70–75
 – effects, 77–80
 – generation, 68, 75
 – radiation, 68
 – source, 68–70
 – transport, 68–75
 Helium–cadmium laser, 57
 Helium–neon laser, 3, 57, 65, 92, 139
 Hematoporphyrin, *see* HpD
 Hematoxylin, 59
 Hemoglobin, 16, 64
 Hemorrhage, 81, 158, 162, 214, 221, 232
 HF* laser, 234
 Hg lamp, 100–102
 High-frequency rotational coronary
 angioplasty (HFRCA), 222
 High-speed photography, 143, 147–148
 Histology, 59, 157, 191
 Ho:YAG laser, 3, 65–66, 92
 Hot tip, 222–223
 HpD, 49–56
 – absorption, 52–53
 – concentration, 52, 54–55
 – consistency, 50–52
 – energy diagram, 53
 – fluorescence, 52–55
 Hydroxyapatite, 59, 122, 182, 232
 Hyperopia, 166, 169, 172, 174
 Hyperthermia, 77–80
 Hypophysis, 213
 Hypothalamus, 213
- Ileum, 237
 India ink, 18
 Integrating sphere, 37–38
 – double, 39
 Intersystem crossing, 48, 53
 Intestine, 237
 Intrastromal ablation, 176–179
 Inverse Bremsstrahlung, *see*
 Bremsstrahlung
 Ionization, 46, 105–107, 113, 128
 Ionization probability, 113–114, 119
 Iridotomy, 161–162
 Iris, 152, 161–162
- Jejunum, 237
 Jet formation, 129–131, 147–149
- Keratin, 227
 Keratoconus, 166
 Keratomileusis, 169–176
 Kidney, 69, 207
 KrF laser, 3, 65, 92, 99–100, 102
 Krypton ion laser, 3, 18
 Kubelka–Munk
 – coefficients, 29, 40
 – theory, 29–31, 35, 40–41, 87
- Lambert’s law, 15, 29, 32, 64, 96
 Lambert–Beer law, 16

- Larynx, 241
- Laser
- bandwidth, *see* Bandwidth
 - chopped pulse, 201–202
 - classification scheme, 7, 253–258
 - continuous wave (CW), 3, 58, 99, 201–202, 253, 265
 - maintenance, 265
 - mode locking, 4–5, 74, 106, 134, 265–267
 - Q-switch, 5, 106, 134, 265, 269
 - superpulse, 201–202
- Laser-induced interstitial thermo-therapy (LITT), 77, 81–87, 206, 211–212
- Laser-welding, 200
- LASIK, 179–180
- Lens, 108, 117, 119, 152, 159–161
- Lens fragmentation, 161
- Leukoplakia, 197
- Lithotripsy, 126, 210–211
- LITT, *see* Laser-induced interstitial thermo-therapy
- Liver, 42, 81, 83–85, 237
- Lung, 42, 247
- Macula, 152–153
- degeneration, 155, 158
- Magnetic resonance, 82, 218
- Maxwell's equations, 27, 108–109
- Medium
- opaque, 15
 - transparent, 15
 - turbid, 25, 28, 33, 43
- Medulla oblongata, 213
- Melanin, 16, 64, 227
- Melting, 58–59, 63, 77–78, 80
- Membrane permeability, 77–78
- Meniscectomy, 236
- Meniscus, 236
- Mesencephalon, 213
- Methylene blue, 18, 51
- Minimally invasive surgery (MIS), 2, 81, 126, 151, 220, 242
- Mode locking, *see* Laser
- Monomer, 89–90
- Monte Carlo simulation, 33–35, 87
- condensed, 35
- MPE value, 258, 260
- mTHPC, 54–56
- Müller matrix, 35
- Multi-photon
- absorption, 98
 - ionization, 106–107
- Muscle, 42, 69
- Mutagenesis, 100–102
- Myocardial infarction, 221
- Myocardium, 42
- Myopia, 166, 169, 172–174
- NaCl, 105, 117
- Naevus flammeus, 228–230
- Naphthalocyanin, *see* Phthalocyanin
- Nd:YAG laser, 3, 57, 65, 80–81, 92, 100, 260, 265, 269
- Nd:YLF laser, 3, 65, 92, 100, 265–269
- Necrosis, 2, 49–50, 54–56, 77–83, 102
- Neoplasia, 201
- Neovascularization, 158
- Nigrosine, 18
- OD value, 260–261
- Odontoblast, 182
- OPO, 74
- Optical breakdown, 4, 18, 103–121, 130–134
- Osteotomy, 232
- Ovarium, 201
- Oxygen
- singlet, 48–49, 54
 - triplet, 48–49
- Pain relief, 57, 183, 220, 238, 247
- Palliative treatment, 238–239
- Panretinal coagulation, 155–156, 158
- Papilla, 152–153
- Pathline portrait, 148–149
- PDT, *see* Photodynamic therapy
- Percutaneous transluminal coronary angioplasty (PTCA), 221–222
- Perfusion, *see* Blood
- Phase function, 23–28, 33, 37
- δ -Eddington, 23
 - Henyey–Greenstein, 23–25, 34, 37
 - Rayleigh–Gans, 23
 - Reynolds, 23
- Phase transition, 68, 77
- Phorbide, 54
- Phosphorescence, 48–49
- Photodecomposition, *see* Decomposition
- Photodynamic therapy (PDT), 49–56, 210–211, 240
- Photokeratitis, 251
- Photorefractive keratectomy (PRK), *see* Keratomileusis
- Photosensitizer, 47–56
- Photosynthesis, 47

- Photothermolysis, 230
 Phthalocyanin, 54
 Piezoelectric transducer, 140
 Pigment, 16–18, 64, 108
 Plaque
 – blood vessel, 221–224
 – tooth, 50, 182, 198
 Plasma
 – absorption, 97, 108–111, 134
 – analysis, 121–125
 – conductivity, 109
 – dielectric factor, 109
 – electron density, 105–108, 111–125, 131–134
 – frequency, 111–112
 – generation, 96–97, 103–111, 128–134
 – ionization, 105–108, 128
 – length, 133
 – lifetime, 115, 120
 – shielding, 97, 111, 132
 – spark, 103, 120, 121
 – spectrum, 121–125
 – temperature, 107, 121–125, 131
 – threshold, 96–97, 105, 112–121, 129
 PMMA, 89–90, 99
 Pockels effect, 5, 267
 Polarization, 11, 35, 58
 Polarized microscopy, 157, 191
 Polyimide, 89
 Polymer, 89–90
 Pons, 213
 Porphyrin, 49–56
 Port wine stain, *see* Naevus flammeus
 Posterior capsulotomy, 159–160
 Probe beam experiment, 139–141, 144–145
 Prostate, 42, 81, 207
 Protein, 16–18, 64, 102
 – denaturation, *see* Denaturation
 Pulp, 181–182, 195, 198
 Pulse
 – femtosecond, 4, 106, 121
 – microsecond, 4, 73–75
 – nanosecond, 73, 88, 106, 117, 126, 133, 139
 – picosecond, 4, 73, 105–106, 115–121, 126, 133, 139, 265–268
 Pupil, 161, 176
 PVDF, 140–142
 Pyrimidine, 100

 Q-switch, *see* Laser
 Quarter-wave plate, 267

 Radial keratectomy (RK), 166–169
 Radial keratotomy, 166
 Radiation
 – infrared (IR), 64, 98, 249–251
 – ionizing, 56, 249
 – non-ionizing, 249
 – ultraviolet (UV), 7, 64, 88–93, 98–102, 249–251
 – visible (VIS), 64, 98, 249–251
 Random walk, 33
 Rayleigh scattering, *see* Scattering
 Rayleigh's law, 19–21
 Reactive black, 18
 Recanalization, 223–224
 Rectum, 237
 Reflectance, 11–14, 39
 Reflection
 – angle, 10–12
 – diffuse, 10, 39, 258
 – specular, 10, 39, 258
 – total, 11
 Reflectivity, 11
 Refraction
 – index, 11, 14
 Refractive power, 165
 Regenerative amplifier, *see* Amplifier
 Repetition rate, 75
 Restenosis
 – arterial, 222, 224
 – gastrointestinal, 238
 – urethral, 208
 Retina, 74, 81, 132, 152–158
 – detachment, 155
 – hazard, 250–251
 – hole, 155
 Retinoblastoma, 155, 158
 Retinopathy, *see* Diabetic retinopathy
 Root canal, 181–182, 198
 Rotating disc mask, 174
 Ruby laser, 2–3, 57, 65

 Saha's equation, 124–125
 Salpingectomy, 206
 Salpingolysis, 206
 Salpingostomy, 206
 Salpinx, 206
 Scanning slit, 174
 Scattering
 – angle, 21, 23, 34
 – anisotropic, 23, 32
 – backward, 23
 – Brillouin, 22, 132
 – coefficient, 20, 27, 37

- elastic, 19, 22
- first-order, 29, 87
- forward, 23
- inelastic, 19, 22
- isotropic, 23, 32, 81
- Mie, 22–23
- phase function, *see* Phase function
- Rayleigh, 19–23, 65
- Schlemm’s canal, 161, 164
- Schrödinger function, 91
- Sclera, 18, 152, 163–164
- Sclerostomy, 18, 163–164
- Seeding, 267
- Shock wave, 126–143
- Similarity relation, 32
- Singlet state, 48, 53
- SiO₂, 117
- Sister chromatid, 100–102
- Skin, 42, 69, 227–230
 - absorption, 16
 - cancer, 250
 - edema, 56
 - erythema, 251
 - hazard, 250–251
 - photosensitization, 54
 - wound healing, 57
- Slit lamp, 154, 174–175
- Snell’s law, 11
- Soft laser, 230
- Speed
 - of light, 11, 109
 - of particle, 135
 - of shock wave, 135, 142–143
 - of sound, 135, 141
- Spike, 5
- Spinal cord, 220
- Stefan–Boltzmann law, 69
- Stenosis
 - arterial, 221, 224
 - gastrointestinal, 238–239
 - laryngeal, 241–242
 - urethral, 208
- Stereotactic neurosurgery, 218–220
- Sterilization, 197–198, 206, 214
- Stokes vector, 35
- Stomach, 237
- Streptococcus sanguis, 50
- Striae of Retzius, 59
- Subcutis, 227

- Tatrazine, 18
- Tattoo, 230–231
- Telegraph equation, 109

- Temperature
 - conductivity, 69
 - tissue, *see* Tissue
- Thalamus, 213
- Therapeutic window, 16, 29
- Thermal birefringence, 269
- Thermal penetration depth, 72
- Thermal relaxation time, 72
- Thermionic emission, 106–107
- Thermomechanical interaction, 59, 185
- Thrombosis, 221
- Thyroid gland, 69
- Ti:Sapphire laser, 3, 5
- Tissue
 - ablation, *see* Decomposition
 - cooling, 77
 - damage, *see* Damage
 - in vitro, 43
 - in vivo, 43
 - inhomogeneity, 10, 16, 43, 89, 93
 - measurement of properties, 37–43
 - necrosis, *see* Necrosis
 - optical properties, 64, 84
 - temperature, 77–79
 - thermal properties, 64
- Tooth, 119, 121–125, 141, 181–196
 - ablation, 61–63, 76, 103–104, 117–118, 192
 - pain relief, 57
- Trabeculoplasty, 162–163
- Trabeculum, 152, 162–163
- Transition probability, 125
- Transmittance, 10, 39
- Transmyocardial laser revascularization (TMLR), 226
- Transport equation, 27, 87
 - vector, 35
- Transurethral resection (TUR), 210–211
- Transurethral ultrasound-guided laser-induced prostatectomy (TULIP), 211
- Triplet state, 48, 53
- Tuba uterina, 201, 206
- Tubal pregnancy, 206
- Tumor
 - diagnosis, 54–55
 - necrosis, 2, 49–50, 54–56, 81–83
 - treatment, 49–52, 81–82, 158, 197, 208, 210, 213, 218, 238–241, 247
- Twin-twin transfusion syndrome, 206
- Type I reaction, 48–49
- Type II reaction, 48–49

- Ultrasound, 82, 226
- Units, 270–271
- Ureter, 207–209
- Urethra, 207–209
- Urethrotomy, 208
- Urinary calculi, 126, 210–211
- Urinary tract, 207
- Uterus, 42, 60, 62, 81, 201

- Vagina, 201, 203
- Vaginal intraepithelial neoplasia (VAIN), 201, 203
- Vaporization, 58–59, 61, 75, 77–78, 80, 156, 202
- Vascularization, 57, 81
- Vasospasm, 223
- Vein occlusion, 155, 158
- Vitreous body, 117, 119, 152, 158
- Vulva, 201, 203
- Vulvar intraepithelial neoplasia (VIN), 201, 203

- Water
 - absorption, 64–66
 - breakdown threshold, 117
 - cavitation, 145
 - content, 68
 - heat conductivity, 69
 - ionization probability, 119
 - plasma absorption, 112
 - reflection, 14
 - refraction, 14
 - shock wave, 135–143
 - thermal penetration depth, 72
 - vaporization heat, 75, 77
- Wound healing, 57–58, 230

- X-ray, 221, 226, 228, 249
- XeCl laser, 3, 65, 92, 99–102
- XeF laser, 3, 65, 92, 100
- Xenon lamp, 1, 5, 267

- Zirconium fluoride fiber, 236

About the Author



Prof. Dr. Markolf Niemz studied physics and bioengineering at the Universities of Frankfurt, Heidelberg, and the University of California at San Diego (UCSD). He received the Master of Science in bioengineering 1989 from UCSD, the Diplom in Physics 1989 from the University of Heidelberg, and the Ph.D. degree in physics 1992 from the University of Heidelberg. In 1996, he joined the Wellman Laboratories of Photomedicine at the Harvard Medical School in Boston. In 1999, he became head of the Optical Spectroscopy department at the Fraunhofer Institute for Physical Measurement Techniques in Freiburg. Since 2000, he has been a director of MABEL (Mannheim Biomedical Engineering Laboratories), a joint venture of the University of Heidelberg and the Mannheim University of Applied Sciences. His research is focused on physics and applications of laser–tissue interactions. For these studies, he was awarded the Karl–Freudenberg Prize by the Heidelberg Academy of Sciences.